Study of the Determinants of Enteric Neuropathy in Experimental Chagas Disease

Harry Langston

Thesis submitted in accordance with the requirements for the degree of
Doctor of Philosophy of the University of London

May 2024

Department of Infection Biology

Faculty of Infectious and Tropical Diseases

LONDON SCHOOL OF HYGIENE & TROPICAL MEDICINE

Primary supervisor: Dr. Michael Lewis
Secondary supervisor: Professor John M. Kelly

Funded by the Medical Research Council, UK and DNDi

Declaration

I, Harry Langston, confirm that the work presented in this thesis is my own. Where information has been derived from other sources, I confirm that this has been indicated in the thesis.

Signed 

Harry Langston, January 2024

Acknowledgments

I would like to express my utmost gratitude and thanks to Michael Lewis for his guidance and supervision throughout this PhD. He is a natural supervisor, and It's a privilege to have been his first PhD student. As I leave the world of parasitology behind (for now) I will closely follow his work in the field, whilst channelling everything I've learnt from him to inspire others one day, as he did for me. I would also like to thank Archie for her unwavering ability to offer help whenever it was needed, and for making me laugh during days I didn't think possible. A huge thanks to John Kelly for his invaluable advice and unique ability to provide feedback in a way that motivated, and for all his support before and during this PhD. A thank you to everyone else in the Kelly group for their help and guidance over the years.

A massive thank you to my incredible parents, without whom none of this would be possible. Their love, support, and genuine interest in what I'm doing has kept me motivated and focussed more than anything ever could. I can't thank them, or my brothers, enough.

I would also like to thank my wonderful partner Rosie for bearing the brunt of my stress throughout this PhD. She kept me afloat, and only with her help and understanding did this process feel doable. A thank you to all my friends who have remained despite the constant cancellation of plans during this write up. To Rhodri for the essential 7 coffee breaks a day, and to Luca and Jason ~~for the constant positive reinforcement.~~

Contents

1. Introduction

1.1 Overview

Chagas disease (CD) is a neglected tropical zoonotic disease caused by the protozoan parasite *Trypanosoma cruzi*. The parasite infects diverse mammalian species and affects 6-8 million people (1). Though CD cases are historically associated with poverty in Latin America, migration patterns have led to an emerging global public health concern, with ~122,000 cases in Europe (2) and ~240,000 cases in the USA (figure 1) (3). Intra and inter-continental migration has driven globalisation of the disease, with transmission by congenital and or blood/organ transfusion/transplant responsible for transmission outside of the insect vectors' distribution. Acute infection typically presents as a non-specific, self-limiting illness or is commonly asymptomatic. Left untreated, the successive latent or asymptomatic phase can persist for the entirety of the host's life, but 30-40% of cases ultimately result in organ dysfunction affecting the heart, digestive tract or both. CD results in ~13,000 deaths annually and 800,000 lost disability adjusted life years (DALYS) (4).

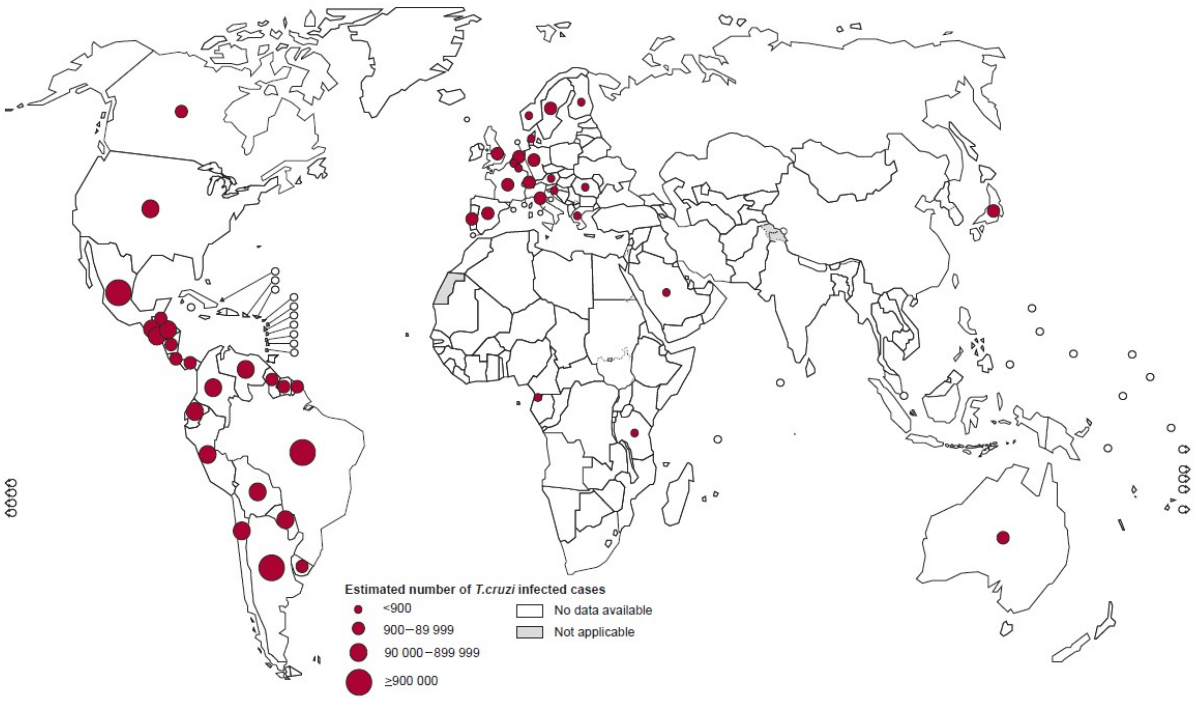

Figure 1: Global distribution of cases of Chagas disease.
Size of red dots correlates with the number of cases in particular regions. This graphic not only highlights the endemic nature of Chagas disease to Latin America, but the growing distribution across USA and Europe. W.H.O, 2018.

There is no vaccine and the viable chemotherapies, benznidazole and nifurtimox, only have a cure rate of 50-70% in the chronic phase of disease. Treatment is not generally advised once advanced cardiac symptoms are established, but is tentatively recommended for asymptomatic chronic patients, despite limited evidence for curative efficacy (5,6) However, there is good evidence supporting treatment in children, acute phase disease and congenital cases (5). These treatments are also synonymous with serious adverse side effects and poor clinical outcomes, which often results in treatment being ended early.

1.2 *T. cruzi* biology and life cycle

Trypanosoma cruzi is a kinetoplastid hemoflagellate protozoan (6). These hemoflaggelates obtain hematin from blood haemoglobin for aerobic respiration, and have diverse life cycle stages with varying positions, orientations, and origin of flagella (7). A kinetoplast is a specialised structure containing the mitochondrial DNA (kDNA) that apposes the nucleus and varies in size and arrangement among species (8). In *T. cruzi* parasites the entire kinetoplast appears as a concave disk with a diameter of 1μm and is 0.1μm thick. kDNA for trypanosomatid parasites is composed of maxicircles and minicircles, with a variation of number between species (8). Minicircles possess a conserved 100-200 base pair repetitive region, with four copies of conserved sequence found in *T. cruzi* (6). They encode the guide RNAs that mediate the RNA editing of cryptic mitochondrial genes transcribed by maxicircle DNA. Kinetoplasts possess highly specialised, adaptive pathways for lipid biosynthesis, which reflect the harsh life-cycle environments, each stage with its own unique requirements for lipid synthesis via type I or type II synthase (6). The genetic lineages in *T. cruzi* have long been recognised (9). The high molecular and phenotypic heterogeneity was first categorised into “zymodemes”, which has

subsequently resulted in the development of a wide variety of markers employed to categorise six distinct lineages, referred to as discrete typing units (DTUs) termed TcI through TcVI (10–14). These DTUs are associated with several epidemiological and pathological features of Chagas disease. TcII, TcV and TcVI are confined to domestic transmission cycles to the south of the Amazon basin, whereby there is an association with considerable human disease (15). TcIII is strongly associated with the nine-banded armadillo (*Dasypus novemcinctus*) in terrestrial transmission cycles throughout South America (15). TcIV is most commonly reported in primates, and seemingly uncommon amongst humans. Distribution is broadly limited to Amazonia and Northern South America. TcI is the most common lineage in sylvatic transmission cycles, infecting arboreal marsupials and triatomines across the American tropics and sub-tropics. TcI parasites are responsible for major human infection in North America, northern South America, with sporadic infections found throughout the southern cone (15). The primary route of transmission to humans is via the hematophagous Triatomine bugs (e.g. *Triatoma infestans*).

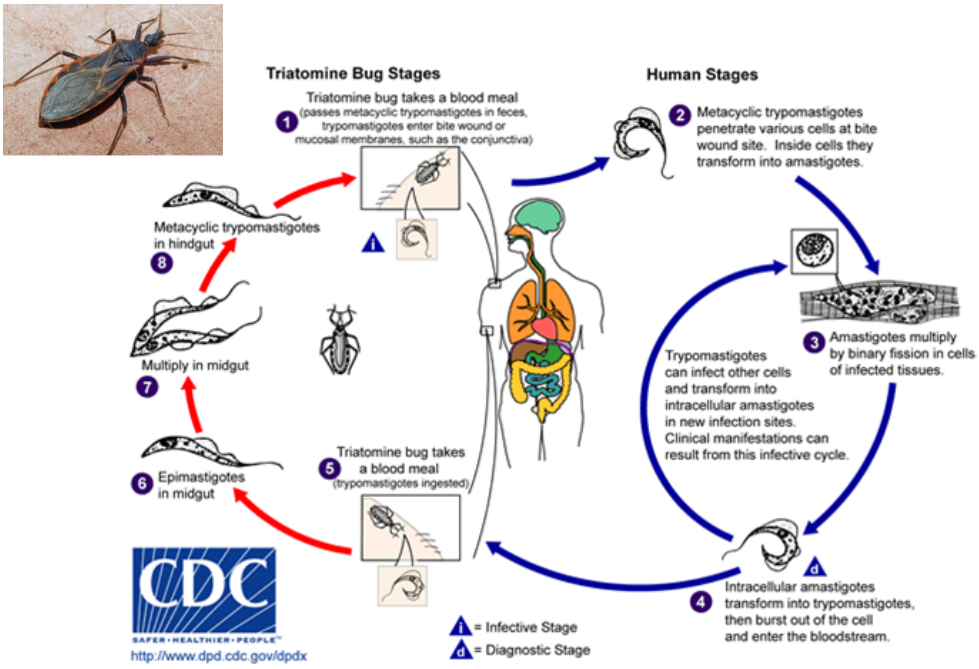

Figure 2. Life cycle of *T. cruzi* infection.

Red arrows depict progression through the Triatomine insect stages, occurring within the midgut of the vector. The blue arrows depict progression through the human/animal host., highlighting the infective metacyclic trypomastote stage, which rapidly becomes intracellular within host tissue. Differentiation from intracellular amastigotes back to blood-form trypomastigotes permits the life cycle to continue following a blood meal from the insect vector. CDC, 2021.

The hematophagous insects pass infective, non-replicating metacyclic trypomastigotes in their faeces onto the skin whilst taking a blood meal – the parasites gain entrance into the host when the area around the blood meal is agitated, resulting in a local inflammatory lesion referred to as a Chagoma. Direct entrance via the conjunctival surfaces can also present as characteristic, unilateral, periorbital swelling. *T. cruzi* utilises phagocytic and non-phagocytic pathways to invade most nucleated host cell types (16). Lysosome action at the cell surface permits trypomastigote entrance into the intracellular milieu and, via parasitophorous vacuoles, the parasite enters the cytosol (17). The intracellular parasites differentiate into amastigotes, which undergo multiple rounds of division via binary fission. The amastigotes differentiate to form a population of pleomorphic bloodstream-form trypomastigotes (BTs) which, once released from the host cell, utilise the haemolymphatic system and their flagellar motility to traffic and disseminate to local tissues to infect new cells, or they may be ingested by a second triatomine bug during a bloodmeal. Ingested parasites differentiate in the gut of the insect to the epimastigote form and these undergo multiple rounds of cellular division, followed by differentiation into infective, highly motile metacyclic trypomastigotes. It should also be noted that *T. cruzi* can also be transmitted between humans congenitally from mother to child, by blood transfusion or organ transplant. The oral transmission route, involving contaminated food and drink, was considered a rare mode of infection but, since 2000, has garnered increased attention due to a series of oral transmission outbreaks associated with fruit drinks contaminated with infected triatomine bugs (18).

There are key differences in the surface membrane protein composition and morphology of *T. cruzi* in different life cycle stages. 30% of identified proteins in the protein coat are expressed in all life cycle stages, with roughly 250 proteins expressed only at one stage of the life cycle (19). The most significant families of surface membrane proteins for host-parasite interactions are: mucins, trans-sialidase, TcGP63, amastin, TcTASV, mucin-associated surface proteins (MASP) and cruzipain (19). *T. cruzi* is covered in a dense and widely distributed layer of mucin-type molecules, constituting the majority of the surface glycoproteins [46]. Mucins are critical in parasite protection, infectivity, and modulation of the host immune response throughout the life cycle (20). Mucins are separated into two mucin gene families: TcMUC and TcSMUG. TcMUC I protein is distributed on the surface membrane of the amastigote form but is also found on the bloodstream trypomastigote forms (19). The trans-sialidase (TS) protein family is a superfamily comprised of ~1430 genes and pseudogenes (21). This family is classified into four groups: TS I, TS II, TS III and TS IV, based on sequence similarity and function. Trypomastigotes rely heavily on TS activity to transfer sialic acid from host glycoconjugates to alactoses of acceptor molecules located on its own surface since they are unable to synthesise it *de novo* (22). After initial invasion, the acquisition of a negatively charged sialic acid coat masks parasites allowing them to circumvent early innate effectors and lysis by serum factors. TS also permits facilitates adhesion to mammalian cells, ensuring parasite viability. Insect dwelling epimastigotes actively express TS-epi, a specific trans-sialidase found in the TS I group, which is not associated with other life-cycle forms. Members from TS group II include ASP-1 and ASP-2, which are amastigote specific surface proteins, and TSA-1 a trypomastigote specific surface antigen. These proteins aid in parasitic invasion

via host-cell attachment and invasion. TSA-1 also induces targeted CD8+ cytotoxic and polyclonal B-cell antibody responses in mice and humans (19).

The GP63 protein family are zinc dependant metalloproteases which serve as host-cell attachment ligands expressed on the surface of trypanosomatids (19). In *Trypanosoma brucei*, the causative agent for African sleeping sickness, GP63 proteins release variant surface glycoproteins from the cell surface during antigenic variation. *T. cruzi* express GP63-like genes (TcGP63), which are thought to be important at multiple life-cycle stages due to it being differentially regulated (23). TcGP63-I is present in all life-cycle stages, bound to the parasites membrane by a C-terminal glycosylphosphatidylinositol (GPI) anchor. There are two discernible isoforms of TcGP63-I found on different life-cycle forms; the glycosylated isoform is found in epimastigotes and amastigotes. The non-glycosylated isoform is present in the metacyclic trypomastigote form, where it is located intracellularly adjacent to the kinetoplast and flagellar pocket (24). Cruzipain (CZ), a cysteine proteinase, is expressed by all developmental forms of the parasite, but in trypomastigotes is only found in the flagellar pocket (25). CZ is responsible for proteolytic activity implicated in parasite virulence and morphogenesis, but also elicits a potent humoral immune response (26). CZ also confers protection against antibody targeting since CZ can digest the Fc region of IgG, inhibiting the binding to FcR (27).

1.3. Clinical aspects

Oral outbreaks have been associated with particularly high fatality rates (>20%) and severe symptoms (28). By contrast, the acute mortality rate in vectorial derived disease is lower, <5% of diagnosed cases, and most cases are not diagnosed (29). Typically, patients experience mild non-specific symptoms including fever, headaches, muscle pains and lymphadenopathy. Parasite entry into the eye can lead to an obvious monocytic infiltration and swelling, referred to as Romana's sign or a 'Chagoma' if the swelling has taken place at the insect bite site. In most patients, acute symptoms resolve within 4-8 weeks and they enter an asymptomatic phase which, in 60-70% of cases, spans the patient's lifetime. This phase is characterised by low blood parasitaemia, but infection can be confirmed by detection of antibodies in serum (29).

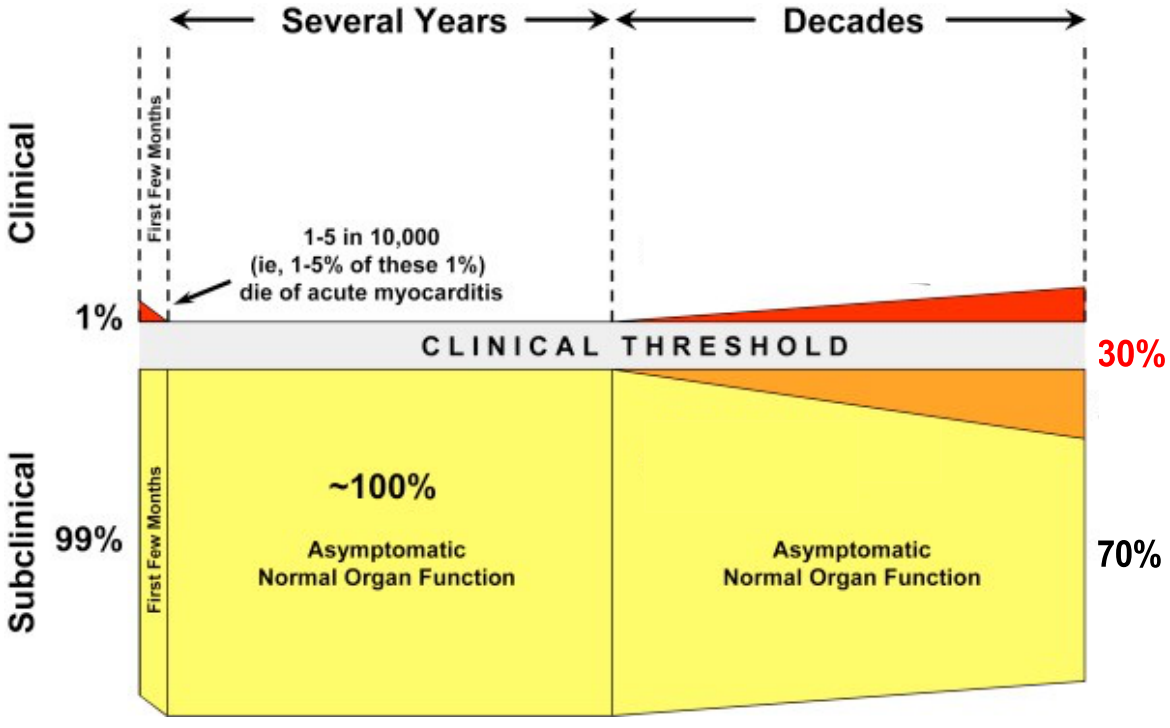

Figure 3. Graphic depicting typical clinical outcomes.
Majority of acute infections are subclinical with >1% of cases being fatal. As the disease transitions through to chronic phase, 70% of infection patients will remain asymptomatic for the duration of their lives. 30% will develop symptomatic organ dysfunction; either cardiomyopathy (fatal) or digestive dysfunction (high morbidity). Figure modified from original source; Bonney and Engman, 2015. (88)

As depicted in Figure 3, the transition from acute to latent phase disease is characterised by subclinical manifestations. Moving through the latent phase into chronic disease, ~70% of cases remain perpetually asymptomatic for the duration of a patient's life. In the remaining ~30% of cases, a range of cardiac sequelae develop at a rate of 2% a year (18) or digestive complications which develop in ~10% of cases, sometimes in combination with cardiac disease (29).

Chagasic cardiomyopathy is a result of conduction issues via autonomic neuronal destruction and dysfunction (30), and/or irreversible fibrosis due to the dysregulated chronic inflammation-wound healing axis (31). There are also microvascular abnormalities, and an increased risk of thrombosis, cardiac embolism and stroke. Digestive sequalae involve the hyperdilation of the oesophagus or large intestine, referred to as digestive 'megasyndromes', and are responsible for significant morbidity. Due to the limited treatment options for alleviating megasyndromes, surgical intervention is used to alleviate the burden of symptoms. This contributes indirectly to the mortality of digestive disease, for example, recent studies have described emergency hospital admissions and/or death of Chagas disease patients due to post-surgical complications (32).

The causative mechanisms underpinning these digestive disease manifestations are largely unknown and constitute a large the focus of this study. It is also not entirely clear why Chagas pathology only occurs focally in certain tissues, in a subset of infected people. This remains one of the longest-standing questions in the field.

1.4 Prevention, diagnosis, and treatment

Control strategies for Chagas disease are two pronged; prevention of vectorial transmission and prevention of new cases through blood transfusion and organ transplantation. The disease vector, triatomine spp, intrudes and resides in households synonymous with thatch roofs, adobe walls, open windows and doors (33). An important vector intervention strategy includes housing improvements, namely, concrete foundations, solid walls and ceilings and window screens which impede insect entry (33). Transmission by blood transfusion has been recognised since 1952 (34). The total number of transfusion cases is thought to roughly 800, with blood control programmes only becoming routine in the 1980's after the HIV pandemic. Screening programmes have been successful, with coverage progressively reaching 100% in many endemic regions over the last 30-40 years. In these regions the residual risk of infection through transfusion is estimated to be 1:200,000 units of blood (35). Due to migration out of endemic regions, and the asymptomatic nature of the disease, transfusion transmission has been described in USA, Spain and Canada. This correlates with the increased number of carriers in these countries with ~240,000 predicted in USA, and ~122,000 across Europe (36). Diagnosing Chagas disease early is critical for successful treatment, but conventional microscopy has limitations. Acute diagnosis is determined by identifying trypomastigotes in thin or thick blood films, which becomes less reliable as the disease progresses and the parasitaemia in the blood decreases. Laboratories use a combination of microscopy, PCR and serology to confirm diagnosis (37). When chronic infection is suspected, the Pan American Health Organization (PAHO) recommends the use of two serological tests, either ELISA or indirect fluorescent antibody tests, to detect antibodies against *T. cruzi* antigen (38).

PCR methods that target kinetoplast DNA (kDNA) and nuclear satellite DNA can detect low numbers of parasites in the blood of acute infections, congenital infections, and some late acute/early chronic stage patients (39,40).However, the range of PCR sensitivity is one parasite per 10ml of blood, so negative results are not conclusive for diagnosis when blood parasitaemia is below the sensitivity range of these assays. PCR is typically used for monitoring treatment efficacy in confirmed Chagas disease cases.

There are currently two chemotherapy treatments available in the clinic: Benznidazole (BZ) and nifurtimox (NFX). Both are nitroimidazole antimicrobial pro-drugs, reduced by a type I nitroreductase (NTR) in the parasite. With benznidazole, this results in the formation of a hydroxylamine derivative, followed by a series of intermediates, before a final dissociation yields glyoxal which is cytotoxic and mutagenic (41). Treatment with benznidazole has an efficacy of 76% in established acute disease (42), which decreases as the patient progresses through latent and chronic phase, with a success rate of 37%, which increases to 62% in children (42,43). Congenital cases have a 96% response rate (44).Treatment in the chronic stage is not generally considered with those experiencing gut complications alone, only when presenting in conjuncture with cardiac manifestations. Both drugs are synonymous with adverse side effects which results in patients being discontinued from treatment; BZ is considered to have a slightly better safety profile than NFX. One study showed only 60% of patients starting treatment complete the course, with 89% experiencing at least one adverse side effect (45). There is plenty of scope for treatment refinement, with the recent BENDITA study aiming to improve the benznidazole dosage regime to limit adverse side effects. The standard treatment regimen is 300 mg for 8 weeks.

In this study 82.8% of patients exhibited no detectible parasites 1 year after treatment. A similar proportion of patients were parasite negative after 1 year following 4 weeks (89.3%) and 2 weeks of treatment (79.3%). This study suggested that treatment was therefore just as effective when the treatment period was reduced by 75%. This also equated to treatment being well-tolerated with no patient dropouts and good safety profiles (46).

There have also been a myriad of prospective treatments coming through the pipeline, but high treatment failures associated with the promising posaconazole (80-90% in chronic treatment) and ravuconazole, which block ergosterol biosynthesis, showcase the obstacles in achieving sterile cure.

1.5 Immunology

T. cruzi mammalian forms display morphological, antigenic and spatial variability which all pose a challenge to the host immune system. *In vivo* and *in vitro* studies have demonstrated that *T. cruzi* can reside and replicate in the cytosol of almost any nucleated mammalian cell (47). Sites for which the parasite has a significant affinity include adipose tissue, cardiomyocytes, phagocytes, smooth muscle, and the skin. By contrast, immune-privileged sites and those characterised by a low blood supply are less affected. Acute pathology is facilitated by the direct lysis of infected cells perturbed by intracellular *T. cruzi* replication and indirectly by the host's inflammatory response (48). Both innate and adaptive immune responses are involved in controlling *T. cruzi* infection.

1.5.1 Innate response

Prior to the adaptive immune response and CD8+ T cell activation, the initial host response is characterised by delayed type I interferon signalling, recruitment and/or activation of neutrophils, macrophages and natural killer (NK) cells (49). This delay is in part due to *T. cruzi* escape from the phagolysosome, which reduces the mortality of the parasite, the release of danger associated molecular patterns (DAMPs), and ultimately avoids activation of many pattern recognition receptors (PRRs) e.g. TLR9 and TLR7. The replication rate of *T. cruzi* is also significantly slower than that of bacteria and viruses. This results in a delay until at least after the first lytic cycle of intracellular replication (4-10 days depending on the parasite strain), yielding ~250 trypomastigotes to establish a threshold necessary for the host to mount a robust response (50).

After host cell lysis, *T. cruzi* becomes a target of the complement pathway (51). The three pathways for complement mediated lysis; classical, alternative and lectin have different initial steps, but converge upon the production of C3 and C5 convertases, which results in the formation of the membrane attack complex (MAC) (51). MAC covalently attaches to target cells, forming pores in pathogen plasma cell membrane, leading to osmolysis (52). Trypomastigotes have a large set of effector mechanisms that provide resistance to complement-mediated lysis. Parasites hinder the lectin pathway via calreticulin, a surface molecule that binds to host mannan-binding lectins (MBLs), preventing the target interaction with parasite mannan (53). Calreticulin also interacts with L-ficolin which inhibits a critical conversion of C4 convertase to C4b, preventing the successful formation of the MAC. As the infection progresses and antibodies are formed, calreticulin also directly disrupts the classical

complement pathway by binding with C1 convertase, preventing its interaction with C4. *T. cruzi* derived calreticulin is able to directly disrupt two complement pathways, but due to the reduction of C3 convertase formation, calreticulin indirectly inhibits the alternative pathway. Trypomastigotes also utilise complement regulatory protein (CRP), a GPI-anchored surface protein that binds to C3b and C4b, disrupting both classical and alternative complement C3 convertase (54). Additionally, complement C2 receptor inhibition trispanning (CRIT), a transmembrane protein, binds and prevents the formation of C3 convertase via lectin and classical complement mediated pathways. Other proteins, including trypomastigote decay-accelerating factor (T-DAF) and gp58/68, form a comprehensive arsenal against complement mediated lysis via C3 convertase inhibition, a key step in all three pathways. By blocking the initial steps of complement pathways, there are additional downstream protective effects independent of the complement immune response. C3b is an opsonin, recognised by macrophages inducing phagocytosis. Upon inhibition of C3b formation, via the mechanisms outlined, *T. cruzi* is additionally protected from macrophage derived parasite lysis (51).

These interactions permit an immunologically silent early acute phase, which allows for a widely disseminated infection pattern with most nucleated cell types subject to invasion (55). Invasion of, or phagocytosis by, myeloid cells facilitates the release of IL-12 and IL-18, which activate natural killer cells (NK). Activated NK cells orchestrate the early acute stage immune response in several ways: i) NK derived cytokines, such as TNF-α, promote a Th1 biased T-cell response. ii) Secretion of IFN-γ activates macrophages, and iii) NK cells also contribute directly to parasite control by cytotoxic action against infected cells (56).

After the parasite's initial intracellular replication cycle, egress of trypomastigotes into the extracellular milieu permits it to invade other local tissue cells or incoming leukocytes, or to traffic to other tissues via the blood or lymphatic system. Rupture releases the supernatants of infected cells, including DAMPs, such as oxidised DNA in extracellular vesicles which are sensed by cyclic GMP-AMP synthase (cGAS) and urate crystals and silica, which activate nucleotide-binding oligomerization doman-like receptors (NLRs) (57,58). This stimulates a myriad of cross-talking signalling pathways, which revolve around a distinct set of transcription factors ultimately responsible for the production of pro-inflammatory cytokines (59,60). Pre-eminent amongst these are IL-12, IFNγ and TNF-α – the hallmarks of type 1 intracellular infection immunity. Upregulation of IL-12 by macrophages is critical for local recruitment of IFNγ+ NK cells, both of which are canonical factors for controlling parasite numbers and preventing acute mortality (61). Moreover, TNF-α plays a similarly pivotal role in tandem with IFNγ to activate trypanocidal effector mechanisms. The principle innate immune effectors for *T. cruzi* control are reactive oxygen and nitrogen species (ROS, RNS). Moreover, macrophage-derived inducible nitric oxide synthase (iNOS) activation and downstream production of the free-radical nitric oxide (NO) is directly parasiticidal *in vitro* through oxidative stress, disrupted energy metabolism, DNA damage, or dysregulation of cytosolic calcium (62) (Fig.4).

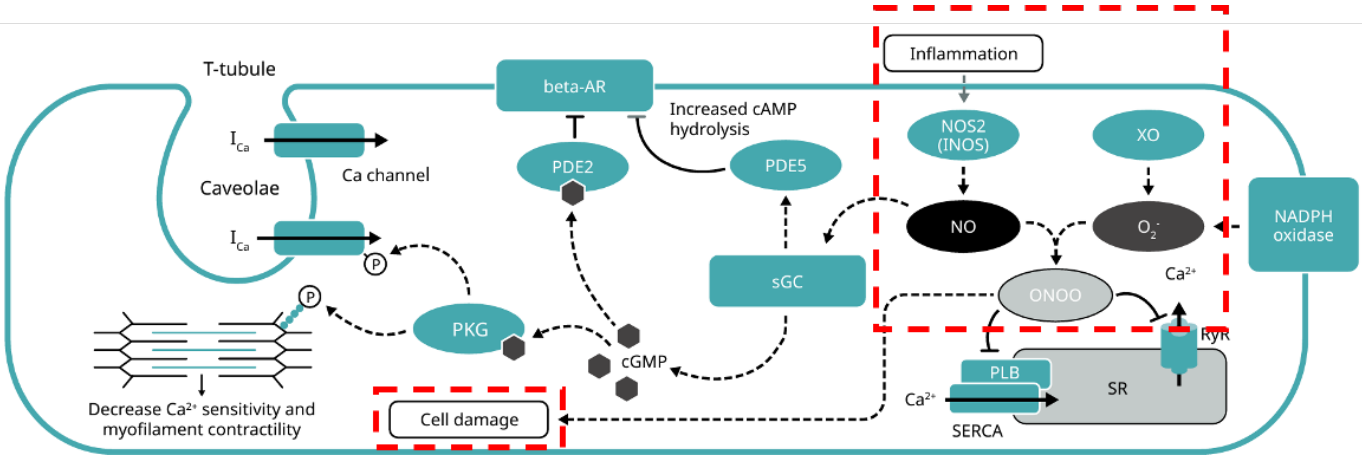

Figure 4. Cellular processes of iNOS mediated cell damage.
The red box highlights aspects of the pathway directly implicated in pathogen defence. All other pathways are of nitric oxide derived cellular homeostasis. Infectious challenge increases inflammation and iNOS expression. Nitric oxide (NO) is synthesised and is directly toxic, but upon reacting with superoxide to form peroxynitrite (ONOO) which greatly enchase the antimicrobial effect effectively causing DNA damage, DNA strand breakage and base modification. ONOO also inhibits phospholamban (PLB) from transporting calcium from the cytosol into the sarcoplasmic reticulum. Chronic blocking of this pump diminishes myofilament contraction, which is particularly critical in regulating cardiac muscle. The second pathway entails the NO derived activation of sGC, which releases cyclic guanosine monophosphate (cGMP). This acts on protein kinase G
(PKG) which results in decreased calcium sensitivity and myofilament contractility.

abcam, 2023.

It is not clear whether the innate responses meaningfully restrain parasite numbers *in vivo* or serve a more indirect role by activating the adaptive response. This is highlighted by infected SCID mice, with intact innate responses but no adaptive immunity, experiencing a widely disseminated disease, exponential parasite replication and inability to survive acute phase (63). *T. cruzi* possesses a well characterized anti-oxidant system, where synergistic enzymes (cytosolic peroxiredoxin, iron superoxide dismutase and glutathione peroxidase 1) are able to neutralize H_2O_2, $O_2^{\bullet-}$ and $ONOO^-$ (64). The high levels of iNOS expression ultimately required, are induced during acute infections and has spearheaded the leading theory that excessive levels of NO are responsible for host tissue damage, for example, nerve ganglion loss in the digestive tract (66,67).

Pro-inflammatory responses ultimately need to be regulated to prevent excessive collateral damage to the host. Although the mechanisms are poorly described, there is evidence that interleukin 10 (IL-10) and Transforming Growth Factor β (TGF- β)

are upregulated and act to dampen the type 1 inflammatory response, reducing the risk of mortality (65). Thus, as the infection progresses into the chronic phase, an equilibrium becomes established between the immune-mediated responses required to contain parasite numbers, and deactivating mechanisms that limit the collateral damage that may result from pro-inflammatory responses. Over time, this immune balance, or rather dysregulation of, probably dictates the severity of disease pathology and disease progression (48).

1.5.2 Adaptive response

B cells

The initial B cell response is polyclonal and not specific to parasite antigens, with parasite specific B cells peaking at day 18 post infection (66). There are ~$2x10^3$ named *T. cruzi* epitopes that prime the adaptive immune response, with each named epitope associated with a specific antibody interaction in both human and animal infection models (67). Certain targets are surface proteins implicated in complement evasion, including gp190, T-DAF, and GPI anchored mucin like glycoproteins, which are targeted by so called “lytic” antibodies (67). Other parasite epitopes that are recognised by antibodies include, but not limited to, mucin associated surface proteins, trans-sialidases, amastigote surface proteins, paraflagellar rod protein, kinetoplast membrane protein 11 and heat shock protein hsp70 (68). This prefaces a mitogenic sensory cascade, which results in T-cell independent B-cell activation and hypergammaglobulinemia. Splenic extrafollicular and germinal centre responses extended from the red pulp are evident as early as 3 days post infection in mice (66). IgM and IgG anti-galactose antibodies are useful for discriminating between early, mid or late-stage Chagas disease due to the changing ratios of the two types of

antibodies as the disease progresses. In early infection there is an IgM bias, and in chronic there is an IgG bias (69). Disappearance of lytic antibodies are identifiers of parasitological cure since they're only present during an active infection or shortly after treatment. Follow up observations of cleared antibody can be assessed years after treatment.

B cells have two important roles in *T. cruzi* infection. First is the production of antibody, and second is the conditioning of T-cell responses. Mouse models lacking mature B cells (μMT mice) exhibit an increase in pro-inflammatory responses, characterised by TNF-α producing CD4+ T cells, and a reduction in levels of the regulatory cytokine IL-10, whilst exhibiting an increased parasitaemia and 100% mortality (70). B-cell responses are as essential as direct effectors against *T. cruzi* as they are mediators of T-cell responses. μMT mice have diminished populations of memory T-cell subsets and T_HI, T_H17, and T_{reg} populations (70), which suggests a significant role for B-cells in the establishment of parasite-specific memory T-cell populations which are themselves critical for parasite control.

CD4+ T cells

CD4+ T cells (T helper cells) primarily modulate the activity of other immune cells. They are characterised by the secretion of cytokines such as IFN-γ , TGF-β and IL-10 which modulate cytotoxic responses and control inflammation (67). In response to *T. cruzi*, increased expression of the chemokine receptor CXCR5 directs CD4+ T cell migration toward B-cells in lymphoid organs, where the local interaction with B-cells facilitates differentiation into follicular helper T cells. The majority of CD4+ T cells differentiate into T-helper cells that migrate and extravasate into inflamed tissue. The secretion of CD40L stimulates dendritic cell maturation and promotes the

recruitment of CD8+ cytotoxic responses. However, the significance of CD4+ cells in inducing critical pathways, such as cytotoxic responses, is uncertain. In a study utilising class II MHC knock-out mice (which cannot present antigen to CD4+ T cells), it was shown that although CD4+ T-cells may facilitate development of CD8+ T-cell responses against *T. cruzi* epitopes, the CD4+ cell type is dispensable for control of the infection. CD8+ T-cell populations expand in response to *T. cruzi* challenge in CD4- T-cell deficient mice (71), with the regulatory IL-21, IL-2, IL-17 and pro-inflammatory cytokine IFN-γ compensated by natural killer cells and γδ-T cells (72). However, using human case studies from *T. cruzi:* HIV/AIDS co-infection does suggest that long term absence of CD4+ T cells has important consequences. As the CD4+ T-cell population plummets, *T. cruzi* infection recrudesces with atypical disease presentations such as lesions in the central nervous system, meningoencephalitis, and skin plaques (73). This highlights the need for caution in interpreting results from experimental animal studies as they may not always capture the situation in infected humans.

CD8+ T cells

CD8+ T cells are a critical agent for controlling *T. cruzi* infection, showcased, for example, by CD8 blocking studies whereby the parasite burden increases, myocarditis is exacerbated and the outcome is 100% fatal (74). Initial activation of the anti-parasite CD8+ T-cell response in lymphoid tissues is initiated by antigen recognition by naïve T-cells via receptor class I MHC molecules on the surface of *T. cruzi*-antigen bearing dendritic cells. The primed CD8+ T-cell populations undergo clonal expansion and traffic to infected tissue sites where they can identify and destroy infected target cells after recognition of cognate peptide:MHC-I on the surface. This is achieved via

cytotoxic perforin/granzyme-mediated and Fas-FasL-mediated apoptosis pathways. Perforin is a pore forming protein that permits the internalisation of granzyme B, triggering caspase activation and cytochrome C leakage into the cytosol via BH3-interacting domain death agonist (Bid) and BCL-2 (apoptotic regulator) interaction (75). The release of cytochrome c interacts with, and matures, caspase 9 via binding to apoptotic protease activating factor (Apaf-1). As the apoptosome forms, caspase-3 is activated which cleaves inhibitors of caspase-activated DNase allowing the fragmentation of DNA and ultimately apoptosis (75). It has been noted that CD8+ cytotoxic mechanisms also have a direct trypanocidal effect on both intracellular and circulating parasites (76). Granulysin is not required for destruction of infected cells but facilitates granzyme penetration of amastigotes. The same process is true of extracellular trypomastigotes, which can be directly destroyed by granzyme B activity in a granulysin-dependant process (67).

In cardiac infiltration, T-cell recruitment is driven by the establishment of chemokine gradients, especially of the CXCR3 ligands, CXCL9 and CXCL10 (77). A low frequency of *T. cruzi* specific CD8+ T-cells is observed in Chagas disease patients with severe cardiomyopathy compared to asymptomatic and mild cardiac patients (78), which highlights the significance of CD8+ T-cells in the prevention and progression of cardiac disease. IFN-γ and TNF-α secretion is critical for the protective function of antigen-specific CD8+ T-cells, by perpetuating iNOS expression from recruited innate effectors such as monocytes, macrophages, or somatic cells in infected tissue (79,80). There is not a straightforward antagonistic link between these cytokines and effectors, since IFN-γ knock out mice exhibit a

severe onset of disease resembling CD4/CD8$^{(-/-)}$. Comparatively, iNOS knock out mice exhibit an initial milder phenotype, but is still 100% fatal after 3 weeks (67).

Overall, the generation of *T. cruzi* specific CD8+ T-cells effectively reduces parasitic burden by >99% compared to the acute peak via the mechanisms outlined above. This effectively limits parasite persistence to niched, focal populations in immunologically permissive sites where parasites can persist through the chronic stage (81,82).

The chronic persistence discovery has suggested theories of an ongoing interaction between host and parasite and, due to the chronicity of infection, a potential contributory role for CD8+ T-cells in tissue damage, including damage to enteric neurons, alongside innate effectors (e.g. iNOS). This is despite there being an incomplete recruitment of CD8+ T cells to parasitic nests in the chronic stage (83). The hyperfocal sites of parasitic persistence, and the inability to routinely find parasites in damaged tissue sites in humans and animal models, was historically taken by some to suggest that tissue damage could be primarily auto-immune -- a hypothesis independent from pathology induced directly by parasitic invasion or immunopathology from parasite-specific response-driven collateral damage. The 'auto-immune' hypothesis is controversial, and despite being reviewed several times in the past few decades (84,85), it has only been discussed in the context of cardiac disease. Self-reactive antibodies and T cells have long been identified in Chagas disease patients and were thought to be evidence of molecular mimicry and immune evasion (86). A direct link between adaptive immune responses as direct drivers of tissue pathology has yet to be established. However, after treatment with benznidazole, parasites are eliminated and both cardiac pathology and humoral mediated autoimmunity is resolved (87,88).

Reinfection and recrudescence of *T. cruzi* infection re-established both myocarditis and autoimmunity. This strongly suggests that the pathology associated with the auto-reactive phenomena is transient and infection-dependent, not a result of a permanent compromise in self-tolerance. This supports the principle that sterile cure of *T. cruzi* infection for example, using anti-parasitic chemotherapy, has the potential to prevent or alleviate clinical symptoms, without risking persistent autoimmune-mediated pathology.

1.6 The enteric nervous system (ENS)

The intestines are home to two neuronal plexuses and four distinct layers (Fig.5). The ENS consists of a highly complex and diverse network of neurons and glial cells, which regulate the autonomic functions of the GI tract (89). The neuronal constituents of the ENS are predominantly arranged into the myenteric nerve plexus and submucosal nerve plexus which span the length of the GI tract, adjacent to the circular and longitudinal smooth muscle layers, in which *T. cruzi* parasites are frequently observed (90).

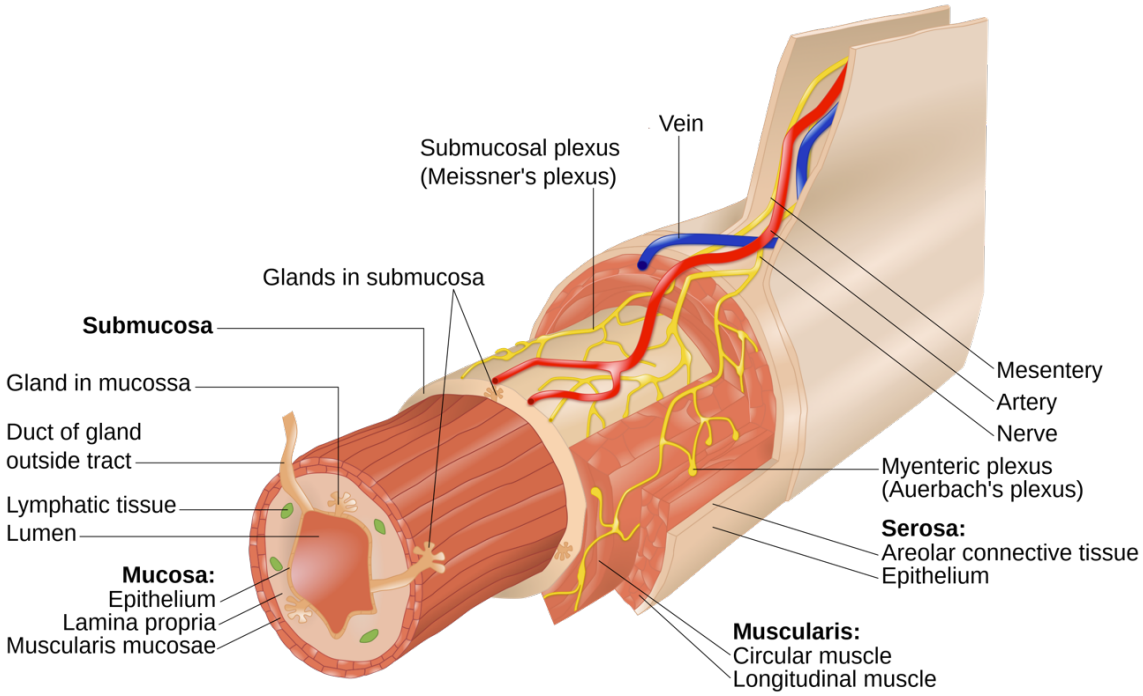

Figure 5. Schematic of the large intestine.
The four layers of the large intestine from the lumen outward are the mucosa, submucosa, muscular layer, and serosa. The muscular layer is made up of two layers of smooth muscle, the inner, circular layer, and the outer, longitudinal layer. The myenteric plexus is situated between the muscle layers, and the submucosal plexus between the circular muscle and the sub-mucosal layer. Key blood vessels consist of superior and inferior mesenteric veins and arteries. Extrinsic nerves connect the enteric nervous system to the central nervous system, also via the mesentery.
Adapted from Wikipedia, 2023.

The ENS is primarily responsible for peristaltic motor, secretory, and immunological cross-talk functions (91). Secondary, more complex behaviours include non-propulsive mixing or segmentation, slow orthograde propulsion via migrating myoelectric complex (MMC), and redistribution of local blood flow (92). The ENS is the largest and most complex unit of the peripheral nervous system and, given its development stems from the neural crest, the ENS has many unique organisational features, as well as features that resemble the central nervous system (CNS) (93).

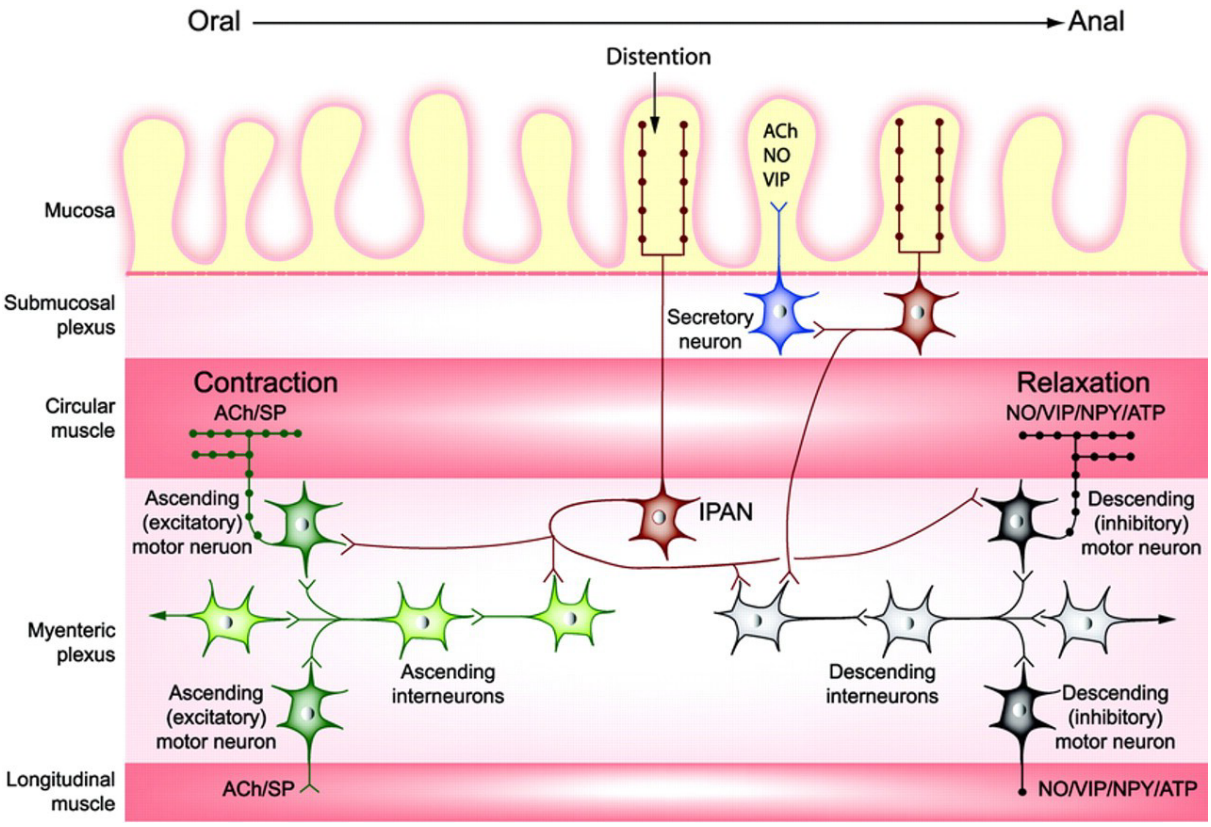

Figure 6. Schematic depicting key components of the enteric nervous system.
In green are excitatory neurons (dark green=motor neurons, light green=interneurons). Excitatory neurons are responsible for contraction of circular and longitudinal muscle via neurotransmitters acetylcholine (Ach) and substance p (SP). Inhibitory neurons (black= motor neurons, white=interneurons) are responsible for the relaxation of the muscle layers via neurotransmitters nitric oxide (NO), vasoactive intestinal peptide (VIP), neuropeptide Y (NPY), ATP. Intrinsic primary afferent neurons (IPAN) are sensory, that detect physiological changes in the luminal environment and communicate between excitatory and inhibitory neurons. Interstitial cells of Cajal are not shown. Extrinsic neurons, connecting ENS circuits to the CNS are not shown.

The primary components of the ENS are summarised above (Fig. 6). The intercommunication between excitatory and inhibitory neurons, orchestrated by the sensory action of intrinsic primary afferent neurons (IPAN), is responsible for peristaltic homeostasis. Functionality is maintained by secretion of the neurotransmitters acetylcholine (ACh) and substance P (SP), which act to contract the circular and longitudinal muscles, and nitric oxide (NO) / vasoactive intestinal peptide (VIP) / neuropeptide Y (NPY) / adenosine triphosphate (ATP) that act to relax the muscles. Not shown are the interstitial cells of Cajal (ICC), which are distributed in the tunica muscularis and serve primarily as electrical pacemakers and

mediators of enteric neurotransmission (94). There are sub-populations of ICC based on regional location; ICC-CM are circular muscle populations, LM are found in the longitudinal muscle, IM are intramuscular, DMP reside in the deep muscular plexus, and SMP reside in the sub-mucosal plexus. ICCs are particularly concentrated in regions innervated by descending inhibitory neurons (95), and have been shown to be receptive to enteric neurotransmitters including the inhibitory NO and SP. The direct antagonism between ICCs and NO has been supported in studies whereby a loss of ICCs results in a loss of NO dependant neurotransmission and effect (94).

The ENS lacks much of the collagen derived connective tissue between neurons, which are non-myelinated, in contrast to most other peripheral and central nervous system (PNS, CNS) neurons. The primary support cell type of the ENS, enteric glial cells, resemble the astroglia of the CNS. Enteric glia fulfil physical and chemical homeostatic functions in the ENS including; upholding maintenance and integrity of the intestinal epithelial barrier, and have been shown to play a role in the regulation of intestinal inflammation (96,97). Enteric glia are characteristically irregular in shape and morphology compared to Schwann cells, another type of glial cell in the CNS. Schwann cells organise and wrap around axons to ‘insulate’ most neurons of the PNS to facilitate efficient, long-distance propagation of nerve impulses. In contrast, in the ENS, the glial cells radiate outward and terminate into small nodes called “end feet”, forming an incomplete glial sheath which separates the enteric nerves from surrounding connective tissue (98). Enteric glia also interact with myriad non-neuronal cell types such as enterocytes, enteroendocrine and immune cells which highlights the heterogeneity of functions within the ENS compartment and its

integration with other organ systems. It is emerging that enteric glia are involved in several pathological disorders (97). Deposits of alpha-synuclein and misfolded proteins are found in enteric neurons and glia, a hallmark of Parkinson's disease and Creutzfeldt-Jakob disease (99).

1.7 Digestive Chagas disease (DCD)

Gastrointestinal dysfunction develops in 10-15% of chronically infected people (48). The definitive clinical manifestation is the occurrence of megaviscera which is characterised by the dilation of one or more regions of the GI tract, usually the oesophagus and/or large intestine. In rare cases, the stomach and small intestine may be affected. Megaoesophagus and megacolon can occur independently of each other, concurrently and/or in conjunction with heart pathology (48).

Megaoesophagus is synonymous with dysphagia, odynophagia, epigastric pain and, in severe cases, malnutrition. Oesophageal achalasia has also been documented, which occurs when the smooth muscle fibres lining the lower oesophageal sphincter contract and are unable to relax (100). In humans, megacolon typically affects the descending colon, sigmoid section, or rectum – or a combination. It is synonymous with constipation and, in severe cases, obstipation, abdominal distension, faecaloma and or sigmoid volvulus (48). Anti-parasitic chemotherapy is not considered as justified for those suffering from GI related symptoms whilst exhibiting normal cardiac function. This is primarily due to a lack of experimental and clinical trial data to suggest treatment would be effective at reversing GI related pathology (101). It is also unknown whether early treatment of asymptomatic individuals would delay or prevent the development of digestive disease symptoms.

Despite chronic GI disease being associated with high morbidity and prevalence, there is far less experimental data on DCD compared to cardiac CD. The neglected nature of DCD is exemplified by the generalised view that mega-syndromes are a result of irremediable denervation of the enteric nervous system (ENS), specifically during the acute phase (102) where trypanocidal inflammatory responses cause collateral damage to neurons, resulting in irreversible agangliosis. Our leading theory for DCD immunopathogenesis is attributed to the denervation of the ENS via IFN-γ- and iNOS-dependent NO production to neurotoxic levels (103) . This is based on a 2004 study, by Arantes et al. The study utilised IFN-γ knock out mice (IFN-$\gamma^{-/-}$) and it was noted there was no evidence of inflammatory infiltration in the intestinal foci or change to neuronal integrity (confirmed by immunoreactivity of PGP 9.5, a general nerve maker) in the myenteric plexus, compared to infected wild type (WT) mice. However, infected $iNOS^{-/-}$ mice experienced higher parasite loads and similar inflammatory infiltrate to WT infected mice, but without any denervation. Between days 5-10 post infection, iNOS activity increased in the WT infected models and was associated with enteric denervation, but both iNOS expression and enteric integrity remained unchanged in both knockouts. Thus, ENS integrity remains intact in the absence of iNOS-derived NO (103). Furthermore, by observing no denervation in infected $iNOS^{-/-}$ mice, despite very high parasite loads, suggests that the denervation is NO specific, and not a result of either a) direct parasitism of neurons, b) a parasite-derived neurotoxin, or c) other inflammatory effectors stemming from other IFN-γ mediated cascades, such as ROS. Other studies found high expression of NO in muscle tissue correlating with local nerve cell degeneration and, more specifically to the cellular localisation to the colon muscle layers, an increased expression of

nicotine adenine dinucleotide phosphate-di-aphorase (NADPH-diaphorase), a type of nitric oxide synthase (104). This echoes neurodegenerative disorders such as Multiple Sclerosis and Alzheimer's disease, where iNOS and high production of NO is directly implicated in denervation synonymous with poor clinical outcomes (105). Moreover, in ulcerative colitis and Crohn's disease patients where NO has been found at concentrations 8-fold higher than normal in the superficial mucosal layers and lumen (106). Additionally, similar clinical outcomes associated with aganglioisis in Hirschsprung disease such as intestinal pseudo-obstruction, colitis and chronic constipation (107) could help formulate hypotheses for general mechanisms and pathways underpinning ENS immunopathology.

Currently there are contrasting denervation hypotheses, particularly with respect to the kinetics of pathology development. Where the contribution of iNOS and NO mediated neuronal death is thought to occur exclusively in the acute phase, the alternative focusses on the importance of chronic parasite persistence and ongoing host-parasite interactions. The latter idea is circumstantially supported by the detection of parasite DNA from the GI tracts of chronic patients and reduced numbers of enteric neurons, glial "support" cells, and "pacemaker" interstitial cells of Cajal (108,109).

Little progress into underlying immunopathogenic mechanisms of DCD has been made, partly because of a lack of a robust animal model of chronic disease. In the pursuit of an animal model studies have been conducted on mouse, rat, rabbit, hamster, dogs, and non-human primates (110). Dogs and mice are considered good models of cardiac Chagas disease as they both reproduce some important clinical

and immunological outcomes identified in human patients (110). In the context of digestive disease, animal model studies have been largely limited to biopsy of GI organs and the counting of neurons, with no functional assays (111). In these models there has also been no link established between parasite infection dynamics and the loss of enteric neurons, other than blood parasitaemia/PCR. Moreover, inbred mice such as C57BL/6, make up a lot of small digestive studies which often lack appropriate controls. However, bioluminescence imaging has now identified the gut as a long-term reservoir for *T. cruzi* in mice. This strongly suggests that continual parasite persistence and associated host responses may dictate the severity of DCD pathology (63).

We have recently developed an experimental digestive Chagas disease (DCD) mouse model has recently been identified that exhibits a consistent and reproducible functional delay in peristalsis. (112). By using a transit time assay whereby mice were fed a red carmine food dye solution, it was shown that C3H/HeN mice infected with TcI-JR parasites develop dysperistalsis from the early acute phase which persists for the duration of infection (102). This phenotype was not observed consistently in other mouse-parasite strain combinations (Fig.7b). Gut dysfunction has been correlated with a reduction of HuC/D expression, a pan-neuronal cell body marker in the myenteric plexus of infected mice (Fig.7b), which also coincided with the colocalization of parasites (green) in space and time (Fig.7c).

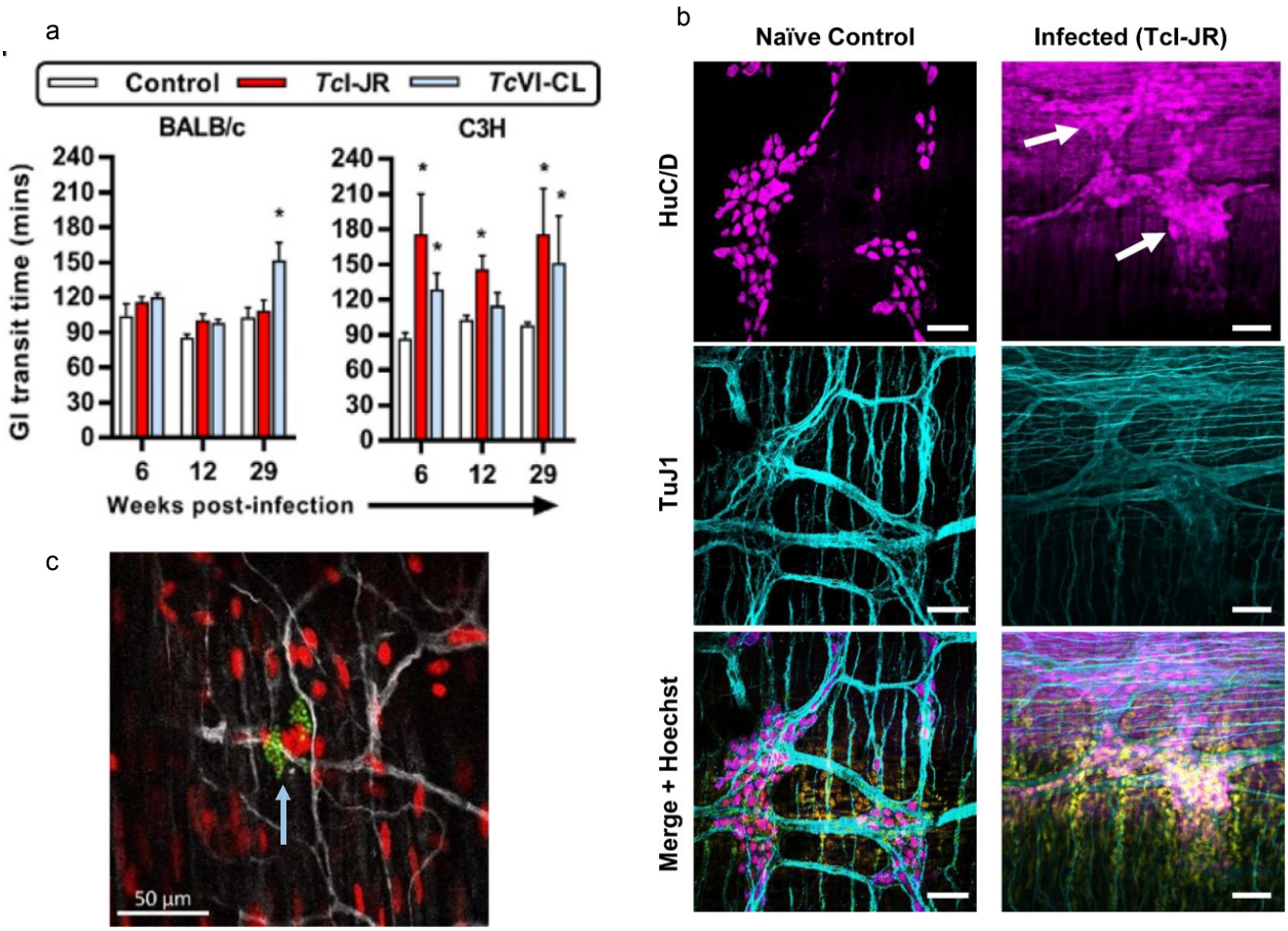

Figure 7. Graphical representation of a gut dysfunction phenotype in 4 different host parasite combinations. a) Graph on the left represents BALB/c mice infected with either TcI-JR (red bars) or TcVI-CL (blue bars). Y-axis is the total time taken to pass a red faecal pellet after being fed with 6% w/v Carmine solution. X-axis is the number of weeks post infection. Graph on the right represents C3H/HeN mice infected with the same parasite strains. A consistent and significant transit time delay is observed throughout the duration of infection in C3H mice infected with TcI-JR parasites, but not in any other mouse parasite combination. This is consistent with damage to the enteric nervous system, observed in b) where white arrows indicate loss of Huc/D (pan-neuronal cell nuclei) staining and lack of normal neuronal soma morphology. c) mNeonGreen *T. cruzi* parasites in green, neurons in white and nuclei in cell red, showing close physical proximity between infected cells and neurons in the colon muscle wall tissue.

Although this DCD model (TcI-JR in C3H mice) exhibits a clear pathological GI phenotype, parasites are in fact consistently observed in the GI tract of all infected mice irrespective of the mouse or parasite strain, so local infection persistence is not sufficient to explain the disease. This suggests, consistent with clinical epidemiology of human DCD, that variability in host-parasite interactions (underpinned by genetics) play a vital role in digestive pathogenesis severity.

The ENS has a diverse range of homeostatic and regulatory roles, and damage to the myenteric plexus is synonymous with DCD manifestations. The intestinal neuro-

immune signalling axes, and the microenvironment of enteric regions is an aspect of DCD that remains understudied. More specifically, the interaction between diverse cell subtypes such as enteric glial cells, resident immune cells, and neuronal cells which may play a role in pathogenesis development in different host/parasite models. These themes are explored within this project.

1.8 Wound healing and tissue repair in the GI tract

Dysregulation of the inflammation and wound-healing cycle has been shown to be the primary cause of cardiac pathology in Chagas disease, where excessive extracellular matrix (ECM) accumulation results in pathological fibrosis and progressive heart failure (113). Chronic parasitism of the GI tract suggests similar dynamics may also shape the progression of DCD alongside damage to and loss of enteric neurons. There are virtually no data on gut-specific immune responses to *T. cruzi* infection, but other diseases provide a potentially useful starting point. In inflammatory bowel disease (IBD), innate immune cells and epithelial cells act broadly by upregulating inducers of reactive oxygen and nitrogen species, facilitating local tissue damage (114). If the collateral damage to local tissue is severe, fibroblasts migrate to the sites of damage. Fibroblasts in the intestinal wall depict a high degree of heterogeneity (115), with those that are able to differentiate to smooth-muscle cells termed myofibroblasts (116). Myofibroblasts are critical in tissue repair in the GI tract due to their migratory functions and *in situ* production of extracellular matrix, which are altered by chronic inflammation (114).

Transforming growth factor (TGF-β) orchestrates the activation of myofibroblasts and induces collagen synthesis and matrix deposition at sites of damage. TGF-β is the most widely distributed mediator of pro-fibrotic pathways, observed in tissue repair of the lungs, liver, pancreas, and skin. Because of this, it is implicated in pathological fibrosis and fibrotic diseases of these tissues, as well as intestinal fibrosis (117). There is no defined model for intestinal fibrosis, due to the spectrum of causative factors, but TGF-β regulates the expression of tissue inhibitor of metalloproteinase (TIMPS) which has been described to be overexpressed in inflammatory bowel disease (118). Moreover, in colitis mouse models where TGF-β has been inhibited, severe fibrotic outcomes are alleviated, but inflammation and tissue damage worsen, due to the role of TGF-β as an inducer of regulatory T cells (117). Trans- differentiation of fibroblasts to myofibroblasts is permitted by TGF-β but Insulin-like growth factor I (IGFI) and interleukin (IL)-4 are also relevant for this transdifferentiation, contributing to both normal and pathological wound healing. Upregulation of both IGFI and TGF-β is observed in myofibroblasts at sites of fibrosis in patients with Crohn's disease (119).

Tissue repair processes have not been described for DCD, but the processes described with other inflammatory intestinal diseases may provide insight into our understanding of chronic GI pathology in our models. There is scope to dissect whether the severity of GI pathology resides with the host's or parasite's genetics and subsequent chronic interactions. More specifically, whether a host can recognise parasites in the colon, and regulate chronic inflammation and tissue repair effectively to limit or compensate for damage to the ENS, resulting in non- or slow progression of DCD. Alternatively, whether a dysregulation of the inflammatory and pro-fibrotic

axis permits severe neurological and tissue damage outcomes with insufficient repair to achieve functional compensation, as we observe with the cardiac disease.

1.9 Aims and Objectives

This project aims to investigate mechanisms of immunopathogenesis and tissue repair in the large intestine during experimental digestive Chagas disease, with a special focus on the enteric nervous system.

Objective 1. Does host-parasite genetics shape experimental DCD severity?

To analyse murine DCD caused by *T. cruzi*, I will first utilise colon tissue from a comparative study of two parasite strains (TcI-JR, TcVI-CL), and two mouse strains (BALB/c, C3H/HeN) at acute and chronic infection timepoints. These models have been shown to have divergent GI transit time delay phenotypes (Fig.4a). I will use histological and immunohistochemical (IHC) approaches to profile key aspects of pathology in colon tissue:

I. Inflammation and tissue architecture using Haematoxylin & Eosin (H&E) staining.
II. Fibrosis using Picro-Sirius red staining.
III. Neuronal damage using IHC targeting neuron-specific tubulin (TuJ1)
IV. Expression of iNOS using IHC

Relevant Papers and Manuscripts:

Local association of Trypanosoma cruzi chronic infection foci and enteric neuropathic lesions at the tissue micro-domain scale*. Archie A. Khan. Harry Langston., et al. PLOS Pathogens. (2021).*

***Pathological and immunological components of experimental Chagas disease*.**

Harry Langston., et al. Manuscript in preparation. (2024).

Objective 2. What drives the onset of acute transit time delay in the experimental DCD model?

The objective is to investigate which aspects of the immune system contribute to the initial development of dysperistalsis; either directly via collateral damage, or indirectly by increasing local parasite burden.

I. Characterise the acute GI dysperistalsis development window at finer resolution, including definition of when the inception of transit time delay occurs.
II. Test the effect of disrupting specific candidate immune effectors on
    a. the dysperistalsis initiation window
    b. immune cell subsets in the colon
    c. parasite loads
    d. ENS pathology

Objective 3. Does anti-parasitic treatment promote gut tissue repair and better DCD outcomes?

Using the TcIJR-C3H model, the objective is to investigate how anti-parasitic benznidazole treatment affects DCD outcomes in terms of peristalsis function and neuro-muscular tissue damage and repair processes.

I. Transit time assays and *in vivo* imaging will be conducted to track peristalsis function and parasite burden respectively.

II. Benznidazole treatment will be employed from week 6 of infection for 20 days to suppress or cure the infection.

III. 5-ethynyl-2′-deoxyuridine (EdU) will be administered to label proliferative cells, with injections to be carried out periodically after treatment is complete.

IV. H&E histological staining will be used to assess inflammation.

V. Immunofluorescence assays will be used to assess retrospective cellular replication within the myenteric plexus as a marker of post-treatment tissue repair or regeneration.

Relevant Papers and Manuscripts:

Enteric nervous system regeneration and functional cure of experimental digestive Chagas disease with trypanocidal chemotherapy*. Archie. A. Khan, Harry Langston., et al. bioRxiv 2022. (Nat. Comm, in revision).*

Objective 4. Explore the potential for broader experimental DCD models, beyond the mouse.

The objective is to expand the scope of investigating experimental Chagas disease with other animal models.

I. Investigate the dynamics of *T. cruzi* infection in a hamster model

Relevant Papers and Manuscripts:

Dynamics of Trypanosoma cruzi infection in hamsters and novel association with progressive motor dysfunction. *Harry Langston, et al. Manuscript submitted; PLoS NTD (in revision, 2023)*

References

1. Lidani KCF, Andrade FA, Bavia L, Damasceno FS, Beltrame MH, Messias-Reason IJ, et al. Chagas disease: From discovery to a worldwide health problem. J Phys Oceanogr. 2019;49(6):1–13.
2. Basile L, Jansà JM, Carlier Y, Salamanca DD, Angheben A, Bartoloni A, et al. Chagas disease in european countries: The challenge of a surveillance system. Eurosurveillance. 2011;16(37):3.
3. Manne-Goehler J, Umeh CA, Montgomery SP, Wirtz VJ. Estimating the Burden of Chagas Disease in the United States. PLoS Negl Trop Dis. 2016;10(11):1–7.
4. Lee Y B. Simulation Models. Lancet infectious diseases. 2013;13(4):342–8.
5. Marin-Neto JA, Rassi A, Morillo CA, Avezum A, Connolly SJ, Sosa-Estani S, et al. Rationale and design of a randomized placebo-controlled trial assessing the effects of etiologic treatment in Chagas' cardiomyopathy: the BENznidazole Evaluation For Interrupting Trypanosomiasis (BENEFIT). Am Heart J. 2008 Jul;156(1):37–43.
6. Maiguashca Sánchez J, Sueto SOB, Schwabl P, Grijalva MJ, Llewellyn MS, Costales JA. Remarkable genetic diversity of Trypanosoma cruzi and Trypanosoma rangeli in two localities of southern Ecuador identified via deep sequencing of mini-exon gene amplicons. Parasit Vectors. 2020 Dec 14;13(1):252.
7. Zeledón RA. Hemoflagellates. 1996.
8. Cavalcanti DP, de Souza W. The Kinetoplast of Trypanosomatids: From Early Studies of Electron Microscopy to Recent Advances in Atomic Force Microscopy. Scanning. 2018;2018:9603051.
9. Miles MA, Souza A, Povoa M, Shaw JJ, Lainson R, Toye PJ. Isozymic heterogeneity of Trypanosoma cruzi in the first autochthonous patients with Chagas' disease in Amazonian Brazil. Nature. 1978 Apr 27;272(5656):819–21.
10. Tibayrenc M, Ward P, Moya A, Ayala FJ. Natural populations of Trypanosoma cruzi, the agent of Chagas disease, have a complex multiclonal structure. Proc Natl Acad Sci U S A. 1986 Jan;83(1):115–9.
11. Tibayrenc M. Genetic epidemiology of parasitic protozoa and other infectious agents: the need for an integrated approach. Int J Parasitol. 1998 Jan;28(1):85–104.
12. Brisse S, Barnabé C, Tibayrenc M. Identification of six Trypanosoma cruzi phylogenetic lineages by random amplified polymorphic DNA and multilocus enzyme electrophoresis. Int J Parasitol. 2000 Jan;30(1):35–44.
13. Marcili A, Lima L, Cavazzana M, Junqueira AC V, Veludo HH, Maia Da Silva F, et al. A new genotype of Trypanosoma cruzi associated with bats evidenced by phylogenetic analyses using SSU rDNA, cytochrome b and Histone H2B genes and genotyping based on ITS1 rDNA. Parasitology. 2009 May;136(6):641–55.
14. Lima L, Espinosa-Álvarez O, Ortiz PA, Trejo-Varón JA, Carranza JC, Pinto CM, et al. Genetic diversity of Trypanosoma cruzi in bats, and multilocus phylogenetic and phylogeographical analyses supporting Tcbat as an independent DTU (discrete typing unit). Acta Trop. 2015 Nov;151:166–77.
15. Carrasco HJ, Segovia M, Llewellyn MS, Morocoima A, Urdaneta-Morales S, Martínez C, et al. Geographical Distribution of Trypanosoma cruzi Genotypes in Venezuela. PLoS Negl Trop Dis. 2012 Jun 26;6(6):e1707.
16. Barrias ES, de Carvalho TMU, De Souza W. Trypanosoma cruzi: Entry into mammalian host cells and parasitophorous vacuole formation. Front Immunol. 2013;4(AUG):1–10.
17. De Noya BA, Díaz-Bello Z, Colmenares C, Ruiz-Guevara R, Mauriello L, Zavala-Jaspe R, et al. Large urban outbreak of orally acquired acute chagas disease at a school in Caracas, Venezuela. Journal of Infectious Diseases. 2010;201(9):1308–15.

18. Sabino EC, Ribeiro AL, Salemi VMC, Di Lorenzo Oliveira C, Antunes AP, Menezes MM, et al. Ten-Year incidence of chagas cardiomyopathy among asymptomatic trypanosoma cruzi-seropositive former blood donors. Circulation. 2013;127(10):1105–15.
19. C. Onyekwelu K. Life Cycle of *Trypanosoma cruzi* in the Invertebrate and the Vertebrate Hosts. In: Biology of Trypanosoma cruzi. IntechOpen; 2019.
20. Frasch ACC. Functional Diversity in the Trans-sialidase and Mucin Families in Trypanosoma cruzi. Parasitology Today. 2000 Jul;16(7):282–6.
21. El-Sayed NM, Myler PJ, Bartholomeu DC, Nilsson D, Aggarwal G, Tran AN, et al. The Genome Sequence of *Trypanosoma cruzi* , Etiologic Agent of Chagas Disease. Science (1979). 2005 Jul 15;309(5733):409–15.
22. Previato J, Andrade AFB, Pessolani MC V., Mendonça-Previato L. Incorporation of sialic acid into Trypanosoma cruzi macromolecules. A proposal for a new metabolic route. Mol Biochem Parasitol. 1985 Jun;16(1):85–96.
23. Kulkarni MM, Olson CL, Engman DM, McGwire BS. Trypanosoma cruzi GP63 proteins undergo stage-specific differential posttranslational modification and are important for host cell infection. Infect Immun. 2009 May;77(5):2193–200.
24. Cuevas IC, Cazzulo JJ, Sánchez DO. gp63 homologues in Trypanosoma cruzi: surface antigens with metalloprotease activity and a possible role in host cell infection. Infect Immun. 2003 Oct;71(10):5739–49.
25. Cerny N, Bivona AE, Sanchez Alberti A, Trinitario SN, Morales C, Cardoso Landaburu A, et al. Cruzipain and Its Physiological Inhibitor, Chagasin, as a DNA-Based Therapeutic Vaccine Against Trypanosoma cruzi. Front Immunol. 2020 Oct 9;11.
26. Schnapp AR, Eickhoff CS, Sizemore D, Curtiss R, Hoft DF. Cruzipain Induces Both Mucosal and Systemic Protection against *Trypanosoma cruzi* in Mice. Infect Immun. 2002 Sep;70(9):5065–74.
27. Truyens C, Carlier Y. Protective host response to Trypanosoma cruzi and its limitations. In: American Trypanosomiasis Chagas Disease. Elsevier; 2017. p. 579–604.
28. Shikanai-Yasuda MA, Carvalho NB. Oral Transmission of Chagas Disease. Clinical Infectious Diseases. 2012 Mar 15;54(6):845–52.
29. Rassi A, Rassi A, Marin-Neto JA. Chagas disease. The Lancet. 2010 Apr;375(9723):1388–402.
30. Saenz LC, Corrales FM, Bautista W, Traina M, Meymandi S, Rodriguez DA, et al. Cardiac sympathetic denervation for intractable ventricular arrhythmias in Chagas disease. Heart Rhythm. 2016 Jul;13(7):1388–94.
31. Lewis MD, Kelly JM. Putting Infection Dynamics at the Heart of Chagas Disease. Trends Parasitol. 2016;32(11):899–911.
32. Bierrenbach AL, Quintino ND, Moreira CHV, Damasceno RF, Nunes M do CP, Baldoni NR, et al. Hospitalizations due to gastrointestinal Chagas disease: National registry. PLoS Negl Trop Dis. 2022 Sep 19;16(9):e0010796.
33. Klotz SA, Shirazi FM, Boesen K, Beatty NL, Dorn PL, Smith S, et al. Kissing Bug (Triatoma spp.) Intrusion into Homes: Troublesome Bites and Domiciliation. Environ Health Insights. 2016;10:45–9.
34. PEDREIRA DE FREITAS JL, AMATO NETO V, SONNTAG R, BIANCALANA A, NUSSENZVEIG V, BARRETO JG. [First tests on the accidental transmission of Chagas disease to man by blood transfusion]. Rev Paul Med. 1952 Jan;40(1):36–40.
35. Schmunis GA, Cruz JR. Safety of the blood supply in Latin America. Clin Microbiol Rev. 2005 Jan;18(1):12–29.

36. Strasen J, Williams T, Ertl G, Zoller T, Stich A, Ritter O. Epidemiology of Chagas disease in Europe: many calculations, little knowledge. Clin Res Cardiol. 2014 Jan;103(1):1–10.
37. Suárez C, Nolder D, García-Mingo A, Moore DAJ, Chiodini PL. Diagnosis and Clinical Management of Chagas Disease: An Increasing Challenge in Non-Endemic Areas. Res Rep Trop Med. 2022;13:25–40.
38. PAHO. Guidelines for the diagnosis and treatment of Chagas disease . 2018.
39. Schijman AG, Altcheh J, Burgos JM, Biancardi M, Bisio M, Levin MJ, et al. Aetiological treatment of congenital Chagas' disease diagnosed and monitored by the polymerase chain reaction. J Antimicrob Chemother. 2003 Sep;52(3):441–9.
40. Angheben A, Boix L, Buonfrate D, Gobbi F, Bisoffi Z, Pupella S, et al. Chagas disease and transfusion medicine: a perspective from non-endemic countries. Blood Transfus. 2015 Oct;13(4):540–50.
41. Hall BS, Wilkinson SR. Activation of benznidazole by trypanosomal type I nitroreductases results in glyoxal formation. Antimicrob Agents Chemother. 2012 Jan;56(1):115–23.
42. Meymandi S, Hernandez S, Park S, Sanchez DR, Forsyth C. Treatment of Chagas Disease in the United States. Curr Treat Options Infect Dis. 2018;10(3):373–88.
43. Morillo CA, Marin-Neto JA, Avezum A, Sosa-Estani S, Rassi A, Rosas F, et al. Randomized Trial of Benznidazole for Chronic Chagas' Cardiomyopathy. New England Journal of Medicine. 2015;373(14):1295–306.
44. Meymandi S, Hernandez S, Park S, Sanchez DR, Forsyth C. Treatment of Chagas Disease in the United States. Curr Treat Options Infect Dis. 2018;10(3):373–88.
45. Jackson Y, Wyssa B, Chappuis F. Tolerance to nifurtimox and benznidazole in adult patients with chronic Chagas' disease. J Antimicrob Chemother. 2020 Mar 1;75(3):690–6.
46. DNDi. the BENDITA study. 2019.
47. Lewis MD, Kelly JM. Putting Infection Dynamics at the Heart of Chagas Disease. Trends Parasitol. 2016;32(11):899–911.
48. Rassi A, Rassi A, Marin-Neto JA. Chagas disease. The Lancet. 2010;375(9723):1388–402.
49. Pérez-Mazliah D, Ward AI, Lewis MD. Host-parasite dynamics in Chagas disease from systemic to hyper-local scales. Parasite Immunol. 2021 Feb 24;43(2).
50. Cardoso MS, Reis-Cunha JL, Bartholomeu DC. Evasion of the Immune Response by Trypanosoma cruzi during Acute Infection. Front Immunol. 2016 Jan 18;6.
51. Cardoso MS, Reis-Cunha JL, Bartholomeu DC. Evasion of the Immune Response by Trypanosoma cruzi during Acute Infection. Front Immunol. 2016 Jan 18;6.
52. Xie CB, Jane-Wit D, Pober JS. Complement Membrane Attack Complex: New Roles, Mechanisms of Action, and Therapeutic Targets. Am J Pathol. 2020 Jun;190(6):1138–50.
53. Ferreira V, Valck C, Sánchez G, Gingras A, Tzima S, Molina MC, et al. The Classical Activation Pathway of the Human Complement System Is Specifically Inhibited by Calreticulin from *Trypanosoma cruzi*. The Journal of Immunology. 2004 Mar 1;172(5):3042–50.
54. Norris KA, Bradt B, Cooper NR, So M. Characterization of a Trypanosoma cruzi C3 binding protein with functional and genetic similarities to the human complement regulatory protein, decay-accelerating factor. J Immunol. 1991 Oct 1;147(7):2240–7.
55. Burleigh BA, Andrews NW. The mechanisms of Trypanosoma cruzi invasion of mammalian cells. Annu Rev Microbiol. 1995;49:175–200.

56. Kayama H, Koga R, Atarashi K, Okuyama M, Kimura T, Mak TW, et al. NFATc1 Mediates Toll-Like Receptor-Independent Innate Immune Responses during Trypanosoma cruzi Infection. PLoS Pathog. 2009 Jul 17;5(7):e1000514.
57. Choudhuri S, Garg NJ. PARP1-cGAS-NF-κB pathway of proinflammatory macrophage activation by extracellular vesicles released during Trypanosoma cruzi infection and Chagas disease. PLoS Pathog. 2020 Apr 21;16(4):e1008474.
58. Silva GK, Costa RS, Silveira TN, Caetano BC, Horta CV, Gutierrez FRS, et al. Apoptosis-Associated Speck–like Protein Containing a Caspase Recruitment Domain Inflammasomes Mediate IL-1β Response and Host Resistance to *Trypanosoma cruzi* Infection. The Journal of Immunology. 2013 Sep 15;191(6):3373–83.
59. Huan Huang, Stefka B Petkova, Alex W Cohen, Boumediene Bouzahzah, John Chan, Jian-nian Zhou. Activation of transcription factors AP-1 and NF-kappa B in murine Chagasic myocarditis. Infect Immun. 2003;71(5):2859–67.
60. Hall BS, Tam W, Sen R, Pereira MEA. Cell-specific Activation of Nuclear Factor-κB by the Parasite *Trypanosoma cruzi* Promotes Resistance to Intracellular Infection. Mol Biol Cell. 2000 Jan;11(1):153–60.
61. Michailowsky V, Silva NM, Rocha CD, Vieira LQ, Lannes-Vieira J, Gazzinelli RT. Pivotal Role of Interleukin-12 and Interferon-γ Axis in Controlling Tissue Parasitism and Inflammation in the Heart and Central Nervous System during Trypanosoma cruzi Infection. Am J Pathol. 2001 Nov;159(5):1723–33.
62. Murphy MP. Nitric oxide and cell death. Biochimica et Biophysica Acta (BBA) - Bioenergetics. 1999 May;1411(2–3):401–14.
63. Lewis MD, Fortes Francisco A, Taylor MC, Burrell-Saward H, Mclatchie AP, Miles MA, et al. Bioluminescence imaging of chronic Trypanosoma cruzi infections reveals tissue-specific parasite dynamics and heart disease in the absence of locally persistent infection. Cell Microbiol. 2014;16(9):1285–300.
64. Piacenza L, Peluffo G, Alvarez MN, Martínez A, Radi R. Trypanosoma cruzi antioxidant enzymes as virulence factors in Chagas disease. Antioxid Redox Signal. 2013 Sep 1;19(7):723–34.
65. Silva JS, Twardzik DR, Reed SG. Regulation of trypanosoma cruziinfections in vitro and in vivo by transforming growth factor β(TGF-β). Journal of Experimental Medicine. 1991;174(3):539–45.
66. Bermejo DA, Amezcua Vesely MC, Khan M, Acosta Rodríguez E V., Montes CL, Merino MC, et al. Trypanosoma cruzi infection induces a massive extrafollicular and follicular splenic B-cell response which is a high source of non-parasite-specific antibodies. Immunology [Internet]. 2011 Jan;132(1):123–33. Available from: https://onlinelibrary.wiley.com/doi/10.1111/j.1365-2567.2010.03347.x
67. Acevedo GR, Girard MC, Gómez KA. The Unsolved Jigsaw Puzzle of the Immune Response in Chagas Disease. Front Immunol. 2018 Aug 24;9.
68. Almeida IC, Milani SR, Gorin PA, Travassos LR. Complement-mediated lysis of Trypanosoma cruzi trypomastigotes by human anti-alpha-galactosyl antibodies. J Immunol. 1991 Apr 1;146(7):2394–400.
69. Chaves AC, Correa Oliveira R, Romanha AJ, Antas PR, Torrico F, Araújo-Jorge TC, et al. Early, intermediate, and late acute stages in Chagas' disease: a study combining anti-galactose IgG, specific serodiagnosis, and polymerase chain reaction analysis. Am J Trop Med Hyg. 1999 Aug 1;61(2):308–14.
70. Serrán MG, Boari JT, Vernengo FF, Beccaría CG, Ramello MC, Bermejo DA, et al. Unconventional pro-inflammatory CD4+ T cell response in B cell-deficient mice infected with Trypanosoma cruzi. Front Immunol. 2017;8(NOV).

71. Marzo AL, Vezys V, Klonowski KD, Lee SJ, Muralimohan G, Moore M, et al. Fully functional memory CD8 T cells in the absence of CD4 T cells. J Immunol. 2004 Jul 15;173(2):969–75.
72. Padilla A, Xu D, Martin D, Tarleton R. Limited role for CD4+ T-cell help in the initial priming of Trypanosoma cruzi-specific CD8+ T cells. Infect Immun. 2007 Jan;75(1):231–5.
73. HIV.gov. Guidelines for the Prevention and Treatment of Opportunistic Infections in Adults and Adolescents with HIV : Chagas Disease. 2023.
74. Tarleton RL, Sun J, Zhang L, Postan M. Depletion of T-cell subpopulations results in exacerbation of myocarditis and parasitism in experimental Chagas' disease. Infect Immun. 1994 May;62(5):1820–9.
75. Boivin WA, Cooper DM, Hiebert PR, Granville DJ. Intracellular versus extracellular granzyme B in immunity and disease: challenging the dogma. Lab Invest. 2009 Nov;89(11):1195–220.
76. Dotiwala F, Mulik S, Polidoro RB, Ansara JA, Burleigh BA, Walch M, et al. Killer lymphocytes use granulysin, perforin and granzymes to kill intracellular parasites. Nat Med. 2016 Feb 11;22(2):210–6.
77. Pontes Ferreira C, Cariste LM, Ferri Moraschi B, Ferrarini Zanetti B, Won Han S, Araki Ribeiro D, et al. CXCR3 chemokine receptor guides Trypanosoma cruzi-specific T-cells triggered by DNA/adenovirus ASP2 vaccine to heart tissue after challenge. PLoS Negl Trop Dis. 2019 Jul;13(7):e0007597.
78. Albareda MC, Laucella SA, Alvarez MG, Armenti AH, Bertochi G, Tarleton RL, et al. Trypanosoma cruzi modulates the profile of memory CD8+ T cells in chronic Chagas' disease patients. Int Immunol. 2006 Mar 1;18(3):465–71.
79. Vespa GN, Cunha FQ, Silva JS. Nitric oxide is involved in control of Trypanosoma cruzi-induced parasitemia and directly kills the parasite in vitro. Infect Immun. 1994 Nov;62(11):5177–82.
80. Hölscher C, Köhler G, Müller U, Mossmann H, Schaub GA, Brombacher F. Defective nitric oxide effector functions lead to extreme susceptibility of Trypanosoma cruzi-infected mice deficient in gamma interferon receptor or inducible nitric oxide synthase. Infect Immun. 1998 Mar;66(3):1208–15.
81. Tarleton RL. CD8+ T cells in Trypanosoma cruzi infection. Semin Immunopathol. 2015 May 29;37(3):233–8.
82. Lewis MD, Francisco AF, Taylor MC, Jayawardhana S, Kelly JM. Host and parasite genetics shape a link between Trypanosoma cruzi infection dynamics and chronic cardiomyopathy. Cell Microbiol. 2016 Oct;18(10):1429–43.
83. Ward AI, Lewis MD, Taylor MC, Kelly JM. Incomplete Recruitment of Protective T Cells Is Associated with Trypanosoma cruzi Persistence in the Mouse Colon. Infect Immun. 2022 Feb 17;90(2):e0038221.
84. Kierszenbaum F. Chagas' disease and the autoimmunity hypothesis. Clin Microbiol Rev. 1999 Apr;12(2):210–23.
85. De Bona E, Lidani KCF, Bavia L, Omidian Z, Gremski LH, Sandri TL, et al. Autoimmunity in Chronic Chagas Disease: A Road of Multiple Pathways to Cardiomyopathy? Front Immunol. 2018;9:1842.
86. Gironès N, Cuervo H, Fresno M. Trypanosoma cruzi-induced molecular mimicry and Chagas' disease. Curr Top Microbiol Immunol. 2005;296:89–123.
87. Soares MB, Pontes-De-Carvalho L, Ribeiro-Dos-Santos R. The pathogenesis of Chagas' disease: when autoimmune and parasite-specific immune responses meet. An Acad Bras Cienc. 2001 Dec;73(4):547–59.

88. Bonney KM, Engman DM. Autoimmune Pathogenesis of Chagas Heart Disease. Am J Pathol. 2015 Jun;185(6):1537–47.
89. Ciechanowski M, Mower-Wade D, Mcleskey SW. Anatomy and physiology of the nervous system. Critical Care Nursing: A Holistic Approach. 2013;(Suppl IV):691–722.
90. Ward AI, Lewis MD, Khan AA, McCann CJ, Francisco AF, Jayawardhana S, et al. In vivo analysis of trypanosoma cruzi persistence foci at single-cell resolution. mBio. 2020;11(4):1–13.
91. Gershon MD. The Enteric Nervous System. Annu Rev Neurosci. 1981 Mar;4(1):227–72.
92. Furness JB. The enteric nervous system and neurogastroenterology. Nat Rev Gastroenterol Hepatol. 2012 May 6;9(5):286–94.
93. Gershon MD. The Enteric Nervous System: A Second Brain. Hosp Pract. 1999 Jul 15;34(7):31–52.
94. Ward SM. Interstitial cells of Cajal in enteric neurotransmission. Gut. 2000 Dec 1;47(90004):40iv–43.
95. Huizinga JD, Berezin I, Daniel EE, Chow E. Inhibitory innervation of colonic smooth muscle cells and interstitial cells of Cajal. Can J Physiol Pharmacol. 1990 Mar;68(3):447–54.
96. Gershon MD, Rothman TP. Enteric glia. Glia. 1991 Jan 12;4(2):195–204.
97. Fleming MA, Ehsan L, Moore SR, Levin DE. The Enteric Nervous System and Its Emerging Role as a Therapeutic Target. Gastroenterol Res Pract. 2020;2020:8024171.
98. Gabella G. Fine structure of the myenteric plexus in the guinea-pig ileum. J Anat. 1972 Jan;111(Pt 1):69–97.
99. Scheperjans F, Derkinderen P, Borghammer P. The Gut and Parkinson's Disease: Hype or Hope? J Parkinsons Dis. 2018 Dec 18;8(s1):S31–9.
100. Vaezi MF. Atypical manifestations of gastroesophageal reflux disease. Vol. 7, MedGenMed : Medscape general medicine. 2005. p. 25.
101. Bern C. Antitrypanosomal therapy for chronic Chagas' disease. N Engl J Med. 2011 Jun 30;364(26):2527–34.
102. Köberle F. The causation and importance of nervous lesions in American trypanosomiasis. Bull World Health Organ. 1970;42(5):739–43.
103. Arantes RME, Marche HHF, Bahia MT, Cunha FQ, Rossi MA, Silva JS. Interferon-γ-Induced Nitric Oxide Causes Intrinsic Intestinal Denervation in Trypanosoma cruzi-Infected Mice. American Journal of Pathology. 2004;164(4):1361–8.
104. Garcia SB, Paula JS, Giovannetti GS, Zenha F, Ramalho EM, Zucoloto S, et al. Nitric oxide is involved in the lesions of the peripheral autonomic neurons observed in the acute phase of experimental Trypanosoma cruzi infection. Exp Parasitol. 1999 Dec;93(4):191–7.
105. Lee SC, Zhao ML, Hirano A, Dickson DW. Inducible nitric oxide synthase immunoreactivity in the Alzheimer disease hippocampus: association with Hirano bodies, neurofibrillary tangles, and senile plaques. J Neuropathol Exp Neurol. 1999 Nov;58(11):1163–9.
106. Kolios G, Valatas V, Ward SG. Nitric oxide in inflammatory bowel disease: a universal messenger in an unsolved puzzle. Immunology. 2004 Dec;113(4):427–37.
107. Brosens E, Burns AJ, Brooks AS, Matera I, Borrego S, Ceccherini I, et al. Genetics of enteric neuropathies. Dev Biol. 2016;417(2):198–208.
108. Vago AR, Silva DM, Adad SJ, Correa-Oliveira R, d'Avila Reis D. Chronic Chagas disease: presence of parasite DNA in the oesophagus of patients without megaoesophagus. Trans R Soc Trop Med Hyg. 2003;97(3):308–9.

109. Vago AR, Macedo AM, Adad SJ, Reis DD, Corrêa-Oliveira R. PCR detection of Trypanosoma cruzi DNA in oesophageal tissues of patients with chronic digestive Chagas' disease. Lancet. 1996 Sep 28;348(9031):891–2.
110. Chatelain E, Konar N. Translational challenges of animal models in Chagas disease drug development: a review. Drug Des Devel Ther. 2015;9:4807–23.
111. Nogueira-Paiva NC, Fonseca K da S, Vieira PM de A, Diniz LF, Caldas IS, Moura SAL de, et al. Myenteric plexus is differentially affected by infection with distinct Trypanosoma cruzi strains in Beagle dogs. Mem Inst Oswaldo Cruz. 2014 Feb;109(1):51–60.
112. Khan AA, Langston HC, Costa FC, Olmo F, Taylor MC, McCann CJ, et al. Local association of Trypanosoma cruzi chronic infection foci and enteric neuropathic lesions at the tissue micro-domain scale. PLoS Pathog. 2021 Aug 23;17(8):e1009864.
113. Lewis MD, Kelly JM. Putting Infection Dynamics at the Heart of Chagas Disease. Trends Parasitol. 2016;32(11):899–911.
114. Rieder F, Brenmoehl J, Leeb S, Schölmerich J, Rogler G. Wound healing and fibrosis in intestinal disease. Gut. 2007 Jan;56(1):130–9.
115. Komuro T. Re-evaluation of fibroblasts and fibroblast-like cells. Anat Embryol (Berl). 1990;182(2):103–12.
116. Gabbiani G, Ryan GB, Majne G. Presence of modified fibroblasts in granulation tissue and their possible role in wound contraction. Experientia. 1971 May 15;27(5):549–50.
117. Motomura Y, Khan WI, El-Sharkawy RT, Verma-Gandhu M, Verdu EF, Gauldie J, et al. Induction of a fibrogenic response in mouse colon by overexpression of monocyte chemoattractant protein 1. Gut. 2006 May;55(5):662–70.
118. McKaig BC, McWilliams D, Watson SA, Mahida YR. Expression and regulation of tissue inhibitor of metalloproteinase-1 and matrix metalloproteinases by intestinal myofibroblasts in inflammatory bowel disease. Am J Pathol. 2003 Apr;162(4):1355–60.
119. Simmons JG, Pucilowska JB, Keku TO, Lund PK. IGF-I and TGF-beta1 have distinct effects on phenotype and proliferation of intestinal fibroblasts. Am J Physiol Gastrointest Liver Physiol. 2002 Sep;283(3):G809-18.

Pathological and immunological components of experimental digestive Chagas disease

Harry Langston, Archie A. Khan, Amanda F Francisco, John M. Kelly, Michael D. Lewis

Department of Infection Biology, London School of Hygiene and Tropical Medicine, Keppel Street, London, WC1E 7HT, United Kingdom

Introduction

Chagas disease (CD), an infection caused by the intracellular protozoan parasite *Trypanosoma cruzi*, affects approximately 6 million people globally. Severe clinical manifestations present in the heart and digestive tract, or both. Principle cardiac presentations include myocarditis, fibrosis, conduction abnormalities, cardiac failure and sudden death (1). There is a disparity between experimental research conducted on cardiac CD and the digestive form; for cardiac CD there is expansive clinically informed research and translatable animal models, which are lacking for digestive CD. Human digestive CD (DCD) is characterised by the progressive dilation and dysfunction of the GI tract (2). Clinically, this presents as abdominal pain, constipation and, in extreme cases, faecaloma. This can progress to severe DCD complications synonymous with substantial oesophageal and or colonic dilation, referred to as mega-syndromes. Dilation is associated with loss or damage to the enteric nervous system, resulting in dysperistalsis and smooth muscle hyperplasia (3,4).

Cardiomyopathy develops in around 33% of individuals, with 10% developing DCD (1). Anti-parasitic chemotherapy is only considered to have an evidence-based justification in patients where cardiac manifestations are present, but not for those presenting with gastrointestinal sequalae only. This is largely due to an absence of any clinical trial data addressing treatment efficacy in the context of digestive outcomes (5). Difficulty for clinical trials, especially for DCD, reside in the widely varying and slow-developing disease outcomes linked to geographical regions (6). Host-parasite genetics plays a pivotal role in the severity of both cardiac and GI disease, with our understanding coming principally from experimental models (7,8).

By utilising bioluminescent parasites expressing a red-shifted luciferase (9), infection dynamics can now be tracked in real-time and correlated with varying severities of pathology. Despite the different infection and pathological profiles across tested murine *T. cruzi* infection models, the gastrointestinal tract was always found to be a primary site of chronic infection (10,11).

DCD is thought to stem from collateral damage to the enteric nervous system, as a result of potent anti-parasitic nitric oxide (NO) synthesis in smooth muscle of the large intestine, predominantly, or even exclusively, in the acute phase (12). Due to the chronicity of CD, and the frequently detected oesophageal and colonic inflammation from patients, it is propounded that chronic parasite-host interactions may also contribute to disease development (13). These data are difficult to interpret because inflammation and parasite loads are transient, and the relationship between parasite and host is highly dynamic over the course of a life-long infection.

This spearheaded the generation of a robust murine model for DCD at LSHTM, to help study the kinetics of infection and pathology simultaneously. C3H/HeN mice infected with TcI-JR parasites elicit a significant gut dysperistalsis phenotype associated with local parasite persistence in GI tissues, which is highly reproducible (7). However, C3H/HeN mice infected with a divergent parasite strain, TcVI-CLBR did not exhibit the sustained dysperistalsis phenotype and neither did BALB/c mice infected with either parasite strain. Here, to test the hypothesis that total GI transit time delays correlate with a distinct immunopathological environment in the colon, we compared pathological features in the DCD model with other mouse-

parasite strain combinations that have GI parasite persistence, but only develop mild or no DCD symptoms.

Materials and methods

Tissue samples

Tissues were obtained from both C3H/HeN and BALB/c mice, infected interperitoneally with either $1x10^3$ TcI-JR-LUC or TcVI-CL-BR parasites. For the chronic experiments, endpoints were 185 days post infection, or 205 days post infection. For the acute, the end point was 42 days post infection. Archive tissue samples were derived from historical experiments originally used in different contexts (14), as well as from pilot DCD experiments and work that led to a recent paper describing the development of the DCD mouse model (15).

Preparing tissue for histology

After necropsy, tissue was fixed in Glyofixx (Epredia) for 24 hours. Fixed tissue was then transferred to 70% ethanol until processing. To process, tissue was dehydrated through a graded alcohol series; 70% - 100% ethanol, 30 minutes in each solution. There were two total immersions in 100% ethanol. Tissue was then cleared in two washes of Histoclear (National Diagnostics) for 11 minutes each. Finally, tissue was incubated in molten paraffin wax for 11 minutes. Processed tissue was then embedded in histology blocks and cut using microtomy. Sections were cut at 3-5 µm and left to air dry overnight. Before staining, the slides had to be deparaffinised to remove excess wax from the tissue. Slides were incubated in two changes of xylene,

5 minutes each, then rehydrated through a graded alcohol series starting from 100% down to 70%.

Haematoxylin and Eosin (H&E) stain

After deparaffinisation, slides were stained in Harris haematoxylin for 8 minutes then washed in running tap water for 5 minutes, or until the water runs clear. Cleaned slides were then differentiated in acid alcohol (1% HCL v/v, 70% ethanol) for 30 seconds with slight agitation. Differentiated tissue slides were then washed in running tap water for 1 minute, then stained in alcoholic Eosin Y for 1 minute. Slides were immediately washed in running tap water until the water ran clear, then cleared in two changes of 100% ethanol for 3 minutes each. Slides were left to air dry and mounted with a coverslip using DPX-based mounting media. Slides were observed using the Leica DM 3000 and analysed using Leia application suite v.4.0.1. Fifteen images per mouse, 5 distal, 5 mid-, 5 proximal colon, at 400x magnification were analysed. Inflammation index was calculated as the the estimated number of cells based on individual cells identified within a set colour threshold.

Picrosirius red stain

After deparaffinisation, slides were stained in Harris haematoxylin for 8 minutes, and washed in running tap water for 10 minutes. Tissue was stained in picrosirius red working solution (0.1% Sirius Red F3B w/v, saturated aqueous picric acid) for 1 hour. Tissue was washed in two changes of acidified water (0.5% glacial acetic acid v/v, distilled water) for 1 minute each. Excess acidified water was shaken off the slide, then dehydrated in two changes of 100% ethanol. After airdrying, slides were mounted with a coverslip using DPX-based mounting media. Slides were observed

using Leica DM 3000 and analysed Leia application suite v.4.0.1.Ten images per mouse, at 400x magnification were analysed.

Immunohistochemistry

After deparaffinisation, slides underwent antigenic retrieval. Slides were placed into a Coplin jar with pre-heated sodium citrate buffer (10 mM sodium citrate, 0.05% Tween-20, pH 6.0). Immersed slides were placed in a water bath at 98^{o}C for 30 minutes. The Coplin jar was removed from the water using heat resistant gloves and left to stand at room temperature for 15 minutes. Slides were removed and quickly shaken to remove excess buffer, and a hydrophobic barrier was drawn around the tissue using a PAP pen. The barrier was left to dry for 2 minutes, ensuring the slide did not dry out completely. 100-150µl of blocking solution (2.5% horse serum, 0.1% Tween-20 in PBS) was added within the hydrophobic barrier, ensuring a meniscus was visible over the tissue. Tissue was blocked for 1 hour, shaken dry and incubated with hydrogen peroxide solution (0.3% H_2O_2 v/v distilled water) for 20 minutes to quench endogenous peroxidase activity, especially important for colon tissue. Slides were washed in three changes of PBS, 5 minutes each and incubated with primary antibody: rabbit anti-iNOS [Abcam, ab15323] 1:50 or rabbit anti-TuJ-1 [Biolegend PRB-435P] 1:1000 or rat anti-BTNL1 [a gift from A. Hayday] 1:1000 or rabbit anti-MARCO [Abcam, ab259264] 1:500. Primary antibodies were diluted to working concentrations in 0.1% PBS-T. Tissue was left to incubate overnight at 4^{o}C in a humidified chamber. Slides were then washed in 3 changes of PBS, 5 minutes each. Tissues were incubated with 100-150µl ImmPRESS horse anti-rabbit IgG or anti-rat IgG horseradish peroxidase (HRP) polymer secondary antibody reagent for 30 minutes, before being washed in three changes of PBS for 5 minutes each. Slides

were then counterstained in filtered Harris haematoxylin for 5 seconds and rinsed in running tap water for 1 minute. Slides were dehydrated in 100% ethanol for 2 minutes, left to airdry, and mounted with a coverslip in DPX-based mounting media. Slides were imaged on Leica DM 3000 and analysed on Leica application suite v.4.0.1.

Whole mount Immunofluorescence

Whole colon was flushed with ice cold PBS using a gavage needle and cut longitudinally along the mesentery line using micro scissors. The open colon tissue was pinned and fixed in paraformaldehyde (4% w/v in PBS). Once fixed, the mucosal layer of the colon was peeled off using fine forceps under a dissection microscope so that only the muscularis layer remains. Peeled tissue was stored in sucrose solution (30% d-sucrose w/v, 0.01% azide) until required. Colon tissue removed from sucrose was washed three times in 0.1% PBS-T, and permeabilised with PBS containing 1% Triton X-100 for 2 hours, followed by blocking for 1 hour (10% sheep serum, 0.5% Triton X-100 in PBS). Tissues were incubated with primary antibodies: Rabbit anti-CD3 monoclonal [Abcam, ab11089] and mouse anti-CD45R [Abcam, ab40763] dilution of 1:500 in PBS-T (PBS, 0.1% Triton X-100) overnight in a humidity chamber at 4^{o}C. Tissues were washed with PBS for 45 minutes, with 3 changes, then incubated with secondary IgG: goat-anti mouse AlexaFluor488; donkey anti-mouse IgG AlexaFluor568 (ThermoFisher), all used at 1:500 in 0.1% PBS-T. Tissue was incubated for 1 hour at room temperature, kept dark, before a final 45-minute PBS wash, with 3 changes. Tissue was counterstained with the DNA-binding dye Hoechst 33342 (1 μg ml^{-1}) for 30 minutes and mounted on glass slides using FluorSavr

mounting medium (Merck). Antibody control samples were not subjected to primary antibody, only secondary.

Whole mounts were examined and imaged using LSM880 confocal microscope, using 20X and 40X objectives. Images were captured as Z-stacks of 12 digital slices. Post image compression and adjustment was performed on FIJI software.

Results

Inflammation

All data derives from colon tissue collected from mice over two independent replicate experiments. Histological analysis was conducted on the smooth muscle layer of the colon of C3H/HeN and BALB/c mice, where infected mice were culled 185 days post-infection (experiment 1) or 205 days post-infection (experiment 2). It is well established from previous bioluminescence imaging that there is parasite persistence at this site, though the infection is sparse and focal (16,17). I compared two parasite strains in terms of various aspects of histopathology, and the first pathology analysed was inflammation, which was made observable by H&E staining.

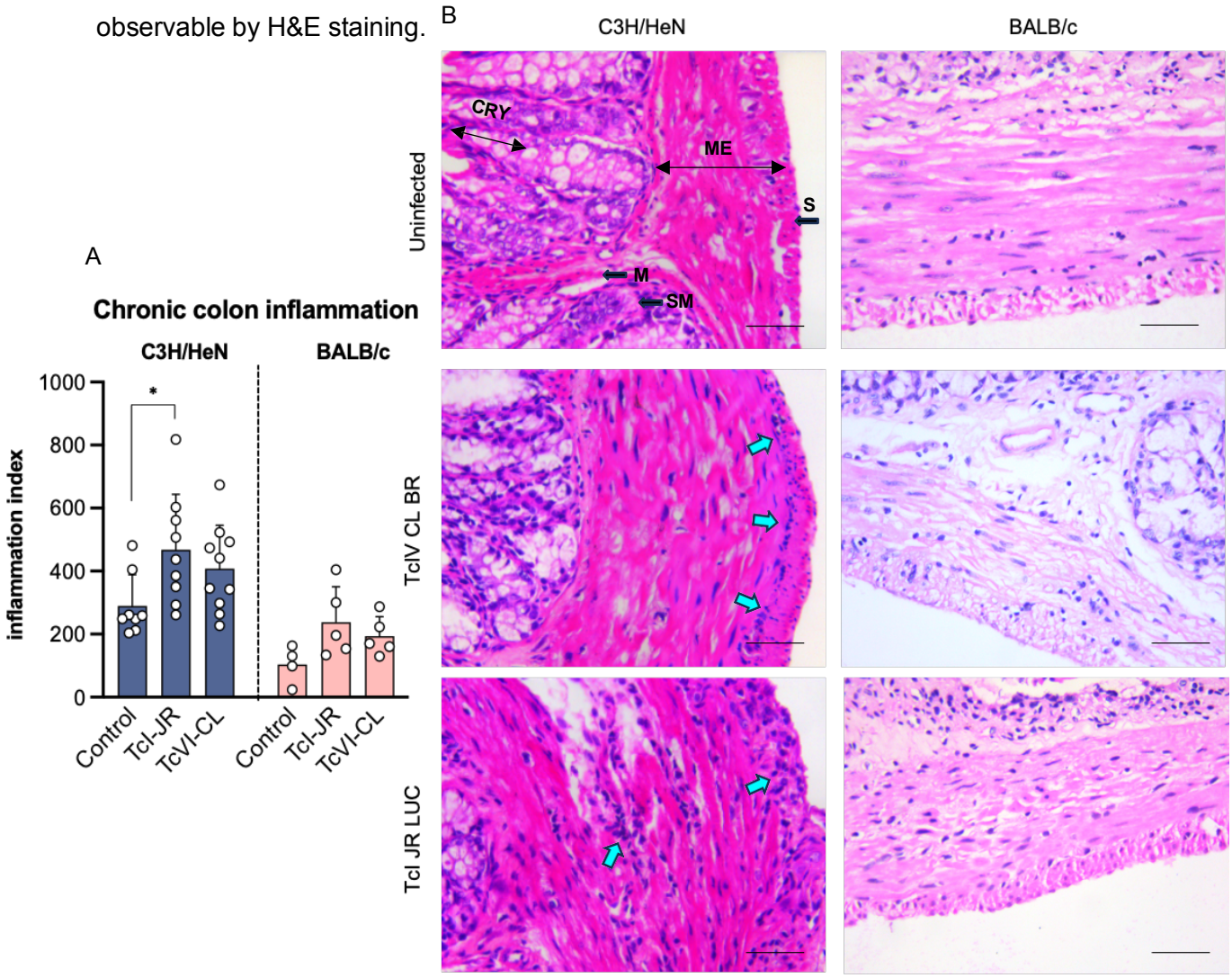

Figure 1. Chronic Inflammation in the smooth muscle layer of the colon in C3H/HeN and BALB/c mice infected with either TcI-JR or TcVI-CLBR parasites.
A) Bar chart depicting the average colonic inflammation index of each mouse parasite combination. For each mouse 15 images were taken at 400x magnification, across all 3 regions of the colon: distal, mid and proximal. 2-way ANOVA were conducted, with aterisk indicating a *p* value of 0.0128. C3H/HeN control *n=8,* TcI-C3H *n=9*, TcVI-C3H *n=10*, BALB/c control *n=4*, TcI-BALB/c *n=5*, TcVI-BALB/c *n=5.* B) Representative images of each mouse parasite combination, at 400x magnification. Sections stained with H&E. Nuclei are stained deep purple, with muscle in pink. Black arrows highlight distinct regions of a large intestine cross sections. S=Serosa, ME=Muscularis externa, SM=Submucosa, M= mucosa, CRY=crypt. Blue arrows indicating distinct inflammatory cell foci. Scale bars are 50µm. Images acquired on Leica v_4.01.

The results (Fig. 1) suggest a significant increase in cellular infiltration in the smooth muscle layer, specifically for the chronic TcI-C3H model (*p=0.0128*). This model causes the most severe digestive Chagas disease symptoms, with a consistent functional transit time delay across the duration of infection (18). The other models experience a milder, more sporadic dysperistalsis phenotype and these results show that this is associated with a lack of evidence of statistically significant pathological inflammation. During analysis, it was qualitatively observed that more cellular infiltration was regionally focal to the proximal region of the colon. To address this, both distal and proximal regions were then quantified separately (Fig. 2).

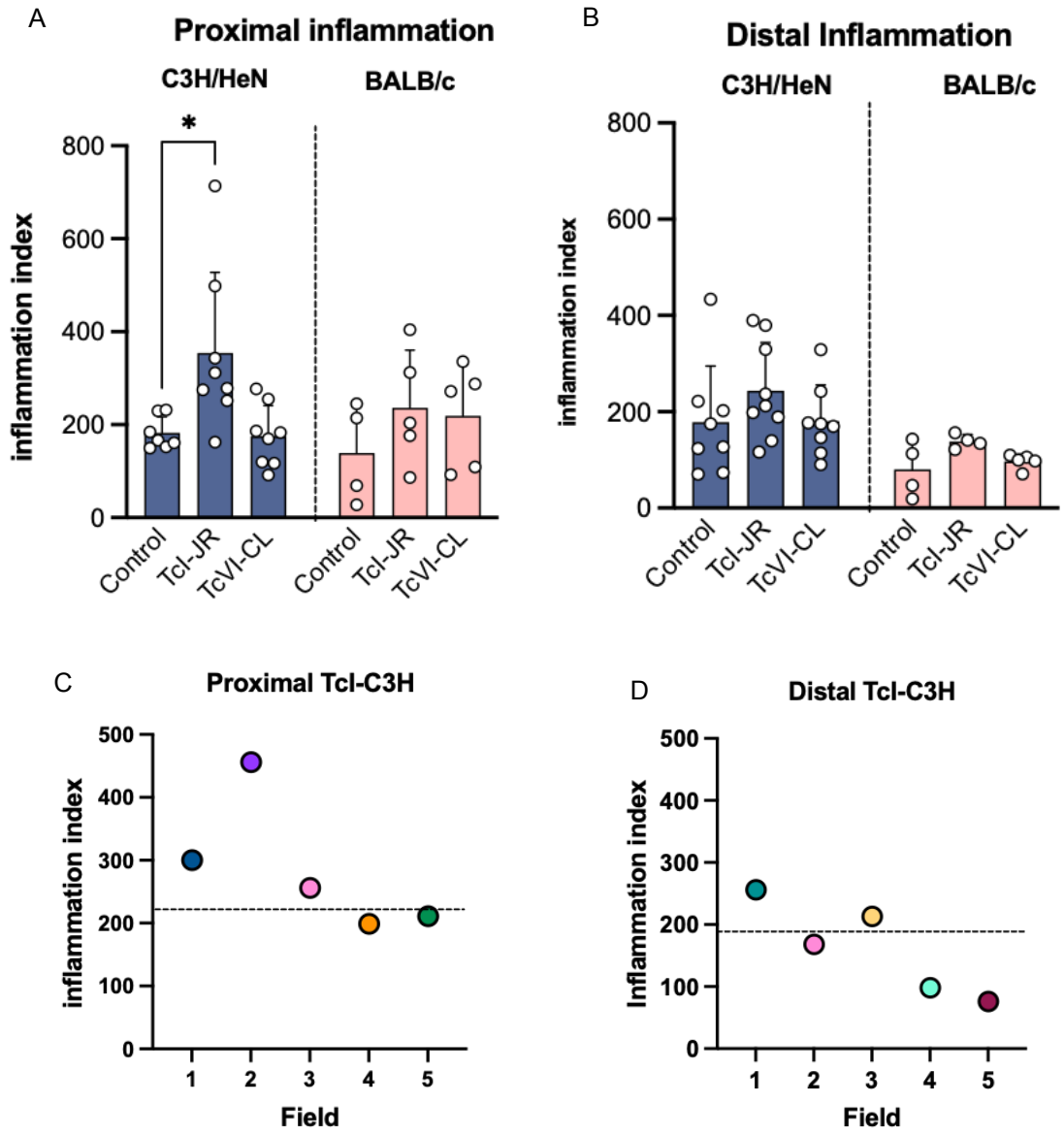

Figure 2. Regional colon specific inflammation in C3H/HeN and BALB/c mice infected with either Tcl-JR or TcVi CL parasites.
A) Bar chart depicting the average inflammation in the proximal region only, of each mouse parasite combination. 5 images taken at 400x magnification for each region for each mouse. 2-way ANOVA was conducted against Tcl-C3H. Asterisk for Tcl-JR vs control indicates a significant difference and a *p* value of 0.0161. C3H/HeN control n=8, Tcl-C3H n=9, TcVI-C3H n=10, BALB/c control n=4, Tcl-BALB/c n=5, TcVI-BALB/c n=5. B) Bar chart depicting the average inflammation in the distal region only. 5 images taken at 400x magnification for each mouse. 2-way ANOVA conducted. C). Scatter plot depicting inflammation data for each of the 5 proximal images from a single representative Tcl-C3H mouse. Dotted line represents uninfected cohort average for proximal colon cellularity only, + 2 standard deviations. D). Scatter plot depicting inflammation data for each of the 5 distal colon images from a single representative Tcl-C3H mouse. Dotted line represents uninfected cohort average for proximal colon cellularity only, + 2 standard deviations.

Upon analysing both the distal and proximal regions, it was evident that quantification of the proximal colon corroborated the qualitative observations of focal inflammation (*p=0.0161*) (Fig. 2a). There was no significant difference between any other mouse-parasite combination in the proximal region. However, although non-significant, there was an

upwards trend in distal inflammation in the TcI-C3H model (Fig. 2b). It was also observed that within the proximal region, cellular infiltration was not consistent across the smooth muscle layer, but more focally distributed (Fig. 2c). Inflammation was also not a consistent feature across the entire proximal tissue region, with, for example, only 3 of the 5 fields viewed presenting with levels of cellularity above 'normal' levels (indicated by the dotted line) in a representative mouse. Similar variability was observed across the distal region (Fig.2d), where, in the example shown, 2 of 5 fields exhibited evidence of higher cellularity than 'normal'. The high cellular counts indicative of inflammatory foci were typically most obvious in the smooth muscle of the proximal region directly adjacent to where the mesenteric adipose tissue attaches (Fig.3).

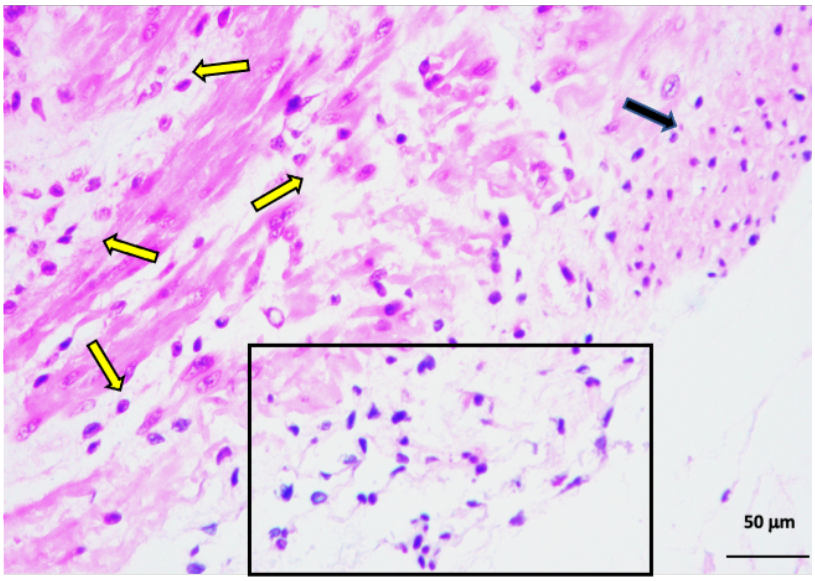

Figure 3. Mesenteric attachment region of the proximal colon in a chronic infection.
Black box indicates the mesentery tissue from a TcI-C3H mouse. Black arrow indicates a putative inflammatory infiltrate in the longitudinal muscle layer, yellow arrows indicate circular muscle layer with a sparse (normal) distribution of nuclei.

There was a high degree of parasitism of GI mesentery tissue observed in the acute phase of infection, with the lipid rich environment thought to be suitable for parasite replication and metabolic activity. Chronically infected mice have a significantly reduced mass of mesentery tissue, which is also rich with blood vessels and lymphatic system which we hypothesise to permit parasite and cellular trafficking to and from the colon (19).

In summary, there is evidence of significant, highly focal inflammation of the proximal colon in the TcI-C3H model only, which may result from lymphocyte trafficking via the mesenteric tissue, which harbours the gut-draining lymph nodes. This circumstantially links

chronic inflammation with the enduring GI transit time delay phenotype in this model. Why inflammation is greater in this model compared to the other three host-parasite strain combinations remains unknown.

Fibrosis

Collagen is present as a component of the extra-cellular matrix in all healthy tissues. It is also deposited when local inflammation triggers the wound-healing process and myofibroblasts synthesise extracellular matrix components (20). In cardaic CD, it is thought that inflammation-wound healing cycles become dysregulated, resulting in pathological levels of collagen synthesis (fibrosis) (21). It is unclear if this also occurs in GI Chagas pathology, so I used a collagen stain to assess if fibrosis is a feature of DCD in our models.

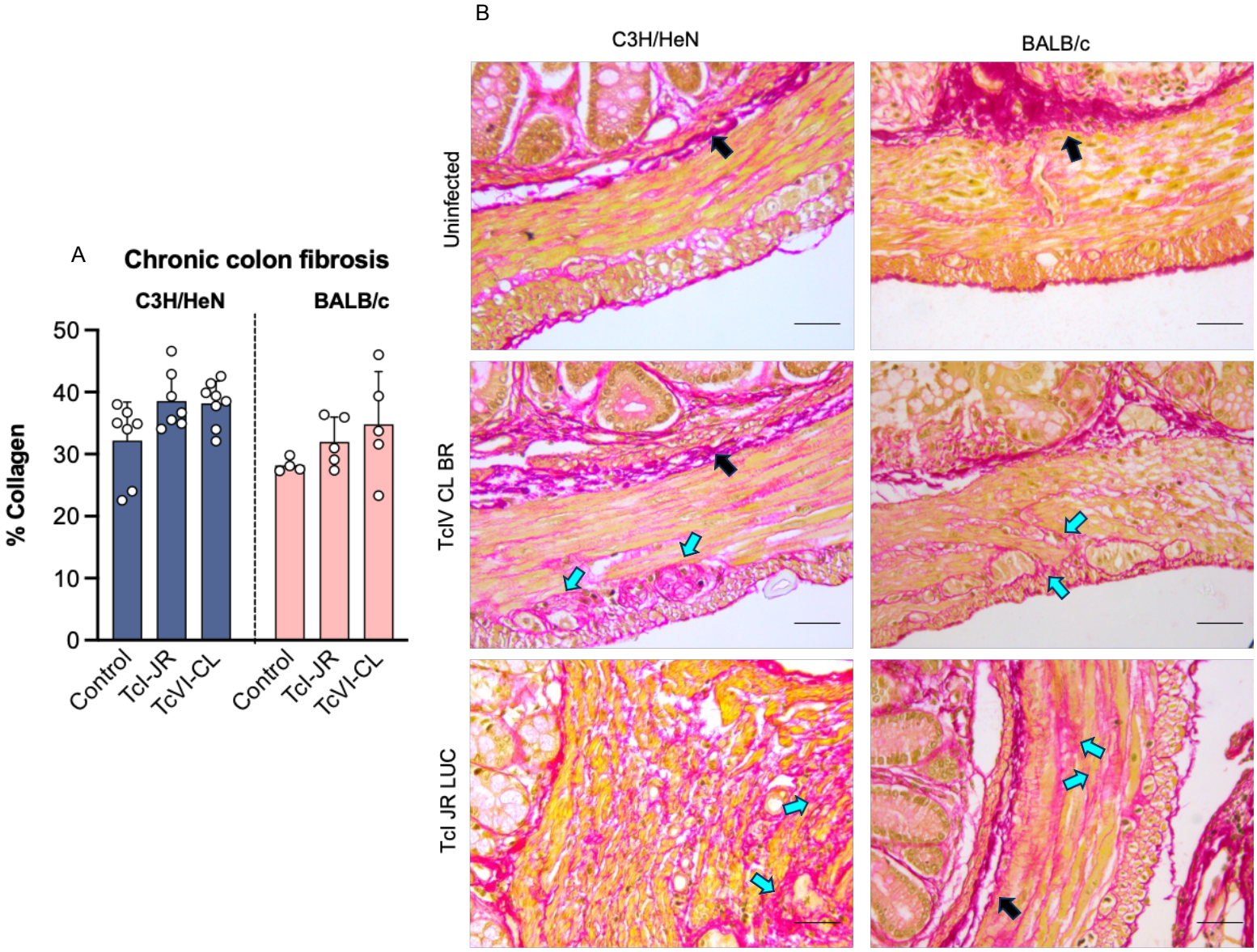

Figure 4. Analysis of collagen content in the smooth muscle layer of the colon in C3H/HeN and BALB/c mice infected with either Tcl-JR or TcVI CL parasites.
A) Bar chart depicting the average percentage of collagen in the colon smooth muscle layer, in each mouse parasite combination. For each mouse 15 images were taken at 400x magnification, across 3 regions of the colon: distal, mid and proximal. A 2-way ANOVA was conducted with no significant differences noted. The mucosal and sub-mucosal layers were manually excluded from image analysis, with a percentage of red/pink pixels being calculated within the longitudinal and circular muscle layers only. C3H/HeN control *n=7* Tcl-C3H *n=7*, TcVI-C3H *n=8*, BALB/c control *n=4*, Tcl-BALB/c *n=5*, TcVI-BALB/c *n=5*. B) Representative images of each mouse parasite combination, at 400x magnification. Sections were stained with PSR. Collagen in pink, and muscle in yellow. Black arrows indicate normal 'band' of sub-mucosal collagen, situated amongst the muscularis mucosae and submucosal plexus. Blue arrows indicate examples of distinct foci of putative excess collagen accumulation within the muscle layer.

An initial question was whether potential changes in collagen content were a result of increased synthesis, or muscle thicknessing/oedema distributing the natural collagen over a larger surface area. The image analysis software that was used does not consider the pixel intensity, only the area occupied by a colour range over a defined threshold. I decided to calculate a percentage of collagen in the smooth muscle layer only as a means of normalising the data whereby images that feature more muscle layer in an image do not skew the data. The results suggested that there were putative foci of excess collagen deposition and the Tcl-C3H model exhibited the highest proportion of smooth muscle collagen, with a 6.3% increase compared to the uninfected control. Nevertheless, overall there was only a non-significant trend towards an increase in average collagen content in the smooth muscle layer of all infected mice compared to uninfected controls (Fig. 4A). As was observed with inflammation, the proximal region was qualitatively a focal region for increased collagen accumulation. To address this, proximal only data were plotted to quantify this regional effect (Fig. 5).

Like the focal inflammation, the distribution of fibrosis was not uniform across the entire muscle layer of all regions of the colon. Although there was no significant increase in average collagen accumulation in the colon overall (proximal, mid- and distal regions combined) for any mouse parasite combination (Fig.4), there was a significant increase specifically in the proximal region of the Tcl-C3H model (*p=0.0278*) (Fig. 5a). Even in the proximal region of the Tcl-C3H model, there was heterogeneity in the location where foci of increased collagen content were observed (Fig. 5b). This is visualised more easily in Fig. 5c which is a complete transverse section of a proximal colon from a Tcl-infected C3H mouse. Directly adjacent to where the mesentery tissue attaches is a high degree of tissue disruption, smooth muscle hyperplasia and fibrosis, which is not observed in the rest of the tissue. Thus, although there was no correlation in total colon inflammation and fibrosis, there was a significant increase in both cellular infiltration and collagen accumulation in the

proximal colon region in the TcI-C3H model, again circumstantially linking these pathological phenomena to the DCD dysperistalsis phenotype.

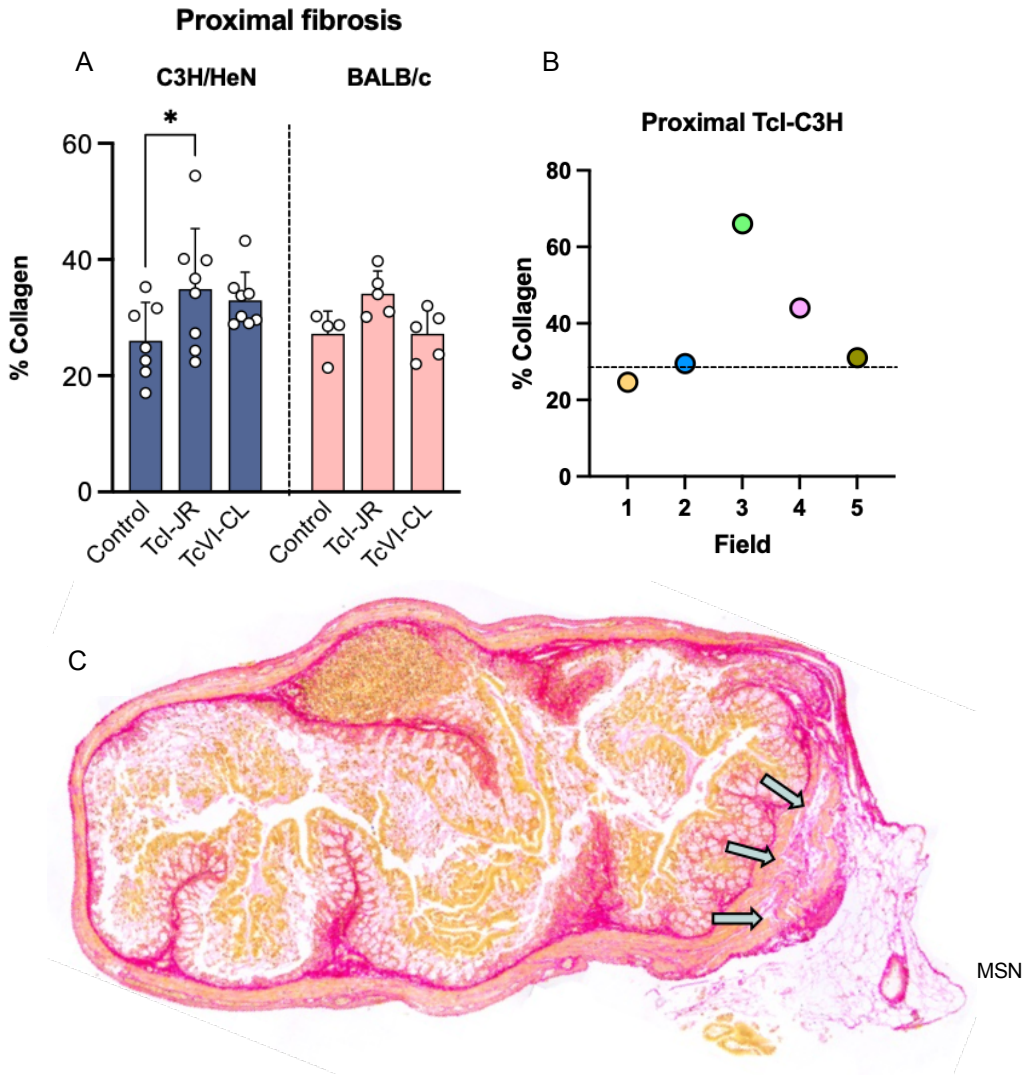

Figure 5. Regional fibrosis in the proximal colon of a chronically infected TcI-C3H mouse
A) Bar plot depicting the percentage of collagen in the smooth muscle layer of the proximal colon only. 2-way ANOVA conducted and the asteriks for TcI-JR vs control indicates a *P* value of 0.0278. C3H/HeN control *n=7*, TcI-C3H *n=8*, TcVI-C3H *n=8*, BALB/c control *n=4*, TcI-BALB/c *n=5*, TcVI-BALB/c *n=5*. B) Scatter plot depicting collagen percentage data for each of the 5 proximal images from a single representative TcI-C3H mouse. Dotted line represents uninfected cohort average, + 2 standard deviations. C) A low magnification image (25X) of a TcI-C3H infected proximal colon. Arrows indicate muscle layer disruption and collagen accumulation next to mesentery (MSN) attachment zone.

Little is known about the interaction between gut immunology, *T. cruzi*, and the resulting DCD pathology. The results of the Arantes et al (2004) study, whereby iNOS was noted as a critical mediator of enteric denervation, is the leading theory, but only the acute phase was studied (Introduction). I used an anti-iNOS antibody in immuno-histological analysis to assess whether iNOS expression differs between the different parasite-mouse strain combinations.

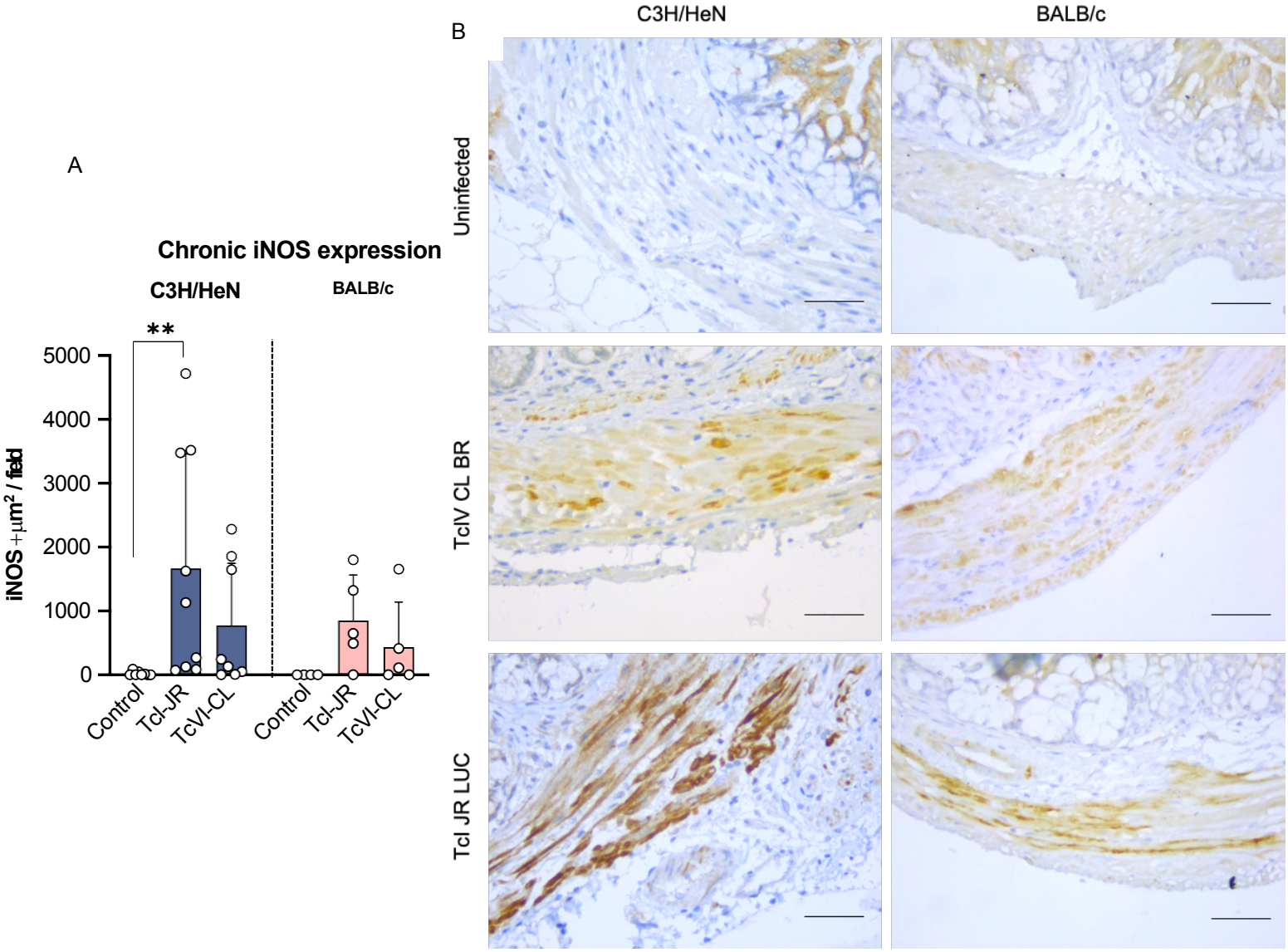

Figure 6. Chronic iNOS expression in the smooth muscle layer of the colon in C3H/HeN and BALB/c mice infected with either Tcl-JR or TcVI CL parasites.
A) graph depicting the average iNOS expression intensity, by area of positive signal, in each mouse parasite combination. The area of the total field was $6.7x10^4$ μm^2, and only the smooth muscle layer was analysed with the rest of the tissue manually excluded. For each mouse, 15 images were taken at 400x magnification, 5 images for each of the 3 regions of the colon: distal, mid and proximal. 2-way ANOVA was conducted, and the 2 asteriks indicate a *P* value of 0.0082. C3H/HeN control *n=8*, Tcl-C3H *n=9*, TcVI-C3H *n=8*, BALB/c control *n=4*, Tcl-BALB/c *n=5*, TcVI-BALB/c *n=5*. B) Representative images of each mouse parasite combination, at 400x magnification. Sections stained with 1:50 anti-iNOS antibody, visualised by oxidised 3,3'-Diaminobenzidine (DAB) precipitate (brown). Tissue counterstained with haematoxylin. Scale bars are 50µm. Images acquired on Leica v_4.01.

The global iNOS expression in the TcI-C3H infected colon smooth muscle layer was significantly higher compared to uninfected control (*p=0.0082*), and the data suggest there is 45% more iNOS protein compared to the TcVI-C3H model (Fig. 6A).

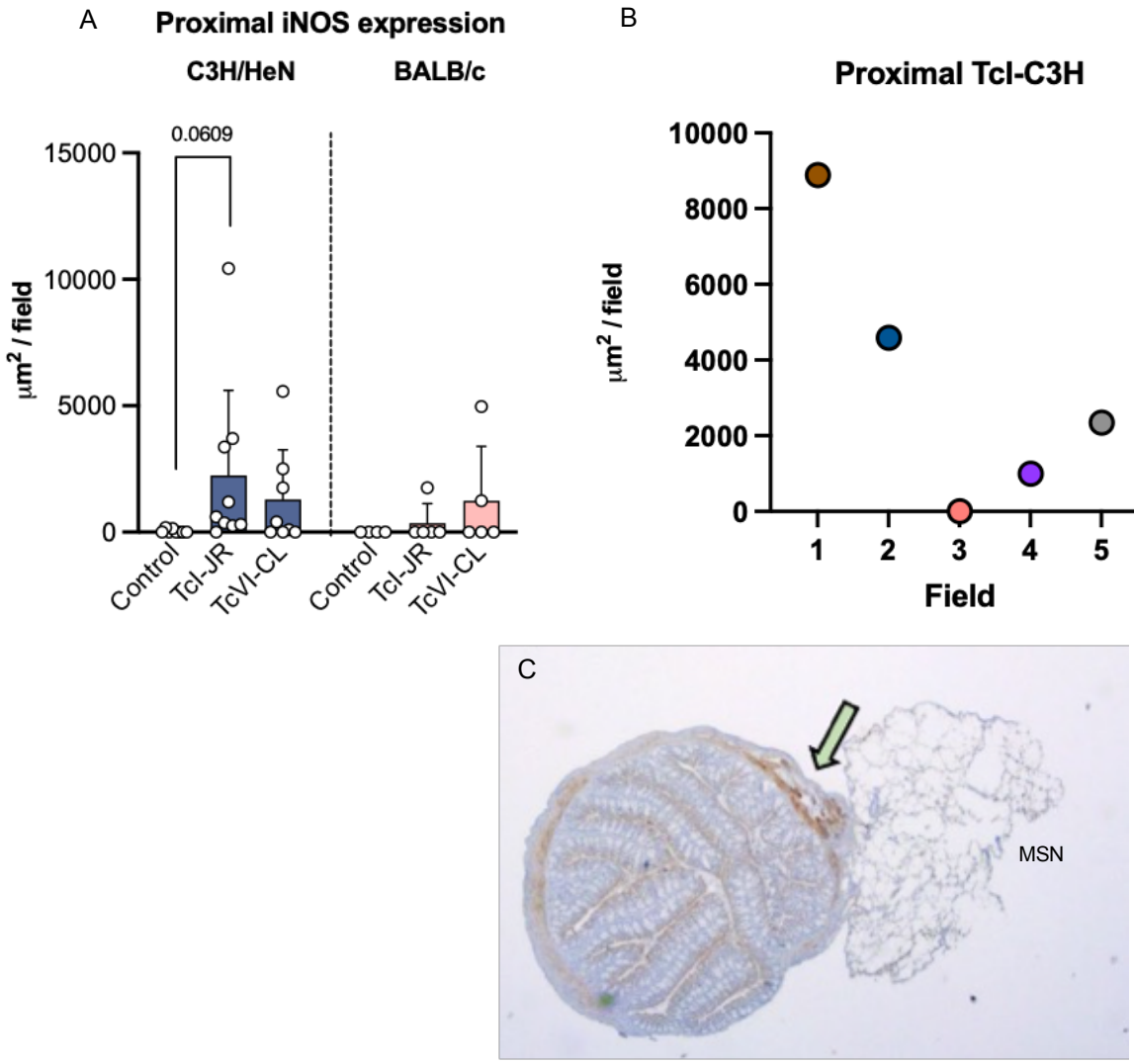

Figure 7. Proximal specific iNOS expression in the smooth muscle layer of a TcI-C3H mouse.
A) Bar plot depicting the area occupied by iNOS+ staining in the smooth muscle layer of the proximal colon only. 2-way ANOVA was conducted and there was no significant difference in any of the groups. C3H/HeN control *n=8*, TcI-C3H *n=8*, TcVI-C3H *n=8*, BALB/c control *n=4*, TcI-BALB/c *n=5*, TcVI-BALB/c *n=5*. B) Scatter plot depicting the distribution of iNOS specific staining across each of the 5 proximal images from a single representative TcI-C3H mouse. C) A low magnification image (25X) of a TcI-C3H infected proximal colon. Arrows indicate intense iNOS expression directly adjacent to mesentery attachment (MSN).

The regional data (Fig. 7A) suggested there was no significant difference in iNOS expression in the proximal region of the colon; however, an overall trend of upregulation was evident (*p*=0.0609). As was the case with other pathologies analysed, iNOS expression was often highly focal, with intense positive signal being predominantly observed in the region where the mesentery tissue attaches to the proximal colon (Fig. 7C).

Enteric innervation analysis

Denervation is a well-documented feature of human DCD, but there is little known regarding the underlying mechanisms. However, some of the functional deficits and clinical manifestations of DCD have been reproduced in experimental mouse models (18). I next investigated whether enteric denervation correlated with the hyperfocal inflammation shown in my H&E and iNOS staining seen in the Tcl-C3H model by utilising a neuronal-specific tubulin antibody (TuJ-1) in an immunohistochemistry (IHC) analysis.

The immunohistochemical staining of the enteric ganglia showed a significant reduction of enteric neuronal TuJ-1 specific signal in the Tcl-C3H model (*p=0.0178*). (Fig. 8a). Similar to the other pathologies, there was a distinct regional focus for the loss of TuJ-1, which was significant only in the proximal colon (Fig. 8b). A qualitatively observed phenotype was the absence of TuJ-1 staining within some enteric ganglia, referred to as the 'white-space' phenotype. This is clearly seen by the black arrows above (Fig. 8c), where the integrity of the ganglia looks disrupted compared to the dense, regular staining seen in the uninfected control.

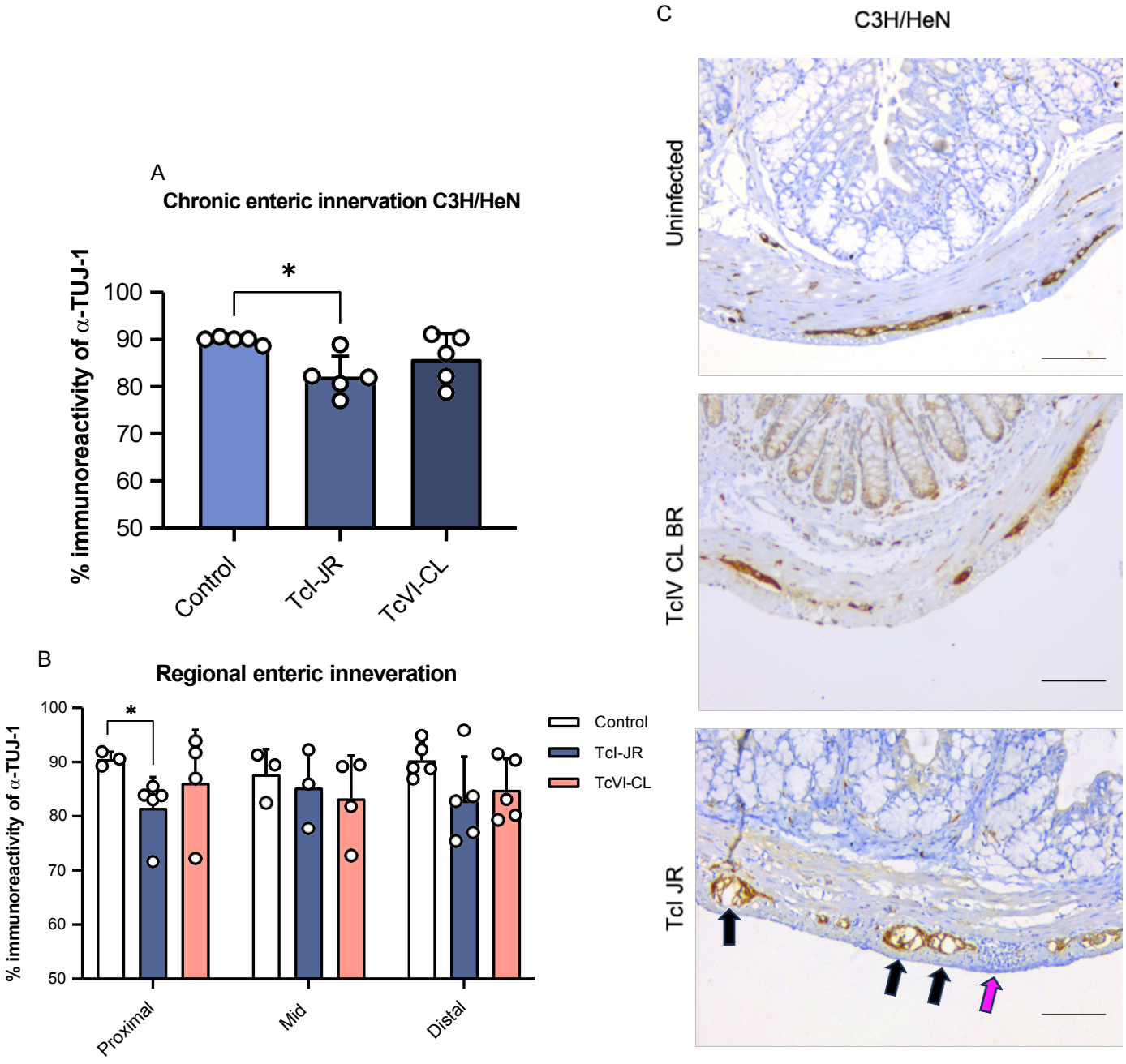

Figure 8. Innervation analysis of the enteric nervous system in the large intestine of C3H/HeN mice infected with either TcVI-CL or TcI-JR parasites.

A) Bar plot depicting the % of positive immunoreactivity of the anti-TuJ1 antibody within the myenteric plexus region. Every myenteric ganglion observed in a section was quantified. An unpaired T-test was conducted, and a significant reduction of immunoreactivity was observed in the TcI-C3H model. Asterik indicates a *p* value of 0.0178. B) The breakdown of total innervation analysis by region. One way ANOVA was conducted, and star indicates *p* value of 0.0494. *n=5* for each group. C) Representative images for each group. Pink arrow pointing to distinct pocket of cellular infiltration adjacent to an enteric neuronal ganglion exhibiting a “white space” phenomenon, depicted by black arrows. Images 200X magnification

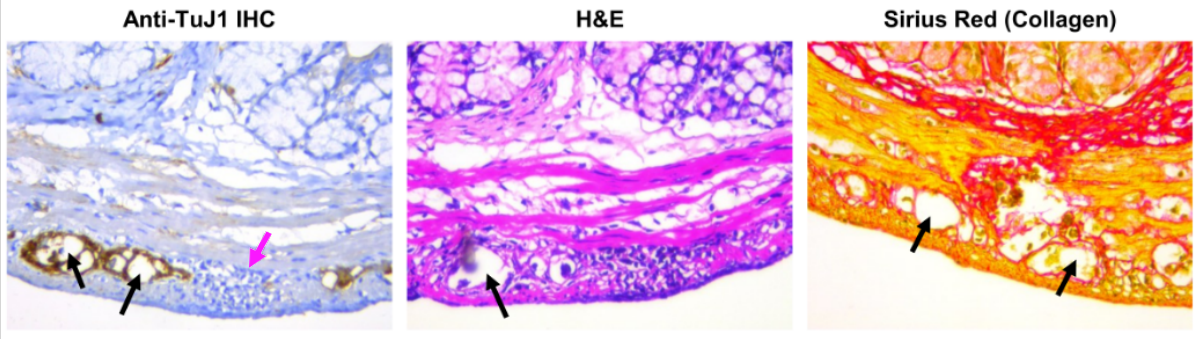

Figure 9. 'White-space' phenomena within enteric ganglia in the TcI-C3H model.
The white space is refractory from conventional histological dyes. On the left panel is the anti-TuJ-1 immunohistochemical stain. Middle panel is a successive section, 5µm deeper than the first panel, stained with H&E. Right panel is a 5µm tissue section taken successively from the one depicted in the middle panel, stained with Picrosirius red. All images taken at 400X magnification.

These intra-ganglionic 'white space' regions were also refractory to conventional histological dyes (Fig. 9). This suggests that the phenotype is not just an absence of neuronal specific tubulin, but the absence of any cells or extracellular matrix. The localised pocket of inflammation directly adjacent to one of these ganglia, indicated by the pink arrow (Fig. 8C, Fig. 9), suggests there is a causative link between the local immune response and the disrupted ganglion phenomenon. In total this was observed in roughly 10% of TcI-C3H ganglia, with varying degrees of cellular ablation.

However, it must also be considered that these 'white space' phenotypes may be artifacts or 'retraction' of nuerons during tissue processing. Moreover, given the absence of higher magnification images, it is difficult to make any conclusive claims regarding the determinants of this 'white space'. Other possibilities include local adipocytes, swelling or vascular changes to muscle fibers, break-off friable tissue, or necrotic muscle tissue. Also, since this phenotype was observed in other models and in periganglionic regions (such as the longitudinal muscle), alternative theories will have to be considered.

In summary, the overall trend suggests neuron specific immunoreactivity is reduced in the TcI-C3H model, potentially associated with the enigmatic 'white-space' phenotype. This correlates with an increase in inflammation, iNOS expression and dysperistalsis in the same model. Each pathology investigated presents with a degree of variability from mouse to mouse, which is also characteristic of the human disease.

Acute stage inflammation and iNOS expression

After determining GI pathology in the chronic phase of infection, H&E and iNOS expression were also assessed in samples from an acute infection experiment. I focussed on the TcI-C3H and TcVI-BALB models, our high morbidity and low morbidity DCD models respectively.

Unlike the chronic phase, during the acute phase there is a widely disseminated infection, with parasites present in most tissues throughout the body. By 6 weeks post infection, there is already a functional GI transit delay in the TcI-C3H model (18), indicating that enteric pathology is sufficiently established within this early timeframe. However, there was no significant increase in cellular infiltration detected in the smooth muscle layer of this DCD model (*p=0.0845)*, but there was a distinct upwards trend (Fig. 10A). Conversely, in closer alignment with the chronic phenotype, there was a significant increase in iNOS expression in this model (*p=0.0015*) (Fig10.B). Thus, iNOS expression appears to be a better correlate of dysperistalsis than generalised inflammation intensity.

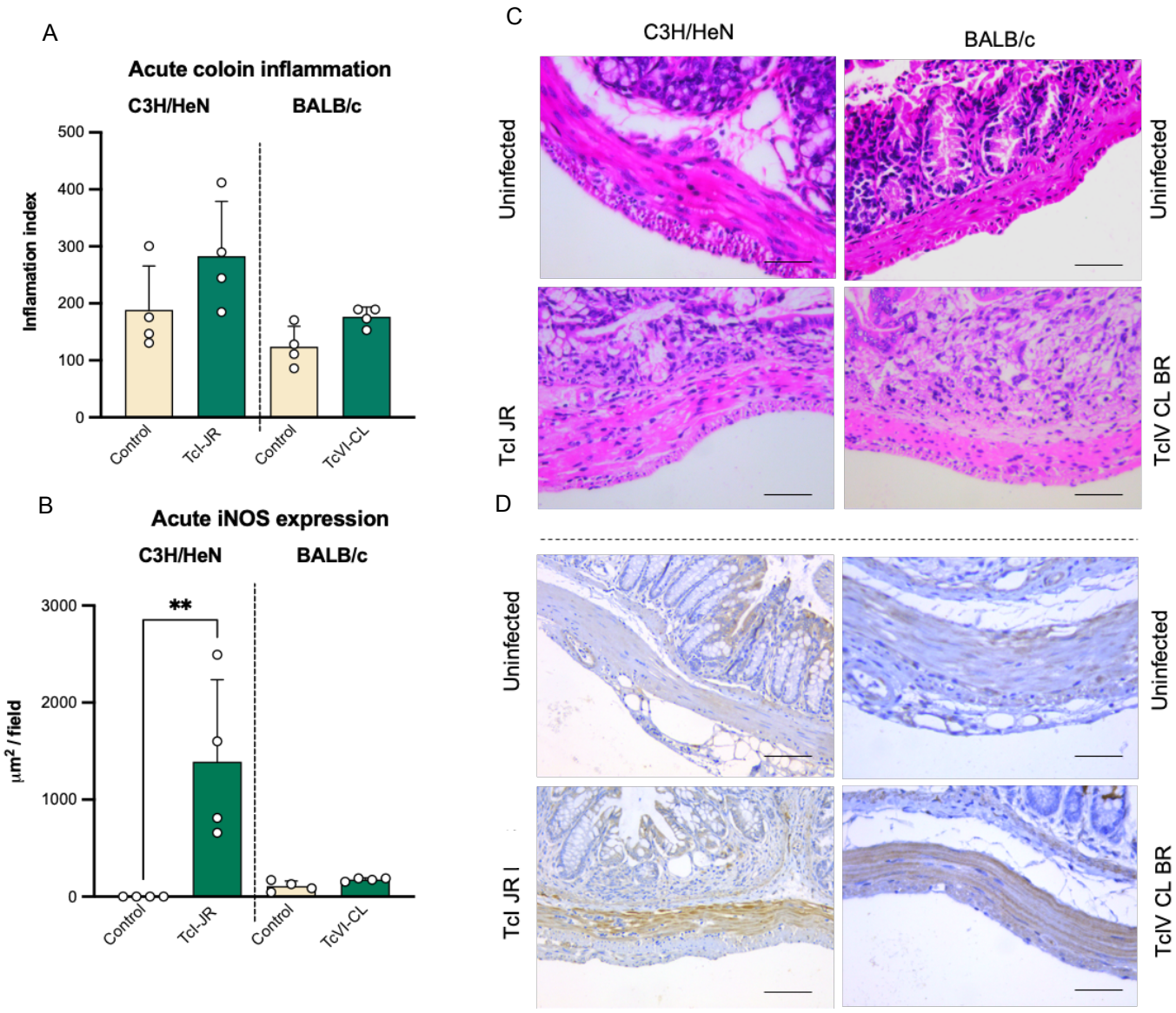

Figure 10. Acute colon Inflammation and iNOS expression in DCD smooth muscle.
All samples are from 6 weeks post infection. A) Bar plot depicting inflammation score of C3H/HeN and BALB/c mice infected with Tcl-JR and TcVI-CL parasite respectively. One way ANOVA was conducted and no significant difference was observed (*p=0.0845* for Tcl-JR vs control in C3H). C3H/HeN control *n=4*, Tcl-C3H *n=4,* BALB/c control *n=4*, TcVI-BALB/c *n=4*. B) Bar plot depicting iNOS expression by area of smooth muscle layer. One way ANOVA was performed, and asteriks indicate a significant difference, with *P* value of 0.0015. C) Representative images of acute colon sections stained with H&E to visualise cellular infiltrates in purple. D) Representative images of acute colon sections stained with anti-iNOS antibody, with specific positive signal visualised by brown DAB precipitate. All images taken at 400X magnification Scale bar=50µm

Acute colonic immune system gene expression

Work conducted by my supervisor (Dr Michael Lewis), with the objective of garnering a broader understanding of the immunological microenvironment in the *T. cruzi*-infected colon, employed the use of NanoString technology to evaluate the expression levels of 547 genes related to the immune system. This technology entailed the use of oligonucleotide probes tagged with gene-specific fluorochrome 'barcodes', which allowed for highly multiplexed mRNA quantification in bulk RNA extracted from colon tissue. The barcode probe-hybridised RNA molecules were digitally counted allowing for analysis of expression levels between different experimental groups. This approach was used to compare naïve C3H/HeN and BALB/c mice against the TcI-C3H (high morbidity) and TcVI-BALB/c (low morbidity) models at 7 weeks post infection (Fig.11). The results from these experiments yielded a series of differentially expressed genes (DEGs) that became candidate factors involved in a) parasite persistence in the colon i.e. DEGs shared in both infection models, and b) development of the DCD phenotype i.e. DEGs uniquely seen in the TcI-C3H model. Two genes of interest from these data were selected, which I carried forward to investigate at a protein level.

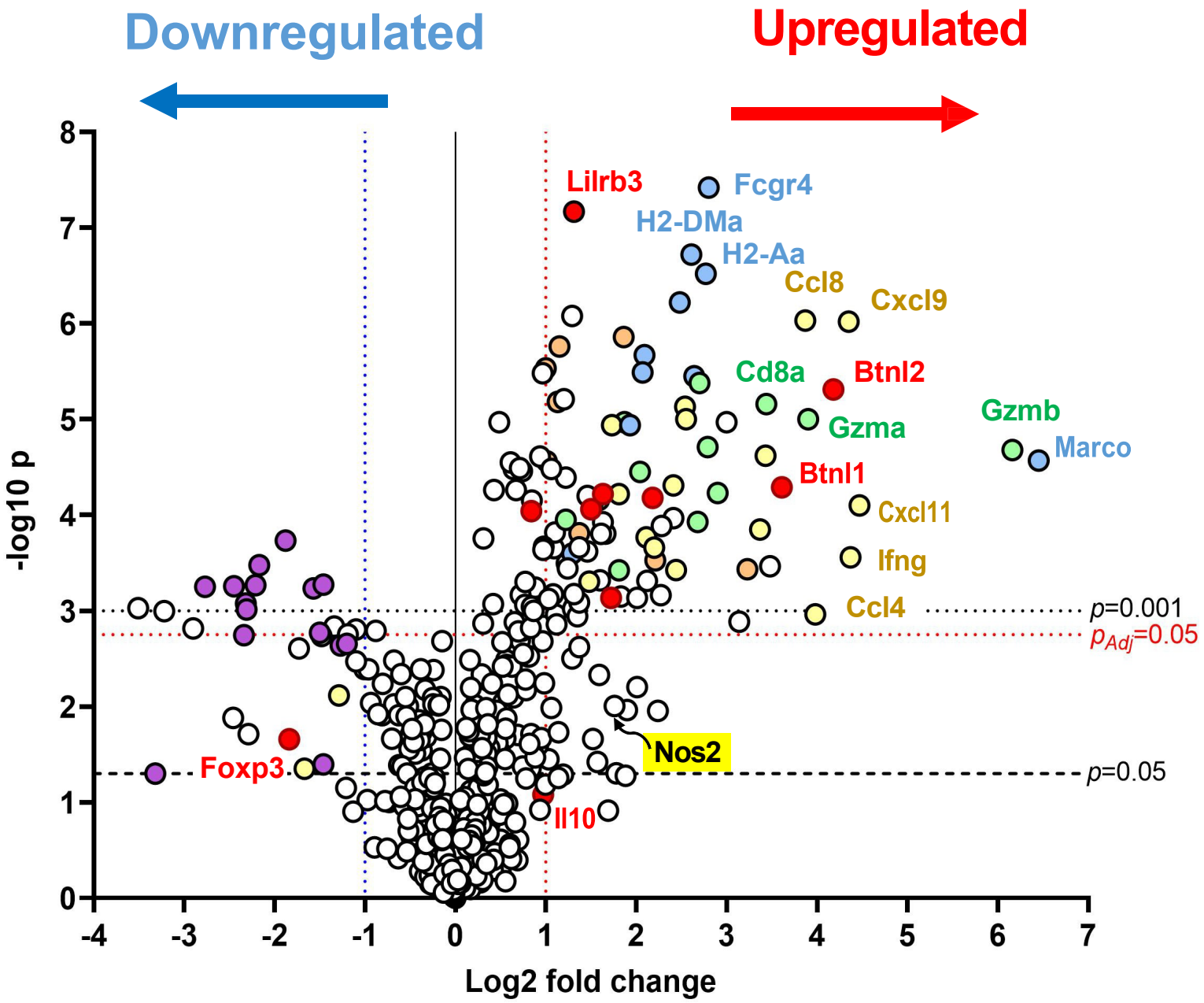

- Cytokines + receptors
- Myeloid APCs/MHC-II
- Cytotoxic lymphocytes
- B cells
- Complement-related
- Deactivating / anti-inflammatory factors

Figure 11. Immune response in the C3H/HeN colon at 7 weeks post infection. A volcano plot depicting the fold change of RNA expression in colon tissue from the DCD model (n=3), compared to naïve C3H control (n=3). All points on the right of the solid vertical black line are upregulated markers, and all points on the left are downregulated, indicated by red and blue arrows respectively. Red dotted line represents an adjusted *p* value of 0.05, acting as a threshold for significantly altered expression levels. Figure legend shows colours assigned to different families of immune markers.

Data courtesy of Michael Lewis, unpublished

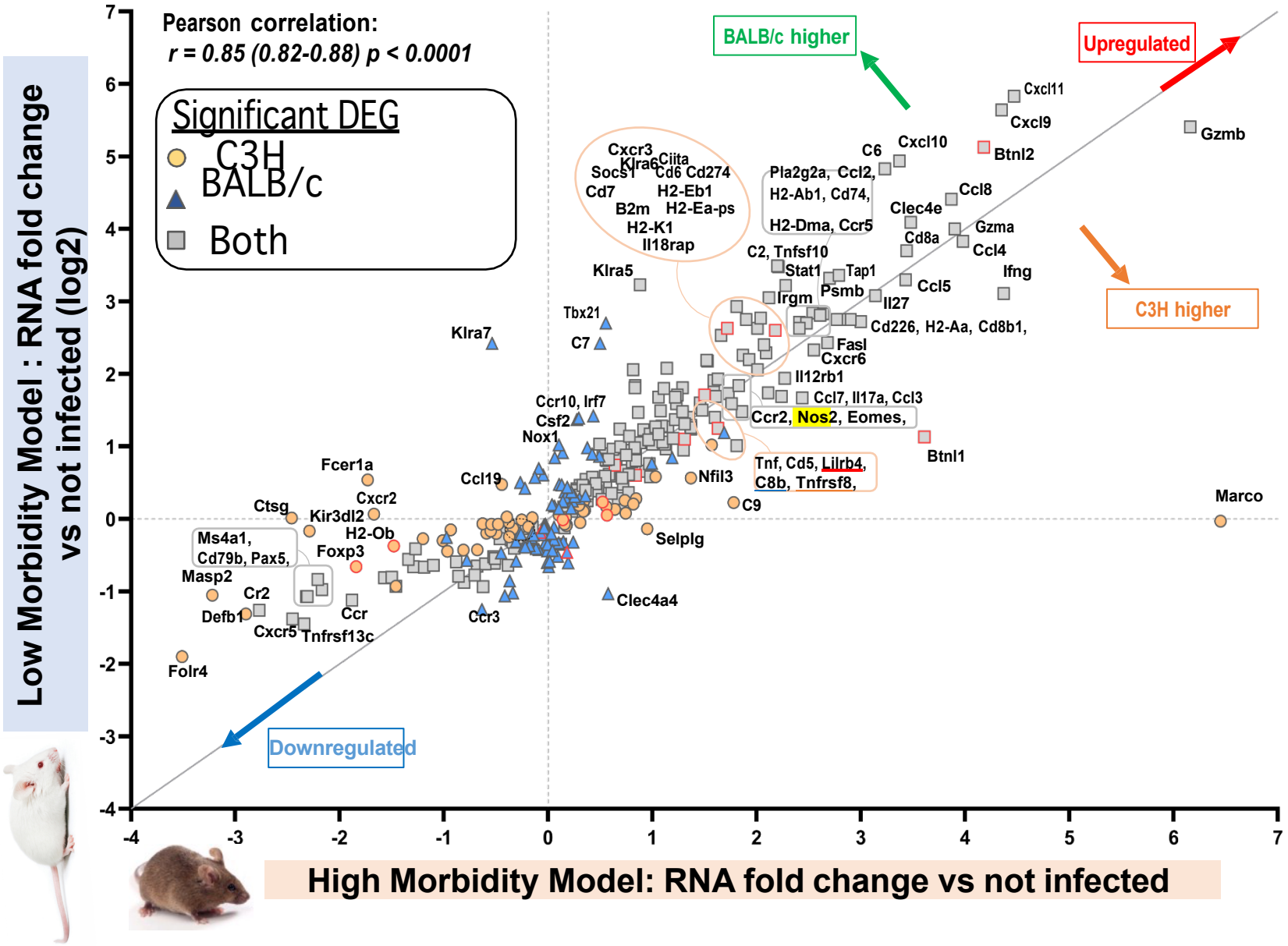

Figure 12. Relative gene expression levels associated with colon immune responses in TcI-JR-infected C3H/HeN and TcVI-CLBR-infected BALB/c mice at 7 weeks post infection. Each data point represents an individual gene for which the x co-ordinate indicates fold-change expression in infected vs naïve C3H control and the y co-ordinate indicates fold-change expression in infected vs naïve BALB/c control. Points on the diagonal line of equivalence are differentially regulated (vs naïve control) to the same extent in both models. Points above the diagonal line of equivalence are more strongly differentially regulated (vs naïve control) in the TcVI-CLBR-infected BALB/c low morbidity model. Points below the diagonal line of equivalence are more strongly differentially regulated (vs naïve control) in the TcI-JR-infected C3H/HeN high morbidity model. *Data courtesy of Michael Lewis, unpublished*

From the volcano plot (Fig. 11) and model comparison plot (Fig. 12) there were clear similarities between the colonic immune gene expression profiles in both models. Chemokines (*Cxcl9,10,11, Ccl5,8*) and markers associated with cytotoxic lymphocytes (*Cd8a, Gzma, Gzmb*) were amongst the most highly upregulated genes in both models, consistent with the well-established role for CD8+ T cells in the control of *T. cruzi* infections. Interestingly, there was also an observed downregulation of multiple B-cell specific markers (e.g. *Cd19, Pax5, Cd79b*) in both models compared to uninfected control mice. *Nos2* was significantly upregulated in both models, but slightly higher in the TcI-C3H model. There was a 1.59-fold increase in the TcVI-BALB model, and 1.76-fold increases in the TcI-C3H model (Fig.11&12). *Nos2* gene expression does not therefore stand out against the full data set as a potential determinant of DCD severity, in contrast to the iNOS IHC-based protein expression data (Fig. 10b). This discordance could be due to week 7 being a late window for detection of *Nos2* gene transcriptional changes, and/or the iNOS protein (and enzyme activity) may be regulated more by post-transcriptional/ translational mechanisms in the different models.

Two genes stood out as being far more strongly upregulated in the high morbidity DCD model (TcI-JR-C3H) than in the low morbidity model (TcVI-CLBR-BALB/c): *Btnl1* (*butyrophilin-like 1*) and *Marco* (*Macrophage Receptor With Collagenous Structure*) (Fig. 12). These were also highly significantly upregulated compared to uninfected controls (Fig. 11)

Butyrophilins are a family of membrane proteins that contribute to immuno-modulation and homeostasis of T-cells, particularly y8-T cells (22). Both *Btnl1* and

Btnl2 were significantly upregulated in the infected C3H colon (Fig. 11), suggesting that butyrophilin-mediated suppression of T-cell activity might be important in a colon specific context in the DCD model. However, *Btnl2* was similarly upregulated in the mild morbidity model whereas *Btnl1* was much more specific to the TcI-C3H high morbidity model (Fig. 12). To our knowledge a role for butyrophilins in Chagas disease has not previously been identified.

Marco was the most strongly upregulated marker in the whole TcI-C3H data set (87-fold vs naïve control). MARCO is a scavenger receptor found on certain subsets of macrophages and acts as a pattern recognition receptor. MARCO regulates phagocytosis and mediates binding and ingestion of unopsinised particles (23). To our knowledge a role for MARCO in Chagas disease has not previously been identified.

Therefore, we hypothesised *Btnl1* and *Marco* were two primary candidates for differentially expressed genes in the TcI-C3H model that could be part of the mechanism of DCD pathogenesis.

Colonic smooth muscle BTNL1 expression

Using immunohistochemistry, colon and oesophagus tissue sections were stained with anti-BTNL1 antibody donated from the Francis Crick Institute (Prof A. Hayday). Tissue from mice culled 7-weeks post infection were used, and the expression of BTNL1 was quantified in the smooth muscle layer of the large intestine only.

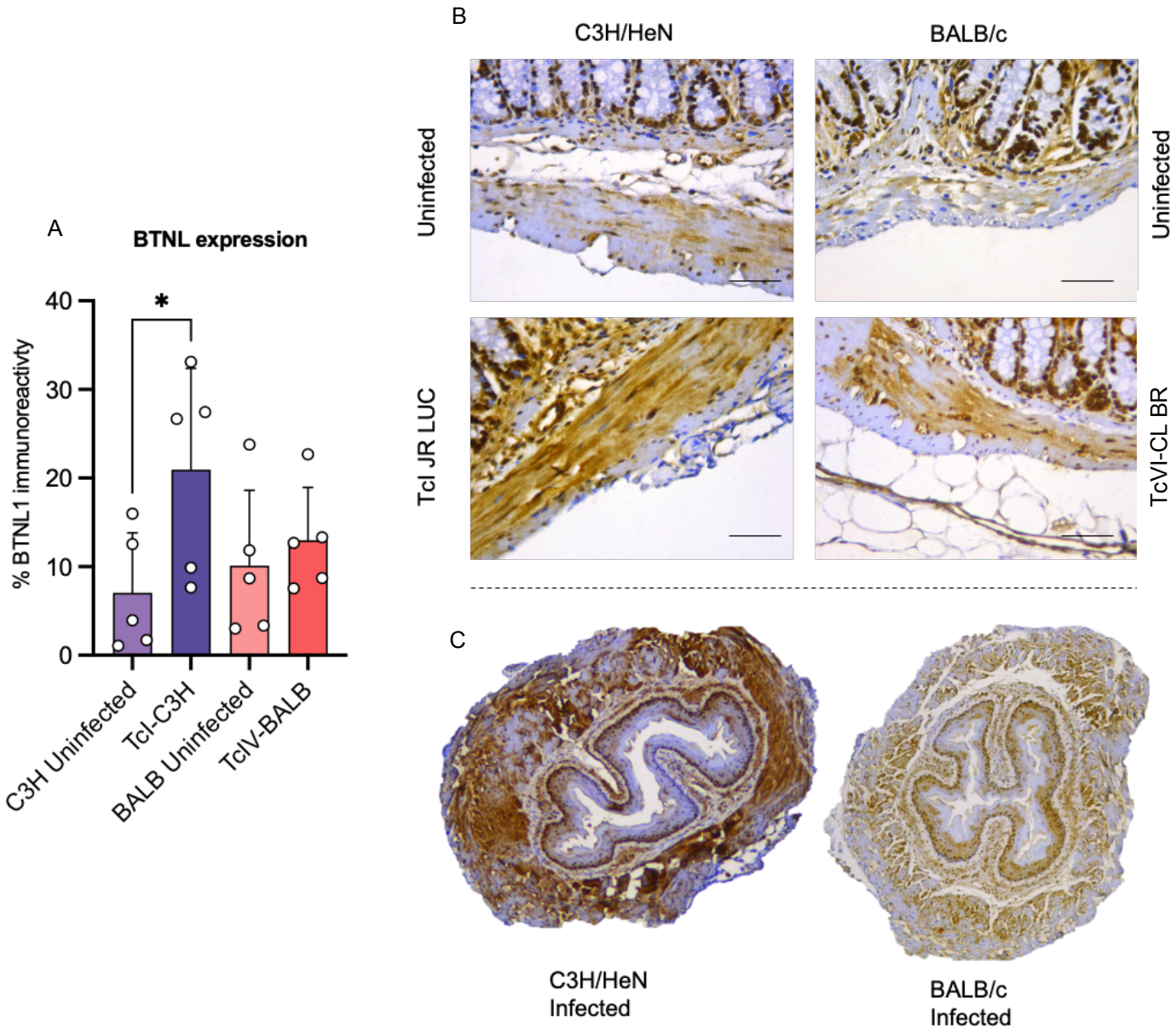

Figure 13. BTNL1 expression in the GI tract from Tcl-C3H and TcVI-BALB/c infection models, with uninfected controls. A) % positive BTNL1 immunoreactivity in the smooth muscle layer only of the large intestine; mucosal layer was excluded from analysis. all groups *n=5*. Unpaired t-test was conducted between each group: the asterik indicates a significant difference between C3H uninfected and Tcl-JR, with a *p* value of 0.0475. Tcl-C3H vs TcVI-BALB was non-significant with a *p* value of 0.2041. There was no significance between the uninfected groups (*p* value of 0.5454). B) Representative images of each experimental group at 400X. BTNL1 specific expression is visualised by oxidised 3,3'-Diaminobenzidine (DAB) precipitate (brown), using a primary antibody concentration of 1:1000. Counterstained with haematoxylin. Scale bar: 50µm C) Low magnification (25x) images of oesophagus from Tcl-C3H and TcVI-BALB mice stained with anti-BTNL antibody.

The corresponding representative images for both the infected groups (Fig. 13B, bottom two panels) shows that BTNL1 signal was intense in the circular muscle, but not in the longitudinal muscle layer. Despite a similar staining pattern, there was observationally more intense and diffuse staining in the TcI-C3H model, which translated to a 21% positive BTNL1 immunoreactivity across the smooth muscle layer of the colon. As was the case with all other analyses conducted thus far, there was a high degree of variability and heterogeneity within each group, including the uninfected. Although not quantified, there was a qualitative difference in BTNL1 expression in the oesophagus between the two infected groups (Fig. 13C). Positive signal was observationally diffuse in both groups, but staining intensity was seemingly greater in the TcI-C3H group. It is important to note that although the NanoString RNA data was used to inform BTNL1 as a prospective immunological candidate for important host-pathogen interactions in the DCD model, in this experiment we used tissue from mice infected one-week longer than those used for RNA expression.

Quantitatively, there was a 3-fold increase in BTNL1 specific signal between the TcI-C3H and C3H uninfected groups ($p=0.0475$) (Fig.13a). There were no other significant differences between any of the other experimental groups. However, there was a 1.6-fold increase in expression in TcI-JR compared to TcVI-BALB ($p=0.2041$). The relative protein expression levels between groups are therefore broadly comparable to the RNA-based Nanostring data (Fig. 12).

Smooth muscle MARCO expression

According to the NanoString data, a massive upregulation of colonic *Marco* RNA was specific to C3H/HeN mice infected with Tcl-JR parasites at 7-weeks post infection (Fig. 12). Here we used immunohistochemistry on the same experimental groups as we did for BTNL1; 7-week post infection mice. Analysis was limited to the smooth muscle layer, with the sub-mucosal and mucosal layers excluded.

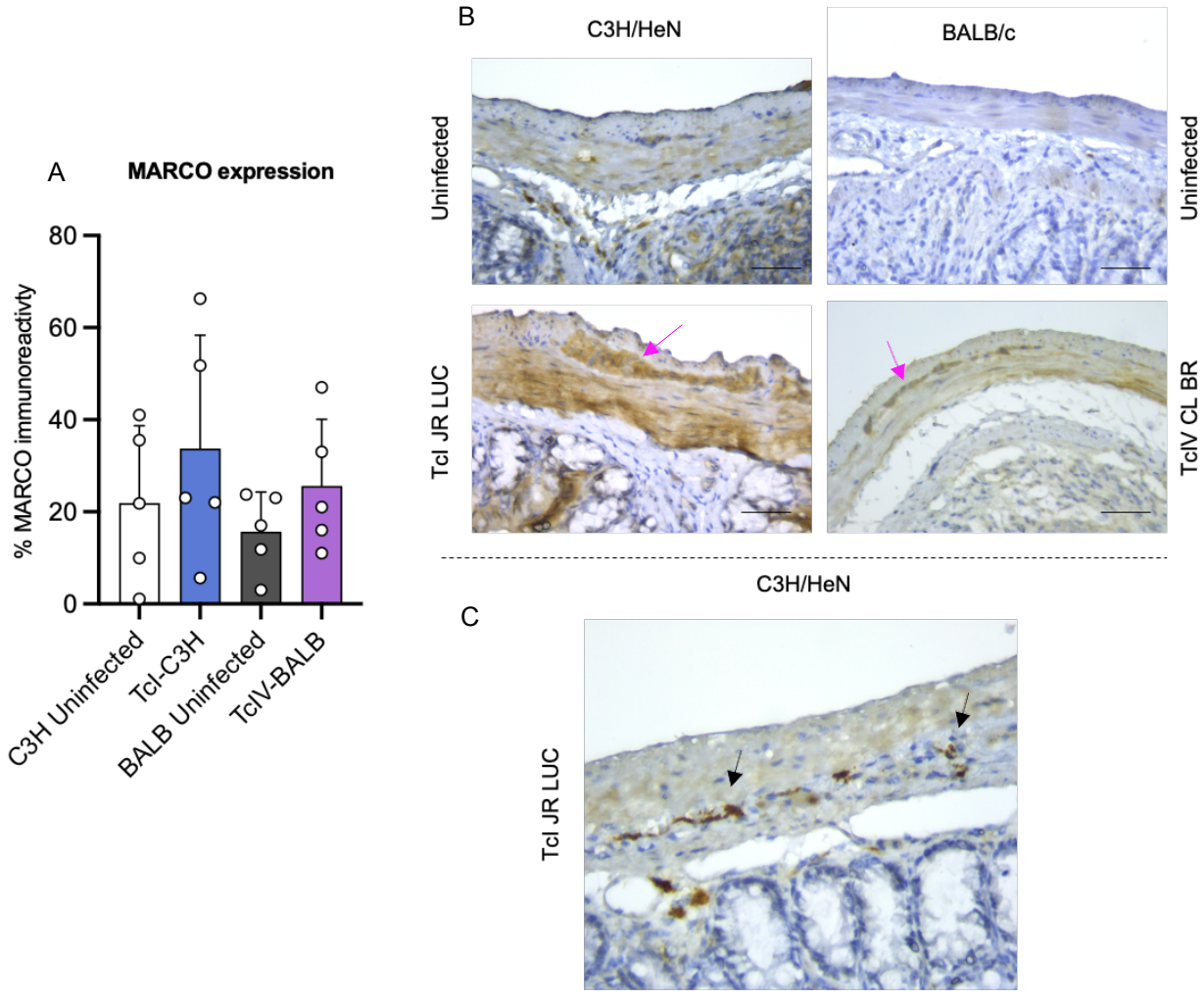

Figure 14. MARCO expression in the colon from Tcl-C3H and TcVI-BALB/c infection models 7 weeks post infection, with uninfected controls.
A) % positive MARCO immunoreactivity in the smooth muscle layer only of the large intestine; mucosal layer is excluded from analysis. All groups *n=5*. Unpaired t-test was conducted between each group, with no significant differences noted. C3H uninfected vs Tcl-C3H (*p* value *0.3999*). Tcl-C3H vs TcVI-BALB (*p* value = 0.5416). C3H uninfected vs BALB uninfected (*p* value =0.4850). B) Representative images of each experimental group at 400x. MARCO specific expression is visualised by oxidised 3,3'-Diaminobenzidine (DAB) precipitate (brown), at a primary antibody concentration of 1:500. Counterstained with haematoxylin. C) Post analysis optimisation showing more focal expression (black arrows) with minimal non-specific background signal; anti-MARCO concentration changed to 1:1,500 and modified blocking solution.

Unlike the significant upregulation of *Marco* RNA in the TcI-C3H model, there was no significant difference in MARCO expression detected at a protein level (Fig.14A). There was, however, an upward trend in both infected groups compared to their respective uninfected control. TcI-C3H mice had 12% on average more MARCO immunoreactivity than C3H control mice (*p=0.3999*), and TcVI-BALB had 10% more than the BALB control group (*p=0.2263*). TcI-C3H had the highest MARCO expression with a percentage smooth muscle expression of 34%, which was 8% higher than TcIV-BALB at 25.6% (*p=0.5416*). However, this is clearly discordant with the 87-fold upregulation of *Marco* mRNA abundance in TcI-C3H infections.

There was no specific pattern to MARCO IHC signal, but qualitatively there was more signal in the circular muscle layer than longitudinal with a diffuse appearance (Fig. 14B). Moreover, it was observed that MARCO signal often presented in the myenteric plexus region, identified by the pink arrows (Fig. 14B). This phenotype was striking, and consistent across both infected cohorts occurring in roughly 59% of TcI-C3H and 43% of TcVI-BALB mice. During analysis, a high degree of background and non-specific signal was observed, including in the naïve controls, resulting in a decision that further optimisation was required. The anti-MARCO antibody concentration was reduced from 1:500 to 1:1500, and the blocking solution was changed from 5% BSA, 0.1% PBS-T, to 10% sheep serum 0.3% PBS-T. This did reduce the background noise, and staining went from diffuse staining of the smooth muscle to single cell-like staining (Fig. 14C). Clusters of intense MARCO+ cells were found in the circular muscle layer, apposing to the submucosal layer (Fig. 14C, black arrows). MARCO staining was still observed in the myenteric ganglia after this

adjustment to protocol. Time constraints of the project prevented further optimisation and validation of a robust anti-MARCO IHC assay.

Summary

Chronic (26-32 weeks post infection)					
Experimental group	**Smooth muscle inflammation (H&E)**	**Smooth muscle fibrosis (PSR)**	**Smooth muscle iNOS expression (IHC)**	**Denervation analysis (IHC)**	
TcI-C3H vs control	Significantly increased	No significant change	Significantly increased	Significantly increased	
TcVI-BALB/c vs control	No significant change	No significant change	No significant change	No significant change	

Acute (6-7 weeks post infection)					
Experimental group	**Smooth muscle inflammation (H&E)**	**Smooth muscle iNOS expression (IHC)**	***Nos2* RNA expression**	**Smooth muscle BTNL1 expression (IHC)**	**Smooth muscle MARCO expression (IHC)**
TcI-C3H vs control	No significant change	Significantly increased	Significantly increased	Significantly increased	No significant change
TcVI-BALB/c vs control	No significant change	No significant change	Significantly increased	No significant change	No significant change

Figure 15. A summary table of each of the major pathology findings in both mild DCD and severe DCD models. Top table (Dark blue) denotes each significant change in chronic pathology (26-32 weeks post infection) across each DCD model assessed (TcI-C3H & TcVI-BALB/c). Bottom table (pink) denotes the significant findings in acute pathology (6-7 weeks post infection) across each DCD model assessed (TcI-C3H & TcIV-BALB/c).

Discussion

Inflammation and fibrosis

It has previously been shown that the TcI-C3H model exhibits a severe and consistent DCD transit phenotype, whereas the TcVI-BALB/c model displays a milder phenotype (Attached paper, (18)). Here we demonstrate that the TcI-C3H model also exhibits an increase in cellular infiltration in the late chronic stage 32 weeks post infection (w.p.i), and an increase in smooth muscle iNOS expression in the acute stage (6 w.p.i) in addition to the chronic stage. The phenotyping of cells comprising the increase of cellular infiltration was beyond the scope of this study, so it is not known if the cells are leukocytic. Following up with CD45+ labelling, or more specifically CD3, CCR2, CD45R for T-cells, monocytes, and B cells respectively, or TE-7 for fibroblastic tissue repair, would help to start categorising infiltration composites in the large intestine. In the cardiac model the inflammatory profile is better defined where, in the chronic stage, the composition is largely lymphocytic (24). T cells predominate the cell types, with a ratio of 3:1 of CD8+ T cells to CD4+ T cells (25). Macrophages, eosinophils, plasma cells, neutrophils and mast cells are also present to a lesser extent (26–28).

There was no significant increase in total colon collagen content, but there was evidence of fibrosis focally to the proximal colon-mesentery junction region. I hypothesise that this area is an important site for parasite trafficking from the colon to other sites throughout the course of infection, such as the skin, in order to achieve transmission back to the triatomine bug. In line with this, a theory has been previously described for the sporadic inflammatory waves, where sporadic trafficking of parasites to the heart causes the pathology synonymous with Chagas disease in

the absence of local cardiac parasite persistence (17). The colon appears to be a ubiquitous immunologically permissive reservoir for parasite persistence in experimental (murine) Chagas disease (17), so the conduit for parasite efflux may be the colon apposing mesentery tissue, which is rich in lymphatics and blood vessels. An initial follow up would be to utilise CD-31 and LYVE-1 labelling for blood vessels and lymphatics respectively, in combination with fluorescent parasites to observe if the blood or lymphatic systems are key for parasite trafficking in the late acute phase through the late chronic phase. It would also be pertinent to conduct a terminal deoxynucleotidyl transferase dUTP nick end labelling (TUNEL) assay, and cell replication assays such as 5-ethyl-2-deoxyuridine (EdU) to assess the tissue damage-repair axis in this area at different stages of infection.

A straightforward link between end-point inflammation and fibrosis is difficult to establish since inflammation is transient, and fibrosis is cumulative. The observations in this study suggest there was no evidence of significant inflammation in the TcVI-CLBR C3H model, but total GI collagen content was similar to that observed for TcI-JR in the same mouse strain. Moreover, there was no significant difference in smooth muscle collagen content between TcI-C3H and any other mouse-parasite combination, which suggests that fibrosis may not mechanistically be linked to transit delay and not a central component of pathogenesis, which contrasts with the case for Chagas cardiomyopathy (21). Here, the link between inflammation and fibrosis is well established. Myocarditis and fibrosis are hallmarks of cardiac disease, despite there being no continuous parasitic persistence in the heart (29). Therefore, continuous parasite persistence in the gut could mean the induction pathway and or dampening of potential fibrosis underscores an intrinsic difference between fibrosis

generation in smooth muscle and cardiac muscle. Moreover, smooth muscle cells may have a higher regenerative capacity, so damaged tissue can be replaced by new muscle cells rather than extracellular matrix (ECM) (30). TGFβ, which is upregulated upon infection with *T.* cruzi is an important mediator of myofibroblast differentiation which produces both collagen and tissue inhibitors of metalloproteinase 1 (TIMP-1) (31). TIMP-1 further promotes production of extracellular matrix including specific collagen subtypes (32). Therefore, the continuous interaction of a number of competing factors could mean the level and severity of GI fibrosis is strongly influenced by host and parasite genetics.

The role of iNOS in DCD

Nitric oxide mediated enteric denervation in the acute stage is the leading theory for the neuropathogenesis associated with DCD, (33). Recent discoveries have challenged the notion that enteric neuropathy occurs predominantly, or even exclusively, in acute stage. The first being that the large intestine is a ubiquitous chronic parasite reservoir in experimental mouse models (17), and the number of neuronal cell bodies in the myenteric plexus decreases throughout the course of infection (Khan et al., in revision; Chapter 3).

These findings suggest ongoing host-parasite interactions continue to contribute to neuropathology throughout the course of infection. In this study there was an increase in smooth muscle iNOS expression in the acute stage, supporting the hypothesis of acute phase iNOS mediated tissue damage. We also observed an increase in expression in the chronic stage, supporting the hypothesis that ongoing host-parasite interactions facilitate gradual development of tissue damage.

Interestingly, there was no correlation between iNOS expression and focal inflammation or loss of enteric ganglia. *Nos2* mRNA was also upregulated in comparable amounts in both TcI-C3H and TcIV-BALB/c at 7w.p.i, but a severe functional deficit and increased inflammation has only been observed in TcI-C3H mice. Overall, this suggests that iNOS may be a feature of digestive pathology development, but not on its own. The inflammatory environments of the chronic stage are different to the acute phase, in that there is an equilibrium between parasite replication and adaptive immunity suppression in the progression to the chronic stage (34). This suggests that mechanisms of pathogenesis in the acute and chronic stages may be different, and result in a variable degree of neuropathogenesis and tissue damage in different host-parasite combinations.

Enteric innervation in DCD

In this study a significant reduction in neuronal tubulin was noted in the TcI-C3H model, which has previously been published (attached paper, (18)). Using IHC and histological approaches on transverse cross-sections, I revealed a 'white-space' phenomena or apparent ablation of cellular material within the myenteric ganglionic space. These areas were refractory to several types of staining. One hypothesis is oedema (plasma leakage) or lipid deposition within the ganglia, perhaps following recent destruction of neurons. Using HuC/D labelling, a pan-neuronal marker, showcased the same phenotype (18). Parasites were also not readily observed focally to the damaged neurons (18), which suggests that direct infection of neurons by parasites is not enough to explain the development of DCD, but more likely act as an inducer of pathology. Histological assessment of neurons presented with limitations in this study. By cutting thin, transverse cross sections, it was difficult to

obtain a global view of the myenteric plexus and the extent of neuropathy, especially since the pathology was sporadic and the number of ganglia per cut section varied. Whole mount IFA is more suitable for neurologic analysis as the myenteric plexus can be more widely sampled, and the use of multi-colour staining permits better characterisation of focal damage. The causative agent for enteric neuropathy is investigated in chapter 2, but a suitable follow up would be by utilising oil-red-o staining on frozen sections to assess if the ganglionic 'white-space' is lipid based.

BTNL1 and MARCO: symptom or cause?

BTNL1 at both an RNA and protein level was higher expressed in the TcI-C3H model. BTNL1 binds to T cells, via an unknown receptor, preventing proliferation via cell cycle arrest without triggering apoptosis (35). The physiological significance of BTNL1 has been demonstrated in an autoimmune *in vivo* model by neutralising BTNL1 activity (35). Inhibition resulted in enhanced T cell proliferation and inflammatory cytokine production (IL-2, IL-17, IL-4, IL-5 and IL-13), suggesting a critical role of BTNL1 in Th2/17 cytokine production. Notably, BTNL1 inhibition also prevented IFN-γ production, which indicates that activated antigen presenting cells (APCs) expressing high levels of BTNL1 are also central to the induction of a Th1 response. In the context of *T. cruzi* infection and DCD, this may suggest that T cells are not direct inducers of tissue damage or enteric neuropathy since we observe a severe functional deficit in the TcI-C3H model and denervation (18), and an unregulated expression of BTNL in the smooth muscle layer which would putatively prevent excessive focal T cell responses. However, since this model exhibits severe pathology, the triggering of BTNL1 expression may be downstream of distinct pathological presentation, or perhaps BTNL1 expression in other models is sufficient

at limiting excessive pathology only up to a certain level. It may be that BTNL1 expression is delayed or 'out of sync' with the waves of parasite egress, reinfection, and inflammation in the TcI-C3H model, so that inhibitory action only reaches sufficient levels once tissue damage has already occurred. This coincides with the upregulation of *Marco* RNA in the TcI-C3H. Macrophages use the scavenger receptor MARCO as part of opsonization of environmental particles and debris (36). We theorise that the MARCO+ population may therefore be higher in the TcI-C3H model due to the higher degree of tissue and ENS damage in this model, and subsequent increase of debris in the microenvironment for MARCO+ macrophages to 'clear up'. MARCO -/- mice treated with TiO_2, an overt environmental particle, presented with enhanced inflammation and chemokine expression, indicating that the clearance of debris serves as an important immune regulator of the lung (37). Therefore, BTNL1 and MARCO upregulation may be 'symptoms' of high tissue damage rather than causes. BTNL1 attempts to dampen an already strong type 1 cellular immune responses, and more MARCO+ macrophages are required to opsonize a higher amount of debris in this model both from infected cells and damaged bystander cells (including neurons), whilst also preventing further inflammatory cascades. In order to expand on the understanding of these two important markers at a protein level, the utilisation of cryo-sectioning and IFA, to better preserve the epitopes, would be recommended.

One aspect of the colon-specific and model-specific microenvironments that was outside the scope of this study was whether pathological immune cell phenotypes are acquired before or after infiltration into the smooth muscle tissue. Some qualitative observations suggest that there may be involvement of tertiary lymphoid

follicles in the colon. Throughout the multiple histopathological analyses in this study, distinct lymphoid follicle-like structures were observed frequently in colon tissue sections.

Figure 16. Transverse cross-section of a distal colon from a Tcl-C3H mouse
Section stained with H&E. Image formed from multiple 100X images stitched together. Black box depicts a typical tertiary lymphoid follicle structure. Green arrows indicate potential egress from follicle to the smooth muscle layer. Scale bar is 500μm.

The structures exhibited marked variability between mice, ranging from ~1000μm in diameter to 3 or 4-fold larger (Fig.16). As well as size, the morphology of the structures varied. Follicles can present as compact structures or appear more dispersed, with potential egress or ingress of cells into the sub-mucosa or smooth muscle layer, as indicated by the green arrows above. The lymphoid structure draws similarities with Peyers patches (PP) found in the small intestine. The literature suggests these structures are secondary/tertiary colonic lymphoid follicles although their location may not be infection-related, since they are also observed in control

mice (38). The structure and potential spatial kinetics observed between infection groups may suggest activation, as it has been demonstrated that these structures provide a suitable microenvironment to facilitate host immune response upon infection of enteric pathogens (39). Apart from initial qualitative observations, it was not clear if these structures were infection related. Using IFA it was initially suggested these lymphoid structures are predominantly B-cell rich (Fig.11).

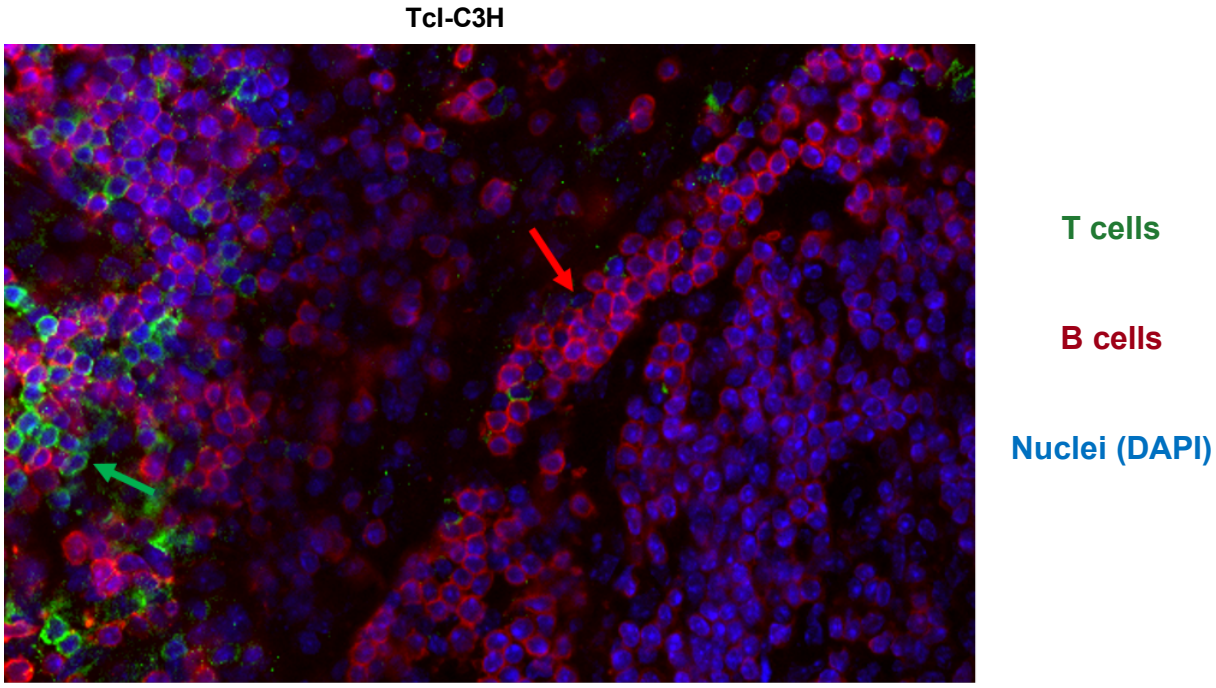

Figure 11. immunofluorescence staining of a lymphoid follicle in a whole mount colon section from a Tcl-C3H mouse.
CD3 cells visualised in green and indicated by green arrow. Rabbit anti-CD3 used at 1:500, visualised with Alexafluor488.B-cells visualised in red, indicated by red arrow. Mouse anti-CD45R used at 1:500, visualised with Alexafluor568. Cell nuclei stained with DAPI. Image taken at 200X magnification on confocal microscope.

B-cells are an important factor of the Th1/IFNy axis response, where IgG1 and IgG3 antibodies are produced to opsonise extracellular parasites (40). There is also evidence that B-cells also regulate T-cell responses essential for controlling *T. cruzi* infection via the production of IL-17 and IL-10 (41). The interaction between B and T-cells causes a strong inflammatory response which, if not regulated, causes host cell lysis and tissue damage (34). In these follicular structures, CD4+ T follicular helper

(Tfh) cell regulation of B cell response may be an important component of the local immune response, however, there are very few data on gut-specific responses including B cell responses, and it would be worth further investigating whether they have a role in promoting parasite persistence, and even neuronal damage.

Interestingly, there was a loss of B cells in both TcI-C3H and TcVI-BALB models inferred from the nanostring data. It would be interesting to investigate whether the loss of these cells corresponds with the size and proliferation activity of these observed structures, or if this is a result of the general permissiveness of the colon. In humans, regulatory B cells are known to produce IL-10 (42). IL-10 is an anti-inflammatory cytokine that dampens the inflammatory immune response contributing to the prevention of excessive tissue damage (43). However, upregulation of IL-10 or Foxp3, the primary T-reg marker, was not observed in the nanostring analysis. To assess the role these lymphoid structures have on immune-pathogenesis or disease control, I envisage utilising activation/proliferation markers such as Ki-67, EdU and CD44. I would like to quantify a difference between activity levels in infection groups. Additionally, I'd like to assess if there's a difference between regions of the colon regarding size, activity and number and follow up with high parameter flow cytometry and spatial transcriptomics, to garner a comprehensive understanding of the immune microenvironment in different colon layers and regions.

Megasyndromes are not a feature of 'severe' DCD model.

A key question about experimental Chagas disease is why megaoesophagus or megacolon are not obvious features of any DCD model. Firstly, the life expectancy of mice ranges between 18-24 months, which limits the longevity of extended chronic

experiments. Therefore, it may be that the experiments to date have not permitted enough time for megasyndromes to develop. In humans, megasyndromes manifest when the neuronal loss in areas of the digestive tract reach at least 55% (44), which may be an outcome of decades long infection. In this study I qualitatively observed a variation in oesophagus size, so conducted a pilot study investigating the thickness of the muscle layer to assess for smooth muscle hyperplasia. The luminal circumference and the total circumference were also measured to assess oesophageal dilation.

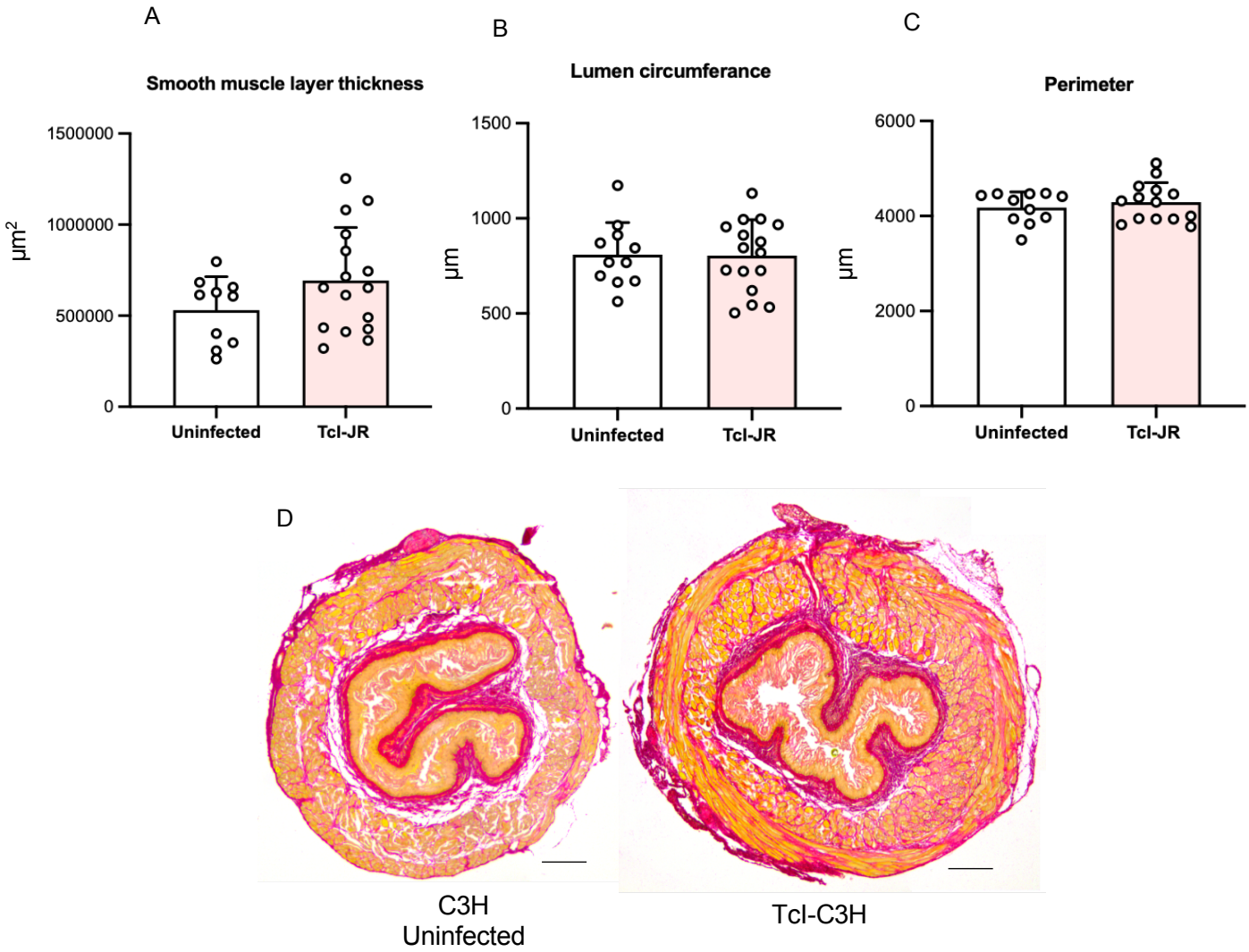

Figure 18. Oesophageal histopathology analysis of chronic Tcl-JR infections in C3H mice, 185 – 205 days post infection.
A) Graph depicting the average smooth muscle layer thickness in µm^2 of C3H uninfected (*n=10)* and Tcl-JR infected mice (*n=16*). Unpaired t test was conducted with *p* value of 0.1277. Area was determined by manually drawing around the smooth muscle layer, excluding submucosal and mucosal layer. The area of the polygon was calculated in Leica Application suite. B) Graph depicting the average circumference of the luminal space of C3H uninfected (*n=10)* and Tcl-JR infected mice (*n=16*). Circumference of lumen was manually drawn with the length of the line calculated in Leica Application suite. Unpaired t-test was conducted with a p value of 0.9527. C) Graph depicting the average total perimeter circumference of C3H uninfected (*n=10)* and Tcl-JR infected mice (*n=16*). Unpaired t-test was conducted with a *p* value of 0.4714.D) Representative images of Tcl-C3H infected and uninfected esophagus. 25x magnification, images comprised of 5 individual images stitched together. Scale bar 500µm.

There was a high degree of heterogeneity in the smooth muscle layer thickness of TcI-C3H mice (Fig.18A). There was no significant difference between infected and uninfected (*p=0.1277*) but, on average, the smooth muscle layer of the infected group was 30.6% thicker (Fig. 18A, 18D). The variability of smooth muscle hyperplasia seen in the oesophagus was similar to the variability observed in each pathological analyses conducted in the large intestine. There was no difference in luminal circumference (*p=0.9527*), with the group averages being within 4μm from the other. Finally, there was no difference in the total perimeter circumference (*p=0.4714*), and the average difference in circumference was only 118 μm. Comparatively, the least variation between infected and uninfected was observed when analysing the total circumference. In summary, the results suggest that after 6 months of *T. cruzi* infection there is, at best, a trend of oesophageal smooth muscle layer thickening, although not significant, without any evidence of organ dilation. Thus, the chronic DCD model currently does not generate significant oesophageal pathology, although the smooth muscle thickening seen in a subset of individual animals suggest further development of the parameters may be worthwhile.

In order to assess whether megasyndromes could be reproduced in a modified version of this model, it would be useful to firstly analyse earlier timepoints e.g. before week 6/7 to study damage, and then at timepoints >1 year. By comparing smooth muscle hyperplasia at late acute, chronic and late chronic timepoints this may reveal the gradual development of megasydromes. Previous studies have noted increased thickness of the colon wall and diffuse muscle cell hypertrophy in experimental models, with the authors characterising these pathologies as ‘mega formation’ (45,46). However, the study utilised a different parasite strain (*Y* strain),

Swiss mice infected at 4 weeks old, a large parasite inoculum, and no corroborating gut functionality assays. Nevertheless, this does suggest that varying model parameters may be a viable route in mimicking human disease outcomes.

It would be pertinent to explore methods to assess the transit functionality of the oesophagus. Currently, the transit time assay is ineffective at investigating the upper regions of the GI tract, since the carmine solution is gavaged directly into the stomach, bypassing the oesophagus. By employing the use of an *ex vivo* isolated organ bath, accurate readings of the isometric or isotonic tissue contraction and release could be assessed. This would provide an insight into the neuron viability and muscle functionality in this region, which could be used in conjuncture with IFA whole mount staining to assess the number of intramuscular neuronal cell bodies, and transverse histological sectioning to assess smooth muscle hyperplasia at several timepoints throughout the course of an infection.

Conclusions

The TcI-C3H DCD model presented with a pathological profile that compliments the previously identified peristalsis functional deficit. The mechanisms underlying the development of this functional delay are unknown, however, iNOS mediated damage is likely to contribute to tissue damage, but in combination with other inflammatory effector pathways. TcVI-BALB/c infection is a good model for asymptomatic infection or slow progressing DCD. Moreover, it may be that TcVI-CLBR is less virulent than TcI-JR as well as possessing different susceptibility in BALB/c and C3H/HeN. Ideally, significant differences between these models need to be followed up e.g. comparing TcVI in C3H and TcI in BALB/c. It would be beneficial to identify

and categorise different severities of experimental DCD models to mimic the heterogeneity observed in human infection. This would allow the assessment of prospective drug therapeutics on digestive disease severities ranging from ‘asymptomatic acute’ to ‘severe symptomatic chronic’. The fundamental questions remaining from this study are:

1. What effectors are responsible for tissue and neuronal damage?
2. Is pathology permanent, or is dysperistalsis reversible?
3. Can megasyndromes be reproduced as a feature of murine experimental Chagas disease?

References

1. Rassi A, Rassi A, Marin-Neto JA. Chagas disease. The Lancet. 2010 Apr;375(9723):1388–402.
2. Iantorno G, Bassotti G, Kogan Z, Lumi CM, Cabanne AM, Fisogni S, et al. The enteric nervous system in chagasic and idiopathic megacolon. Am J Surg Pathol. 2007 Mar;31(3):460–8.
3. Jabari S, de Oliveira EC, Brehmer A, da Silveira ABM. Chagasic megacolon: enteric neurons and related structures. Histochem Cell Biol. 2014 Sep 25;142(3):235–44.
4. Köberle F. The causation and importance of nervous lesions in American trypanosomiasis. Bull World Health Organ. 1970;42(5):739–43.
5. Bern C. Antitrypanosomal therapy for chronic Chagas' disease. N Engl J Med. 2011 Jun 30;364(26):2527–34.
6. Coura JR, Borges-Pereira J. Chagas disease. What is known and what should be improved: a systemic review. Rev Soc Bras Med Trop. 2012 Jun;45(3):286–96.
7. Khan AA, Langston HC, Costa FC, Olmo F, Taylor MC, McCann CJ, et al. Local association of Trypanosoma cruzi chronic infection foci and enteric neuropathic lesions at the tissue micro-domain scale. PLoS Pathog. 2021 Aug 23;17(8):e1009864.
8. Lewis MD, Francisco AF, Taylor MC, Jayawardhana S, Kelly JM. Host and parasite genetics shape a link between Trypanosoma cruzi infection dynamics and chronic cardiomyopathy. Cell Microbiol. 2016;18(10):1429–43.
9. Branchini BR, Ablamsky DM, Davis AL, Southworth TL, Butler B, Fan F, et al. Red-emitting luciferases for bioluminescence reporter and imaging applications. Anal Biochem. 2010 Jan 15;396(2):290–7.
10. Santi-Rocca J, Fernandez-Cortes F, Chillón-Marinas C, González-Rubio ML, Martin D, Gironès N, et al. A multi-parametric analysis of Trypanosoma cruzi infection: common pathophysiologic patterns beyond extreme heterogeneity of host responses. Sci Rep. 2017 Aug 21;7(1):8893.
11. Lewis MD, Fortes Francisco A, Taylor MC, Burrell-Saward H, Mclatchie AP, Miles MA, et al. Bioluminescence imaging of chronic Trypanosoma cruzi infections reveals tissue-specific parasite dynamics and heart disease in the absence of locally persistent infection. Cell Microbiol. 2014;16(9):1285–300.
12. Arantes RME, Marche HHF, Bahia MT, Cunha FQ, Rossi MA, Silva JS. Interferon-γ-Induced Nitric Oxide Causes Intrinsic Intestinal Denervation in Trypanosoma cruzi-Infected Mice. American Journal of Pathology. 2004;164(4):1361–8.
13. Côbo E de C, Silveira TP, Micheletti AM, Crema E, Adad SJ. Research on Trypanosoma cruzi and Analysis of Inflammatory Infiltrate in Esophagus and Colon from Chronic Chagasic Patients with and without Mega. J Trop Med. 2012;2012:232646.
14. Lewis MD, Francisco AF, Taylor MC, Jayawardhana S, Kelly JM. Host and parasite genetics shape a link between Trypanosoma cruzi infection dynamics and chronic cardiomyopathy. Cell Microbiol. 2016 Oct;18(10):1429–43.
15. Khan AA, Langston HC, Costa FC, Olmo F, Taylor MC, McCann CJ, et al. Local association of Trypanosoma cruzi chronic infection foci and enteric neuropathic lesions at the tissue micro-domain scale. PLoS Pathog. 2021 Aug 23;17(8):e1009864.
16. Ward AI, Lewis MD, Khan AA, McCann CJ, Francisco AF, Jayawardhana S, et al. In vivo analysis of trypanosoma cruzi persistence foci at single-cell resolution. mBio. 2020;11(4):1–13.

17. Lewis MD, Francisco AF, Taylor MC, Jayawardhana S, Kelly JM. Host and parasite genetics shape a link between Trypanosoma cruzi infection dynamics and chronic cardiomyopathy. Cell Microbiol. 2016 Oct;18(10):1429–43.
18. Khan AA, Langston HC, Costa FC, Olmo F, Taylor MC, McCann CJ, et al. Local association of Trypanosoma cruzi chronic infection foci and enteric neuropathic lesions at the tissue micro-domain scale. PLoS Pathog. 2021 Aug 23;17(8):e1009864.
19. Booth LA, Smith TK. Lipid metabolism in Trypanosoma cruzi: A review. Mol Biochem Parasitol. 2020 Nov;240:111324.
20. Wynn TA, Vannella KM. Macrophages in Tissue Repair, Regeneration, and Fibrosis. Immunity. 2016 Mar;44(3):450–62.
21. Lewis MD, Kelly JM. Putting Infection Dynamics at the Heart of Chagas Disease. Trends Parasitol. 2016;32(11):899–911.
22. Herrmann T, Karunakaran MM. Butyrophilins: γδ T Cell Receptor Ligands, Immunomodulators and More. Front Immunol. 2022 Mar 17;13.
23. Kanno S, Hirano S, Sakamoto T, Furuyama A, Takase H, Kato H, et al. Scavenger receptor MARCO contributes to cellular internalization of exosomes by dynamin-dependent endocytosis and macropinocytosis. Sci Rep. 2020 Dec 11;10(1):21795.
24. Bonney K, Engman D. Chagas Heart Disease Pathogenesis: One Mechanism or Many? Curr Mol Med. 2008 Sep 1;8(6):510–8.
25. Molina HA, Kierszenbaum F. Interaction of human eosinophils or neutrophils with Trypanosoma cruzi in vitro causes bystander cardiac cell damage. Immunology. 1989 Feb;66(2):289–95.
26. Tanowitz HB, Kirchhoff L V, Simon D, Morris SA, Weiss LM, Wittner M. Chagas' disease. Clin Microbiol Rev. 1992 Oct;5(4):400–19.
27. Melo RCN, D'Ávila H, Fabrino DL, Almeida PE, Bozza PT. Macrophage lipid body induction by Chagas disease in vivo: putative intracellular domains for eicosanoid formation during infection. Tissue Cell. 2003 Feb;35(1):59–67.
28. Elias FE, Vigliano CA, Laguens RP, Levin MJ, Berek C. Analysis of the presence of Trypanosoma cruzi in the heart tissue of three patients with chronic Chagas' heart disease. Am J Trop Med Hyg. 2003 Feb;68(2):242–7.
29. Lewis MD, Fortes Francisco A, Taylor MC, Burrell-Saward H, Mclatchie AP, Miles MA, et al. Bioluminescence imaging of chronic Trypanosoma cruzi infections reveals tissue-specific parasite dynamics and heart disease in the absence of locally persistent infection. Cell Microbiol. 2014;16(9):1285–300.
30. Laumonier T, Menetrey J. Muscle injuries and strategies for improving their repair. J Exp Orthop. 2016 Dec 22;3(1):15.
31. Hall BS, Pereira MA. Dual Role for Transforming Growth Factor β-Dependent Signaling in *Trypanosoma cruzi* Infection of Mammalian Cells. Infect Immun. 2000 Apr;68(4):2077–81.
32. Drygiannakis I, Valatas V, Sfakianaki O, Bourikas L, Manousou P, Kambas K, et al. Proinflammatory cytokines induce crosstalk between colonic epithelial cells and subepithelial myofibroblasts: Implication in intestinal fibrosis. J Crohns Colitis [Internet]. 2013;7(4):286–300. Available from: http://dx.doi.org/10.1016/j.crohns.2012.04.008
33. Arantes RME, Marche HHF, Bahia MT, Cunha FQ, Rossi MA, Silva JS. Interferon-γ-Induced Nitric Oxide Causes Intrinsic Intestinal Denervation in Trypanosoma cruzi-Infected Mice. American Journal of Pathology. 2004;164(4):1361–8.
34. Pérez-Mazliah D, Ward AI, Lewis MD. Host-parasite dynamics in Chagas disease from systemic to hyper-local scales. Parasite Immunol. 2020;(August):1–16.

35. Yamazaki T, Goya I, Graf D, Craig S, Martin-Orozco N, Dong C. A Butyrophilin Family Member Critically Inhibits T Cell Activation. The Journal of Immunology. 2010 Nov 15;185(10):5907–14.
36. Arredouani MS, Palecanda A, Koziel H, Huang YC, Imrich A, Sulahian TH, et al. MARCO Is the Major Binding Receptor for Unopsonized Particles and Bacteria on Human Alveolar Macrophages. The Journal of Immunology. 2005 Nov 1;175(9):6058–64.
37. Arredouani M, Yang Z, Ning Y, Qin G, Soininen R, Tryggvason K, et al. The Scavenger Receptor MARCO Is Required for Lung Defense against Pneumococcal Pneumonia and Inhaled Particles. J Exp Med. 2004 Jul 19;200(2):267–72.
38. Buettner M, Lochner M. Development and Function of Secondary and Tertiary Lymphoid Organs in the Small Intestine and the Colon. Front Immunol. 2016;7:342.
39. Buettner M, Lochner M. Development and function of secondary and tertiary lymphoid organs in the small intestine and the colon. Front Immunol. 2016;7(SEP):1–11.
40. Bermejo DA, Amezcua Vesely MC, Khan M, Acosta Rodríguez E V., Montes CL, Amezcua Vesely MC, et al. Trypanosoma cruzi infection induces a massive extrafollicular and follicular splenic B-cell response which is a high source of non-parasite-specific antibodies. Immunology. 2011;132(1):123–33.
41. Bermejo DA, Jackson SW, Gorosito-Serran M, Acosta-Rodriguez E V, Amezcua-Vesely MC, Sather BD, et al. Trypanosoma cruzi trans-sialidase initiates an ROR-?t-AHR-independent program leading to IL-17 production by activated B cells. Nat Immunol [Internet]. 2013;14(5):514–22. Available from: http://www.ncbi.nlm.nih.gov/pmc/articles/PMC3631452/%5Cnhttp://www.ncbi.nlm.nih.gov/pmc/articles/PMC3631452/pdf/nihms445334.pdf
42. Glass MC, Glass DR, Oliveria JP, Mbiribindi B, Esquivel CO, Krams SM, et al. Human IL-10-producing B cells have diverse states that are induced from multiple B cell subsets. Cell Rep. 2022 Apr;39(3):110728.
43. Gazzinelli RT, Wysocka M, Hieny S, Scharton-Kersten T, Cheever A, Kühn R, et al. In the absence of endogenous IL-10, mice acutely infected with Toxoplasma gondii succumb to a lethal immune response dependent on CD4+ T cells and accompanied by overproduction of IL-12, IFN-gamma and TNF-alpha. J Immunol. 1996 Jul 15;157(2):798–805.
44. Tafuri WL, Maria TA, Lopes ER. [Myenteric plexus lesions in the esophagus, jejunum and colon of chronic chagasic patients. Electron microscopy study]. Rev Inst Med Trop Sao Paulo. 1971;13(2):76–91.
45. Ricci MF, Béla SR, Moraes MM, Bahia MT, Mazzeti AL, Oliveira ACS, et al. Neuronal Parasitism, Early Myenteric Neurons Depopulation and Continuous Axonal Networking Damage as Underlying Mechanisms of the Experimental Intestinal Chagas' Disease. Front Cell Infect Microbiol. 2020 Oct 15;10.
46. Campos CF, Cangussú SD, Duz ALC, Cartelle CT, Noviello M de L, Veloso VM, et al. Enteric Neuronal Damage, Intramuscular Denervation and Smooth Muscle Phenotype Changes as Mechanisms of Chagasic Megacolon: Evidence from a Long-Term Murine Model of Tripanosoma cruzi Infection. PLoS One. 2016 Apr 5;11(4):e0153038.

LONDON SCHOOL of HYGIENE &TROPICAL MEDICINE

London School of Hygiene & Tropical Medicine
Keppel Street, London WC1E 7HT

T: +44 (0)20 7299 4646
F: +44 (0)20 7299 4656
www.lshtm.ac.uk

RESEARCH PAPER COVER SHEET

Please note that a cover sheet must be completed for each research paper included within a thesis.

SECTION A – Student Details

Student ID Number	1601186	**Title**	Mr
First Name(s)	Harry		
Surname/Family Name	Langston		
Thesis Title	Study of the Determinants of Enteric Neuropathy in Experimental Chagas disease		
Primary Supervisor	Michael Lewis		

If the Research Paper has previously been published please complete Section B, if not please move to Section C.

SECTION B – Paper already published

Where was the work published?	PLOS pathogens		
When was the work published?	23/08/2021		
If the work was published prior to registration for your research degree, give a brief rationale for its inclusion	A key figure from my study was included in this paper in a different context to that of my study. This provided wider scope and signficance to my findings.		
Have you retained the copyright for the work?*	**No**	Was the work subject to academic peer review?	**Yes**

*If yes, please attach evidence of retention. If no, or if the work is being included in its published format, please attach evidence of permission from the copyright holder (publisher or other author) to include this work.

SECTION C – Prepared for publication, but not yet published

Where is the work intended to be published?	/
Please list the paper's authors in the intended authorship order:	/
Stage of publication	Choose an item.

SECTION D – Multi-authored work

For multi-authored work, give full details of your role in the research included in the paper and in the preparation of the paper. (Attach a further sheet if necessary)	I contributed in ongoin discussions and gave advice about the work in the form of lab meetings, or in 1-on-1 meetings with the primary author (Archie. A. Khan) and or with the praimary supervisor of the project (Michael. D. Lewis). I provided data for figure 5 (Fig5.a, Fig5.b) I processed, embdedded, cut and stained all tissue for these figures. For a) I stained colon sections from chronically infected mice with Heamatolxyin & Eosin, n=10, for three different experimental groups. I collected 5 images per mouse per region of the colon (total 15 images per mouse) and conducted a full qunatitiative histological anlysis, caluclating the extent of inflammation in the smooth muscle layer of each image. I then plotted the data using PRISM and ran suitable statisitical analyses. I provided representative images and updated the methods section accoridingly. For b) I firstly optomised the anti-Tubb3 (Tuj-1) antibody for immunhistochemistry. Once optomised I stained sections from the same mice as I did for the H&E. I imaged all ganglia visible and analysed each image twice. I manually exluded every aspect of the field of view on the serosa side, the sub-mucosal and mucosal layer, so that analysis was only conducted on the nuerons in the smooth muscle layer (myenteric plexus). I calculated the +immunoreactivity of anti-Tuj-1 antibody in each ganglia, I also calculated the 'white space' within each ganglia, and calcualted the percent of postiive immunoreactivty agasint negative 'white space' per ganglia.

SECTION E

Student Signature	
Date	

Supervisor Signature	
Date	

PLOS PATHOGENS

RESEARCH ARTICLE

Local association of *Trypanosoma cruzi* chronic infection foci and enteric neuropathic lesions at the tissue micro-domain scale

Archie A. Khan[1], Harry C. Langston[1], Fernanda C. Costa[1], Francisco Olmo[1], Martin C. Taylor[1], Conor J. McCann[2], John M. Kelly[1], Michael D. Lewis[1]*

1 Department of Infection Biology, London School of Hygiene and Tropical Medicine, London, United Kingdom, **2** Stem Cells and Regenerative Medicine, University College London, Institute of Child Health, London, United Kingdom

* michael.lewis@lshtm.ac.uk

OPEN ACCESS

Citation: Khan AA, Langston HC, Costa FC, Olmo F, Taylor MC, McCann CJ, et al. (2021) Local association of *Trypanosoma cruzi* chronic infection foci and enteric neuropathic lesions at the tissue micro-domain scale. PLoS Pathog 17(8): e1009864. https://doi.org/10.1371/journal.ppat.1009864

Editor: Mattie Pawlowic, UNITED KINGDOM

Received: April 14, 2021

Accepted: August 4, 2021

Published: August 23, 2021

Data Availability Statement: All relevant data are within the manuscript and its Supporting Information files.

Funding: The research was supported by funding from the Medical Research Council (New Investigator Research Grant MR/R021430/1 award to MDL and Project Grant MR/T015969/1 award to JMK, https://mrc.ukri.org/) and the European Union's Seventh Framework Programme (Marie Curie International Outgoing Fellowship award to MDL, grant agreement no. 625810, https://ec.

Abstract

Digestive Chagas disease (DCD) is an enteric neuropathy caused by *Trypanosoma cruzi* infection. The mechanism of pathogenesis is poorly understood and the lack of a robust, predictive animal model has held back research. We screened a series of mouse models using gastrointestinal tracer assays and *in vivo* infection imaging systems to discover a subset exhibiting chronic digestive transit dysfunction and significant retention of faeces in both sated and fasted conditions. The colon was a specific site of both tissue parasite persistence, delayed transit and dramatic loss of myenteric neurons as revealed by whole-mount immunofluorescence analysis. DCD mice therefore recapitulated key clinical manifestations of human disease. We also exploited dual reporter transgenic parasites to home in on locations of rare chronic infection foci in the colon by *ex vivo* bioluminescence imaging and then used fluorescence imaging in tissue microdomains to reveal co-localisation of infection and enteric nervous system lesions. This indicates that long-term *T. cruzi*-host interactions in the colon drive DCD pathogenesis, suggesting that the efficacy of anti-parasitic chemotherapy against chronic disease progression warrants further pre-clinical investigation.

Author summary

Chagas disease (American trypanosomiasis) is caused by the protozoan parasite *Trypanosoma cruzi*. Chagas disease has two types, the cardiac form and the digestive form; some patients have symptoms of both. How the parasite causes digestive disease is poorly understood. It is known that damage to the gut's nervous system is an important factor, but it has been unclear exactly where and when this damage occurs during the course of an infection and also why only a subset of infected people suffer from this outcome. We studied infections in mice and found certain combinations of strains of parasites and mice that exhibited symptoms similar to human digestive Chagas patients, including a problem with peristalsis that localised specifically to the colon. Using parasites that were genetically engineered to emit both bioluminescent and fluorescent light, we tracked infections over

europa.eu/research/fp7/index_en.cfm). The funders had no role in study design, data collection and analysis, decision to publish, or preparation of the manuscript.

Competing interests: The authors have declared that no competing interests exist.

time and were able to analyse rare infected cells deep within the muscle tissue of the wall of the colon. We found evidence of damaged neurons in the same location as these infection foci over 6 months after initial infection. Our results show that digestive Chagas disease probably develops as a result of chronic infection and inflammation, which potentially changes approaches to treatment.

Introduction

Chagas disease (CD) is caused by infection with the protozoan parasite *Trypanosoma cruzi*, which affects approximately 6 million people. There are two principal forms of CD, cardiac and digestive. The most prevalent cardiac presentations include myocarditis, fibrosis, arrhythmias, microvascular abnormalities, progressive heart failure and sudden death [1]. Cardiac CD has been the subject of intensive experimental research and many predictive animal models are available to support translation into the clinic. Human digestive CD (DCD) is characterised by progressive dilatation and dysfunction of sections of the GI tract [2,3]. Symptoms include achalasia, abdominal pain, constipation and faecaloma. Eventually, massive organ dilatation results in megasyndromes, usually of the colon and/or oesophagus. Dilatation is associated with loss of enteric neurons leading to peristaltic paralysis and smooth muscle hypertrophy. Treatments are largely limited to dietary and surgical interventions [4]. The lack of a robust small animal model of enteric CD has been a major block on basic and translational research.

Of symptomatic CD patients, ~65% have cardiomyopathy, 30% enteropathy and 5% have both, with digestive disease most common in Bolivia, Chile, Argentina and Brazil [1]. Anti-parasitic chemotherapy has not been considered justifiable for *T. cruzi*-positive individuals with digestive symptoms, but normal heart function, as no clinical trials have addressed treatment efficacy in the context of digestive outcomes [5]. Challenges for clinical trials include the highly variable and unpredictable clinical outcomes of *T. cruzi* infection, the extended time frame for disease development and, especially in the context of DCD, a paucity of experimental data [6]. Molecular and cellular explanations of DCD pathogenesis also lag far behind the advances made for Chagas cardiomyopathy.

The lack of progress in developing treatments for DCD may also be connected to the idea that megasyndromes result from irreversible enteric denervation, specifically during the *acute* phase of infection [7,8], in which anti-parasitic inflammatory responses are thought to cause iNOS-dependent collateral damage to neurons, leading to aganglionosis [7,9]. Further age-related nerve degeneration was posited to gradually unmask these parasite-driven losses, leading to progressive organ dysfunction on a timescale of years to decades [7]. However, the frequent detection of *T. cruzi* and signs of active inflammation in oesophageal and colonic tissues from patients circumstantially suggests that chronic parasite persistence may contribute to disease development [10–17]. Furthermore, experimental bioluminescence imaging and tissue PCR studies in mice revealed that the GI tract is a major long-term reservoir of *T. cruzi* infection [18–22]. Adult enteric neurogenesis has been described in response to chemically-mediated tissue injury [23] and in the steady state [24]. A series of advances has also highlighted previously unappreciated levels of interconnectedness between the gut's immune and nervous systems [25–27]. We therefore sought to develop murine DCD models suitable to address the hypothesis that host-parasite interactions in the chronically infected gut might impact continuously on the enteric nervous system (ENS) and musculature to drive disease pathogenesis.

Here, we studied a series of parasite and mouse strain combinations to identify several models with significant digestive motility dysfunction. Using a combination of bioluminescence and fluorescence *in vivo* and *ex vivo* imaging techniques, we demonstrate that chronic *T. cruzi* persistence, gut motility delay and enteric neuronal damage are co-localised within discrete foci in the colonic muscularis. This indicates that DCD tissue pathology and transit dysfunction are likely driven by *T. cruzi* persistence in the colon and the associated chronic inflammatory response. DCD should therefore be considered as potentially preventable by anti-parasitic chemotherapy. It also opens the way to investigate the molecular and cellular basis of pathogenesis and *T. cruzi* immune evasion.

Results

A subset of *T. cruzi* mouse infection models display chronic digestive transit time delays

We previously developed a series of mouse models of *T. cruzi* infection based on parasites transgenically expressing the luciferase variant *Ppy*RE9h, which serves as an orange-red light emitting *in vivo* reporter protein [28]. Host-parasite combinations of BALB/c and C3H/HeN mice and TcVI-CL Brener (CLBR) and TcI-JR strain parasites permit long-term tracking of the course and distribution of infections in individual animals (Fig 1A). These models, which exhibit a spectrum of Chagas heart disease severities [19], were screened for gastrointestinal (GI) transit time delays, a common feature of DCD, by oral feeding of a red dye tracer (carmine). Three of the four host-parasite combinations took significantly longer than control uninfected mice to pass the tracer at acute phase, 3 weeks post-infection (p.i.), and/or at 6 weeks p.i. transition phase (Fig 1B). During the early chronic phase, 12 and 18 weeks p.i., only the TcI-JR-infected C3H mice displayed the delay phenotype, which became markedly more severe as the infection developed into the later chronic phase at 24 and 30 weeks p.i. Milder, but still significant transit delay phenotypes also emerged in the other three models.

T. cruzi as a species encompasses a high level of genetic diversity structured across six major lineages [29–31]. To test whether and at what level the strong digestive transit delay phenotype in C3H mice was conserved, we tested a further eight *T. cruzi* strains from five lineages (4x TcI, 1x TcII, 1x TcIII, 1x TcIV and 1x TcVI) using the carmine transit assay (S1 Fig). Two more strains were identified showing evidence of delayed transit: TcI-SN3 and TcVI-Peru. This type of pathology is therefore a relatively rare, strain-specific trait in *T. cruzi*. It occurs in both TcI and TcVI strains, but is not conserved within lineages.

Parasite persistence within the GI tract

We selected the TcI-JR-infected C3H mouse as the most suitable model of experimental chronic DCD. The transit time delay in these animals (Fig 1B) did not show a correlation with the overall parasite burden, which dropped by approximately two orders of magnitude from the acute peak to the level seen in the chronic phase (Fig 1A). Much of the bioluminescence signal in whole animal imaging derives from parasites in the skin [18,19], so we quantified organ-specific parasite loads using *ex vivo* imaging at 3, 6 and 30 weeks p.i. (Fig 2A). Parasitism was consistently detected in the GI tract, in foci distributed from the stomach to the rectum, being relatively more intense in the stomach and large intestine compared to the small intestine (Fig 2A and 2B). All sites exhibited significantly lower parasite loads in the chronic than acute phase (Fig 2B). There was a positive correlation between endpoint GI parasite loads and the severity of transit delay during the acute phase (3 weeks p.i.), but there were no such quantitative associations in the transition (6 weeks) or chronic (30 weeks) phases (Fig 2C).

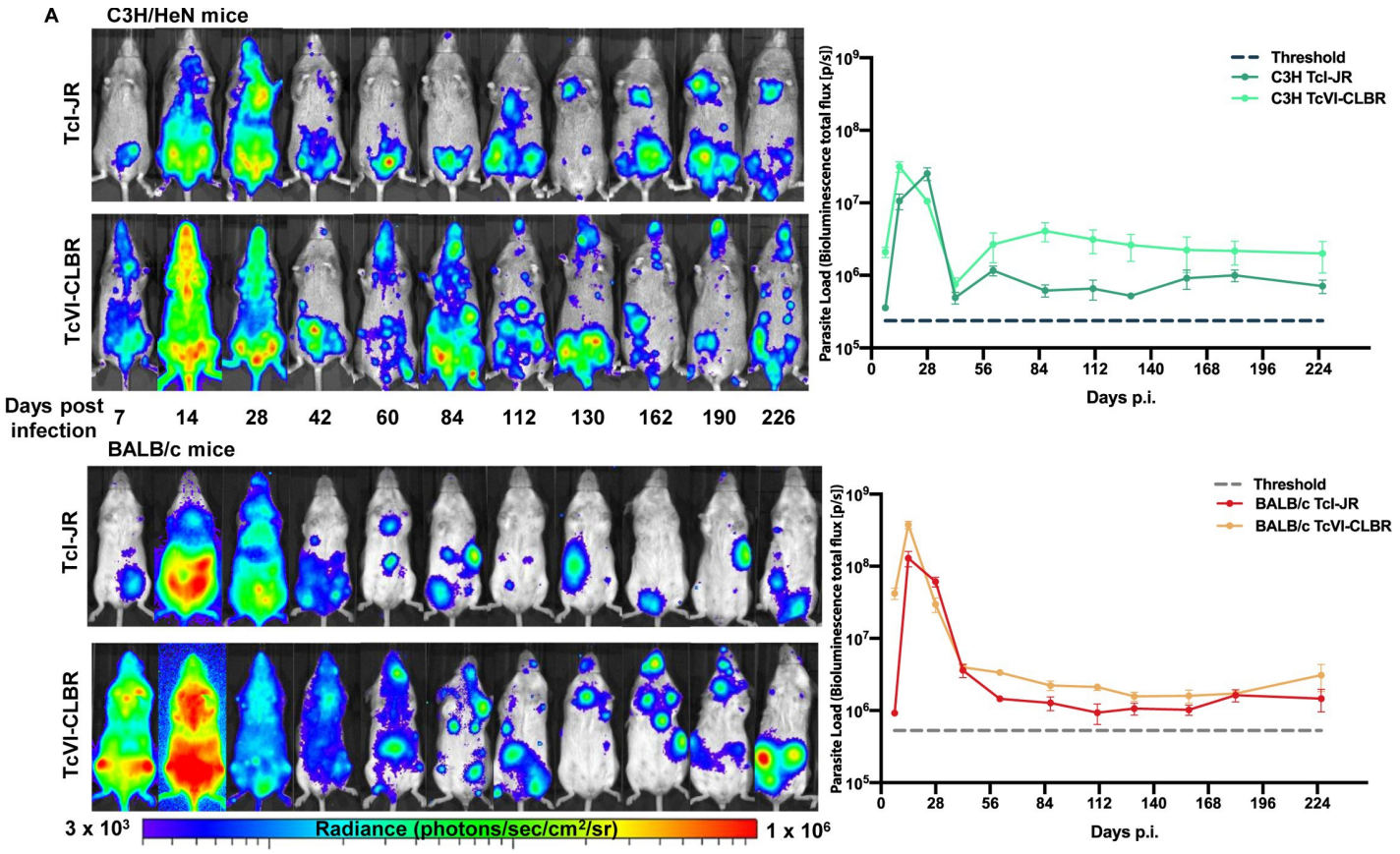

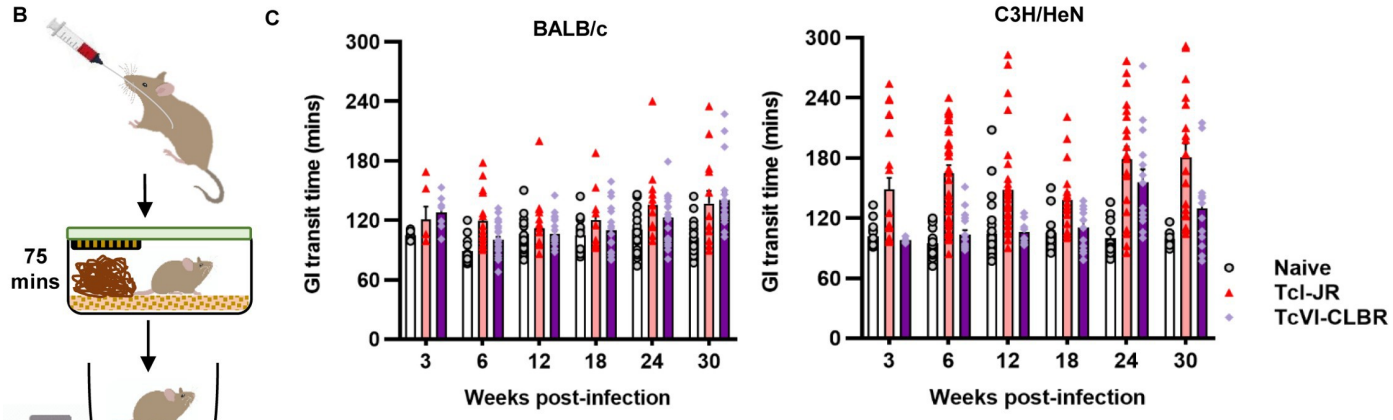

Mouse	Comparison | Week p.i.	3	6	12	18	24	30
		p value (1-way ANOVA)					
BALB/c	Naive vs. Tc-JR	0.273	**<0.0001**	0.61	0.293	**0.034**	**0.019**
	Naive vs. TcVI-CLBR	**0.039**	0.119	0.999	0.84	0.322	**0.004**
	Tc-JR vs. TcVI-CLBR	0.728	**0.005**	0.556	0.471	0.345	0.957
C3H/HeN	Naive vs. Tc-JR	**0.002**	**<0.0001**	**<0.0001**	**0.007**	**<0.0001**	**<0.0001**
	Naive vs. TcVI-CLBR	0.998	0.728	0.962	0.944	**0.001**	0.22
	Tc-JR vs. TcVI-CLBR	**0.002**	**<0.0001**	**0.003**	**0.047**	0.536	**0.013**

Fig 1. Bioluminescence imaging *T. cruzi* infection models and digestive transit dysfunction screen. A. Ventral images of female C3H/HeN (top panels) and BALB/c mice (bottom panels) representing TcI-JR (1st and 3rd panel) and TcVI-CLBR (2nd and 4th panel) course of infection. Images were captured using *in vivo* bioluminescence imaging. Overlaid log-scale pseudocolour heat maps are representative of bioluminescence intensity; the log-scale range is indicated in units of radiance. Adjacent line plots show parasite load represented as average bioluminescence of TcI-JR C3H/HeN (n = 10–24), TcVI-CLBR C3H/HeN (n = 5–12), TcI-JR BALB/c (n = 5–12) and

TcVI-CLBR BALB/c (n = 9–22) infected mice against days post infection (p.i.). Limit of detection of bioluminescence is indicated as threshold by dashed line. **B.** Schematic diagram of the carmine red-dye assay to measure gastrointestinal (GI) transit time delay in mice. **C.** Bar plots show GI transit time vs. weeks post-infection (p.i.) of BALB/c (left) and C3H/HeN (right) mice in the following groups: naive control BALB/c (n = 8–18), TcI-JR BALB/c (n = 6–17), TcVI-CLBR BALB/c (n = 10–29), naive control C3H/HeN (n = 12–35), TcI-JR C3H/HeN (n = 18–38) and TcVI-CLBR C3H/HeN (n = 6–17). Table (bottom) summarises statistical comparisons of GI transit time delay between groups. All statistically significant values are highlighted (red). Data are expressed as mean ± SEM. Statistical significance was tested using one way ANOVA followed by Tukey's HSD test.

https://doi.org/10.1371/journal.ppat.1009864.g001

Evidence of chronic GI parasitism was found for other models displaying milder or transient transit dysfunction (C3H –TcVI-CLBR, BALB/c–TcI-JR, BALB/c–TcVI-CLBR, C3H –TcI-SN3, C3H –TcVI-Peru) but also some with normal transit times (C3H –TcI-ArePe, C3H –TcIII-Arma18) (S1 and S2 Figs). Overall the *ex vivo* imaging analyses showed that GI transit time delays (Fig 1) coincided with the persistence of *T. cruzi* in the GI tract (Fig 2) in the principal C3H –TcI-JR model. The relationship between transit dysfunction and gut parasitism,

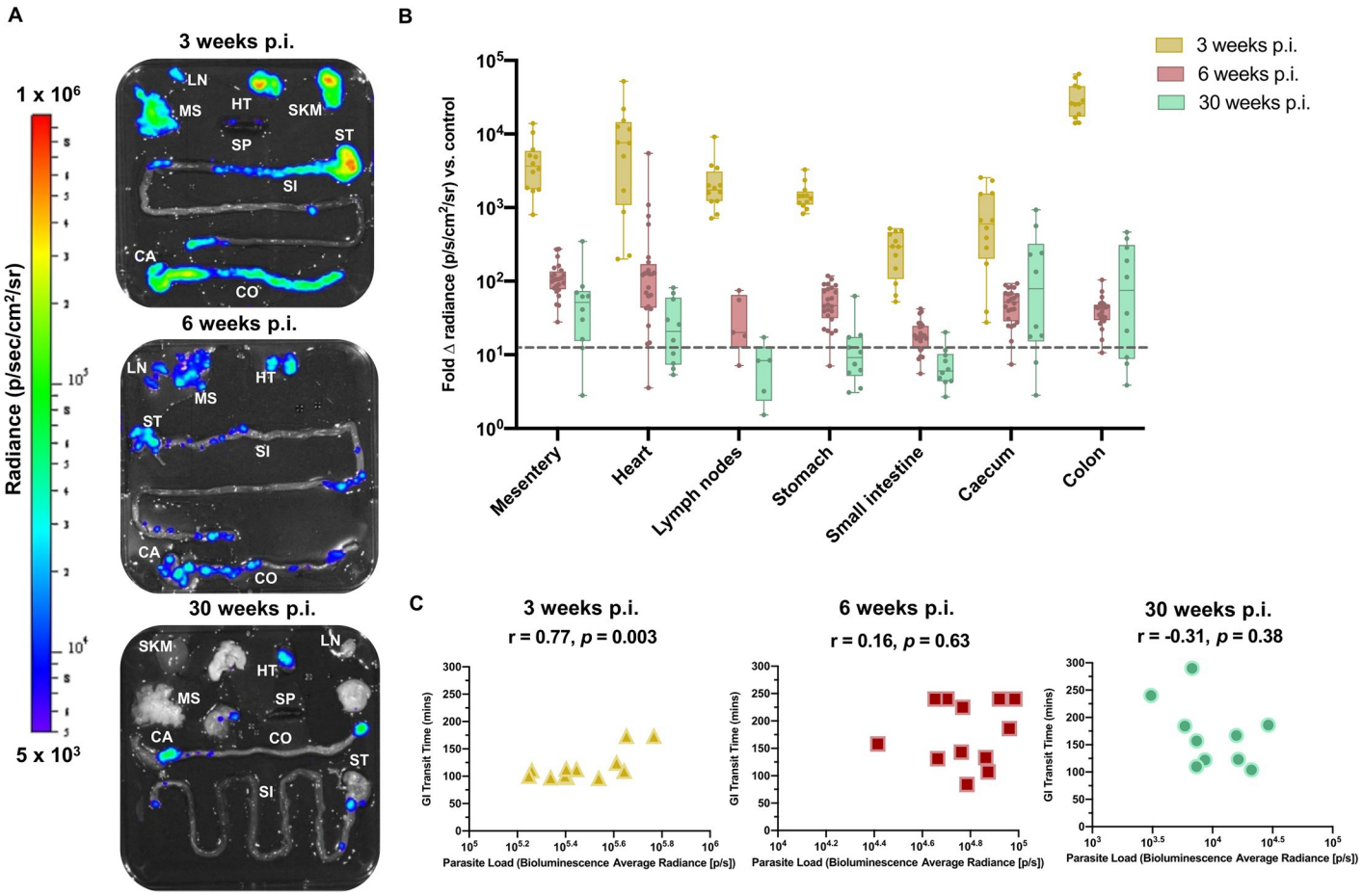

Fig 2. Tissue parasite distribution kinetics in TcI-JR-infected C3H/HeN mice. A. Representative images show parasite distribution in different organ tissue (lymph nodes—LN, gut mesenteric tissue—MS, heart—HT, spleen—SP, skeletal muscle—SKM, stomach—ST, small intestine—SI, caecum—CA and colon—CO) of a TcI-JR infected C3H mouse at 3, 6 and 30 weeks post-infection (p.i.) using *ex vivo* bioluminescence imaging. Overlaid log-scale pseudocolour heat maps are representative of bioluminescence intensity; the log-scale range is indicated in units of radiance. **B.** Box-plots show infection intensity of different organ tissue at 3 (n = 12 per group), 6 (n = 24 per group except n = 5 lymph nodes) and 30 (n = 10 per group except n = 5 lymph nodes) weeks p.i. Data points are expressed as fold change in bioluminescence vs. naïve controls. Limit of detection is denoted as dashed line. The horizontal line within each box indicates median and the whiskers denotes minimum and maximum values of each dataset. **C.** Scatter plots show correlation between gastrointestinal transit time and end-point parasite densities expressed as the aggregate bioluminescence radiance of the GI tract regions at 3 (n = 10), 6 (n = 12) and 30 (n = 10) weeks p.i.; r denotes Pearson's correlation coefficient and p-value represents a measure of statistical significance.

https://doi.org/10.1371/journal.ppat.1009864.g002

however, depends on additional factors because (i) there was not a consistent correlation between delay severity and infection intensity over time, and (ii) GI parasite persistence occurs apparently ubiquitously across different mouse-parasite strain combinations (Figs 2 and S2, [19,32]), yet only a subset have a functional DCD phenotype.

Regional dissection of the transit delay phenotype reveals localisation to the colon

The transit time delay seen in symptomatic DCD animals was not explained by differences in body weight or intestine length (S3 Fig). This suggested a functional impairment to peristalsis, as seen in human DCD. Our next aim was to determine the digestive tract region(s) in which the transit time delay was localised. To do this we fed mice with red and green fluorescent tracers (Rhodamine- and FITC-conjugated 70 kDa dextran, respectively) at variable time intervals prior to *ex vivo* imaging. An interval of 5 minutes was used to test whether stomach emptying was delayed. No significant differences were detected in infected animals compared to controls (Fig 3A), either at 6 or 30 weeks p.i. There was a significant difference in stomach weight at 6 weeks p.i. (Fig 3B), which may indicate increased retention of matter more solid than the tracer.

To measure small intestine dysfunction, we initially analysed tracer transit after 45 minutes and observed a trend for delay in infected mice during the acute but not the chronic phase (Fig 3C). At 3 weeks p.i. there was also significantly increased organ weight (Fig 3D), so we extended analysis at this time point using an increased parasite inoculum and extended the tracer interval time to 60 minutes. Here, we observed evidence of significant small intestine transit delay (Figs 3E and S4).

We next assessed colonic transit using a 90 minute interval after the fluorescent tracer feed. Fluorescence transit appeared similar in infected and control mice at 3 and 6 weeks p.i. (Fig 4A). Unlike the timings used to study transit delay in the upper intestinal tract (Fig 3), the method was less reliable to study the colon in isolation because substantial amounts of dye were still present in the small intestine and we could not quantify any dye that was excreted. Nevertheless, large intestine weights were significantly increased in infected mice at 6 and 30 weeks p.i. (Fig 4B) suggesting a site-specific dysfunction. We therefore employed an alternative assay in which mice were fasted for 4 hours prior to post-mortem analysis of colon lumen contents. *T. cruzi* infected animals showed significantly greater retention of faeces inside the colon than controls, as shown by pellet counts and both wet and dry total faecal weights, ruling out altered water absorption as an explanation (Fig 4C). The colon-localised transit delay phenotype was highly significant at 6 weeks p.i. and endured into the chronic phase, at 30 weeks p.i. (Fig 4C). By varying the fasting time (0, 2 and 4 h) we showed that this phenotype was maintained irrespective of stomach fullness and showed distal colon faecal impaction developing in *T. cruzi* infected mice within this timeframe (Fig 4D). The other *T. cruzi* strains exhibiting signs of total GI transit delay in the carmine assay (SN3, Peru, CLBR) also showed significant retention of faeces after 4 hour fasting, whereas strains with normal carmine transit times did not (S5 Fig). Thus, when GI transit dysfunction occurs in murine chronic *T. cruzi* infections it is predominantly localised to the colon.

To further investigate whether the observed functional constipation phenotype was accompanied by alterations at the molecular level, we used RT-qPCR to measure transcript abundance for 12 neuronal and inflammatory response genes in colon tissue from chronically infected mice (Fig 4E). Neuron-specific tubulin β-3 (*Tubb3*) and neuronal nitric oxide synthase (*Nos1*) genes were strongly downregulated by ~75% compared to naïve control mice. Expression of excitatory substance P and inhibitory vasoactive intestinal peptide (*Vip*) ENS

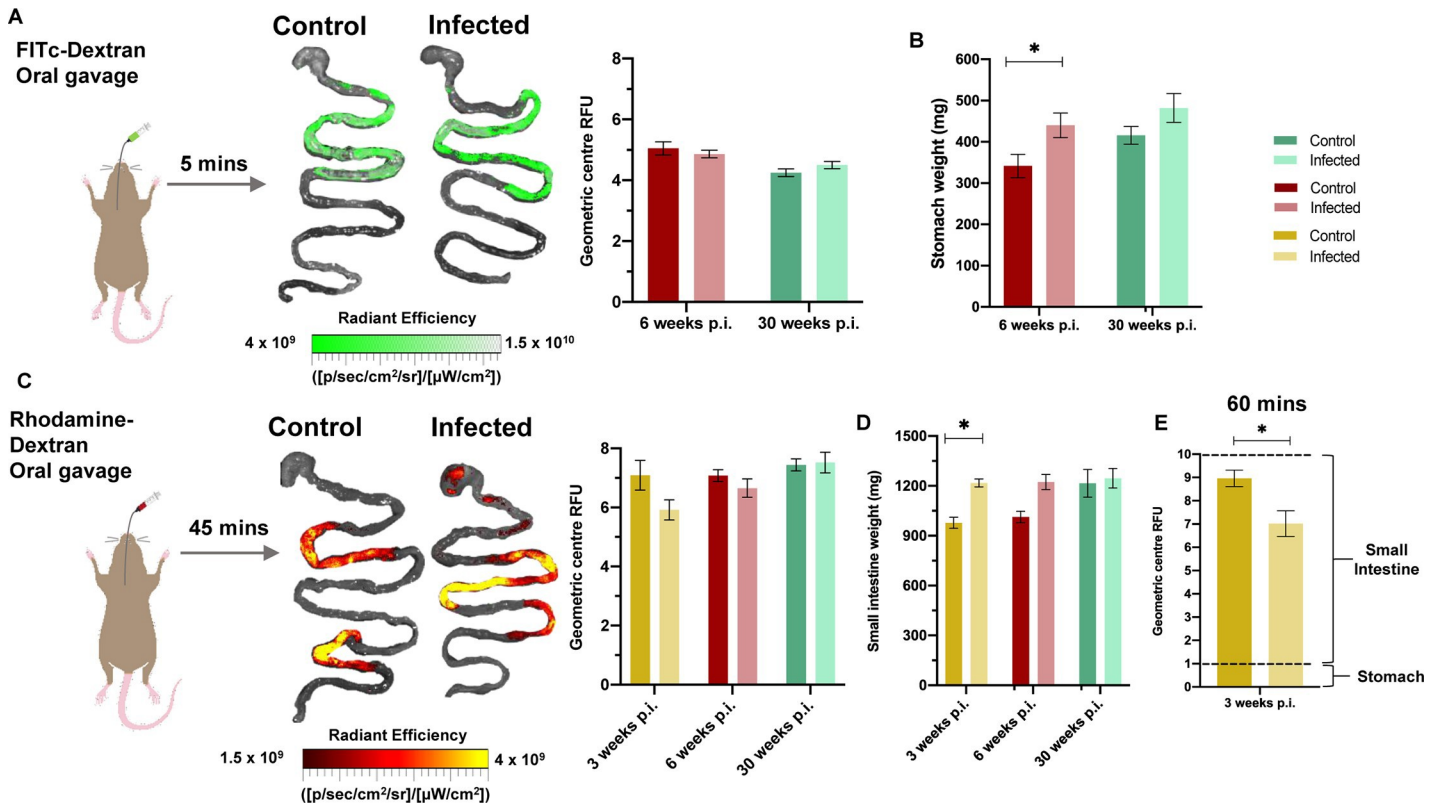

Fig 3. Fluorescent tracer imaging assays for stomach emptying and small intestine transit. A. Schematic diagram of a mouse receiving oral gavage of a green fluorescent marker, FITc-conjugated 70 kDa dextran, 5 minutes prior to termination to trace stomach emptying delay during infection. Representative images of stomach and small intestine are superimposed with traces of FITc-dextran travelling through stomach into small intestine to show transit difference between control and TcI-JR C3H/HeN infected mice. Linear-scale pseudocolour heat map shows minimum and maximum fluorescence intensity of 70-kDa FITC-dextran. Quantification of FITC-dextran fluorescence in control naïve and TcI-JR C3H/HeN is shown in the adjacent bar plot at 6 (n = 12 per group) and 30 (n = 5 per group) weeks post-infection (p.i.). Fluorescence is expressed as geometric centre which is centre mass of the marker. **B.** Bar plot shows post-mortem weights of stomach with contents at 6 (n = 7 per group) and 30 (n = 5 per group) weeks p.i. **C.** Similar schematic diagram and bar plot at 3 (n = 4 per group), 6 (n = 4 per group) and 30 (n = 5 per group) weeks p.i. using a red fluorescent marker, rhodamine-dextran, to target small intestine transit. Linear-scale pseudocolor heat map shows minimum and maximum fluorescence intensity of rhodamine-dextran. **D.** Small intestine weights shown in bar plot at 3 (n = 4 per group), 6 (n = 7 per group) and 30 (n = 5 per group) weeks p.i. **E.** Bar plot shows quantification of rhodamine-dextran fluorescence administered 60 minutes before termination of mice at 3 weeks p.i. (n = 4 per group). Dashed lines on bar plots show the GI segment number corresponding to the geometric centre score (0–1 = stomach, 1–10 = small intestine, proximal to distal). Data are expressed as mean ± SEM. Statistical significance was tested using unpaired two-tailed Student's t test ($^{\wr}P < 0.05$).

https://doi.org/10.1371/journal.ppat.1009864.g003

neurotransmitters was also decreased, but to a lesser extent. No evidence of altered transcript abundance was found for markers of other enteric neuronal subtypes, tyrosine hydroxylase (*Th*) and choline acetyltransferase (*Chat*), tropomyosin receptor kinases (*Ntrk1*/2/3) or nerve growth factor receptor (*Ngfr*). Taken together, these data indicate a possible downregulation of the enteric nitrergic transmission associated with GI dysfunction in DCD mice, recapitulating observations in human Chagas megasyndromes as well as other enteric neuropathies [16,33–36].

Chronic infection foci and enteric neuronal damage at organ and tissue micro-domain scales

Our next aim was to investigate disease pathogenesis in this model and commonalities with human DCD. Colon tissue from TcI-JR chronically infected mice (> 210 days p.i.) contained significant lymphocytic inflammatory infiltrates that were diffusely and focally distributed in the smooth muscle layers (Fig 5A). Immunohistochemical labelling of the nerve plexuses

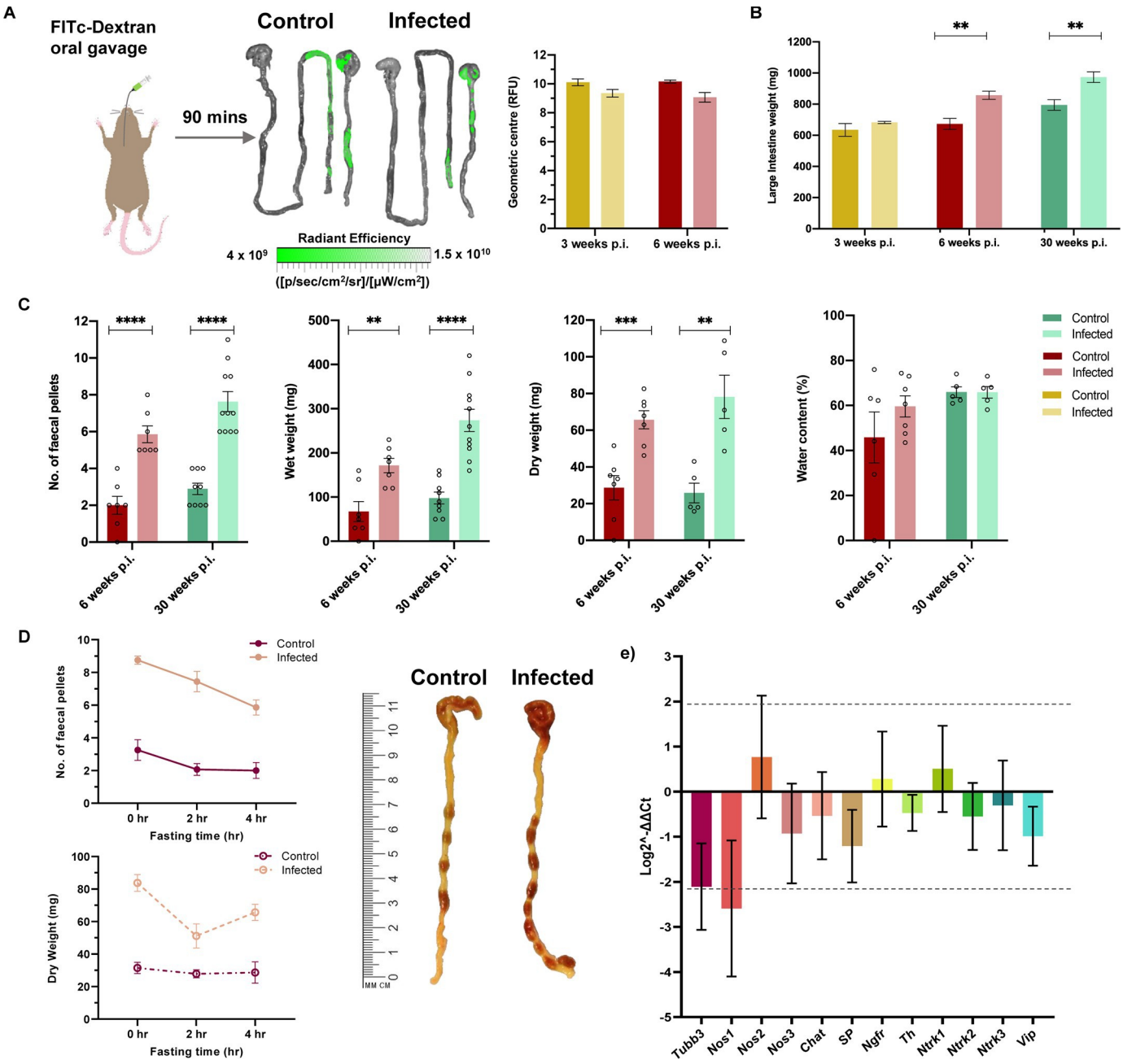

Fig 4. Evidence of colonic transit dysfunction in experimental digestive Chagas disease model. A. Schematic diagram of a mouse receiving oral gavage of a green fluorescent marker, FITC-conjugated 70 kDa dextran, 90 min prior to termination to trace large intestine transit delay during infection. Representative images of stomach, small and large intestine are superimposed with traces of FITC-dextran travelling through small into large intestine to show transit difference between control and TcI-JR C3H/HeN infected mice. Linear-scale pseudocolor heat map shows minimum and maximum fluorescence intensity of FITC-dextran. Bar plots show quantification of FITC-dextran fluorescence in the large intestine of mice at 3 ($n = 4$ per group) and 6 ($n = 4$ per group) weeks post-infection (p.i.). Fluorescence is expressed as geometric centre which is centre mass of the marker. **B.** Bar plot shows post-mortem weights of large intestine at 3 ($n = 4$ per group), 6 ($n = 7$ per group) and 30 (control $n = 9$, TcI-JR $n = 11$) weeks p.i. **C.** Faecal output analyses between control and TcI-JR C3H/HeN infected mice are expressed as faecal pellet count, wet and dry weight, and percentage of water content at 6 ($n = 7$ per group) and 30 weeks p.i. ($n = 5$–11 per group). **D.** Quantification of the effect of different fasting times on faecal output of mice: number of faecal pellets ($n = 4$–16 per group) and dry faecal weight ($n = 4$–7 per group). Images of mouse large intestine showing faecal impaction during infection at 30 weeks p.i. after 4 hours fasting compared to control. Scale bar is in cm and mm. Data are expressed as mean ± SEM. Statistical significance was tested using unpaired two-tailed Student's t test ($^{\wr\wr}P < 0.01$; $^{\wr\wr\wr}P < 0.001$, $^{\wr\wr\wr\wr}P < 0.0001$). **E.** RT-qPCR analysis by log2-fold change in RNA expression of neuronal markers, including pan-neuronal tubulin β-3 (*Tubb3*), neurotransmitter production (*Nos1*, *Chat*, *SP*, *Th*, *Vip*), neuronal growth factor receptors (*Ngfr*, *Ntrk1*, *Ntrk2*, *Ntrk3*), and non-neuronal NOS isoforms *Nos2* and *Nos3*. RNA was from colon tissue of C3H/HeN naïve control and TcI-JR infected mice ($n = 5$ per group, biological replicates). Data are expressed as $Log2^{-\Delta\Delta Ct} \pm$ SD. Dashed line represents mean ± 2SD based on distribution of naïve group values.

https://doi.org/10.1371/journal.ppat.1009864.g004

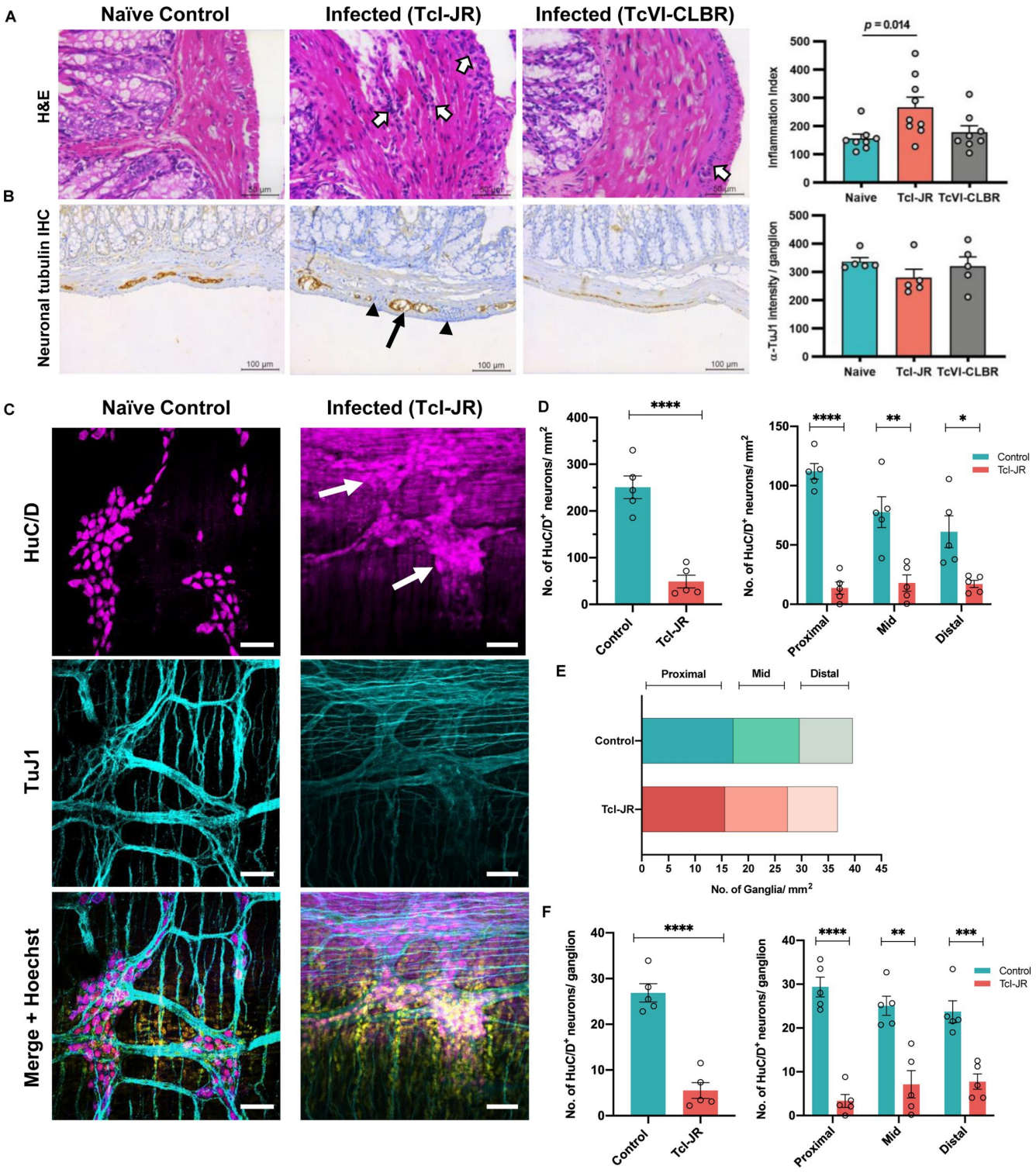

Fig 5. Effects of chronic *T. cruzi* infection on the enteric nervous system. A. Representative brightfield images of 5 μm thick colon sections stained with haematoxylin-eosin. Samples were cut as transverse cross-sections and images are oriented to show the mucosa to the left of the smooth muscle layers and serosa at the right edge. Inflammatory infiltrates are apparent in infected samples, visible as increased numbers of haematoxylin (purple) stained nuclei (white arrows). Images were taken at 400X magnification, scale bar = 50 μm. Adjacent bar plot shows number of nuclei per field to quantify cellular infiltration in TcI-JR ($n = 8$), TcVI-CLBR ($n = 10$) infected mice compared to naïve controls ($n = 8$). **B.** Representative brightfield images of 5 μm thick colon sections to detect neuropathology during *T. cruzi* infection detected by immunohistochemistry. Samples were cut as transverse cross-sections and images are oriented to

show the mucosa above the smooth muscle layers and serosa at the lower edge. Sections were labelled with a pan-neuronal antibody (TuJ1) detected as (3,3'-Diaminobenzidine, DAB) chromogen deposits (brown) and counter-stained with haematoxylin (blue), with signal predominantly localising to the myenteric neural plexus situated between the circular and longitudinal muscle layers. Black triangles indicate inflammatory foci, black arrow indicates disorganised TuJ1 distribution in a myenteric ganglion. Images were taken at 200X magnification, scale bar = 50 μm. Adjacent bar plot shows percentage of neuronal tubulin (TuJ1) immunoreactivity in naïve control ($n = 8$), TcI-JR- ($n = 8$) and TcVI-CLBR ($n = 9$) infected mice. **C.** Representative immunofluorescent confocal images of whole-mount colon samples to show the change in anti-HuC/D stained neuronal cell bodies (magenta, top panel) and anti-Tuj1 stained neural network (cyan, middle panel) in the myenteric plexus during *T. cruzi* infection. Bottom panel shows merged images with DAPI nuclei stain (yellow). White arrows indicate damaged ganglionic neuronal cell bodies. Images were taken at 400X magnification, scale bar = 50 μm. **D.** Bar plots show number of HuC/D positive neuronal cell bodies per field of view in naïve control and TcI-JR infected whole colon samples (left) and from selected regions of the colon: proximal, mid and distal (right; $n = 5$ per group, all). **E.** Quantification of number of ganglia in naïve control and TcI-JR infected samples from proximal, mid and distal colon ($n = 5$ per group). **F.** Bar plots show number of HuC/D positive neuronal cell bodies per ganglion in naïve control and TcI-JR infected whole colon samples (left) and from selected regions of the colon: proximal, mid and distal (right; $n = 5$ per group, all). All data and images are obtained from matched naïve control and infected mice at 30 weeks post-infection. Data are expressed as mean ± SEM. Statistical significance was tested using unpaired two-tailed Student's t test ($^{\wr}P < 0.05$; $^{\wr\wr}P < 0.01$; $^{\wr\wr\wr}P < 0.001$, $^{\wr\wr\wr\wr}P < 0.0001$).

https://doi.org/10.1371/journal.ppat.1009864.g005

within the muscle layers showed that the total amount of neuron-specific tubulin (TuJ1) protein within myenteric ganglia was lower on average in infected mice, but this was not statistically significant (Fig 5B). However, there was a conspicuous spatial disorganisation of TuJ1 in a subset of ganglia, associated with the appearance of anomalous internal acellular structures in these ganglia, which were refractory to common histological dyes (Figs 5B and S6). To investigate this with greater precision, we used whole mount immunofluorescence analysis of the neuronal cell body marker HuC/D. This revealed a dramatic loss of neurons across the proximal, mid and distal colon myenteric plexus (Figs 5C and 5D). This was not a product of a reduced number of ganglia (Fig 5E), rather a highly significant reduction in neurons per ganglion (Fig 5F).

A critical question for rational design of therapies for DCD is whether *T. cruzi* and the associated host response continues to drive ENS pathology during the chronic phase of infection. At this stage, very few colon cells are infected at any one time and parasite foci are spatiotemporally dynamic, with an intracellular lytic cycle lasting 1–2 weeks before motile trypomastigotes migrate within and between tissues [37]. Thus, any temporal association between infection and ENS damage is likely highly localised and rare at any snapshot in time. Indeed, there was no correlation between chronic endpoint parasite loads in colon regions and the level of local denervation (Fig 6A). We also observed both denervated and intact myenteric ganglia immediately adjacent to each other (Fig 6B). Using dual bioluminescent-fluorescent reporter parasites [38] we were able to visualise rare chronic infection foci at single cell resolution. In most cases, infected cells were early in the proliferative cycle, with 10–50 amastigote forms, and they were located in close proximity to intact enteric nerve fibres (Figs 6C and S7). We also captured a very rare, mature pseudocyst at the point of rupture, with thousands of intracellular parasites and trypomastigote forms escaping the site (Fig 6D). The ENS at the level of this pseudocyst was almost completely ablated, whereas the overlying and laterally adjacent ENS networks were intact (Fig 6E). Taken together, our data demonstrate there is an enduring association, at a highly localised tissue micro-domain scale, between chronic parasitism of the gut wall and ENS lesions.

Discussion

Understanding of the mechanism of DCD pathogenesis remains rudimentary and a lack of experimental tools hampers progress. Post-mortem and biopsy studies of human DCD cases found reduced numbers of enteric neurons and glial cells, often coincident with intact parasites, *T. cruzi* DNA or antigen and inflammatory infiltrates [2,10–17,39,40]. These are

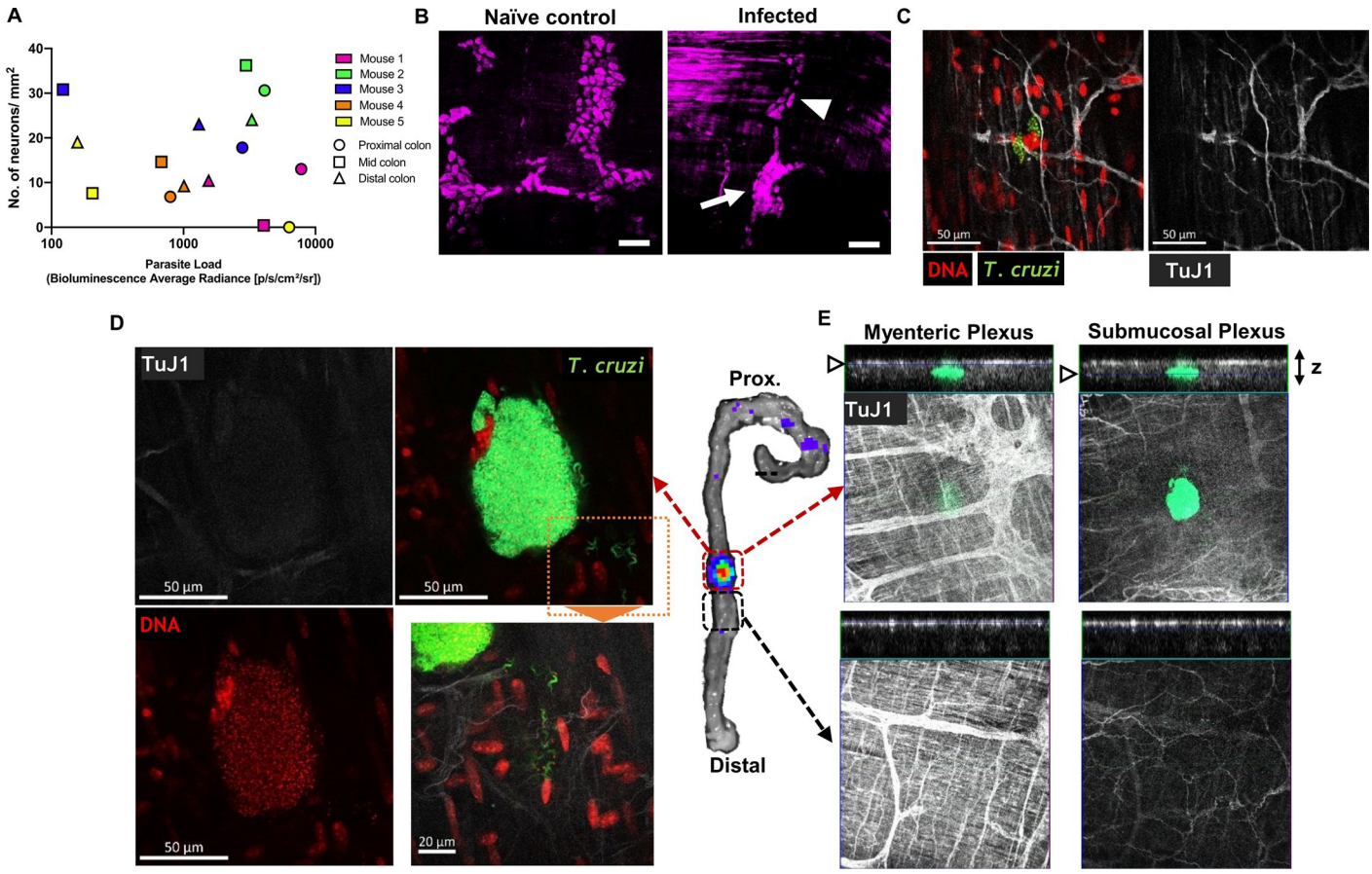

Fig 6. Chronic phase colonic *T. cruzi* infection foci and ENS ablation at the tissue micro-domain scale. A. Lack of correlation between end-point colon parasite loads measured by *ex vivo* bioluminescence intensity and degree of colon myenteric plexus denervation. **B–E.** Whole mount immunofluorescence analysis of colonic muscularis from C3H mice chronically infected with *T. cruzi*. **B.** HuC/D^{+} neuronal cell bodies in colonic myenteric ganglia. Naïve control shows normal morphology; infected mice exhibit adjacent ganglia with both intact (arrowhead) and disrupted (arrow) staining patterns. **C.** Imaging individual *T. cruzi* (mNeonGreen^{+}) infected cells at early stage of parasite replication cycle adjacent to intact enteric neuron fibres (TuJ1^{+}). **D–E.** Bioluminescence *ex vivo* image (centre)-guided analysis of parasitized and parasite-free tissue micro-domains. **D.** Mature parasite pseudocyst containing >1000 flagellated trypomastigotes with extracellular trypomastigotes in the local tissue parenchyma (inset) with faint neuronal (TuJ1) staining. **E.** Z-stack slices at the level of myenteric and submucosal neuronal plexuses showing highly localised loss of TuJ1 staining around the rupturing parasite pseudocyst.

https://doi.org/10.1371/journal.ppat.1009864.g006

important insights into late and terminal disease states, but they provide limited information on pathogenesis and relationships with infection load or distribution over time, which can only realistically be studied in animal models. *T. cruzi* infected mice do not develop advanced digestive megasyndromes resembling those in humans, but these are late stage manifestations that usually take many years to develop. Nevertheless, denervation and other features of nascent enteropathy have been described in several mouse models at the histological level [27,41–45]. Delayed transit has also been reported [44,46,47], but neither the GI region involved, nor associations with infection dynamics have been determined. In this study, we present new experimental chronic *T. cruzi* infection imaging models that, crucially, feature co-localised colonic parasite persistence, denervation and delayed transit as a key functional symptom of DCD.

Our data show that the transit delay seen in chronically infected mice predominantly localises to the colon. It should be noted that in humans, digestive disease affects the oesophagus at a similar frequency [40,48], but we did not study this region, mainly because of the technical challenges targeting a functional assay to the murine oesophagus [49]. Also, evidence indicates

the murine oesophagus is not chronically parasitized by *T*. *cruzi*, or is below the limit of detection for imaging, which might reflect intrinsic anatomical differences between mice and humans in the upper GI tract [50]. The colon, therefore, presents better opportunities for experimental investigation of pathways connecting infection, inflammation and tissue damage. Moreover, enteric neuronal lesions and losses are the central feature in all digestive forms of Chagas disease [51], so the focus on the colon in this model is likely to generate data that can usefully be extrapolated, with due caution, to other GI regions including the oesophagus. There are also wider reasons to be optimistic about the translational value of these murine DCD models. For example, they perform well in predicting the efficacy of anti-parasitic drugs in clinical trials, in terms of both cure of infection and impact on cardiac tissue pathology [52].

The digestive manifestations of Chagas disease predominantly occur in parts of South America where the majority of human *T*. *cruzi* infections are caused by strains from lineages TcII, TcV and TcVI. Conversely, DCD is apparently far rarer north of the Amazon basin, where most human infections involve TcI. While this geographical association may well be circumstantial, being confounded by eco-epidemiological factors and human population genetic variability [53,54], it is still noteworthy that, in mice, a) GI transit delays were strain and not lineage-specific; and b) the most robust phenotype was caused by a TcI strain. There have been reports of TcI infections in humans with symptoms of digestive disease in Colombia [55,56], and they probably also occur in Venezuela [51] and Mexico [57]. It may be that disease presentation is milder in TcI-endemic areas without progression to megasyndromes and is less likely to be diagnosed. It should also be acknowledged that *in vitro* culture adaptation, genetic manipulation and clonal selection may be factors affecting the strain-specific phenotypes observed in our work. Nevertheless, our data still enable us to conclude that both host and parasite genetics contribute to murine DCD susceptibility. With respect to the host, evidence to date indicates that the digestive tract is probably a ubiquitous reservoir of chronic infection in mice. Disease severity was higher in C3H/HeN than BALB/c mice, a finding previously observed for murine cardiac CD [19], and is consistent with the heterogeneous clinical outcomes observed in humans [1].

A key conclusion is that gut parasitism alone is not sufficient as an explanation for DCD development, though it is likely to be a pre-requisite. The quantity and quality of the host's immune and tissue repair responses are likely to be central to disease resistance and susceptibility, yet understanding of gut-specific immunity in Chagas disease is mainly limited to descriptions of the general composition of inflammatory infiltrates, which are rich in T and NK cells [2,13,16]. Other outstanding questions include whether the patchiness of ENS damage is explained by the stochastic distribution of parasites, or because particular subsets of ganglia or neurons differ in susceptibility [58], and if so, why? We focussed on analysis of neurons in the myenteric plexus, but it will be important to explore other ENS components, including potential regulatory or neuroprotective functions of enteric glial cells [2,16,59] and broader factors known to influence neuro-immune interactions in the gut, such as host metabolism [60] and microbiota [61].

Analysis of the kinetics of disease development in our main DCD model (TcI-JR infected C3H mice) showed that the intensity of gut parasitism was somewhat correlated with the degree of transit delay around the peak of the acute phase of infection, but this correlation disappeared after the transition to the chronic phase. Transit assays and imaging were done on different days, so it may be that in the acute phase, where parasite loads are very high and more evenly distributed, snapshot parasite load measurements are more representative of wider time frames than they are in the chronic phase, when parasites are more focal and levels fluctuate substantially within and between individual hosts over time [18]. Also, the main effector causing collateral damage to the ENS in the acute phase is likely to be excessive NO

production via iNOS [9], however, the later transition and chronic inflammatory environments are different situations, in that they promote an equilibrium between parasite replication and suppression by host adaptive immunity [62]. Neuro-immune networks in the gut are also highly diverse [63], so additional mechanisms of pathogenesis may come into play during the chronic phase. Investigation of parasite virulence and variability in the host immune response will therefore be required to gain further insight into the determinants of susceptibility and resistance.

In summary, by combining live parasite imaging and gut tracer analyses, we found enduring associations between infection of the colon and local transit impairment at >6 months post-infection, and moreover at the tissue micro-domain scale between single infected cells and ENS lesions. Our results challenge the theory that DCD is a result of collateral damage to the ENS, resulting specifically from the acute inflammatory response against *T. cruzi* [7,64]. They support the interpretation that the presence of *T. cruzi* and inflammatory infiltrates in GI tissues of human DCD patients reflects a long-term association between parasite persistence and disease development [11,13,15]. However, this still does not prove a causal relationship between local infection and pathogenesis, nor the kinetics of the process; this will require elimination of *T. cruzi* at defined time points through anti-parasitic chemotherapy, for example using benznidazole or nifurtimox. More importantly, such experiments will help to predict whether treatment of chronic infections might have the potential to prevent or alleviate DCD in humans.

Materials and methods

Ethics statement

All *in vivo* experiments were performed in accordance with UK Home Office regulations under the Animal Scientific Procedure Act (ASPA) 1986, within the framework of project license 70/8207 or P9AEE04E, and were approved by LSHTM Animal Welfare Ethical Review Board.

Parasites and infections

Transgenic clones of *T. cruzi* TcI-JR and TcVI-CLBR constitutively expressing the red-shifted firefly luciferase variant *PPy*RE9h [28], alone or fused to mNeonGreen, were described previously [19,38]. Equivalent clones for other *T. cruzi* strains were generated by transfection of the DNA construct pTRIX2-RE9h (TcI-C8, TcI-X10/4, TcIII-Arma18, TcVI-Peru), or by cas9-mediated replacement of the LucRE9h gene with dual reporters, namely LucRE9h::Neon (TcVI-CLBR, TcII-Pot7a, TcIV-X10610) and LucRE9h::mScarlet (TcI-ArePe, TcI-SN3), using the T7 RNA polymerase/cas9 system [38]. *In vitro* epimastigotes were cultivated in supplemented RPMI-1640 medium at 28˚C with 150 μg ml^{-1} G418 or hygromycin B, 5 μg ml^{-1} puromycin or 10 μg ml^{-1} blasticidin as appropriate. Metacyclic trypomastigotes (MTs) from stationary phase cultures were used to infect MA104 monkey kidney epithelial cell monolayers in MEM media + 5% FBS at 37˚C and 5% CO_2. Tissue culture trypomastigotes (TCTs) were obtained from the supernatant of infected cells after 5 to 21 days, depending on the parasite strain.

Animals and infections

Female BALB/c and C3H/HeN mice, postnatal days 42–56, were purchased from Charles River (UK). Female CB17 SCID mice were bred in-house. All mice were housed on a 12 h

light/dark cycle, with food and water available *ad libitum* unless otherwise stated. Mice were maintained under specific pathogen-free conditions in individually ventilated cages.

SCID mice were infected with up to 5×10^5 *in vitro*-derived TCTs in 0.2 ml PBS via i.p. injection. All infected SCID mice developed fulminant infections and were euthanised at or before humane end-points. Blood trypomastigotes (BTs) were derived from parasitaemic SCID mouse blood directly or after enrichment, achieved by allowing blood samples to settle for 1 h at 37˚ C. BALB/c and C3H mice were infected by i.p injection of 10^3 or 10^4 BTs or TCTs depending on the experiment.

At experimental end-points, mice were sacrificed by ex-sanguination under terminal anaesthesia (Euthatal/Dolethal 60 mg kg^{-1}, i.p.) or by cervical dislocation. Organs and tissues of interest were excised, imaged (see below) and either snap-frozen, fixed in 10% Glyo-Fixx (Shandon) or transferred to ice-cold DMEM media. The weight of organs and tissues of interest were recorded.

Total GI transit time assay

Mice were gavaged p.o. with 200 μl of 6% w/v Carmine red dye solution in 0.5% methyl cellulose mixed in distilled water and returned to their home cage. After 75 min, mice were individually separated into containers and the time of excretion of the first red faecal pellet was recorded. A maximum assay cut-off time of 4 h was implemented. Total intestinal transit time was calculated as the time taken from gavage to output of the first red pellet.

In vivo bioluminescence imaging

Mice were injected with 150 mg kg^{-1} D-luciferin i.p., then anaesthetised using 2.5% (v/v) gaseous isoflurane in oxygen. After 10–20 min, bioluminescence imaging was performed using an IVIS Lumina II or Spectrum system (PerkinElmer), with acquisition time and binning adjusted according to signal intensity. Mice were revived and returned to cages after imaging. To estimate parasite burden in live mice, regions of interest (ROIs) were drawn to quantify bioluminescence expressed as total flux (photons/second) [18,19]. The detection threshold was determined using uninfected control mice. All bioluminescence data were analysed using LivingImage v4.7.3.

Ex vivo bioluminescence imaging

Mice were injected with 150 mg kg^{-1} D-luciferin i.p. 5–7 min before euthanasia. Trans-cardiac perfusion was performed with 10 ml of 0.3 mg ml^{-1} D-luciferin in PBS. Tissues and organs of interest (typically lymph nodes, heart, spleen, skeletal muscle, GI tract and associated mesenteries) were collected and soaked in PBS containing 0.3 mg ml^{-1} D-luciferin. Bioluminescence imaging was performed as above. To quantify parasite load as a measure of infection intensity, bioluminescence was calculated by outlining ROIs on each sample and expressed as radiance (photons $second^{-1}$ cm^{-2} sr^{-1}). Fold change in radiance was determined by comparing samples from infected mice with the equivalent tissues from uninfected, age-matched control mice. To determine the detection threshold, fold change in radiance of empty ROIs on images from infected mice was compared with matching empty ROIs on images from uninfected controls [18].

Fluorescent tracer transit assay

Mice were fasted (or not) for 2 or 4 h before euthanasia. They were administered FITC-conjugated 70 kDa dextran (100 μl, 5 mg ml^{-1} d.H_2O) or Rhodamine-conjugated 70 kDa dextran

(100 μl, 10 mg ml^{-1} d.H_2O) by oral gavage 5, 45 or 90 min before euthanasia to target the stomach, small or large intestine transit, respectively. As an extension of the *ex vivo* bioluminescence necropsy (see above), fluorescence images were obtained using excitation filters set at 465/535 nm and emission filters at 502/583 nm for FITC/Rhodamine (f-stop: 16, exposure: 2 s). The relative fluorescence of the tracers was measured from the images by drawing ROIs using LivingImage 4.7.3 software. The GI tract images starting from the stomach to the colon were cut digitally in 15 equal segments and the centre of mass (geometric centre) of the signals were determined. The geometric centre was calculated using the following equation, GC = ∑ (% of total fluorescent signal per segment ϟ segment number) / 100) [65].

Faecal analyses

The colon tissue was separated and cleaned externally with PBS. The faecal pellets were gently removed from the lumen of the colon, counted and the combined wet weight was recorded. The faecal pellets were collected into a 12-well plate and left to dry in a laminar flow cabinet overnight. The dry weight was then recorded and the percent water content was estimated as the difference between wet and dry weights.

Histopathology and Immunohistochemistry

Paraffin-embedded, fixed tissue blocks were prepared and 3–5 μm sections were stained with haematoxylin and eosin as described [19,32]. For tubulin β-3 immunohistochemistry, sections were subjected to heat-induced epitope retrieval by incubation in 10 mM sodium citrate, 0.05% Tween20 for 30 min at 95˚C then cooled and rinsed in distilled water. Sections were blocked with 10% sheep serum and 1% BSA in TBS for 30 min then incubated at 4˚C overnight with 1 μg ml^{-1} rabbit polyclonal anti- tubulin β-3 IgG (Biolegend) and 1% BSA in TBS. Sections were then washed with 0.025% Triton X-100 in TBS and endogenous peroxidase activity was quenched with 3% H_2O_2 for 30 min. Bound primary antibody was labelled with excess volume of HRP polymer anti-rabbit IgG reagent (Vector Labs) with 1% BSA in TBS for 30 min. Slides were then washed as previously and incubated with DAB (Thermo) for 5 min. Sections were counterstained with haematoxylin and mounted with DPX.

Images were acquired using a Leica DFC295 camera attached to a Leica DM3000 microscope. For analysis of inflammation, nuclei were counted automatically using the Leica Application Suite V4.5 software (Leica). DAB intensity was analysed as integrated density in ImageJ.

Immunofluorescence analysis

Colon tissues were transferred into ice-cold DMEM after necropsy. Tissues were cut open along the mesentery line, rinsed with PBS, then stretched and pinned on Sylgard 184 plates. The mucosal layer was peeled away using forceps under a dissection microscope and the remaining muscularis wall tissue was fixed in paraformaldehyde (4% w/v in PBS) for 45 min at room temperature. Tissues were washed with PBS for up to 45 min at room temperature and permeabilised with PBS containing 1% Triton X-100 for 2 h, followed by blocking for 1 h (10% sheep serum in PBS containing 1% Triton X-100). Tissues were incubated with primary antibodies (mouse anti-HuC/D IgG clone 16A11 at 1:200 [Thermofisher], rabbit polyclonal anti-tubulin β-3 IgG at 1:500 [Biolegend]) in PBS containing 1% Triton X-100 for 48 h at 4˚C. Tissues were washed with PBS, then incubated with secondary IgG (goat anti-mouse AlexaFluor-546, goat anti-rabbit AlexaFluor-633, both 1:500, ThermoFisher) in PBS containing 1% Triton X-100 for 2 h and counterstained with Hoechst 33342 (1:10 000) at room temperature. To assess antibody specificity, control tissues were incubated without the primary antibody. Tissues were mounted on glass slides using FluorSave mounting medium (Merck).

Whole mounts were examined and imaged with a LSM880 confocal microscope using a 40X objective (Zeiss, Germany). Images were captured as Z-stack scans of 21 digital slices with an interval of 1 μm optical thickness. Five Z-stacks were acquired per region (proximal, mid and distal colon), per animal. Cell counts were performed on Z-stacks after compression into a composite image using the cell counter plug-in of FIJI software. Neuronal density was calculated as the number of HuC/D$^+$ neuron cell bodies per field of view. HuC/D signal was associated with high background outside ganglia in samples from infected mice, attributed to binding of the secondary anti-mouse IgG to endogenous IgG, so ENS-specific analysis was aided by anti-TuJ1 co-labelling and assessment of soma morphology. The number of intact ganglia in each myenteric plexus image was also counted, along with number of HuC/D$^+$ neurons per ganglia.

RT-qPCR

Colon tissue samples were snap frozen on dry ice and stored at −70˚C. For RNA extraction, samples were thawed and homogenised in 1 ml Trizol (Invitrogen) per 30–50 mg tissue using a Precellys 24 homogeniser (Bertin). To each sample, 200 μl of chloroform was added and mixed by vortex after which the phases were separated by centrifugation at 13,000 g at 4˚C. RNA was extracted from the aqueous phase using the RNeasy Mini Kit (Qiagen) with on-column DNAse digestion as per manufacturer's protocol. The quantity and quality of RNA was assessed using Qubit Fluorimeter (Thermofisher). cDNA was synthesised from 1 μg of total RNA using Superscript IV VILO mastermix (Invitrogen), as per manufacturer's protocol, in reaction volumes of 20 μl. A final cDNA volume of 100 μl was made by adding RNase-free DEPC water (1:5 dilution) and stored at −20˚C until further use. qPCR reactions contained 4 μl of cDNA (1:50 dilution) and 200 nM of each primer (S1 Table) and QuantiTect SYBR Green PCR master mix (Qiagen) or SensiFAST SYBR Hi-ROX kit (Bioline). Reactions were run using Applied Biosystems 7500 fast RT-PCR machine (Thermofisher) as per manufacturer's protocol. Data were analysed by the ΔΔCt method [66] using murine *Gapdh* as the endogenous control gene.

Statistics

Individual animals were used as the unit of analysis. No blinding or randomisation protocols were used. Statistical differences between groups were evaluated using unpaired two-tailed Student's t-test or one-way ANOVA with Tukey's post-hoc correction for multiple comparisons. Pearson correlation analyses was used to evaluate relationships between variables. These tests were performed in GraphPad Prism v.8 or R v3.6.3. Differences of $p < 0.05$ were considered significant.

Supporting information

S1 Fig. Gastrointestinal transit dysfunction screen in mice infected with different strains of *T. cruzi*. Data are gastrointestinal (GI) transit times at indicated weeks post-infection (p.i.) for C3H/HeN mice in the following infection groups: naive control ($n = 4$–6), TcI-ArePe ($n = 1$–4), TcI-SN3 ($n = 4$), TcI-SylvioX10/4 ($n = 4$) and TcI-C8 ($n = 4$), TcII-Pot7a ($n = 4$), TcIII-Arma18 ($n = 3$–4), TcIV-X10610 ($n = 4$) and TcVI-Peru ($n = 3$).
(TIF)

S2 Fig. *Ex vivo* analysis of parasite tissue distributions for TcI-SN3, TcI-ArePe, TcIII-Arma18 and TcVI-Peru strains of *T. cruzi*. A. Bioluminescence signal intensity (blue, low, to red, high) in tissue samples from chronically infected C3H/HeN mice. Samples, from

top left to right, lung, heart, genito-urinary system, liver, GI mesentery, peritoneum, skeletal muscle, visceral adipose, large intestine, small intestine, stomach and oesophagus. **B.** Frequency of parasite detection in the indicated organs/tissues. TcI-SN3 $n = 4$, TcI-ArePe $n = 4$, TcIII-Arma18 $n = 3$, TcVI-Peru $n = 2$.
(TIF)

S3 Fig. Anatomical measures of gastrointestinal *T. cruzi* infection mouse models. A. Body weights of naïve control ($n = 3$–10), TcI-JR ($n = 5$–22) and TcVI-CLBR ($n = 5$–20) infected C3H/HeN (left) and BALB/c mice (right) vs. days post-infection (p.i.). **B.** Bar plots show length of small intestine and colon of control and TcI-JR C3H/HeN mice at 3 ($n = 24$ per group), 6 ($n = 27$ per group) and 30 ($n = 5$ per group) weeks p.i. Data are expressed as mean ± SEM.
(TIF)

S4 Fig. Fluorescent tracer imaging assay for gastrointestinal (GI) transit in high inoculum acute *T. cruzi* infection. Schematic diagram of a mouse receiving oral gavage of a green fluorescent marker, FITC-conjugated 70 kDa dextran, 60 or 120 or 180 minutes prior to termination to trace localised GI transit delay during acute infection. Quantification of FITC-dextran fluorescence in different parts of the GI tract (SI 1 –SI 10: small intestine scored into 10 equal sections, proximal to distal) of naïve control and TcI-JR C3H/HeN ($n = 4$ per group) mice at 3 weeks post-infection. All mice in this experiment were infected with a high inoculum of TcI-JR parasites (10^4). Data are expressed as mean ± SEM.
(TIF)

S5 Fig. Comparison of colonic transit dysfunction in different models of experimental digestive Chagas disease. Faecal output analyses are expressed as faecal pellet count, wet and dry pellet weight at 30 weeks post-infection (p.i.) in the following groups: naive control ($n = 7$–11), TcI-JR ($n = 5$–11), TcI-SN3 ($n = 4$), TcI-ArePe ($n = 1$), TcIII-Arma18 ($n = 3$), TcVI-Peru ($n = 3$) and TcVI-CLBR ($n = 4$–5).
(TIF)

S6 Fig. Myenteric neuronal plexus lesions in *T. cruzi* infection. Colon tissue samples from C3H mice with chronic TcI-JR infections were cut as transverse cross-sections and images are oriented to show the mucosa above the smooth muscle layers and serosa at the lower edge. Acellular structures (arrows) within myenteric plexus ganglia that are refractory to staining by the indicated method. 400X magnification.
(TIF)

S7 Fig. Chronic phase colonic *T. cruzi* infection foci of TcI-SN3 parasites in the ENS. Representative immunofluorescent z-stack confocal images of whole-mount colonic muscularis from C3H mice chronically infected with fluorescent TcI-SN3 (mScarlet$^+$) parasites. Image shows the localisation of TcI-SN3 parasites (red) in the submucosal layer of the ENS stained with anti-TuJ1 (white). DAPI (cyan) shows DNA and white circle indicates DNA of the parasite nest. Images were taken at 400X magnification, scale bar = 50 μm.
(TIF)

S1 Table. Quantitative PCR target gene and primer information.
(DOCX)

Acknowledgments

We thank Herna´n Carrasco, Michael Miles, Manuel Sa´nchez-Moreno, Omar Triana and Matthew Yeo for sharing parasite strains and the LSHTM Biological Services Facility staff for technical support and animal husbandry.

Author Contributions

Conceptualization: Conor J. McCann, John M. Kelly, Michael D. Lewis.

Formal analysis: Archie A. Khan, Harry C. Langston, Michael D. Lewis.

Funding acquisition: Michael D. Lewis.

Investigation: Archie A. Khan, Harry C. Langston, Fernanda C. Costa, Michael D. Lewis.

Methodology: Archie A. Khan, Fernanda C. Costa, Martin C. Taylor, Conor J. McCann, Michael D. Lewis.

Resources: Francisco Olmo, Martin C. Taylor, Conor J. McCann, John M. Kelly, Michael D. Lewis.

Supervision: John M. Kelly, Michael D. Lewis.

Validation: Archie A. Khan, Francisco Olmo, Martin C. Taylor, Michael D. Lewis.

Visualization: Archie A. Khan, Harry C. Langston, Michael D. Lewis.

Writing – original draft: Archie A. Khan, Michael D. Lewis.

Writing – review & editing: Archie A. Khan, Harry C. Langston, Fernanda C. Costa, Francisco Olmo, Martin C. Taylor, Conor J. McCann, John M. Kelly, Michael D. Lewis.

References

1. Rassi A Jr, Rassi A, Marin-Neto JA. Chagas disease. Lancet. 2010; 375(9723):1388–402. https://doi.org/10.1016/S0140-6736(10)60061-X PMID: 20399979
2. Iantorno G, Bassotti G, Kogan Z, Lumi CM, Cabanne AM, Fisogni S, et al. The enteric nervous system in chagasic and idiopathic megacolon. Am J Surg Pathol. 2007; 31(3):460–8. https://doi.org/10.1097/01.pas.0000213371.79300.a8 PMID: 17325489
3. Meneghelli UG. Chagasic enteropathy. Rev Soc Bras Med Trop. 2004; 37(3):252–60. https://doi.org/10.1590/s0037-86822004000300012 PMID: 15330067
4. Rassi A, de Rezende JM, Luquetti AO, Rassi A. Clinical phases and forms of Chagas disease. In: Telleria J, Tibayrenc M, editors. American Trypanosomiasis Chagas Disease (Second Edition). London: Elsevier; 2017. p. 653–86.
5. Bern C. Antitrypanosomal Therapy for Chronic Chagas' Disease. New Engl J Med. 2011; 364 (26):2527–34. https://doi.org/10.1056/NEJMct1014204 PMID: 21714649
6. Ribeiro I, Sevcsik AM, Alves F, Diap G, Don R, Harhay MO, et al. New, improved treatments for Chagas disease: from the R&D pipeline to the patients. PLoS Negl Trop Dis. 2009; 3(7):e484. https://doi.org/10.1371/journal.pntd.0000484 PMID: 19582163
7. Ko¨ berle F. Chagas' disease and Chagas' syndromes: the pathology of American trypanosomiasis. Adv Parasitol. 1968; 6(63):63–116. https://doi.org/10.1016/s0065-308x(08)60472-8 PMID: 4239747
8. de Oliveira RB, Troncon LE, Dantas RO, Menghelli UG. Gastrointestinal manifestations of Chagas' disease. Am J Gastroenterol. 1998; 93(6):884–9. https://doi.org/10.1111/j.1572-0241.1998.270_r.x PMID: 9647012
9. Arantes RM, Marche HH, Bahia MT, Cunha FQ, Rossi MA, Silva JS. Interferon-gamma-induced nitric oxide causes intrinsic intestinal denervation in *Trypanosoma cruzi*-infected mice. Am J Pathol. 2004; 164(4):1361–1368. https://doi.org/10.1016/s0002-9440(10)63222-1 PMID: 15039223
10. Adad SJ, Andrade DCdS, Lopes ER, Chapadeiro E.s Contribuic¸ão ao estudo da anatomia patolo´gica do megaesoˆfago chaga´sico. Rev I Med Trop. 1991; 33:443–50.
11. Vago AR, Macedo AM, Adad SJ, Reis DdA´, Corrêa-Oliveira R. PCR detection of *Trypanosoma cruzi* DNA in oesophageal tissues of patients with chronic digestive Chagas' disease. Lancet. 1996; 348 (9031):891–2. https://doi.org/10.1016/S0140-6736(05)64761-7 PMID: 8826826
12. Vago AR, Silva DM, Adad SJ, Correa-Oliveira R, d'Avila Reis D. Chronic Chagas disease: presence of parasite DNA in the oesophagus of patients without megaoesophagus. Trans R Soc Trop Med Hyg. 2003; 97(3):308–9. https://doi.org/10.1016/s0035-9203(03)90155-6 PMID: 15228249

13. Corbett CE, Ribeiro U, Jr., Prianti MG, Habr-Gama A, Okumura M, Gama-Rodrigues J. Cell-mediated immune response in megacolon from patients with chronic Chagas' disease. Dis Colon Rectum. 2001; 44(7):993–8. https://doi.org/10.1007/BF02235488 PMID: 11496080

14. Lages-Silva E, Crema E, Ramirez LE, Macedo AM, Pena SD, Chiari E. Relationship between *Trypanosoma cruzi* and human chagasic megaesophagus: blood and tissue parasitism. Am J Trop Med Hyg. 2001; 65(5):435–41. https://doi.org/10.4269/ajtmh.2001.65.435 PMID: 11716095

15. da Silveira ABM, Arantes RME, Vago AR, Lemos EM, Adad SJ, Correa-Oliveira R, et al. Comparative study of the presence of *Trypanosoma cruzi* kDNA, inflammation and denervation in chagasic patients with and without megaesophagus. Parasitology. 2005; 131(05):627–34. https://doi.org/10.1017/S0031182005008061 PMID: 16255821

16. da Silveira ABM, Lemos EM, Adad SJ, Correa-Oliveira R, Furness JB, D'Avila Reis D. Megacolon in Chagas disease: a study of inflammatory cells, enteric nerves, and glial cells. Hum Pathol. 2007; 38 (8):1256–64. https://doi.org/10.1016/j.humpath.2007.01.020 PMID: 17490721

17. de Castro Coˆbo de E, Silveira TP, Micheletti AM, Crema E, Adad SJ. Research on *Trypanosoma cruzi* and Analysis of Inflammatory Infiltrate in Esophagus and Colon from Chronic Chagasic Patients with and without Mega. J Trop Med. 2012; 2012:232646. https://doi.org/10.1155/2012/232646 PMID: 22131997

18. Lewis MD, Francisco AF, Taylor MC, Burrell-Saward H, McLatchie AP, Miles MA, et al. Bioluminescence imaging of chronic *Trypanosoma cruzi* infections reveals tissue-specific parasite dynamics and heart disease in the absence of locally persistent infection. Cell Microbiol. 2014; 16(9):1285–300. https://doi.org/10.1111/cmi.12297 PMID: 24712539

19. Lewis MD, Francisco AF, Taylor MC, Jayawardhana S, Kelly JM. Host and parasite genetics shape a link between *Trypanosoma cruzi* infection dynamics and chronic cardiomyopathy. Cell Microbiol. 2016; 18(10):1429–43. https://doi.org/10.1111/cmi.12584 PMID: 26918803

20. Silberstein E, Serna C, Fragoso SP, Nagarkatti R, Debrabant A. A novel nanoluciferase-based system to monitor *Trypanosoma cruzi* infection in mice by bioluminescence imaging. PLoS ONE. 2018; 13(4): e0195879. https://doi.org/10.1371/journal.pone.0195879 PMID: 29672535

21. Francisco AF, Lewis MD, Jayawardhana S, Taylor MC, Chatelain E, Kelly JM. The limited ability of posaconazole to cure both acute and chronic *Trypanosoma cruzi* infections revealed by highly sensitive *in vivo* imaging. Antimicrob Agents Chemother. 2015; 59(8):4653–61. https://doi.org/10.1128/AAC.00520-15 PMID: 26014936

22. Santi-Rocca J, Fernandez-Cortes F, Chillo´n-Marinas C, Gonza´lez-Rubio M-L, Martin D, Gironès N, et al. A multi-parametric analysis of *Trypanosoma cruzi* infection: common pathophysiologic patterns beyond extreme heterogeneity of host responses. Sci Rep. 2017; 7(1):1–12. https://doi.org/10.1038/s41598-016-0028-x PMID: 28127051

23. Laranjeira C, Sandgren K, Kessaris N, Richardson W, Potocnik A, Vanden Berghe P, et al. Glial cells in the mouse enteric nervous system can undergo neurogenesis in response to injury. J Clin Invest. 2011; 121(9):3412–24. https://doi.org/10.1172/JCI58200 PMID: 21865647

24. Kulkarni S, Micci M-A, Leser J, Shin C, Tang S-C, Fu Y-Y, et al. Adult enteric nervous system in health is maintained by a dynamic balance between neuronal apoptosis and neurogenesis. Proc Natl Acad Sci USA. 2017; 114(18):E3709–E18. https://doi.org/10.1073/pnas.1619406114 PMID: 28420791

25. Muller PA, Koscso´ B, Rajani Gaurav M, Stevanovic K, Berres M-L, Hashimoto D, et al. Crosstalk between Muscularis Macrophages and Enteric Neurons Regulates Gastrointestinal Motility. Cell. 2014; 158(2):300–13. https://doi.org/10.1016/j.cell.2014.04.050 PMID: 25036630

26. Gabanyi I, Muller PA, Feighery L, Oliveira Thiago Y, Costa-Pinto Frederico A, Mucida D. Neuro-immune Interactions Drive Tissue Programming in Intestinal Macrophages. Cell. 2016; 164(3):378–91. https://doi.org/10.1016/j.cell.2015.12.023 PMID: 26777404

27. do Carmo Neto JR, Vinicius da Silva M, Braga YLL, Florencio da Costa AW, Fonseca SG, Nagib PRA, et al. Correlation between intestinal BMP2, IFNγ, and neural death in experimental infection with *Trypanosoma cruzi*. PLoS ONE. 2021; 16(2):e0246692. https://doi.org/10.1371/journal.pone.0246692 PMID: 33561140

28. Branchini BR, Ablamsky DM, Davis AL, Southworth TL, Butler B, Fan F, et al. Red-emitting luciferases for bioluminescence reporter and imaging applications. Anal Biochem. 2010; 396(2):290–7. https://doi.org/10.1016/j.ab.2009.09.009 PMID: 19748472

29. Machado CA, Ayala FJ. Nucleotide sequences provide evidence of genetic exchange among distantly related lineages of *Trypanosoma cruzi*. Proc Natl Acad Sci USA. 2001; 98(13):7396–401. https://doi.org/10.1073/pnas.121187198 PMID: 11416213

30. Westenberger SJ, Barnabe´ C, Campbell DA, Sturm NR. Two hybridization events define the population structure of *Trypanosoma cruzi*. Genetics. 2005; 171(2):527–43. https://doi.org/10.1534/genetics.104.038745 PMID: 15998728

31. Lewis MD, Llewellyn MS, Yeo M, Acosta N, Gaunt MW, Miles MA. Recent, Independent and Anthropogenic Origins of *Trypanosoma cruzi* Hybrids. PLoS Negl Trop Dis. 2011; 5(10):e1363. https://doi.org/10.1371/journal.pntd.0001363 PMID: 22022633

32. Lewis MD, Francisco AF, Jayawardhana S, Langston H, Taylor MC, Kelly JM. Imaging the development of chronic Chagas disease after oral transmission. Sci Rep. 2018; 8(1):11292. https://doi.org/10.1038/s41598-018-29564-7 PMID: 30050153

33. Nascimento R, Martins P, Duarte J, d'A´ vila Reis D. Decrease of Nitrergic Innervation in the Esophagus of Patients with Chagas Disease: Correlation with Loss of Interstitial Cells of Cajal. J Int J Pathol Clin Res. 2017; 3:059.

34. Dickson EJ, Heredia DJ, McCann CJ, Hennig GW, Smith TK. The mechanisms underlying the generation of the colonic migrating motor complex in both wild-type and nNOS knockout mice. Am J Physiol Gastrointest Liver Physiol. 2010; 298(2):G222–G32. https://doi.org/10.1152/ajpgi.00399.2009 PMID: 19959818

35. McCann CJ, Cooper JE, Natarajan D, Jevans B, Burnett LE, Burns AJ, et al. Transplantation of enteric nervous system stem cells rescues nitric oxide synthase deficient mouse colon. Nat Commun. 2017; 8:15937. https://doi.org/10.1038/ncomms15937 PMID: 28671186

36. Rivera LR, Poole DP, Thacker M, Furness JB, Motility. The involvement of nitric oxide synthase neurons in enteric neuropathies. Neurogastroenterol Motil. 2011; 23(11):980–8. https://doi.org/10.1111/j.1365-2982.2011.01780.x PMID: 21895878

37. Ward AI, Lewis MD, Khan AA, McCann CJ, Francisco AF, Jayawardhana S, et al. *In Vivo* Analysis of *Trypanosoma cruzi* Persistence Foci at Single-Cell Resolution. mBio. 2020; 11(4):e01242–20. https://doi.org/10.1128/mBio.01242-20 PMID: 32753495

38. Costa FC, Francisco AF, Jayawardhana S, Calderano SG, Lewis MD, Olmo F, et al. Expanding the toolbox for *Trypanosoma cruzi*: A parasite line incorporating a bioluminescence-fluorescence dual reporter and streamlined CRISPR/Cas9 functionality for rapid *in vivo* localisation and phenotyping. PLoS Negl Trop Dis. 2018; 12(4):e0006388. https://doi.org/10.1371/journal.pntd.0006388 PMID: 29608569

39. Da Silveira A, Freitas M, De Oliveira E, Neto S, Luquetti A, Furness J, et al. Neuronal plasticity of the enteric nervous system is correlated with chagasic megacolon development. Parasitology. 2008; 135 (11):1337–42. https://doi.org/10.1017/S0031182008004770 PMID: 18664306

40. Ko¨berle F. Enteromegaly and Cardiomegaly in Chagas Disease. Gut. 1963; 4(4):399–405.

41. Campos CF, Cangussu´ SD, Duz ALC, Cartelle CT, Noviello MdL, Veloso VM, et al. Enteric Neuronal Damage, Intramuscular Denervation and Smooth Muscle Phenotype Changes as Mechanisms of Chagasic Megacolon: Evidence from a Long-Term Murine Model of *Trypanosoma cruzi* Infection. PLoS ONE. 2016; 11(4):e0153038. https://doi.org/10.1371/journal.pone.0153038 PMID: 27045678

42. Ricci MF, Be´la SR, Moraes MM, Bahia MT, Mazzeti AL, Oliveira ACS, et al. Neuronal Parasitism, Early Myenteric Neurons Depopulation and Continuous Axonal Networking Damage as Underlying Mechanisms of the Experimental Intestinal Chagas' Disease. Front Cell Infect Microbiol. 2020; 10:583899. https://doi.org/10.3389/fcimb.2020.583899 PMID: 33178632

43. Moreira NM, Zanoni JN, de Oliveira Dala´lio MM, de Almeida Arau´jo EJ, Braga CF, de Arau´jo SM. Physical exercise protects myenteric neurons and reduces parasitemia in *Trypanosoma cruzi* infection. Exp Parasitol. 2014; 141:68–74. https://doi.org/10.1016/j.exppara.2014.03.005 PMID: 24667137

44. Oda JY, Bele´m MO, Carlos TM, Gouveia R, Luchetti BFC, Moreira NM, et al. Myenteric neuroprotective role of aspirin in acute and chronic experimental infections with *Trypanosoma cruzi*. Neurogastroenterol Motil. 2017; 29(10):1–13. https://doi.org/10.1111/nmo.13102 PMID: 28524628

45. Maifrino LB, Liberti EA, Watanabe I, De Souza RR. Morphometry and acetylcholinesterase activity of the myenteric neurons of the mouse colon in the chronic phase of experimental *Trypanosoma cruzi* infection. Am J Trop Med Hyg. 1999; 60(5):721–5. https://doi.org/10.4269/ajtmh.1999.60.721 PMID: 10344641

46. de Oliveira GM, de Melo Medeiros M, da Silva Batista W, Santana R, Arau´jo-Jorge TC, de Souza AP. Applicability of the use of charcoal for the evaluation of intestinal motility in a murine model of *Trypanosoma cruzi* infection. Parasitol Res. 2008; 102(4):747–50. https://doi.org/10.1007/s00436-007-0829-8 PMID: 18163190

47. de Souza AP, Sieberg R, Li H, Cahill HR, Zhao D, Arau´jo-Jorge TC, et al. The role of selenium in intestinal motility and morphology in a murine model of *Typanosoma cruzi* infection. Parasitol Res. 2010; 106 (6):1293–8. https://doi.org/10.1007/s00436-010-1794-1 PMID: 20195635

48. Lopes ER, Rocha A, Meneses AC, Lopes MA, Fatureto MC, Lopes GP, et al. Prevalência de megas em necro´psias realizadas no triaˆngulo mineiro no per´ıodo de 1954 a 1988. Rev Soc Bras Med Trop. 1989; 22(4):211–5. https://doi.org/10.1590/s0037-86821989000400008 PMID: 2518668

49. Osman KL, Kohlberg S, Mok A, Brooks R, Lind LA, McCormack K, et al. Optimizing the Translational Value of Mouse Models of ALS for Dysphagia Therapeutic Discovery. Dysphagia. 2020; 35(2):343–59. https://doi.org/10.1007/s00455-019-10034-9 PMID: 31300881

50. Hugenholtz F, de Vos WM. Mouse models for human intestinal microbiota research: a critical evaluation. Cell Mol Life Sci. 2018; 75(1):149–60. https://doi.org/10.1007/s00018-017-2693-8 PMID: 29124307

51. Jd Rezende. Chagasic mega syndromes and regional differences. New Approaches in American trypanosomiasis research Pan Am Health Org Sci Publ. 1975; 318:195–205.

52. Chatelain E, Scandale I. Animal models of Chagas disease and their translational value to drug development. Expert Opin Drug Discov. 2020; 15(12):1381–402. https://doi.org/10.1080/17460441.2020.1806233 PMID: 32812830

53. Miles M, Cedillos R, Povoa M, de Souza A, Prata A, Macedo V. Do radically dissimilar *Trypanosoma cruzi* strains (zymodemes) cause Venezuelan and Brazilian forms of Chagas' disease? Lancet. 1981; 317(8234):1338–40. https://doi.org/10.1016/s0140-6736(81)92518-6 PMID: 6113312

54. Messenger LA, Miles MA, Bern C. Between a bug and a hard place: *Trypanosoma cruzi* genetic diversity and the clinical outcomes of Chagas disease. Expert Rev Anti Infect Ther. 2015; 13(8):995–1029. https://doi.org/10.1586/14787210.2015.1056158 PMID: 26162928

55. Panesso-Go´mez S, Pavia P, Rodr´ıguez-Mantilla IE, Lasso P, Orozco LA, Cuellar A, et al. *Trypanosoma cruzi* Detection in Colombian Patients with a Diagnosis of Esophageal Achalasia. Am J Trop Med Hyg. 2018; 98(3):717–23. https://doi.org/10.4269/ajtmh.17-0417 PMID: 29405099

56. Flo´rez O, Esper J, Higuera S, Barraza MF, Cabrera HB, Mantilla JC, et al. Chagasic megacolon associated with *Trypanosoma cruzi* I in a Colombian patient. Parasitol Res. 2010; 107(2):439–42. https://doi.org/10.1007/s00436-010-1874-2 PMID: 20502919

57. Sa´nchez-Guille´n MC, Lo´pez-Colombo A, Ordo´ñez-Toquero G, Gomez-Albino I, Ramos-Jimenez J, Torres-Rasgado E, et al. Clinical forms of *Trypanosoma cruzi* infected individuals in the chronic phase of Chagas disease in Puebla, Mexico. Mem Inst Oswaldo Cruz. 2006; 101(7):733–40. https://doi.org/10.1590/s0074-02762006000700005 PMID: 17160280

58. Jabari S, de Oliveira EC, Brehmer A, da Silveira AB. Chagasic megacolon: enteric neurons and related structures. Histochem Cell Biol. 2014; 142(3):235–44. https://doi.org/10.1007/s00418-014-1250-x PMID: 25059649

59. Boesmans W, Lasrado R, Vanden Berghe P, Pachnis V. Heterogeneity and phenotypic plasticity of glial cells in the mammalian enteric nervous system. Glia. 2015; 63(2):229–41. https://doi.org/10.1002/glia.22746 PMID: 25161129

60. Hossain E, Khanam S, Dean DA, Wu C, Lostracco-Johnson S, Thomas D, et al. Mapping of host-parasite-microbiome interactions reveals metabolic determinants of tropism and tolerance in Chagas disease. Sci Adv. 2020; 6(30):eaaz2015. https://doi.org/10.1126/sciadv.aaz2015 PMID: 32766448

61. Veiga-Fernandes H, Pachnis V. Neuroimmune regulation during intestinal development and homeostasis. Nat Immunol. 2017; 18(2):116–22. https://doi.org/10.1038/ni.3634 PMID: 28092371

62. Pe´rez-Mazliah D, Ward AI, Lewis MD. Host-parasite dynamics in Chagas disease from systemic to hyper-local scales. Parasite Immunol. 2021; 43(2):e12786. https://doi.org/10.1111/pim.12786 PMID: 32799361

63. Yoo BB, Mazmanian SK. The Enteric Network: Interactions between the Immune and Nervous Systems of the Gut. Immunity. 2017; 46(6):910–26. https://doi.org/10.1016/j.immuni.2017.05.011 PMID: 28636959

64. Ko¨berle F. The causation and importance of nervous lesions in American trypanosomiasis. B World Health Organ. 1970; 42(5):739–43. PMID: 4988694

65. Miller MS, Galligan JJ, Burks TF. Accurate measurement of intestinal transit in the rat. J Pharmacol Methods. 1981; 6(3):211–7. https://doi.org/10.1016/0160-5402(81)90110-8 PMID: 7329070

66. Schmittgen TD, Livak KJ. Analyzing real-time PCR data by the comparative CT method. Nat Protoc. 2008; 3:1101. https://doi.org/10.1038/nprot.2008.73 PMID: 18546601

Chapter 2: Investigating the parasite-immune axis in the initiation of gut dysfunction in acute stage experimental Chagas disease.

2.1 Introduction

The gastrointestinal tract is innervated by neuronal networks that synergistically coordinate critical homeostatic functions such as peristalsis, pathology, and wound healing (1). Upon infectious challenge, an aberrant microenvironment may develop and impact negatively on these neurological tissues, or alternatively a neuroprotective response may be initiated (2). This process has yet to be studied in detail for DCD, but research in a variety of experimental systems suggests that it is likely to be regulated by bi-directional crosstalk between neurons and immune cells.

Intestinal neuro-immune axis

The *muscularis externa* layer of the GI tract, where the majority of the enteric nervous system (ENS) resides between the circular and longitudinal smooth muscle layers, is also the resident site of abundant MHCII+ Cd11b+ CX_3CR1+ muscularis macrophages (MMs), which are in close physical proximity to enteric ganglia (3). These macrophages are phenotypically distinct, characterised by tissue-protective expression of *Arg1* for arginase production, *Il10* and *cd163* for regulating inflammation, *Mrc1* for immune homeostasis via endocytosis of glycoproteins, and *Retnla* for dampening T_H2 responses and promoting tissue repair (4). To highlight the focal significance of MMs to enteric transit function, MM-deficient mice present with atypical and asynchronous muscle contraction and slower intestinal motility due to the absence of the MM-derived growth factor bone morphogenetic protein 2 (BMP2) (3). BMP2 signals directly on enteric neurons via bone morphogenic protein

receptors to organise muscle contraction. Reciprocally, enteric neurons facilitate MM preservation in the smooth muscle via production of CSF1, a key macrophage survival factor. There is a degree of heterogeneity within MM populations and where they reside in the intestinal milieu. A subset of CX_3CR1+ MMs are self-maintained by embryo-derived progenitors in the gut, in contrast to the majority of intestinal macrophages that originate from sustained trafficking of bone marrow derived monocytes (5). Self-sustaining macrophages reside across multiple intestinal layers, including the sub-mucosa where they have niched functions in adhesion and angiogenesis (5). Despite the wider distribution, self-maintaining macrophages are independently critical to enteric homeostasis, as depletion of them results in caspase-3-mediated apoptosis and reduced intestinal transit time (5). During an infection challenge by some enteric bacteria neuronal-MM cross talk ensures neuronal protection from excessive inflammation. Primarily, via neuronal moderation of tissue protective M2-like (anti-inflammatory/tissue-protective) MM populations in the myenteric plexus, in which polyamines are generated via β2 adrenergic receptor (β_2AR) on MMs in response to the neurotransmitter norepinephrine (noradrenaline). This in turn limits inflammasome mediated damage to enteric neurons after the clearance of pathogens, which would otherwise lead to long-lasting motility defects (6).

Although not as well defined, the adaptive immune system also interacts with the ENS in several ways (7). Neuronal communication with B cells and CD4+ and CD8+ T cells contributes critically to immune tolerance and the integrity of the intestinal barrier (8). For example, a signalling cascade originating from efferent vagal nerves reaches the spleen and, via β_2AR, communicates with choline acetyltransferase

(ChAT)+ T cells, which can in turn produce the neurotransmitter acetylcholine (Ach) (9).

In the gut, local T-cell generated Ach interacts with MMs, which inhibits TNF-α production and limits excessive inflammation. Ach also directly modulates T-cell function via M_3 muscarinic Ach receptor (M3R), which has been directly implicated in host defence against murine hookworm and *Salmonella Typhimurium* infection (10). Dysregulated signalling between CD8+ T cells and the ENS is also implicated during systemic infection with Chikungunya, West Nile and Zika flaviviruses which leads to slowed GI motility and bowel dilation (11). The GI dysmotility was identified to be a result of CD8+ T-cell mediated enteric neuron death in the acute phase, validated by the finding that CD8+ T cell deficiency alleviated the transit time delay whilst preventing enteric neuron death. Conversely, introducing flavivirus-primed CD8+ T cells resulted in myenteric denervation and the delayed transit time phenotype to return (11). CD8+ T-cell mediated myenteric and submucosal denervation could also be a factor of IBD. CD8+ T-cell recruitment to these nerve plexuses correlated with significant damage and severe intestinal transit delays (12). The mechanisms behind neuronal destruction in this dysregulated signalling between neurons and CD8+ T-cells in these settings are not known, but in a mouse model of autoimmune enteric ganglionitis cell-to-cell mediated neuronal death has been shown to require perforin and TNFα, but not Fas/FasL signalling (13).

B cells, upon activation in the GI tract, typically switch from IgM to IgA-producing plasma cells for anti-pathogenic responses (14). The evidence for neuronal signalling contribution with B cells appears to be similar to T cells, with Ach

promoting plasma cell differentiation, with populations seen apposing Peyer's patches in the small intestine and mucosal nerves across the GI tract (15). Validating the bi-directional communication between nerves and B cells, neuron-derived vasoactive intestinal peptide (VIP) induces IgA production *in vitro*, and signalling via β2AR promotes IL-4 dependent Ig production. Another neurotransmitter, noradrenaline, directly inhibits Th2-dependent plasma cell differentiation (16). In experimental autoimmune encephalomyelitis
(EAE) models, where antibody responses target neuronal cell surfaces and synaptic proteins, a distinct interaction with peripheral nervous systems, including the ENS, has been identified. In these models, mice present with an increased colonic transit time and atypical glial fibrillary acid protein (GFAP) expression in the ENS (17). Upon B-cell depletion, mice presented with normal gut motility. Moreover, serum from multiple sclerosis patients or autoimmune encephalitis mice exhibited increased immunoreactivity against ENS neurons and glial cells (17).

In summary, the neuronal-immunological axis is finely balanced to ensure pathological challenge is neutralised without excessive local tissue or neurological damage. The microenvironment of neurological tissues is maintained in homeostasis by signalling between neurons and multiple immune cell types, but when this system is dysregulated, neurological and functional symptoms can manifest. The mechanisms of immune-mediated enteric neuropathies are vast and differ between infectious and non-infectious contexts. However, aspects of the immune response may contribute to both cases.

Neuroinflammation and cell death

Neuroinflammation is the process by which the inflammatory response occurs within neuronal spaces, such as the brain, CNS, or peripheral nervous systems, with cellular infiltrates closely opposing neurons (18). Cytokines, chemokines and reactive oxygen species are produced by either resident cells such as microglia and astrocytes in the CNS, or by endothelial cells and local or peripheral immune cells, which can damage neurons by collateral damage or targeted destruction (18). Neurodegenerative diseases are good case studies for dissecting the mechanistic basis of inflammatory neuropathy. The accumulative amyloidogenic proteins on neurons, which are synonymous with Alzheimer's disease (AD), Parkinson's' disease (PD), Amyotrophic lateral sclerosis (ALS) and Creutzfeldt-Jakob's disease (CJD), are directly neurotoxic, and these aggregates also trigger neuroinflammation which further perpetuates pathology (19).

Pattern recognition receptors (PRRs) directly recognise amyloid deposits as damage-associated molecular patterns (DAMPs). As plaques develop, other markers of neurodegeneration are released including, but not limited to; heat-shock proteins, extracellular matrix components (fibrinogen and fibronectin), mitochondrial DNA and cytochrome c (20). Supramolecular organising centres (SMOCs) assembled on various intracellular sites, organise effector enzymes after PRR activation via DAMPs (21). The downstream signalling from SMOCs can contribute to neurotoxicity by promoting the production of inflammatory mediators such as reactive oxygen species (ROS) and reactive nitrogen species (RNS) e.g., nitric oxide (NO). Examples of specific SMOC produced inflammatory mediators include the proteolytic cleavage of caspase-1, which triggers the secretion of the pro-inflammatory cytokine IL-1,

whereas signalling through MyD88 results in secretion of tumour necrosis factor NF-KB and subsequently type 1 interferons (22,23). These pro-inflammatory cytokines result in neuronal apoptosis via a process known as excitotoxicity, which occurs through cytokine mediated overstimulation of synaptic receptors (24). NO is a primary inflammatory by-product of the innate immune response produced by inducible nitric oxide synthase (iNOS). iNOS is synonymous with a wide range of immunity pathways since it is regulated by major immunity transcription factors such as NF-KB, signal transducer and activator of transcription (STAT1), and interferon regulatory factors (IRFs) (25). NO is also a retrograde neurotransmitter and is additionally produced by neuronal nitric oxide synthetase (nNOS) to aid in intracellular signalling in neurons (26). Subsequently, overproduction of NO results in neurotoxicity by inhibiting neurotransmitter recycling. In the CNS, activation of microglia is associated with increased expression of iNOS, and subsequently NO and RNS. This pro-inflammatory pathway is implicated in a neurodegenerative context as immunostaining of iNOS is increased in PD brains (27). ROS, more specifically the oxygen superoxide anion, is also implicated in neurotoxicity by broad-acting oxidation of critical proteins and nucleic acids acting to impair cellular functions and DNA repair.

Direct inflammation mediated cell death is also implicated in response to certain DAMPs and TNF-α activity (19). DAMPs released from dead cells perpetuate a feedback loop whereby the same PRRs continuously recognise the original DAMP(19). There are two mechanisms of cell death synonymous with the inflammatory cascade outlined thus far with neurodegeneration and neuroinflammation. Inflammatory damage and stress results in necroptosis, which is

unprogrammed cell death, or apoptosis, which is programmed cell death (19). Necroptosis is a caspase-8 independent mechanism, orchestrated by the necrosome. Upon cell death, a secondary inflammatory response is perpetuated due to the release of cytokines, chemokines, and DAMPS into the extracellular milieu (28). Necroptosis is associated with signal transduction events downstream of TNF-a and IL-1, regulated by receptor-interacting protein kinase 1 (RIPK1) and RIPK3, which are also independently associated with inflammation irrespective of cell death (29). Conversely, apoptosis is caspase-8 dependent and results in a controlled, immunologically silent cell death, as the integrity of the plasma membrane is maintained, and the intracellular contents are not exposed (29). In addition to immune cell mediated cell death, neurons can directly initiate cell death since TNF-α receptors and caspase-8 receptors, such as CD95, are located on neuronal surfaces (30).

Adaptive immune effectors also contribute to progression of neurodegenerative diseases (21). The chronicity of pro-inflammatory cytokine action mentioned previously (TNF-α, IL-1 IFN-y) permit peripheral immune cells to cross the blood brain barrier (BBB) (31). Infiltrated effector T-cells can produce the same neurotoxic cytokines that disrupted the integrity of the BBB, which directly interact with receptors on neurons (32). CD8+ T-cell action can be neurotoxic through both direct and collateral means (33). Multiple Sclerosis (MS) is a T-cell mediated autoimmune inflammatory disease, which is a good case study for the neurotoxic effect of CD8+ T cells. Here, CD8+ T-cells target oligodendrocytes (myelinating cells of CNS) by forming an immunological synapse with MHC-I molecules presenting self-derived peptides on target cells (34). These autoreactive CD8+ T cells then release perforin

and granzymes from cytotoxic granules in a unidirectional secretory pathway, ensuring only the cell being targeted is destroyed. However, cell destruction can also occur through nonconfined release, via a constitutive multidirectional nongranule pathway (33). Nonconfined release, coupled with leakage of perforin and granzymes from the formed immunological synapse results in collateral damage to neighbouring cells (34).

To summarise, there is a myriad of immunological mediated mechanisms that contribute to neuropathy, providing a broad framework for the investigation of digestive Chagas disease (DCD). In DCD it is not clear which effectors drive the denervation observed in the enteric nervous system. Our current understanding and theories of enteric neuropathy suggest a significant amount of damage to the ENS occurs in the acute phase of *T. cruzi* infection, which involves both innate and adaptive, cellular and humoral immune responses. A better understanding of the similarities and differences between the pathogenic mechanisms underpinning DCD and other (better studied) neuroinflammatory and neurodegenerative diseases could accelerate the development of diagnostic and therapeutic tools.

Neuropathy in Chagas disease

Denervation has long been identified as a clinical manifestation of Chagas disease, with Fritz Köberle's seminal studies (35,36) establishing rates of denervation in organs from 800 Chagas disease patient autopsies in Brazil. Across the GI tract for the colon and oesophagus, megasyndromes were associated with >55% and >95% denervation respectively, but even patients who did not have megasyndromes had lower neuron counts than normal. This established denervation beyond these critical

thresholds as the primary theory for megasyndrome development in the GI tract. Colonic denervation recently reproduced in DCD models exhibiting severe transit time delays (37).

From Kberle's studies it was established that the cardiac denervation threshold was much lower at 25%, which would contribute to conduction issues associated with arrythmia and cardiomyopathy. Sympathetic denervation of chagasic hearts occurs in the acute phase of infection and is characterised by depletion of cardiac norepinephrine (38). The mechanism behind Chagas related neuropathy, in both organ systems remains unknown, but leading theories revolve around parasite persistence. This theory focuses on the mechanical rupture of parasitized cells and neurons, and the release of parasitic and cellular debris, including PAMPs and DAMPs, which elicits a secondary local immune response (39). The regulatory gene expression of specific pro-inflammatory cytokines in the acute phase, that have previously been mentioned in the context of neuroinflammation, complements the inflammatory contribution to neuropathy. Th1 factors are upregulated: IFN-y, TNF-α, IL-6, IL-17, TGF-β (39). Interestingly, IFN-y, IL-6, IL-17 and TGF-β are also upregulated in the chronic stage of disease with the addition of IL-12, which is not convincingly unregulated in the acute phase (39). The IL-12/IFN-y/iNOS axis is essential in not only controlling parasite numbers, but a determinant in preventing parasite infection reaching the CNS. For example, IL-12 knockout mice, from late acute phase, show signs of neurological manifestations marked by hind limb paralysis and unbalanced gait. This correlated with increased lesions in the brain (40).

Our leading theory for the denervation of the enteric nervous system is collateral damage as a result of iNOS synthesised NO in the acute phase (41). In Arantes et al's 2004 study (42), they infected iNOS$^{-/-}$ knock-out mice and discovered that parasite burden increased by ~6-fold in the absence of NO production, but that the immunostaining of PGP 9.5, a cytoplasmic protein in neurons, remained consistent with immunostaining in wild type controls (41). This theory is being brought into question in light of discovering the large intestine being a main reservoir of chronic parasitic persistence (37).

Early theories for generalised neuropathy in *T. cruzi* infection include parasitic neurotoxin secretion. The basis of the theory was that upon destruction of parasite nests there is a release of cytotoxic or cytolytic substances that act upon local ganglion cells (43). The hypothetical neurotoxin has never been identified however, early electron microscopy images documenting the loss of neurons with apposing cytotoxic lymphocytes has been significant in strengthening of the neuroinflammation hypothesis (44). Proponents of the neurogenic theory have suggested that the correlation between neuronal cell loss and impairment of neurohormonal circuits can be explained by autoimmune dependent mechanisms. Here the autonomous nervous system is targeted by auto-reactive cytotoxic lymphocytes, resulting in cycles of catecholamine cardiotoxicity, myocytolysis, and heart failure (45). In the cardiac model, antibodies to a number of self-antigens are produced during *T. cruzi* infection (46). Targets include actin, myosin binding protein C, myosin, tropomyosin in addition to muscarinic and adrenergic receptors such as *β*-adrenergic receptors (anti-β1AR and anti-p2β) (47). The significance of auto-antibodies on disease severity is questioned, with studies suggesting titres of anti- *β*-adrenergic receptors

are linked with severe outcomes associated with dilated cardiomyopathy and systolic heart failure (48), whilst others suggest that antibody titres do not correlate with disease severity and that cardiac damage as a result of *T. cruzi* induced auto-immunity may not be antibody mediated at all (49,50).

Prior studies of neuropathogenesis linked to *T. cruzi* infection suffer from several drawbacks. Human studies are largely limited to autopsies and only reflect end-stage disease states. Data relating to cardiac disease may lack relevance for digestive disease. The few experimental mouse studies that have focussed on digestive disease have used lethal acute infection levels and/or lacked integration of data on parasite loads, immune responses, denervation and functional consequences for peristalsis. The development of the new murine DCD model provides much improved opportunities to investigate the mechanism of enteric neuropathy.

2.2 Rationale for the study

The primary rationale for this study comes from the identification of an initiation window of gut dysperistalsis from the transit time assay referred to in chapter 1. This will focus on C3H/HeN mice infected with Tcl-JR parasites, our previously identified high morbidity DCD model.

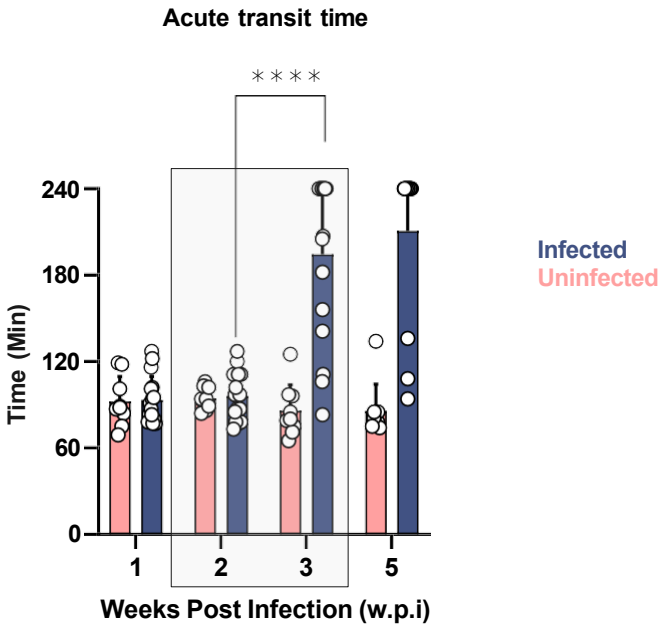

Figure 2.2.1: **Bar plots showing mean total transit time from C3H/HeN mice infected with 1x10^3 Tcl-JR-luc parasites and uninfected controls.**
Transit time assay assessing total time taken to pass red faecal pellet after feeding with 6% (w/ v) Carmine solution. *n = 16* for infected group, *n=21* for uninfected group. Unpaired, two-tailed t – test was conducted, with the asteriks indicating *P* value <0.0001. Overlaid box highlights the 'dysperistalsis initiation' window.

There was a clear initiation of gut dysfunction between weeks 2 and 3 post-infection in the DCD model (Fig. 2.2.1). Interestingly, this window is only apparent in the high morbidity DCD model and not in other mouse-parasite combinations (Fig. 2.2.2b (37). The narrow time window also coincides with progression to peak parasitaemia (Fig. 2.2.2a).

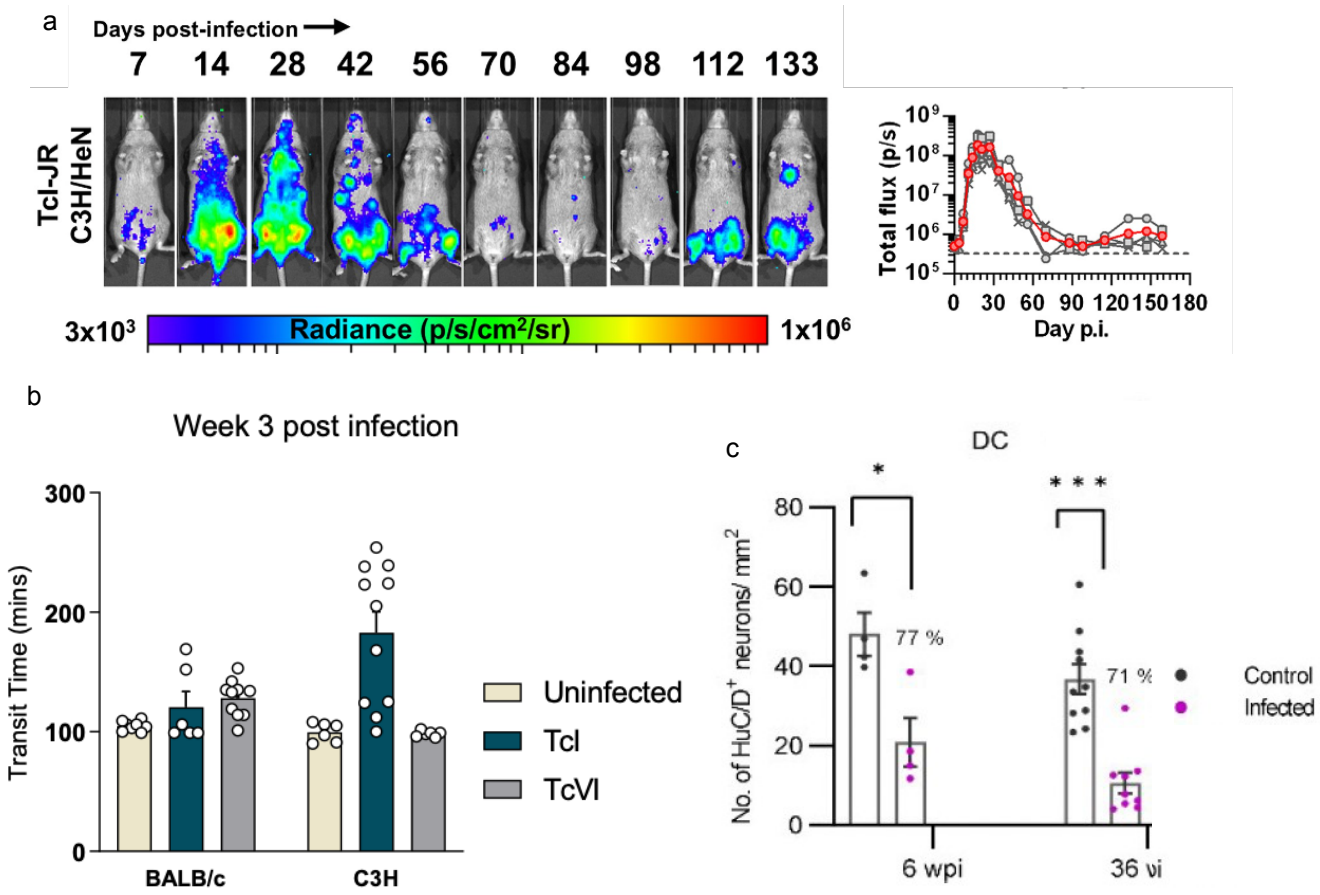

Fig. 2.2.2: Previous data that informs the current study.
a) *in vivo* bioluminescence profile of C3H/HeN mice infected with Tcl-JR parasites throughout the course of infection, with the average signal plotted in a line graph. Peak parasitaemia at 28 days post infection. Figure adapted from Lewis et al, 2016 (107). b) The transit time of different mouse-parasite strain combinations at week 3 post infection. The only delay present at this timepoint was in the Tcl-C3H combination. A. Khan, unpublished. Unpaired t-test was conducted between Tcl-C3H and uninfected, p= 0.0037. c) HuC/D positive neuron count in the large intestine (distal colon) of Tcl-C3H model at week 6 nd week 36 post infection. Figure adapted from A. Khan., et al (2023).

By week 6 post infection there is evidence of significant denervation, with a 77% reduction in the distal colon of the Tcl-C3H model, which worsens by week 36 (Fig. 2.2.2c). This shows that a significant amount of neuronal damage occurs in the acute phase of this model, but not exclusively. We are unsure if any repair or recovery processes occur between acute and chronic stage disease, but ongoing host-parasite interactions induce further damage between these timepoints. It is not known what occurs in the timepoints leading up to week 6 post infection, other than the histopathological data I produced in chapter 1. I showed there was evidence of

inflammation in the smooth muscle layer and increased iNOS expression (Chapter 1).

With the identification of this transit time delay initiation window there is plenty of scope to investigate a myriad of prospective effectors that may be responsible for the clear digestive disease outcomes in this model. I identified several immunomodulatory and chemical strategies to target candidate pathways that I hypothesized could be driving pathogenesis.

I set out to achieve the following aims:

1. To design an acute *in vivo* experiment whereby immune-regulatory and or trypanocidal treatments would be administered for a 7 day regimen to test their effects on the initiation and severity of GI transit time delay.
2. To evaluate the colon-specific immunological impact of treatments via flow cytometry.
3. To assess the pathological impacts of these treatments on the structural integrity of the ENS using immunofluorescence assays.

The objective of this study was to investigate whether manipulating the early infection and immune response dynamics would affect the instigation of gut dysfunction in the DCD model. The downstream analyses would confirm if any alleviation or exacerbation of this phenotype correlates with ENS integrity.

This study will help garner a deeper understanding on the initiation of acute dysperistalsis in experimental DCD and assist the exploration of whether the

prospective pathways identified in this window might warrant further study as potential drivers of chronic pathology. This will shed light on how prospective therapeutic intervention could prevent the development of DCD pathology.

2.3 Experimental plan

The aim of the study was to improve our understanding of the causative effectors responsible for the initiation of gut dysperistalsis (by measure of tranist time delay) in the DCD mouse model between weeks 2 and 3 post-infection. This study consisted of three independent experiments designed to assess the reproducibility of a core set of well-established treatment groups (benznidazole, cyclophosphamide) and also allow for iterative introduction of additional or adjusted experimental arms informed by the results as the study progressed.

Experiment 1

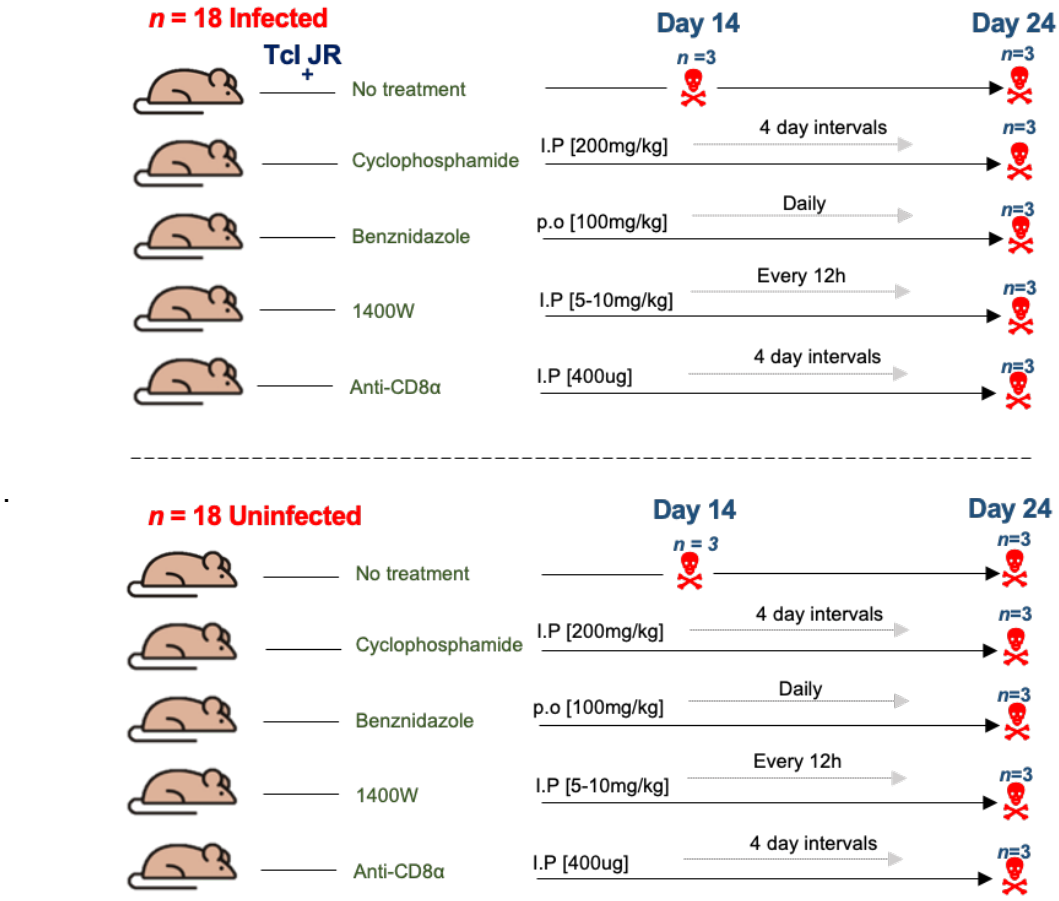

.

Figure 2.3.1 Schematic depicting the pilot plan.
Female C3H/HeN mice only, aged 6-8 weeks old. *n*=18 for the infected cohort, depicted above the dotted line. *n=18* for the uninfected cohort, below the dotted line. Infected cohort inoculated with $5x10^3$ TcI-JR LUC, i.p. Both cohorts were split *n*=3 for each treatment. Treatments, depicted in green, began at 14 d.p.i. Corresponding dosages and treatment intervals are shown above each arrow, which represents the 7 day treatment window. Endpoint was 24 d.p.i.

The treatments were designed to knockdown or deplete specific immune targets or parasites as follows:

- **Benznidazole**: Anti-parasitic chemotherapy was used to reduce the *T. cruzi* load to test the hypothesis that the ongoing presence of the parasite is required for the development of the GI transit time delay.
- **Cyclophosphamide:** Pan-immune suppression targeting leukocytes non-specifically to test the hypothesis that the immune response *per se* is required for the development of the GI transit time delay.
- **1400W:** iNOS enzymatic inhibitor treatment was used to reduce iNOS mediated NO production to test the hypothesis that NO-dependent tissue damage is required for the development of GI transit time delay. Informed by Arantes, 2004 study and immunohistochemistry data shown in chapter 1.
- **Anti-CD8α:** Anti-CD8+ IgG-mediated depletion of CD8+ T cells was used to test the hypothesis that the key effector of the adaptive cellular immune against *T. cruzi,* contributes to the development of the GI transit time delay whilst also distinguishing against the humoral response.
- **Anti-CCR2 (MC-21):** This well-established tool for inflammatory monocyte depletion was used to test the hypothesis that direct monocyte action or indirect differentiation to macrophages contribute to the development of GI transit time delay. Target was informed by the large, model specific, upregulation of genes implicating monocyte recruitment to the colon i.e. CCR2, CCR5, and contributory ligands CCL 2, 3, 4, 5, 7 and 12 (Chapter 1, M.Lewis, unpublished).

- **IgG Isotype controls:** Corresponding dosage concentration was matched to MC-21 and anti-CD8α dose concentration to exclude the effect of non-specific antigen binding on GI transit time delay.
- **Untreated controls:** Infected mice subject to no treatment were used as benchmarks for *in vivo* bioluminescence parasite burden and GI transit time by which treatment effects can be compared.
- **Uninfected controls:** Used as healthy, negative controls, against which treatment effects can be compared.

In the pilot, depicted above, C3H/HeN mice were infected with a 'high dose' [$5x10^3$] of JR-LUC parasites, which we were confident would elicit a clear and reproducible dysperistalsis phenotype (37). The primary readout from this experiment was transit time assays conducted at each week of infection. Transit time readouts at week 2 were the pre-treatment reference, with the change in transit times at week 3 used to evaluate the effect of each treatment on DCD pathology development. One infected and one uninfected control group were not subject to any treatments. Weekly *in vivo* bioluminescence imaging was used to monitor parasite burdens. All other confirmatory methods of treatment efficacy were implemented downstream of the *in vivo* phase of the experiment. Specifically, multi-colour flow cytometry was conducted on single cell colon suspensions to evaluate the efficiency of knockdown of CD8+ T cells in the anti-CD8a treated group, and CD45+ cells (leukocytes) in the cyclophosphamide treated group.

Immunofluorescence antibody staining in whole mount sections was used to assess the structural integrity of the myenteric plexus and to visualise iNOS expression in

the colonic smooth muscle layers. Additionally, an infected and uninfected group were sacrificed at week 2, as pre-treatment reference groups.

Second experiment (additional groups)

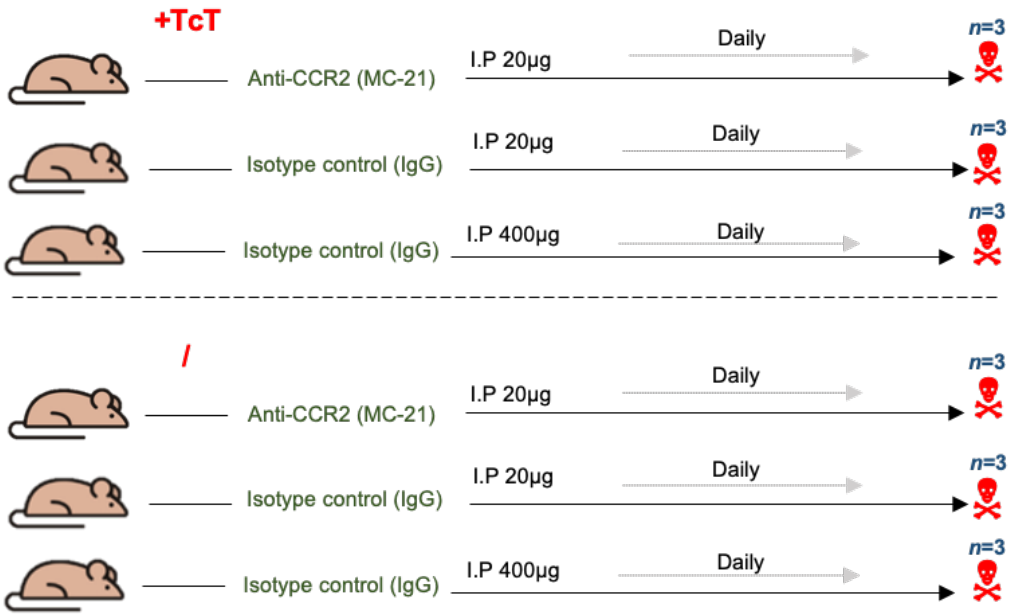

Figure 2.3.2 Schematic depicting the additions to the initial experiment design (see Figure 2.3.1a).
Female C3H/HeN mice only, aged 6-8 weeks old. *n=9* for the infected cohort, depicted above the dotted line. *n=9* for the uninfected cohort, below the dotted line. Infected cohort inoculated with $5x10^3$ tissue culture trypomastigotes (TcT) Tcl-JR LUC, I.P. Both cohorts were split *n*=3 for each treatment. Treatments, depicted in green, begin at 14 d.p.i. Corresponding dosages and treatment intervals are shown above each arrow, which represents the 7 day treatment window. Endpoint was 24 d.p.i.

In the second experiment, the inoculum remained the same at $5x10^3$ parasites and all the treatments showcased in figure 2.3.1 were repeated. An anti-CCR2 treatment for targeting the egress of inflammatory monocytes from the bone marrow (MC-21) (51) was introduced to test the hypothesis that these components of the innate immune system are responsible for development of GI transit time delay.

Two isotype IgG controls were included, corresponding to the anti-CD8a and MC-21 IgG treatment concentrations. All confirmatory methods remained the same, with an adjustment to the flow antibody panel (see methods) to also allow evaluation of

the impact on myeloid cells (e.g. expression of Ly6C and CD11b) to be observed in response to MC-21 treatment.

Third experiment

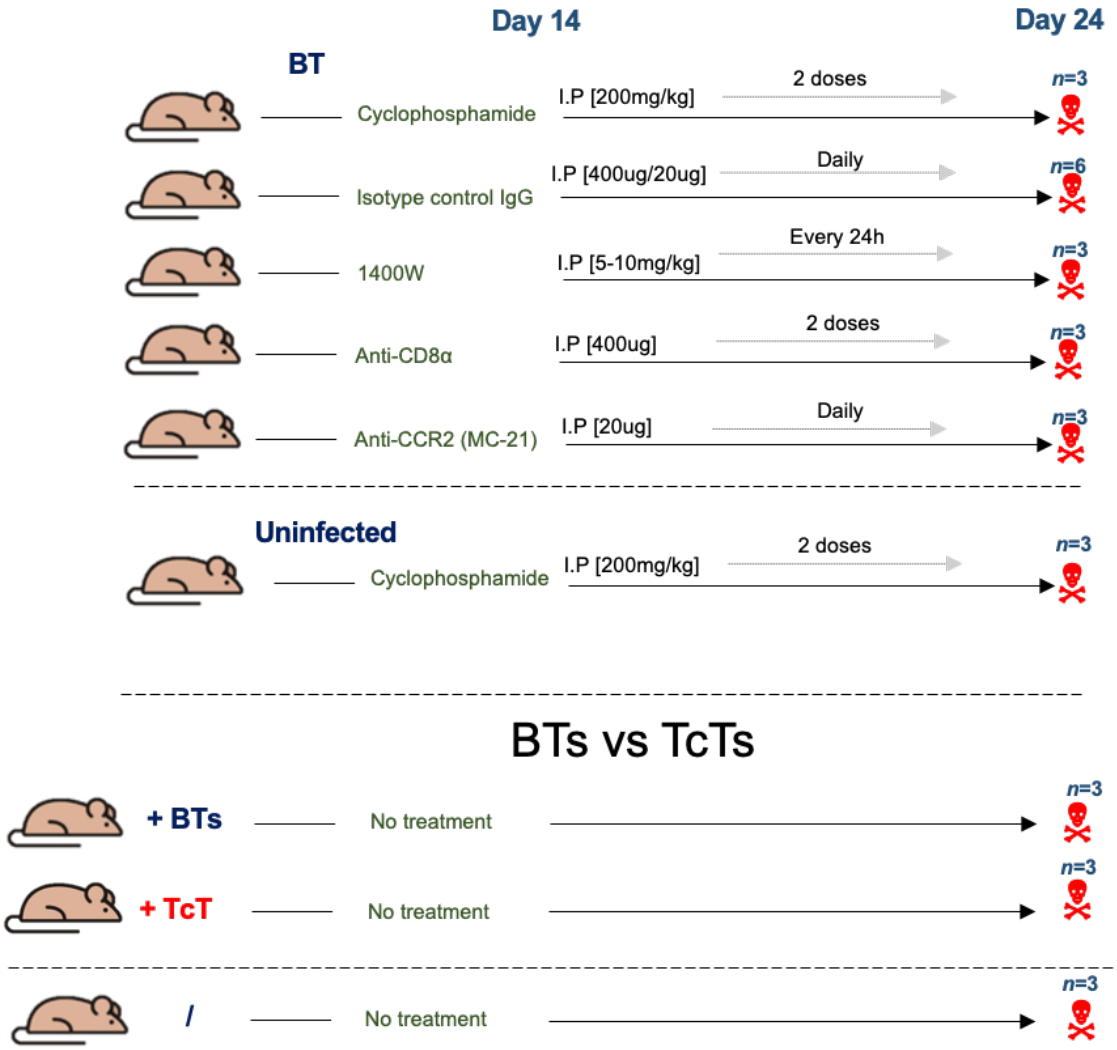

Figure 2.3.3. Schematic depicting the third experiment. Female C3H/HeN mice only, aged 6-8 weeks old. *n*=21 for the BT infected cohort, *n*= 3 for the TCT infected cohort, and *n*= 6 uninfected cohort. Infected cohort inoculated with $5x10^3$ Tcl-JR LUC, i.p Both cohorts were split *n*=3 for each treatment. Treatments, depicted in green, begin at 14 d. p.i. Corresponding dosages and treatment intervals are shown above each arrow, which represents the 7-day treatment window. Endpoint was 24 d.p.i. An additional experiment was conducted to compare infection with blood trypomastigotes (BTs) and tissue culture trypomastigotes (TcT).

The final experiment repeated most of the previous groups, but also had some key differences from the first two: The benznidazole treated group was omitted because the treatment effect noted from the previous experiments was consistently

reproduced with strong statistical significance. As mice were limited, priority was given to groups with variable treatment outcomes. The only uninfected controls were for the cyclophosphamide treated group to increase confidence that the effects were infection dependent as opposed to treatment having a non-specific effect on transit time. There was also an additional 'mini' comparative experiment between tissue culture-derived and blood-derived trypomastigote (TCTs and BTs) infected, untreated control mice, to assess intrinsic differences in infection kinetics between the different infection methods used in the previous experiments. Due to time constraints, the only downstream assays were *ex vivo* imaging and weighing of the spleen, caecum, stomach, mesentery adipose and brain.

2.4 Methods and materials

2.4.1 Murine infections and bioluminescence imaging

Parasites

The study used aliquots of frozen tissue culture trypomastigotes (TCT), of the TcI-JR strain of *T. cruzi* (JR-LUC), parasites that express the red-shifting firefly luciferase variant *PPy*RE9h, as previously described (49). Parasites were thawed at room temperature, sedimented by centrifugation at 10,000x g for 5 minutes, washed in 1ml complete media (MEM media, +5% FBS), sedimented and resuspended in 250ul complete medium. After 1-hour incubation at 37^{o}C, active parasites were counted using a haemocytometer and the population density was adjusted to the required concentration.

Animals and infections

All animal work was performed under UK home office project licence (PPL P9AEE04E4) and approved by the LSHTM Animal Welfare Ethical Review Board. Procedures were in accordance with the UK animals (Scientific procedures) Act 1986 (ASPA).

Female C3H/HeN and CB17 SCID mice were purchased from Charles River (UK). Animals were maintained under specific pathogen-free conditions in individually vented cages (no more than 6 per cage at any time, no fewer than 2). Animals experienced a 12-hour light/dark cycle, with access to food and water *ad libitum*. Prior to treatments, the cage bedding of C3H/HeN mice was redistributed to equalise the microbiome between the mice and reduce any cage effects bought about by separate housing. All mice were subject to the same extrinsic factors (handling time, time under anaesthesia, and time outside their respective cages).

The study comprised a core experiment conducted in triplicate, with some variations between replicates:

In experiment 1 and 3, two SCID mice were inoculated with $2x10^4$ and $4x10^4$ JR-LUC blood trypomastigotes (BTs) respectively in 0.2ml D-PBS via intraperitoneal (I.P) injection. 21 days post infection, BTs were harvested from the SCID mice via cardiac bleed. Harvested parasites were used to infect C3H/HeN mice (4 – 8 weeks old) at $5x10^3$ per mouse via I.P. injection.

In experiment 2 and a small subset of mice in experiment 3, C3H/HeN mice were inoculated with $5x10^3$ JR-LUC TCTs i.p. derived from the supernatant of an *in vitro* infected MA104 cell monolayer.

At experimental end-points, mice were sacrificed by cervical dislocation, followed by a secondary confirmatory method (exsanguination).

In vivo imaging

Mice were injected with 150 mg kg^{-1} d-lucerfin I.P., and anaesthetized using 2.5% (v/v) gaseous isoflurane before being and placed in an IVIS spectrum (PerkinElmer) for bioluminescence imaging. Image acquisition settings were dependent on signal intensity, with exposure time of 1-5 minutes and binning set to small, medium or large. After imaging, mice were placed in a tub atop a heat pad for recovery from anaesthesia prior to being returned to cages. Bioluminescence was quantified using regions of Interest (ROI) created by polygon tools on Living Image 4.7.4. Whole body total flux (photons sec^{-1}) was the primary read-out of interest, as a proxy for *in vivo* parasite burden.

Ex vivo imaging

Food was withdrawn from the cages 2.5 hours prior to sacrifice. 7 minutes before euthanasia, mice were injected with 150 mg kg^{-1} d-luciferin I.P. During necropsy the caecum, stomach, mesentery adipose and brain were placed in a light refractory 24 well plate with 1ml of d-luciferin (15 mg/ml). Plates were imaged in the IVIS spectrum (PerkinElmer) under the same conditions as described for *in vivo* imaging. Total flux

(photons sec^{-1}) was quantified for each organ, by drawing same sized ROI for each well, using Living Image 4.7.4.

2.4.2 Procedures and treatments

Total GI transit time assay

6% carmine red dye working solution was made with 0.5% methyl cellulose (w/v) in distilled water, sonicated and kept at room temperature – as previously described (53)

Carmine solution was administered to mice via oral gavage (0.2ml), before returning them to their cages for 60 minutes. They were then placed into individual containers and observed every 2-3 minutes. The difference between the time of gavage and the passing of the first red stained faecal pellet was calculated as the total GI transit time. The maximum cut-off time was 4 hours, employed for isolation concerns and welfare of the mice.

Benznidazole treatment (Experiments 1 & 2)

Benznidazole was prepared from powder at 10 mg ml^{-1} by dissolving in HPMC vehicle solution (0.5 % w/v hydroxypropyl methylcellulose, 0.5% v/v benzyl alcohol, 0.4% v/v Tween 80 in deionised water). Benznidazole was sonicated prior to use and then administered via oral gavage at a dose concentration of 100 mg kg^{-1}, daily for 7 days starting at 15 dpi.

Anti-CD8α IgG treatment (Experiments 1, 2 & 3)

Anti-murine CD8 (lyt-2), IgG clone YTS 169.4 was purchased as a working solution from 2BScientific in PBS, at 1mg ml^{-1} (cat: Ab00166-2.0-VXF). 0.4ml at 400µg per dose [20 mg kg^{-1}] was administered via I.P. infection. Two doses were administered with a 3 day interval between doses. Due to the expected immunosuppressive effects of the treatment, mice were weighed frequently to monitor any progression towards humane end-points i.e. loss of >20% weight. Mice were also frequently observed for hallmarks of severe outcomes i.e. reluctance to feed or drink freely for more than 4-6 hours, or loss of balance. A corresponding IgG2b isotype control antibody (LTF-2), at the same concentration, was administered to allocated control mice.

Cyclophosphamide treatment (Experiments 1, 2 & 3)

Cyclophosphamide working solution was prepared from powder at 20 mg ml^{-1} by dissolving in d-PBS, sonicated and kept at 4^{o}C until needed. Cyclophosphamide was administered via I.P. at 200 mg kg^{-1}. Two doses were administered with a 3 day interval. Due to the expected immunosuppressive effects of the treatment, mice were weighed frequently to monitor humane end-points i.e. loss of >20% weight. Mice were also frequently observed for hallmarks of severe outcomes i.e: reluctance to feed or drink freely for more than 4-6 hours, or loss of balance.

1400W treatment (Experiments 1, 2, & 3)

The iNOS inhibitor 1400w di-hydrochloride (Tocris. cat: 1415), was made into a working solution by reconstituting at 0.75mg ml^{-1} in D-PBS. The working solution had

to be made fresh immediately before use and administered at a dosing concentration of 7.5mg kg^{-1} I.P. 1400W was administered daily for 7 days.

MC-21 treatment (Experiments 2 & 3)

MC-21 anti-CCR2 IgG antibody, was donated by Prof. M. Mack from University Hospital Regensburg, as a working solution. The concentration was adjusted for 20µg per dose [1mg kg^{-1}], and administered via I.P. injection daily for 7 days. A corresponding IgG2b isotype control antibody purchased from Bioxcell (cat: #BE0086), adjusted to the same concentration, and administered to allocated control mice.

2.4.3. Flow cytometry

Single cell preparations from large intestine:

<u>Stock solutions</u>

Dithiothreitol (DTT): Sigma D0632, dissolve 1.54g in 10ml Milli-Q water, filter and store at 4^{o}C short term

Ethylenediaminetetraacetic acid (EDTA): 500mM stock solution; dissolve 18.6g in 90ml water and adjust pH to 8.0 with NaOH. Top up to 100ml final volume. Store at room temperature

Liberase TL: (Roche, cat: 05-401-020-001). Dilute 5mg vial in 0.5ml RPMI for 10 mg/ml stock. Store at -20^{o}C.

DNase I: (Sigma, cat: DN25). Make up 3mg/ml stock in Milli-Q water and store at -20^{o}C.

Procedure

Mice were fasted for 2.5 hours, with drinking water kept *ad libitum*, then culled by cervical dislocation. After euthanization, mice were sprayed externally with 70% ethanol, opened along the mid-line and perfused trans-cardially with 10 ml PBS. The colon was dissected as quickly and aseptically as possible, ensuring the main areas of mesentery adipose were removed. The tissues were transferred to a Petri dish on ice with 10ml R3 media (RPMI, 10mM HEPES, 3% FBS, L-Glutamine, Pen/Strep,) with 50μM β-mercaptoethanol added just prior to use. Tissue was transferred to dry filter paper, and residual connective tissue and fat was removed. Faecal pellets were carefully removed, before the colon was opened longitudinally with fine scissors. The opened colon was rinsed with fresh R3 media ensuring all impacted and residual faecal material was removed. The tissue was then added to 10ml Hanks' Balanced Salt Solution, with calcium and magnesium (HBSS+/+), before being shaken vigorously by hand for 30 seconds. After sieving, the tissue was kept in R3 media, on ice, until previous steps were repeated for all animals.

A 6 well plate was filled with 2ml of serum free media (SFM) warmed to 37^{o}C. The tissue, kept in R3 media, was vortexed briefly and the supernatant discarded. The tissue was transferred to the 6-well plate and cut into 1cm pieces without ripping or tearing the tissue. The tissue pieces were transferred to 10ml of pre-warmed DTT-EDTA washing media (SFM, 5mM EDTA, 1mM DTT), and incubated for 20 minutes in a shaking 37^{o}C incubator, at 250rpm, to remove mucus and epithelial cells. After incubation, the tissue was strained and transferred to 10ml SFM and vortexed to remove excess EDTA.

Digestion media was made fresh with working volumes of 2ml for uninfected tissue and 4ml for infected tissue: SFM, 2.5% liberase (w/v), 1% DNAse (v/v).

1ml of digestion media was added to a 12 well plate, and the tissue from one mouse added to a single well. Using fine scissors, the tissue was minced as fine as possible so pieces could pass through a pastette. The entire contents of each well was transferred to corresponding 15ml falcon tube, and topped up with an additional 1ml (uninfected) or 3ml (infected) digestion media. Tubes were placed in a shaking 37^{o}C incubator, at 250rpm, for 40-60 minutes. At the end of incubation, 6ml of R10 media (RPMI, 10mM HEPES, 10% FBS, L-Glutamine, Pen/Strep + 50μM β-mercaptoethanol) was added to each tube to stop digestion. The suspension was poured into a 6-well plate through a 70μm cell strainer. The contents left in the strainer were mashed through with a plunger from a 5ml syringe, with the digestion tube then rinsed with 5ml R10 media before being poured through the strainer again. Everything was transferred to a 15ml falcon tube, and all samples were kept cold on ice going forward. Tubes were centrifuged for 5 minutes at 400x*g*, 4 ^{o}C. The supernatant was discarded and the pellet was washed in 10ml of R3 media, and centrifuged again. The final pellet was resuspended in 0.1ml cold PBS and kept on ice.

2.4.4. Single cell preparations from spleen

Spleens collected during necropsy were kept in R3 media on ice until ready. Spleens were mashed through a 70μm cell strainer into 5ml R3 media, with an additional 5ml being used for rinsing . In some cases, spleens from replicate mice were pooled. The suspension was centrifuged at 400x*g* for 10 minutes, with supernatant discarded and pellet resuspended in 1ml (uninfected) or 2 ml (infected)

Ammonium–chloride–potassium (ACK) buffer and left to incubate for 5 minutes at room temperature, to lyse red blood cells. 13 or 14 ml of cold PBS was added and centrifuged again. The pellet was resuspended in 1ml per gram of tissue (FB) Flow Buffer (1 x PBS, 0.05% azide, 2mM EDTA, 0.5% BSA) and kept on ice until ready.

2.4.5. Cell surface antibody staining of colon and spleen suspensions

Tubes were prepared for each sample along with the following controls using pooled excess cells from the samples:

1) Unstained control
2) Compensation controls
    a) Single stained controls (one for each antibody)
    b) Live/Dead (L/D) viability dye only control
3) A Fluorescence minus one (FMO) for each antibody

For the L/D control, 100µl of pooled spleenocytes were heated to 56°C for 20 minutes then immediately placed on ice. For all samples, 90µl of cells were added to new 15ml tubes, and 0.5µl Zombie Yellow viability dye (BioLegend, cat: 423103) was added to each tube apart from the unstained control, the single antibody compensation controls and the L/D FMO control. Samples were incubated for 20 minutes at room temperature, in the dark. After incubation, 10µl Mouse FcBlock reagent was added to every tube and left to incubate in the fridge for 10 minutes. Tubes were placed on ice, and 100µl FB was added to the unstained control and the L/D control. 100µl 2X single antibody solution / antibody cocktail / FMO cocktail was added to the appropriate tubes and stained on ice for 30 minutes in the dark. The antibody panels, with dilution factors are shown in tables 1 and 2 overleaf.

Table 1. Flow cytometry antibody panel 1

First panel: 17/10/22 – 21/4/23

Laser	FL	Channel	Filter	Ab	Conjugate	Dilution factor
488nm	1	B530	530/30	CD3e	FITC	200
	2	B585	585/42	NKp46	PE	100
	3	B610	610/20			
	4	B660	660/20	TCRd	PE-Cy5	200
	5	B695	695/40			
	6	B780	780/60	B220	PE-Cy7	200
633nm	7	R670	670/30	CD44	APC	200
	8	R730	730/45			
	9	R780	780/60	CD8a	APC-eF780	300
405nm	10	V450	450/50	CD4	eF450	400
	11	V500	525/50	Zombie-Yellow		500
	12	V605	605/12			
	13	V650	655/8			
	14	V711	710/50			
	15	V786	780/60	CD45	SB780	400

Table 2. Flow cytometry antibody panel 2

Second panel: 21/4/23

Laser	FL	Channel	Filter	Ab	Conjugate	Dilution factor
488nm	1	B530	530/30	CD3e	FITC	200
	2	B585	585/42	NKp46	PE	100
	3	B610	610/20			
	4	B660	660/20			
	5	B695	695/40	CD11c	PerCP-Cy5.5	400
	6	B780	780/60	B220	PE-Cy7	400
633nm	7	R670	670/30	NOS2	APC	400
	8	R730	730/45			
	9	R780	780/60	CD8a	APC-eF780	300
405nm	10	V450	450/50	CD4	eF450	400
	11	V500	525/50	Zombie-Yellow		500
	12	V605	605/12	Ly6C	BV605	400
	13	V650	655/8			
	14	V711	710/50	CD11b	BV711	400
	15	V786	780/60	CD45	SB780	400

Note that the anti-CD8α clone used for flow cytometry staining was distinct from the one used in the *in vivo* depletion treatment.

After incubation, 5ml cold FB was added before centrifuging at 400x*g* for 5 minutes. The supernatant was discarded and the pellet was resuspended in 0.2ml FB. The cell suspension was fixed with 0.2ml paraformaldehyde (4% w/v in PBS) on ice for 30 minutes. After fixation, 5ml FB was added to cell suspension, and it was centrifuged at 400x*g* for 5 minutes. The pellet was then resuspended 0.5ml FB and kept in the fridge, protected from light.

2.4.6 Intracellular iNOS staining of fixed cells (panel 2 only)

After cell surface staining, cells were permeabilised for intracellular antibody staining. Fixed cells were kept at 4^{o}C overnight were centrifuged at 400x*g* and the pellet was resuspended in 1x BD Perm/Wash buffer (PWB) for 15 minutes on ice, to permeabilise the cell surface membrane. 2X anti-iNOS antibody solution was prepared in permeabilization wash buffer (PWB), enough for 100µl per sample, and incubated on ice, in the dark for 45 minutes. After staining, cells were washed in 1ml PWB, centrifuged at 400x*g* for 5 minutes and resuspended in 0.5ml FB.

Cell suspensions were passed through 70µm cell strainer into FACS tubes and run on a three-laser Becton Dickinson LSRII Flow Cytometer (Violet 405nm, Blue 488nm, Red 633nm). The gating strategy and analysis was conducted using FlowJo_v10.8.1. Becton Dickinson Fortessa X-20, 4-laser was also used at the University of York.

2.4.7 Immunofluorescence staining and analysis

During necropsy, 2cm of distal colon was transferred to 10% DMEM and kept on ice. The tissue was cut longitudinally along the mesentery attachment line, then washed in PBS before being stretched and pinned on Sylgard 184 silicon polymer dishes. The pinned tissue was fixed in paraformaldehyde (4% w/v in PBS) overnight at 4^{o}C. Fixed tissue was rinsed in sucrose washing solution (15% d-sucrose w/v, 0.01% azide) and stored in sucrose storage solution (30% d-sucrose w/v, 0.01% azide) and kept at 4^{o}C until ready to be stained.

Using a dissection microscope, the mucosal layer was peeled away using forceps, leaving the muscularis wall tissue. The tissue was then washed for 45 minutes in PBS, with 3 changes, at room temperature. The tissue was then permeabilised with PBS containing 1% Triton X-100 for 2 hours, followed by blocking for 1 hour (10% sheep serum in PBS, 0.5% Triton X-100).

Tissues were incubated with primary antibodies: Human antineuronal nuclear antibody type1 (anti-ANNA-1/anti-“Hu”), donated by Dr Vanda Lennon from Mayo Clinic, Rochester MN, used at a dilution of 1:7500, rabbit anti-iNOS polyclonal [ab3523, Abcam] 1:50, and rat anti-GFAP monoclonal IgG, clone 2.2B10 at 1:500 [ThermoFisher] in 500µl PBS-T (PBS, 0.1% Triton X-100) for 4 nights in a humidity chamber at 4^{o}C. Tissues were washed with 0.5 ml PBS for 45 minutes, with 3 changes, then incubated with secondary IgG: goat anti-human IgG AlexaFluor647; donkey anti-rat IgG AlexaFluor488; donkey anti-rabbit IgG AlexaFluor568, all 1:500 in 0.5 ml 0.1% PBS-T. Tissues were incubated for 1 hour at room temperature, kept dark, before a final 45 minute wash 0.5 ml PBS. Tissues were counterstained with

Hoechst 33342 DNA dye (1 μg ml^{-1} in PBS) for 30 minutes and mounted on glass slides using FluorSave mounting medium (Merck). For antibody control samples the primary antibody was omitted. The whole mounts were examined and imaged using an LSM880 confocal microscope, using 20X and 40X objectives. Images were captured as Z-stacks of 12 3μm thick slices ensuring the full thickness of the myenteric plexus was captured. Three Z-stacks were taken per sample, chosen at random. Post-acquisition image compression was performed on FIJI software.

2.4.8 Blood film preparations

3μl of peripheral blood was taken from each mouse via a tail snip procedure. Collected blood was pipetted onto the top of the slide, and by using another slide angled at 30-45^{o}, was spread thinly across the slide. Three films were collected for each mouse, fixed in methanol for 1 minute and rinsed with running tap water for 1 minute. A working giemsa solution was made at a concentration of 1:9 with deionised water and stained for 15 minutes. Slides were washed in running tap water for 5 minutes and left to air dry. Slides were imaged by bright field microscopy on Leica DM 3000, and slides were scanned on 40x for monocytes and parasites.

2.5. Results

2.5.1 Monitoring parasite burdens

In order to assess the impact that each treatment had on parasite loads, *in vivo* bioluminescence imaging was utilised at each week of infection. Importantly, the pre-treatment reference at 2 w.p.i was conducted the day prior to treatments starting, to ensure an accurate post-treatment comparison.

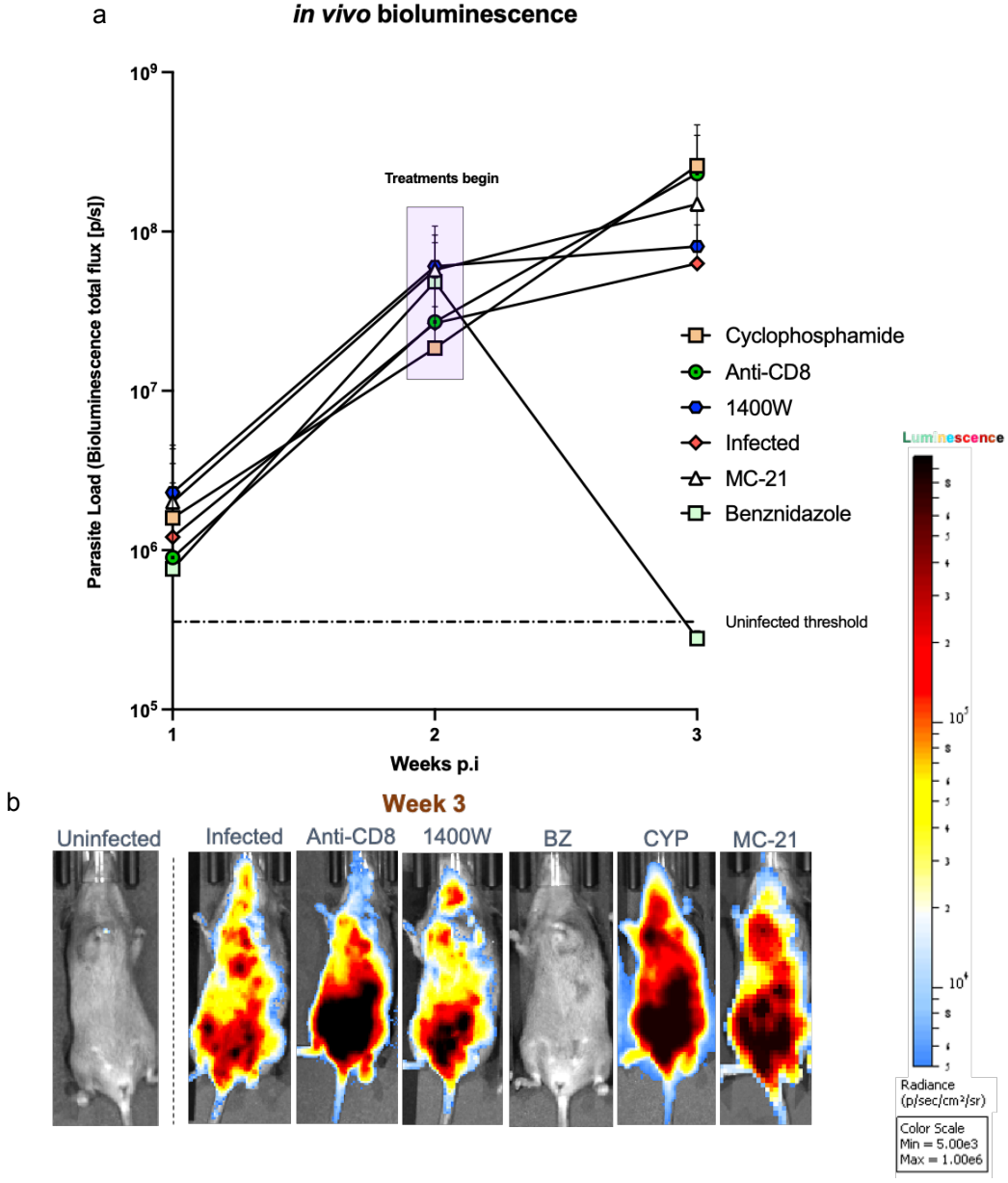

Figure 2.5.1.1. *in vivo* bioluminescent imaging of each experimental group before and after treatments. a) Pooled total flux (parasite burden) data from all 3 experiments on a logarithmic scale. Uninfected threshold indicative of the mean average of all uninfected mice imaged. Legend on the right refers to each treatment and infected cohort includes isotype controls. b) Visual representation of bioluminescent signal after 7 days of treatment for each group. Light blue represents low signal, dark red/black is high signal. Cyclophosphamide (*n=9*)., Anti-CD8 (*n*=9), 1400W (*n*=9), infected (*n*=13), MC-21 (*n*=6), benznidazole (n=6). All mice were injected with 150 mg kg^{-1} d-luciferin i.p 7 mins before imaging. Ordinary one-way ANOVA was conducted

As depicted in figure 2.5.1.1 there was a degree of variability in parasite burden between groups after each treatment i.e. at 3 w.p.i. This allowed for an intra-timepoint comparison to assess which treatment results in the highest parasite burden, by comparing each treatment group to the infected, untreated control at week 3. Cyclophosphamide treated mice had on average a 3.1-fold higher parasitic burden than untreated controls (p=<0.0009), which was the highest level of infection of any group. The parasite distribution was widely disseminated, with intense signal in the lower abdomen and left side of the chest – an infection pattern consistent in all infected groups. (Fig 2.5.1.1b) The anti-CD8a treated group exhibited a 2.7-fold greater parasitic burden on average than the untreated controls (p=0.0074). It displayed on average the second highest bioluminescence of any group, second to the cyclophosphamide treated group which had 13% more signal. The MC-21-treated group had the third highest parasite burden at end-point, with a 1.37-fold difference between the untreated control (p=0.467). There was little separating the 1400W-treated and infected untreated control groups, with the 1400W group resulting only in a 0.27-fold difference, which was not statistically significant (p=0.998). As expected, the benznidazole treated group exhibited a 2,250-fold reduction in signal on average (p=0.0050), with the end point total flux being equivalent to the background luminescence measured for the uninfected control group. This is easily visualised in Figure 2.5.1.1a, where the cyclophosphamide, anti-CD8a and MC-21 treated groups have the 3 most intense signal profiles post-treatment, and the benznidazole treated group has a complete absence of signal. On average, the anti-CD8a treated group had signal 3.3-fold greater than the IgG [400µg] (*p=0.0491*), and MC-21 had signal 1.5-fold greater than the IgG [20µg] (*p=0.384*) (2.5.1.2).

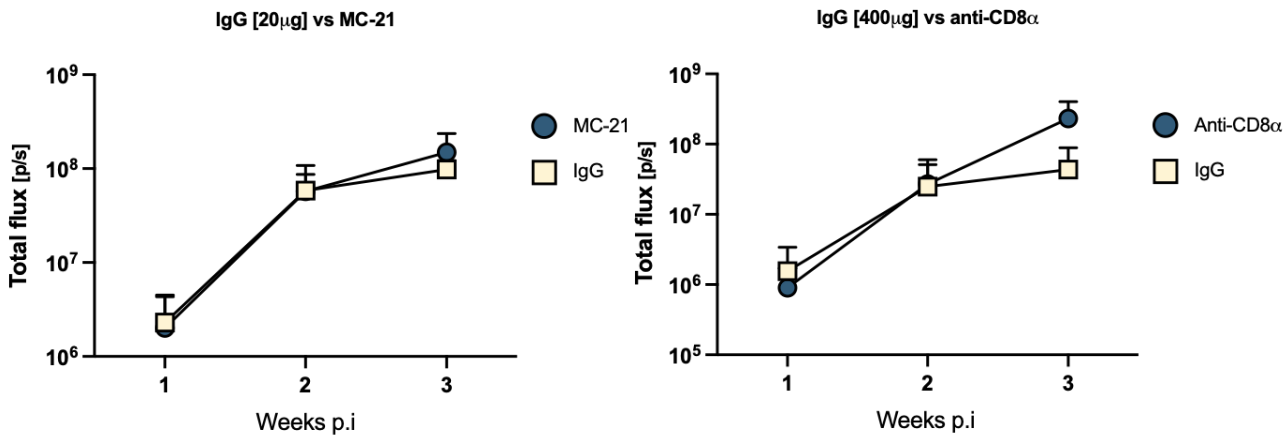

Figure 2.5.1.2 Total average flux of both IgG control groups.
a) MC-21 total flux (circle) against corresponding IgG control (square) at a dose concentration of 20μg. *p=0.484* (IgG control: *n=4,* MC-21 *n=6*). b) Anti-CD8a total flux (circle) against corresponding IgG control (square) at a dose concentration of 20μg. *p=0.0491* (IgG control: *n=7,* anti-CD8a *n=9*).

It was also possible to assess the parasite burden changes within the same treatment group over time, by plotting individual inter-time point graphs (see overleaf). This helped to account for the variation in pre-treatment infection intensity observed between individual mice.

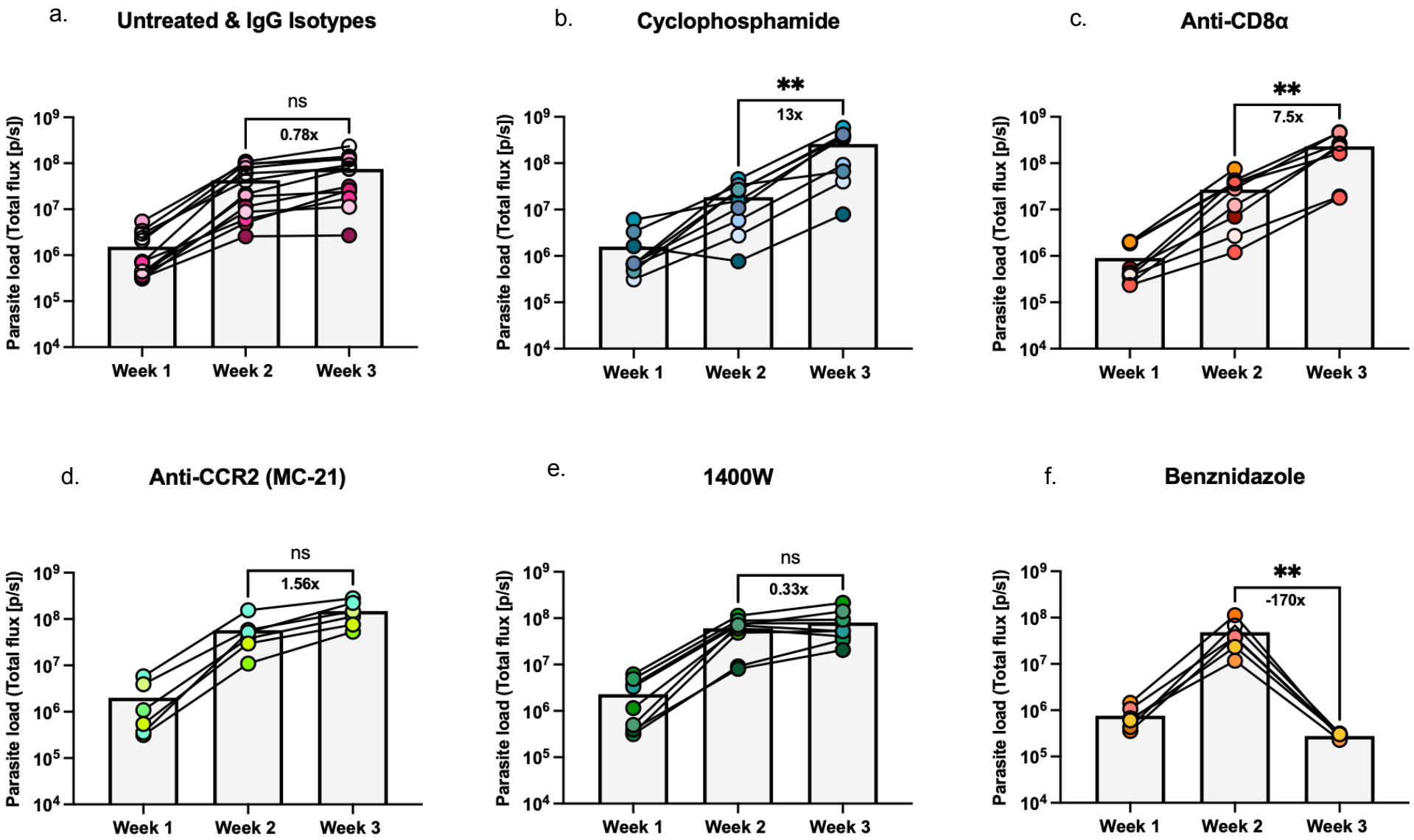

Figure 2.5.1.3. Bioluminescent signal throughout entire experiment of C3H/HeN mice infected with Tcl-JR parasites subject to each treatment.
Each individual treatment group is presented on a logarithmic scale. Bars show the group mean and each data point represents an individual mouse. *n* = 9 for cyclophosphamide treated group, anti-CD8a and 1400W. *n* = 6 for MC-21 and benznidazole groups. *n* = 13 for pooled infected & isotype control. Unpaired, two-tailed *t* –test conducted between weeks 2 and 3 (the treatment window). a) Cyclophosphamide treated group; asterisks indicate *p* value of 0.003 corresponding with a 13x increase in parasite burden after treatment. b) Anti-CD8a treated group, stars indicating *p* value of 0.0028 corresponding with a 7.5x increase in parasite burden after treatment. c) MC-21 treated group, no significant difference in parasite burden after treatment. d) 1400W treated group, no significant difference in parasite burden post treatment. e) Untreated and isotype control groups, no significant difference in parasite burden between weeks 2 and 3. f) benznidazole treated group, with asterisk indicating a *p* value of 0.0025 corresponding with a 170x reduction of parasite burden post treatment.

Visualising the pre - vs. post-treatment changes in parasite burden for each individual group allowed us to track the rate of change in parasite burden in response to the treatments. The cyclophosphamide treated group b) exhibited the steepest increase in parasite burden of 13-fold between 2 and 3 w.p.i. This was a vast difference compared to the untreated/isotype-treated infections a), which depicted a 'natural' infection propagation, where the fold increase is 0.78 between 2- and 3-weeks post-infection. The increase observed in the cyclophosphamide group was not surprising, since the broad suppression of the immune system is well known to facilitate an unchallenged disseminated infection (54). Similarly, with a specific suppression of CD8+ T cells, c), there was a 7.5-fold increase in parasite numbers post-treatment. Again, this was expected because CD8+ T cells are essential for parasite control (55). There was no significant difference in parasite burden between either MC-21, 1400W and the untreated controls. However, MC-21 treatment did lead to a trend of slightly higher parasite numbers than the untreated cohort. This suggested that inflammatory monocytes may play a small role in controlling parasites, but the study sample size may have been too small to have the statistical power to detect this. Predictably, benznidazole reduced the level of infection by 170-fold which, as depicted in figure 2.5.1.3a, was below the detection threshold defined using the uninfected control groups.

2.5.2. Gastrointestinal *ex vivo* imaging

Whilst *in vivo* imaging allowed estimation of the total parasite burden in an entire mouse, it was difficult to extrapolate which specific organs and tissues were infected. Gastrointestinal specific parasitic burden, measured immediately *post mortem* at the

3 w.p.i. end-point, provided insight into the effects of each treatment on local parasite loads and helped interpret pathological gut dysfunction phenotypes.

There was an evident degree of variability in organ specific parasite burdens after each treatment. The pooled GI bioluminescent flux was the stomach and caecum specific bioluminescence signal pooled together (Fig.2.5.2.1a). This was used for overall comparative parasitism of the GI tract in this experiment. There was no significant change in bioluminescence signal in response to 1400W or MC-21 treatments, compared to infected control (*p=0.314*, *p=0.951*). Benznidazole treated mice had bioluminescent signal in these pooled tissues line with uninfected control thresholds (depicted by the dotted line) i.e., the infection was either completely cured or suppressed below the limit of detection. The cyclophosphamide treated group exhibited a significant increase in GI bioluminescence (*p=0.0020*) compared to the untreated, with an increase of 10.6-fold and the highest bioluminescence signal of any experimental group. After cyclophosphamide, the anti-CD8a treated group exhibited the second highest signal with an 8.2-fold increase in bioluminescent signal compared to the untreated group, although it was not at the level of significance (*p=0.198*).

There was a range of individual variability within each treatment group, including the cyclophosphamide and anti-CD8a treated groups where signal was consistently higher for each organ on average than the untreated. However, this variability was not treatment dependent since it was also readily observed in infected, untreated control groups. There was a smaller degree of variability in the benznidazole treated group, which supports the notion that parasite infection dynamics are heterogeneous irrespective of immune integrity.

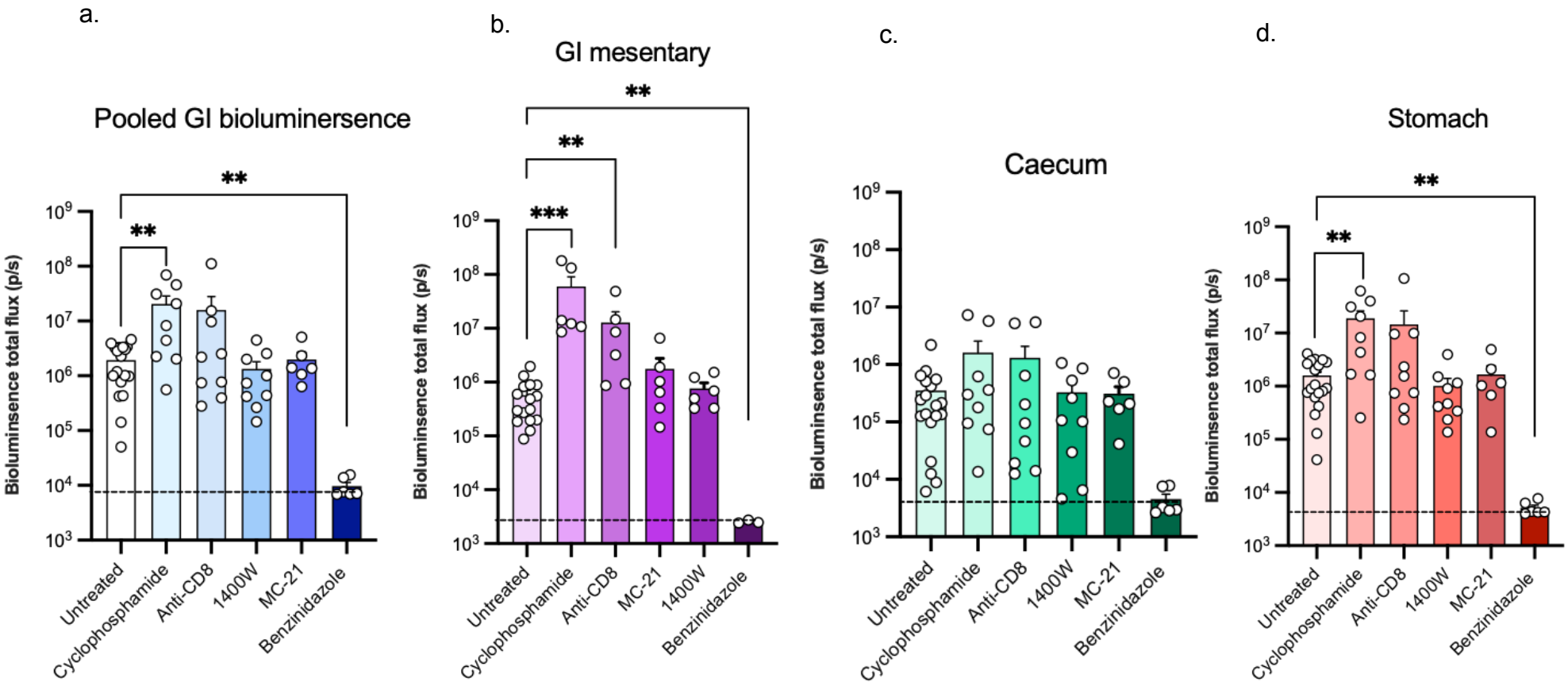

Figure 2.5.2.1. *Ex vivo* bioluminescence imaging of gastrointestinal organs only, at 24 days post infection, from all 3 experiments.
All mice were injected with 150 mg kg^{-1} d-lucerfin I.P 7 minutes before sacrifice. All tissue was incubated in luciferin (2% v/v/ in d-PBS) during necropsy, and imaged. Dotted line represents the uninfected control average bioluminescence for each organ, plus 2 standard deviations. a) Total GI flux is the sum of stomach and caecum bioluminescence signal, with a significant difference between cyclophosphamide treated groups and infected control. Asterisks indicate a *p* value of 0.0020 between Cyclophosphamide and untreated, and *p* of 0.0037 between benznidazole and untreated, obtained using an ordinary one-way ANOVA, b) Mesentery adipose specific bioluminescence removed from large intestine during necropsy and imaged in the Spectrum and exposed for 3-5 minutes, with a binning of 4-12 in to avoid saturation. A significant difference was observed in the cyclophosphamide treated group against infected control, with asteriks representing a *p* value of 0.0042 between cyclophosphamide and untreated, *p*=0.0115 for Anti-CD8 vs Untreated, *p=0.0073*, obtained using ordinary one-way ANOVA. c) Caecum specific bioluminescence. Caecum removed from small intestine during necropsy and incubated in luciferin. Tissue imaged at a 5-minute exposure, with large binning. d) Stomach specific bioluminescence signal. Stomach removed during necropsy and incubated in luciferin and imaged at 2–5-minute exposure, binning medium to large. Asterisks represents a *p* value of 0.0015 between cyclophosphamide treated group and untreated group, *p=0.0061* for benznidazole vs untreated.

The total flux in the GI mesentery (a contiguous set of adipose-rich connective tissues, anchoring segments of the intestine to the abdomino-pelvic cavity wall), Fig.2.5.2.1b), depicted the highest increases in treatment-dependent parasite signals of all imaged tissues. The cyclophosphamide treated group exhibited a 104-fold increase compared to the infected, untreated control (*p=0.0020*). There was a 226-fold reduction in parasite burden in the benznidazole treated group compared to the untreated control (*p=0.0037*). Following similar trends seen in the pooled GI signal, the MC-21 and 1400W treatment groups had similar parasite loads in the mesentery to that of the untreated control group.

The caecum (Fig. 2.5.2.1c) is a pouch at the most proximal side of the large intestine. It is the only organ analysed that exhibited no significant differences in signal between the infected control and any of the treatment groups, suggesting infection in this organ was the least affected by treatments. However, benznidazole treatment, just as in the mesentery, resulted in bioluminescence signal falling to background levels. The stomach specific signal (Fig.2.5.2.1d) also displayed a range of variability within each treatment group, but cyclophosphamide treated mice exhibited the only significant increase in parasite burden compared to infected control with an 11-fold increase (*p=0.0015*). There was a significant reduction in signal in response to benznidazole of 308-fold (*p=0.0061*).

In summary, cyclophosphamide treatment resulted in significantly increased GI-specific parasite loads. Anti-CD8a treatment led to higher average parasite loads, but this was only statistically significant in the mesentery tissue. Benznidazole cleared parasites below the limit of detection in all sites. Neither 1400W nor MC-21

had any effect. The GI-specific infection results were therefore consistent with the whole animal *in vivo* imaging data.

2.5.3 Immune profile of Digestive Chagas Disease large intestine

The following flow cytometry experiments and data were from a pilot study. This was conducted as one of my final experiments with no time for repeats, so there were clear limitations when interpreting results and with the conclusions drawn. Caveats are outlined in full in the discussion (2.6.5).

~5cm of the large intestine from each mouse was removed during necropsy and processed into single cell suspensions. The suspensions were stained using a range of antibodies (see methods) to delineate immune cell subsets and analysed using flow cytometry.

The aim of this was two-fold; first to confirm the immune-modulatory treatment efficacies in the colon; and second, to garner deeper insight into the microenvironment of the large intestine during acute *T. cruzi* infection, and in response to each treatment.

Using FMO, negative controls and compensation controls the initial gating strategy shown in 2.5.3.1 was designed. This gating strategy, in particular identifying CD45+ (all leukocytes) and CD3+ CD8+ populations (CD8+ T cells), allowed for quantification and confirmation of colon-specific target cell depletion in response to cyclophosphamide and anti-CD8a treatments respectively. Using counting beads, it was possible to establish total counts of cell subtype populations to calculate the percentage change in response to treatment.

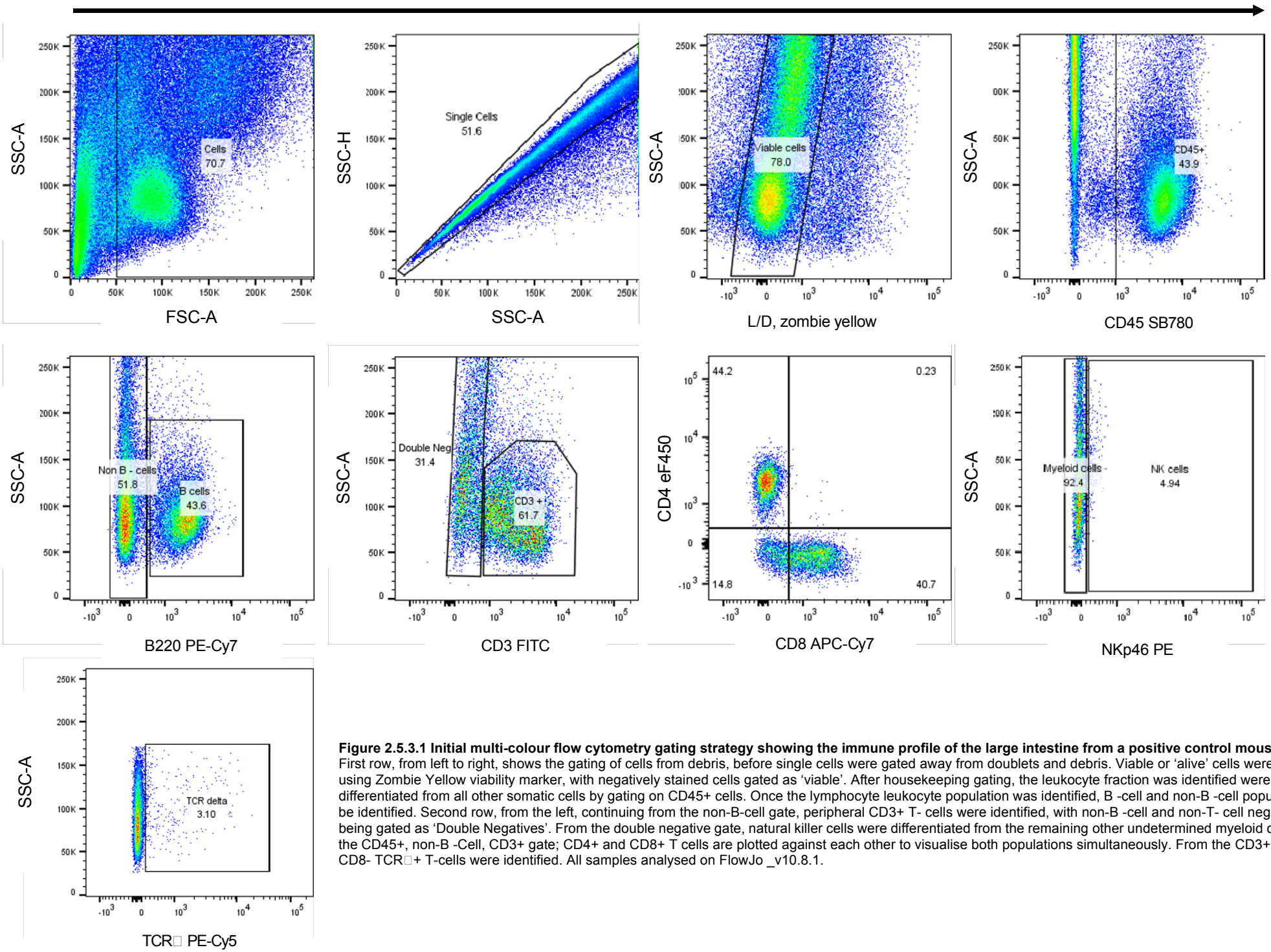

Figure 2.5.3.1 Initial multi-colour flow cytometry gating strategy showing the immune profile of the large intestine from a positive control mouse. First row, from left to right, shows the gating of cells from debris, before single cells were gated away from doublets and debris. Viable or 'alive' cells were identified using Zombie Yellow viability marker, with negatively stained cells gated as 'viable'. After housekeeping gating, the leukocyte fraction was identified were differentiated from all other somatic cells by gating on CD45+ cells. Once the lymphocyte leukocyte population was identified, B -cell and non-B -cell populations could be identified. Second row, from the left, continuing from the non-B-cell gate, peripheral CD3+ T- cells were identified, with non-B -cell and non-T- cell negative cells being gated as 'Double Negatives'. From the double negative gate, natural killer cells were differentiated from the remaining other undetermined myeloid cells. From the CD45+, non-B -Cell, CD3+ gate; CD4+ and CD8+ T cells are plotted against each other to visualise both populations simultaneously. From the CD3+ gate, CD4- CD8- TCR□+ T-cells were identified. All samples analysed on FlowJo _v10.8.1.

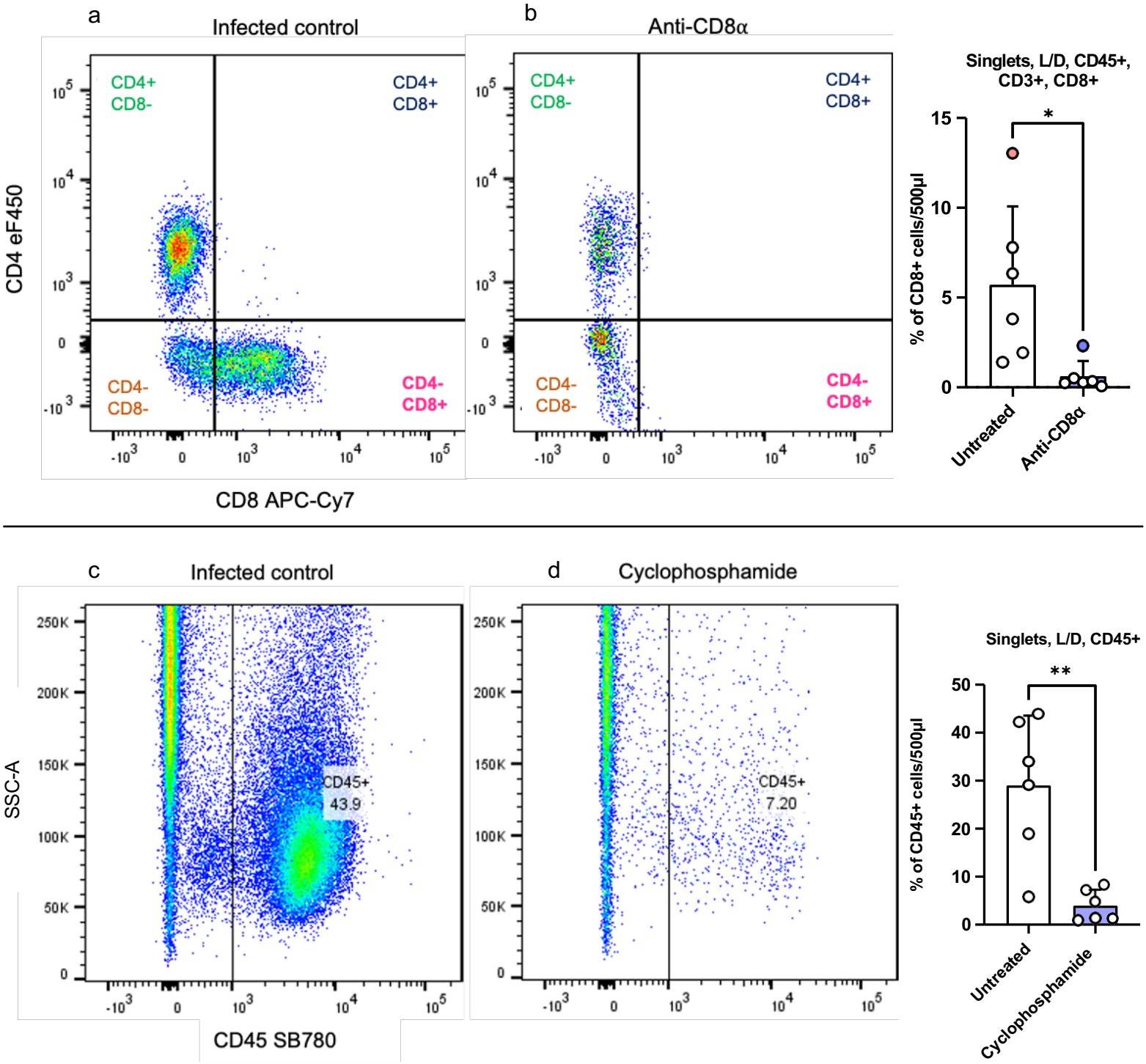

Figure 2.5.3.2 Representative flow plots.
a) Untreated control plot: CD8 vs CD4 plot on the L/D, CD45+, CD3+, CD8 vs CD4 population gate. Lower right quadrant represents CD8+ T cell population. b) Plot of anti-CD8a treated mouse on the same gate, with lower right quadrant representing CD8+ T cell population. Graph depicting the total CD8+ T cell population, by percent, in infected untreated control and anti-CD8a treated mice. Unpaired t-test was conducted, and asterisk indicates a *p* value of 0.0184. Red and blue data point are to indicate outlier. c) infected control vs cyclophosphamide treated SSC vs CD45+plot on the viable singlet population L/D, CD45+ gate. d) Graph depicting the total CD45+ cell population, by percent, in infected control mice and cyclophosphamide treated mice. Unpaired t-test was conducted, with star indicating a *p* value of 0.0021.

Figure 2.5.3.2 are representative plots for both cyclophosphamide and anti-CD8a treated infected mice. In a) I qualitatively observed the reduction in colonic CD8+ T cell populations, contained in the lower right quadrant, in the anti-CD8a treated mice compared to the infected control plot. This depletion was corroborated by calculating the percentage population of CD8+ T cells, shown in b), where an average 89% reduction was noted across all anti-CD8a treated infected mice (*p=<0.0184*). This was achieved using counting beads to first calculate total number of cells per sample, then gating through singlets>L/D>CD45+>non-B-cell>CD3+ and calculating the percent of CD8+ cells of the sample, normalised for each. In cyclophosphamide treated mice I anticipated a reduction of total immune cells, which can be visualised in the representative CD45+ gates in c). This reduction was calculated, and in d) there was a significant reduction of leukocytes in all cyclophosphamide treated infected mice with an average 85% knock-down (*p=0.0021*). We also used an anti-CD8a matching IgG2b isotype control, to increase confidence in treatment specificity, a representative plot is shown below.

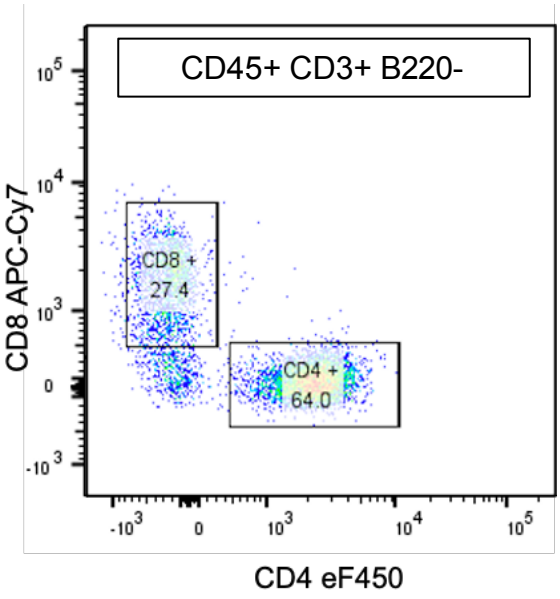

Figure 2.5.3.3 Representative flow plot for IgG isotype [400µg].

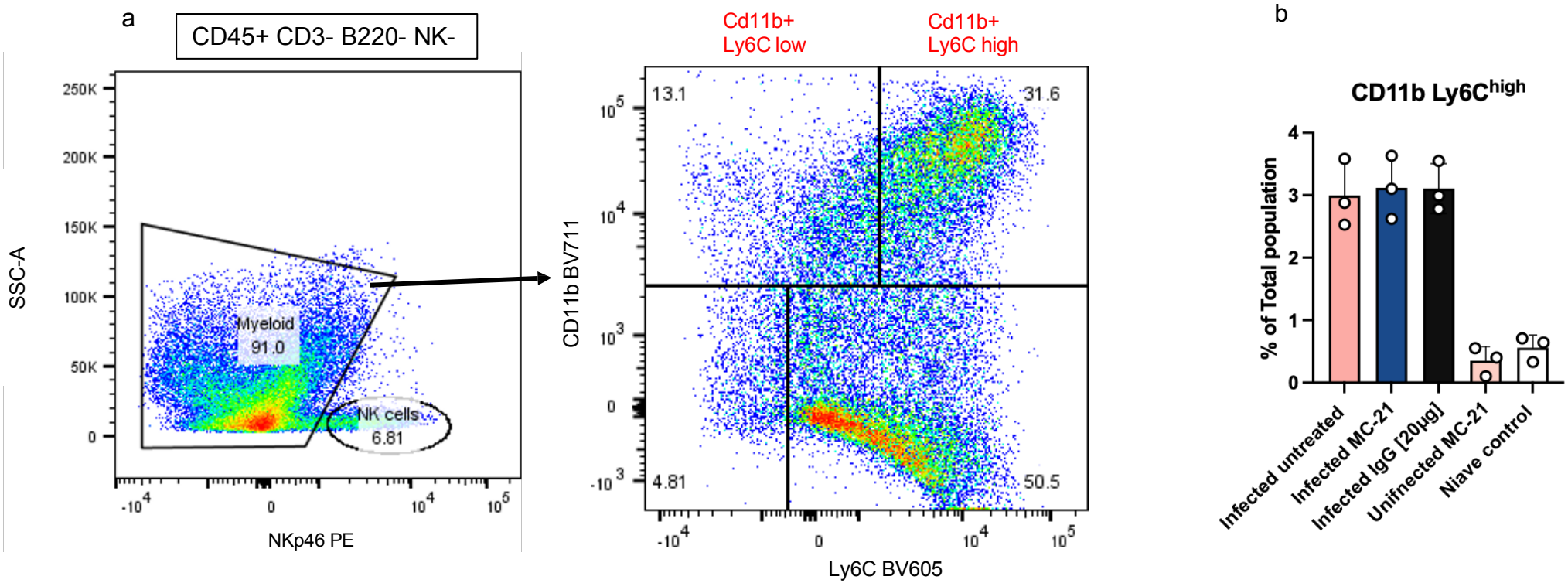

Figure 2.5.3.4 Flow plots showing use of new panel to analyse colon cells from an MC-21 treated mouse.
The adjusted antibody panel remained largely similar, with the addition of more myeloid specific targets. a) A plot showing Ly6cC vs CD11b, through the following gates: CD45+, CD3-, NK-B220- Myeloid +. Two populations of Ly6C+ can be visualised, Cd11b high and Cd11b low. b) depicts a comparison of CD11b+ Ly6C^{high} + populations in MC-21 treated infected and uninfected groups, as well as infected and uninfected controls. One-way ANOVA conducted: infected untreated vs MC-21 (*p=0.98867*), infected untreated vs uninfected MC-21 (*p=<0.0001*), infected untreated vs Naïve control (*p=<0.0001*), Infected untreated vs Infected IgG (*p=0.9903*).

With the addition of MC-21 anti-CCR2 treatment in the second and third experiments, we designed a more expansive antibody panel to include additional myeloid markers (see Methods), which could be used to evaluate the depletion of monocytes. Monocytes can be grouped into two classifications: Ly6C^{high}, which possess the surface markers CD11b+ and CD115+ and chemokine receptors CC-chemokine receptor 2 ^{high} (CCR2high) CX_3CR1low, and Ly6C^{low} which possess the surface markers CD11b$^+$ CD115$^+$ and chemokine receptors CCR2^{low}CX_3CR1^{high} (56). CCR2-C-C-motif chemokine ligand 2 (CCL2) signaling results in Ly6C^{high} monocyte egress from bone marrow, and conformational changes to the vascular cell adhesion molecule 1 (VCAM-1), which permits transmigration into inflamed tissue (57). Ly6C^{high} display developmental plasticity and, upon maturing to M1 macrophages, they coordinate the innate immune response through the activation of the inflammasome after exposure to pathogen-damage-associated molecular patterns (PAMPs) (58,59). They release proinflammatory cytokines (IL-1, IL-6, IL-8, TNF-α), and also have a high antimicrobial capability including potent capacity for phagocytosis and secretion of nitric oxide (NO) whilst also contributing to tissue degradation and T-cell activation (56). Since Ly6C^{high} monocytes traffic from the bone-marrow in a CCR2-dependant manner, MC-21, as a CCR2+ target, is specific against this monocyte subset (60).

In the steady-state, Ly6C^{high} monocytes differentiate into Ly6C^{low} which patrol the circulatory system. This sub-set interacts using different chemokines to Ly6C^{high} (CX_3CR1), which is refractory from CCR2 inhibition. Ly6C^{low} monocytes can differentiate into M2 macrophages, which contribute the anti-inflammatory process via the secretion of IL-10, and promote tissue repair (61).

Surprisingly, there was not an obvious reduction, and no significant difference, in Ly6C^{high} monocytes in the MC-21 treated groups compared to their respective controls (Fig. 2.5.3.4). The treatment window for this experiment was 7 days, but the treatment regime for MC-21 was limited to 5 days as per advice from the donor of the antibody. Mice generate an antibody response against the anti-CCR2 antibody after 48 hours of the final dose, rendering it ineffective (M. Mack *personal communication*) and in this experiment the final dose was ~72 hours before the tissue was processed for flow cytometry. Therefore, it is possible that monocyte depletion had been achieved, but their numbers had rebounded by the time of tissue collection. In the final experiment, upon repeating the MC-21 treatment arm, I did not process any tissue for flow cytometry, but collected blood at day 5 post-treatment with the aim of counting monocytes manually to confirm treatment efficacy.

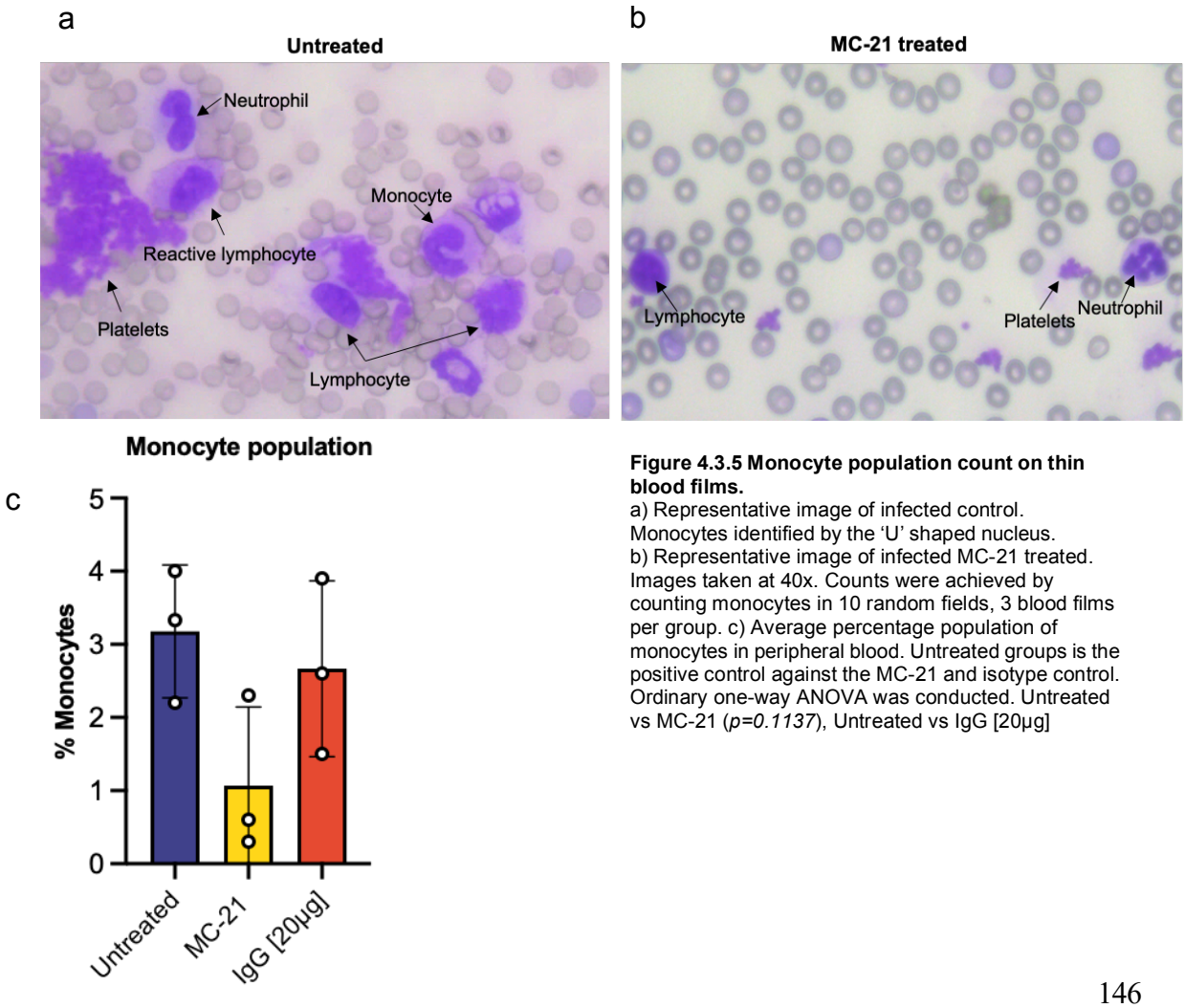

Figure 4.3.5 Monocyte population count on thin blood films.
a) Representative image of infected control. Monocytes identified by the 'U' shaped nucleus. b) Representative image of infected MC-21 treated. Images taken at 40x. Counts were achieved by counting monocytes in 10 random fields, 3 blood films per group. c) Average percentage population of monocytes in peripheral blood. Untreated groups is the positive control against the MC-21 and isotype control. Ordinary one-way ANOVA was conducted. Untreated vs MC-21 (*p=0.1137*), Untreated vs IgG [20µg]

The average monocyte population in the anti-CCR2 (MC-21) treated group was 2.6-fold lower compared to the IgG[20µg] isotype (*p=0.1612*) and 3-fold lower than the untreated control (*p=0.1137*). This observed reduction was not significant, likely due to the low statistical power associated with the small sample size (n=3) of each group.

The flow cytometry data were also used to build unique colonic immune profiles of certain treatment groups from the first experiment only. Using the first antibody panel it was possible to quantify the comparative differences between all immune markers across the groups. Firstly, a total number of stained cells were counted. Then, using counting beads, the different cell populations were normalised allowing an accurate percentage change to be calculated against the infected control. First the total number of CD45+ cells was quantified for each treatment group (Fig. 2.5.3.6a).

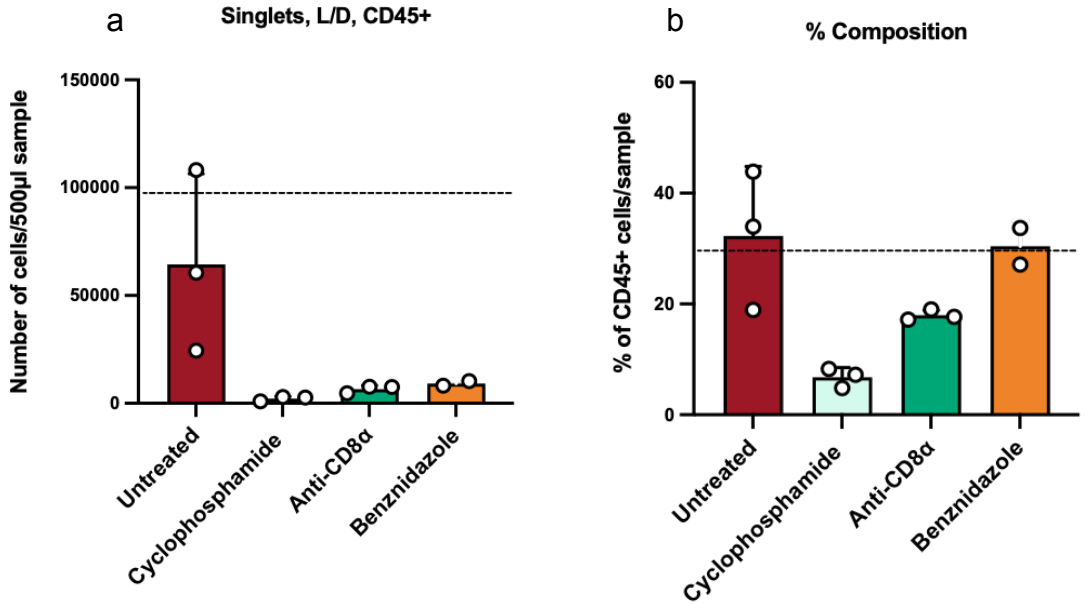

Figure 2.5.3.6. Bar plots showing proportion of colonic CD45+ cells in each experimental group.
a) Total number of CD45+ cells in the colon of each treatment group at 21 days post infection. Gates used: Cells, singlets, L/D, CD45+. The dotted line represents the average CD45+ count in the uninfected control + 2 SD. One way ANOVA conducted: Untreated vs Cyclophosphamide (*p=0.138*), Untreaded vs anti-CD8a (*p=0.315*), Untreated vs benznidazole (*p=0.561*). *n=3* for each group, *n=2* for benznidazole due to poor yield during sample collection. b) The standardised percentage of cells in each processed colon that were CD45%. Dotted line represents the uninfected average. One-way ANOVA conducted: Untreated vs Cyclophosphamide (*p=0.0078*), Uninfected vs anti-CD8a (*p=0.0981*), uninfected vs benznidazole (*p=0.983*).

There was a treatment trend in each of the treated groups compared to the untreated control, although not significantly different. There was a 86% reduction in the CD45% population in the cyclophosphamide treated group, compared to the untreated group (*p=0.0078*). The CD45+ population in the cyclophosphamide treated group was also 22% of the amount CD45+ seen in the benznidazole group. There was 44% fewer CD45+ cells in the anti-CD8a compared to the untreated (*p=0.0981*). The low sample size within each group, and the absence of the MC-21 treated group, was due to general analysis only being viable on the first experiment with the initial antibody panel. This was a result of complications during data processing of the second flow cytometry experiment (see section 4.6.5).

Within the CD45+ gate, the population for each other maker was counted and compared (Fig. 2.5.3.7).

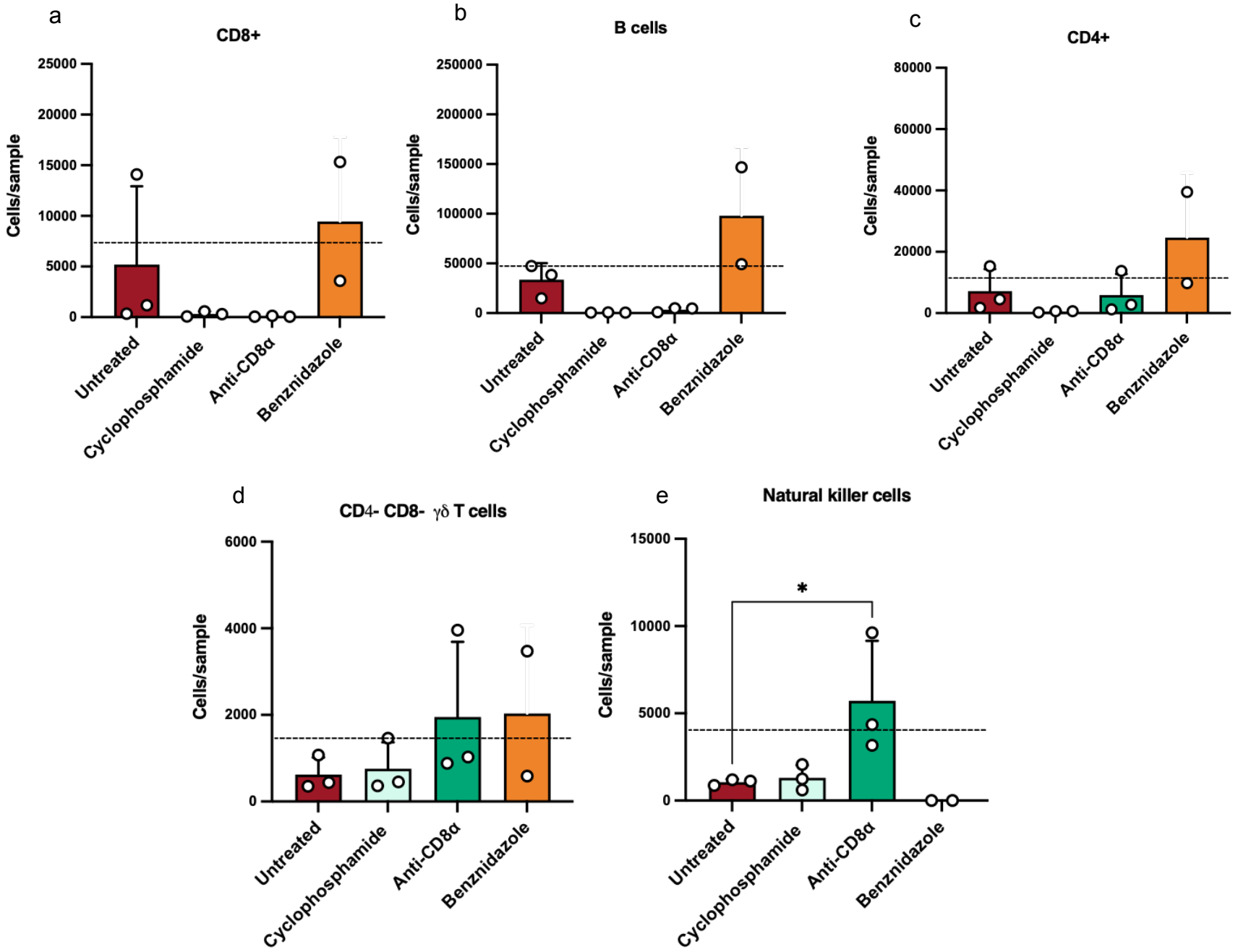

Figure 2.5.3.7. The population of immune markers in the colon of different experimental treatment groups.
a) The population of CD8+ T cells gated within singlets, L/D and CD45+. One way ANOVA was conducted between each treatment group and the untreated. Untreated vs cyclophosphamide *(p=0.5594*) vs benznidazole (*p=0.7159).* b) The population of B cells gated within singlets, L/D and CD45+, B220+. One way ANOVA conducted between each treatment group and the untreated. Cyclophosphamide (*p=0.3942*), Anti-CD8a (*p=0.4618*), benznidazole (*p*=0.0888). c) The population of CD4+ T cells gated within singlets, L/D and CD45+, B2 20-, CD3+, CD4+. One way ANOVA conducted. between each treatment group and the untreated. Cyclophosphamide (*p= 0.7391*), Anti-CD8a (p= *0.9968*), benznidazole (*p=0.1945*). d) The population of γδ T cells gated within singlets, L/D and CD45+, B220-, CD3+, CD4-, CD8-. One way ANOVA conducted between each treatment group and the untreated. Cyclophosphamide (*p=0.9983*), Anti-CD8a (*p=0.4829*), benznidazole (*p=0.5223*). e) The population of natural killer cells gated within singlets, L/D and CD45+, B220-, CD3-. One way ANOVA conducted between each treatment group and the untreated. Cyclophosphamide (*p=0.9969*), Anti-CD8a (*p=0.0464*), benznidazole (*p=0.8750*).

In each of the total cell counts the uninfected controls exhibited a higher average than the untreated. This was due to a major outlier in the uninfected group, coupled with a low sample size (*n=3*).

From the immune profiles there were several observed treatment effects (Fig. 2.5.3.7). The CD8+ populations in the colon fell below the uninfected average +2SD in every treatment group except the benznidazole group. The anti-CD8a treated group averaged a population of 0.034%, suggesting CD8 T cell depletion was almost total (refer to for confirmation of CD8+ knockdown in both experiments). Cyclophosphamide treatment also reduced the CD8+ population by 11-fold (*p=0.5594*). An additional *t*-test was conducted to re-assess significance, but the outcome was similar (*p=0.104*). There were similar trends observed with B cell populations but at higher cell populations compared to CD8+ cells for each group (Fig. 2.5.3.7b). The untreated group exhibited a 9.5-fold greater B cell population than observed in the anti-CD8a group (*p=0.2114*), which suggests there might be a knock-on effect of CD8+ T cell depletion on B cell activity in the colon of infected mice. Similarly, with CD8+ T cell populations, there was a downward trend of B cell population in response to cyclophosphamide treatment with a 655-fold reduction in population, which was significant when an additional *t*-test was conducted (One way ANOVA: *p*=0.1030*,* t-test: *p*=0.0274). Interestingly, there was no change of CD4+ cell populations between untreated and anti-CD8a treated (*p= 0.9968*) (Fig. 2.5.3.7c). I hypothesise that in the absence of CD8+ T cells there is less competition for cytokine or mitogen activity for CD4+ T cell differentiation and/or proliferation (see Discussion). A similar cyclophosphamide treatment trend was observed in the CD4+ T cell population with a 14-fold reduction (one-way ANOVA: *p=0.7391,* t-test: *p*=0.1802) (Fig.2.5.3.7c).

With the γδ T cells and natural killer cell populations there were rare upward trends observed in the cyclophosphamide treated group, and in the anti-CD8a treated groups (Fig. 2.5.3.7 d&e). In the anti-CD8a treated group, we observed a 3-fold increase in γδ T cells (p=0.0363) and 5-fold increase in natural killer cells compared to untreated (p=0.031). This is theorised to be a compensatory mechanism to subsidise the absence of CD8+ T cells. Interestingly, despite an 86% reduction in CD45+ cells in cyclophosphamide treated mice compared to untreated mice (Fig.2.5.3.6), the remaining 14% had similar γδ T cell population compared to uninfected control (*p=0.9983*), and similar in natural killer cell populations compared to untreated group (*p=0.9969)*, suggesting these cell types are less susceptible to this drug.

Using the second immuno-phenotyping panel, it was possible to quantify iNOS+ cell populations. The aim was to initially screen if immune (CD45+) or non-immune (CD45-) cells were the cellular source of iNOS, in a way that could explain alleviation or exacerbation of pathology associated with an increase or decrease of source cells, in response to the various treatments. Firstly, the total number of iNOS+ events were calculated where it was evident that MC-21 and anti-CD8a treated groups had the highest number of total iNOS+ cells (Fig. 2.5.3.7a). Both groups exhibited significantly increased iNOS+ events against the uninfected control (*p=0.0027*, *p=0.0467* respectively), and there were no significant differences observed in infected untreated (*p=0.1162*), cyclophosphamide (*p=0.6333*), and benznidazole (*p=0.9954*) groups. Within the total iNOS+ population, the CD45+ population was gated to determine a percentage population of immunologically sourced iNOS (Fig. 2.5.3.7c), and non-immunologically sourced iNOS (Fig. 2.5.3.7b).

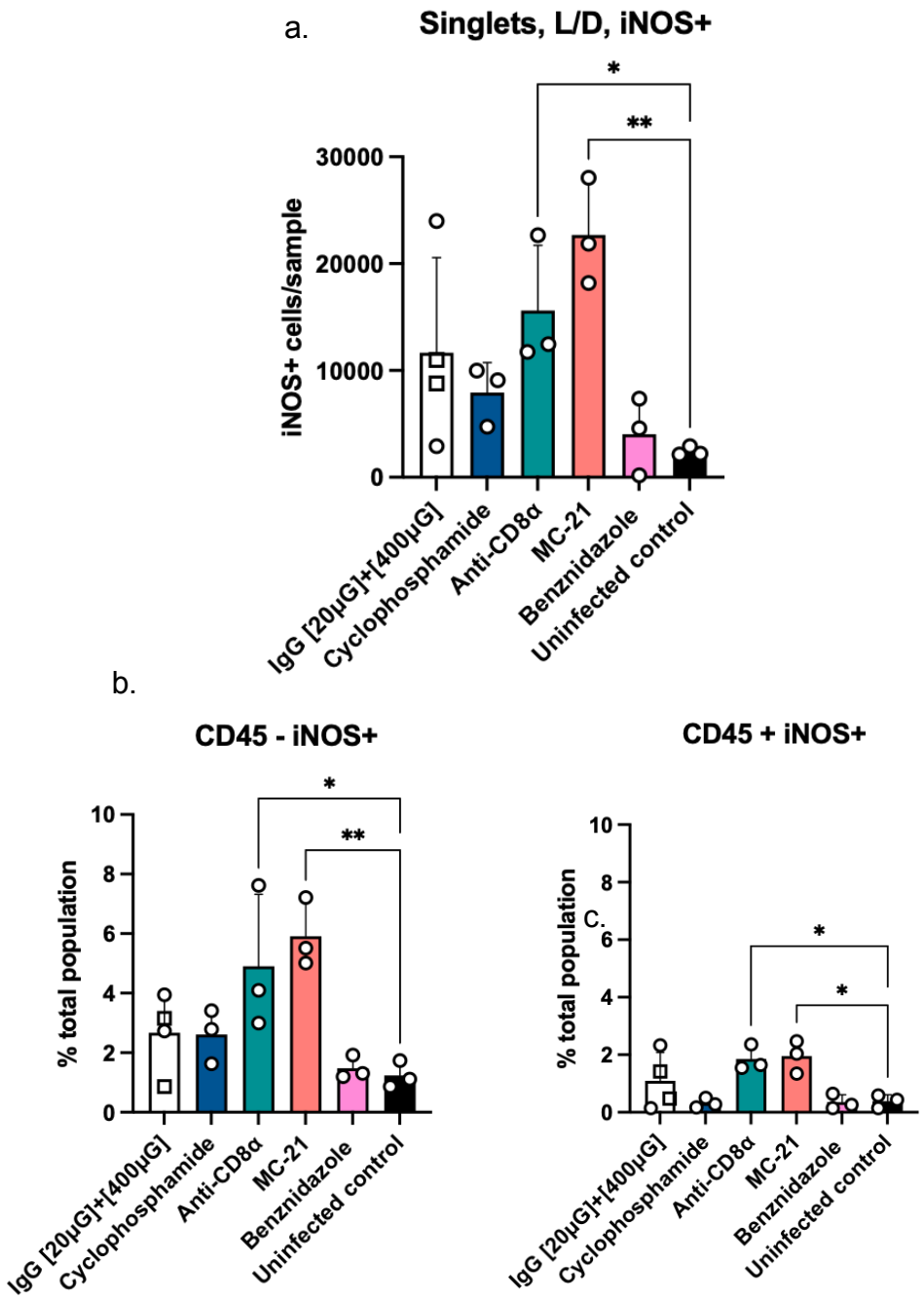

Figure 4.3.8. Bar plots depicting NOS2iNOS+ cell populations in the large intestine.
a) Total number of iNOS+ cells (Singlets, L/D, iNOS+). One way ANOVA conducted: all vs uninfected control. Asterisks indicate a significant difference for: Anti-CD8a vs uninfected control (*p=0.0467*), and MC-21 vs uninfected control (*p=0.0027*). No significant difference between Isotype infected controls vs uninfected control (*p=0.1162*), cyclophosphamide (*p=0.6333*), and benznidazole (*p=0.9954*). b) Shows the percentage proportion of iNOS+ cells that are not leukocytic. One way ANOVA was conducted; all vs uninfected control. Stars indicate a significant difference; for MC-21 vs Uninfected control indicate a *p* value of 0.0083, and for anti-CD8a vs uninfected control stars indicate a *p* value of 0.0385. Squares in IgG bar are IgG [400µg], circles [20 µg]. c) Shows the proportion of NOS2 iNOS+ cells that are leukocytic, co-staining with CD45. One way ANOVA conducted; all vs uninfected control. Stars indicate a significant difference; for MC-21 vs uninfected control indicate a *p* value of 0.0207 and for anti-CD8a vs uninfected control a *p* value of 0. 0121. Relative percentage was calculated using counting beads, and gating strategy was established using NOS2 iNOS FMO control. Data processed on FlowJo.

After gating it was evident that the iNOS+ colonic cellular compartment is predominantly non–leukocytic in each treatment group (Fig 4.3.8 b&c). In the infected, isotype-treated controls, 1.09% of immune cells (CD45+) were iNOS

producing, compared to 2.67% of non-immune (CD45-) cells. Neither population was significantly higher than in the uninfected group despite a 1.13-fold (*p=0.3892*) and 1.79-fold (*p=0.4824*) increase respectively. There were similar trends in both iNOS+ populations in response to each treatment. MC-21 treated mice exhibited the highest iNOS expression of any experimental group in both leukocytic and non-leukocytic populations (Fig.4.3.8). There was a strongly significant increase compared to the uninfected group in the CD45- compartment (*p=0.0029*), and a significant increase in the CD45+ compartment (*p=0.0207*). There was also a significant increase between MC-21 treated and IgG isotype group (*p=0.0192*) in the non-leukocytic compartment but not in the leukocytic (*p=0.2410*).

The anti-CD8a treated mice had the second highest iNOS+ population in both compartments, with a 0.84-fold increase (*p=0.0166*) in the CD45-population and 0.70-fold (*p=0.0304*) in the CD45+population. The cyclophosphamide treated group had a CD45- iNOS expressing cell population that was 0.73-fold and 0.99-fold higher than the benznidazole (*p=0.1166*) and uninfected control group (*p=0.5770*) but had the lowest leukocyte iNOS+ population of all groups. This low iNOS+ leukocyte compartment compliments the depletion of CD45+ colonic cell population observed in cyclophosphamide treatment. In the leukocytic and non-leukocytic populations, uninfected control and benznidazole groups are separated by only 0.04% and 0.2% respectively. The similar iNOS+ populations in these groups corelated with the absence of parasites, evidenced by the lack of *in vivo* and *ex vivo* bioluminescence signal.

2.5.4. Effect of treatments on GI transit time

To assess gut peristalsis functionality, transit time assays were conducted at each of the 3 weeks of infection. Gut dysfunction, or more specifically dysperistalsis, in infected mice is characterised by a significantly longer transit time at week 3 than week 2 or a significantly longer transit time than uninfected controls at any timepoint.

Across the 3 experiments conducted, the inoculum [$5x10^3$ parasites] comprised either tissue culture trypomastigotes or blood trypomastigotes. To test the validity of pooling of experimental data from animals that received different types of trypomastigote, a comparison of transit times was conducted.

At weeks 1 and 2 every mouse used across all 3 experiments infected with either blood trypomastigotes or tissue culture trypomastigotes were plotted. The data points at week 3 represent only those that were not subject to any treatment.

A similarly significant increase was observed in both inoculum methods between weeks 1 and 2 (Fig. 2.5.4.1) This phenotype had not been readily observed in previous individual experiments where transit time assays were conducted at the same time points. Although the increase between weeks 1 and 2 was only 29% (p= *<0.0001*) in the TCT group and 23% (p=*0.0007*) in the BT group in this timeframe, the pooling of data and consequent increase in samples size shows that the onset of gut dysfunction is earlier than originally thought. Between week 2 and 3, TCT infected mice present with a 75% increase in transit time on average (p= *<0.0001*), and BT infected mice with 63% (p= *<0.0001*). The much larger effect size for increased transit time in both groups cements week 2 – 3 as a suitable window in which to test interventions.

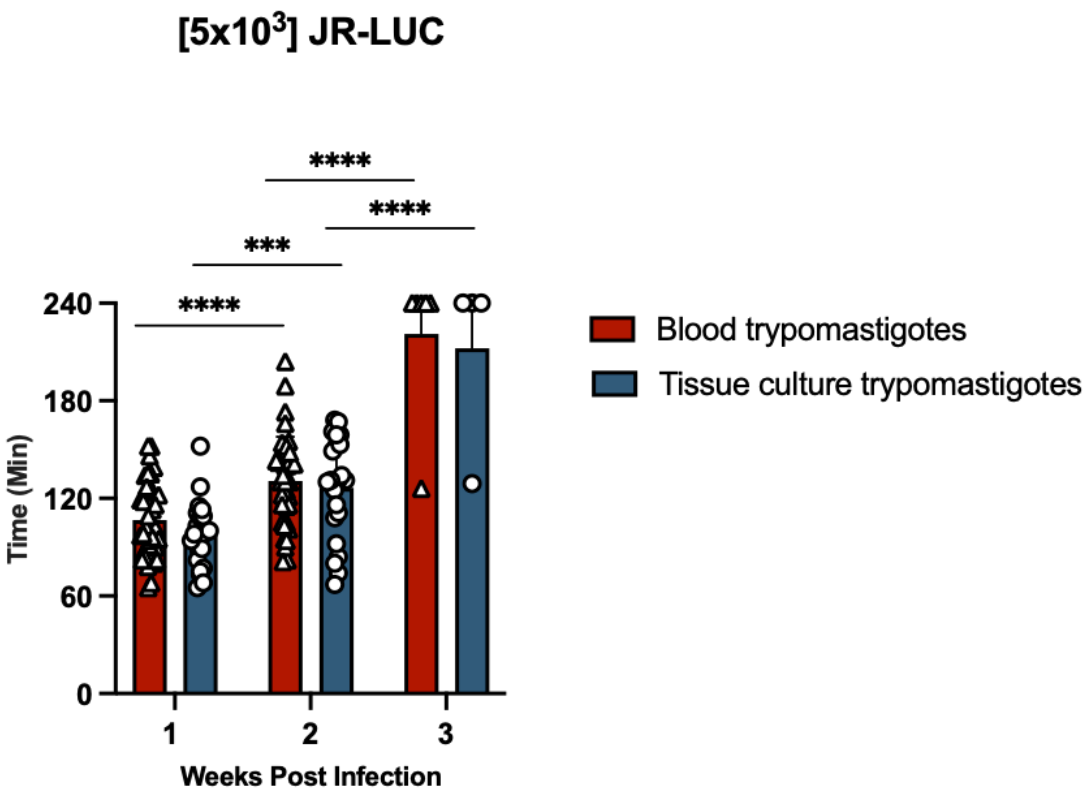

Figure 2.5.4.1 Bar plot depicting the transit time of mice infected with either blood trypomastigotes (triangles) or tissue culture trypomastigotes (circles).
The dosage of both inoculation methods was identical, at [5x10^3], injected intraperitoneally. Unpaired, two-tailed t-test conducted between week 1 and 2 for both groups. Stars for blood trypomastigotes, between weeks 1 and 2 represent a *p* value of <0.0001. Stars for tissue culture trypomastigotes between weeks 1 and 2 represent a *p* value of 0.0007. There was no significance between the inocula at week 2 *(p=0.583*). There is a major increase between weeks 2 and 3 for both groups: Blood trypomastigotes (*p=<0.0001*), tissue culture trypomastigotes (*p=<0.0001*), but there was no difference between the groups at week 3 post infection (*p=0.7935*). Blood trypomastigotes *n=39* weeks, 1&2, *n= 4* at week 3. Tissue culture trypomastigotes *n=22* weeks 1&2, *n=5* week 3.

There was no significant difference between TCT and BT when comparing transit time at week 2 post infection (*p=0.583*), and week 3 post infection (*p=0.7935*). This increased confidence that inoculating with either BT or TCT had no comparable impact on transit time dysfunction development, justifying the pooling of data across all 3 experiments.

In this study, the first transit time assay was performed 7 days after infection. The second on the day treatments began at 14 days post infection, and finally on the last day the treatment intervention window, at 21 days post infection.

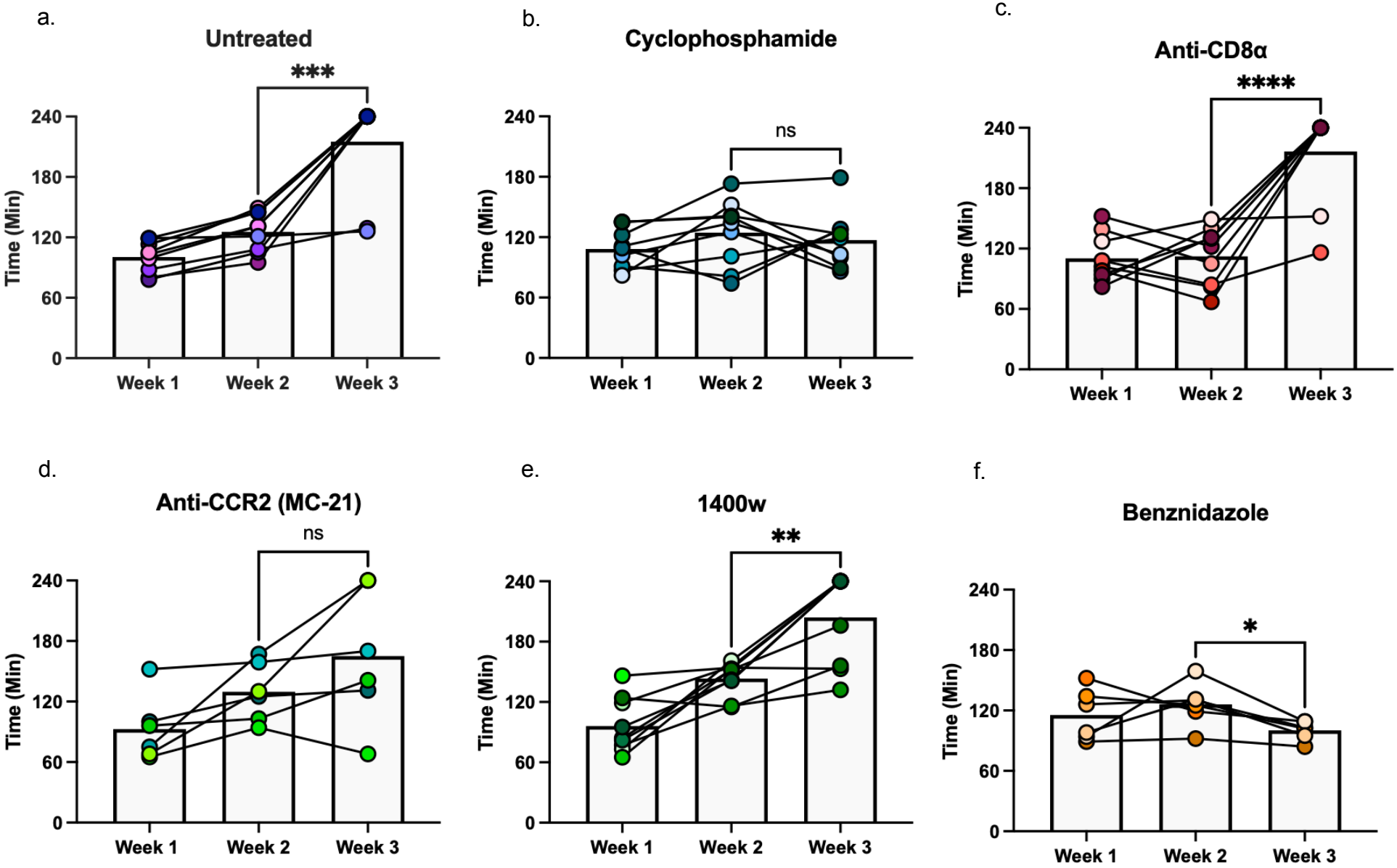
a.
Untreated
***
240
180
120
60
0
Time (Min)
Week 1
Week 2
Week 3
b.
Cyclophosphamide
ns
240
180
120
60
0
Time (Min)
Week 1
Week 2
Week 3
c.
Anti-CD8α
****
240
180
120
60
0
Time (Min)
Week 1
Week 2
Week 3
d.
Anti-CCR2 (MC-21)
ns
240
180
120
60
0
Time (Min)
Week 1
Week 2
Week 3
e.
1400w
**
240
180
120
60
0
Time (Min)
Week 1
Week 2
Week 3
f.
Benznidazole
*
240
180
120
60
0
Time (Min)
Week 1
Week 2
Week 3

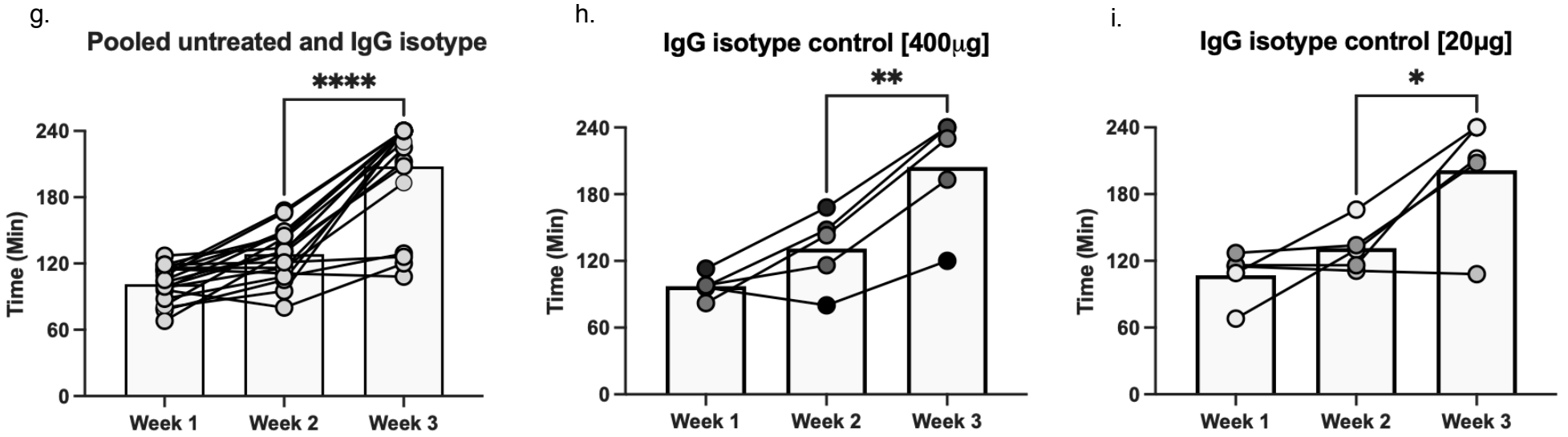

Figure 2.5.4.2 Graphs depicting transit times data at weeks 1, 2 and 3 post infection, assessing the development of gut dysfunction in response to immune-regulatory modulatory or trypanocidal treatments.
C3H/HeN mice were infected with $5x10^3$ JR-LUC parasites, with each treatment covering a 7-day window between the second and third week of infection. Transit time assay entails feeding mice carmine solution (6% w/v) via oral gavage and timing the duration it takes to pass a red faecal pellet. The bars represent average transit time at each timepoint, with each data point assigned its own colour to represent each mouse within the group and the lines links serial data points for the individual mice. The maximum cut-off for the experiment was 240 minutes. a) Transit time data for Untreated cohort (*n=9*) throughout, paired t-test conducted between week 2 and 3 (*p=0.0005*). b) Transit time data for cyclophosphamide treated mice (*n=9*) throughout, a paired t-test was conducted between week 2 and 3 (*p=0.5948*). c) Transit time data for anti-CD8a treated mice (*n=9*) throughout, paired t-test conducted between week 2 and 3 (*p=<0.0001*). d) Transit time for anti-CCR2 (MC-21) treated mice (*n=6*) throughout, paired t-test conducted between week 2 and 3 (*p=0.1043*). e) Transit time for 1400W treated mice (*n=9*) throughout, paired t-test conducted between week 2 and 3 (*p=0.0011*). f) Transit time data for benznidazole treated mice (*n=6*) throughout, paired t-test conducted between week 2 and 3 (*p=0.0108*). g) Transit time data for the pooled untreated cohort, including both IgG isotype controls [400μg and 20μg] (*n=19*) throughout, paired t-test conducted between week 2 and 3 (*p=<0.0001*). h) Transit time data for the IgG isotype [400μg] control (*n=5*) throughout., paired t-test between week 2 and 3 (*p=0.0279*). i) Transit time data for the IgG isotype [20μg] control (*n=5*) throughout., paired t-test between week 2 and 3 (*p=0.0268*)

The standard infection phenotype for the initiation of transit time delay is depicted by the untreated plot (Fig. 2.5.4.2a). Between weeks 2 and 3 there was an average 72% increase in transit time (*p=0.0005*), with all but two mice reaching the 240-minute cut off. Contrastingly, the cyclophosphamide treated group did not develop a transit time delay as there was no difference between weeks 2 and 3 (*p=0.5948*). The average transit time was reduced post treatment by 5.6% (Fig. 2.5.4.2b). The prevention of the dysperistalsis phenotype, by measure of an average decrease in transit time, was only shared with benznidazole treatment where there was a significant reduction after treatment (*p=0.0108*), even though the two treatments had completely opposite impacts on parasitic burden (section 2.5.1).

Conversely, the anti-CD8a treated group showcased the highest average post-treatment transit time of 216.4 minutes, which was an increase of 92.9% during the treatment window (*p=<0.0001*), with all but two mice reaching the maximum cut off time across the three experiments. This outcome reflected most closely that of the untreated infected control, which had an increased transit time of 72% between weeks 2 and 3. Thus, depletion of CD8+ T cells had no significant impact on the transit time delay phenotype in the DCD model.

Anti-CCR2 (MC-21) treated mice were the only treatment group that exhibited a non-significant increase in transit time post treatment (*p=0.1043*). This coincided with a high degree of variability between individual mice in the week 3 transit time, supported by a mean of 170 minutes and standard deviation calculated at 61.1 mins. Thus, depletion of monocytes led to an intermediate transit time phenotype that

was less severe than was seen in the untreated or dose-matched isotype control mice.

The 1400W treated group also exhibited a degree of variability in treated mice, with half reaching the maximum cut-off and half ranging from 132 to 196 minutes. However, there was still a significant increase of 42.5% and an average transit time of 204.1 minutes post-treatment (*p=0.0011*). Thus, chemical inhibition of iNOS activity appeared to have no significant impact on the transit time phenotype in the DCD model.

For both anti-CD8a and anti-CCR2 (MC-21) treatment, a matching dose concentration of IgG2b isotype was used to account for non-specific antigen binding in vivo, or other off-target effects of antibody treatment. From the transit time data of the isotype controls, it was clear that the transit time profiles were different to their corresponding treatments and comparable with untreated controls, irrespective of the dose concentration [400µg/20µg]. Despite there being a 20-fold difference in isotype antibody concentrations administered, there was a negligible impact on post-treatment transit time: MC-21 isotype control had an increase of 53.4% and anti-CD8a isotype had an increase of 56.2%. This provides confidence that the effects of treatment observed were the result of antigen specific binding, and not off-target effects of the antibody treatments.

To allow more of a direct comparison between each group at the final post-treatment time point I plotted each end point average together (Fig. 2.5.4.3).

a.

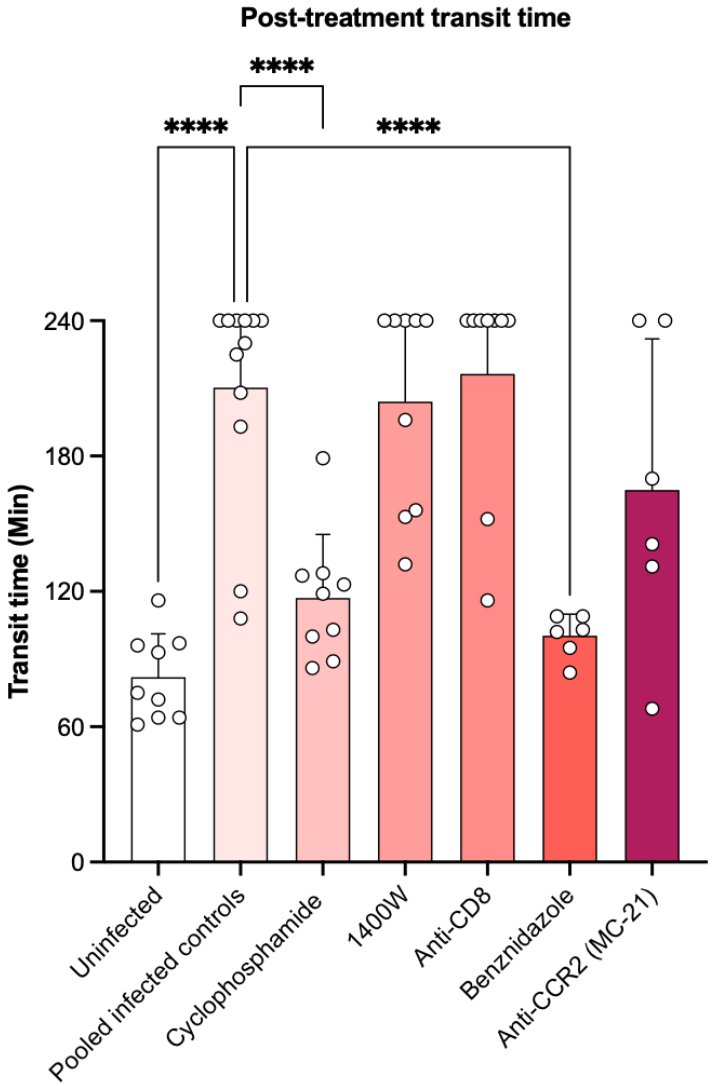

b.

Comparison	*p* value One way ANOVA (all vs all)
Uninfected vs Infected	<0.0001
Uninfected vs Cyclophosphamide	0.5602
Uninfected vs 1400W	<0.0001
Uninfected vs anti-CD8α	<0.0001
Uninfected vs Benznidazole	0.9799
Uninfected vs anti-CCR2 (MC-21)	0.0068
Pooled infected vs Cyclophosphamide	<0.0001
Pooled infected vs 1400W	0.9999
Pooled infected vs anti-CD8α	0.9999
Pooled infected vs Benznidazole	<0.0001
Pooled infected vs anti-CCR2 (MC-21)	0.3238
Cyclophosphamide vs 1400W	0.0009
Cyclophosphamide vs anti-CD8α	0.0001
Cyclophosphamide vs Benznidazole	0.9873
Cyclophoshphamide vs anti-CCR2 (MC-21)	0.3213
1400W vs anti-CD8α	0.9955
1400W vs Benznidazole	0.0003
1400W vs anti-CCR2 (MC-21)	0.5645
Anti-CD8α vs Benznidazole	<0.0001
Anti-CD8α vs anti-CCR2 (MC-21)	0.2421
anti-CCR2 (MC-21) vs benznidazole	0.1203

Figure 2.5.4.3. Post treatment transit time for each experimental group.
a) Average transit time for each treatment group at week 3 post infection, after 1 week of infection. Each data point represents data for individual mice, and 240 minutes was experimental cut off. Plotted is a one-way ANOVA, all vs Pooled infected control. *p=<0.0001* for uninfected, cyclophosphamide and benznidazole. b) Table depicting *p* values from a one-way ANOVA where each group was compared to the other. Dark red indicates ****, which lightens as stars decrease. Treatment conditions are described in methods (2.4.2)

The significant reduction in transit time at end point in cyclophosphamide treated, benznidazole treated and uninfected groups (p = <0.0001) represents a marked alleviation of the development of gut dysfunction, compared to that of untreated infected mice. This suggests that cyclophosphamide and benznidazole treatment both prevent gut dysfunction developing in this critical 2–3-week window, despite the treatments having divergent physiological effects.

The anti-CCR2 (MC-21) group had an intermediate phenotype. There was no significant difference between the pooled infected control (*p=0.3238*) and a significant difference compared to uninfected (*p=0.0068*), but no significant difference compared to both the cyclophosphamide treated (*p=0.3213*) and benznidazole treated (*p=0.1203*) groups, both of which alleviated the transit time phenotype. Anti-CCR2 (MC-21) was also the only treated group that exhibited a non-significant increase in transit time between weeks 2 and 3 (Fig. 2.5.4.2d), whilst the matching IgG isotype control developed a significant delay (Fig. 2.5.4.2i).

There was no significant difference in transit time in the 1400W treated (*p=0.*999) group compared to infected control group. This was also observed in the anti-CD8a treatment group (*p=0.999*). This denotes an exacerbation of, or a negligible impact on, development of gut dysfunction. There was also no significant difference between these two groups (*p=0.9955*).

As mentioned previously, there was a high degree of variability in the MC-21 and 1400W treated groups, with 33.3% and 55.5% of mice reaching the maximum cut-off respectively. This suggests the downstream effects of these treatments on the

development of dysfunction were inconsistent. Moreover, the average transit time of MC-21 treated mice was 21.2% lower post treatment than observed in the 1400W group at the same timepoint. The degree of variability suggests the mechanistic effect of the treatments is dependent on interactions within the host, potentially permitted by differing parasite burden and or localisation within each mouse.

Uninfected mice were also subject to each treatment (Fig. 2.5.4.4, overleaf). This was to assess whether the transit time changes observed in the infected cohorts could be explained as an intrinsic effect of the immuno-modulatory or chemotherapeutic treatments on normal gut physiology, even in the absence of *T. cruzi* infection.

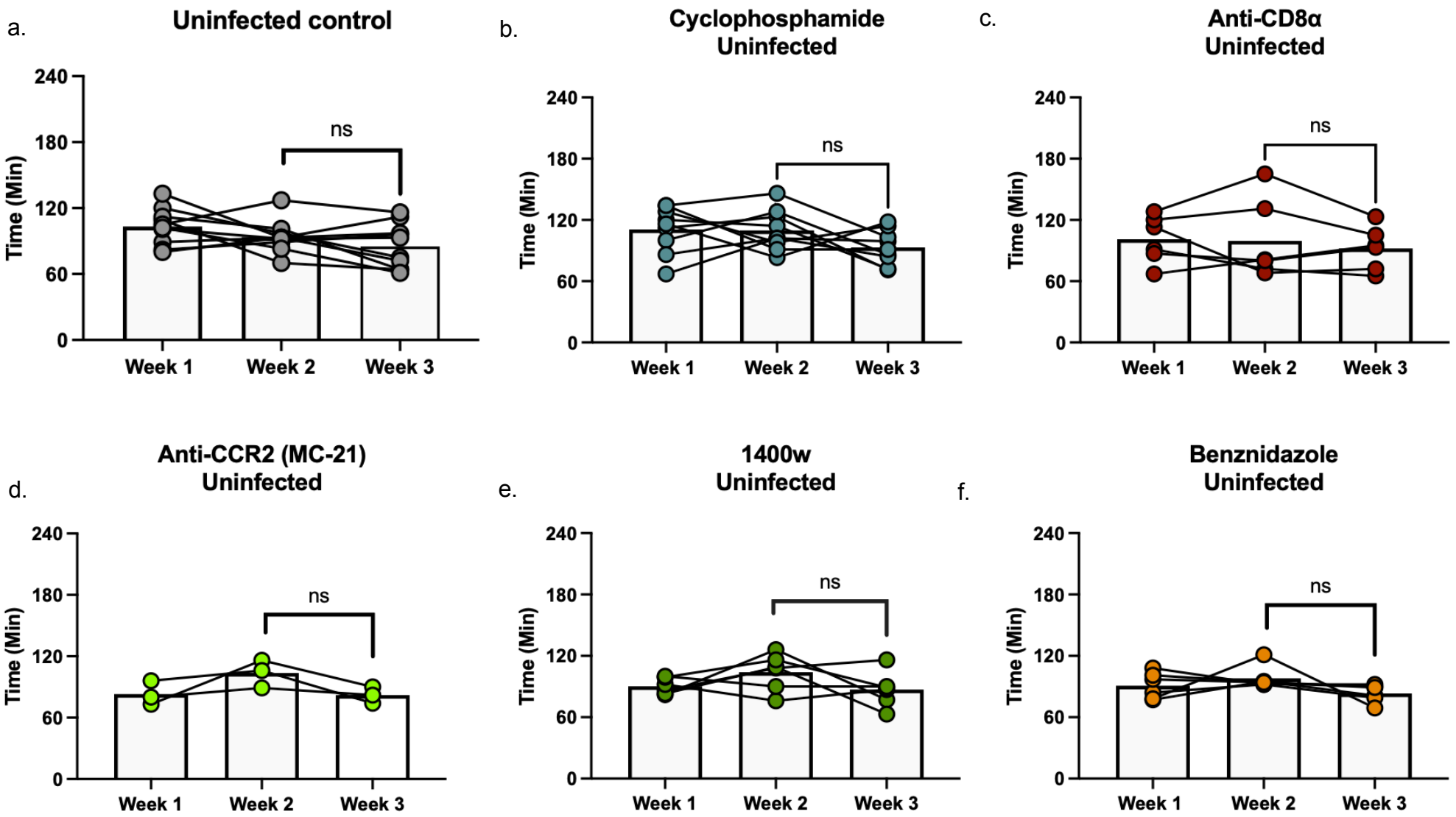

Figure 2.5.4. 4.Transit time data for uninfected C3H/HeN mice subject to each treatment.
All mice treated under the same conditions as corresponding infected cohorts. Bars are the mean average of each individual mouse, which are each represented by circular data points. Lines link serial data points of each individual mouse. Unpaired t-test conducted between week 2 and 3, with no significant difference noted in any of the treatment groups. a) *n* = 9, b) *n* =6, c) *n* =6, d) *n* =6, e) *n* = 3, f) *n* = 10.

The transit time data from the uninfected cohort shows that none of the treatments caused peristalsis-related side-effects such as diarrhoea, constipation or other abnormalities that would have complicated interpretation of data collected from the *T. cruzi*-infected cohorts. The average transit time post-treatment in each of the groups were all within 10 minutes of each other and did not exhibit the levels of inter-individual variability in response to each of the treatments that was seen in the infected cohort. Therefore, the effects observed for the treatments are *T. cruzi*-infection dependent.

To further validate the findings from the post-treatment transit time assay, the total number of faecal pellets in the large intestine during necropsy (after 2.5 hours fasting) were counted. Increased faecal retention has previously been shown to be a reliable indicator of digestive pathology that correlates with transit time delay (37). As well as counting pellets, the mesentery tissue and spleens were weighed during necropsy to corroborate infection status and disease severity post treatment.

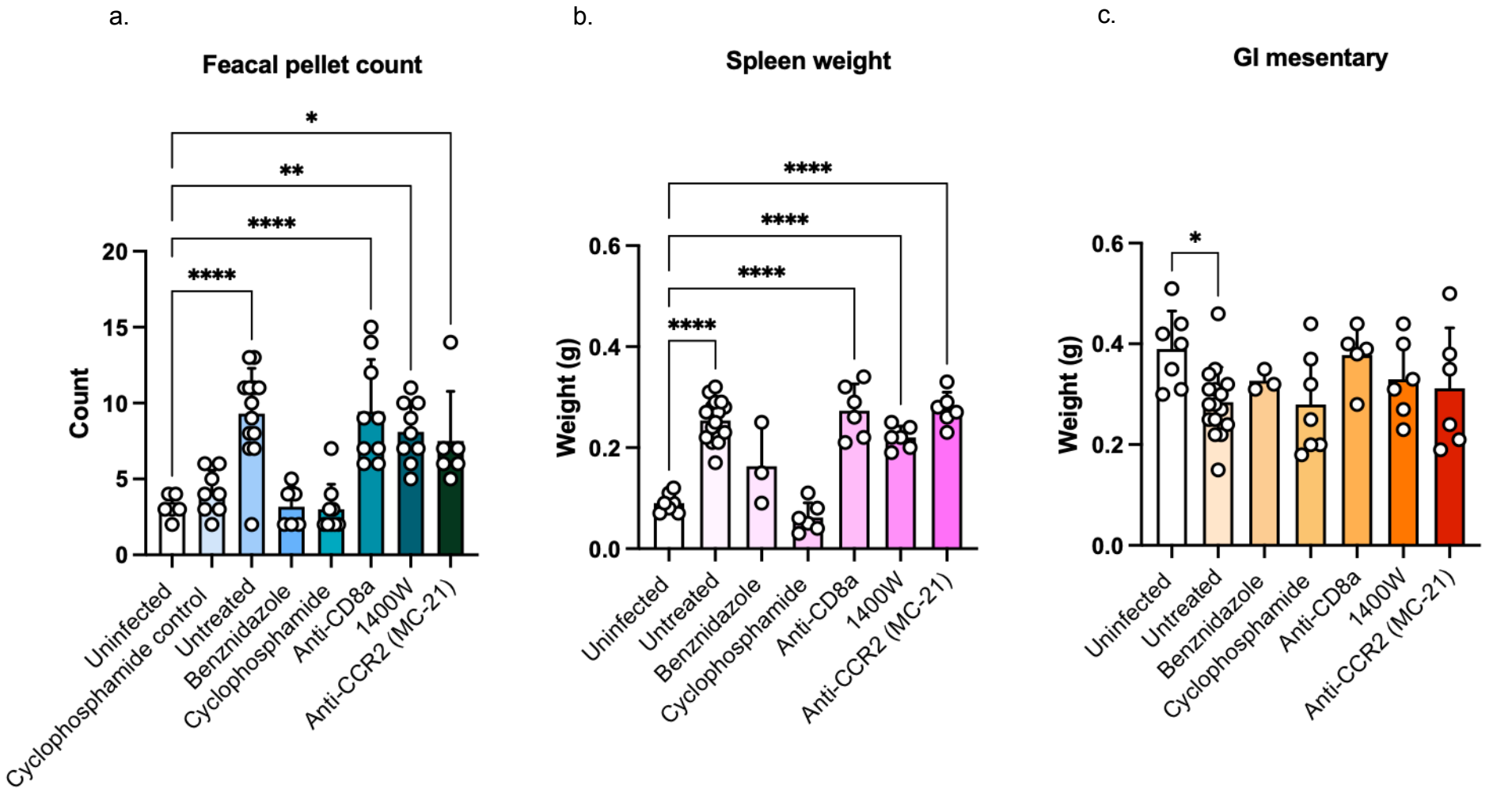

Figure 2.5.4.5 All necropsy assays conducted across each of the 3 experiments.
a) Graph depicting the total count of faecal pellets remaining in the large intestine at point of sacrifice. All mice were fasted for 2.5 hours prior to culling. One way ANOVA was conducted, all vs uninfected control conducted, with asterisks indicating a *p* value of <0.0001 between infected control and anti-CD8α against uninfected control. There was also a significant difference between 1400W and uninfected control, with a *p* value of 0.0015. Asterisk between MC-21 and uninfected control resembles a *p* value of 0.0154. b) The spleen weight of each mouse during necropsy, across 3 experiments. One way ANOVA was performed, with a strong significant difference noted between all groups except cyclophosphamide and benznidazole, against uninfected control. Asterisks represent *p* value of <0.0001 in each treatment group. c) Weight of mesentery adipose tissue from each mouse, removed from the intestines during necropsy. One way ANOVA was conducted, with only one significant difference observed between infected and uninfected control. Asterisk represents a *p* value of 0.0312.

High retention of faeces within the colon is, as with delayed transit time, a strong indicator of pathological gut dysfunction. The treated groups that exhibited a strong significant transit time delays (anti-CD8α and 1400W) each had significantly higher faecal pellet retention than the uninfected control, cyclophosphamide treated and benznidazole treated groups, indicating that the two assays broadly corroborated each other.

The size of the spleen was also an indicator of both active and past *T. cruzi* infection. It was evident that the spleen weight of each infected group, except for cyclophosphamide and benznidazole treated, was significantly greater than the uninfected control (Fig. 2.5.4.5b). Cyclophosphamide treatment had a direct effect on the size and proliferative activity of the spleen, consistent with the targeted depletion of leukocytes (see section 2.5.3). The intermediate weight of the spleen in benznidazole treatment (not significantly different from uninfected or untreated controls), despite successfully clearing parasites, is likely indicative of the recently cleared or strongly suppressed infection (see section 2.5.1).

The weight of the mesentery tissue between infected and uninfected was significantly decreased, which is consistent with increased parasite localisation from the *ex vivo* data and previous observations of atrophy of this tissue (37). All the treated groups except anti-CD8α followed a similar trend, though the loss of mesenteric tissue was not significant, perhaps due to smaller sample sizes than the untreated control group reducing the power to detect small differences. However, the similar mesentery weight to uninfected control in the anti-CD8α treated group despite the increased parasite burden (Fig. 2.5.4.5c) is an interesting finding.

2.5.5. Assessing the immunopathogenesis of the enteric nervous system.

In the DCD mouse model, the reduced ability to pass faeces is caused by enteric nervous system ablation, indicated by a loss of HuC/D+ (37) or ANNA-1+ neuronal cell bodies in the myenteric plexus (chapter 3), which disrupts regular peristaltic activity. It was important to identify whether the transit time phenotypes observed in this acute phase experiment were also associated with ENS damage, or if other treatment-specific mechanisms could have been driving the development of (or protection from) a transit time delay.

To assess ENS integrity, a triple immunofluorescence staining assay was performed (Fig. 2.5.5.1), comprising a range of targets chosen to provide an accurate account of enteric nervous system changes, to corroborate the gut dysfunction phenotype noted in each treatment group:

- ANNA-1 is a neuronal cell body specific marker; these are clustered inside the ganglia of the myenteric and submucosal plexuses.
- GFAP is a glial cell marker. Glial cells provide physical and biochemical support to neurons aiding in the maintenance of their environment.
- iNOS is a known effector of inflammation and apoptosis via nitric oxide.
- Nuclei were visualised using Hoechst 33342 to label DNA.

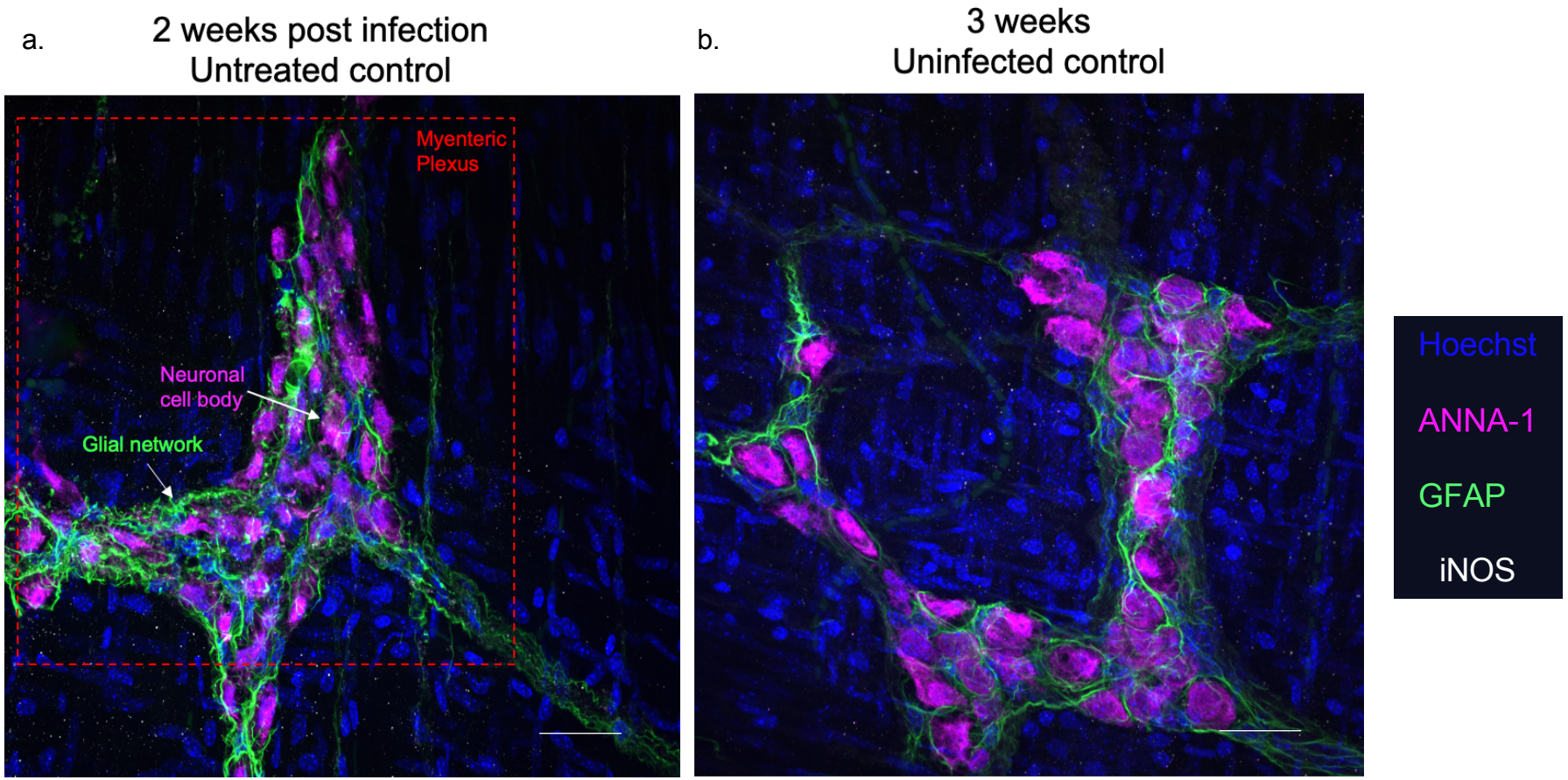

Figure 2.5.5.1 Representative images of a colon myenteric plexus ganglion for the primary comparative controls.
a) compressed Z-stack of a 2-week post infection, pre-treatment control. b) compressed Z-stack of an uninfected naïve control at 3 weeks. Each image composed of 10 slices each with 1.03 µm thickness, captured at 400x 400X magnification. Human anti-ANNA-1 primary antibody labelled with anti-human Alexa fluor647 Rat anti-GFAP primary antibody labelled with secondary anti-rat Alexa fluor488. Rabbit anti-iNOS primary antibody at 1:50 labelled with anti-rabbit Alexa fluor568. Cell nuclei stained with Hoechst 33342.
Scale bar 50µm.

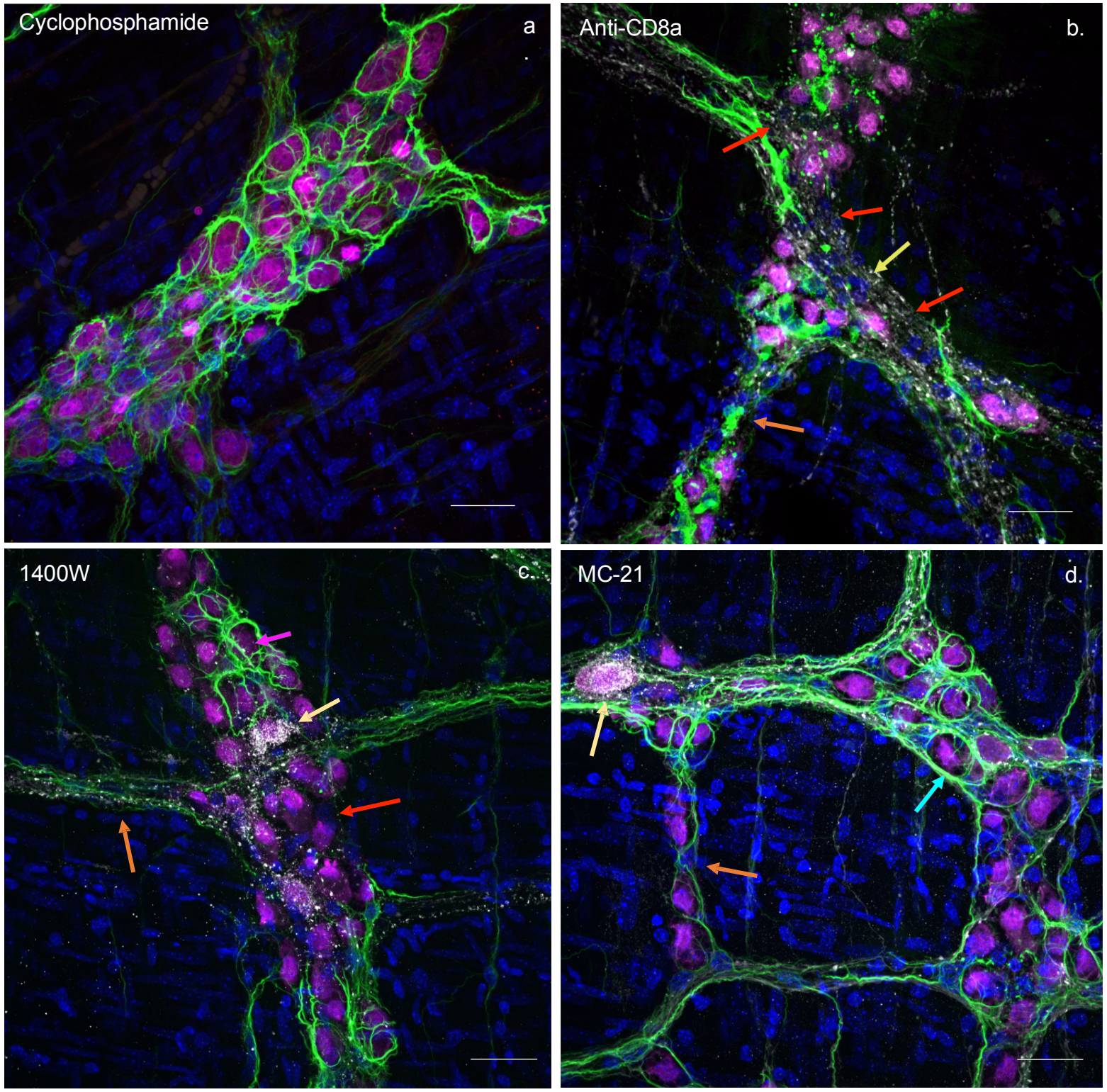
Cyclophosphamide
a
.
Anti-CD8a
b.
1400W
c.
MC-21
d.

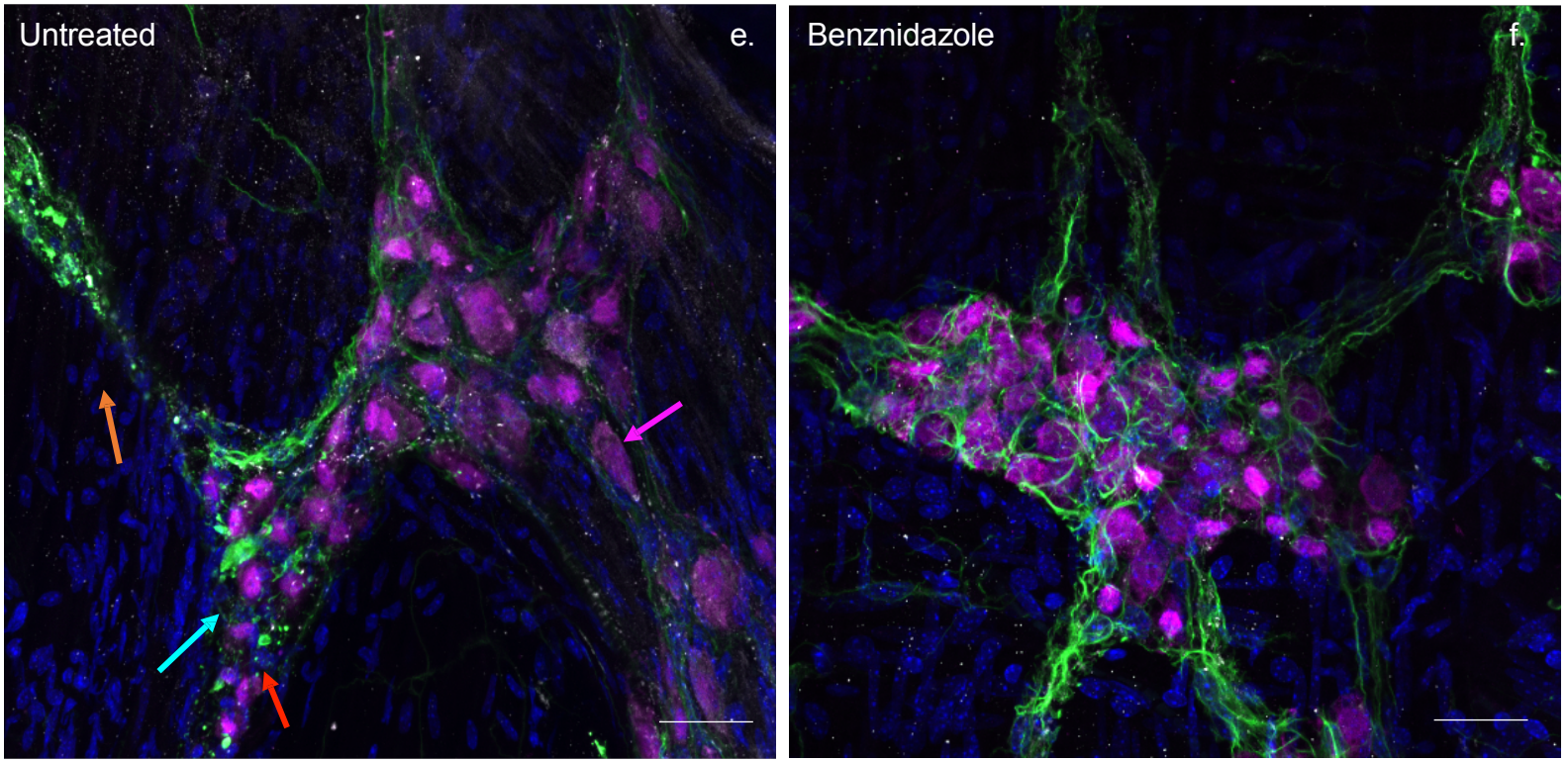

Figure 2.5.5.2 Representative images of the myenteric plexus each infected treated group, after a week of treatment.
Whole mount distal colon stained with anti- ANNA-1, anti-GFAP, anti-iNOS and cell nuclei stained with Hoechst 33342. a) Cyclophosphamide. b) anti-CD8a c) 1400W. d) MC-21. e) Untreated. f) Benznidazole. On each image, red arrows indicate an example of the absence of neuronal cell bodies and/ or ablation of normal plexus structures. Yellow arrows indicate an examples of iNOS positive staining in the vicinity of neuronal cell bodies. Orange arrows indicate an examples of thinning of glial cell network. Blue arrows indicate an example of the 'shrinking' of neuronal cell bodies. Pink arrows indicate an example of neuronal cell bodies without visible nucleus. Scale bar: 50μm.

The phenotype of delayed transit time was clearly associated with an ablation of, or damage to, components of the ENS. Conversely, the groups that exhibited an alleviation or prevention of gut dysfunction development exhibited little to no change to the integrity of the ENS. There was also visible iNOS expression in the regions of damaged neurons in some images. When present, iNOS expression was in some cases diffuse within the ganglionic structure, as depicted by white staining in b), the anti-CD8a treated group. In other cases, expression presented more focally, where iNOS co-localised with ANNA-1 neuronal cell bodies depicted by yellow arrows in the MC-21 and 1400W treated groups. Moreover, there may also be cross-reactivity with nNOS which is constitutively expressed in central and peripheral neurons (62).
It is important to note that the caveat that positive staining of iNOS protein expression does not necessarily infer ongoing enzymatic activity of iNOS and production of NO. Moreover, there was no evidence of parasite nests in the myenteric plexus, although identification of lone parasites was difficult as this was restricted to looking for parasite DNA (kDNA).

The cyclophosphamide treated group, in which transit delay did not develop despite increased parasitic burden, had a predominantly healthy ENS. There was only minor evidence of sporadic marring of neuronal cell bodies, high or ENS-localised iNOS expression, or loss of integrity to the glial cell network. I theorised that this damage was primarily parasite derived, suggesting direct parasite damage is not sufficient to cause a transit time delay at this timepoint. This damage could also be a result of residual cyclophosphamide resistant immune cells. Moreover, compared to the uninfected control, there was qualitatively more intense GFAP staining in the cyclophosphamide treated group. A potential explanation for this may be an upregulation of glial cells in

response to the additional parasite challenge provoked by cyclophosphamide immunosuppression, and enhanced requirement to aid in neuronal repair and support during and after treatment.

In Fig. 2.5.5.2b I observed a substantial and obvious damage to the ENS associated with anti-CD8a treatment-dependent disease exacerbation. There was evidence of widespread and near-complete neuronal cell body ablation within this region of the myenteric plexus, as shown by red arrows, and evidence of Hoechst (DNA)-negative cell bodies indicative of cell death. Within the ganglionic structure there was also evidence of diffuse iNOS expression with the highest levels presenting where no neuronal cell bodies remained (Fig. 2.5.5.3).

Anti-CD8α

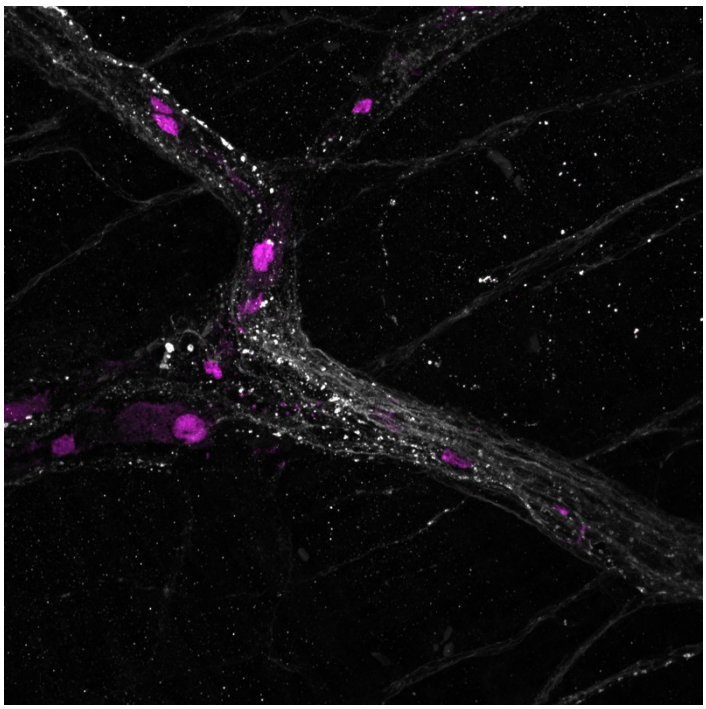

Figure.2.5.5.3. Representative image of high myenteric iNOS expression (white) in an acutely infected colon. Absence of ANNA-1 neuronal cell body staining (magenta). GFAP and Nuclei channels were omitted from the image. Magnification 400x

There was a high degree of variability of ENS presentation in the MC-21 treated group, consistent with the broad observed range of transit times. However, where

damage was noted, its complexion was similar to that of the 1400W treated group (Fig. 2.5.5.2 c&d). There was also evidence of neuronal cell body thinning, where there was a qualitative reduction in neuronal cell body size. There was also similar apparent glial cell network thinning and iNOS co-localising with ANNA-1 neuronal cell bodies. The complexion of the infected control (untreated) enteric nervous system and damaged structures was similar to that of the 1400W and MC-21 treated groups, but not as obvious as the anti-CD8a treated group (Fig. 2.5.5.2b). The key difference between the high pathology groups, at least qualitatively, was the frequency at which damaged ganglia were observed. As was the case with each treatment group, there were intact ganglia amongst the damaged, as has been previously reported for the standard DCD model, consistent with the focal nature of *T. cruzi* infection (37). From what was observed in each group, the anti-CD8a treated ENS exhibited the highest number of damaged ganglia compared to each group, with intact 'healthy' looking structures only sparsely observed in the myenteric plexus (Fig. 2.5.5.2b). This suggested that anti-CD8a treatment did not simply fail to prevent the development of a transit time delay but may have exacerbated and accelerated the development of pathology compared to the infected untreated controls. This may have been masked by the 4-hour maximum cut-off time used in the live transit time assay. Contrary to this hypothesis, it should be acknowledged that average faecal pellet counts were not significantly increased by anti-CD8a treatment, but this assay would also presumably have an upper limit.

The benznidazole treated group, as with the cyclophosphamide treated group, exhibited a largely healthy ENS with even rarer and negligible neuronal damage, compared to what was observed in the cyclophosphamide treated and uninfected control group.

2.6 Discussion

2.6.1. Summary of results

Experimental group	Parasite load	GI parasite load	iNOS+ cells	Transit time	ENS damage
Uninfected control	/	/	**2419.33** 1.2% CD45- 0.4% CD45+	97 min (baseline)	/
Untreated control	High	High	**11664.8** 2.7% CD45- 1.1% CD45+	208 min (Significantly delayed)	High
Benznidazole	Undetectable	Undetectable	**4042.67** 1.5% CD45- 0.35% CD45+	109 min (no delay)	Negligible
Cyclophosphamide	Significantly increased. (13-fold)	Significantly increased. (11-fold)	**7931.67** 2.6% CD45- 0.2% CD45+	117 min (no delay)	Very low
Anti-CD8 α	Significantly increased. (7.5- fold)	Significantly increased. (8-fold)	**15653** 4.9% CD45- 1.9% CD45+	216 min (Significantly delayed)	Very High
1400W	Non-Significantly increased. (0.33-fold)	No significant difference	No flow data	204 min (Significantly delayed)	High
Anti-CCR2 (MC-21)	Non-Significantly increased. (1.56-fold)	No significant difference	**22693.7** 6% CD45- 2% CD45+	165 min (non- significant increase)	Highly variable

Table.2.6.1. Summary of experimental results findings in study.
Parasite loads were determined by bioluminesence signal both *in vivo* and *ex vivo*. Total iNOS+ cells indicated in bold, with the percentage of leukocyte derived (CD45+) and non-leukocyte derived (CD45-) populations indicated below. Transit time is the average transit time of each group relative to baseline (uninfected control). The ENS damage was scored qualitatively by observing IFA images.

2.6.2 Immunosuppression and anti-parasitic treatment both normalise gut function.

DCD mice treated with cyclophosphamide presented with a 12-fold increase in parasite burden between weeks 2 and 3 on infection due to strong and broad-based suppression of the immune system. However, a transit time delay did not develop. This suggests that high parasite numbers in the GI tract are not sufficient to explain the development of acute gut neuropathy. This ruled out a direct parasite-driven pathology caused by, for example, infection of the enteric neurons or production of a neurotoxin by the parasite, as has been previously hypothesized (43). Benznidazole mice exhibited the same post-treatment transit time phenotype (i.e. normal peristalsis), but with a parasite burden reduced to undetectable levels. Therefore, a synergistic interaction between *T. cruzi* parasite persistence and immune action is key to the initiation of transit time delay in the DCD model in the acute phase. Since the GI tract is a ubiquitous parasitic reservoir in experimental Chagas disease, the interaction between host and parasite is ongoing which facilitates chronic inflammation and ongoing pathology development throughout the course of an infection. It is not far fetched therefore, to assume the interactions permitting development of ENS pathology in the acute phase are not exclusive mechanistic contributors to disease outcomes seen in the chronic stage. As a result of cyclophosphamide treatment, there was an 86% reduction of CD45+ cells across the group (Fig. 2.5.3.2). Although the sub-typing of the remaining 14% wasn't possible within the scope of this study, using the flow cytometry data it was possible to exclude γδ T cell and natural killer cells as prospective pathogenic effectors, since there was a 22% and a 23% in these populations respectively, compared to the untreated control, and there was no development of a transit time delay. However,

there was a significant increase in natural killer cells in the anti-CD8a treated group, which suggests that the same cell types may have different roles in response to different treatments. Natural killer cells are apparently cyclophosphamide resistant cells, but they may be dependent on other cyclophosphamide sensitive cell types for a pathogenic effector function. Although significantly increased in the anti-CD8a treated group when compared to the untreated control, there was no significant difference in natural killer cells when compared to the cyclophosphamide treated group (*p=0.0951*). This suggests that this cell type may have a contributary role, either directly or indirectly, in pathogenesis, but not an exclusive one.

The neuroprotective intervention of cyclophosphamide in digestive Chagas disease has in fact been described previously (63). Here, in the chronic stage of a large vesper mouse (*Calomys callosus*) infection model, cyclophosphamide prevented excessive neuronal loss in both the oesophagus and colon by means of reducing the proinflammatory response via nitric oxide and the proliferative capacity of splenocytes (63). It should be noted that this study lacked uninfected controls and did not analyse parasite loads or transit function. In addition to reduced neuron loss, a morphometric analysis of the neurons was conducted with enhancement of neuronal volume, area and perimeter noted. Upon comparing ‘young’ mice, there was no significant alterations in the number of neurons, but in the ‘old’ mice there was reduced neuronal loss in those treated with cyclophosphamide. However, this protection in the older animals may be independent of *T. cruzi* infection, since a degree of age-related nerve degeneration may be masked by cyclophosphamide by means of reducing ROS and RNS production, rendering the downstream effect of age-related reduction of antioxidant scavengers negligible (64).

One critical follow up question to my findings is which specific immune effectors are being depleted by cyclophosphamide, preventing the development of immune mediated enteric neuropathy and dysperistalsis? Cyclophosphamide treatment casts a wide net, especially when high doses are used as near-complete eradication of hematopoietic multipotent stem cells, which can differentiate into both myeloid and lymphoid lineages, can be achieved. 200 mg kg^{-1}, the dose used in this study, has shown to reduce splenic T-cell populations (CD4+, CD8+, CD4-CD25+, CD4+CD25+) by >90% in C3H/HeN mice, with the peak decrease occurring on day 4 (65). When the dose is reduced to 20 mg kg^{-1} the population of CD4+ and CD8+ T cells reduce by ~50%, but CD4+CD25+ T_{reg} cells are reduced by ~85% and recover slowly compared to CD4+, resulting in a low ratio of CD4+CD25+ T cells to CD4+ T cells throughout the course of treatment (65). This highlights that certain immune cells are more sensitive to cyclophosphamide, and adjustable doses can be used for selective suppression of CD4+CD25+. Cyclophosphamide treatment also works differently for different mouse strains. One study showed a 200 mg kg^{-1} dose on two inbred strains (DBA/2J, BALB/cByJ) presented with differing outcomes on neutrophil depletion (66). This suggests that mouse and dose combinations could be adjusted and further optimised for targeted depletion of cell subtypes. In the context of this study, this could be used to help identify the CD45+ iNOS expressing cells that are significantly increased in the anti-CD8a and anti-CCR2 (MC-21) treated cohorts. The primary leukocytic candidates for iNOS expression are monocytes/macrophages, T cells and dendritic cells (67). With the results presented so far, CCR2+ monocyte lineages and CD8+ T cells were targeted for depletion, which resulted in a high degree of variability in transit time in the former, and a consistent delay in the latter. An explanation for the phenotypic variability within the anti-CCR2 treatment group

could be that the treatment had an inconsistent effect across the group. This could be due to varying parasite infection foci between each mouse, resulting in CCR2+ trafficking to inflamed tissues not consistently observed across the group. However, the transit time in MC-21 treated group was not significantly increased post treatment, and the average (165 mins) is between the untreated control (208 mins) and the cyclophosphamide treated group (117 mins) (Fig. 2.5.4.3). This suggests that monocyte depletion can potentially account for half the overall effect of cyclophosphamide.

There is scope to investigate the anti-CCR2 treatment effects further, but also to investigate other specific cell subtypes, such as dendritic cells as individual contributors to pathology by NO dependant or independent mechanisms. In cancer therapy, cyclophosphamide influences dendritic cell homeostasis and promotes IFN type 1 secretion (68) Moreover, skin derived migratory dendritic cells and plasmacytoid dendritic cells in the lymph nodes and spleen have lower sensitivity against cyclophosphamide (69) than the previously mentioned T_{reg} cells, which are sensitive to very low doses. This provides scope for targeted depletion of T_{reg} activity which would prevent T_{reg} lymphocyte-activation gene 3 (LAG3) binding to MHC class II molecule inhibition of dendritic cell maturation and function, theoretically increasing dendritic cell populations (70). Since T_{reg} also regulate other T cells, including CD8+ T cells, the downstream effect of T_{reg} targeting could be an increase of cytotoxic effectors which, as per the results of CD8+ depletion in this study, we know are not direct contributors to GI pathology. This dose modulation of cyclophosphamide would allow dendritic cells to be evaluated as pathology contributors, and cement CD8+ T cells as non-pathogenic contributors of parasite control.

Another prospective candidate for pathological effectors, which have not been singularly targeted for depletion in this study, would be mast cells. Mast cells have a large variety of receptors and respond to an array of stimuli including microbial, immune, and neural (71). Interestingly, NO is responsible for a potent regulatory role for mast cell degranulation and is protective in the allergy model (72). Here, inhibition of NOS2 increased allergen-induced histamine release *in vivo* resulting in exacerbated cardiac anaphylaxis presumably through the unregulated mast cell activity (73). Mast cells express receptors for neurotransmitters (Acetylcholine and serotonin) and neuropeptides (substance P and VIP) and nitric oxide (71). In the intestinal mucosa, mast cells contribute to local homeostasis by promoting water and ion secretion, stimulation of innate and adaptive responses, wound healing, and peristalsis (74). Moreover, increased numbers and activation of mast cells, has been observed in the intestine of patients with inflammation associated intestinal diseases and, interestingly, functional gastrointestinal disorders (71) which makes them a viable candidate in the scope of experimental DCD as an iNOS independent mechanism of pathogenesis.

During imaging of the ENS of each experimental group, it was qualitatively observed that the cyclophosphamide treated group exhibited higher levels of GFAP (glial cell marker) expression compared to other treatment groups (Fig. 4.6.2, also compare 4.5.1a with 4.5.2a).

Cyclophosphamide

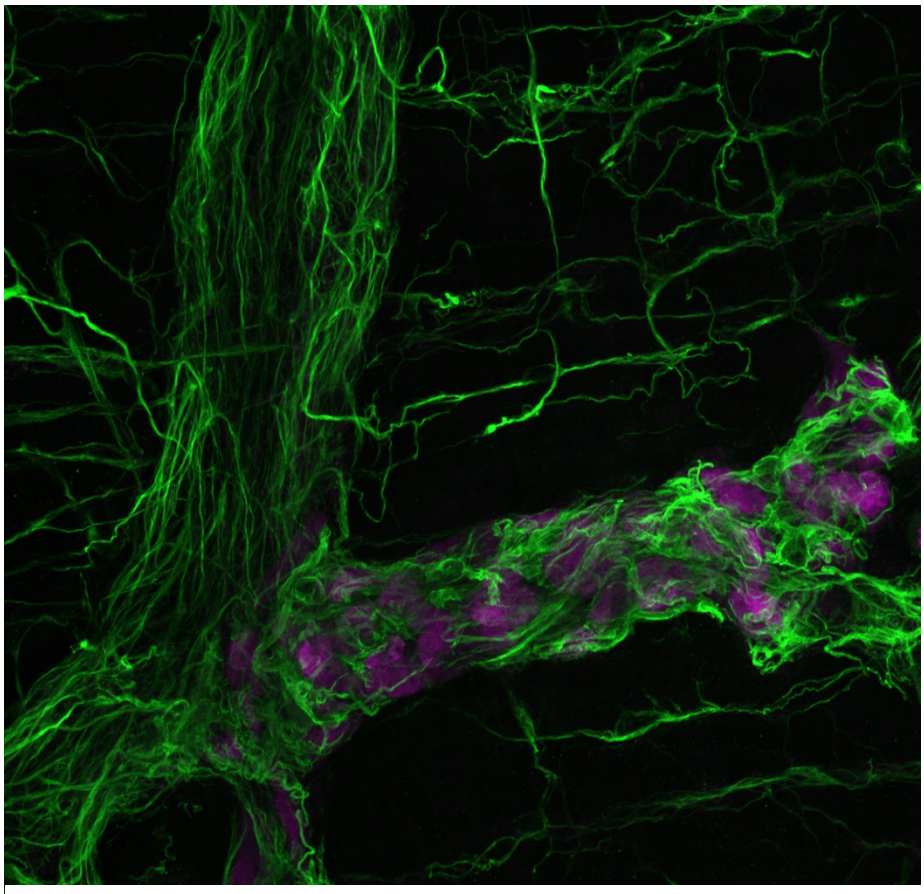

Figure.4.6.2 Representative image of cyclophosphamide treated "DCD" mouse myenteric plexus, 3 weeks post infection, with high GFAP expression.
GFAP in green and neuronal cell bodies in magenta

The GFAP staining was both myenteric and intramuscular and was qualitatively observed to be densely expressed within the ganglionic space, particularly around ANNA-1 neuronal cell bodies with long uninterrupted, bundled projections seen extending outwards (Fig. 4.6.2). Cyclophosphamide treated mice had a consistently low transit time with a negligible amount of variation. This was unusual compared to other treatment groups, except for benznidazole, that showcased greater heterogeneity in the post-treatment transit time.

This potentially suggests that cyclophosphamide treatment created a consistent, suitable, and unique microenvironment that permitted a repair mechanism, possibly involving gliogenesis, to support or protect enteric neurons against the significantly increased parasite burden in the absence of an active immune system. Enteric glia have pleotropic roles, and are essential for virtually all ENS mediated gastrointestinal functions (75). The importance of enteric glia is highlighted in gastrointestinal diseases that are a result of altered glia such as ulcerative colitis, Parkinson's disease, Crohn's disease and infectious enteritis (76). The neuroprotective aspects of enteric glial cells are highlighted by the phenotype of mice with experimental ablation of GFAP+ cells using the HSV thymidine kinase – ganciclovir system (77). This resulted in enteric neuron loss, impaired intestinal motility, altered epithelial barrier cell barrier, and severe inflammation (77). Gliogenesis, the generation of glial population form multipotent neural stem cells (75), could explain the observed increase in GFAP expression which goes unregulated without immune-mediated damage in response to parasite presence. It has been previously noted that the rate of gliogenesis in the myenteric plexus of adult mice is low under steady state conditions, with 2-3% of myenteric glia proliferating during a 12-week period in adult mice (78). The rate of gliogenesis increases in response to injury and inflammation with a common progenitor as mucosal glia (79). In addition to stem cell derived gliogenesis, GFAP upregulation is seen in reactive astrogliosis which occurs in response to inflammation and is characteristic of glial scar formation in the central nervous system (80,81). While there is little work exploring glial scars in an enteric context, the molecular and functional similarities between astrocytes in the CNS and enteric glia suggest that a similar process may be occurring in this region in response to parasite prevalence,

inflammation and microenvironment because of immune-regulatory treatments (80,81).

2.6.3 CD8+ T cells: critical for parasite control but not DCD pathology.

The depletion of CD8+ T cells and the subsequent lack of impact on the development of dysperistalsis suggests there is no direct role for cytotoxic T cells in promoting gut pathology development. The anti-CD8a treated mice had a similar parasite burden to that of the cyclophosphamide treated group (Fig. 2.5.1.3), but presented with the steepest increase of transit time, post treatment, of any group (Fig. 2.5.4.2). This suggested that anti-CD8a treatment did not simply fail to prevent the development of a transit time delay but may have exacerbated and accelerated the development of pathology compared to the infected untreated controls. This may have been masked by the 4-hour maximum cut-off time used in the live transit time assay. Contrary to this hypothesis, it should be acknowledged that average faecal pellet counts were not significantly increased by anti-CD8a treatment. The lack of a role for CD8+ T cells on pathology development is likely due to the highly regulated specificity of cytotoxic activity, ensured by its restriction to infected cells presenting *T. cruzi* antigen in the context of MHC-I molecules, and the consequently limited scope for 'collateral' damage to host tissue (82). Cytotoxic T cells possess cytotoxins such as perforin and granzymes, synthesised *de novo,* which contribute to targeted cell death. Cytotoxic T cells orient their Golgi apparatus and microtubules to focus the point of secretion on the point of contact with a target cell. If the T cell is attached to multiple targets, the organelles are re-orientated to ensure target destruction of one target at a time (82).This suggests that the only direct contributory role CD8+ T-cells could have on gut dysfunction development is the targeted destruction of parasitised neurons.

It has been demonstrated that enteric neurons can be parasitized in mice (83). However, the frequency at which this tropism was identified was rare which further suggests the contribution of CD8+ T cells toward enteric neuropathy is negligible. The prominent parasitized cell type were myocytes in the circular muscle layer, suggesting the cytotoxic effects of CD8+ T cells could potentially contribute to more generalised tissue damage (83). Overall, the data suggest that in untreated infected mice, CD8+ T cells are not causing neurotoxicity and in fact may have an indirect role in limiting the severity of gut pathology via suppression of parasite numbers, mainly in smooth muscle cells.

Interestingly, anti-CD8a treated mice had an average GI mesentery weight similar to that of the uninfected control mice (Fig. 2.5.4.5), despite exhibiting increased parasite loads (Fig. 2.5.2.1). This suggests that CD8+ T cells could be driving mesentery tissue atrophy, presumably linked to their role as the primary effector cell type targeting parasites in this region. In an obesity study it was found that both CD4+ and CD8+ T cells infiltrate the adipose tissue leading to M1 macrophage accumulation and an increase of CXCR3 expression on CD8+ T cells (84). In the context of adipose inflammation, it was suggested that the cross talk between CD8+ T cells, CD4+ and adipocytes facilitate and maintain inflammation in the adipose tissue microenvironment (84). Moreover, adipocytes can serve as antigen presenting cells to regulate the T cell mediated immune response by secreting adipokines such as leptin, IL-6 and TNF-α that regulate local inflammation and differentiation of T cells (85). In normal conditions, there is a high *T. cruzi* burden observed in the GI mesentery during the acute phase and, sometimes, in the chronic stage, although the precise cell types that are parasitized in this tissue have not been established. Overall, it can be concluded that local cytotoxic interactions

could result in the characteristic atrophy of adipose, in combination with parasite egress. The different effects of CD8 T cell depletion on the ENS and mesentery suggests that their contribution to different aspects of *T. cruzi* infection pathogenesis is likely to be tissue-context dependent.

2.6.4. The role of iNOS and CCR2+ monocytes in the development of dysperistalsis is uncertain.

As covered in the introduction, the leading theory for enteric denervation in DCD is IFNγ-driven iNOS production in the setting of an acute lethal *T. cruzi* infection (41). Certain caveats exist in that study, including the use of Tc-I *Y* strain which is considered highly virulent (86). Moreover, the scope of the study was limited to the acute phase since iNOS$^{-/-}$ mice exhibited a 100% mortality rate within 3 weeks of infection. Based on the results of the current study, the significance and exclusivity of iNOS activity on the development of gut dysfunction is, however, uncertain for a number of reasons: the 1400W treated mice still developed a significant transit time delay; there was an increase in colonic smooth muscle iNOS expression in the BALB/c model which does not exhibit a severe transit time delay (chapter 1); high throughput RNA nanostring data of the colon did not note a large *Nos2* upregulation in the high morbidity DCD model, but also an increase in the low morbidity model (chapter 1); and cyclophosphamide treated mice in this study had the same percentage population of CD45-iNOS+ cells, than the uninfected control, yet no development of pathology. The large intestine is a major reservoir for parasite persistence in the chronic phase of disease (87), and enteric neuropathy, by

measure of HuC/D-based neuron counts, worsens between week 6 post infection and week 36 (Archie Khan, unpublished). Therefore, chronic persistence and the subsequent ongoing host-parasite interactions continue to contribute to the gradual develop of pathology over time. Moreover, the specific inhibition of iNOS activity in the 1400W treated group had a negligible effect on the development of gut dysfunction, suggesting iNOS activity is not exclusively responsible for severe pathological outcomes in the acute phase.

Inflammatory monocytes may be contributing to pathology through iNOS independent pathways. In chapter 1 I showed a significant increase of smooth muscle inflammation in the acute and chronic stage disease (Fig. 2). It has been shown that monocytes contribute to cardiac pathology in Chagas disease patients, with symptomatic patients exhibiting an increased percentage of inflammatory monocytes and IL-6 cytokine levels - a biomarker for severe cardiac outcomes (88). In colonic disease of *Toxoplasa gondii*, CCR2+ monocytes play a critical role in gut inflammation where they are the dominant immune cell type populating the large intestine and, upon depletion, prevented the development of GI pathology (89). Here, the anti-CCR2 (MC-21) treated group exhibited the highest population of iNOS+ cells of any treatment group, and although there was high inter-individual variability, on average there was evidence of protection from DCD symptoms. This heterogeneity suggests that gut-infiltrating CCR2+ monocytes might contribute to the development of a transit delay, but are unlikely to be essential by themselves. Anti- CCR2 treated mice also had variable *in vivo* bioluminescence and ENS structure, suggesting that the caution should be applied to interpretation of this phenotype.

However, it would be premature to assume iNOS and NO have a negligible role in pathology as it has long been identified as a contributor for neuronal damage in diseases associated with inflammation including, peripheral nerve damage associated with diabetes (90), degeneration of dopaminergic neurons in Parkinson's disease (91), demyelination of nerves in multiple sclerosis (92), and Alzheimer's disease (93) and there is likely a role in Chagas disease, but not in the capacity currently identified. I theorise that iNOS expression does contribute to pathology, but not exclusively. The high CD45- iNOS expression in the MC-21 treated group could be a compensatory mechanism for depletion of leukocytic expressors. From the IFA images, the expression pattern of iNOS is suggestive of being glial cell derived and is therefore the primary candidate for non-leukocytic section of NO. This could correlate with a high local parasite burden in the acute phase, but not for chronic enteric neuropathy where neuronal damage does not quantitatively correlate with end-point parasite loads (37), likely reflecting the more focal and fluctuating infection dynamics. In a murine colitis study, upregulation of glial NO correlates with the peak of chemically induced colonic inflammation (94). NO concentration was measured by immunoreactivity for nitrated proteins, which primarily colocalized with GFAP immunoreactivity within the myenteric plexus (94). Moreover, NO production and protein nitrification coincided with neuron death, highlighting how glial cell produced NO production can dictate pathological outcomes in an inflammatory model. An important aspect to note was that concentrations of glial cell-derived NO was only significantly increased compared to naïve mice at the peak of inflammation (94). In the context of this chapter, this may imply that the neuro-immune axis and communication through cytokinetic pathways is important to trigger glial cell secreted NO. This could explain why glial NO was not sufficient to cause neuronal damage in

the cyclophosphamide treated group, despite the observed increase in GFAP immunoreactivity and parasite burden. The alternative theory could be that both leukocytic and non-leukocytic iNOS expression is required for pathological levels of NO to be produced.

In the context of this study, non-leukocytic sources of iNOS were more frequent than CD45+ sources. In addition to glial cell produced iNOS other sources could be vascular smooth muscle cells (95), smooth muscle cells (96) and epithelial cells in the gut (97). A more focussed investigation into of immune-regulatory treatments, namely 1400W, treatments on non-leukocytic iNOS production would be a suitable addition upon repeating this experiment.

2.6.5. Experimental caveats and future directions

Several experimental dosing caveats were recognised. Prior to the study, I was unsure of dosing concentration, route of treatment and the administration frequency of the iNOS inhibitor 1400W. Published concentrations of *in vivo* 1400W ranged from 5-10 mg kg^{-1} with dosing regimens that varyied from every 6 hours to every 24 hours, with one study even employing the use of an ALZET mini-osmotic pump surgically implanted under the skin of mice, which released low dose 1400W every hour (98–103). 1400W has a proposed half-life of 6 hours (104), and with our dosing schedule of once every 24 hours it is likely we were observing experimental outcomes (imaging, transit time, IFA) within waves of inhibited and regained iNOS activity. I conducted Griess assays (nitrite detection assay) on pure splenocytes, splenoctyes spiked with *T. cruzi* lysate, and on blood plasma from 1400W treated mice, and each assay was inconclusive. This means it remains unclear whether

1400W was actually achieving any meaningful inhibition of iNOS activity in our system.

Therefore, there is scope for refinement and optimisation of the 1400W dosing protocol, since other iNOS inhibition methods are not suitable for the question being addressed. Other prospective chemical inhibitors such as L-NAME are not suitable due to the broad acting inhibition of nitric oxide progenitors, including iNOS, nNOS, eNOS and NOS (101). Moreover, transgenic mice would not be suitable because the study is investigating the inhibition of iNOS within a specific timeframe. Transgenic mice in which iNOS gene deletion is inducible, or manipulation of the availability of the iNOS substrate L-arginine could be explored in future.

There were also caveats for the anti-CCR2 (MC-21) dosing regimen. Using MC-21, monocytes could only be depleted for a maximum of 5 days by daily injection and the clearance of monocytes occurs within 3 hours of the first dose. MC-21 neutralising antibodies are generated 5 days after the initial dose rendering the treatment ineffective, which posed a limiting step of using MC-21 in this study. The identified transit delay development window was at least 7 days and delaying by or ending treatment by 48 hours could result in the incomplete depletion of monocytes. i.e: monocyte dependent pathology might be established between day 19 and day 21 post-infection when anti-MC-21 antibodies are generated, giving rise to the intermediate transit time phenotype observed. The treatment schedule was to end treatment 48 hours prior to sacrifice, so it may be that protection from monocyte derived tissue damage wore off around day 19-20 post-infection. The difference in

measured monocyte frequencies for day 15 (fresh blood film Giemsa) vs day 21 (flow cytometry) is consistent with this interpretation.

Several studies utilising this MC-21 regime have confirmed CCR2 monocyte depletion (32,51,105) including in the GI tract in a chronic toxoplasmosis study (106). Nevertheless, most *in vivo* studies have been with hamsters, BALB/c or C57BL6/J mice, not C3H/HeN, so it is not known if the depletion efficacy varies in the DCD model. Due to the results of the MC-21 treated group (variable transit time, pellet counts) a robust follow up would be to use CCR2 null transgenic mice.

There were distinct complications with generation of flow cytometry data. The LSRII Flow Cytometer available at LSHTM was out of service during the time of the second experiment, so samples could not be run fresh. Fixed samples were eventually taken to the University of York where certain compensation controls and FMO controls were not viable, and so data for certain markers across most groups were not reliably collected. In addition, the flow cytometer laser configuration differed substantially from the LSHTM instrument. Ultimately, all data collected from the second experiment were not pooled with the first. The statistical power was therefore low for these treatment groups and the observed trends would need to be confirmed with more analysis. There were some unexpected results, such as uninfected groups exhibiting higher leukocyte counts than the infected in some cases. This could be a result of increased difficulty to dissociate immune cells from the infected colons, perhaps due to upregulation of integrins resulting in stronger binding to ECM. Moreover, the infected tissue was more ‘fragile’ than uninfected, so during necropsy and processing for flow cytometry it may have been more difficult to keep the cells

alive/viable. When repeated, increased protocol optimisation could ensure increased cell count/viability.

For future directions:

- It would be beneficial to adjust the transit time experimental cut off. It is likely that the severity of transit delay in groups has been masked by the 240-minute cut off. It has been anecdotally observed that red faecal pellets from some mice reaching this cut off have been observed in the large intestine during necropsy the following day. By extending the cut off it would be possible to assess whether the transit delay phenotype is exacerbated in response to treatments, as opposed to being limited to suggesting there's no change in pathology development vs infected control. However, additional protocol refinements would be required to address animal welfare concerns associated with isolating mice in individual observation containers for > 4 hours.
- To follow up the qualitative evaluation of ENS damage, a full neuronal cell body quantification using anti-ANNA-1 or HuC/D would be beneficial in quantifying the extent of enteric neuropathy to compare between each treatment group. This was only outside the scope of this project due to time limitations.
- It would be beneficial to selectively target exclusively gut resident populations of immune cells to assess the effect on the immune-neuronal axis on the development of transit delay, without the caveat that treatments also impact host-parasite interactions in other organs.

- If the DCD phenotype could be identified in a C57BL/6 mouse, the potential of creating transgenic mice to assess the effect of knock down, or upregulation of, specific immune or neuronal markers on peristaltic function could be considered. This could include iNOS$^{-/-}$ and the effect on gut function, B6.129S4-*Ccr2*^{tm1Ifc}/J which are defective in monocyte recruitment during infectious challenge, B6;129S- *Gfap*^{tm1Mes}/J or B6.129X1-*Nfe2l2*^{tm1Ywk}/J which are defective in regulating oxidate stress. This approach would also introduce the potential to design therapeutics to alleviate innate transit delay in these mice.

2.7. References

1. Rao M, Gershon MD. The bowel and beyond: the enteric nervous system in neurological disorders. Nat Rev Gastroenterol Hepatol. 2016 Sep 20;13(9):517–28.
2. Ahrends T, Aydin B, Matheis F, Classon CH, Marchildon F, Furtado GC, et al. Enteric pathogens induce tissue tolerance and prevent neuronal loss from subsequent infections. Cell. 2021 Nov;184(23):5715-5727.e12.
3. Muller PA, Koscsó B, Rajani GM, Stevanovic K, Berres ML, Hashimoto D, et al. Crosstalk between Muscularis Macrophages and Enteric Neurons Regulates Gastrointestinal Motility. Cell. 2014 Aug 28;158(5):1210.
4. Gabanyi I, Muller PA, Feighery L, Oliveira TY, Costa-Pinto FA, Mucida D. Neuro-immune Interactions Drive Tissue Programming in Intestinal Macrophages. Cell. 2016 Jan 28;164(3):378–91.
5. De Schepper S, Verheijden S, Aguilera-Lizarraga J, Viola MF, Boesmans W, Stakenborg N, et al. Self-Maintaining Gut Macrophages Are Essential for Intestinal Homeostasis. Cell. 2018 Oct 4;175(2):400-415.e13.
6. Matheis F, Muller PA, Graves CL, Gabanyi I, Kerner ZJ, Costa-Borges D, et al. Adrenergic Signaling in Muscularis Macrophages Limits Infection-Induced Neuronal Loss. Cell. 2020 Jan 9;180(1):64-78.e16.
7. Jacobson A, Yang D, Vella M, Chiu IM. The intestinal neuro-immune axis: crosstalk between neurons, immune cells, and microbes. Mucosal Immunol. 2021 May;14(3):555–65.
8. Wang L, Zhu L, Qin S. Gut Microbiota Modulation on Intestinal Mucosal Adaptive Immunity. J Immunol Res. 2019;2019:4735040.
9. Rosas-Ballina M, Olofsson PS, Ochani M, Valdés-Ferrer SI, Levine YA, Reardon C, et al. Acetylcholine-synthesizing T cells relay neural signals in a vagus nerve circuit. Science. 2011 Oct 7;334(6052):98–101.
10. Darby M, Schnoeller C, Vira A, Culley FJ, Bobat S, Logan E, et al. The M3 muscarinic receptor is required for optimal adaptive immunity to helminth and bacterial infection. PLoS Pathog. 2015 Jan;11(1):e1004636.
11. White JP, Xiong S, Malvin NP, Khoury-Hanold W, Heuckeroth RO, Stappenbeck TS, et al. Intestinal Dysmotility Syndromes following Systemic Infection by Flaviviruses. Cell. 2018 Nov 15;175(5):1198-1212.e12.
12. van Diest SA, Stanisor OI, Boeckxstaens GE, de Jonge WJ, van den Wijngaard RM. Relevance of mast cell-nerve interactions in intestinal nociception. Biochim Biophys Acta. 2012 Jan;1822(1):74–84.
13. Sanchez-Ruiz M, Iorgu AM, Küster F, Hellmich M, Brunn A, Deckert M. CD8 T cell–Derived Perforin and TNF-α Are Crucial Mediators of Neuronal Destruction in Experimental Autoimmune Enteric Ganglionitis. Am J Pathol. 2021 Jun;191(6):1064–76.
14. Hoffman W, Lakkis FG, Chalasani G. B Cells, Antibodies, and More. Clin J Am Soc Nephrol. 2016 Jan 7;11(1):137–54.
15. Zhang X, Lei B, Yuan Y, Zhang L, Hu L, Jin S, et al. Brain control of humoral immune responses amenable to behavioural modulation. Nature. 2020 May;581(7807):204–8.
16. Kohm AP, Sanders VM. Suppression of antigen-specific Th2 cell-dependent IgM and IgG1 production following norepinephrine depletion in vivo. J Immunol. 1999 May 1;162(9):5299–308.

17. Spear ET, Holt EA, Joyce EJ, Haag MM, Mawe SM, Hennig GW, et al. Altered gastrointestinal motility involving autoantibodies in the experimental autoimmune encephalomyelitis model of multiple sclerosis. Neurogastroenterology and motility. 2018 Sep;30(9):e13349.
18. DiSabato DJ, Quan N, Godbout JP. Neuroinflammation: the devil is in the details. J Neurochem. 2016 Oct;139 Suppl 2(Suppl 2):136–53.
19. Sušjan-Leite P, Ramuta TŽ, Boršić E, Orehek S, Hafner-Bratkovič I. Supramolecular organizing centers at the interface of inflammation and neurodegeneration. Front Immunol. 2022 Aug 1;13.
20. Thundyil J, Lim KL. DAMPs and neurodegeneration. Ageing Res Rev. 2015 Nov;24:17–28.
21. Kagan JC, Magupalli VG, Wu H. SMOCs: supramolecular organizing centres that control innate immunity. Nat Rev Immunol. 2014 Dec 31;14(12):821–6.
22. Martinon F, Burns K, Tschopp J. The Inflammasome. Mol Cell. 2002 Aug;10(2):417–26.
23. Ye L, Huang Y, Zhao L, Li Y, Sun L, Zhou Y, et al. IL-1β and TNF-α induce neurotoxicity through glutamate production: a potential role for neuronal glutaminase. J Neurochem. 2013 Jun;125(6):897–908.
24. Kessing CF, Tyor WR. Interferon-α Induces Neurotoxicity Through Activation of the Type I Receptor and the GluN2A Subunit of the NMDA Receptor. Journal of Interferon & Cytokine Research. 2015 Apr;35(4):317–24.
25. Tewari D, Sah AN, Bawari S, Nabavi SF, Dehpour AR, Shirooie S, et al. Role of Nitric Oxide in Neurodegeneration: Function, Regulation, and Inhibition. Curr Neuropharmacol. 2020 Dec 31;19(2):114–26.
26. Picón-Pagès P, Garcia-Buendia J, Muñoz FJ. Functions and dysfunctions of nitric oxide in brain. Biochim Biophys Acta Mol Basis Dis. 2019 Aug 1;1865(8):1949–67.
27. Bal-Price A, Brown GC. Inflammatory Neurodegeneration Mediated by Nitric Oxide from Activated Glia-Inhibiting Neuronal Respiration, Causing Glutamate Release and Excitotoxicity. The Journal of Neuroscience. 2001 Sep 1;21(17):6480–91.
28. Seifert L, Miller G. Molecular Pathways: The Necrosome-A Target for Cancer Therapy. Clin Cancer Res. 2017 Mar 1;23(5):1132–6.
29. Khoury MK, Gupta K, Franco SR, Liu B. Necroptosis in the Pathophysiology of Disease. Am J Pathol. 2020 Feb;190(2):272–85.
30. Vernet-der Garabedian B, Derer P, Bailly Y, Mariani J. Innate immunity in the Grid2Lc/+ mouse model of cerebellar neurodegeneration: glial CD95/CD95L plays a non-apoptotic role in persistent neuron loss-associated inflammatory reactions in the cerebellum. J Neuroinflammation. 2013 May 15;10:65.
31. Ferrari CC, Depino AM, Prada F, Muraro N, Campbell S, Podhajcer O, et al. Reversible Demyelination, Blood-Brain Barrier Breakdown, and Pronounced Neutrophil Recruitment Induced by Chronic IL-1 Expression in the Brain. Am J Pathol. 2004 Nov;165(5):1827–37.
32. Anderson KM, Olson KE, Estes KA, Flanagan K, Gendelman HE, Mosley RL. Dual destructive and protective roles of adaptive immunity in neurodegenerative disorders. Transl Neurodegener. 2014 Dec 13;3(1):25.
33. Melzer N, Meuth SG, Wiendl H. CD8 $^{+}$ T cells and neuronal damage: direct and collateral mechanisms of cytotoxicity and impaired electrical excitability. The FASEB Journal. 2009 Nov 30;23(11):3659–73.
34. Kaskow BJ, Baecher-Allan C. Effector T Cells in Multiple Sclerosis. Cold Spring Harb Perspect Med. 2018 Apr 2;8(4).

35. Köberle F. The causation and importance of nervous lesions in American trypanosomiasis. Bull World Health Organ. 1970;42(5):739–43.
36. Köberle F. Chagas' disease and Chagas' syndromes: the pathology of American trypanosomiasis. Adv Parasitol. 1968;6:63–116.
37. Khan AA, Langston HC, Costa FC, Olmo F, Taylor MC, McCann CJ, et al. Local association of Trypanosoma cruzi chronic infection foci and enteric neuropathic lesions at the tissue micro-domain scale. PLoS Pathog. 2021 Aug 23;17(8):e1009864.
38. Machado CRS, Camargos ERS, Guerra LB, Moreira M da C V. Cardiac autonomic denervation in congestive heart failure: Comparison of Chagas' heart disease with other dilated cardiomyopathy. Hum Pathol. 2000 Jan;31(1):3–10.
39. Teixeira ARL, Hecht MM, Guimaro MC, Sousa AO, Nitz N. Pathogenesis of chagas' disease: parasite persistence and autoimmunity. Clin Microbiol Rev. 2011 Jul;24(3):592–630.
40. Michailowsky V, Silva NM, Rocha CD, Vieira LQ, Lannes-Vieira J, Gazzinelli RT. Pivotal role of interleukin-12 and interferon-gamma axis in controlling tissue parasitism and inflammation in the heart and central nervous system during Trypanosoma cruzi infection. Am J Pathol. 2001 Nov;159(5):1723–33.
41. Arantes RME, Marche HHF, Bahia MT, Cunha FQ, Rossi MA, Silva JS. Interferon-γ-Induced Nitric Oxide Causes Intrinsic Intestinal Denervation in Trypanosoma cruzi-Infected Mice. American Journal of Pathology. 2004;164(4):1361–8.
42. Arantes RME, Marche HHF, Bahia MT, Cunha FQ, Rossi MA, Silva JS. Interferon-γ-Induced Nitric Oxide Causes Intrinsic Intestinal Denervation in Trypanosoma cruzi-Infected Mice. American Journal of Pathology. 2004;164(4):1361–8.
43. Köberle F. The causation and importance of nervous lesions in American trypanosomiasis. Bull World Health Organ. 1970;42(5):739–43.
44. Tafuri WL, Maria TA, Lopes ER, Chapadeiro E. [Electron microscopy of the myocardium in human trypanosomiasis cruzi]. Rev Inst Med Trop Sao Paulo. 1973;15(6):347–70.
45. Dávila DF, Núñez TJ, Odreman R, de Dávila CAM. Mechanisms of neurohormonal activation in chronic congestive heart failure: pathophysiology and therapeutic implications. Int J Cardiol. 2005 Jun 8;101(3):343–6.
46. Bonney KM, Luthringer DJ, Kim SA, Garg NJ, Engman DM. Pathology and Pathogenesis of Chagas Heart Disease. Annual Review of Pathology: Mechanisms of Disease. 2019 Jan 24;14(1):421–47.
47. Bonney KM, Taylor JM, Daniels MD, Epting CL, Engman DM. Heat-Killed Trypanosoma cruzi Induces Acute Cardiac Damage and Polyantigenic Autoimmunity. PLoS One. 2011 Jan 21;6(1):e14571.
48. Rodeles LM, Vicco MH, Bontempi IA, Siano A, Tonarelli G, Bottasso OA, et al. Combined analysis of cross-reacting antibodies anti- β 1 <scp>AR</scp> and anti-B13 in advanced stages of Chagas heart disease. Tropical Medicine & International Health. 2016 Dec 24;21(12):1545–51.
49. Talvani A, Rocha MOC, Ribeiro AL, Borda E, Sterin-Borda L, Teixeira MM. Levels of anti-M2 and anti-β1 autoantibodies do not correlate with the degree of heart dysfunction in Chagas' heart disease. Microbes Infect. 2006 Aug;8(9–10):2459–64.
50. Bonney KM, Gifford KM, Taylor JM, Chen C -I., Engman DM. Cardiac damage induced by immunization with heat-killed *<scp>T</scp> rypanosoma cruzi* is not antibody mediated. Parasite Immunol. 2013 Jan 13;35(1):1–10.
51. Mack M, Cihak J, Simonis C, Luckow B, Proudfoot AEI, Plachý J, et al. Expression and Characterization of the Chemokine Receptors CCR2 and CCR5 in Mice. The Journal of Immunology. 2001 Apr 1;166(7):4697–704.

52. Lewis MD, Francisco AF, Taylor MC, Jayawardhana S, Kelly JM. Host and parasite genetics shape a link between Trypanosoma cruzi infection dynamics and chronic cardiomyopathy. Cell Microbiol. 2016 Oct;18(10):1429–43.
53. Khan AA, Langston HC, Costa FC, Olmo F, Taylor MC, McCann CJ, et al. Local association of Trypanosoma cruzi chronic infection foci and enteric neuropathic lesions at the tissue micro-domain scale. PLoS Pathog. 2021 Aug 23;17(8):e1009864.
54. Bustamante JM, Craft JM, Crowe BD, Ketchie SA, Tarleton RL. New, combined, and reduced dosing treatment protocols cure Trypanosoma cruzi infection in mice. J Infect Dis. 2014 Jan 1;209(1):150–62.
55. Bustamante JM, Bixby LM, Tarleton RL. Drug-induced cure drives conversion to a stable and protective CD8+ T central memory response in chronic Chagas disease. Nat Med. 2008 May;14(5):542–50.
56. Yang J, Zhang L, Yu C, Yang XF, Wang H. Monocyte and macrophage differentiation: circulation inflammatory monocyte as biomarker for inflammatory diseases. Biomark Res. 2014 Dec 7;2(1):1.
57. Audoy-Rémus J, Richard JF, Soulet D, Zhou H, Kubes P, Vallières L. Rod-Shaped monocytes patrol the brain vasculature and give rise to perivascular macrophages under the influence of proinflammatory cytokines and angiopoietin-2. J Neurosci. 2008 Oct 8;28(41):10187–99.
58. Mouhadeb O, Ben Shlomo S, Cohen K, Farkash I, Gruber S, Maharshak N, et al. Impaired COMMD10-Mediated Regulation of Ly6Chi Monocyte-Driven Inflammation Disrupts Gut Barrier Function. Front Immunol. 2018;9:2623.
59. Yang P, Liu L, Sun L, Fang P, Snyder N, Saredy J, et al. Immunological Feature and Transcriptional Signaling of Ly6C Monocyte Subsets From Transcriptome Analysis in Control and Hyperhomocysteinemic Mice. Front Immunol. 2021 Feb 25;12.
60. Brühl H, Cihak J, Schneider MA, Plachý J, Rupp T, Wenzel I, et al. Dual role of CCR2 during initiation and progression of collagen-induced arthritis: evidence for regulatory activity of CCR2+ T cells. J Immunol. 2004 Jan 15;172(2):890–8.
61. Auffray C, Fogg D, Garfa M, Elain G, Join-Lambert O, Kayal S, et al. Monitoring of blood vessels and tissues by a population of monocytes with patrolling behavior. Science. 2007 Aug 3;317(5838):666–70.
62. Forstermann U, Sessa WC. Nitric oxide synthases: regulation and function. Eur Heart J. 2012 Apr 1;33(7):829–37.
63. Caetano LC, Zucoloto S, Kawasse LM, Toldo MPA, do Prado JC. Does cyclophosphamide play a protective role against neuronal loss in chronic T. cruzi infection? Dig Dis Sci. 2008 Nov;53(11):2929–34.
64. Castelli V, Benedetti E, Antonosante A, Catanesi M, Pitari G, Ippoliti R, et al. Neuronal Cells Rearrangement During Aging and Neurodegenerative Disease: Metabolism, Oxidative Stress and Organelles Dynamic. Front Mol Neurosci. 2019;12:132.
65. Motoyoshi Y, Kaminoda K, Saitoh O, Hamasaki K, Nakao K, Ishii N, et al. Different mechanisms for anti-tumor effects of low- and high-dose cyclophosphamide. Oncol Rep. 2006 Jul;16(1):141–6.
66. Watters JW, Kloss EF, Link DC, Graubert TA, McLeod HL. A mouse-based strategy for cyclophosphamide pharmacogenomic discovery. J Appl Physiol. 2003 Oct;95(4):1352–60.
67. Xue Q, Yan Y, Zhang R, Xiong H. Regulation of iNOS on Immune Cells and Its Role in Diseases. Int J Mol Sci. 2018 Nov 29;19(12).

68. Sistigu A, Viaud S, Chaput N, Bracci L, Proietti E, Zitvogel L. Immunomodulatory effects of cyclophosphamide and implementations for vaccine design. Semin Immunopathol. 2011 Jul 25;33(4):369–83.
69. Nakahara T, Uchi H, Lesokhin AM, Avogadri F, Rizzuto GA, Hirschhorn-Cymerman D, et al. Cyclophosphamide enhances immunity by modulating the balance of dendritic cell subsets in lymphoid organs. Blood. 2010 Jun 3;115(22):4384–92.
70. Vignali DAA, Collison LW, Workman CJ. How regulatory T cells work. Nat Rev Immunol. 2008 Jul;8(7):523–32.
71. Albert-Bayo M, Paracuellos I, González-Castro AM, Rodríguez-Urrutia A, Rodríguez-Lagunas MJ, Alonso-Cotoner C, et al. Intestinal Mucosal Mast Cells: Key Modulators of Barrier Function and Homeostasis. Cells. 2019 Feb 8;8(2).
72. COLEMAN JW. Nitric oxide: a regulator of mast cell activation and mast cell-mediated inflammation. Clin Exp Immunol. 2002 Jun 28;129(1):4–10.
73. Masini E, Gambassi F, Bello MG, Mugnai L, Raspanti S, Mannaioni PF. Nitric oxide modulates cardiac and mast cell anaphylaxis. Agents Actions. 1994 Jun;41(S1):C89–90.
74. Bischoff SC. Role of mast cells in allergic and non-allergic immune responses: comparison of human and murine data. Nat Rev Immunol. 2007 Feb;7(2):93–104.
75. Seguella L, Gulbransen BD. Enteric glial biology, intercellular signalling and roles in gastrointestinal disease. Nat Rev Gastroenterol Hepatol. 2021 Aug;18(8):571–87.
76. Sharkey KA. Emerging roles for enteric glia in gastrointestinal disorders. J Clin Invest. 2015 Mar 2;125(3):918–25.
77. Bush TG, Savidge TC, Freeman TC, Cox HJ, Campbell EA, Mucke L, et al. Fulminant jejuno-ileitis following ablation of enteric glia in adult transgenic mice. Cell. 1998 Apr 17;93(2):189–201.
78. Joseph NM, He S, Quintana E, Kim YG, Núñez G, Morrison SJ. Enteric glia are multipotent in culture but primarily form glia in the adult rodent gut. J Clin Invest. 2011 Sep;121(9):3398–411.
79. Laranjeira C, Sandgren K, Kessaris N, Richardson W, Potocnik A, Vanden Berghe P, et al. Glial cells in the mouse enteric nervous system can undergo neurogenesis in response to injury. J Clin Invest. 2011 Sep;121(9):3412–24.
80. Benvenuti L, D'Antongiovanni V, Pellegrini C, Antonioli L, Bernardini N, Blandizzi C, et al. Enteric Glia at the Crossroads between Intestinal Immune System and Epithelial Barrier: Implications for Parkinson Disease. Int J Mol Sci. 2020 Dec 2;21(23):9199.
81. Leven P, Schneider R, Schneider L, Mallesh S, Vanden Berghe P, Sasse P, et al. β-adrenergic signaling triggers enteric glial reactivity and acute enteric gliosis during surgery. J Neuroinflammation. 2023 Nov 8;20(1):255.
82. Chaplin DD. Overview of the immune response. J Allergy Clin Immunol. 2010 Feb;125(2 Suppl 2):S3-23.
83. Ward AI, Lewis MD, Khan AA, McCann CJ, Francisco AF, Jayawardhana S, et al. *In Vivo* Analysis of Trypanosoma cruzi Persistence Foci at Single-Cell Resolution. mBio. 2020 Aug 25;11(4).
84. Kiran S, Kumar V, Murphy EA, Enos RT, Singh UP. High Fat Diet-Induced CD8+ T Cells in Adipose Tissue Mediate Macrophages to Sustain Low-Grade Chronic Inflammation. Front Immunol. 2021;12:680944.
85. Gyamfi D, Awuah EO, Owusu S. Molecular aspects and biochemical regulation of diabetes mellitus. In: Molecular Nutrition: Carbohydrates. Elsevier; 2019. p. 35–57.
86. Queiroga TBD, Pereira N de S, da Silva DD, Andrade C de M, de Araújo Júnior RF, Brito CR do N, et al. Virulence of Trypanosoma cruzi Strains Is Related to the

Differential Expression of Innate Immune Receptors in the Heart. Front Cell Infect Microbiol. 2021;11:696719.
87. Lewis MD, Fortes Francisco A, Taylor MC, Burrell-Saward H, Mclatchie AP, Miles MA, et al. Bioluminescence imaging of chronic Trypanosoma cruzi infections reveals tissue-specific parasite dynamics and heart disease in the absence of locally persistent infection. Cell Microbiol. 2014;16(9):1285–300.
88. Gómez-Olarte S, Bolaños NI, Echeverry M, Rodríguez AN, Cuéllar A, Puerta CJ, et al. Intermediate Monocytes and Cytokine Production Associated With Severe Forms of Chagas Disease. Front Immunol. 2019;10:1671.
89. Saraav I, Cervantes-Barragan L, Olias P, Fu Y, Wang Q, Wang L, et al. Chronic *Toxoplasma gondii* infection enhances susceptibility to colitis. Proceedings of the National Academy of Sciences. 2021 Sep 7;118(36).
90. Fujimoto M, Shimizu N, Kunii K, Martyn JAJ, Ueki K, Kaneki M. A role for iNOS in fasting hyperglycemia and impaired insulin signaling in the liver of obese diabetic mice. Diabetes. 2005 May;54(5):1340–8.
91. Knott C, Stern G, Wilkin GP. Inflammatory regulators in Parkinson's disease: iNOS, lipocortin-1, and cyclooxygenases-1 and -2. Mol Cell Neurosci. 2000 Dec;16(6):724–39.
92. Bö L, Dawson TM, Wesselingh S, Möurk S, Choi S, Kong PA, et al. Induction of nitric oxide synthase in demyelinating regions of multiple sclerosis brains. Ann Neurol. 1994 Nov 8;36(5):778–86.
93. Lee SC, Zhao ML, Hirano A, Dickson DW. Inducible Nitric Oxide Synthase Immunoreactivity in the Alzheimer Disease Hippocampus: Association with Hirano Bodies, Neurofibrillary Tangles, and Senile Plaques. J Neuropathol Exp Neurol. 1999 Nov;58(11):1163–9.
94. Brown IAM, McClain JL, Watson RE, Patel BA, Gulbransen BD. Enteric Glia Mediate Neuron Death in Colitis Through Purinergic Pathways That Require Connexin-43 and Nitric Oxide. Cell Mol Gastroenterol Hepatol. 2016 Jan;2(1):77–91.
95. Bernhardt J, Tschudi MR, Dohi Y, Gut I, Urwyler B, Bühler FR, et al. Release of nitric oxide from human vascular smooth muscle cells. Biochem Biophys Res Commun. 1991 Oct;180(2):907–12.
96. Vallance P. GENERAL CARDIOLOGY: Endothelial function and nitric oxide: clinical relevance. Heart. 2001 Mar 1;85(3):342–50.
97. Sonar SA, Lal G. The iNOS Activity During an Immune Response Controls the CNS Pathology in Experimental Autoimmune Encephalomyelitis. Front Immunol. 2019 Apr 4;10.
98. Nemec A, Pavlica Z, Petelin M, Crossley DA, Šentjurc M, Jerin A, et al. Systemic use of selective iNOS inhibitor 1400W or non-selective NOS inhibitor l-NAME differently affects systemic nitric oxide formation after oral Porphyromonas gingivalis inoculation in mice. Arch Oral Biol. 2010 Jul;55(7):509–14.
99. Garvey EP, Oplinger JA, Furfine ES, Kiff RJ, Laszlo F, Whittle BJR, et al. 1400W Is a Slow, Tight Binding, and Highly Selective Inhibitor of Inducible Nitric-oxide Synthase in Vitro and in Vivo. Journal of Biological Chemistry. 1997 Feb;272(8):4959–63.
100. Xu J, Luo Y, Yuan C, Han L, Wu Q, Xu L, et al. Downregulation of Nitric Oxide Collaborated with Radiotherapy to Promote Anti-Tumor Immune Response via Inducing CD8+ T Cell Infiltration. Int J Biol Sci. 2020;16(9):1563–74.
101. Nowicki B, Singhal J, Fang L, Nowicki S, Yallampalli C. Inverse Relationship between Severity of Experimental Pyelonephritis and Nitric Oxide Production in C3H/HeJ Mice. Infect Immun. 1999 May;67(5):2421–7.

102. Reeves KJ, Reed MWR, Brown NJ. The role of nitric oxide in the treatment of tumours with aminolaevulinic acid-induced photodynamic therapy. J Photochem Photobiol B. 2010 Dec 2;101(3):224–32.
103. Klug F, Prakash H, Huber PE, Seibel T, Bender N, Halama N, et al. Low-Dose Irradiation Programs Macrophage Differentiation to an iNOS+/M1 Phenotype that Orchestrates Effective T Cell Immunotherapy. Cancer Cell. 2013 Nov;24(5):589–602.
104. Rota C, Bergamini S, Daneri F, Tomasi A, Virgili F, Iannone A. N-Acetylcysteine negatively modulates nitric oxide production in endotoxin-treated rats through inhibition of NF-kappaB activation. Antioxid Redox Signal. 2002 Feb;4(1):221–6.
105. Maus U, von Grote K, Kuziel WA, Mack M, Miller EJ, Cihak J, et al. The Role of CC Chemokine Receptor 2 in Alveolar Monocyte and Neutrophil Immigration in Intact Mice. Am J Respir Crit Care Med. 2002 Aug 1;166(3):268–73.
106. Saraav I, Cervantes-Barragan L, Olias P, Fu Y, Wang Q, Wang L, et al. Chronic *Toxoplasma gondii* infection enhances susceptibility to colitis. Proceedings of the National Academy of Sciences. 2021 Sep 7;118(36).
107. Lewis MD, Francisco AF, Taylor MC, Jayawardhana S, Kelly JM. Host and parasite genetics shape a link between Trypanosoma cruzi infection dynamics and chronic cardiomyopathy. Cell Microbiol. 2016 Oct;18(10):1429–43.

Chapter 3: Does functional recovery after anti-parasitic chemotherapy correspond with tissue repair in experimental DCD?

3.1. Introduction

Clinical manifestations and diagnosis

In most individuals, irrespective of the route of parasite transmission, acute *T. cruzi* infection is usually asymptomatic. When symptoms do occur, they usually present as non- specific manifestations which include fever, enlargement of the lymph nodes and liver, and subcutaneous oedema. In vector borne transmission, signs of infection via the ocular mucous membranes results in a characteristic Romaña sign, which is classified as periorbital swelling. An ECG might reveal cardiac abnormalities including sinus tachycardia, first-degree atrioventricular block, low QRS voltage and primary T-wave changes (1), although these manifestations are not consistently observed and few acute infections are investigated in this way. In congenitally infected infants, hypotonicity, fever, anaemia and hepatosplenomegaly are the most common symptoms, with the development occurring within the first few weeks of delivery (2).

The annual rate of cardiomyopathy development in intermediate / chronic stage infections is 2% per year (3), but clinical outcomes can range from life-long asymptomatic disease to severe morbid outcomes in the form of mega-digestive manifestations or sudden death. Outcomes are related to pathological involvement of the heart, gastrointestinal tract, or both, referred to as the cardio-digestive form.

Gastrointestinal dysfunction, namely megaoesophagus, megacolon, or both, develops in up to 15% of chronically infected patients and, although not associated with a high rate of mortality, does significantly alter the quality of life of those affected. Megacolon typically presents in the sigmoid segment, rectum or descending colon, or a combination of all three. The chronic cardiac form presents with a high mortality, with just under a third (~30%) of individuals presenting with conduction abnormalities, arrythmias, apical aneurysms and sudden death (4).

Diagnosing Chagas disease in the chronic phase is difficult. Cardiac manifestations of symptomatic patients can be detected by ECG, with the most common abnormalities being right bundle branch block, abnormal Q waves and low voltage of QRS. The combination of right bundle block branch block with left anterior fascicular block is the hallmark of Chagas cardiac involvement. Diagnosis of the digestive form of disease resides with positive serology in combination with identification of gastrointestinal sequelae, namely dysregulated myoelectrical activity, alterations of gastric emptying and distension, hypoperistalsis, pyloric hypertrophy, and organ dilation, usually observed by a barium swallow and/or enema imaging test (5). Diagnostic efficacy is precarious in the chronic stage since parasitaemia is scarce (1), and the presence of IgG antibodies against *T. cruzi* antigens needs to be detected via two different serological methods to confirm diagnosis; either ELISA, indirect immunofluorescence or hemagglutination (6). PCR for confirming the presence of *T. cruzi* DNA is not routinely reliable due to poor standardisation, and the transient presence of parasites in the blood, but is useful to confirm diagnosis in combination with positive serology (6). Moreover, PCR is applicable to confirm treatment failure, but not for confirmation of treatment success since the absence of

parasite DNA in blood samples does not confirm absence of infection in other tissues. (6)

Evidence basis of treatment regimes

As per recommendations by the Ministry of Health in Brazil in 2018 (7), and a clinical review in 2007 of Chagas disease in the United States (8), treatment is only strongly recommended for acute infections, infection in children and for reactivated infections e.g. linked to HIV co-infection or anti-transplant rejection treatments. Treatment for chronic stage infections is considered justified for those up to the age of 18, but is not suggested for those suffering from advanced cardiac disease or megaoesophagus. Benznidazole and nifurtimox are currently the only two drugs with proven efficacy against *T. cruzi* infection (1). Benznidazole has a better safety and efficacy profile, so is usually the first-line treatment, despite it still being synonymous with adverse side effects and low patient compliance (9).

The Benznidazole Evaluation for Interrupting Trypanosomiasis (BENEFIT) trial unambiguously identified the benefit of treatment in preventing congenital transmission, and scrutinised the use of benznidazole for mild to moderate cardiomyopathy as treatment of chronic disease did not significantly reduce the rate of the primary clinical outcome (10,11). Benznidazole treatment for patients with digestive symptoms without any cardiac involvement is not considered to have an evidence-based rationale because clinical trials to date have not included GI-related outcomes. Treatment is limited to palliative care, with approaches for advanced megaoesophagus focused on aiding food and liquid transit, such as sublingual nitrites and nifedipine to relax the lower oesophageal sphincter. Patients with early

developed megaoesophagus can be treated with surgical interventions e.g. laparoscopic Heller's myotomy and fundoplication (12). Other treatment options are fibre-rich diets and laxatives to offset colonic dysfunction, with surgical resection considered for patients where conservative measures fail.

Overall, there is a lack of pre-clinical and clinical data on whether *T. cruzi* infected adults, who are asymptomatic should be treated with benznidazole in order to delay or prevent progression to symptomatic Chagas disease (7,13). The key questions are whether treatment intervention in the chronic stage helps alleviate established pathology, and or prevents further pathology developing.

Recent developments have been made on the effect of stage-specific treatment on cardiac pathology, with use of highly sensitive bioluminescence imaging and histopathological assessment in experimental mouse models (14). The efficacy of benznidazole in preventing cardiac fibrosis in C3H/HeN mice infected with TcI-JR parasites, a host-parasite combination known to cause significant cardiac and digestive pathology, was recently assessed (15,16). The model exhibits similarities observed in human chronic infection, including a high degree of heterogeneity in cardiac fibrosis (17). In this experimental model, sterile curative treatment during both acute and chronic stage of infection prevented the development of cardiac fibrosis (14). When compared to BALB/c mice infected with TcVI-CLBR parasites, treatment during the acute phase starting from day 14- or 22-days post infection also resulted in the prevention of fibrosis development (14). However, unlike the TcI-C3H model, if treatment was delayed until the chronic phase, to day 110 post infection, high levels of fibrosis were observed, similar in severity to infected (untreated)

controls, suggesting that treatment had no effect on cardiac pathology development in this model. This failed alleviation of disease severity is in line with the rationale of why benznidazole treatment is not considered justified in the chronic stage of human disease (10,11). These experimental findings demonstrated that antiparasitic treatment efficacy in the chronic phase resides strongly with the strain of parasite, and genetics of the host. Critically, it also demonstrates that clinically relevant cardiac manifestations can be alleviated if treatment begins in the acute phase.

As described in the previous chapters, the TcI-C3H model also exhibits a consistent GI transit functional delay throughout the course of infection, with dysperistalsis correlating with a loss of enteric neurons and continued parasite persistence in the colon (16). Similar to the cardiac pathology observed in these mice, digestive disease severity was higher in this model than BALB/c. The heterogeneity in clinical outcomes between parasite-mouse genetic combinations appears consistent with human epidemiology, with the TcI-C3H model being more suitable for investigating host-parasite kinetics and disease development in the GI tract. BALB/c mice were refractory to development of a consistent GI functional delay with either TcVI-CLBR or TcI-JR parasites, despite the digestive tract being a major reservoir for chronic infection in both cases (15). This demonstrates that local parasitism is not sufficient for the development of digestive dysfunction. The condition and viability of the host's immune and tissue repair responses at a microdomain level is therefore likely central to disease resistance and susceptibility (16).

The mechanism or mechanisms of enteric denervation is thought to derive from collateral damage from local potent anti-parasitic inflammation, as explored in chapter 2. Here I aim to use a similar experimental framework, but with a focus on GI tissue repair processes at a microdomain level in response to benznidazole mediated cure or suppression of *T. cruzi* infection.

Here we will utilise the DCD model and test the hypothesis that benznidazole treatment 6 weeks after *T. cruzi* infection can prevent or reduce GI disease severity.

3.2 Manuscript #2, Khan et al 2022

Khan AA, **Langston HC**, Walsh L, Roscoe R, Jayawardhana S, Francisco A, Taylor MC, McCann CJ, Kelly JM, Lewis MD; Enteric nervous system regeneration and functional cure of experimental digestive Chagas disease with trypanocidal chemotherapy. *bioRxiv* (2022) 12.14.520395;
doi: https://doi.org/10.1101/2022.12.14.520395; Nat. Comm. In revision.

LONDON SCHOOL of HYGIENE &TROPICAL MEDICINE

London School of Hygiene & Tropical Medicine
Keppel Street, London WC1E 7HT

T: +44 (0)20 7299 4646
F: +44 (0)20 7299 4656
www.lshtm.ac.uk

RESEARCH PAPER COVER SHEET

Please note that a cover sheet must be completed for each research paper included within a thesis.

SECTION A – Student Details

Student ID Number	1601186	**Title**	Mr
First Name(s)	Harry		
Surname/Family Name	Langston		
Thesis Title	Study of the derminants of enteric neuropathy in experimental Chagas disease		
Primary Supervisor	Dr. Michael Lewis		

If the Research Paper has previously been published please complete Section B, if not please move to Section C.

SECTION B – Paper already published

Where was the work published?			
When was the work published?			
If the work was published prior to registration for your research degree, give a brief rationale for its inclusion			
Have you retained the copyright for the work?*	Choose an item.	Was the work subject to academic peer review?	Choose an item.

*If yes, please attach evidence of retention. If no, or if the work is being included in its published format, please attach evidence of permission from the copyright holder (publisher or other author) to include this work.

SECTION C – Prepared for publication, but not yet published

Where is the work intended to be published?	Nature Communications (unrevised version on BioRxiv)
Please list the paper's authors in the intended authorship order:	Archie.A. Khan, Harry. C. Langston, Louis Walsh, Rebbecca Roscoe, Shiromani Jayawardhana, Amanda F. Francisco, Martin.C. Taylor, Connnor. J. McCann, John. M. Kelly, Michael. D. Lewis.
Stage of publication	**Undergoing revision**

SECTION D – Multi-authored work

For multi-authored work, give full details of your role in the research included in the paper and in the preparation of the paper. (Attach a further sheet if necessary)	i) In Unrevised version: Extended Figure 1.h. A full histological qunatification of four distinct infection status groups (Control, Untreated, Benznidazole treated:relapse, Benznidazole treated: cured. I performed the tissue processing, embedding of tissue into paraffin blocks, cutting transverse sections using micotomy, and staining with Heamotoxylin and Eosin. I then quantified the extent of inflammation in the smooth muscle layer of the distal colon, and averaged the total number of nuceli from 5 images. I produced the bar plots on Prism and ran statistics (ordinary one-way ANOVA). I wrote the corresponding methods section; lines 402-405. I contributed to ongoing discussions about data in lab meetings and in 1-on-1 meetings with Archie, the primary auhor. ii) In revised version (still in revision) I contributed to additional data after initial reviewers comments. Multi-stain immunofluoresecent images, with cell proliferation/reploication labelling (EdU), nueronal cell body labelling (ANNA-1) and Glial cell labelling (GFAP) in mice with different infection statuses (Control, untreated, treated:cured, treated:relapse). I peformed all animal husbandry, treatment with benznidazole (with cover provided from Michael Lewis) and pulsing with EdU. I performed neropsies with Michael Lewis and Archie Khan, and processed tissue for cryosectioning. I fixed, embedded and cut the tissue using a cryostat. I used confocal microscpy to obtain 10 images per distal colon, per mouse, in the form of Z-stacks. I performed a total EdU+ cell count in two spatial contexts: ganglionic and peri-ganglionic, and provided corresponding quantification plots. I also cut and stained some additional colon sections for H&E staining from a previous, late benznodazole treatment (24 weeks post infection), experiment.

SECTION E

Student Signature	[redacted]
Date 15.11.23	

Supervisor Signature	Michael Lewis
Date	16.11.23

Enteric nervous system regeneration and functional cure of experimental digestive Chagas disease with trypanocidal chemotherapy

Archie A. Khan[1], Harry C. Langston[1], Louis Walsh[1], Rebecca Roscoe[1], Shiromani Jayawardhana[1], Amanda F. Francisco[1], Martin C. Taylor[1], Conor J. McCann[2], John M. Kelly[1], Michael D. Lewis[1*]

[1] Department of Infection Biology, London School of Hygiene and Tropical Medicine, Keppel Street, London, WC1E 7HT, United Kingdom

[2] Stem Cells and Regenerative Medicine, University College London, Great Ormond Street Institute of Child Health, London, United Kingdom

*Corresponding author

Email: michael.lewis@lshtm.ac.uk

Abstract

Digestive Chagas disease (DCD) is an enteric neuropathy caused by *Trypanosoma cruzi* infection. There is a lack of evidence on the mechanism of pathogenesis and rationales for treatment. We used a mouse model that recapitulates key clinical manifestations to study how infection dynamics shape DCD pathology, and the impact of treatment with the front-line drug benznidazole. Curative treatment at 6 weeks post-infection resulted in sustained recovery of GI transit function, whereas sub-curative treatment led to infection relapse and gradual return of DCD symptoms. Neuro-immune gene expression profiles shifted from chronic inflammation to a tissue repair signature after cure, accompanied by increased glial cell activity and regenerative neurogenesis in the myenteric neuronal plexus. Delaying treatment until 24 weeks post-infection led to a partial reversal of the DCD phenotype, suggesting the accumulation of permanent tissue damage over the course of chronic infection. Our study shows that murine DCD pathogenesis is sustained by chronic *T. cruzi* infection and is not an inevitable consequence of acute stage denervation. The risk that irreversible enteric neuromuscular tissue damage and dysfunction will develop highlights the importance of prompt diagnosis and treatment. Finally, these findings support the concept of treating asymptomatic *T. cruzi* infected individuals with benznidazole to prevent DCD development.

Introduction

Chagas disease (CD), or American trypanosomiasis, is a neglected tropical disease with a prevalence of 6.5 million cases, a burden of 10,000 deaths per year, 275, 000 DALYs and economic costs reaching US$7 billion per year (1, 2). The large majority of cases occur in endemic regions of Latin America, but there is a clear long-term trend of globalisation (3-5). CD is caused by *Trypanosoma cruzi*, a protozoan parasite, which is primarily transmitted to humans by blood-feeding insect vectors (triatomine bugs), but it can also be acquired congenitally or from contaminated blood transfusions, organ transplants and foodstuffs (6). Anti-parasitic treatment is limited to the nitroheterocyclic drugs, nifurtimox and benznidazole. Both have long dosing schedules and can cause significant toxicity (7, 8). Daily benznidazole treatment for 60 days is the current standard of care because side effects are considered less severe than for nifurtimox. Recent trial data show that reducing the duration of treatment to 2 weeks may be justified (9).

Upon transmission, *T. cruzi* invades target cells of diverse types and begins an approximately weekly cycle of replication, host cell lysis and dissemination. In most cases, adaptive immunity suppresses parasite numbers to very low levels; sterile clearance is considered rare (10, 11). Clinical manifestations affecting the heart and/or GI tract develop in around one third of chronically infected people. Benznidazole treatment is recommended for all acute, congenital and immunosuppression-related reactivation cases, as well as chronic infections in children and women of childbearing age (12). However, the evidence for the efficacy of benznidazole in terms of chronic disease progression and outcomes is limited. Treatment showed no significant benefit compared to placebo in terms of preventing death or disease progression in patients who already had symptomatic cardiac Chagas disease (8). There are no clinical or pre-clinical data on the impact of treatment on digestive Chagas disease (DCD) outcomes.

DCD is an enteric neuropathy characterised by progressive dilatation and dysfunction of sections of the GI tract (13, 14). Symptoms include achalasia, abdominal pain, constipation and faecaloma. Eventually, massive organ dilatation results in megasyndromes, usually of the colon and/or oesophagus. Dilatation is associated with loss of enteric neurons leading to peristaltic paralysis and smooth muscle hypertrophy. Options for DCD management are limited to palliative and surgical interventions (15), often implemented in emergency scenarios late in the disease course, with significant mortality risk (16).

DCD is thought to stem from collateral damage to enteric neurons caused by anti-parasitic inflammatory immune responses in the muscle wall of the affected region of the GI tract (17). Beyond this, the mechanism and kinetics of denervation, and therefore a rationale for treatment, are poorly defined. The inability to detect gut-resident parasites in chronic infections supported a model of acute phase damage unmasked by further ageing-related denervation (18). Molecular detection of *T. cruzi* DNA and inflammatory infiltrates in post-mortem and biopsy studies of human DCD circumstantially suggests that chronic parasite persistence may contribute to disease development (19-27). These data from late and terminal disease states are difficult to interpret in respect of relationships between pathogenesis and infection load or distribution over time. Experimental bioluminescence imaging and tissue PCR studies in mice showed that the GI tract is a major long-term reservoir of infection with diverse *T. cruzi* strains (28-32). This led to the development of a robust mouse model of DCD, which features significantly delayed GI transit associated with co-localised parasite persistence and enteric neuronal lesions in the wall of the large intestine (33). Here, we utilised this model to formally test the hypothesis that benznidazole-mediated cure of *T. cruzi* infection can either prevent DCD, or reduce its severity.

Results

Benznidazole-mediated cure of *T. cruzi* infection in the experimental DCD model

We have developed C3H/HeN mice infected with bioluminescent TcI-JR parasites as a model of chronic DCD (33)(Fig. 1). Subsets of mice were treated with benznidazole or vehicle at 6 weeks post-infection (wpi) (Fig. 1a, b). At this time, parasite loads are already in sharp decline as a result of adaptive immunity. *In vivo* bioluminescence imaging (BLI) showed that untreated mice transitioned to a stable, low-level chronic infection. In contrast, parasite loads in benznidazole treated mice became undetectable (Fig. 1b, 1c). This was corroborated by splenomegaly, low body weight and loss of GI mesenteric tissue at 36 wpi in the untreated infected group. In all cases, the read-outs reversed closer to control baseline after curative benznidazole treatment (Fig. 1d, Extended Data Fig. 1). *In vivo* and *ex vivo* BLI identified a subset of infected, BZ-treated mice (n = 11/27, 41%) in which the infection had relapsed (Fig. 1b, 1c, 1e). Of these, 5 (19 %) infections were only detectable by post-mortem *ex vivo* imaging of internal organs (Fig. 1e). Retrospective comparison of body weights and parasite loads showed there was no difference at the start of treatment between animals that were cured and those that relapsed (Extended Data Fig. 2). Relapse infections were most often localised to GI tissues, in contrast to the broadly disseminated pattern seen in the infected group (Fig. 1f, 1g). Of note, in the

context of cardiac Chagas disease, relapse infections rarely localised to the heart (2/11, 18%), which was a site of frequent and high intensity parasitism in the untreated group (16/18, 89 %) (Fig. 1f, 1g). Overall, our findings show that benznidazole treatment at 6 wpi achieves 60 % parasitological cure in this experimental DCD model with infection relapse cases often localised to the GI tract.

Benznidazole treatment restores normal GI transit function associated with re-innervation

In the DCD model there is a highly significant delay in GI transit time in infected mice compared to uninfected controls ((33), Fig. 2a, 2b, 2c). Benznidazole chemotherapy rapidly reversed the transit delay phenotype to uninfected control baseline (Fig. 2b, 2c). Immediately prior to initiation of treatment, the mean GI transit time was 184 minutes in infected mice compared to 103 minutes in uninfected controls (Fig. 2b). In the untreated infection group, the delay remained significant, although it initially eased in line with immune-mediated parasite load reduction and then gradually worsened as the chronic phase progressed (Fig. 2b, 2c). Curative benznidazole treatment led to permanent restoration of normal transit times. Importantly, relapse infections were associated with the return of a significant transit delay, but this remained less severe than for the infected group (Fig. 2b, 2c, Extended Data Fig. 2). At the experiment end point, we analysed faecal retention in the colon after a period of fasting. This showed a clear constipation phenotype associated with an increased number of faecal pellets and weight in untreated infections. This was alleviated in benznidazole cured mice, but not in relapsed infections (Fig. 2d, 2e, 2f and Extended Data Fig. 1e). We also observed significant normalisation of caecum weight in cured mice (Extended Data Fig. 1c).

Given the central role of denervation in human DCD, we next evaluated the impact of infection and benznidazole-mediated treatment on the enteric nervous system (ENS). The number of neuronal cell bodies in the proximal colon myenteric plexus of infected-untreated mice was reduced by 70 % and 86% at 6 and 36 wpi respectively (Fig. 2g, 2h). The distal colon showed a similar pattern, with 77 % fewer neurons than uninfected control mice at 6 wpi and 71% at 36 wpi. Benznidazole-mediated cure of infection led to recovery of neuron numbers by 36 wpi, with only 47% and 21% less than the uninfected control mean in the proximal and distal myenteric plexus respectively. Denervation in relapsed mice was significant, but of lower magnitude (69% proximal, 56% distal) than for infected-untreated mice (Fig. 2g, 2h), in line with their intermediate transit delay phenotype (Fig. 2b - f).

We observed a morphologically heterogeneous population of HuC/D^{+} myenteric neuronal bodies in colon samples from benznidazole-cured mice. A subset of these neurons resembled those seen in

healthy control ganglia, while another subset appeared atypically smaller and rounder with weaker anti-HuC/D reactivity. These were commonly present in the same ganglion as neuronal cell bodies with normal morphology and neighbouring healthy control-like myenteric ganglia (Fig. 2g). Together, these data show that benznidazole treatment reverses the transit time and constipation phenotypes in the DCD mouse model, and that this is associated with substantial recovery of myenteric neuron density, particularly in the distal colon. In mice in which infection relapsed, transit time delay returns but not to levels observed in untreated infected controls, with an intermediate recovery of myenteric innervation.

Distinct gene expression profiles for chronic, relapsed and cured infections.

To further investigate how the balance of infection and host immunity impacts on the ENS during *T. cruzi* infection, we performed Nanostring multiplex analysis of host gene expression, focussing on immune response (n = 491) and ENS (n = 17) genes. In mice with untreated chronic infections (36 wpi), there were 128 significantly differentially expressed genes (DEGs) compared to uninfected controls in colon tissue, of which 108 were up- and 20 down-regulated (Fig. 3a, 3b). These evidenced a type 1-polarised inflammatory response involving class I and class II antigen presentation (e.g. *Ciita, Tap1, Psmb9, B2m; H2-Aa, H2-Ab1, Cd74*), cytokines/chemokines (e.g. *Ifng*, *Il21, Tnf; Cxcl9, Cxcl10, Ccl5*), transcription factors (e.g. *Stat1,-2,-3,-6, Irf1,-88*), cytotoxic lymphocyte markers and effectors (*Cd8a, Cd8b1, Cd226, Gzmb, Fasl, Prf1)*, complement factors (*C2, C6, C4a, C3, C7, C1qb*) and Fc receptors (*Fcgr1,-4,-3, Fcer1a,-1g*). There was also evidence of significant dysregulation at the pathway level for antigen presentation, interferon signalling, apoptosis and phagocytosis (Fig. 3d, Extended Data Fig. 3a). Consistent with the enduring capacity of *T. cruzi* to survive in this inflammatory environment and the need to prevent excessive GI tissue damage, the up-regulated DEG set included a diverse range of immuno-inhibitory mediators: *Btnl1, Btnl2, Cd274* (PD-L1)*, Socs1, Lilrb4, Lilrb3, Lair1, Tnfaip3, Serping1*.

Next, we evaluated the impact of benznidazole treatment on host gene expression in the contexts of sterile cure and infection relapse. Relapsed infections were associated with a larger DEG set (n = 179 vs uninfected) than untreated chronic infections. The majority, 58.6%, were same direction DEGs as chronic infections, but the data also revealed relapse-specific changes (Fig. 3b, Extended Data Fig. 4). Notably, these included stronger upregulation of 54 genes, including *Cd8a*, *Cd8b1, Ccl5, Cxcl1, Gzmb* and *Ifng,* and unique up-regulation of cytotoxic effectors *Gzma* and *Fas*, leukocyte markers *Cd4*, *Cd7* and *Cd27*, transcription factors (*Batf3*, *Ikzf4*, *Irf5*, *Nfil3*) and the components of integrins α4β1 (VLA-

4), α5β1 (VLA-5), αLβ2 (LFA-1), αMβ2 (MAC-1). Given the lower and less disseminated parasite loads seen in these animals (Fig. 1), this broader gene expression profile is consistent with enhanced control of *T. cruzi*, enduring for months after non-curative treatment.

Colon tissue from benznidazole cured mice had gene transcript abundances equivalent to uninfected controls for 119 (93%) of the 128 DEGs that were identified in untreated chronic infections, indicating near complete reversion to homeostasis (Fig. 3). At the pathway level, there were no significant differences between cured and uninfected groups (Extended Data Fig. 4). Nevertheless, cured mice did have a distinct profile compared to uninfected control mice, comprising 44 DEGs (40 up- and 4 down-regulated genes) (Fig. 3b, 3c, 3e). Of note, the most up-regulated gene set was enriched for neuronal markers (*Rbfox3* (NeuN), *Nefl*, *Tubb3*), enteric glial cells (EGCs) (*S100b*, *Gfap*, *Plp1*), genes associated with neural development (*Ngf*, *Frmpd4*) and neurotransmission (*Nos1*). The EGC marker *S100b* was the only switched direction DEG, with reduced expression in chronic infections and increased expression in cured mice (Fig. 3e). Furthermore, multiple genes involved in tissue repair and regeneration were also highly significant DEGs in cured mice, including *Notch2*, *Tgfb2*, *Tgfbr1*, *Tgfb3* and *Zeb1.* Sterile cure of *T. cruzi* infection therefore results in dissipation of the chronic inflammatory environment in the colon and induction of a tissue repair program that encompasses key components of the ENS.

Neuro-glial impact of benznidazole treatment of *T. cruzi* infections

Nitrergic neuronal inhibitory signalling is critical for homeostatic control of peristalsis and its disruption is linked to a range of enteric neuropathies, including human DCD (34). Evidence for altered *Nos1* gene expression in our experimental model ((33); Fig. 3c, 3e) led us to analyse the expression of the corresponding protein (neuronal NOS, nNOS) in myenteric neurons from the proximal and distal colon using immunofluorescence. The number of distal colon $nNOS^+$ neurons was significantly reduced in untreated and relapse infections compared to uninfected controls (Fig. 4a, 4b). In benznidazole-cured animals, $nNOS^+$ neuron density remained lower on average than uninfected controls, but the difference was not statistically significant (Fig. 4a, 4b).

The RNA-based analyses strongly implicated EGCs in post-cure tissue repair (Fig. 3c, 3e, Extended Data Fig. 3b), so these were further analysed at the protein level. Immunofluorescence analysis of neuro-glial network morphology (Fig. 4c) clearly showed EGCs (glial fibrillary acidic protein, $GFAP^+$) wrapped around neurons (neuron-specific β-tubulin, $TuJ1^+$) in the myenteric plexus for all groups. Networks of

GFAP$^+$ EGCs in samples from untreated infections showed the weakest staining intensity and contained fragmented aggregates and patches in the plexus compared to controls, cured and relapsed mice. Conversely, GFAP staining in samples from benznidazole treated animals exhibited control-like glial morphology with a dense network, which was also preserved in relapsed infections (Fig. 4c). Western blot analysis of GFAP protein expression revealed bands at 75 kDa, larger than reference brain GFAP protein (50 kDa), which most likely reflects gut-specific post-translational modification. A second band was observed in both infected-untreated and relapse groups at approximately 70 kDa, indicating altered GFAP protein structure as a feature of DCD pathology. Benznidazole treatment induced doubling of the GFAP protein abundance compared to controls and disappearance of the secondary band, while the relapse infection group showed a more moderate increase overall and a minor secondary band (Fig. 4d, 4e). In combination, the RNA- and protein-based data provide evidence that sterile cure of *T. cruzi* infection is followed by increased EGC activity in the colonic myenteric plexus, which may contribute to the recovery of normal transit.

Delayed treatment improves GI function to a lesser extent than early treatment

Most cases of human Chagas disease are associated with chronic *T. cruzi* infections. We therefore investigated treatment initiated at 24 wpi, to assess the impact on DCD in the chronic stage (Fig. 5). The bioluminescence profile of the infected-untreated mice followed a similar pattern as previously shown (Fig. 1a, 1e). Treatment with benznidazole at 24 wpi resulted in elimination of parasite bioluminescence by 30 wpi (Fig. 5a, 5b), a gradual gain of body weight (Extended Data Fig. 5a) and reversal of splenomegaly (Fig. 5c). Relapses of infection were detected in 30% (3/10) of the treated mice with reappearance of the bioluminescence signal, mostly in the abdominal area (Fig. 5a, 5b and 5d). *Ex vivo* imaging at end-point necropsy of infected mice (48 wpi) showed the highest intensity and frequency of infection in the heart and GI tract compared to other organs (Fig. 5e). Although there were only 3 relapse cases, the distribution of infections amongst organs and tissues appeared to have a similar profile to the acute stage treatment (Fig. 5e, 5f).

As expected, there was a significantly longer GI transit time ($\bar{x}$ = 184 mins) in infected, untreated mice at all chronic time-points compared to uninfected controls (Fig. 5g, 5h). Transit time in sterile cured mice improved to an intermediate level ($\bar{x}$ = 144 mins), which was stable over for the duration of the experiment, indicating a partial recovery of function (Fig. 5g, 5h). The relapse mice initially showed strong improvements in transit time post-treatment, but by the end point, they transitioned towards an increased transit time ($\bar{x}$ = 174 mins), close to the delay seen in infected-untreated mice (Fig. 5g,

5h). When we analysed colonic faecal retention, there was stronger evidence for recovery of GI function in cured mice. This constipation phenotype was significantly alleviated after benznidazole-mediated cure of infection, while there was no significant improvement in mice where infection relapsed after treatment (Fig. 5i and Extended Data Fig. 5e). Retrospective comparison of pre-treatment body weights, parasite loads and transit times showed that there were no significant differences between benznidazole treated mice that were cured compared to relapsed (Extended Data Fig. 6). In summary, when treatment was delayed until the chronic phase of infection, the observed sterile parasitological cure rate was slightly higher than for treatment at 6 weeks (70% vs 59%) and there was more modest recovery of GI transit function. Therefore, the timing of anti-parasitic treatment is an important factor affecting the degree to which GI function can be restored in DCD.

Discussion

Treatment for DCD is limited to palliative dietary adjustments and surgical interventions with significant mortality risk (16). Lack of data has prevented a consensus on whether *T. cruzi* infected adults who are asymptomatic should be treated with anti-parasitic chemotherapy (4, 12, 35). Our findings in a pre-clinical mouse model provide evidence that prompt treatment with benznidazole can prevent chronic DCD. When treatment was delayed until the chronic phase, sterile cure of infection only resulted in a partial GI functional recovery, indicating that some tissue pathology reaches an irreversible stage. This echoes the results of clinical trials of benznidazole in late-stage chronic Chagas cardiomyopathy patients, in which the drug performed no better than placebo in preventing disease progression or death (8). Further work is required to determine the point at which cure of infection will cease to yield functional improvement in DCD. Nonetheless, our findings provide a pre-clinical *in vivo* evidence base supporting the concept that the earlier anti-parasitic chemotherapy is initiated, the greater the chances of preventing or delaying the progression of digestive disease.

In the context of DCD, our results provide insight into the dynamic relationships between *T. cruzi* infection, host responses, ENS damage and tissue repair. Most denervation occurred in the acute phase of infection, yet the complete and sustained normalisation of GI transit function after benznidazole treatment at 6 weeks shows that these acute losses are not sufficient to explain chronic disease symptoms, contrary to early theories of DCD aetiology (18) . Transient functional improvement in untreated controls in the early chronic phase further supports this conclusion (33). Over time, chronic infection of the GI tract led to further neuron losses and gradual decline in GI function.

Moreover, in cases of failed treatment, relapses of *T. cruzi* infection were associated with a return to GI dysfunction. Together, these data support the conclusion that chronic infection actively drives disease, as has been circumstantially suspected from the detection of parasites in GI tissues from human DCD patients (19-27). However, the disease aetiology is more complex than anticipated because neither parasite load, nor the degree of denervation directly predicted the severity of functional impairment. This might be explained by compensatory plasticity of the remaining ENS and/or extrinsic circuitry in the denervated colon (36). As seen in the CNS, it is also possible that the existing ENS neural circuit rewires to compensate for the neuronal loss by rebalancing the excitatory and inhibitory outputs of the network (37). Our neuro-immune gene expression analysis indicated that the broader balance of inflammatory, regulatory and tissue repair factors at play in the infected colon also contributes to the DCD phenotype.

Why the GI tract serves as a long-term permissive site for *T. cruzi* has been unclear because there have been minimal data on gut-specific immune responses. At the transcriptional level, we found that chronic infection of the colon is associated with a robust type 1 inflammatory response, dominated by markers of $CD8^+$ T cell recruitment, similar to that seen in studies of other tissue types (10, 38-42). The discovery that at least 9 genes with immuno-inhibitory potential were also upregulated suggests that there are host-intrinsic mechanisms that limit tissue damage, yet also enable *T. cruzi* persistence. We previously found that chronic *T. cruzi* infection is restricted to a few rare foci, which can be widely scattered within the colonic smooth muscle layers and are regularly re-seeded in new locations by motile trypomastigotes (33, 43). Here, we analysed RNA from full thickness colon tissue and, for selected markers of neurons and glia, immuno-fluorescence analysis of the myenteric plexus. Therefore, a key challenge now will be to determine how infection and immune response dynamics relate to specific cell types, and how these in turn shape pathology at finer spatial and temporal scales.

The extent to which the adult ENS is capable of repair and regeneration is a fundamental question, with relevance across diverse enteric neuropathies. We observed a recovery of myenteric plexus neuron numbers in mice several months after sterile cure of *T. cruzi* infection. There are several potential neurogenic mechanisms that could underly this replenishment. It has been proposed that enteric neurons are regularly replaced from a population of neural stem cells as part of gut homeostasis (44), however, the majority of studies indicate that enteric neurogenesis is absent, or extremely limited in the steady-state adult gut (45-50). Regeneration of the ENS involves neurogenesis from enteric glial cell pre-cursors after chemical injury using benzalkonium chloride (BAC) or Dextran Sulfate Sodium (DSS) (46, 47, 49, 50) and from extrinsic Schwann cell pre-cursors in mouse models of

Hirschprung's disease (51, 52). Our approach did not enable us to define the ontogeny of new neurons, but the data suggest that glial cells are likely to be involved. We saw upregulation of the canonical glial markers GFAP and S100β specifically in sterile cured mice, as well as PLP1, which corresponds to the subset of glial cells that differentiate into neurons in the DSS colitis model (47). Transcriptional changes in healing colon tissue also comprised up-regulation of the stem cell transcription factor *Zeb1*, which regulates epithelial–mesenchymal transition (53) and neuronal differentiation in the CNS (54), including from radial glial-like cells in the adult hippocampus (55). We also saw up-regulation of *Ngf* and *Notch2*, critical regulators of neurogenesis; Notch signalling in particular has been implicated in maintenance of the neural progenitor pool and controlling glial to neuronal differentiation in the CNS (56) and the gut (57, 58). The *T. cruzi* infection and cure approach may therefore open new experimental opportunities to study adult neurogenesis and inform the development of regenerative therapies for enteric neuropathies, most especially DCD.

Materials and Methods

Parasites

This study used the TcI-JR strain of *T. cruzi* parasites constitutively expressing the red-shifted firefly luciferase variant *PPy*RE9h, as previously described (29). Epimastigotes were cultured *in vitro* in supplemented RPMI-1640 medium at 28°C under selective drug pressure with 150 µg ml^{-1} G418. MA104 monkey kidney epithelial cell monolayers were infected with metacyclic trypomastigotes, obtained from stationary phase cultures, in MEM media + 5% FBS at 37°C and 5% CO_2. After 5 to 10 days, tissue culture parasites (TCTs) were harvested from the culture supernatant and aliquots from a single batch were cryopreserved in 10% DMSO. For *in vivo* infections, TCTs were thawed at room temperature, sedimented by centrifugation at 10,000x *g* for 5 minutes, washed in 1 ml complete medium, sedimented again and resuspended in 250 µl complete medium. After 1 hr incubation at 37°C, active parasites were counted and the suspension was adjusted to the required density.

Animals and Infections

All animal procedures were performed under UK Home Office project license P9AEE04E, approved by LSHTM Animal Welfare Ethical Review Board and in accordance with Animal Scientific Procedure Act (ASPA) 1986 regulations. Female C3H/HeN mice, aged 6-8 weeks, were purchased from Charles River (UK) and habituated for 1-2 weeks before experiments. All CB17 SCID mice used were female and bred

in-house. Mice were housed in individually ventilated cages on a 12 hr light/dark cycle. They had access to food and water available *ad libitum* unless otherwise stated. Mice were maintained under specific pathogen-free conditions. Humane end-points were loss of >20% body weight, reluctance to feed or drink freely for more than 4-6 hours, loss of balance or immobility.

Inocula of 1×10^5 TCTs were used to infect SCID mice via i.p. injection. After 3 weeks, motile blood trypomastigotes (BTs) were derived from the supernatant of cardiac whole blood after passive sedimentation of mouse cells for 1 hr at 37°C. C3H/HeN mice were infected with 1 x 10^3 BTs in 0.2 ml PBS via i.p. injection. The benznidazole treatment schedule was 100 mg kg^{-1} day^{-1} for 20 consecutive days via oral gavage. Benznidazole was prepared from powder form at 10 mg ml^{-1} by dissolving in vehicle solution (0.5 % w/v hydroxypropyl methylcellulose, 0.5% v/v benzyl alcohol, 0.4% v/v Tween 80 in deionised water).

At experimental end-points, mice were killed by exsanguination under terminal anaesthesia (Euthatal/Dolethal 60 mg kg^{-1}, i.p.) or by cervical dislocation. Selected organs and tissue samples were cleaned with PBS and either snap-frozen on dry ice, fixed in 10 % Glyofixx or transferred to ice-cold DMEM medium to suit different downstream analysis methods.

Total GI transit time assay

Carmine red dye solution, 6% in 0.5% methyl cellulose (w/v) in distilled water was administered to mice by oral gavage (200 µl). Mice were returned to their home cage for 75 mins, after which they were placed in individual containers and observed. The time of excretion of the first red-stained faecal pellet was recorded and the mouse was returned to its cage. A cut off time of 4 hours was employed as the maximum GI transit delay for the assay for welfare reasons. Total GI transit time was calculated as the time taken to expel the first red pellet from the time of gavage.

***In vivo* bioluminescence imaging**

Mice were injected with 150 mg kg^{-1} D-luciferin i.p., then anaesthetised using 2.5% (v/v) gaseous isoflurane in oxygen. Bioluminescence imaging was performed after 10-20 minutes using an IVIS Lumina II or Spectrum system (PerkinElmer). Image acquisition settings were adjusted dependent on signal saturation (exposure time: 1 – 5 min; binning: medium to large). After imaging, mice were placed on a heat pad for revival and returned to cages. Whole body regions of interest (ROIs) were

drawn on acquired images to quantify bioluminescence, expressed as total flux (photons sec^{-1}), to estimate *in vivo* parasite burden in live mice (28). The detection threshold was determined using uninfected control mice. All bioluminescence data were analysed using Living Image v4.7.3.

Ex vivo bioluminescence imaging

Food was withdrawn from cages 4 hours prior to euthanasia. Five to seven minutes prior to euthanasia, mice were injected with 150 mg kg^{-1} D-luciferin i.p.. After euthanasia, mice were perfused trans-cardially with 10 ml of 0.3 mg ml^{-1} D-luciferin in PBS. Typically, organs collected included heart, liver, spleen, lungs, skin, peritoneum, the GI tract, the genitourinary system and their associated mesenteries, as well as samples of hindlimb skeletal muscle and visceral adipose. These were soaked in PBS containing 0.3 mg ml^{-1} D-luciferin prior to imaging, which was performed as described above. Parasite load in each organ tissue was quantified using a measure of infection intensity. To do this, bioluminescence per organ or tissue sample was calculated by outlining ROIs on each sample and expressed as radiance (photons sec^{-1} cm^{-2} sr^{-1}). Radiances from equivalent organs/tissues of age-matched, uninfected control mice were measured and the fold change in bioluminescence for each test sample was calculated. The detection threshold was determined by scoring the presence of *T. cruzi* infection foci of at least 10 contiguous bioluminescent pixels at radiance $\geq 3 \times 10^3$ photons sec^{-1} cm^{-2} sr^{-1}. These criteria were established by reference to a set of images from uninfected control animals (59).

Faecal analyses

Isolated colon tissue was cleaned externally with PBS and faecal pellets were gently teased out of the lumen. Faecal pellets were counted and collected in 1.5 ml tubes. Wet weights were recorded and then the tubes were left to dry in a laminar flow cabinet overnight; dry weights were measured the following day.

Histopathology

Paraffin-embedded fixed tissue blocks were prepared and 3-5 µm sections were stained with haematoxylin and eosin as described (29). Images were acquired using a Leica DFC295 camera attached to a Leica DM3000 microscope. For analysis of inflammation, nuclei were counted automatically using the Leica Application Suite V4.5 software (Leica).

406

407 **Immunofluorescence analysis**

408

409 After necropsy, excised colon tissues were transferred from ice-cold DMEM to PBS. Tissues were cut
410 open along the mesentery line, rinsed with PBS, then stretched and pinned on Sylgard 184 plates.
411 Under a dissection microscope, the mucosal layer was carefully peeled away using forceps and the
412 remaining muscularis wall tissue was fixed in paraformaldehyde (4% w/v in PBS) for 45 minutes at
413 room temperature. Next, tissues were washed with PBS for 45 minutes, with 3 changes, at room
414 temperature and permeabilised with PBS containing 0.5% Triton X-100 for 2 hours, followed by
415 blocking for 1 hour (10% sheep serum in PBS containing 0.5% Triton X-100). Tissues were incubated
416 with primary antibodies (mouse anti-HuC/D IgG clone 16A11 at 1:200 [ThermoFisher], rabbit anti-
417 tubulin β-3 (TuJ1) polyclonal IgG at 1:500 [Biolegend], rat anti-GFAP monoclonal IgG clone 2.2B10 at
418 1:500 [ThermoFisher], rabbit anti-nNos polyclonal IgG at 1:500 [ThermoFisher]) in PBS containing 0.5%
419 Triton X-100 for 48 hours at 4°C. Tissues were washed with PBS for 30 minutes with three changes,
420 then incubated with secondary IgG (goat anti-mouse Alexa546, goat anti-rabbit Alexa633, goat anti-
421 rat, all 1:500, ThermoFisher) in PBS containing 0.5% Triton X-100 for 2 hours and counterstained with
422 Hoechst 33342 (1 μg ml^{-1}) at room temperature. Control tissues were incubated with only secondary
423 antibodies (without primary antibodies) to assess antibody specificity. Tissues were mounted on glass
424 slides using FluorSave mounting medium (Merck).

425

426 Whole mounts were examined and imaged with a LSM880 confocal microscope using a 40X objective
427 (Zeiss, Germany). Images were captured as Z-stack scans of 21 digital slices with interval of 1 μm
428 optical thickness. Five Z-stacks were acquired per region (proximal and distal colon), per animal. Cell
429 counts were performed on Z-stacks after compression into a composite image using the cell counter
430 plug-in of FIJI software. Neuronal density was calculated as the number of HuC/D^+ or $nNOS^+$ neuron
431 cell bodies per mm^2. HuC/D signal was associated with high background outside ganglia in samples
432 from infected mice, attributed to binding of the secondary anti-mouse IgG to endogenous IgG, so ENS-
433 specific analysis was aided by anti-TuJ1 co-labelling and assessment of soma morphology.

434

435 **Western Blot**

436

437 Frozen colon tissue samples were lysed in RIPA Buffer and the total protein concentration was
438 quantified using a BCA assay kit as per manufacturer's protocol (ThermoFisher). Lysates were obtained
439 from three independent biological samples per group and pooled into a single sample for analysis.

Polyacrylamide gel electrophoresis was performed to separate proteins using 4-20% stain-free TGX gels (Bio-Rad). Proteins were visualised by UV-induced fluorescence using a Chemidoc imaging system (Bio-Rad) to verify equal loading of samples. The most abundant protein band in each loading control sample was used for quantification. Proteins were transferred to nitrocellulose membranes in a trans-blot turbo transfer system (Bio-Rad). Membranes were blocked for 30 minutes using 5% skimmed milk in PBST and then probed with rat anti-GFAP primary antibody (1:2000, cat # 13-0300, Thermo Scientific) overnight at 4°C, followed by incubation with HRP-conjugated goat anti-rat secondary antibody (1:5000, cat # 31460 Thermo Scientific) for 2 hours at room temperature and visualisation using enhanced chemiluminescence (ECL kit, GE Healthcare Life Sciences). Data were analysed using the gel analysis package in FIJI.

RNA extraction

Frozen tissue samples were thawed in 1 ml Trizol (Invitrogen) per 30-50 mg tissue and immediately homogenised using a Precellys 24 homogeniser (Bertin). 200 µl of chloroform was added to each sample and mixed by vortex. The aqueous phase was separated by centrifugation at 13,000 g at 4°C and RNA was purified using the RNeasy Mini Kit (Qiagen) with on-column DNAse digestion, as per manufacturer's protocol. A Qubit Fluorimeter (ThermoFisher) and/or a Nanodrop instrument was used to assess RNA quality and quantity.

RT-qPCR

cDNA was synthesised from 1 µg of total RNA using Superscript IV VILO mastermix (Invitrogen), as per manufacturer's protocol, in reaction volumes of 20 µl. qPCR reactions were carried out using QuantiTect SYBR green master mix (Qiagen) with 200 nM of each primer and 4 µl of cDNA diluted 1/50 in DEPC water. Reactions were run using an Applied Biosystems Fast 7500 machine (ThermoFisher) as per manufacturer's protocol.

A final cDNA volume of 100 µl was made by adding RNase-free DEPC water (1: 5 dilution) and stored at −20 °C until further use. qPCR reactions consisted of 10µl QuantiTect SYBR green master mix, 6 µl of forward and reverse primer mix (200 nM; design in Supplementary Table 1) and 4 µl of cDNA diluted 1/50 in DEPC water. For No-RT and no template control reactions, 4 µl of solution from the No-RT cDNA reaction and DEPC water were added respectively. Reactions were run using an Applied

Biosystems Fast 7500 machine (ThermoFisher) as per manufacturer's protocol. Data were analysed by the ΔΔCt method (60) using murine *Oaz1* as the endogenous control gene.

Nanostring gene expression analysis

RNA was adjusted to 30-60 ng μl^{-1} and analysed on a Nanostring nCounter system (Newcastle University, UK). We used a "PanelPlus" set of target probes comprising the standard mouse immunology nCounter codeset (XT-CSO-MIM1-12) and a custom selection of 20 probes from the mouse neuroinflammation and neuropathology codesets: *Acaa1a, Adora2a, Cck, Ch25h, Cidea, Drd1, Drd2, Gfap, MAPt, Nefl, Ngf, Nos1, Npy, P2rx7, Pla2g4a, Pla2g5, Plp1, Rbfox3, S100b* and *Tubb3*. The core immunology codeset comprised 547 protein-coding test genes, 14 house-keeping control genes, 6 positive binding control probes and 8 negative binding control probes. Fifty nine test genes were below a detection threshold limit (mean negative control bound probe count + 3 SDs) and were excluded from the analysis. The final codeset comprised probes for 508 test genes and was analysed using nSolver 4.0. Data were normalised in the Basic Analysis module with positive control and housekeeping gene normalisation probe parameters both set to geometric mean. Normalised data were then imported to the Advanced Analysis module and used to analyse differential gene expression between groups and pathway scores using default parameters. Samples were annotated with their run number as a confounding variable.

Statistics

Individual animals were used as the unit of analysis. No blinding or randomisation protocols were used. Statistical differences between groups were evaluated using 2-tailed, unpaired Student's *t*-test one-way ANOVA with Tukey's post-hoc correction for multiple comparisons. These tests were performed in nSolver 4.0, GraphPad Prism v.8 or R v3.6.3. Differences of $p < 0.05$ were considered significant.

Figure Legends

Figure 1: Evaluation of benznidazole treatment outcomes in a mouse model of digestive Chagas disease.

a, Schematic representation of the experimental timeline. **b,** Representative *in vivo* bioluminescence images for each group of mice: uninfected controls (Control), *T. cruzi* infected and untreated

(Infected), treated with benznidazole and parasitologically cured (BZ-Cured), and relapse infections after benznidazole treatment failure (BZ-Relapsed). *Ex vivo* bioluminescence images show parasite localisation in the indicated organs and tissue samples (liver- LV, lymph nodes - LYN, lungs - LN, gut mesenteric tissue - MS, heart - HT, spleen - SP, skeletal muscle - SKM, visceral fat - VF, stomach - ST, small intestine - SI, large intestine - LI, skin - SK, carcass - CAR, genitourinary system - GUS, and peritoneum - PT). Bioluminescence intensity is expressed on log-scale pseudocolour heat maps (range expressed in units of radiance). **c,** Line plots show course of infection as mean total bioluminescent flux (p/s) per mouse. Infected, *n* = 18, except *n* =10 at 9 and 22 wpi, *n* = 47 at 6 wpi and *n* = 50 at 3 wpi; BZ-cured, *n* = 16, except *n* = 17 at 12 and 18 wpi, *n* = 8 at 9 wpi and *n* = 7 at 22 wpi, and BZ-relapsed, *n* = 11, except *n* = 5 at 9 and 22 wpi. Dashed lines show thresholds: uninfected control mean auto-luminescence (dark brown dashed line) and mean ± 2SD (light brown dotted lines). **d,** Spleen weights at post-mortem of control (*n* = 17), infected (*n* = 14), BZ-Cured (*n* = 16) and BZ-Relapsed (*n* = 11) groups. **e,** Parasite bioluminescence intensity detected in individual BZ-Relapse mice after the end of benznidazole treatment (12 wpi). Data up to 36 wpi are from whole animal *in vivo* imaging and for 42 wpi are the sum of bioluminescent flux signals detected in organs and tissue samples imaged *ex vivo*. Dashed line shows uninfected control mean auto-luminescence threshold. **f,** Dot plot and **g**, box plot show relative *ex vivo* infection intensities in the indicated organs/tissue at 42 wpi. Data are expressed as the mean fold change in bioluminescent radiance vs. the uninfected control mean for groups (f) and individual mice (g). In dot plot **f**, the circle sizes indicate the percentage of mice with bioluminescence positive (BL^+) signal and the circle colours show the infection intensity (fold change of mean bioluminescent radiance vs uninfected control). Infected, *n* = 18; except skin, GUS and other *n* = 17; BZ-Cured, *n* = 16 and BZ-Relapsed, *n* = 11 mice. Statistical significance was tested using one-way ANOVA followed by Tukey's HSD test (*$P < 0.05$, ***$P < 0.001$, **** $P < 0.0001$).

Figure 2: Benznidazole-mediated cure of infection reverses digestive Chagas disease phenotype and promotes ENS recovery.

a, Schematic representation of the carmine red dye tracer method to measure transit time delay in mice. **b,** Line plots show change in mean total GI transit time over the course of 36 weeks of *T. cruzi* infection for infected (*n* = 18, except *n* = 46 at 6 weeks post-infection (wpi)), benznidazole (BZ) treated and cured (BZ-Cured; *n* = 16, except *n* = 17 at 12 and 18 wpi) and benznidazole treated and relapsed (BZ-Relapsed; *n* = 11) mice compared with uninfected controls (*n* = 20). Cream overlaid bar shows BZ treatment window (6-9 wpi, 20 daily doses). **c,** Bar plots show final GI transit times at 36 wpi for individual mice. Control *n* = 19, infected *n* = 18, BZ-Cured *n* = 16 and BZ-Relapsed *n* = 11. **d, e,** Bar plots show number of faecal pellets number (d) and dry weight (e) retained in the colon after 4 hours of

fasting at 42 wpi for control (*n* = 20), infected (*n* = 18), BZ-Cured (*n* = 16) and BZ-Relapsed (*n* = 11) mice. **f,** Representative images of large intestines corresponding to the data in d and e. Scale bar = 2 cm. **g,** Representative immunofluorescence images of enteric neuronal cell bodies (HuC/D$^+$, magenta) in the colon myenteric plexus from control, infected, BZ-cured and BZ-relapsed mice. White arrowhead indicates denervated ganglia (absence of defined soma). Magnified region of the BZ-Cured image shows intact control-like neuronal cell bodies, indicated by white arrows. In a 500 µm laterally adjacent region of the BZ-Cured ENS, a morphologically heterogeneous neuronal cell population is observed: white arrows indicate intact control-like neuron soma morphology and white stars indicate atypical neuron soma morphology. The magenta to white heat map scale corresponds to pixel fluorescence intensity. **h,** Bar plots show the densities of HuC/D-positive neurons in proximal and distal colon (PC, DC) before (6 wpi) and after BZ treatment (36 wpi) of control (*n* = 4 at 6 wpi, *n* = 10 at 36 wpi), infected (*n* = 4 at 6 wpi, *n* = 9 at 36 wpi), BZ-Cured (*n* = 7) and BZ-Relapsed (*n* = 8) groups. Data are expressed as mean ± SEM. Statistical significance was tested using one-way ANOVA followed by Tukey's HSD test (*$P < 0.05$, **$P < 0.01$, ***$P < 0.001$ **** $P < 0.0001$).

Figure 3: Enteric neuro-immune gene expression signatures associated with *T. cruzi* infection and benznidazole treatment outcomes.

a, Volcano plots of the $\log_2$-transformed fold change and significance ($-\log_{10}$ *p* value) of differentially expressed genes (DEGs) in colon tissue from *T. cruzi* infected (red shades), benznidazole treated and cured (BZ-Cured; blue shades) and benznidazole treated and relapsed (BZ-Relapsed; purple shades) vs. uninfected control C3H/HeN mice; and BZ-Cured vs. infected (green shades) mice. Lighter coloured shaded dots indicate statistical significance of $P < 0.05$ and darker shaded dots $P < 0.001$. **b,** Venn diagrams show same-direction differentially expressing genes (DEG) shared between infected, BZ-Cured and BZ-Relapsed groups for all genes analysed (left, n shows number of genes) and transcription factors (right) (threshold of $p < 0.05$ vs uninfected controls in at least one of the groups). Arrows indicate up- and down-regulation. **c,** Relative change in neuro-glial genes between the indicated experimental groups; colour intensity corresponds to fold change ($\log_2$) expression vs uninfected controls. **d,** Signalling pathway scores for each group. **e,** Comparison of directionality and extent of gene expression change in chronically infected and BZ-cured mice vs uninfected controls (*n* = 163 genes that are significant DEGs in at least one group). Red circles are DEGs specific to the chronic, untreated infections, blue triangles are DEGs specific to the BZ-Cured mice and grey squares are DEGs shared by both groups. Diagonal dashed line is the line of equivalence. Vertical and horizontal dashed lines indicate position for genes with identical expression levels as uninfected controls in chronic infection and BZ-cured mice respectively. Infected and uninfected controls *n* = 6, BZ-Cured and BZ-

Relapsed *n* = 3. Statistical significance was determined by 2-tailed, unpaired Student's *t*-test for each gene (**P* < 0.05, ***P* < 0.01, ****P* < 0.001, **** *P* < 0.0001).

Figure 4: Enteric nitrergic neuron and glial cell dynamics in chronic *T. cruzi* infections and after benznidazole treatment.

a, b, Representative immunofluorescence images (a) and quantification (b) of nNOS$^+$ neurons in the colonic myenteric plexus of control (*n* = 10), infected (*n* = 9), benznidazole treated cured (BZ-Cured, *n* = 7 in proximal [PC] and *n* = 8 in distal colon [DC]) and benznidazole treated relapsed (BZ-Relapsed, *n* = 8 in PC and *n* = 7 in DC) mice. Bar plots show density of nNOS$^+$ neuronal cell bodies. **c,** Representative immunofluorescence images of myenteric plexus enteric glial cells (EGCs, GFAP$^+$, gold to yellow fluorescence intensity scale) and enteric neural network (TuJ1$^+$, blue to cyan fluorescence intensity scale) in the indicated experimental groups. Top panel shows merged images of GFAP$^+$ and TuJ1$^+$ cells. Bottom panel shows images of morphologically diverse GFAP$^+$ enteric glial cells in a second example ganglion revealed on a red to yellow fluorescence intensity scale. White arrows show aberrant EGC morphology and white stars show activated EGC morphology. All confocal images (**a** and **c**) were taken at 400X magnification, scale bar = 50 µm. Colour heat map scale shows pixel fluorescence intensity. **d, e,** Western blot analysis of GFAP in full thickness colon tissue lysates. Bar plot (d) and paired dot plot (e) show normalised GFAP protein abundance as a ratio of uninfected controls). For all groups, the sample analysed was a pooled lysate of 3 independent biological replicates (mice)). The blot in **d** shows α-GFAP staining using 12 µg of each lysate (corresponding to the bar plot groups above). Total protein was visualised using tryptophan trihalo-crosslinking gels for loading control and normalisation; the most abundant protein band is shown. GFAP abundance differences were validated by analysing replicate gels with two lysate quantities (12 and 21 µg) as indicated in plot **e**.

Figure 5: Impact of chronic phase benznidazole treatment on experimental digestive Chagas disease.

a, b Representative *in vivo* bioluminescence (BL) image series (a) and quantification (b) of *T. cruzi*-infected C3H/HeN mice before and after treatment with benznidazole (BZ) at 24 weeks post-infection (wpi). *Ex vivo* images show distribution and intensity of infection in internal organs and tissue samples (liver - LV, lungs - LN, gut mesenteric tissue - MS, heart - HT, spleen - SP, skeletal muscle - SKM, visceral fat - VF, stomach - ST, small intestine - SI, large intestine - LI, genitourinary system - GUS, and peritoneum - PT) at necropsy. BL intensity (radiance) is expressed as log-scale pseudocolour heat maps. **I**nfected mice *n* = 8, except *n* = 19 at 6 and 12 wpi, *n* = 16 at 24 wpi and *n* = 20 at 3 wpi; benznidazole treated and cured (BZ-Cured; *n* = 7) and benznidazole treated and relapsed (BZ-Relapsed; *n* = 3). Dashed lines show thresholds: uninfected control mean auto-luminescence (dark

blue dashed line) and mean ± 2SD (light blue dotted lines). **c,** Spleen weights of control (*n* = 6), infected (*n* = 8), BZ-Cured (*n* = 6) and BZ-Relapsed (*n* = 3) groups. **d,** *In vivo* BL intensity of individual BZ-Relapsed mice after treatment at 24 wpi. Thresholds shown as uninfected control mean auto-luminescence (grey line) and mean ± 2SD (grey dotted lines). **e,** Dot plot and **f**, box plot show relative *ex vivo* infection intensities in the indicated organs/tissue at 48 wpi. Data are expressed as the mean fold change in bioluminescent radiance vs. the uninfected control mean for groups (e) and individual mice (f). In dot plot **e**, the circle sizes indicate the percentage of mice with bioluminescence positive (BL^+) signal and the circle colours show the infection intensity (fold change of mean bioluminescent radiance vs uninfected control). Infected *n* = 8, BZ-Cured *n* = 6 and BZ-Relapsed *n* = 3 mice. **g,** Mean GI transit time of control (*n* = 5, except *n* = 11 at 24 wpi and *n* = 6 at 30 wpi), infected (*n* = 9, except *n* = 23 at 24 wpi and *n* = 8 at 30 wpi), BZ-Cured (*n* = 7) and BZ-Relapsed (*n* = 3) mice. Cream overlaid bar shows BZ treatment window (24 - 27 wpi, 20 daily doses). **h,** Bar plots show final GI transit times at 46 wpi for individual mice. Control *n* = 5, infected *n* = 9, BZ-Cured *n* = 7 and BZ-Relapsed *n* = 3. **i,** Bar plots show number of faecal pellets number (left) and dry weight (right) retained in the colon after 4 hours of fasting at 48 wpi for control (*n* = 6), infected (*n* = 8), BZ-Cured (*n* = 6) and BZ-Relapsed (*n* = 3) mice. Data are expressed as mean ± SEM. Statistical significance was tested using one-way ANOVA followed by Tukey's HSD test (*$P < 0.05$, **** $P < 0.0001$).

References

1. Gómez-Ochoa SA, Rojas LZ, Echeverría LE, Muka T, Franco OH. Global, Regional, and National Trends of Chagas Disease from 1990 to 2019: Comprehensive Analysis of the Global Burden of Disease Study. Global Heart. 2022;17(1):59.

2. Lee BY, Bacon KM, Bottazzi ME, Hotez PJ. Global economic burden of Chagas disease: a computational simulation model. Lancet Infect Dis. 2013;13(4):342-8.

3. Irish A, Whitman JD, Clark EH, Marcus R, Bern C. Updated Estimates and Mapping for Prevalence of Chagas Disease among Adults, United States. Emerging Infectious Diseases. 2022;28(7):1313-20.

4. Suárez C, Nolder D, García-Mingo A, Moore DAJ, Chiodini PL. Diagnosis and Clinical Management of Chagas Disease: An Increasing Challenge in Non-Endemic Areas. Research and Reports in Tropical Medicine. 2022;13:25-40.

5. Navarro M, Navaza B, Guionnet A, López-Vélez R. Chagas disease in Spain: need for further public health measures. PLoS Neglected Tropical Diseases. 2012;6(12):e1962.

6. Pérez-Molina JA, Molina I. Chagas disease. Lancet. 2018;391(10115):82-94.

643 7. Berenstein AJ, Falk N, Moscatelli G, Moroni S, González N, Garcia-Bournissen F, et al.
644 Adverse Events Associated with Nifurtimox Treatment for Chagas Disease in Children and Adults.
645 Antimicrobial Agents and Chemotherapy. 2021;65(2).
646 8. Morillo CA, Marin-Neto JA, Avezum A, Sosa-Estani S, Rassi AJ, Rosas F, et al. Randomized
647 Trial of Benznidazole for Chronic Chagas' Cardiomyopathy. New England Journal of Medicine.
648 2015;373(14):1295-306.
649 9. Torrico F, Gascón J, Barreira F, Blum B, Almeida IC, Alonso-Vega C, et al. New regimens of
650 benznidazole monotherapy and in combination with fosravuconazole for treatment of Chagas
651 disease (BENDITA): a phase 2, double-blind, randomised trial. Lancet Infect Dis. 2021;21(8):1129-40.
652 10. Pérez-Mazliah D, Ward AI, Lewis MD. Host-parasite dynamics in Chagas disease from
653 systemic to hyper-local scales. Parasite Immunology. 2021;43(2):e12786.
654 11. Buss LF, Campos de Oliveira-da Silva L, Moreira CHV, Manuli ER, Sales FC, Morales I, et al.
655 Declining antibody levels to *Trypanosoma cruzi* correlate with polymerase chain reaction positivity
656 and electrocardiographic changes in a retrospective cohort of untreated Brazilian blood donors. PLoS
657 Neglected Tropical Diseases. 2020;14(10):e0008787.
658 12. PAHO. Guidelines for the diagnosis and treatment of Chagas disease. 2018.
659 13. Iantorno G, Bassotti G, Kogan Z, Lumi CM, Cabanne AM, Fisogni S, et al. The enteric nervous
660 system in chagasic and idiopathic megacolon. Am J Surg Pathol. 2007;31(3):460-8.
661 14. Meneghelli UG. Chagasic enteropathy. Rev Soc Bras Med Trop. 2004;37(3):252-60.
662 15. Pinazo MJ, Cañas E, Elizalde JI, García M, Gascón J, Gimeno F, et al. Diagnosis, management
663 and treatment of chronic Chagas' gastrointestinal disease in areas where *Trypanosoma cruzi*
664 infection is not endemic. Gastroenterología y Hepatología.
665 16. Bierrenbach AL, Quintino ND, Moreira CHV, Damasceno RF, Nunes M, Baldoni NR, et al.
666 Hospitalizations due to gastrointestinal Chagas disease: National registry. PLoS Neglected Tropical
667 Diseases. 2022;16(9):e0010796.
668 17. Arantes RME, Marche HHF, Bahia MT, Cunha FQ, Rossi MA, Silva JS. Interferon-γ-Induced
669 Nitric Oxide Causes Intrinsic Intestinal Denervation in *Trypanosoma cruzi*-Infected Mice. Am J Pathol.
670 2004;164(4):1361-8.
671 18. Köberle F. The causation and importance of nervous lesions in American trypanosomiasis. B
672 World Health Organ. 1970;42(5):739-43.
673 19. Adad SJ, Andrade DCdS, Lopes ER, Chapadeiro E. Contribuição ao estudo da anatomia
674 patológica do megaesôfago chagásico. Rev I Med Trop. 1991;33:443-50.

675 20. Vago AR, Macedo AM, Adad SJ, Reis DdÁ, Corrêa-Oliveira R. PCR detection of Trypanosoma
676 cruzi DNA in oesophageal tissues of patients with chronic digestive Chagas' disease. Lancet.
677 1996;348(9031):891-2.
678 21. Vago AR, Silva DM, Adad SJ, Correa-Oliveira R, d'Avila Reis D. Chronic Chagas disease:
679 presence of parasite DNA in the oesophagus of patients without megaoesophagus. Transactions of
680 the Royal Society of Tropical Medicine and Hygiene. 2003;97(3):308-9.
681 22. Corbett CE, Ribeiro U, Jr., Prianti MG, Habr-Gama A, Okumura M, Gama-Rodrigues J. Cell-
682 mediated immune response in megacolon from patients with chronic Chagas' disease. Diseases of
683 the Colon and Rectum. 2001;44(7):993-8.
684 23. Lages-Silva E, Crema E, Ramirez LE, Macedo AM, Pena SD, Chiari E. Relationship between
685 *Trypanosoma cruzi* and human chagasic megaesophagus: blood and tissue parasitism. The American
686 Journal of Tropical Medicine and Hygiene. 2001;65(5):435-41.
687 24. da Silveira ABM, Arantes RME, Vago AR, Lemos EM, Adad SJ, Correa-Oliveira R, et al.
688 Comparative study of the presence of *Trypanosoma cruzi* kDNA, inflammation and denervation in
689 chagasic patients with and without megaesophagus. Parasitology. 2005;131(05):627-34.
690 25. da Silveira ABM, Lemos EM, Adad SJ, Correa-Oliveira R, Furness JB, D'Avila Reis D.
691 Megacolon in Chagas disease: a study of inflammatory cells, enteric nerves, and glial cells. Human
692 Pathology. 2007;38(8):1256-64.
693 26. de Castro Côbo de E, Silveira TP, Micheletti AM, Crema E, Adad SJ. Research on *Trypanosoma*
694 *cruzi* and Analysis of Inflammatory Infiltrate in Esophagus and Colon from Chronic Chagasic Patients
695 with and without Mega. Journal of Tropical Medicine. 2012;2012:232646.
696 27. Pinto L, Schijman AG, Alonso-Padilla J, Lozano D, Torrico MC, Gamba P, et al. Molecular
697 detection and parasite load of *Trypanosoma cruzi* in digestive tract tissue of Chagas disease patients
698 affected by megacolon. Acta Trop. 2022;235:106632.
699 28. Lewis MD, Francisco AF, Taylor MC, Burrell-Saward H, McLatchie AP, Miles MA, et al.
700 Bioluminescence imaging of chronic *Trypanosoma cruzi* infections reveals tissue-specific parasite
701 dynamics and heart disease in the absence of locally persistent infection. Cell Microbiol.
702 2014;16(9):1285-300.
703 29. Lewis MD, Francisco AF, Taylor MC, Jayawardhana S, Kelly JM. Host and parasite genetics
704 shape a link between *Trypanosoma cruzi* infection dynamics and chronic cardiomyopathy. Cell
705 Microbiol. 2016;18(10):1429-43.
706 30. Silberstein E, Serna C, Fragoso SP, Nagarkatti R, Debrabant A. A novel nanoluciferase-based
707 system to monitor *Trypanosoma cruzi* infection in mice by bioluminescence imaging. PLOS ONE.
708 2018;13(4):e0195879.

709 31. Francisco AF, Lewis MD, Jayawardhana S, Taylor MC, Chatelain E, Kelly JM. The limited ability
710 of posaconazole to cure both acute and chronic *Trypanosoma cruzi* infections revealed by highly
711 sensitive in vivo imaging. Antimicrobial Agents and Chemotherapy. 2015;59(8):4653-61.
712 32. Santi-Rocca J, Fernandez-Cortes F, Chillón-Marinas C, González-Rubio M-L, Martin D, Gironès
713 N, et al. A multi-parametric analysis of *Trypanosoma cruzi* infection: common pathophysiologic
714 patterns beyond extreme heterogeneity of host responses. Scientific Reports. 2017;7(1):1-12.
715 33. Khan AA, Langston HC, Costa FC, Olmo F, Taylor MC, McCann CJ, et al. Local association of
716 *Trypanosoma cruzi* chronic infection foci and enteric neuropathic lesions at the tissue micro-domain
717 scale. PLoS Pathog. 2021;17(8):e1009864.
718 34. Rivera LR, Poole DP, Thacker M, Furness JB. The involvement of nitric oxide synthase
719 neurons in enteric neuropathies. Neurogastroenterology and Motility. 2011;23(11):980-8.
720 35. Villar JC, Perez JG, Cortes OL, Riarte A, Pepper M, Marin-Neto JA, et al. Trypanocidal drugs
721 for chronic asymptomatic *Trypanosoma cruzi* infection. The Cochrane database of systematic
722 reviews. 2014;2014(5):Cd003463.
723 36. Brierley SM, Linden DR. Neuroplasticity and dysfunction after gastrointestinal inflammation.
724 Nature Reviews Gastroenterology & Hepatology. 2014;11(10):611-27.
725 37. Barrett DG, Deneve S, Machens CK. Optimal compensation for neuron loss. Elife.
726 2016;5:e12454.
727 38. Nogueira LG, Santos RHB, Fiorelli AI, Mairena EC, Benvenuti LA, Bocchi EA, et al. Myocardial
728 gene expression of T-bet, GATA-3, Ror-t, FoxP3, and hallmark cytokines in chronic Chagas disease
729 cardiomyopathy: an essentially unopposed TH1-type response. Mediators of Inflammation.
730 2014;2014.
731 39. Ferreira LR, Ferreira FM, Nakaya HI, Deng X, Cândido DD, de Oliveira LC, et al. Blood Gene
732 Signatures of Chagas Cardiomyopathy With or Without Ventricular Dysfunction. J Infect Dis.
733 2017;215(3):387-95.
734 40. Acevedo GR, Girard MC, Gómez KA. The Unsolved Jigsaw Puzzle of the Immune Response in
735 Chagas Disease. Frontiers in Immunology. 2018;9(1929).
736 41. Roffê E, Marino APMP, Weaver J, Wan W, de Araújo FF, Hoffman V, et al. *Trypanosoma cruzi*
737 Causes Paralyzing Systemic Necrotizing Vasculitis Driven by Pathogen-Specific Type I Immunity in
738 Mice. Infection and Immunity. 2016;84(4):1123-36.
739 42. Higuchi MdL, Gutierrez PS, Aiello VD, Palomino S, Bocchi E, Kalil J, et al.
740 Immunohistochemical characterization of infiltrating cells in human chronic chagasic myocarditis:
741 Comparison with myocardial rejection process. Virchows Archiv. 1993;423(3):157-60.

742 43. Ward AI, Lewis MD, Khan AA, McCann CJ, Francisco AF, Jayawardhana S, et al. *In Vivo*
743 Analysis of *Trypanosoma cruzi* Persistence Foci at Single-Cell Resolution. mBio. 2020;11(4):e01242-
744 20.
745 44. Kulkarni S, Micci M-A, Leser J, Shin C, Tang S-C, Fu Y-Y, et al. Adult enteric nervous system in
746 health is maintained by a dynamic balance between neuronal apoptosis and neurogenesis. PNAS.
747 2017;114(18):E3709-E18.
748 45. Virtanen H, Garton DR, Andressoo J-O. Myenteric Neurons Do Not Replicate in Small
749 Intestine Under Normal Physiological Conditions in Adult Mouse. Cellular and Molecular
750 Gastroenterology and Hepatology. 2022;14(1):27-34.
751 46. Belkind-Gerson J, Hotta R, Nagy N, Thomas AR, Graham H, Cheng L, et al. Colitis induces
752 enteric neurogenesis through a 5-HT4–dependent mechanism. Inflammatory Bowel Diseases.
753 2015;21(4):870-8.
754 47. Belkind-Gerson J, Graham HK, Reynolds J, Hotta R, Nagy N, Cheng L, et al. Colitis promotes
755 neuronal differentiation of Sox2+ and PLP1+ enteric cells. Scientific reports. 2017;7(1):1-15.
756 48. Vicentini FA, Keenan CM, Wallace LE, Woods C, Cavin J-B, Flockton AR, et al. Intestinal
757 microbiota shapes gut physiology and regulates enteric neurons and glia. Microbiome. 2021;9(1):1-
758 24.
759 49. Laranjeira C, Sandgren K, Kessaris N, Richardson W, Potocnik A, Berghe PV, et al. Glial cells in
760 the mouse enteric nervous system can undergo neurogenesis in response to injury. The Journal of
761 Clinical Investigation. 2011;121(9).
762 50. Joseph NM, He S, Quintana E, Kim YG, Núñez G, Morrison SJ. Enteric glia are multipotent in
763 culture but primarily form glia in the adult rodent gut. J Clin Invest. 2011;121(9):3398-411.
764 51. Uesaka T, Nagashimada M, Enomoto H. Neuronal Differentiation in Schwann Cell Lineage
765 Underlies Postnatal Neurogenesis in the Enteric Nervous System. The Journal of Neuroscience.
766 2015;35(27):9879-88.
767 52. Uesaka T, Okamoto M, Nagashimada M, Tsuda Y, Kihara M, Kiyonari H, et al. Enhanced
768 enteric neurogenesis by Schwann cell precursors in mouse models of Hirschsprung disease. Glia.
769 2021;69(11):2575-90.
770 53. Zhang P, Sun Y, Ma L. ZEB1: at the crossroads of epithelial-mesenchymal transition,
771 metastasis and therapy resistance. Cell Cycle. 2015;14(4):481-7.
772 54. Singh S, Howell D, Trivedi N, Kessler K, Ong T, Rosmaninho P, et al. Zeb1 controls neuron
773 differentiation and germinal zone exit by a mesenchymal-epithelial-like transition. eLife.
774 2016;5:e12717.

775 55. Gupta B, Errington AC, Jimenez-Pascual A, Eftychidis V, Brabletz S, Stemmler MP, et al. The
776 transcription factor ZEB1 regulates stem cell self-renewal and cell fate in the adult hippocampus. Cell
777 Reports. 2021;36(8):109588.
778 56. Imayoshi I, Sakamoto M, Yamaguchi M, Mori K, Kageyama R. Essential roles of Notch
779 signaling in maintenance of neural stem cells in developing and adult brains. The Journal of
780 Neuroscience. 2010;30(9):3489-98.
781 57. McCallum S, Obata Y, Fourli E, Boeing S, Peddie CJ, Xu Q, et al. Enteric glia as a source of
782 neural progenitors in adult zebrafish. Elife. 2020;9.
783 58. Okamura Y, Saga Y. Notch signaling is required for the maintenance of enteric neural crest
784 progenitors. Development. 2008;135(21):3555-65.
785 59. Lewis MD, Francisco AF, Jayawardhana S, Langston H, Taylor MC, Kelly JM. Imaging the
786 development of chronic Chagas disease after oral transmission. Scientific Reports. 2018;8(1):11292.
787 60. Schmittgen TD, Livak KJ. Analyzing real-time PCR data by the comparative CT method.
788 Nature Protocols. 2008;3:1101.

789

790 Acknowledgements

791 We thank Hernán Carrasco for sharing parasite strains, Jody Phelan for helping with R scripts and the
792 LSHTM Biological Services Facility staff for technical support and animal husbandry. The work was
793 funded by an MRC New Investigator Research Grant (MR/R021430/1) and an EU Marie Curie
794 Fellowship (grant agreement no. 625810).

795 **Figure 1**

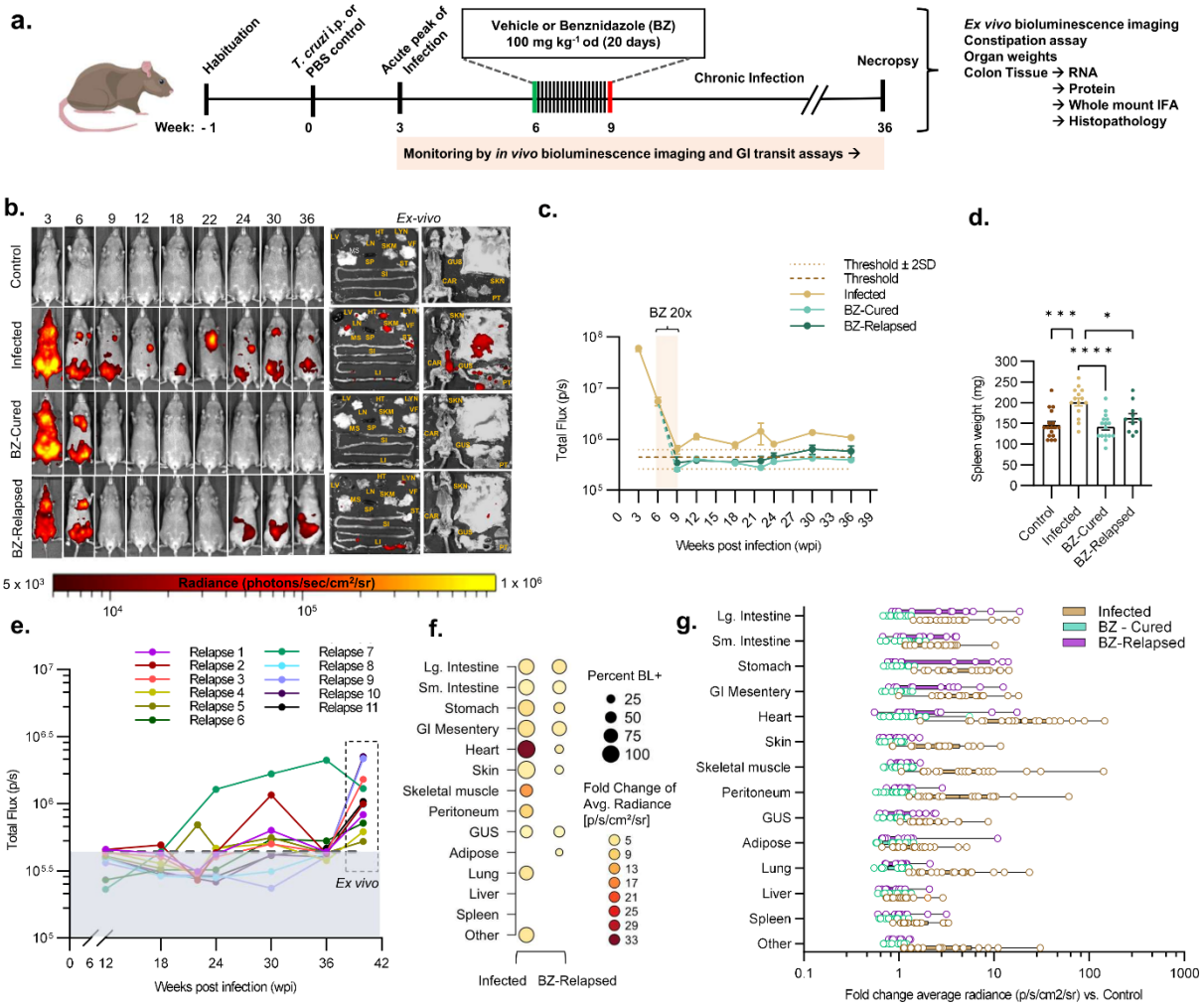

796

Figure 2

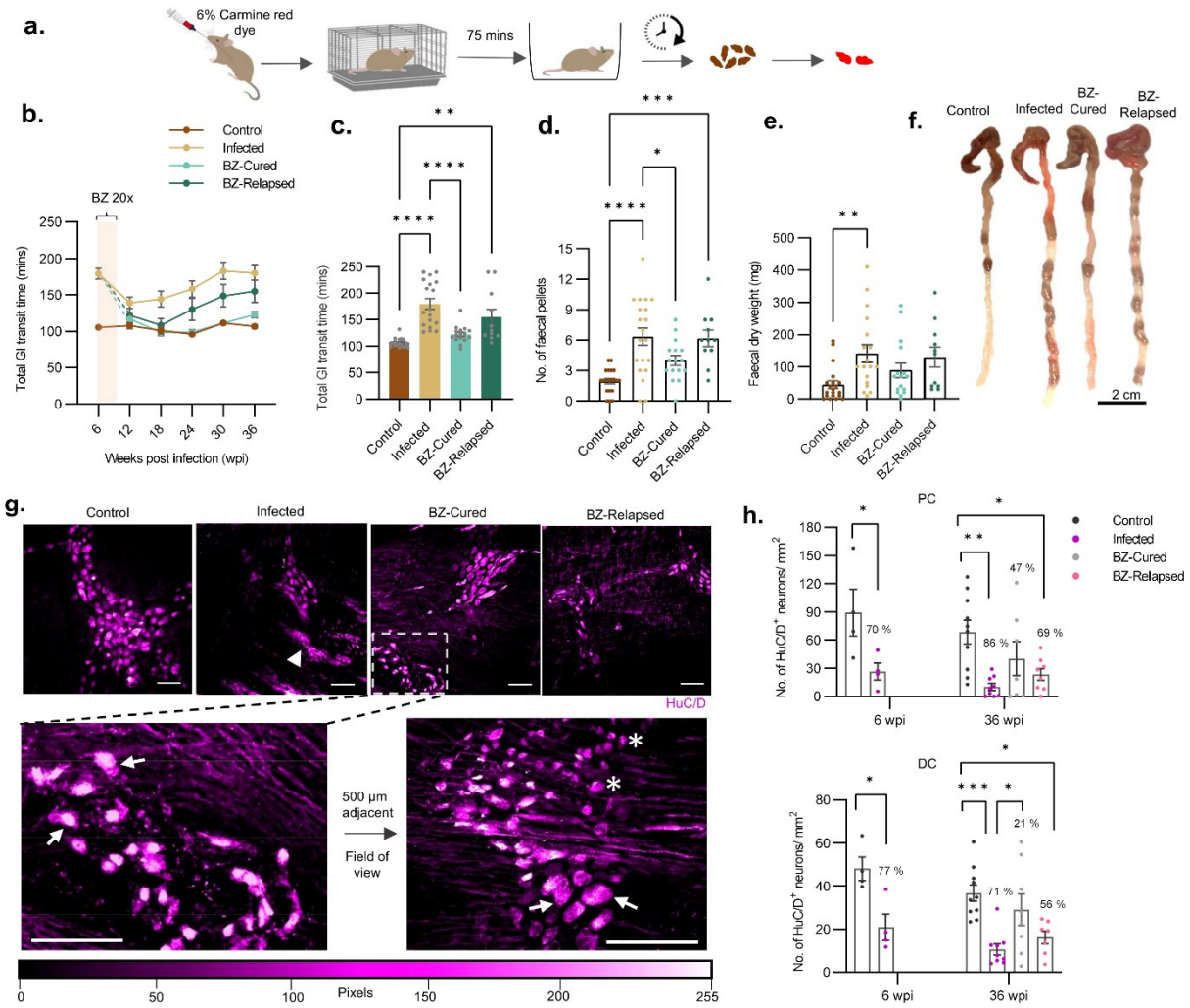

Figure 3

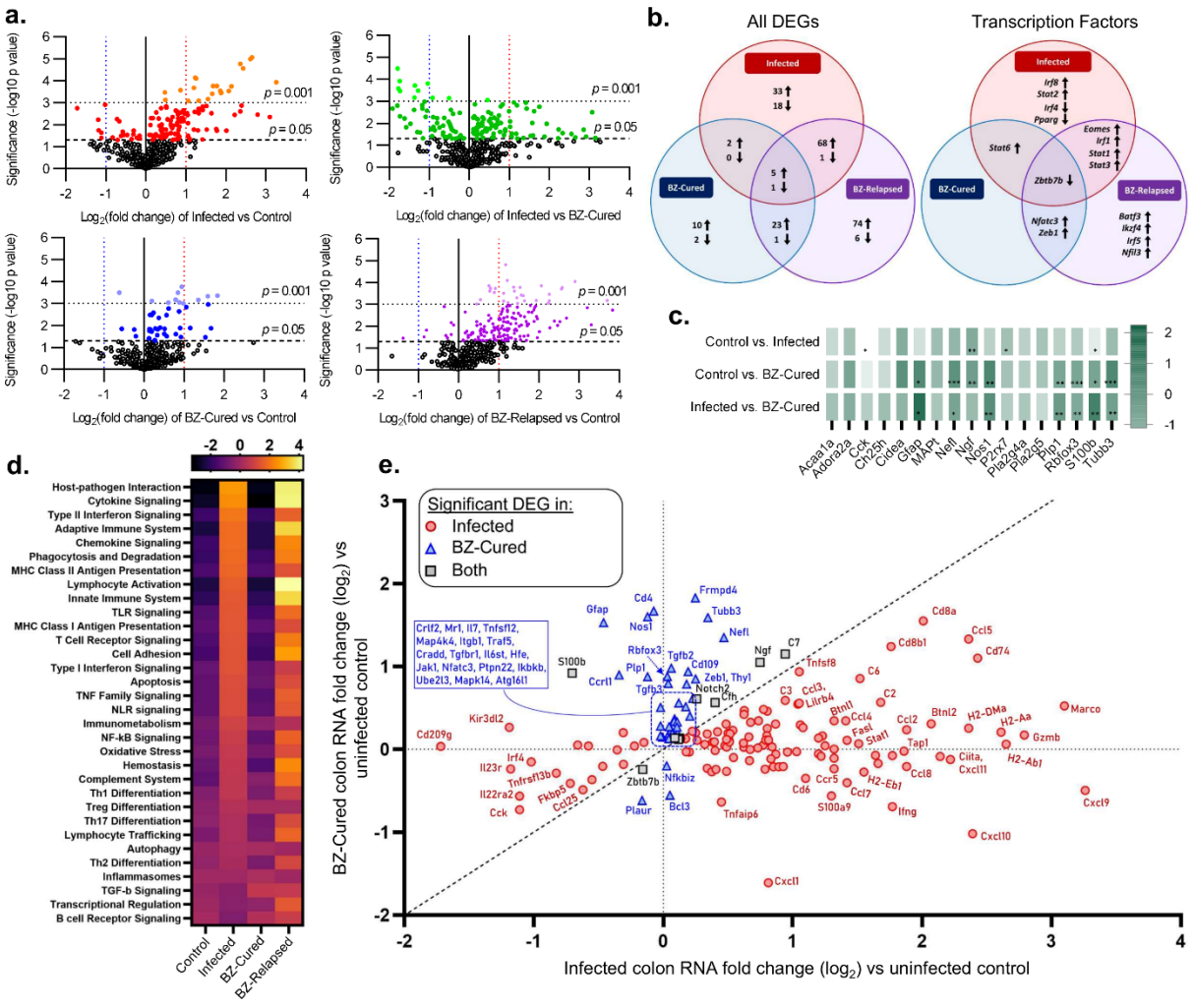

801 **Figure 4**

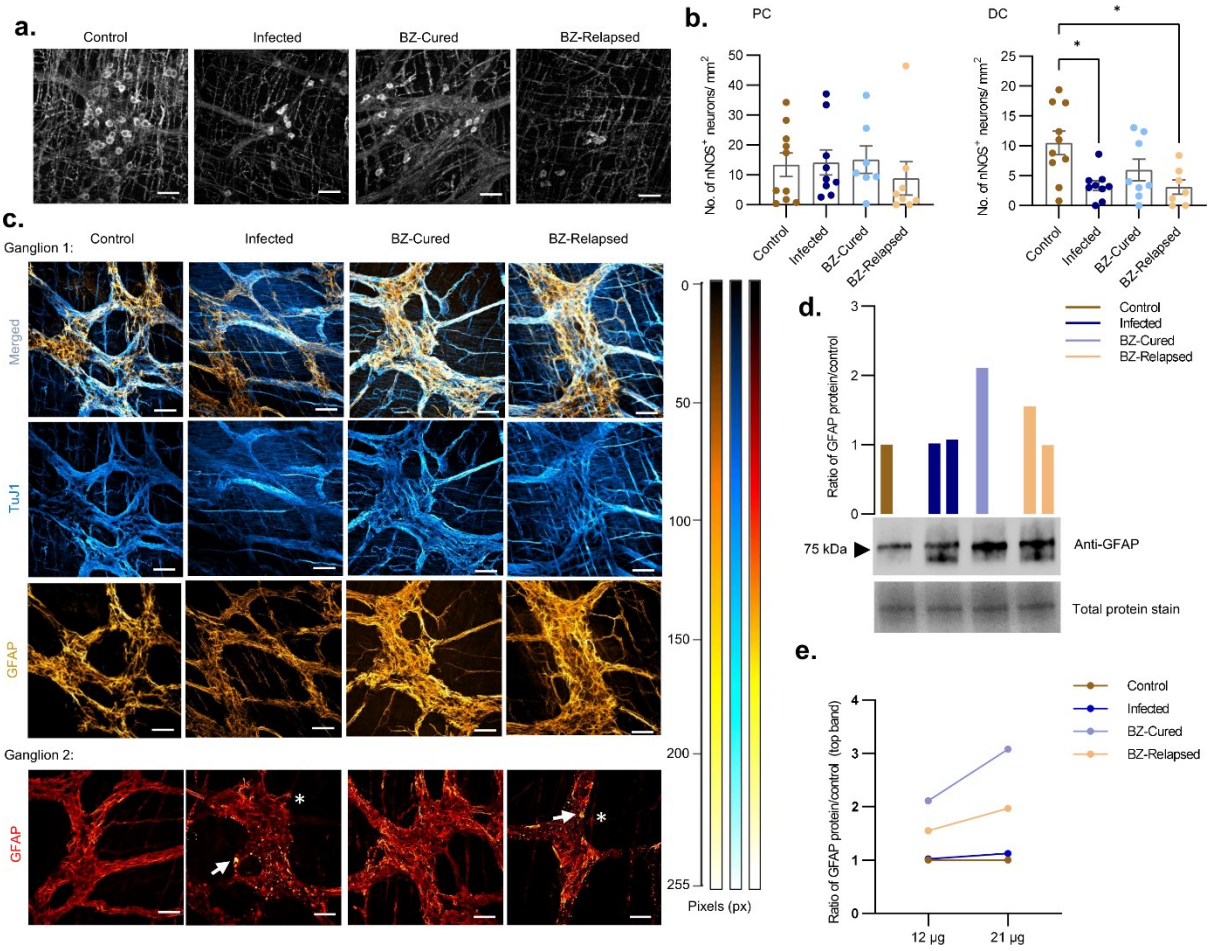

802

803 **Figure 5**

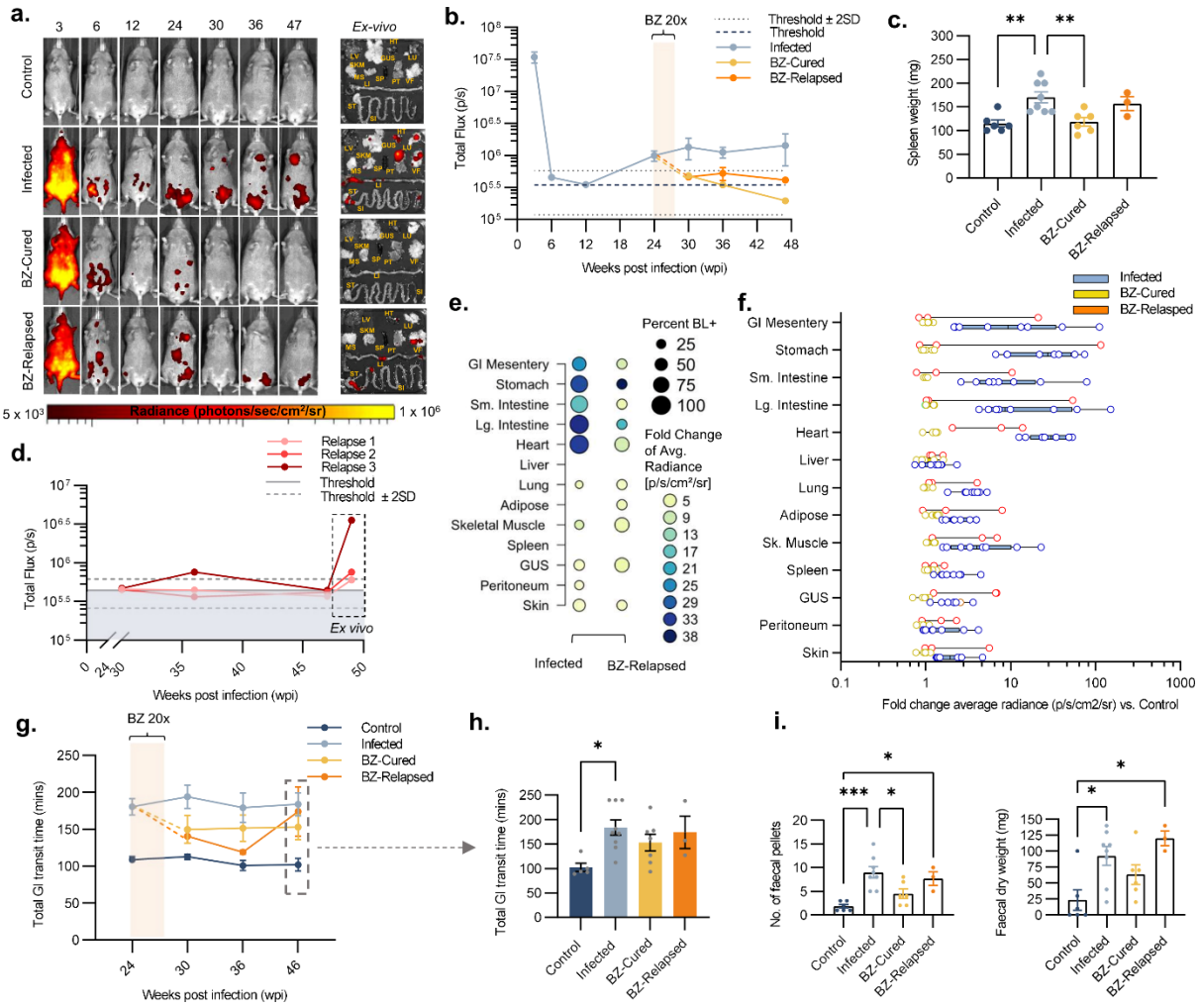

804

Extended Data

Extended Data Figure 1: Additional GI assays after benznidazole treatment initiated at 6 weeks post-infection. a, Body weight line plots of control (*n* = 15; except *n* = 10 at 3, 6, 9, 22 and 36 wpi), infected (*n* = 10, except *n* = 25 at 0 and 3 wpi, and *n* = 24 at 6 wpi), benznidazole treated and cured (BZ-Cured; *n* = 7, except *n* = 8 at 9, 12 and 18 wpi) and benznidazole treated and relapsed (BZ-Relapsed; *n* = 5) mice. Cream bar on line plots show benznidazole treatment window (6 - 9 wpi). Bar plots show **b,** GI mesentery **c,** caecum **d,** stomach and **e,** wet faecal pellet weight of control (*n* = 20), infected (*n* = 18), BZ-Cured (*n* = 16) and BZ-Relapsed (*n* = 11) mice. **f,** Average daily water and, **g,** food intake per mouse of uninfected control (*n* = 2 cages, 10 mice), infected (*n* = 4 cages, 20 mice) and BZ-treated (*n* = 6 cages, 30 mice) mice over two weeks (35 – 37 wpi). **h**, Representative brightfield images of 5 µm thick colon transverse sections stained with haematoxylin-eosin (mucosa bottom; smooth muscle layers top). Images were taken at 400X magnification, scale bar at 50 µm. **i**, Adjacent bar plot shows number of nuclei per field to quantify cellular infiltration in control (*n* = 7), infected (*n* = 7), BZ-Cured (*n* = 8) and BZ-Relapsed (*n* = 6) mice. End-point data **b, c, d, e, h** and **i** are from 36 wpi. Statistical significance was tested using one-way ANOVA followed by Tukey's HSD test (**P* < 0.05).

Extended Data Figure 2: Pre-treatment characteristics and relapse kinetics after benznidazole treatment initiated at 6 weeks post-infection. a-c, Bar plots show characteristics of BZ-Cured (*n* = 18) and BZ-Relapsed (*n* = 11) mice retrospectively segregated at the point of treatment initiation (6 weeks post-infection (wpi)): **a,** body weight; **b,** bioluminescence intensity (total flux); and **c,** GI transit time. **d, e,** Comparison of parasite load (expressed as total flux) and transit time in BZ-Relapsed (*n* = 11) mice. The dot plot (d) shows pairwise correlation for all time points for individual animals, while the line plot (e) shows the group mean (+/- SEM) for bioluminescence (red line, left y axis) and transit time (blue line, right y axis) over time. Experimental end-point was at 36 wpi. Statistical significance was tested using one-way ANOVA followed by Tukey's HSD test (**P* < 0.05, ***P* < 0.01, ****P* < 0.001, **** *P* < 0.0001).

Extended Data Figure 3: Gene expression analysis of immunoregulatory and neuro-glial genes. a, Pathway level analysis of immunoregulatory differential gene expression (*n* = 4 all) and **b,** qPCR analysis of additional neuronal and glial cell marker gene expression (*n* = 4 all). All mice were treated with benznidazole at 6 weeks post-infection (wpi) and RNA was extracted from colon tissue harvested at 36 wpi.

Extended Data Figure 4: Analysis of differential gene expression in post-treatment relapsed infections. a, Volcano plot of the $\log_2$-transformed fold change and significance ($-\log_{10}$ *p* value) of differentially expressed genes (DEGs) in colon tissue from infected vs. benznidazole-treated relapsed (BZ-Relapsed) mice. **b,** Heat maps show relative change in neuro-glial genes between BZ-Relapsed vs. control (uninfected) or infected groups. Colour intensity indicates fold change ($\log_2$) expression level. **c,** Comparison of directionality and extent of gene expression change in infected and BZ-Relapsed mice vs controls (*n* = 230 genes that are significant DEGs in at least one group). Red circles are DEGs specific to the infected group, purple triangles are DEGs specific to the BZ-Cured mice and grey squares are DEGs shared by both groups. Diagonal dashed line is the line of equivalence. Vertical and horizontal dashed lines indicate position for genes with identical expression levels as controls in infected and BZ-Relapsed mice respectively. Infected and controls *n* = 6, BZ-Relapsed *n* = 3. All mice were treated with benznidazole at 6 weeks post-infection and RNA was extracted from colon tissue harvested at 36 wpi. Statistical significance was determined by 2-tailed, unpaired Student's *t*-test for each gene (**P* < 0.05, ***P* < 0.01, ****P* < 0.001, **** *P* < 0.0001).

Extended Data Figure 5: Additional GI assays after benznidazole treatment initiated at 24 weeks post-infection. a, Line plots show body weight of control (*n* = 5, except *n* =10 at 0, 3 and 24 weeks post-infection (wpi)), infected (*n* = 9, except *n* = 25 at 0 and 3 wpi, *n* = 20 at 6 wpi, *n* = 23 at 12 wpi, and *n* = 22 at 24 wpi), benznidazole treated cured (BZ-Cured; *n* = 7) and benznidazole treated relapsed (BZ- relapsed; *n* = 3) mice. Overlaid cream bar shows the BZ treatment window (24 - 27 wpi, 20 daily doses). Bar plots show **b,** mesentery, **c,** stomach **d,** caecum and **e,** faecal wet weight of control (*n* = 5), infected (*n* = 8), BZ-Cured (*n* = 3 - 6) and BZ-Relapsed (*n* = 3) mice at 36 wpi. Statistical significance was tested using one-way ANOVA followed by Tukey's HSD test (***P* < 0.01).

Extended Data Figure 6: Pre-treatment characteristics of relapses compared with cures for benznidazole treatment initiated at 24 weeks post-infection. Bar plots show characteristics of benznidazole treated and cured (BZ-Cured, *n* = 7) and benznidazole treated and relapsed (BZ-Relapsed, *n* = 3) mice retrospectively segregated at the point of treatment initiation (24 weeks post-infection (wpi)): **a,** body weight; **b,** bioluminescence intensity (total flux) and **c,** total GI transit time.

869 **Extended Data Figure 1**

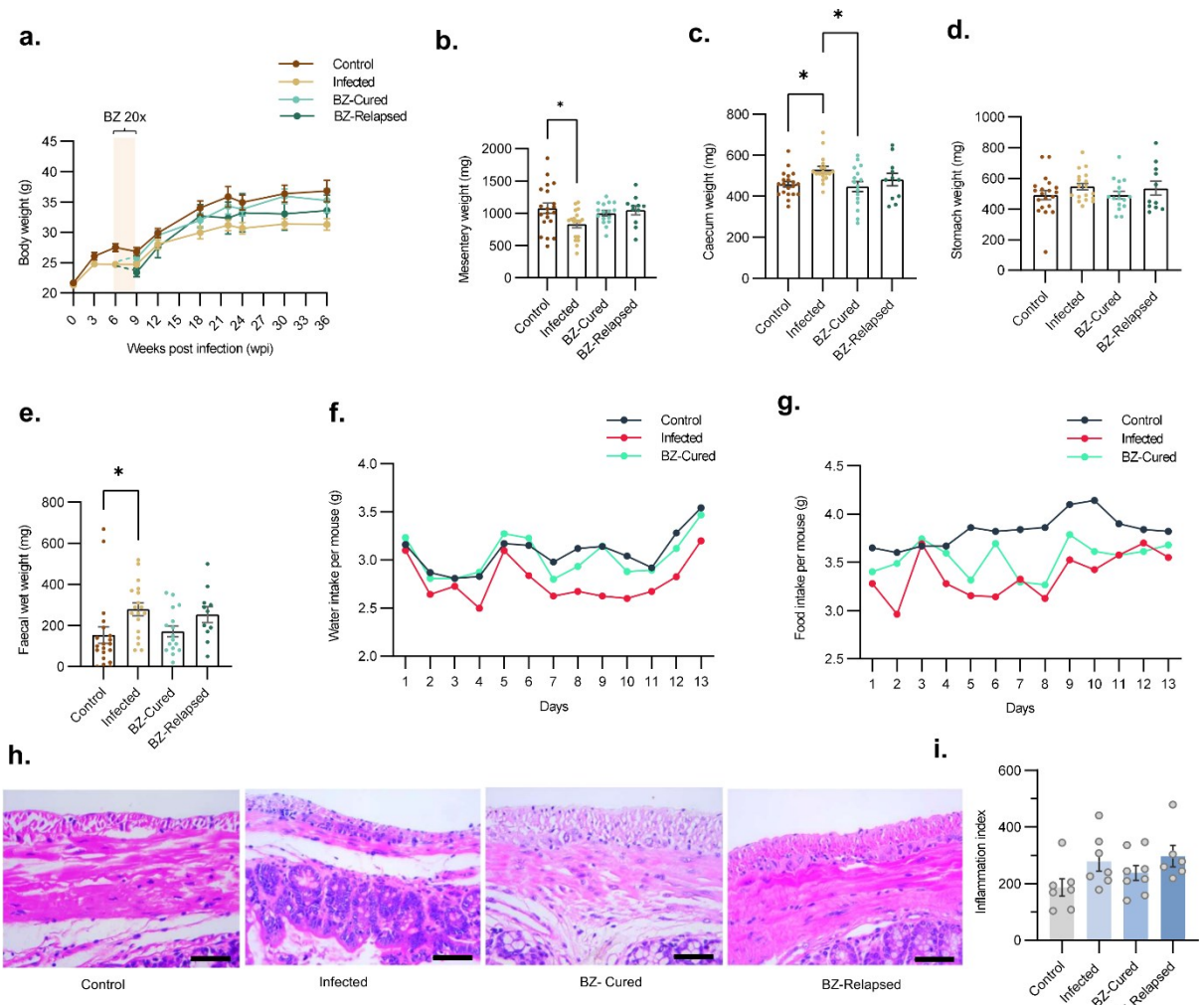

870

871 **Extended Data Figure 2**

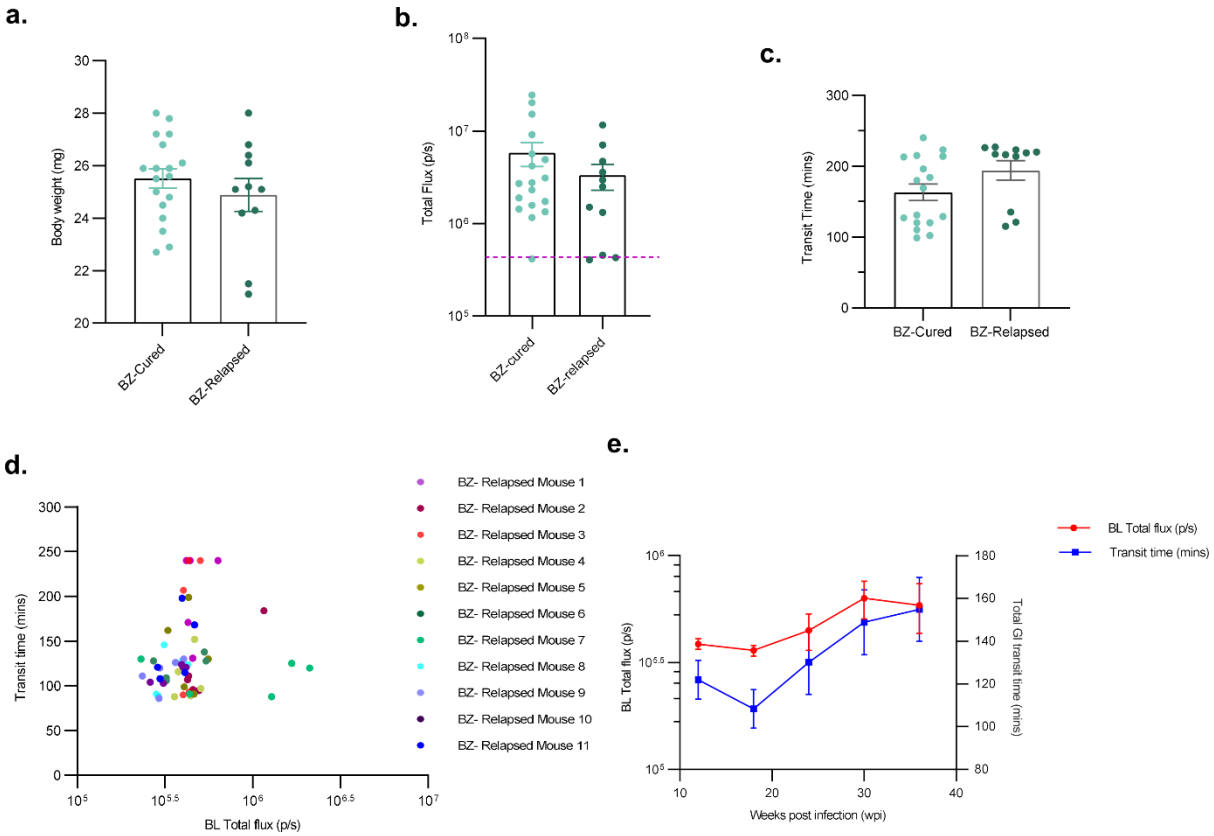

872

873 **Extended Data Figure 3**

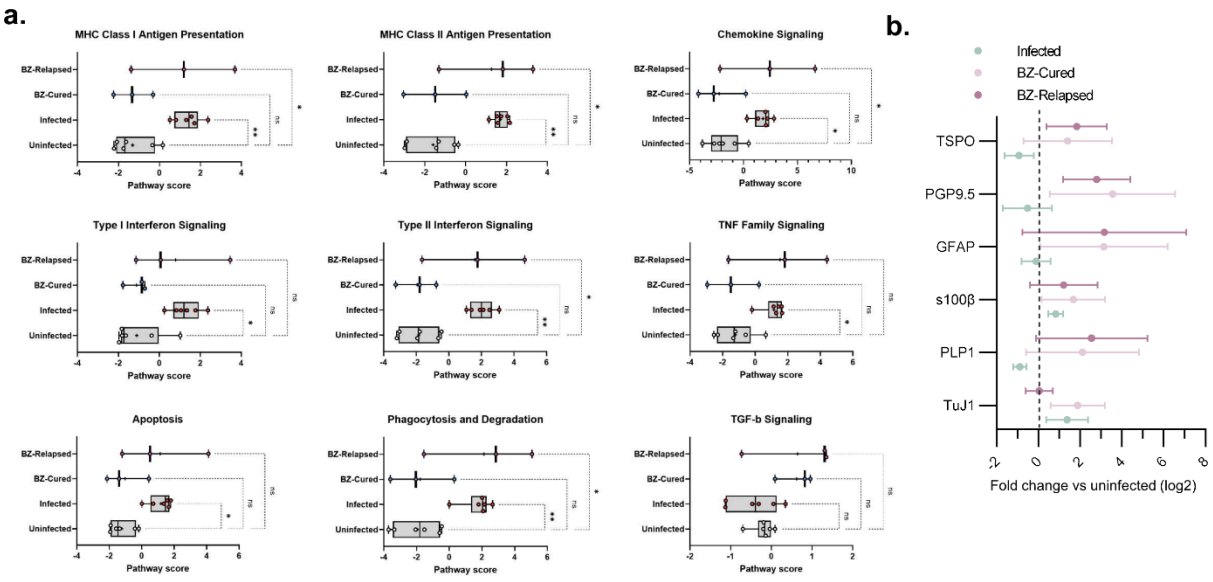

874

Extended Data Figure 4

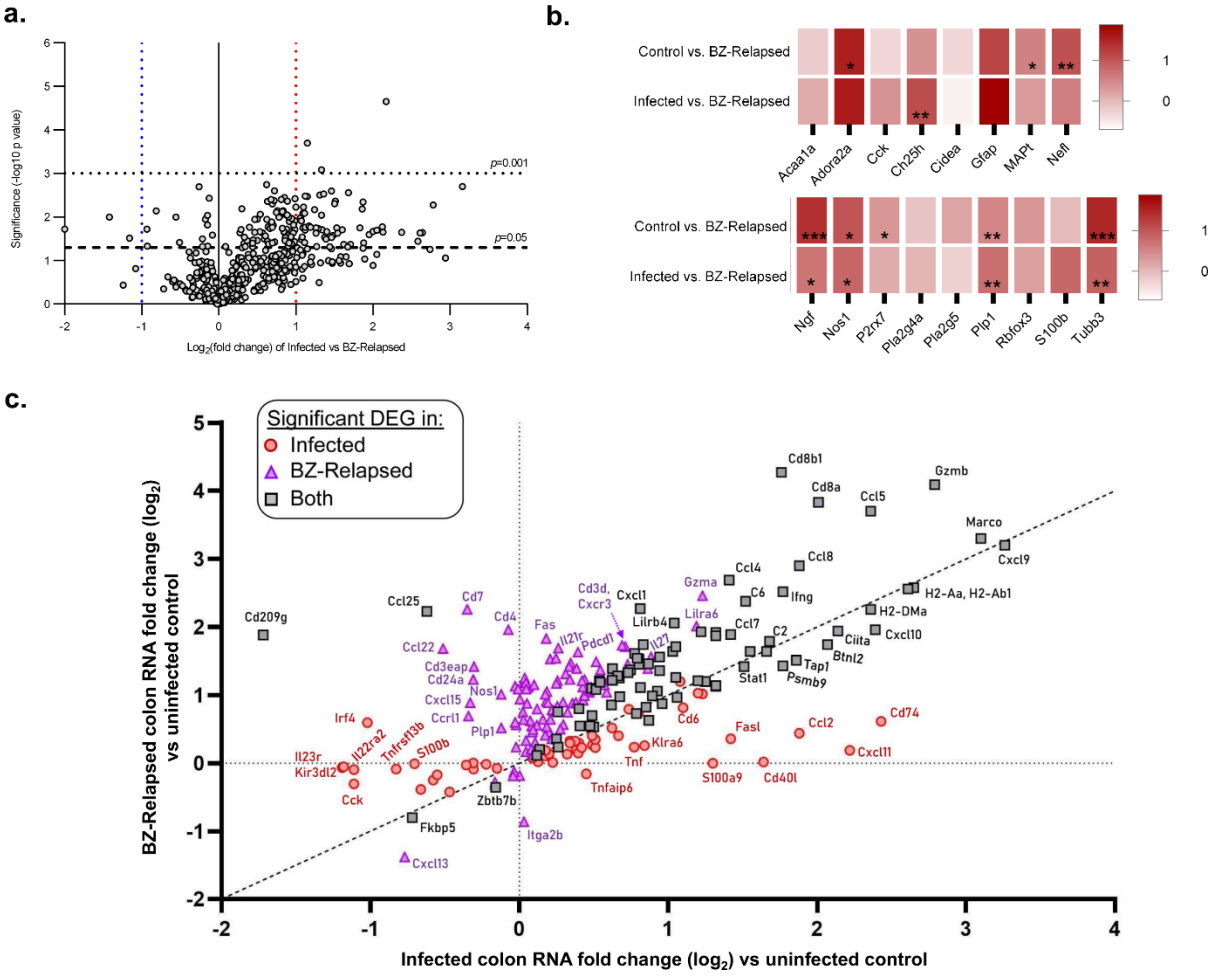

877 **Extended Data Figure 5**

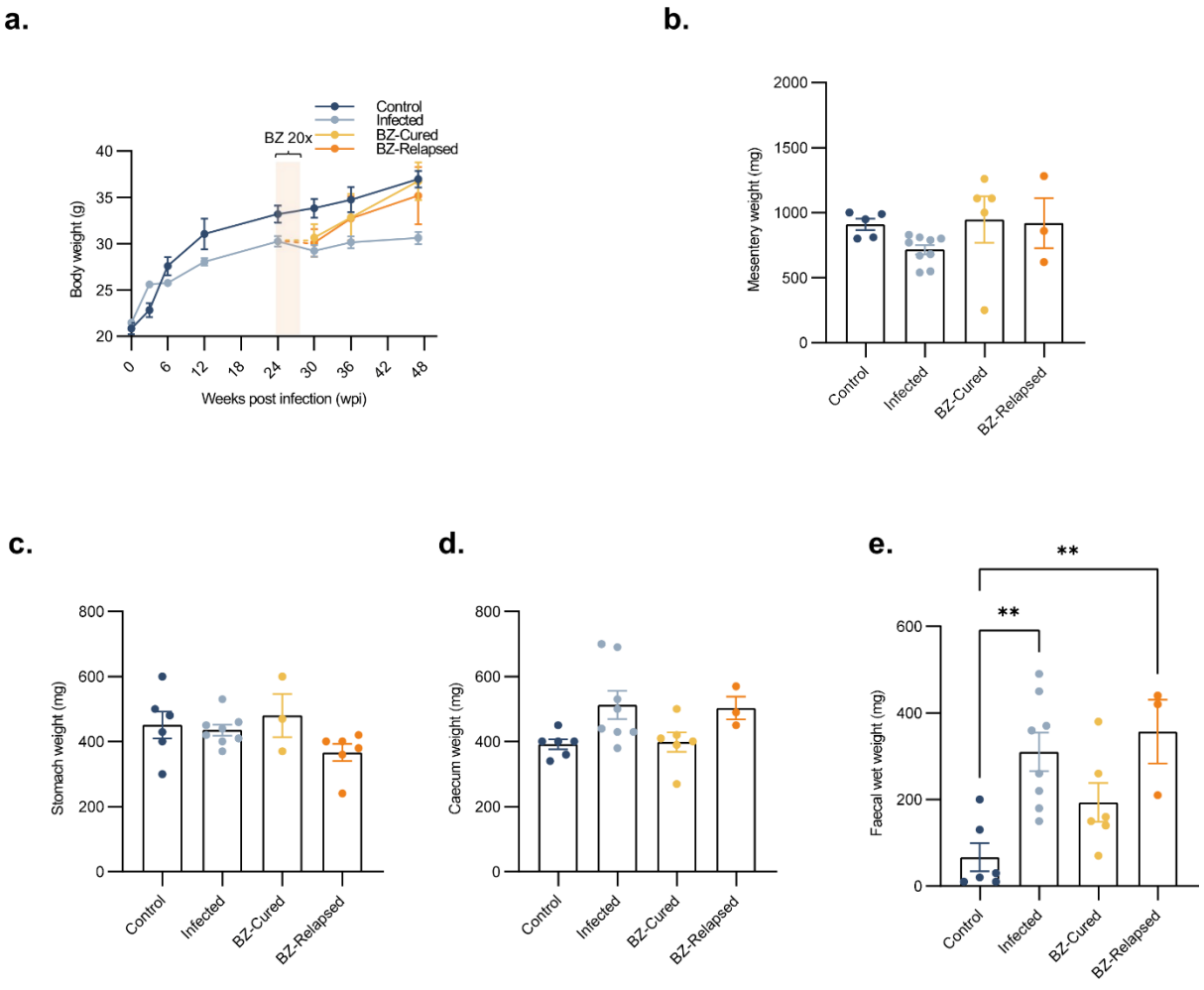

878

879 **Extended Data Figure 6**

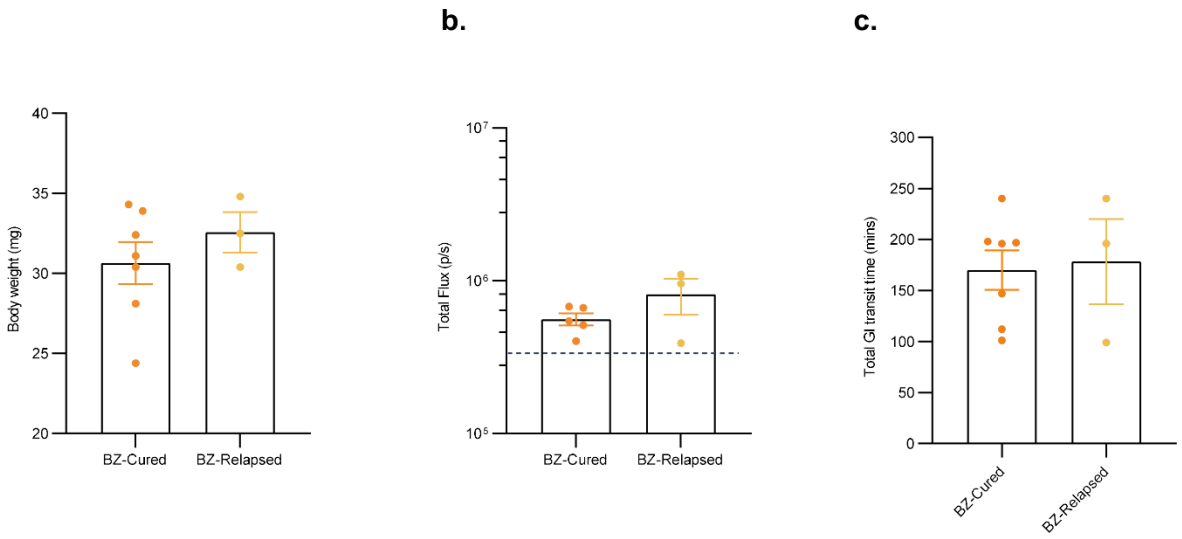

880

881

882 **Supplementary Table 1: qPCR experiment primer design.**

Gene	Forward Primer (5'-3')	Reverse Primer (5'-3')	Amplicon Size (bp)
Oaz1	GTGGTGGCCTCTACATCGAG	AGCAGATGAAAACGTGGTCAG	120
TuJ1	CAGGGCCATTCTGGTGGACT	TAGTGCCCTTTGGCCCAGTT	135
Gfap	GCAAGAGACAGAGGAGTGGT	CTCTTCCTGTTCGCGCATTT	196
Plp1	GGCGACTACAAGACCACCAT	CAAACTTGTCGGGATGTCCT	154
Tspo	ACTGTATTCAGCCATGGGGTA	ACCATAGCGTCCTCTGTGAAA	75
S100b	GACTCCAGCAGCAAAGGTGAC	CATCTTCGTCCAGCGTCTCCA	228
PGP9.5 (Uchl1)	CCTGTGGTACCATCGGGTTG	GGCTCTATCTTCGGGGGACA	125

883

3.3 Adult Neurogenesis Frameworks for ENS Repair and Regeneration in the DCD Model

There is a dogma that the development of neurons, or neurogenesis, does not occur in humans after 2 years of birth (18). This means that neurons are a canonical terminally differentiated cell type, and dead neurons could not be replaced. More recently it has been recognised that adult neurogenesis is possible but is still considered very limited (19). In the CNS the predominant source of adult neurogenesis is differentiation of radial glial-like stem cells (Fig3.3.1).

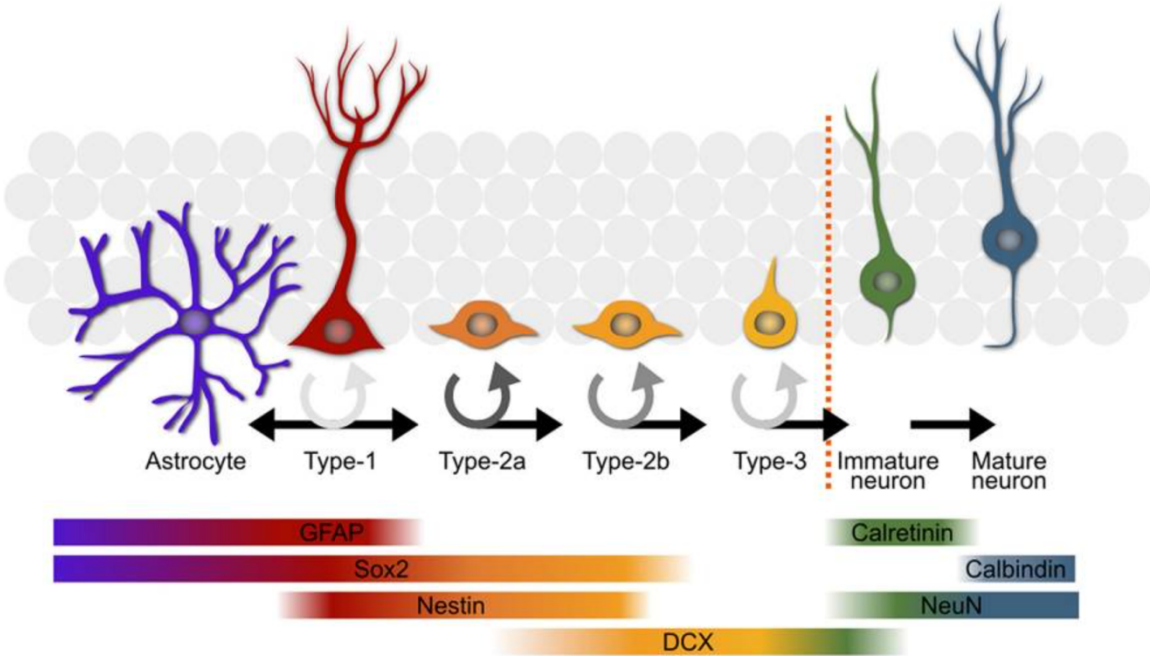

Figure 3.3.1. Overview of commonly used model of adult hippocampal neurogenesis.
Different colours represent different cell types. Type-1 stem cell (red) can directly produce astrocytes (purple) or generate progenitor cells (orange/yellow) which occur in successive stages become becoming mature neurons (blue) or are eliminated via apoptosis. The black horizontal arrows dictate which direction differentiation occurs, whereas the circular arrows represent proliferation rate. The darker the circular arrow, the more proliferative a population is. The key biomarkers for each stage correspond with the expression in different cell types, indicated by colour. Glial fibrillary acidic protein (GFAP) is an intermediate filament protein, SOX2 is a transcription factor that maintains pluripotency of stem cells, nestin is a type XI filament protein, doublecortin (DCX) is microtubule protein expressed by neuronal pre-cursor cells, calretinin is a calcium binding protein expressed on nueral cells, calbindin protects from apoptotic cell death, NeuN is a marker for postmitotic neurons.

Figure adapted from R.W. Overall et al., 2016 (19)

It has been proposed that enteric neurons can also be replaced or replenished in a process involving neuronal stem cells as part of gut homeostasis (20). There is good evidence that glial cells and enteric neurons share the same the neurogenic pre-cursors and can act as neurogenic precursors by reactivating neurogenic transcriptional programmes in response to injury (Fig. 3.3.2) (21).

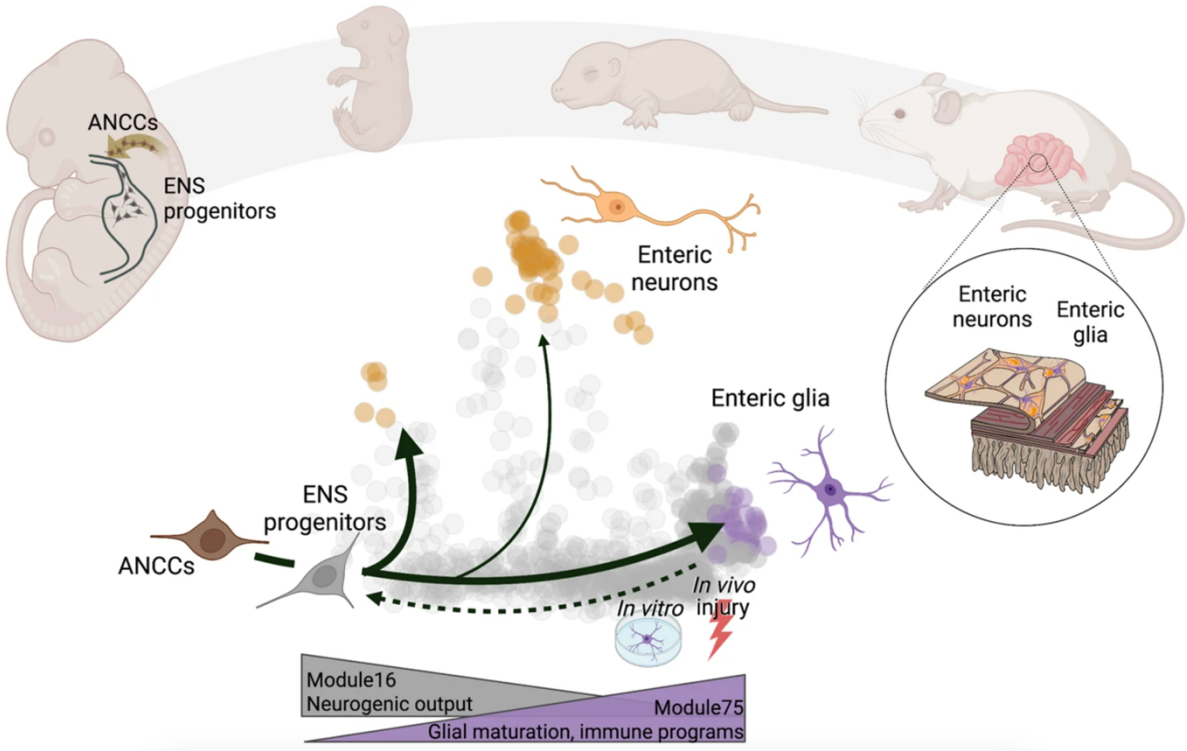

Figure 3.3.2. Branching model of lineage decisions in the enteric nerous system underpinning the neurogenic potential of adult glia. Autonomic neuronal crest cells (ANCCs) become enteric nervous system (ENS) progenitors upon invasion of the foregut. A default differentiation trajectory results in mature enteric glia formation, indicated by the horizontal curved black arrow. From this trajectory are other branches which occur at different timepoints during embryonic and early postnatal periods. Regulation levels of transcription modules are indicated by either grey or purple triangles, with gene module (GM) 16, which underlies active neurogenic activity becoming downregulated, whereas those related to glial maturation and immune function (GM75) are upregulated. The dotted line is of particular interest in the context of this study, as it suggests reverse of de-differentiation of glia response as they can transit upstream of their developmental axis in response to injury.

Figure adapted from A. Laddach et al., 2023. (73)

In the attached pre-print (Khan et al., 2022) an upregulation of *Ngf* and *Notch,* two critical regulators for neurogenesis, was observed in DCD mice after benznidazole treatment. Notch1 signalling, in particular, has been implicated in neuronal progenitor maintenance and the orchestrating of the glial-to-neuronal differentiation axis, in the CNS (22) and gut (23).

The extent by which the adult ENS is capable of repairing and regenerating in response to varying challenges is a fundamental question. In the attached preprint there was also an observed recovery in myenteric plexus neuron numbers, months after benznidazole-mediated cure of *T. cruzi* infection. However, the experimental approach did not allow us to define the ontogeny of new neurons.

The two key questions to expand on these findings are:

1. Do the neurogenic pre-cursors in our DCD model differentiate directly, or does the process involve cell division?
2. Are glial cells the neurogenic pre-cursors?

3.4. Objectives

Using the TcIJR-C3H model, the objective is to investigate how anti-parasitic benznidazole treatment affects DCD outcomes in terms of peristalsis function and neuro-muscular tissue damage and repair processes.

I. Transit time assays and *in vivo* imaging will be conducted to track peristalsis function and parasite burden respectively.
II. Benznidazole treatment will be employed from week 6 of infection for 20 days to suppress or cure the infection.
III. 5-ethynyl-2′-deoxyuridine (EdU) will be administered to label proliferative cells, with injections to be carried out periodically after treatment is complete.
IV. Immunofluorescence assays will be used to assess retrospective cellular replication within the myenteric plexus as a marker of post-treatment tissue repair or regeneration.

3.5 Methods and materials

Murine infections and bioluminescence imaging

Parasites

The study used aliquots of frozen tissue culture trypomastigotes (TCTs), of the TcI-JR strain of *T. cruzi* (JR-LUC) parasites that express the red-shifted firefly luciferase variant *PPy*RE9h, as previously described (24). Parasites were thawed at room temperature, sedimented by centrifugation at 10,000x *g* for 5 minutes, washed in 1ml complete media (MEM media, +5% FBS, +PenStrep) at 37^{o}C, sedimented and resuspended in 250ul complete medium. After 1-hour incubation at 37^{o}C, active (motile) parasites were counted using a haemocytometer and the population density was adjusted using PBS to the required concentration.

Animals and infections

All animal work was performed under UK home office project licence (PPL P9AEE04E4) and approved by the LSHTM Animal Welfare Ethical Review Board. Procedures were in accordance with the UK animals (Scientific procedures) Act 1986 (ASPA).

Female C3H/HeN and CB17 SCID mice were purchased from Charles River (UK). Animals were maintained under specific pathogen-free conditions in individually vented cages (no more than 6 per cage at any time, no fewer than 2). Animals experienced a 12-hour light/dark cycle, with access to food and water *ad libitum*. Prior to treatments, cage bedding of C3H/HeN mice was redistributed to equalise the microbiome between the mice and reduce any cage effects brought about by

separate housing. All mice were subject to the same extrinsic factors (handling time, time under anaesthesia, and time outside their respective cages).

This data in this chapter derive from two independent experiments. In both cases, SCID mice were inoculated with $2x10^4$ (n=1) and $4x10^4$ (n=1) JR-LUC thawed TCTs in 0.2ml d-PBS via intraperitoneal (I.P) injection. At 21 days post infection, bloodstream form trypomastigotes (BTs) were harvested from the SCID mice via cardiac bleed under terminal anaesthesia. Harvested parasites were used to infect C3H/HeN mice (6-8 weeks old) at $1x10^3$ BTs in total diluted in PBS, via I.P. injection.

At experimental end-points, mice were sacrificed by a lethal dose of Dolethal (Pentabarbital sodium 1000 mg kg^{-1} i.p.), followed by exsanguination or cervical dislocation as a secondary confirmatory method.

***In vivo* bioluminescence imaging**

Mice were injected with 150 mg kg^{-1} d-lucerfin I.P., and anaesthetized using 2.5% (v/v) gaseous isoflurane before being and placed in an IVIS spectrum (PerkinElmer). Mice were imaged every 3 weeks ± 1 week, from the first week of infection. Image acquisition settings were dependent on signal intensity and set to maximise signal while preventing saturation. Exposure time: 1-5 minutes; binning: small, medium or large. After imaging, mice were placed in a tub on a heat pad for recovery from anaesthesia and then returned to cages. Bioluminescence was quantified using regions of Interest (ROI) created by polygon tools on Living Image 4.7.4. Whole body total flux (photons sec^{-1}) was the primary read-out of interest, as an estimate of the *in vivo* parasite burden.

Ex vivo bioluminescence imaging

Food was withdrawn from the cages for 2.5 hours prior to euthanasia. 7 minutes before euthanasia, mice were injected with 150 mg kg^{-1} d-luciferin I.P. During necropsy, the caecum, stomach, mesentery adipose and, in some cases, brain were placed in a light refractory 24 well plate with 1ml of d-lucerfin. Plates were imaged in the IVIS spectrum (PerkinElmer) under the same conditions as described for *in vivo* imaging. Total flux (photons sec^{-1}) was quantified for each organ, by drawing same sized ROI for each well, using Living Image 4.7.4.

Total GI transit time assay

6% carmine red dye working solution was made with 0.5% methyl cellulose (w/v) in distilled water, sonicated and kept at room temperature – as previously described (16) Carmine solution was administered to mice via oral gavage (0.2 ml), before returning them to their cages for 60 minutes rest, after which they were placed into individual containers and observed. The difference between the time of gavage and the passing of the first red stained faecal pellet was calculated as the total GI transit time. The maximum cut off for the assay was 4 hours, employed for isolation concerns and welfare of the mice.

Benznidazole treatment

Benznidazole was prepared from powder at 10 mg ml^{-1} by dissolving in HPMC vehicle solution (0.5 % w/v hydroxypropyl methylcellulose, 0.5% v/v benzyl alcohol, 0.4% v/v Tween 80 in deionised water). Benznidazole was administered via oral gavage at a dose concentration of 100 mg kg^{1}, daily for 18 successive days in experiment 1, and 20 successive days in experiment 2.

Cure and Relapse Criteria

Relapsed infections were identified during *in vivo* bioluminescence imaging by the clustering of 10 or more contiguous pixels anywhere on the body at a minimum luminescence threshold of 5 x 10^3 p/s/cm^2/sr. The luminescence threshold was then reduced to 3 x 10^3 p/s/cm^2/sr and if the clustering of pixels expanded (consistent with light emission from an infection focus source), relapse was confirmed. To further confirm *in vivo* identified relapses, *ex vivo* bioluminescence imaging during necropsy was used. For mice with undetectable bioluminescent signal *in vivo*, if a cluster of 10 or more pixels were observed in any tissue sample at a luminescence threshold of 5 x 10^3 p/s/cm^2/sr , the mice were identified as relapsed, and confirmed at a threshold of 3 x 10^3 p/s/cm^2/sr. These thresholds were established based on the levels of auto-luminescence background signal in uninfected control mouse images.

***In vivo* 5-Ethynyl-deoxyuridine (EdU) pulsing**

An EdU stock was made to 2.5 mg ml^{-1} in Dulbecco's PBS, aliquoted to 4ml and kept at -20^{o}C until ready to use. In experiment 1, EdU was administered via I.P. injection, 0.2ml [25 mg kg^{-1}] on two successive days in weeks 10, 12 and 16 post infection. In experiment 2, EdU was administered at [25 mg kg^{-1}] at weeks 9, 10 and 11 post infection, with doses on two successive days for each week. The protocol was modified from a previously described method (25) whereby the labelling target was replicating parasites, compared to host cells here.

Preparing tissue for cryosectioning

During necropsy, 1 cm of distal colon was transferred to paraformaldehyde (4% w/v in PBS) and fixed overnight. Fixed tissue was washed in a sucrose washing solution

(15% d-sucrose w/v, 0.01% azide) before being stored in storage sucrose solution (30% d-sucrose w/v, 0.01% azide) and kept at 4^{o}C. Tissue was later embedded for cryosectioning. An embedding solution of sucrose and gelatine (10% w/v, 7.5% w/v in PBS) was warmed to 37 ^{o}C to liquify, and 1ml was pipetted into peel-away moulds before being refrigerated at 4^{o}C for 20 minutes to set. Meanwhile, tissues kept in sucrose solution were washed in PBS for 5 minutes at room temperature to remove excess sucrose. The tissue was gently placed on the hardened gelatine base and covered with molten embedding solution using a cut P1000 pipette tip, ensuring there were no air bubbles and that all the tissue was completely submerged. The embedded tissue block was then returned to 4^{o}C, for 45 minutes to set. 100 ml of ice cold isopentane (2-methyl-butane) was poured into a glass beaker with a thermometer. Dry ice was slowly added until the isopentane was at -40 ^{o}C, and dry ice was added as needed to ensure the temperature was consistent. The embedded tissues were carefully cut out of the moulds with a scalpel and lowered into the isopentane for 1 minute until the gelatin turned pale white. The frozen tissue block was then removed using forceps, wrapped in aluminium foil and kept on dry ice, ensuring the tissue did not thaw out. Embedded tissue blocks were kept at -80^{o}C until sectioning.

Cryosectioning

After calibrating the cryostat at -21 ^{o}C, gelatin embedded tissue blocks were placed inside the cryostat chamber to equilibrate for 30-45 minutes. A drop of optimal cutting temperature compound (OCT) was placed in the middle of the chuck and the tissue block was mounted, ensuring the colon tissue was oriented so that transverse cross-section cuts could be made. More OCT was added to ensure the tissue was

mounted securely and would not detach during cutting. The chuck was cooled in the cryostat chamber for ~ 30 minutes. The chuck was positioned in the chuck holder, and slowly the embedded tissue was trimmed at 100μm per cut, until a full cross-section of tissue was visible. The cryostat was then set to 50μm for sectioning, and successive sections were collected on labelled superfrost microscope slides, with 3 sections adhered per slide. The slides were left to air dry at room temperature for 30 minutes and then stored at -20 ^{o}C until staining.

EdU click reaction.

Slides were taken from -20^{o}C and brought up to room temperature. Tissue sections were marked with a hydrophobic PAP pen-drawn elipse and the hydrophobic barrier was left to dry before continuing. Tissue sections were permeabilised with PBS-T (1% v/v Triton X-100 in PBS) for 45 minutes in a humidity chamber to prevent evaporation. Meanwhile, the EdU labelling solution was made using components from a Click-iT EdU cell proliferation kit according to the manufacturer's instructions (Invitrogen). On ice, 50μl 10x click EdU reaction buffer was added to a 1.5 ml Eppendorf wrapped in foil. 390 μl of deionized water was added and mixed quickly using a pipette tip. 10 μl copper protectant was then added, followed by 1.2 μl of AlexaFlour-555 picolyl azide and finally 50 μl 1x reaction buffer additive. Typically, the labelling solution made was enough for staining 5 tissue sections at 100 μl each. The labelling solution was mixed well and kept on ice, protected from light. After permeabilization, sections were washed in PBS for 5 minutes and stained with the EdU labelling solution for 30 minutes, protected from light in a humidity chamber. Sections were then washed in PBS for 5 minutes ready for downstream immunofluorescence assays.

Immunofluorescence staining

After post-EdU washing, the sections were blocked for 1 hour (10% sheep serum in PBS, 0.5% Triton X-100). Tissues were incubated with primary antibodies: Human "ANNA-1" antisera (anti-Hu), donated by V. Lennon (Mayo Clinic, Rochester MN), used at a dilution of 1:7500, and rat anti-GFAP monoclonal IgG, clone 2.2B10 at 1:500 dilution [Thermofisher] in PBS-T (PBS, 0.1% Triton X-100) for 4 nights in a humidity chamber at 4^{o}C. Tissues were washed with PBS for 45 minutes, with 3 changes, then incubated with secondary IgG: goat anti-human IgG AlexaFluor647 and donkey anti-rat IgG AlexaFluor488, both at 1:500 in 0.1% PBS-T. Tissues were incubated for 1 hour at room temperature, kept dark, before a final 15 minute PBS wash. Tissue was DNA counterstained with Hoechst 33342 (1 μg ml^{-1}) for 30 minutes and mounted with a glass coverslip using FluorSave mounting medium (Merck). Antibody control samples were not subject to primary antibody, only secondary.

Tissue sections were examined and imaged using the LSM880 confocal microscope, using 20X and 40X objectives. Images were captured as Z-stacks of 12 digital slices of 2μm. Post-image compression was performed on FIJI software. A total of 10 Z-stacks were taken per mouse. EdU counts and co-localisation events were determined on each individual slice of a z-stack, with the z-stack being compressed to confirm co-localisation and to create representative images.

3.6 Results

3.6.1 Experimental plans

The aim of the study was to investigate what effect benznidazole treatment would have on digestive chagas disease manifestations, informed by use of transit time assays, and the cellular basis of post-treatment neurogenesis. To explore the treatment effect on total GI transit time, I first designed a chronic experiment where C3H/HeN mice were infected with 1x10^{3} Tcl-JR parasites, with a cohort being treated with benznidazole at 100 mg kg $^{-1}$ from week 6 post infection for 18 consecutive days (Fig. 3.6.1a).

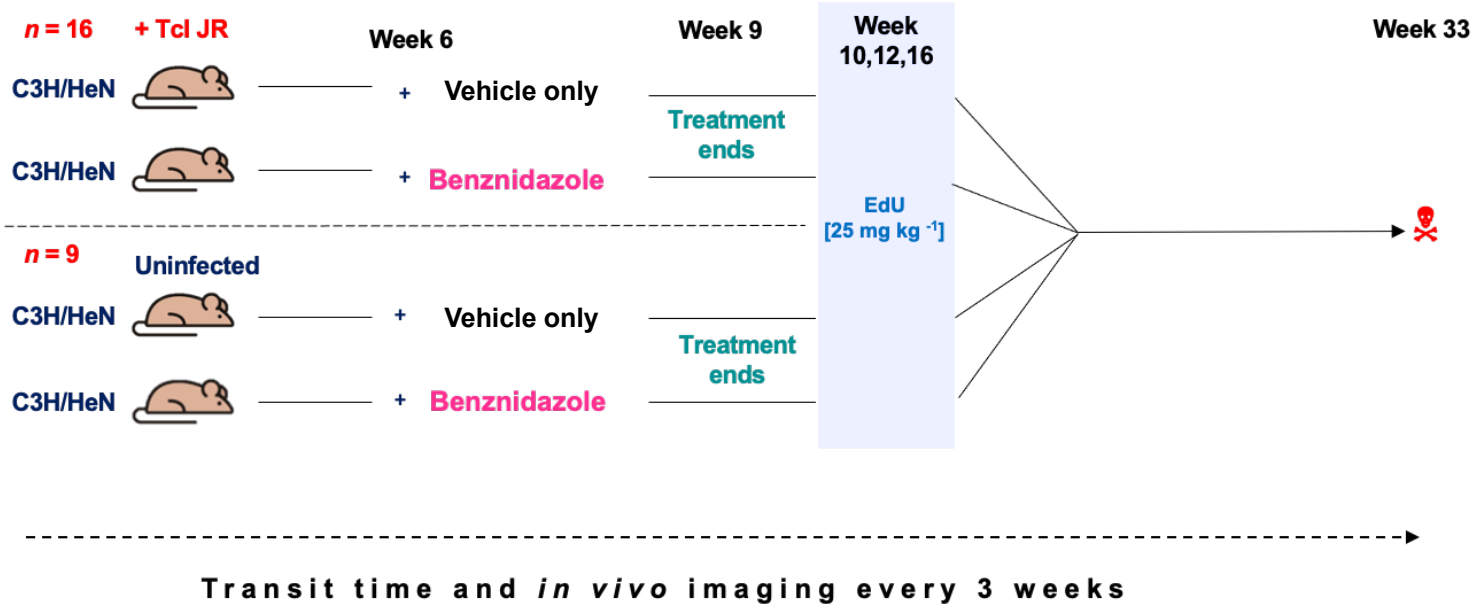

Figure 3.6.1a. Schematic depicting a chronic *in vivo* experiment to assess the impact of benznidazole treatment on gut dysfunction. C3H/HeN mice, aged 6-8 weeks old, were either infected (*n=16)* or uninfected (*n=9*). Infected mice, inoculated with 1x10^{3} Tcl-JR parasites, are above the dotted line. All other conditions are the same between the infected cohort and uninfected cohorts, with all mice subject to *in vivo* imaging and transit time assays every 3 weeks. Treated mice were dosed with benznidazole via oral gavage daily for 18 consecutive days, with untreated mice given HPMC vehicle only. After benznidazole treatment ended, dosing with EdU began at week 10 for all mice, except for 2 negative controls. Mice were dosed twice in each of the three treatment weeks, with 25 mg kg $^{-1}$ IP. The end-point of the experiment was week 33.

5-ethynyl-2′-deoxyuridine (EdU) staining is a method for retrospectively detecting DNA synthesis and cell proliferation during a defined window of time (26). EdU is a thymidine analogue which incorporates itself into nascent DNA, made visible by a downstream ‘click’ chemistry reaction on tissue sections. The reaction entails the covalent binding of an added fluorescent azide to the incorporated EdU, catalysed by copper (I), which can then be visualised by fluorescent imaging (26). In the context of this experiment, we used EdU staining as a method of observing cells that underwent proliferation after benznidazole treatment in (ganglionic) and around (peri-ganglionic) myenteric plexus ganglia, which was interpreted as a proxy for ENS wound healing, including gliosis and neurogenesis.

The window for putative neurogenesis is unknown, therefore, the rationale for pulsing with EdU over weeks 10, 12 and 16 was to cover a ‘long window’. Transit time has previously been observed to ‘normalise’ in infected TcI-C3H mice in this period, even without treatment (16). Uninfected mice were also treated with benznidazole to ensure no secondary therapeutic effect, such as constipation or diarrhoea, was a by-product of the treatment. *In vivo* bioluminescence imaging was conducted every 3 weeks to monitor parasitic burden throughout the course of infection, and to evaluate cures and relapses in the treated cohort. Transit time assays were also conducted every three weeks to monitor gut function throughout the course of the experiment and in response to treatment.

A second experiment was designed to pulse for EdU to cover a ‘short window‘ of putative neurogenesis at earlier time points, weeks 9, 10 and 11, in combination with an earlier experimental end-point (12 weeks) to observe wound healing processes

more intensively in the peristalsis 'normalisation' window immediately after the end of benznidazole treatment.

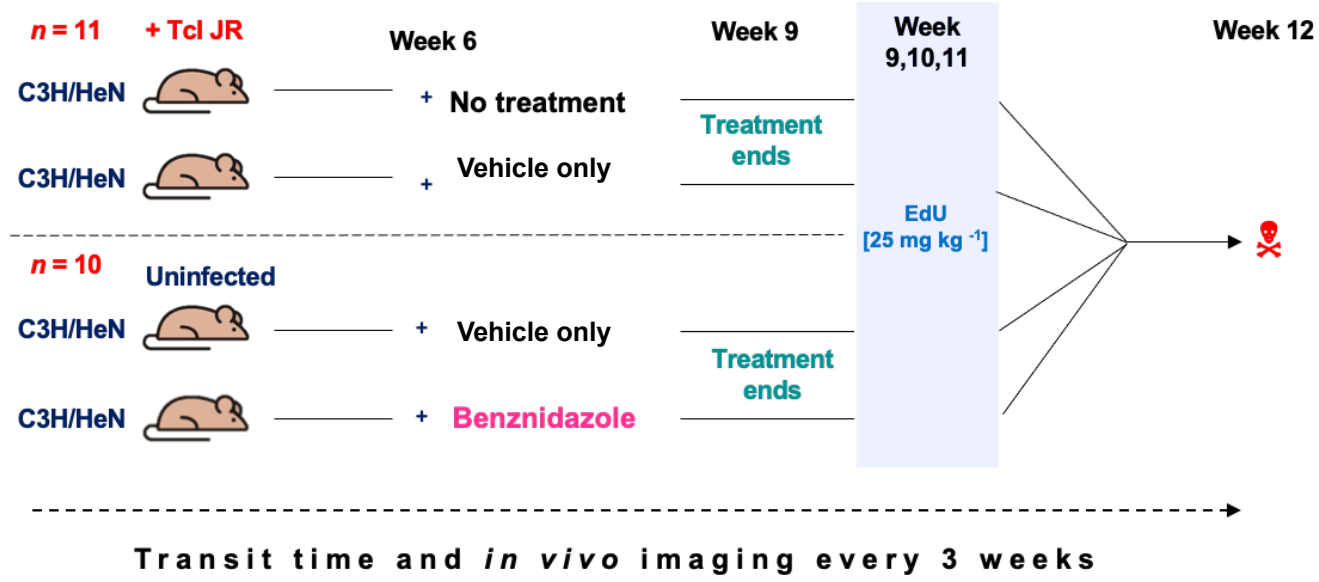

Figure 3.6.1b. Schematic depicting the second experiment. As per the previous experiment, C3H/HeN mice were infected with $1x10^3$ Tcl-JR parasites. Daily treatment with benznidazole began at week 6 post infection for 20 consecutive days, ending on week 9. The same week, pulsing with EdU began with two 25 mg ml^{-1} doses a week, in weeks 9, 10 and 11 post-infection. Mice were sacrificed on week 12 post-infection. *In vivo* imaging and transit time assays was conducted at weeks 1,3,5,6,9 and 12.

The second experiment was similar to the first, but with two key differences. The first was the end point of 12 weeks post infection instead of 33 weeks post infection. The rationale was to collect tissue for analysis to cover both a 'short' and 'long' window of putative ENS repair and regeneration, coinciding with the observed 'normalisation' of transit time after benznidazole treatment. The 12-week experiment additionally allowed us to investigate whether similar processes occur in untreated, infected mice, which show a temporary normalisation of transit times around this time point.

The neuron cell bodies (soma) in the enteric nervous system would be observed using a widely used human antiserum reagent, ANNA-1, which contains autoantibodies to the neuron-specific RNA binding Hu proteins that also cross-react

with mouse orthologues (27). With the revised EdU dosing schedule we were also able to visualise cell division events, tissue repair, and cellular infiltration in the window leading up to this 12-week transit time phenotype. As with the first experiment, *in vivo* imaging and transit time assays were conducted periodically.

3.6.2. 33 week “long repair window” experiment

3.6.2.1 Monitoring parasite burden

To assess the parasite burden throughout the course of the experiment, *in vivo* bioluminescence imaging was utilised periodically to match corresponding transit time data that was collected 24 hours prior. This allowed us to closely assess the fluctuations of transit time in line with changes of parasite burden. Importantly, monitoring parasite burden allowed us to systematically assess benznidazole treatment efficacy. Representative *in vivo* images for each week imaged during the 33-week chronic infection experiment are overleaf (Fig. 3.6.2.1.1).

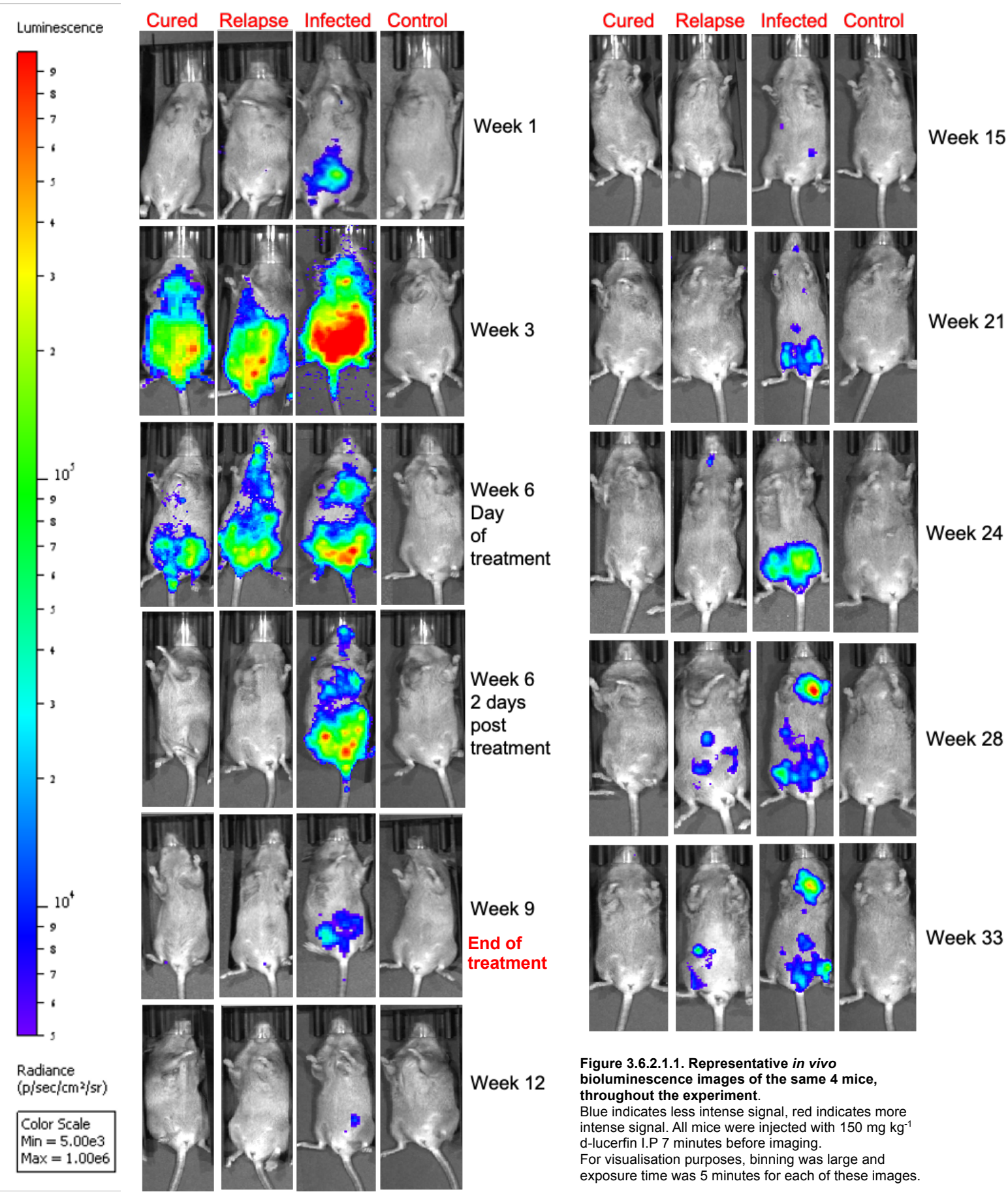

Figure 3.6.2.1.1. Representative *in vivo* bioluminescence images of the same 4 mice, throughout the experiment.
Blue indicates less intense signal, red indicates more intense signal. All mice were injected with 150 mg kg^{-1} d-lucerfin I.P 7 minutes before imaging.
For visualisation purposes, binning was large and exposure time was 5 minutes for each of these images.

Here we visualised the dynamic nature of *T. cruzi* infection throughout the course of an infection spanning both acute and chronic stages. Peak parasitaemia was at week 3 post infection, and treatment began at week 6. We observed that bioluminescence signals reduced to background levels as quickly as 2 days post treatment (Fig. 3.6.2.1.1). Parasite burden in the infected untreated cohort fluctuated, and between weeks 12-15 bioluminescence signal was limited to small foci in the lower abdomen. We also observed a high occurrence of infection relapse in the treated cohort, with 6/8 treated mice developing *in vivo* signals throughout the course of infection and/or *ex vivo* signals detected during necropsy. In the representative image (Fig. 3.6.2.1.1) the relapsed mouse example (second from left panel) developed a signal focus in the upper neck region at week 24 post infection, 16 weeks after treatment concluded. This further developed by week 28 where the signal was in three distinct foci in the upper, mid left and mid right abdomen. By week 33 the intensity had increased in the mid left and spread to the lower left abdomen. The average *in vivo* bioluminescence was quantified for each treatment group (Fig. 3.6.2.1.2a) and with the treatment group split by relapse and cure (Fig. 3.6.2.1.2b).

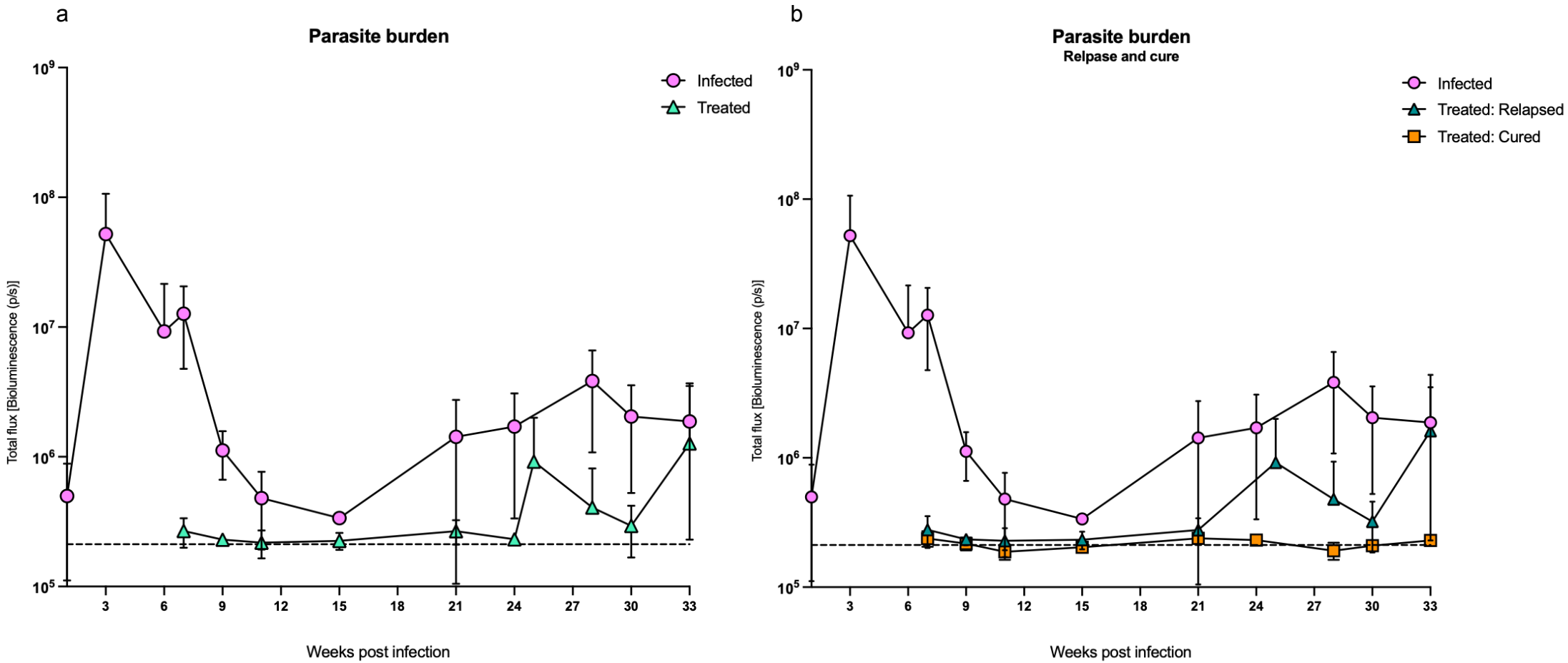

	Comparison	Week post infection							
		9	12	15	21	24	28	30	33
C3H/HeN	Uninfected vs Infected	<0.0001	0.0177	<0.0001	0.0219	0.0215	0.0004	0.0227	0.2832
	Uninfected vs Treated	0.9435	0.9369	0.1793	0.9719	0.5073	0.9503	0.2637	0.4994
	Infected vs Treated	<0.0001	0.0174	<0.0001	0.018	0.1834	0.0007	0.4461	0.8051
Statistics		*p* value (one-way ANOVA)							

Figure 3.6.2.1.2. Parasite burden. a) Graph depicting average total flux [p/s] for each group, on a logarithmic scale. Infected cohort represented by pink circles (*n=5*), treated cohort represented by green triangle (*n=8*). Horizontal dotted line is the mean uninfected threshold +2 standard deviations. The infected cohort at week 3 post infection had an *n*= 11. Three Infected mice were lost to sudden death between this time point and week 6 post infection.
b) Graph depicting average total flux [p/s] for each group, with treated cohort split into treated: relapse, represented by green triangles (*n=6*) and treated: cured, represented by orange squares (*n=2*). One-way ANOVA was conducted at each timepoint, with *p* values depicted for each comparison (Uninfected vs infected, uninfected vs treated, infected vs treated) in table format.

There was substantial heterogeneity in the infected untreated cohort, with a variable parasite burden throughout the course of the experiment. This was most evident from week 21 post infection (Fig. 3.6.2.1.2a) Before treatment began, between weeks 3 and 6 post infection, there were 3 sudden deaths in the infected cohort, reducing the *n* from 16 to 13. Eight of these infected mice were treated with benznidazole from week 6. There was a characteristic dip in parasite burden in the untreated infected group from week 9 to week 15, which then began to rise. However, parasite burden never reached the peak of acute phase (week 3), remaining around an order of magnitude lower. In the treated cohort, 75% of mice (6/8) relapsed. Relapse was determined by *in vivo* signal being detected at any point post treatment or, in the absence of *in vivo* signal, *ex vivo* signal during necropsy. We first detected *in vivo* signal in one treated mouse at week 12 post infection, two at week 21 post infection and two at week 24 post infection, with one additional mouse having no detectable signal until necropsy *ex vivo* imaging. These relapses explain the high degree of variability in the treated parasite burden, as average signal in the treated: cured group when plotted independently stayed at levels observed in the untreated infected group (Fig. 3.6.2.1.2b). Despite the high percentage of relapse, there was no significant difference between the treated and uninfected control groups at any timepoint post treatment, as per the *p* values from one-way ANOVAs (Fig. 3.6.2.1.2). There was a consistent significant difference between uninfected and infected untreated throughout the entire experiment, until week 33 post infection. There was a significant reduction in parasite burden in response to treatment compared to the infected untreated cohort in five of the eight timepoints, with the high degree of variability in the infected group, and the presence

of relapses in the treated, at weeks 24, 30 and 33 resulting in no significant difference at these timepoints (Fig. 3.6.2.1.2).

I decided to plot the total bioluminescence for each individual mouse at each timepoint so the heterogeneity between each group and the fluctuations in signals for individual mice over time are easier to visualise (Fig. 3.6.2.1.3).

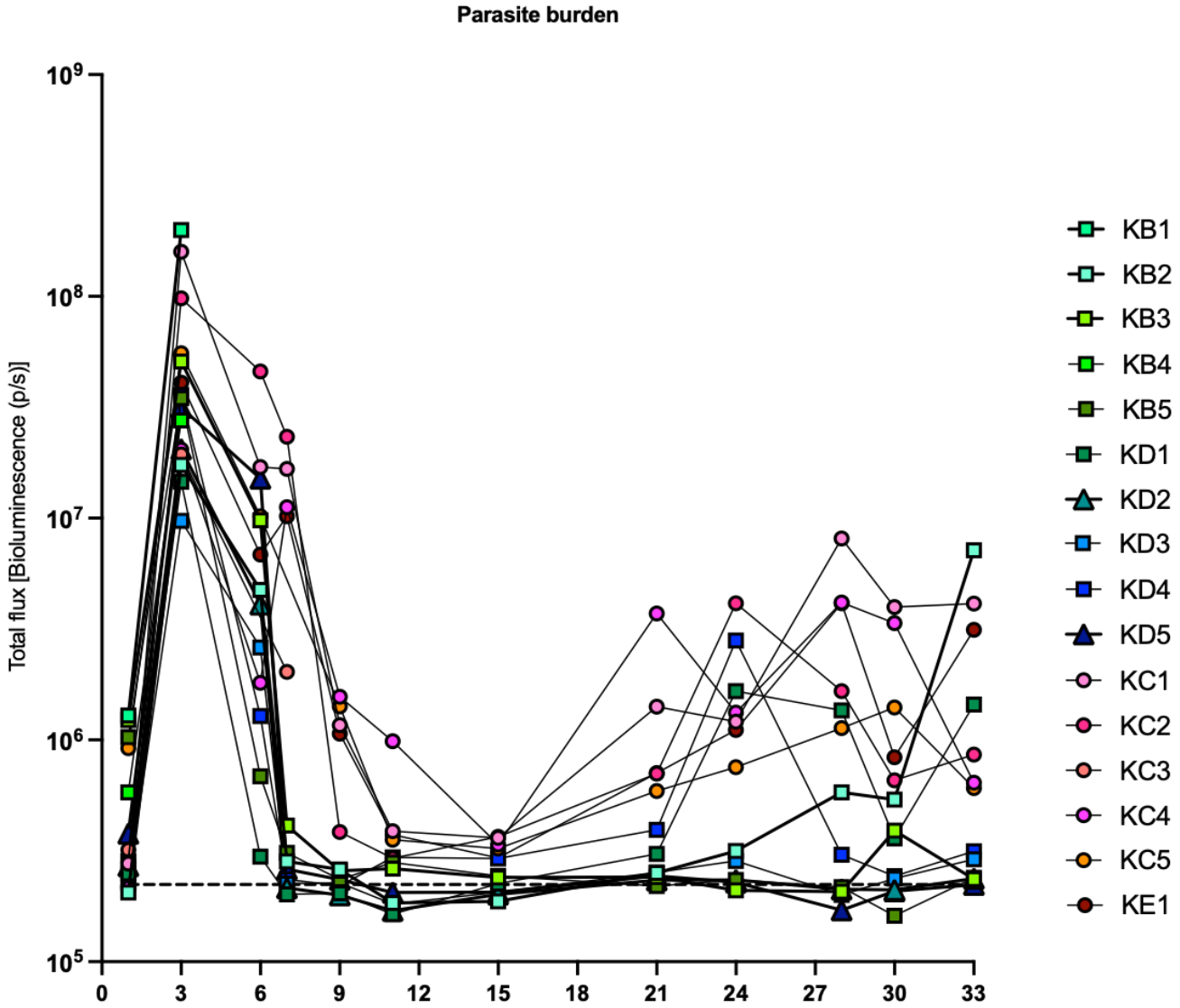

Figure 3.6.2.1.3. Graph depicting total flux [p/s] for every individual mouse, on a logarithmic scale.
Each individual mouse code is in the legend, with those that were treated with benznidazole represented by different shades of green and blue, with relapsed mice represented by squares, and cured mice with triangles. Infected untreated mice are represented by circles of different shades of red, pink, and orange. The average uninfected total flux +2SD is represented by a dotted line.

From the individual plots, the heterogeneity and variability in the infected cohort (Red, pink, orange) was easily observable week by week (Fig. 3.6.2.1.3). The bioluminescence signals in the mice that relapsed were visible from week 15 post infection, with KD4 (dark blue) the first to develop signal. The signal increased sharply between week 21 and 24 by 7.1-fold, where it was the mouse with the second highest parasite burden at that timepoint. KD1 also experienced a steep increase in the same window, with signal increasing 5.4-fold. KB2 developed signal at week 24 which steadily increased by week 28, reduced slightly by week 30 before increasing by 13.3-fold by week 33 ending the experiment with the highest parasite burden of all infected mice, irrespective of treatment status. The other relapsed mice, KD3 and KD5 only had minor increases in bioluminescent signal from week 21. KB5 had *in vivo* signal similar to background levels throughout the experiment, with *ex vivo* confirming relapse. *Ex vivo* imaging was used to confirm treatment efficacy and to assess where parasites were predominantly situated in the chronic stage infection (Fig. 3.6.2.1.4).

Ex vivo imaging

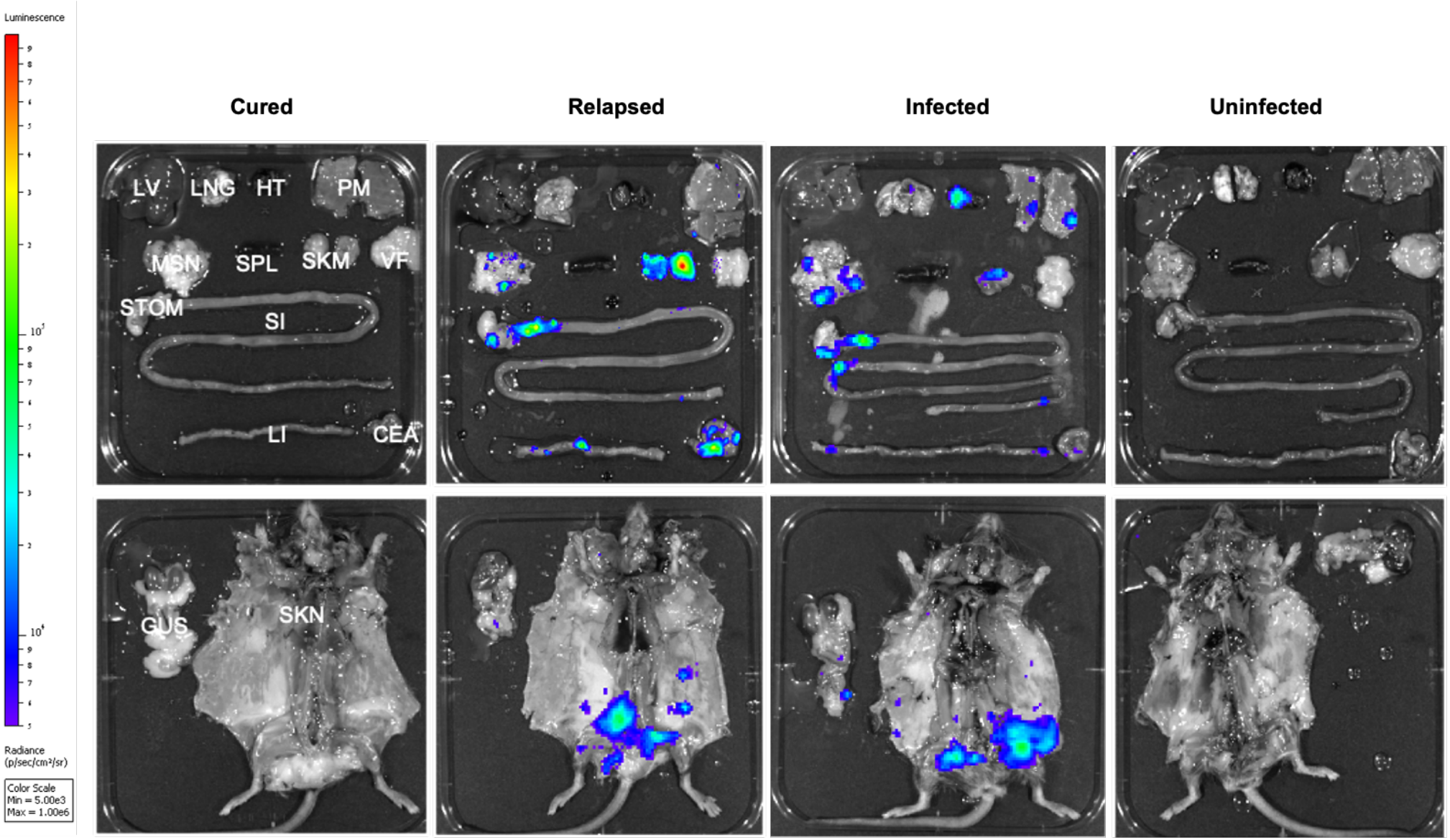

Figure 3.6.2.1.4 Representative *ex vivo* layout for each experimental group.
LV=liver, LNG=lungs. HT=heart. PM=peritoneum, MSN=mesentery tissue, SPL=spleen, SKM=skeletal muscle, VF=visceral fat, STOM= stomach, SI=small intestine, LI=large intestine, CEA=caecum, SKN= kin and carcass, GUS=genitourinary system. Images captured at 5-minute exposure, with a large binning. Blue represents lower intensity of signal and red higher intensity.

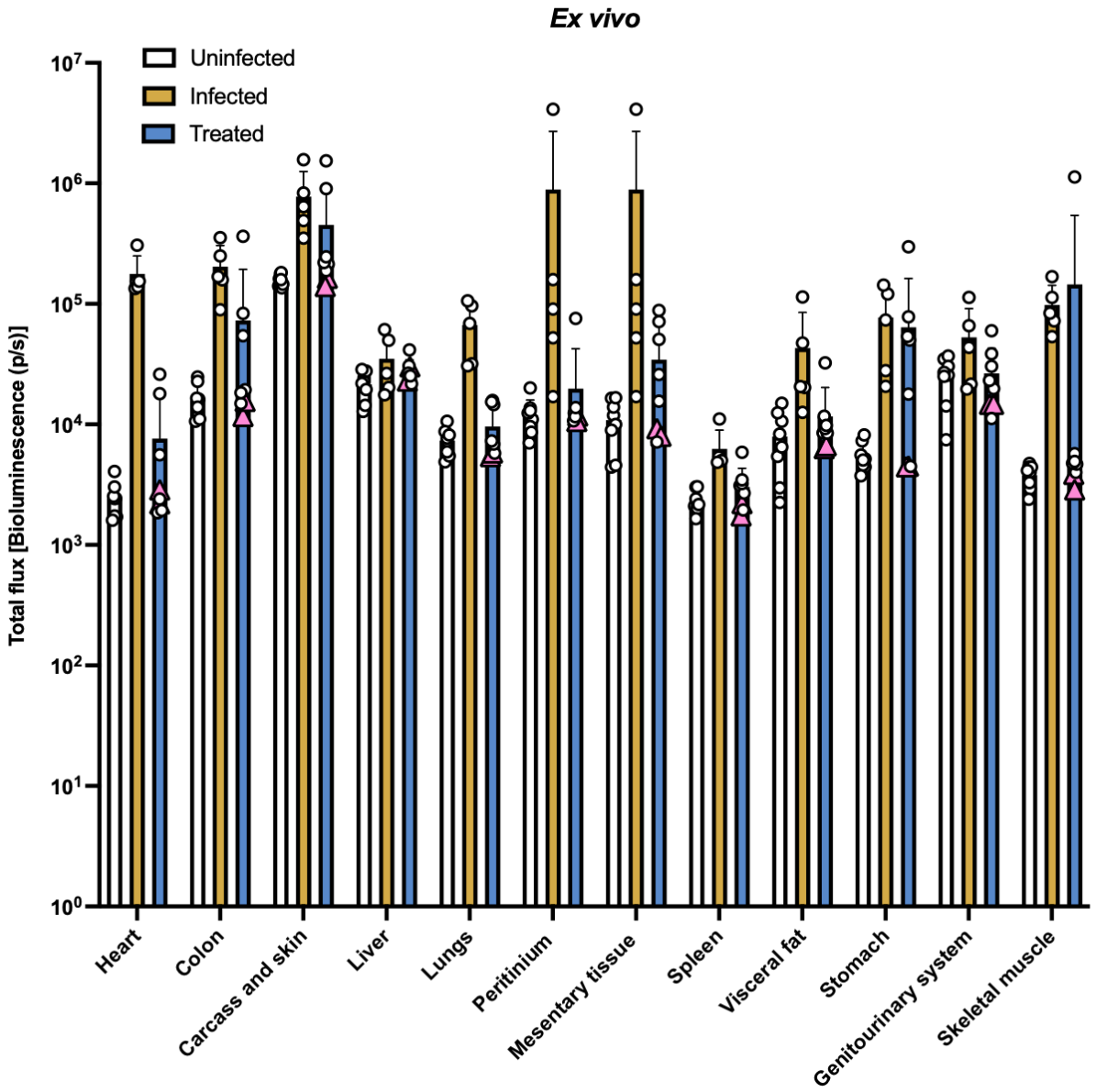

	Comparison	Organ											
		Heart	Colon	Carcass	Liver	Lungs	Peritiunum	Mesentary	Spleen	Visceral fat	Stomach	G.S	Skm
C3H/HeN	Uninfected vs Infected	<0.0001	0.0002	0.0031	0.0887	0.0005	0.1969	0.0026	0.0008	0.021	0.0028	0.0941	<0.0001
	Uninfected vs Treated	0.9527	0.4274	0.302	0.4491	0.9605	0.9998	0.5904	0.6251	0.9319	0.2137	0.9916	0.5059
	Infected vs Treated	<0.0001	0.0469	0.3276	0.484	0.0007	0.2022	0.0173	0.0047	0.0401	0.7893	0.1147	0.9414
Statistics		*p* value (one-way ANOVA)											

Figure 3.6.2.1.5 Average bioluminescence of each organ by experimental group.
G.S=genitourinary system, Skm=skeletal muscle. Total flux was obtained by drawing regions of interest around each organ individually. One-way ANOVA conducted for each organ separately, with *p* values for each comparison in table format. Exposure time and binning adjusted if saturation occurred, with exposure time ranging from 1-5 minutes and binning from medium to large. Pink triangles indicate data from mice assessed as cured.

In the representative relapsed *ex vivo* image (Fig. 3.6.2.1.4) end-point parasite persistence was limited to the GI mesentery tissue, skeletal muscle, stomach, caecum and large intestine, as well as lower body skin. However, it should be noted that this pattern was not consistent across all relapse cases. Three relapsed mice had *ex vivo* signal in the GI mesentery tissue, only one had signal in the skeletal muscle, four had signal in the stomach, one in the caecum, three in the large intestine, and three in the skin.

All of the infected untreated mice had signal in the colon, which complements previous finds of this site being a main reservoir of chronic infection (28). There was no significant difference in average bioluminescence signal between benznidazole-treated and uninfected mice for any of the organs (Fig. 3.6.2.1.5 table). There was a significant difference between infected untreated mice and uninfected controls for most organs, notably including the heart, lungs, colon, stomach and skeletal muscle. There was also a very strong significant difference between infected untreated and treated mice for heart- and lung-specific infection, but no significant difference in the skeletal muscle due to one relapsed mouse exhibiting a strong signal focus in that tissue (Fig. 3.6.2.1.4&5). This was also the case with the stomach and skin, where on average there was no difference between the infected untreated and treated groups due to these sites being distinct sites of parasite relapse infections. Despite the colon also being a common site for *ex vivo* signal in the relapsed mice, it was of significantly lower intensity compared to the infected untreated group. On average there was a very strong signal in the lungs in the infected untreated groups which has been observed in the chronic stage previously (15,28,29).

Overall, these data show that there is a large degree of intrinsic variability in parasite burden in the untreated cohort. Moreover, in the treated cohort those that were cured exhibited bioluminescent signal in line with background levels, whereas the rest of the treated cohort exhibit heterogeneity due to relapses occurring at different timepoints. Variability was also observed in the *ex vivo*, with 66.6% of relapsed mice experiencing bioluminescent signal in the colon.

3.6.2.2 Assessing gut transit function.

Gut transit function was assessed periodically throughout the course of the experiment using a total GI transit time assay (Fig. 3.6.2.2.1).

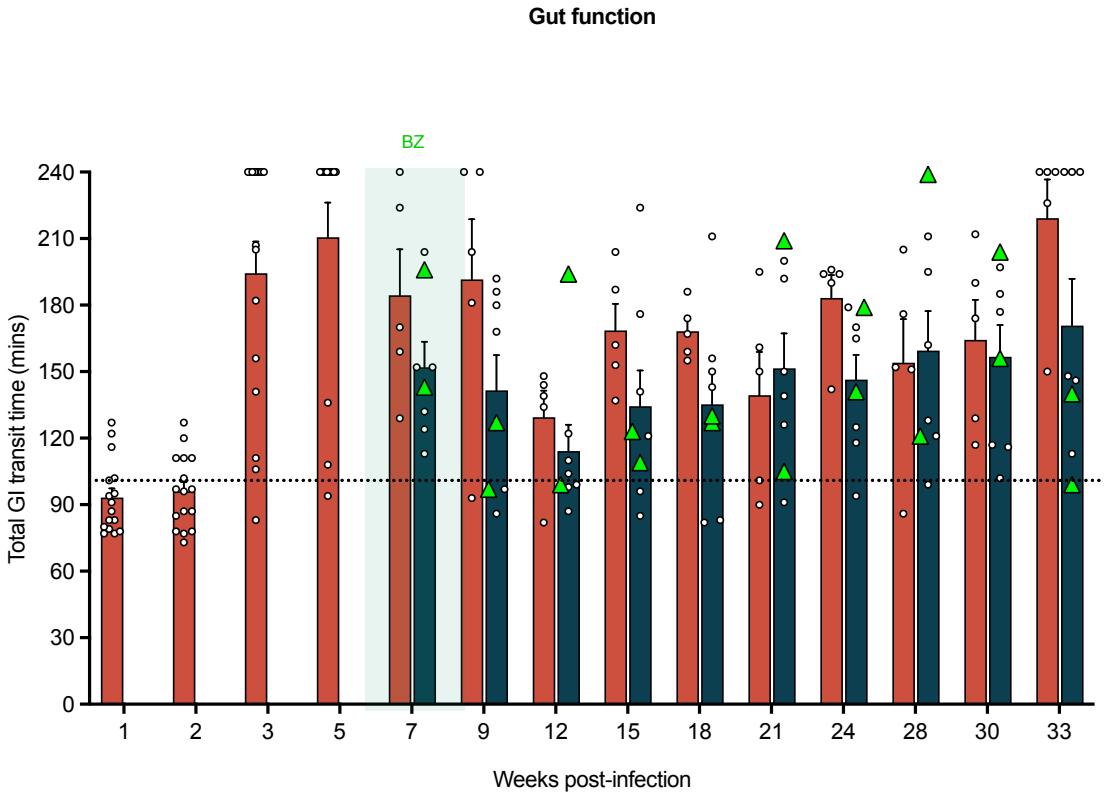

	Comparison	Week post infection								
		7	9	12	15	18	21	24	28	30	33
C3H/HeN	Uninfected vs Infected	0.0186	<0.0001	0.0354	0.0013	0.0184	>0.9999	0.1697	0.1697	0.0186	0.0189
	Uninfected vs Treated	0.0436	0.0147	0.1214	0.0161	0.2305	0.9262	0.0786	0.0786	0.0204	0.7038
	Infected vs Treated	0.006	0.009	0.6045	0.2233	0.225	0.9262	0.9705	0.9705	0.9218	0.234
Statistics		*p* value (one-way ANOVA)									

Figure 3.6.2.2.1. Graph depicting the total GI transit time for each experimental group throughout the course of the experiment. The red bar represents the infected cohort, which splits from week 6 into infected untreated (red) and infected benznidazole-treated (blue). Green triangles in the treated group represent treated cures. The black line running horizontal represents the mean transit time of uninfected control mice +2SD, The light green box represents the benznidazole treatment window of 18 successive days, starting from week 6 post infection. One-way ANOVA was conducted at each time point for each comparison. *p* values highlighted in red represent significant differences within that comparison.

The transit time for the infected cohort, just as with the *in vivo* bioluminescent signal, was variable both within and between timepoints. The overall trend of the infected mouse average transit time was similar to previous work on the TcI-C3H model (16). A consistent transit time delay developed at 3 weeks post infection until week 9 before improving around week 12. The dysfunction then slowly re-established throughout late acute phase/early chronic phase. This is represented by the *p* values calculated at each timepoint in this experiment. There was a strong, significant difference at week 7 post infection (*p=0.0186*) which strengthens by week 9 (*p=<0.0001*). The average delay fell at week 12 but remained significantly delayed (*p=0.0354*). A significant delay was re-established at week 15 (*p=0.0013*) through to week 18 (*p=0.0184*). Interestingly, between weeks 21-28 there was no significant delay. This was likely facilitated by a series of low outliers in those weeks, and a high average transit time for the uninfected control at week 24. A significant delay returned at week 30 (*p=0.0186*) and remained at week 33 (*p=0.0189*).

After benznidazole treatment began at week 6 post infection, the transit time in the infected treated group was significantly reduced by week 7 compared to the infected untreated group (*p=0.006*) but was still significantly delayed compared to the uninfected control (*p=0.0436*). The reduced transit time was maintained at week 9, whereby treatment had concluded (*p=0.009*). By week 12 the infected treated cohort was still trending downwards, but since the infected untreated group also began trending down there was no significant difference between the two groups. Interestingly, from week 18 post infection where the transit time in the infected untreated group was significantly increased compared to the uninfected control, there was no significant difference between the infected treated group and

uninfected control transit times (*p=0.2305*). The transit time in the treated group became a lot more varied from week 21 as the relapses within the group become established. Despite this, there remained no significant difference between the infected treated and the uninfected control between weeks 21 and 28. At week 30 post infection the effect of relapsed infection in the treated group became even more apparent. There was no significant difference between the treated infected group and the untreated infected group (*p=0.9218*), and a significant difference compared to the uninfected control (*p=0.0204*). However, at week 33 post-infection a treatment effect returned and there was no significant difference in transit time between the infected treated group compared to the uninfected control group (*p=0.7038*), but a significant delay in the infected untreated group compared to uninfected control (*p=0.0189*). A treatment effect, albeit mild, was present irrespective of relapse or cure. The treated group had an average lower transit time than the infected untreated group throughout the experiment and had no significant difference in transit time with the uninfected control group at 60% of the timepoints.

To assess how the large percentage of relapsed mice affected the average of the treated cohort throughout the experiment, I decided to split the group into treated: cured and treated: relapsed and plotted them separately. However, because of the low rate of cure (25%) the treated: cured group had an *n* of 2, and ultimately low statistical power.

f

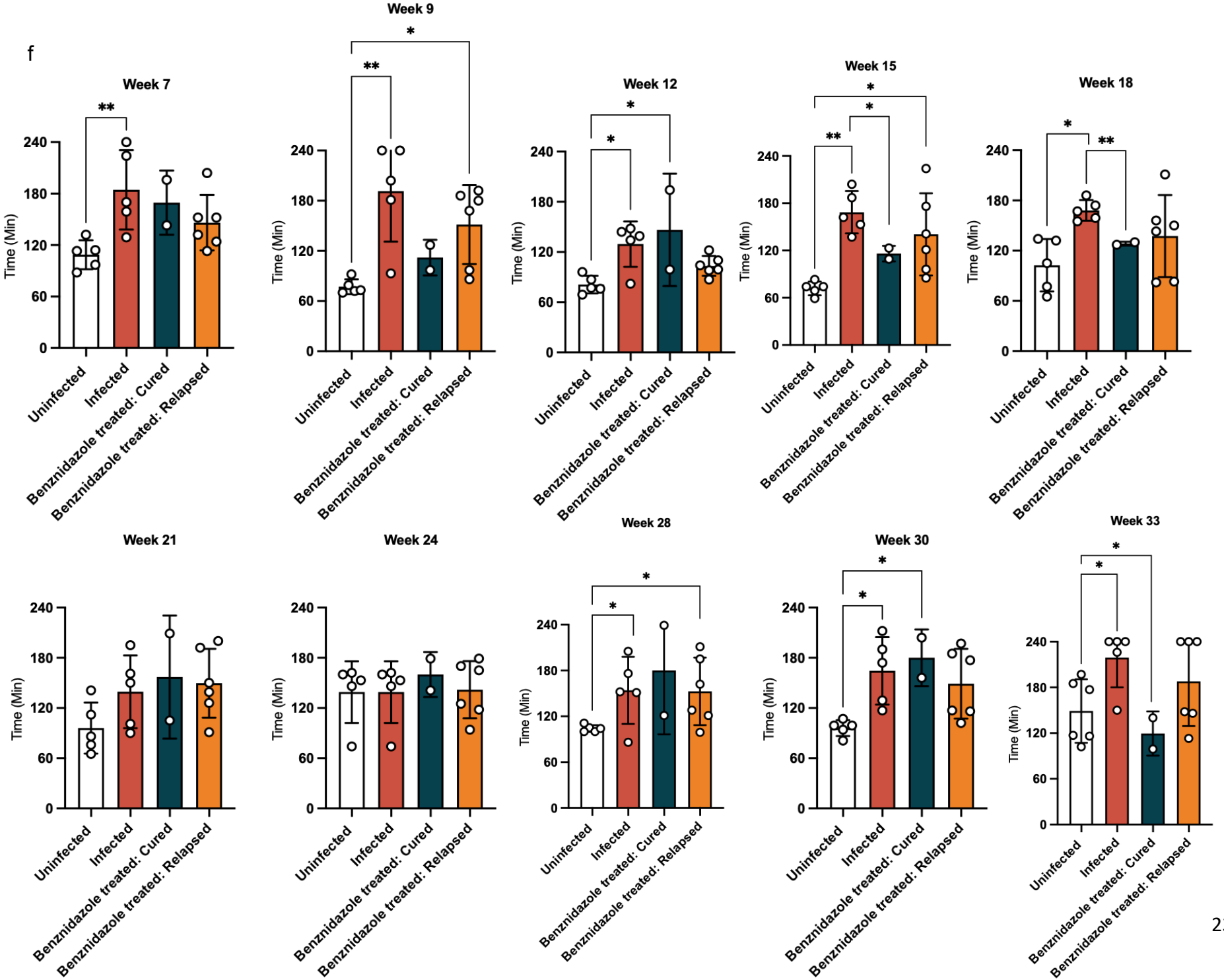
Week 7
Week 9
Week 12
Week 15
Week 18
Week 21
Week 24
Week 28
Week 30
Week 33
Time (Min)
0
60
120
180
240
Uninfected
Infected
Benznidazole treated: Cured
Benznidazole treated: Relapsed
*
**

	Comparison	Week post infection									
		7	9	12	15	18	21	24	28	30	33
C3H/HeN	Uninfected vs Cured	0.3084	0.0932	0.0312	0.4534	0.8045	0.3507	0.8911	0.1796	0.0306	0.8654
	Uninfected vs Relapsed	0.4407	0.1762	0.4691	0.0259	0.3706	0.2038	0.9991	0.0381	0.0979	0.496
	Infected vs cured	0.9103	0.2674	0.8416	0.0496	0.0079	0.9587	0.8911	0.8784	0.9479	0.0242
	Infected vs Relapsed	0.2823	0.0093	0.3417	0.5581	0.4766	0.9775	0.9991	>0.9999	0.8812	0.6902
	Cured vs Relapsed	0.89	0.7433	0.1899	0.8239	0.9881	0.9965	0.9206	0.8535	0.6965	0.1768
	Statistics	*p* value (one-way ANOVA)									

Figure 3.6.2.2.2. Graphs (previous page) depicting the transit times of each treatment group at each timepoint, with the addition of treated: cured and treated: relapsed groups.
The sample size of the uninfected and infected group remains the same, but treated: cure *n*=2 and treated: relapse *n*=6. One-way ANOVA was conducted at each time point for each comparison. *P* values highlighted in red represent significant differences within that comparison.

The first difference observed was at week 9 post infection, where the treated group was pooled there was a significant difference against the uninfected control. Here there is no significant difference between the treated: cured (p=0.0932). At week 15 post infection we observed a key difference. Here we noted no significant difference in transit time between the uninfected and treated: cured group (p=0.4534), a significant difference between the uninfected and treated: relapsed group (p=0.0259), a significant difference between the infected and treated: cured group (p=0.0496) and no significant difference between the infected and treated: relapsed group (p=0.5581). This positive treatment effect supported the rationale for splitting the treated cohort. This trend continued to week 18, where a strong significant difference was observed between the infected and treated: cured group (p=0.0079). There weren't any noticeable differences between the pooled treated group and split between weeks 21 and 24 post infection. However, at week 28 there was a significant difference between uninfected control and treated: relapsed (p=0.0381) and no difference between uninfected and treated: cured (0.1796). In the pooled data there was no difference between the uninfected and pooled treated cohort, suggesting that the relapses were masking a normalising transit time in the treated: cured cohort. At week 30 there was a significant difference between the uninfected and treated: cures, with the cured cohort averaging the highest transit time of any

group. This is likely a result of the low sample size masking the heterogeneity and variably observed in each group irrespective of treatment or infection status. This is supported by the transit time data at week 33, where the treated: cured group had the lowest average transit time of any group, including the uninfected control although not significant (p=0.8654). At week 33 in the pooled treated cohort, there was no significant difference between uninfected and treated, but once split a difference between uninfected and treated: relapse was discovered (p=0.0242) with the treated: cured remaining no different to the uninfected control (p=0.8654). These data suggest that the relapses were possibly masking a more convincing treatment effect than when all treated animal data were pooled, irrespective of cure vs relapse status.

The primary caveat, in addition to the low number of cures, is that all relapsed mice were pooled together from week 7, irrespective of when each individual mouse relapsed. As mentioned previously, the timepoints at which relapse occurred were scattered across the late acute/early chronic stage, with the addition of one confirmed only upon necropsy. This might mean that ‘normal’ transit time from early time points from a mouse that relapsed as late as week 24 of the experiment, would affect the accuracy of the group average. However, there was a significant transit delay in the treated: relapse group at week 15, before 66.7% of the ‘relapsed’ mice had detectable *in vivo* signal. This suggests that gut dysfunction could preface or occur independently of high/detectable parasitaemia.

3.6.3. 12 week “short repair window” experiment

In the chronic (33 week) study we noted that both the infected untreated and infected treated groups had near-normal transit times at 12 weeks post-infection, as observed in earlier work (Khan et al 2021). At week 12 both groups presented with their lowest average transit time across the experiment. Despite this, the *p* value at this time points out that there was still a significant difference in transit time between the infected and uninfected (*p=0.0354*), but no significant difference between the treated and uninfected (*p=0.1214*) (Fig. 3.6.2.2.2). When the treated cohort was segregated into cures and relapses, there was no significant difference between relapsed mice and uninfected (*p=0.4691*). Previously, using IFA it has been discovered that at week 6 post-infection (late acute phase/early chronic phase), infected mice had a decreased neuronal count in the enteric nervous system, confirmed by the loss of anti-HuC/D immunoreactive cell bodies (Khan et al 2021, 2022). By late chronic phase (week 33-36), the neuronal loss had become more substantial, suggesting that the decline in gut dysfunction correlates with neuronal loss and establishes gradually throughout disease progression. It was also noted that between weeks 12-18 post infection there was a transient improvement in transit time. The mechanistic and physiological processes that permit this improvement are not known.

In the chronic study, week 12 post infection was the first timepoint after the full benznidazole treatment regime had been completed. As mentioned, the treated cohort did not have a lower average transit time at any other timepoint than at week 12. In this 12-week experiment we therefore set out to understand if this recovery in transit function is associated with ENS repair, including neuronal recovery and tissue healing.

3.6.3.1. Monitoring parasite burden

In vivo imaging was conducted throughout the experiment to monitor parasite burden (Fig. 3.6.3.1.1). Weeks 5 and 6 were pre-treatment timepoints, with benznidazole treatment beginning for an infected cohort from week 6, with a daily treatment regimen running though week 9 post infection.

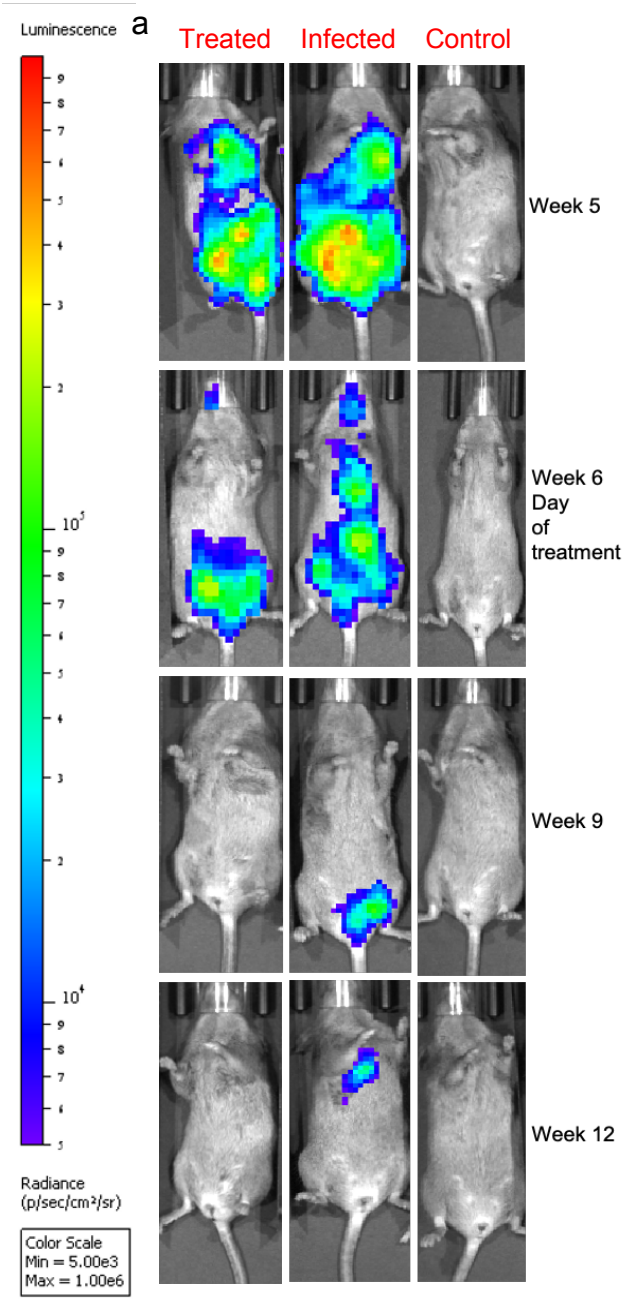

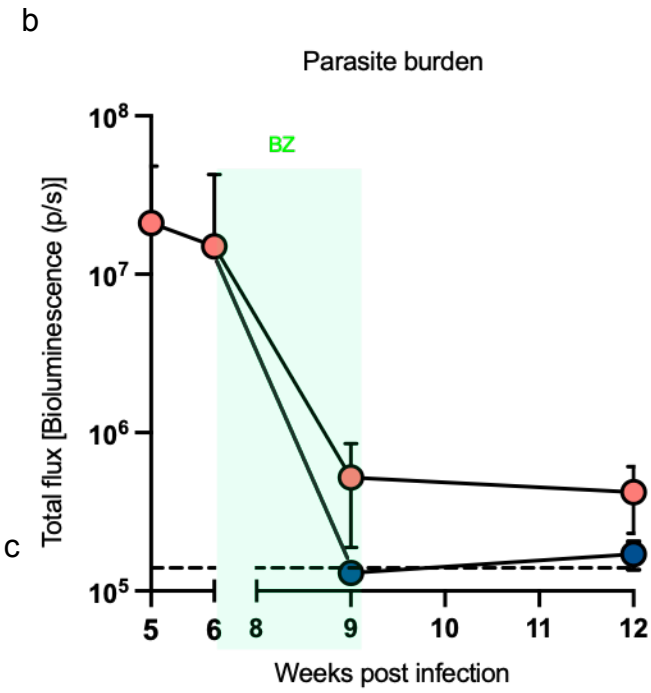

c

	Comparison	Week post infection		
		6	9	12
C3H/HeN	Uninfected vs Infected	0.006	0.0427	0.0158
	Uninfected vs Treated	/	0.9998	0.9295
	Infected vs Treated	/	0.0441	0.0277
Statistics		*p* value (one-way ANOVA)		

Figure 3.6.3.1.1. Monitoring parasite burden.
a) Representative *in vivo* images of each experimental group following the same mice through the experiment duration. Treatment began at week 6 post infection. Blue colouration indicates less intense signal, red indicates more intense signal. All mice were injected with 150 mg kg^{-1} d-lucerfin I.P 7 minutes before imaging. B) Graph depicting average total flux [p/s] for each group, on a logarithmic scale. Infected cohort represented by pink (*n=9*) and treated cohort represented by green (*n=9*). Horizontal dotted line is the mean uninfected threshold +2 standard deviations. Green box represents treatment window. c) Table depicting One-way ANOVA evaluation at each timepoint, with *p* values depicted for each comparison (Uninfected vs infected. uninfected vs treated. infected vs treated).

From the representative images we see a loss of detectable signal in the benznidazole treated mouse in weeks 9 and 12 (Fig. 3.6.3.1.1a). This was reflected by the group average as there was no significant bioluminescent signal detected compared to the uninfected control at week 9 (*p=0.9998*) and week 12 (*p=0.9295*). The infected untreated group had a reduction in parasite burden between week 6 and week 9, but the bioluminescent signal remained significantly higher than the infected treated group at this time point (*p= 0.0441*) and at week 12 (*p=0.0277*), where the signal reduced further.

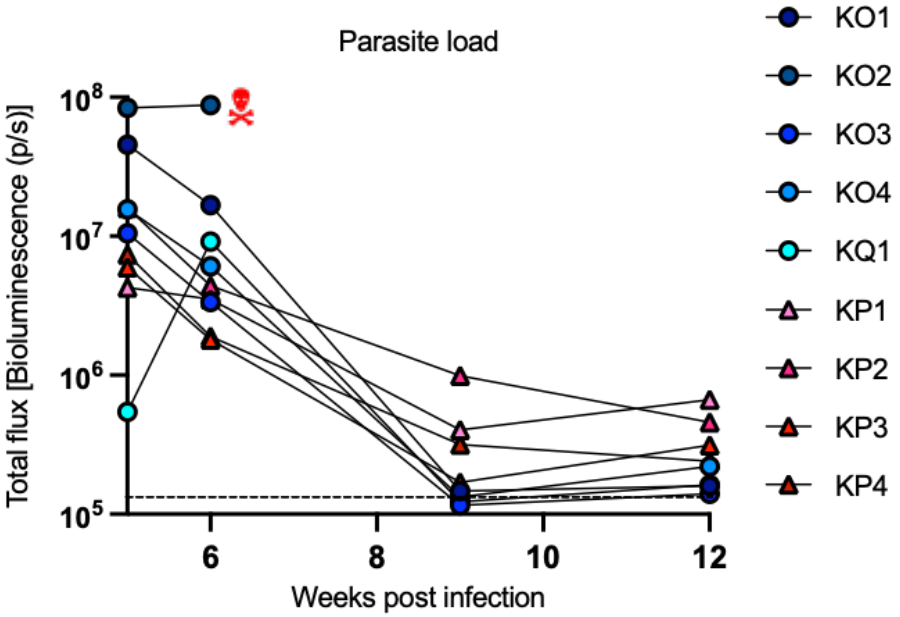

Figure 3.6.3.1.2. Graph depicting total flux [p/s] for each individual mouse, on a logarithmic scale.
Each individual mouse code is in the legend, with those that were treated with benznidazole represented by circles in different shades of blue. Infected untreated mice are represented by triangles in shades of red/pink. The mean +2SD uninfected total flux is represented by a dotted line.

From the individual plots we observed a degree of heterogeneity in parasite burden in the infected untreated group (red/pink dots), but not in the treated. There were two sudden deaths, one occurring in the infected group before treatment (week 5) and one earmarked for treatment, which is highlighted in Fig. 3.6.3.1.2 that died on the first day of treatment. From week 6 of the experiment, once treatments began, it was *n=4* for the treatment group and *n=4* for infected untreated group.

Ex vivo imaging

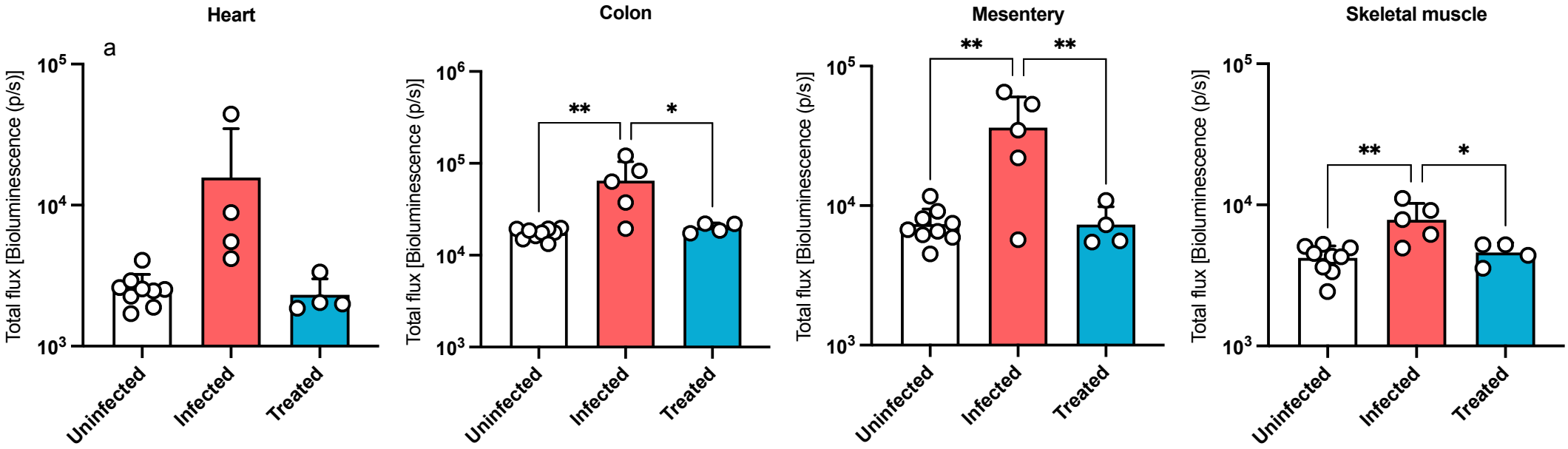

b

	Comparison	Organ												
		Heart	Colon	Skin	Carcass	Liver	Lungs	Peritiunum	Mesentary	Spleen	Visceral fat	Stomach	G.S	Skm
C3H/HeN	Uninfected vs Infected	0.0515	0.0024	0.0252	0.01	0.0357	0.0238	0.0022	0.0023	0.0736	0.0188	0.0274	0.3997	0.0013
	Uninfected vs Treated	0.9989	0.9762	0.9855	0.9714	0.7424	0.5961	0.9979	>0.9999	0.8072	0.8504	0.9924	0.9445	0.8984
	Infected vs Treated	0.2213	0.0142	0.0496	0.0392	0.2596	0.0112	0.0102	0.0093	0.0547	0.0201	0.0572	0.3672	0.0126

Figure 3.6.3.1.3. ***Ex vivo*** **bioluminescence quantification 12 weeks post infection**
a) Average bioluminescence present in each organ for each experimental group. b) a table depicting the *p* values obtained from one-way ANOVA comparing each experimental comparison. G.S=genitourinary system, Skm=skeletal muscle. Total flux was obtained by drawing regions of interest around ach organ individually. One-way ANOVA conducted for each organ separately, with *p* values for each comparison in table format. Exposure time and binning adjusted if saturation occurred, with exposure time ranging from 1-5 minutes and binning from medium to large.

Ex vivo imaging was used to evaluate treatment efficacy at end point, and to identify which organs were reservoirs for parasite burden at week 12 of infection, when *in vivo* signal in infected mice plummets to its lowest. In the graph (Fig. 3.6.3.1.3a), the organs with the highest average signal peaks in the infected untreated group was the skin, colon, carcass, stomach, and GI mesentery tissue. There was a significant increase in bioluminescence signal in each of the infected organs compared to the uninfected except for heart, spleen, and genitourinary system (Fig. 3.6.3.1.3b). Moreover, there was a significant reduction in bioluminescent signal in the infected benznidazole-treated group compared to the infected untreated in most organs, and critically the colon (*p=0.0142*) where there was a 3.2-fold difference. There was no significant difference in bioluminescence in the infected treated group and uninfected group in any of the organs imaged, confirming that benznidazole suppressed parasite numbers to undetectable levels.

3.6.3.2. Assessing gut function

GI transit time was evaluated every 3 weeks of the experiment, with daily benznidazole treatment beginning at week 6 post infection for 20 consecutive days and concluding at week 9 post infection (Fig. 3.6.3.2.1). The overall trend of the infected untreated group (red bar) follows that observed in the chronic experiment. Transit time delay developed steadily up through week 9 post infection, where the delay was significant compared to the uninfected (*p=0.0003*) and the infected treated mice (*p=0.0027*).

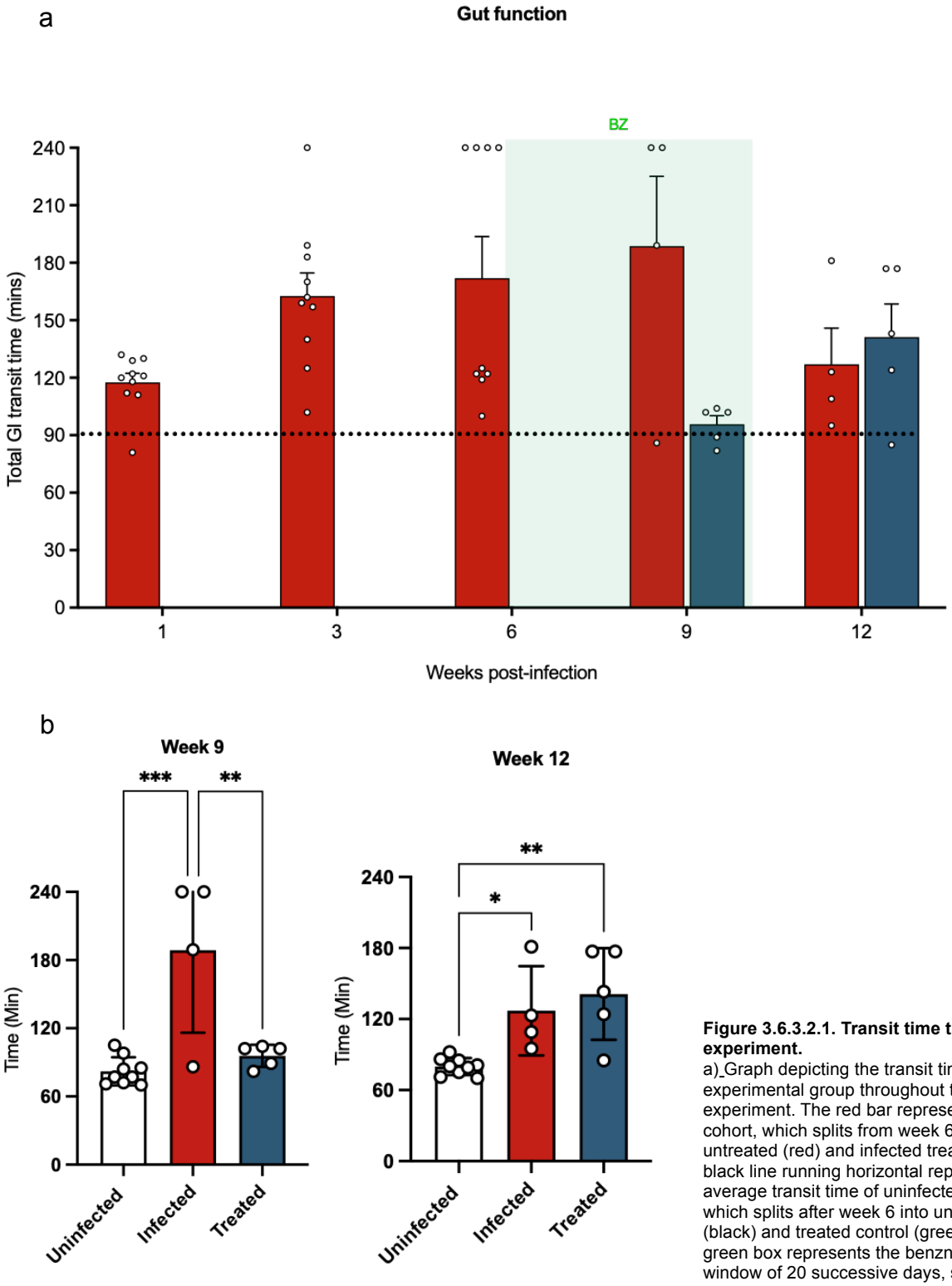

	Comparison	Week post infection	
		9	12
C3H/HeN	Uninfected vs Infected	0.0003	0.0262
	Uninfected vs Treated	0.7554	0.0025
	Infected vs Treated	0.0027	0.7134
	Statistics	*p* value (one-way ANOVA)	

Figure 3.6.3.2.1. Transit time throughout experiment.
a) Graph depicting the transit time for each experimental group throughout the course of the experiment. The red bar represents the infected cohort, which splits from week 6 into infected untreated (red) and infected treated (blue). The black line running horizontal represents the average transit time of uninfected control mice, which splits after week 6 into untreated control (black) and treated control (green). The light green box represents the benznidazole treatment window of 20 successive days, starting from week 6 post infection. b) individual graphs for week 9 and week 12 transit time. c) One-way ANOVA was conducted at each time point for each comparison. *P* values highlighted in red represent significant differences within that comparison.

In line with expectations, the average transit time then fell by 39% in the infected untreated group at week 12, to a degree where no significant difference between the infected untreated and treated group was observed (*p=0.7134*). A significant difference in transit time was still observed between the uninfected group and both the infected untreated (*p=0.0262*) and the treated (*p=0.0025*). This partially corroborates what was observed in the chronic experiment, where the average transit time in the infected untreated group fell at week 12 but remained significantly delayed against the uninfected group. However, unlike in previous experiments (Khan et al biorxiv; Figure 3.3.2 f&g), a mild but significant delay re-developed in the benznidazole-treated group.

3.6.3.3 Investigating ENS repair in the myenteric plexus

EdU was pulsed in each of the mice in defined windows after benznidazole treatment, allowing us to visualise cellular replication retrospectively. This enabled us to begin to investigate ENS repair processes even though most of the benznidazole treatments failed in terms of infection relapse and/or re-development of transit delays.

To re-cap, in the 33 week experiment, EdU was pulsed at weeks 10, 12 and 16 post infection to target a putatively long repair window, while in the 12-week experiment EdU was pulsed at weeks 9, 10 and 11 post infection, to target a putatively short repair window. (17)

3.6.3.3.1: Chronic 33 week ‘long repair window’ experiment

Transverse cross sections of the distal colon were stained for IFA. In addition to EdU, Anti-Hu antisera (ANNA-1) was used to label neuronal cell bodies in the myenteric plexus in between the longitudinal and circular muscle layers of the colon. Anti-GFAP (monoclonal IgG) was used to label glial fibrillary acidic protein, which is an intermediate filament protein expressed by ENS glial cells.

There was a high degree of variability of EdU+ signal across the different experimental groups (Fig. 3.6.2.2.1). Importantly, despite the mice being culled at a relatively late chronic stage (33 weeks post infection), we pulsed with EdU in the late early chronic stage after benznidazole treatment, so were observing cell proliferation events retrospectively. With a focus on the smooth muscle layer, we were particularly interested in the spatial distribution of EdU+ cells. EdU+ cells were categorised as either ganglionic (found within the boundaries of an enteric neuronal plexus ganglion) or peri-ganglionic (found in the smooth muscle and connective tissue regions circumambient to ganglia). As an example, in the infected treated image, we can observe five ganglionic EdU+ cells and 13 peri-ganglionic EdU+ cells (Fig. 3.6.2.2.1a). Co-localisation of EdU (orange) and either ANNA-1 (magenta) or GFAP (green) suggests active proliferation of those cell types, or a precursor of those cell types, at the point of at least one of the pulses of EdU. The white arrow (Fig.3.6.2.2.1a) highlights an observed co-localisation of incorporated EdU on the periphery of a neuronal cell body. This is more easily observed in the YZ plane, where it appears the EdU+ signal is nestled within the cell body space.

Example EdU IFA images

Infected treated

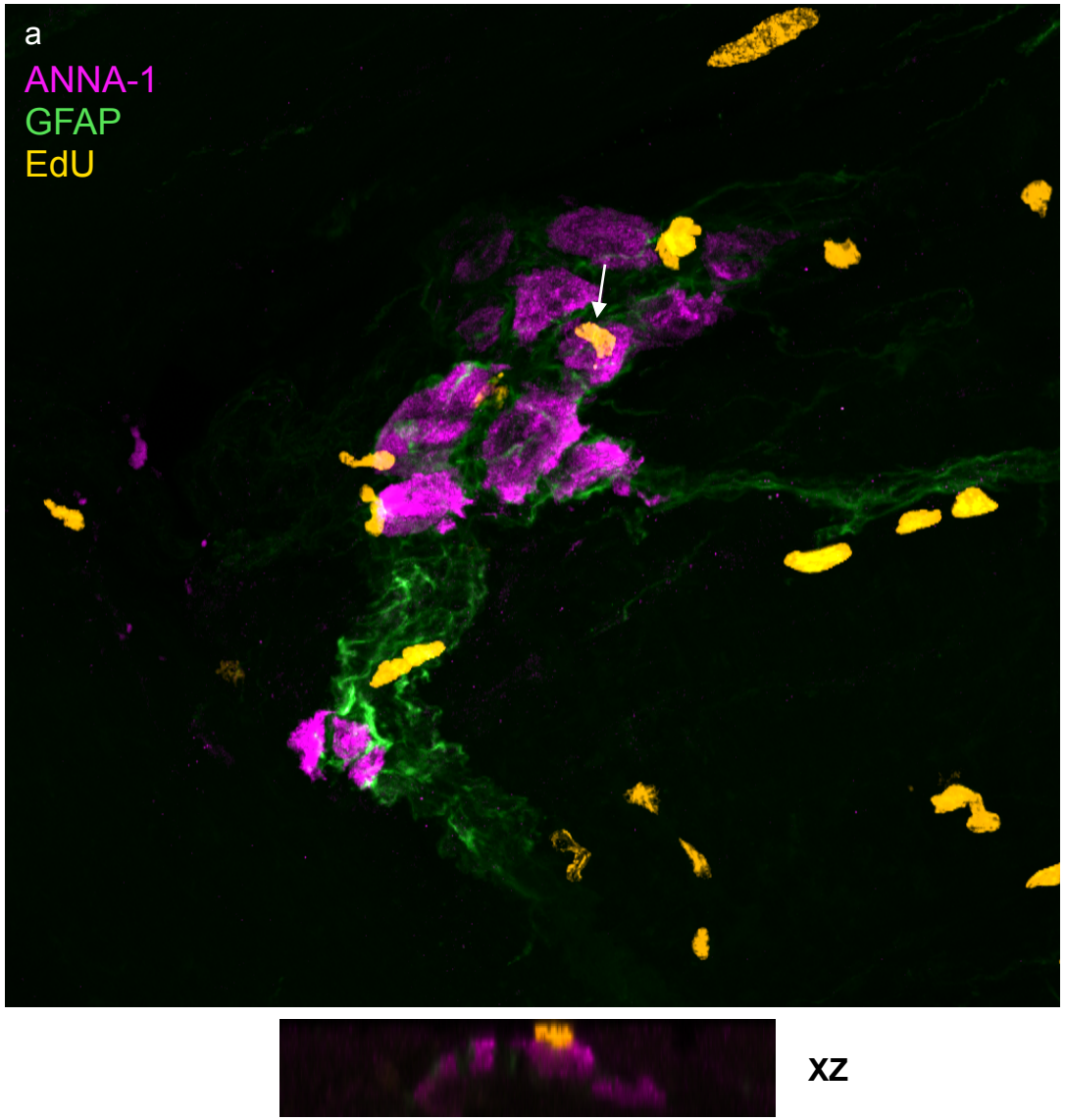

Infected treated

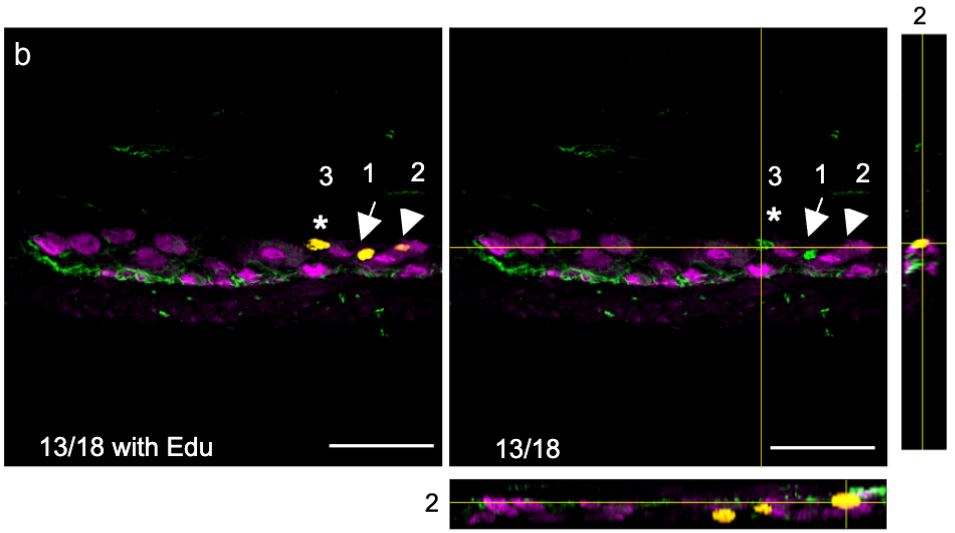

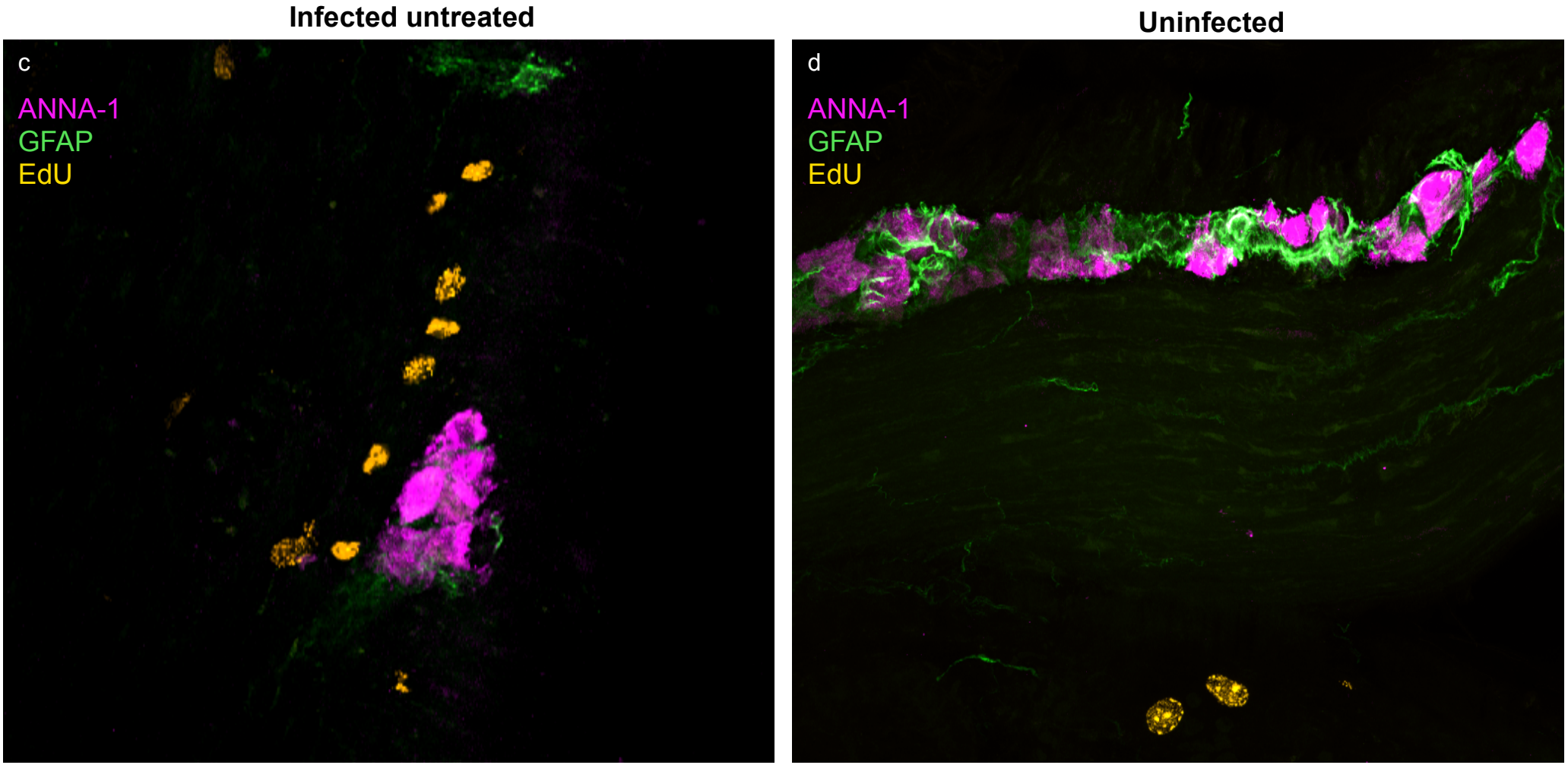

Figure 3.6.2.2.1 Representative images of EdU+ANNA-1+ colocalization events in the large intestine, at 33 weeks.
EdU treatment occurred between during weeks 10, 12 and 16 post infection. a) An image from an infected benznidazole treated mouse. White arrow indicates an EdU+ ANNA-1+ neuronal cell body. To better show the localisation, orthogonal view displays the 3D image in two 2D views; top to bottom (XZ) and left to right (YZ). XZ and YZ orthogonal views of identified Edu+ANNA-1+ cell body give a 3D spatial context of signal co-localisation. b) Image from A. Khan et al (2023) revised manuscript. Each panel depicts slice #13 from a Z-stack of 18 total slices. Left panel with the EdU channel on, and right panel without EdU channel. Arrows labelled '2' indicate EdU+ANNA+ co-localisation with corresponding orthogonal views. Arrows 1 and 3 indicate EdU+GFAP+ co-localisation. c. Image from an infected untreated mouse. d. Image from an uninfected control mouse. Each image is a compressed Z-stack of 20 slices each with 1.03 μm thickness, captured at 400x magnification.

In Fig. 3.6.2.2.1b we can observe the same phenotype in another treated mouse, with the arrow labelled ‘2’ on both panels pointing to the same cell with the EdU channel on and off. The corresponding orthogonal views show the EdU+ signal is amongst the ANNA-1+ structure. This is distinct from the other two EdU+ cells in this ganglion, which are GFAP+.

In the infected untreated samples, we observed many proliferating cells around the ganglia, with a cluster of cells visible in the representative example image (Fig. 3.6.2.2.1c). There was also a paucity of normal neuronal cell bodies and glial filament, consistent with the denervation previously documented in this mouse model (16). We hypothesise that many of these EdU+ cells are putative immune cells or cells involved in the tissue repair process. Any immune cells observed here were not likely immune effector cells, but long-term tissue resident memory cells. This is due to EdU being pulsed at week 10, 12 and 16 post-infection, meaning any EdU+ cell must have remained in the tissue for a minimum of 17 weeks.

In the uninfected controls, we rarely observed EdU+ cells either within the ganglia or the smooth muscle layer. EdU+ cells were visualised in the mucosal layer, presumably associated with homeostatic turnover of this region (Fig. 3.6.2.2.1) (30).

EdU cells were counted and categorised for each group to garner insights into tissue and neuronal homeostasis during this period of infection.

a

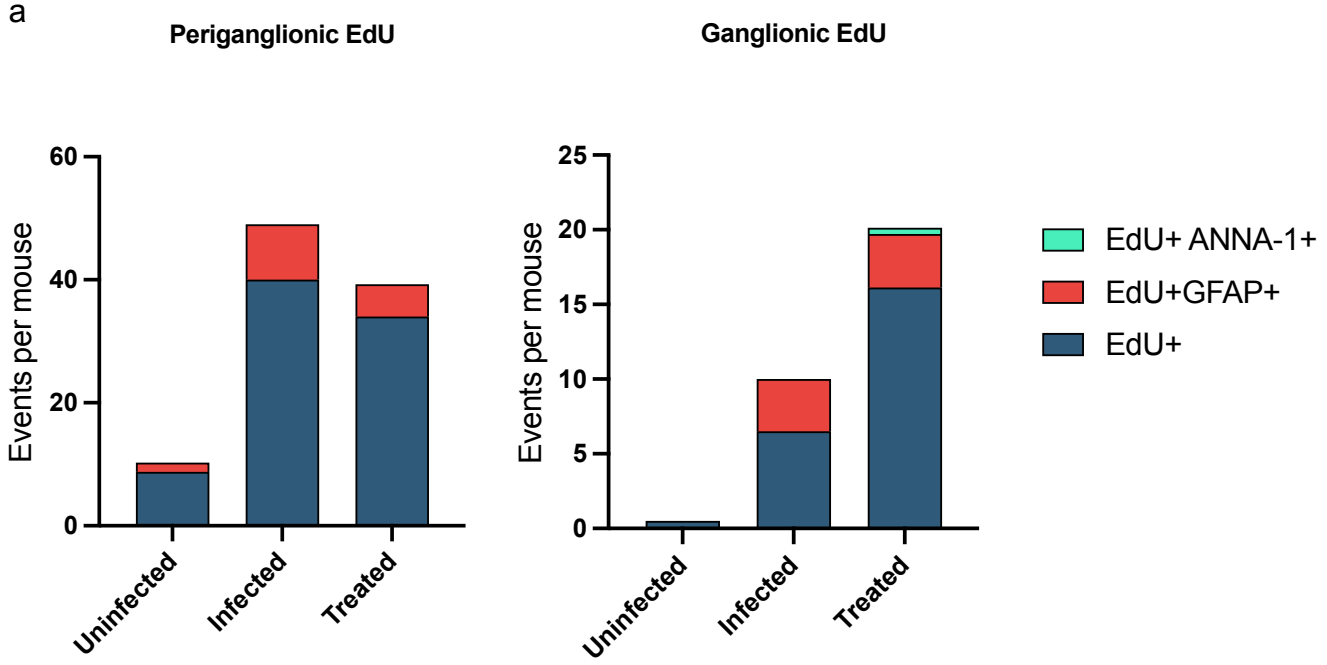

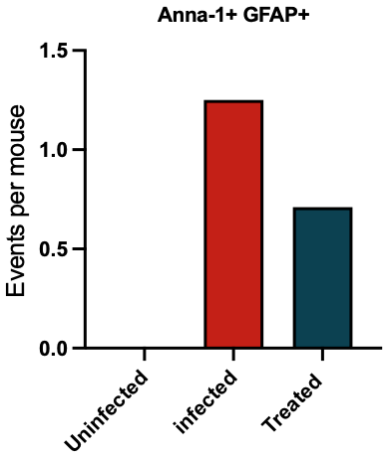

Figure 3.6.2.2.2. 'Long repair window"
a). Graphs depicting the distribution of EdU+ events in both the smooth muscle and connective tissue around ENS ganglia (Peri-ganglionic) and within the ganglionic structures (Ganglionic). The total number of EdU positive cells was counted and grouped by location and co-localisation then normalised as events per mouse in each experimental group. In the peri-ganglionic regions, the events per mouse were as follows: Uninfected; 8.75 EdU+, 1.5 EdU+ GFAP+. Infected: 40 EdU+, 9 EdU+GFAP+. Treated: 34 EdU+, 5.3 EdU+GFAP+. Within myenteric neurons, the events per mouse were as follows: Uninfected; 0.5 EdU+. Infected; 6.5 EdU+, 3.5 EdU+GFAP+, 1.25 ANNA-1+GFAP+. Treated; 16.14 EdU+, 1.29 EdU+ANNA-1+, 3.57 EdU+GFAP+, 0.71 ANNA-1+GFAP+. b) Table showing total number of EdU+ events by location and co-localisation.
Mice treated with benznidazole 6 weeks post infection, and pulsed with EdU at weeks 10, 12 and 16. Mice sacrificed 33 weeks post infection.

b

33 week experiment	EdU events					Non-EdU
Group	Ganglionic EdU+	Peri-ganglionic EdU+	EdU+ ANNA+	Ganglionic EdU+GFAP	Peri-ganglionic EdU+GFAP	ANNA+ GFAP+
Treated	113	238	3	25	37	5
Infected	26	160	0	14	36	5
Uninfected	2	35	0	0	6	0

We observed slightly more peri-ganglionic total EdU+ events per mouse in the infected untreated group (40) than treated (34), and more ganglionic total EdU+ events in the infected treated group (16.1) against untreated (6.5) (Fig3.6.2.2.2a). Peri-ganglionic EdU+ GFAP+ glial cell colocalization events were more frequent in the infected untreated group (9) than treated (5.3), with rare observations also made in the uninfected control (1.5). Ganglionic EdU+GFAP+ glial cells were not observed in any of the uninfected controls, with a similar number of events observed in both treated and untreated infected group; 3.57 and 3.50 respectively. Thus, enteric glial cell proliferation appeared to be increased in *T. cruzi* infected mice, but benznidazole treatment did not have a noticeable effect on it.

Importantly, EdU+ ANNA-1+ neuron colocalization events were only observed in the infected treated group, with a total of 3 counted occurring at an average of 0.43 events per mouse. Although this cell phenotype was very rare, this does indicate that there is a proliferative phase in at least some neurogenesis events after benznidazole-mediated cure of *T. cruzi* infection.

Other key differences were a total of 57 more ganglionic EdU+ events, excluding co-localisation events, occurring in the treated group than the untreated (Fig3.6.2.2.2b) and, conversely, more peri-ganglionic EdU+ events occurring on average in the untreated group than treated. However, a caveat to this assessment was the absence of statistical analysis. The minimal EdU+ staining across the uninfected controls suggests these events were driven by either infection and treatment, or both. The co-labelling of GFAP and EdU was indicative of active proliferation of glial support cells (Fig. 3.6.2.2.3a). In the representative example image overleaf, the

white arrow indicates a yellow cell, confirming the co-labelling of GFAP in green and EdU in red. This was confirmed in the YZ and XZ plane images where there is an overlap of signal from both labels throughout the cell structure. Upon splitting the channels, it was evident that the morphology of the co-labelled cell was visible in both the EdU and GFAP channel independently (Fig. 3.6.2.2.3b). This phenotype was also observed in the infected untreated group.

Interestingly, there was a total of five ANNA-1+ GFAP+ colocalization events (Fig. 3.6.2.2.2), even though these markers are typically considered as neuron- and glial cell-specific respectively. These were EdU-negative cells in all cases and observed in both infected untreated and treated groups, which averaged to 0.71 and 1.25 events per mouse after data were normalised to the sample size of each group. No events of this type were observed in the uninfected group.

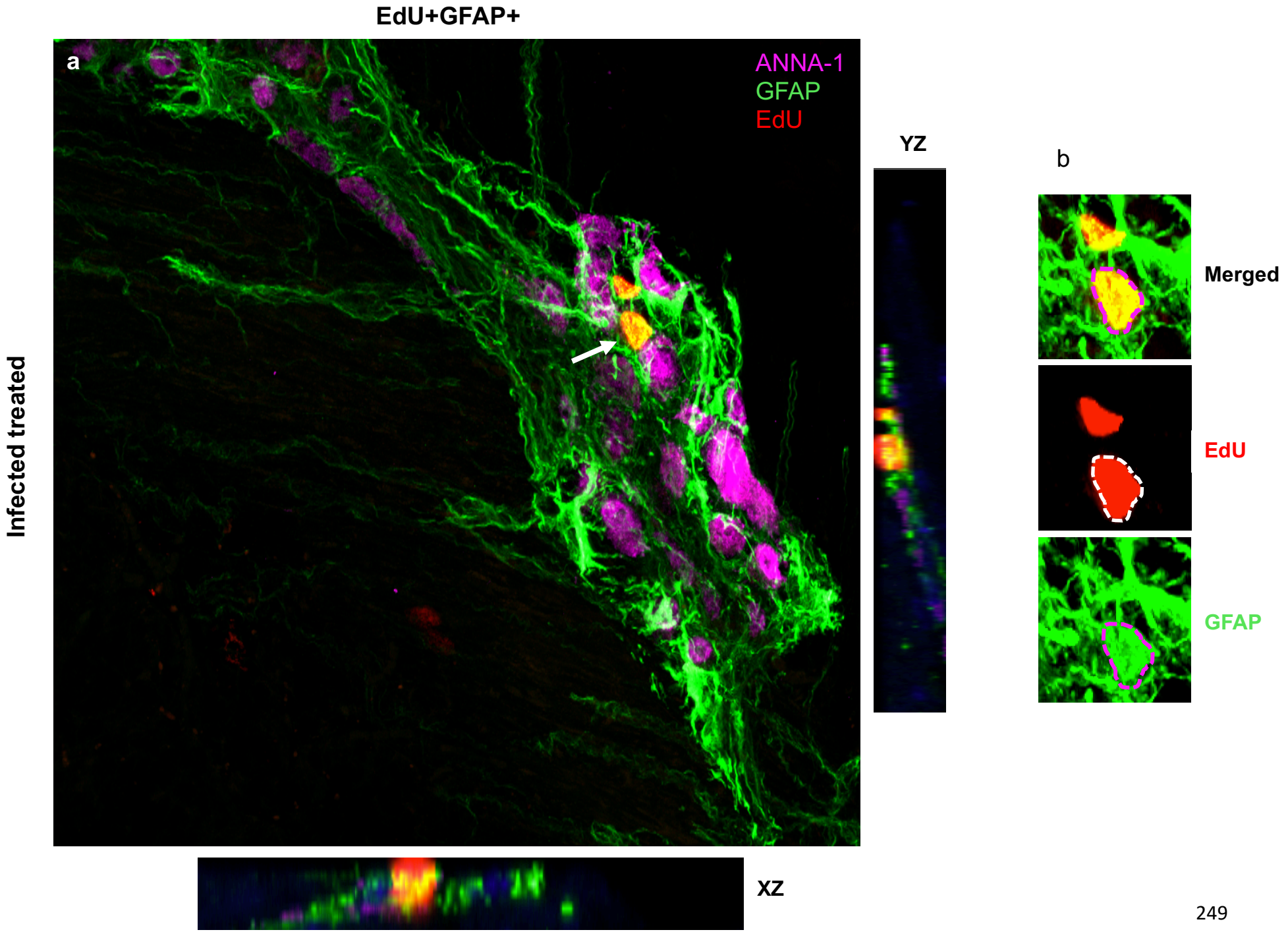
EdU+GFAP+
a
ANNA-1
GFAP
EdU
YZ
XZ
Infected treated
b
Merged
EdU
GFAP

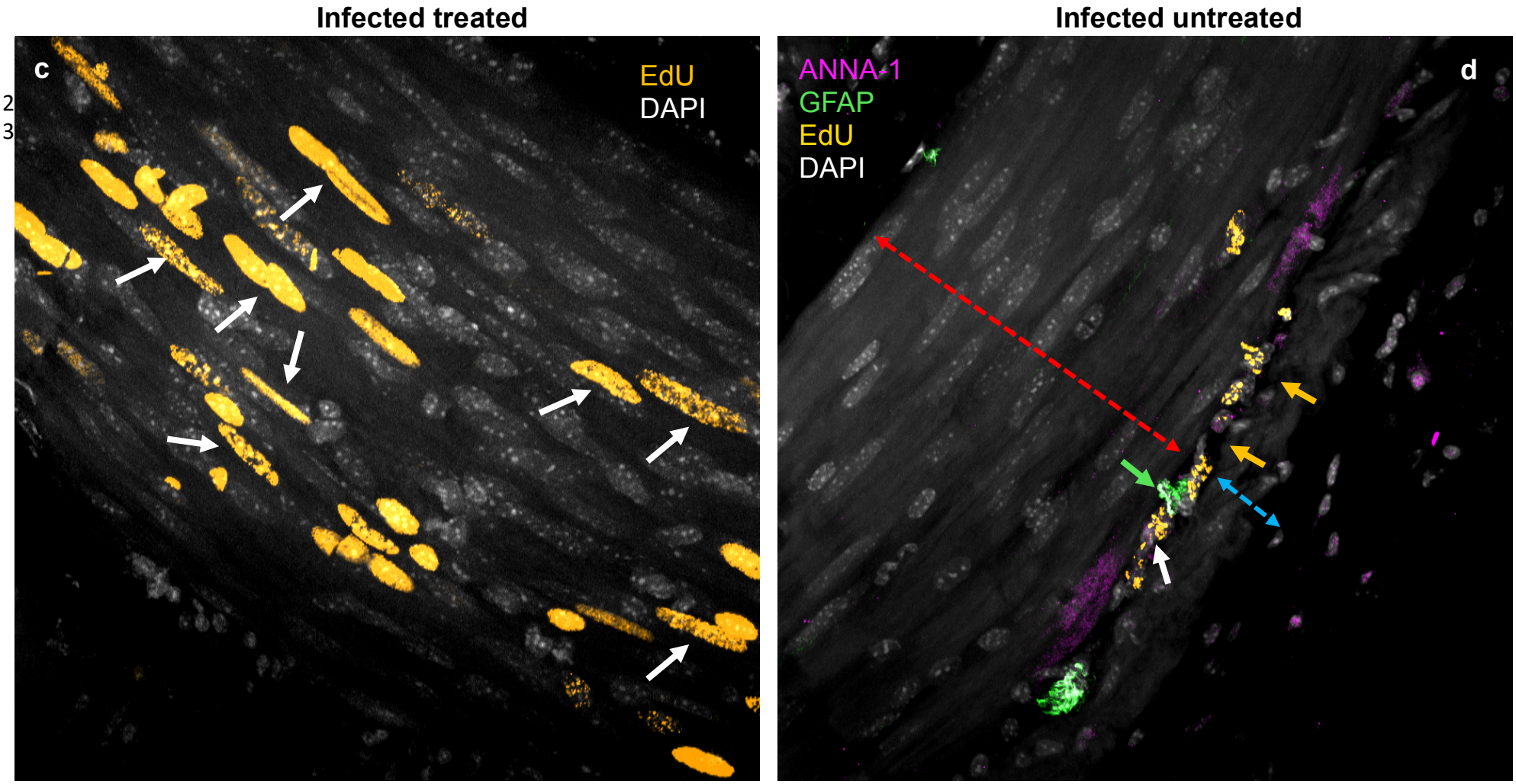

Figure 3.6.2.2.3. Additional observed EdU phenotype in the "long repair window" where EdU was pulsed at weeks 10, 12 and 16 post infection.
a) Image of enteric ganglia from an infected treated mouse, showcasing a colocalization of EdU (red) and GFAP (green) highlighted by a white arrow. YZ and XZ planes included, showing 'yellow' foci of overlap. b) Split channels showing this same colocalising event showcasing the morphological similarities of both markers in a spatial context. Morphology of the co-labelled nucleus outlined in white. c) large number of progeny of proliferating cells in the circular muscle layer of the large intestine. Arrows indicate morphologically distinct elongated nuclei. Many different morphologies can be observed in distinct clusters. d) Image showcasing cell proliferation indicated by 'fragmented' EdU activity in the myenteric space between the circular muscle layer, the length of which indicated by red arrow, and longitudinal muscle layer indicated by blue arrow. All images taken at 400x magnification. ANNA-1 visualised in magenta, EdU in orange, GFAP in green and DAPI nuclear staining in white/grey.

There was also evidence of EdU-incorportating cells across the smooth muscle layer in regions associated with an absence of neuronal or glial cell marker reactivity (Fig. 3.6.2.2.3c). There was a varying morphology of these EdU+ cells including observed elongated nuclei, reminiscent of myofibroblasts (31) highlighted by white arrows in the circular muscle layer. We theorise the rounder more uninform cells are likely to be leukocytes, with specific subsets remaining for the rest of the experiment. A local influx of infiltrates, across the smooth muscle layer and myenteric space, could be associated with the absence of neuronal staining. However, the EdU+ effector cells responsible for this would unlikely still be focal at 33 weeks post infection.

We also observed EdU+ signal in between the circular and longitudinal muscle layers, where the myenteric plexus resides (Fig. 3.6.2.2.3d). The length of the circular muscle layer is represented by a red arrow, and longitudinal muscle layer with a blue arrow. Situated between the layers resides the myenteric plexus, and in this image we saw an absence of ANNA-1+ neuron staining, but an unusual pattern of EdU+ signal. The speckled appearance of EdU, indicated with the white arrow, forms the typical arrangement and cytomorphology of ganglia usually observed in this region (Fig 3.6.2.2.3d). There was also a small pocket of glial cells, indicated with the green arrow, that were also positive for EdU. This suggested that the area may have been damaged (denervated) and was undergoing repair at the time of sampling. There was visible damage to the ganglionic area, with an ablation of neurons and regions refractory to nuclear staining indicated by orange arrows. This was similar to the neuronal “white space” phenomena outlined in chapter 1.

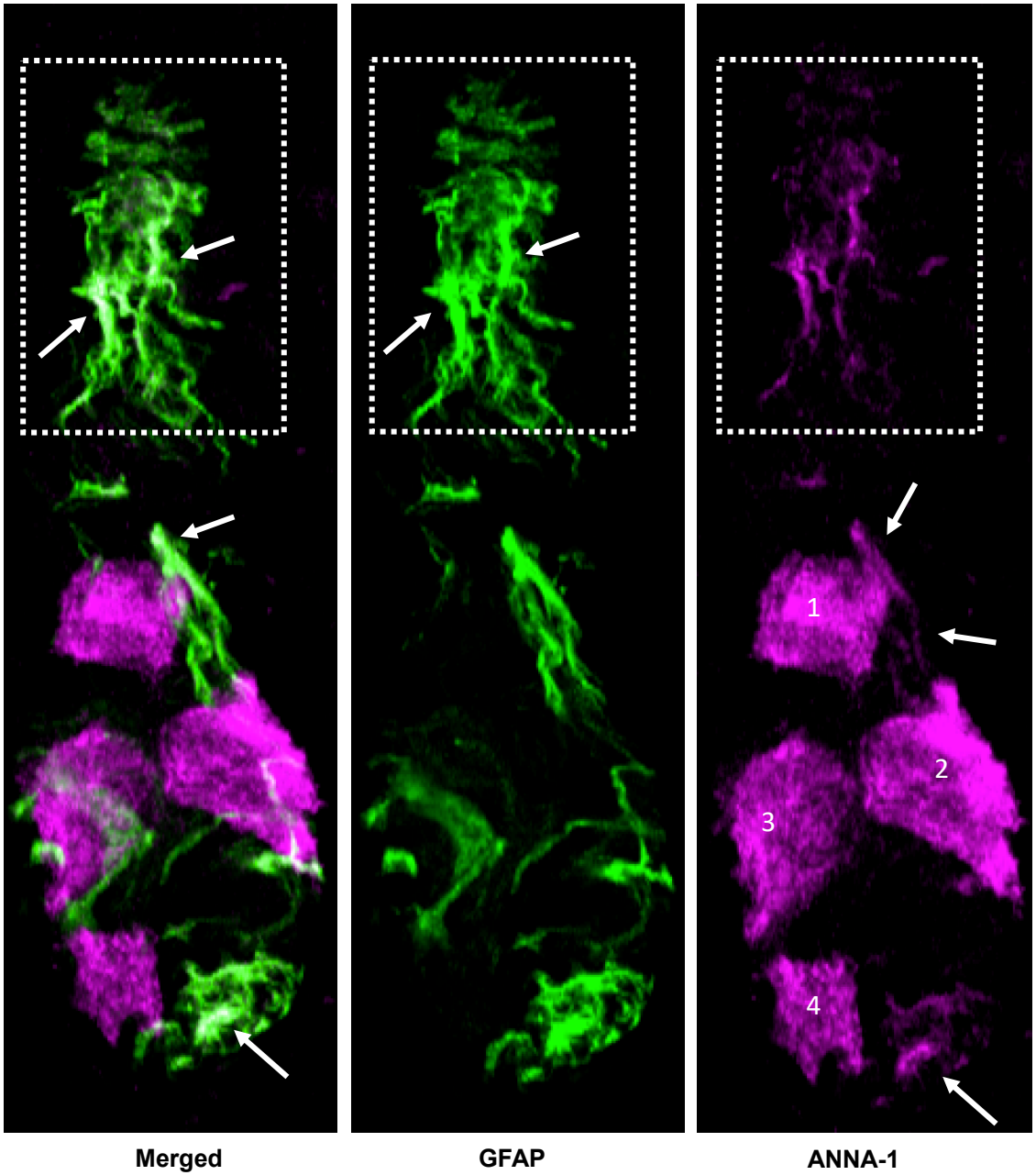

Figure 3.6.2.2.4. Example of ANNA-1 and GFAP colocalization in the myenteric plexus from a treated infection in the "long repair window".
Left panel depicts the merged GFAP and ANNA-1 channels. White arrows indicate co-labelling of the two markers where white areas highlight merging of signal. Middle panel is the GFAP only channel, with the arrow indicating the absence of intense white areas seen in the merged image. Right panel is ANNA-1 channel only, with arrows indicating similar fibrillary morphology observed with in the GFAP only channel, and dotted box showing a large region of co-expression resulting in the white regions in panel 1.

ANNA-1+ GFAP+ co-staining was observed in both infected treated and untreated, but not in uninfected controls. Here, in an infected untreated representative example (Fig. 3.6.2.2.4), we demonstrate co-occurrence of both markers. Co-localisation occurred in a distinct fibrillar morphology, indicated by the dotted box, and suggests there was a common progenitor for these structures. The fibrillary structure, in the dotted box, is predominantly GFAP+ with much of the area ANNA-1-. Moreover, observing the ANNA-1 only and merged channel, it was clear there was no aspect of ANNA-1 specific staining in this region that wasn't also GFAP+. This may indicate the occurrence of a metaplasia event, whereby neurons may be trans-differentiating into glial cells, or vice versa, to maintain the integrity of the ganglion after collateral damage by the immune system and or infectious challenge by parasites. Alternatively, these cells may be stem cell derived, transiently expressing markers of both neuronal and glial prior to selection of a particular fate pathway.

Since this dual glial/neuronal marker expression phenomenon was not observed in the uninfected control cohort, we conclude that it was probably dependent on current or past *T. cruzi* infection, although this phenotype was still very rare in the infected and treated groups. We also observed that this co-expression was not focal to one area of a ganglion (Fig. 3.6.2.2.4). Throughout the entire ganglionic structure there was evidence of ANNA-1+ GFAP+ regions, often continuous structures stemming from the neuronal cell bodies, such as from cell body 1 and 2 (Fig. 3.6.2.2.4). Interestingly, the four primary cell bodies in the ANNA-1 channel were all GFAP-. This allowed us to exclude cross-reactivity of antibodies as an explanation, and increased confidence that the co-staining observed was true and specific.

3.6.3.3.2. 12 week ‘short repair window’ experiment

Just as with the chronic experiment, transverse cross sections of the distal colon were stained for IFA. Representative images are shown for each experimental group, with the aim to identify co-expression and co-localisation events at an earlier time course than depicted in the first experiment. EdU was pulsed during the infection window prefacing the natural reduction of transit time delay in the infected group and in the window immediately following the end of benznidazole treatment in the treated group.

Infected treated

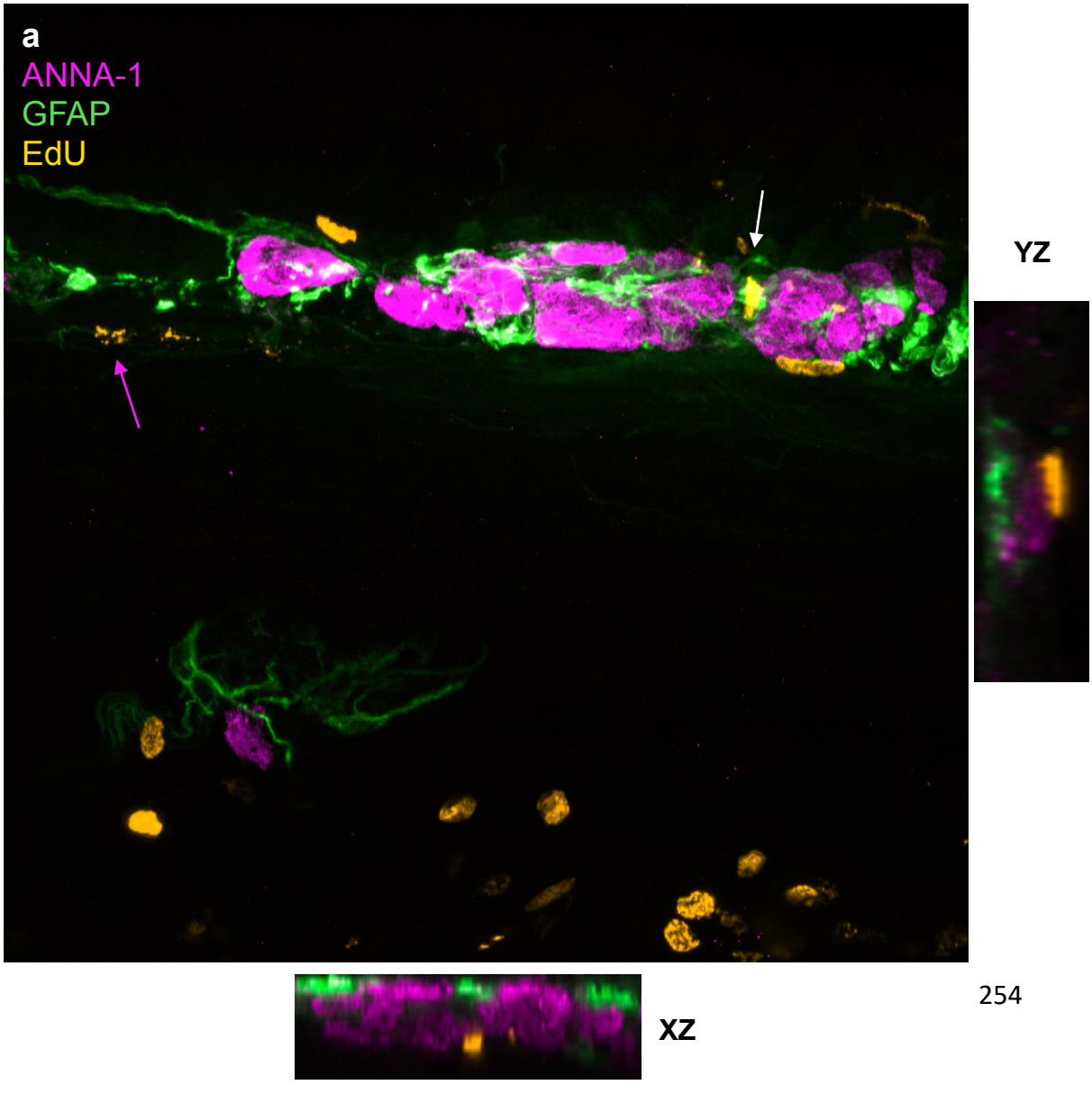

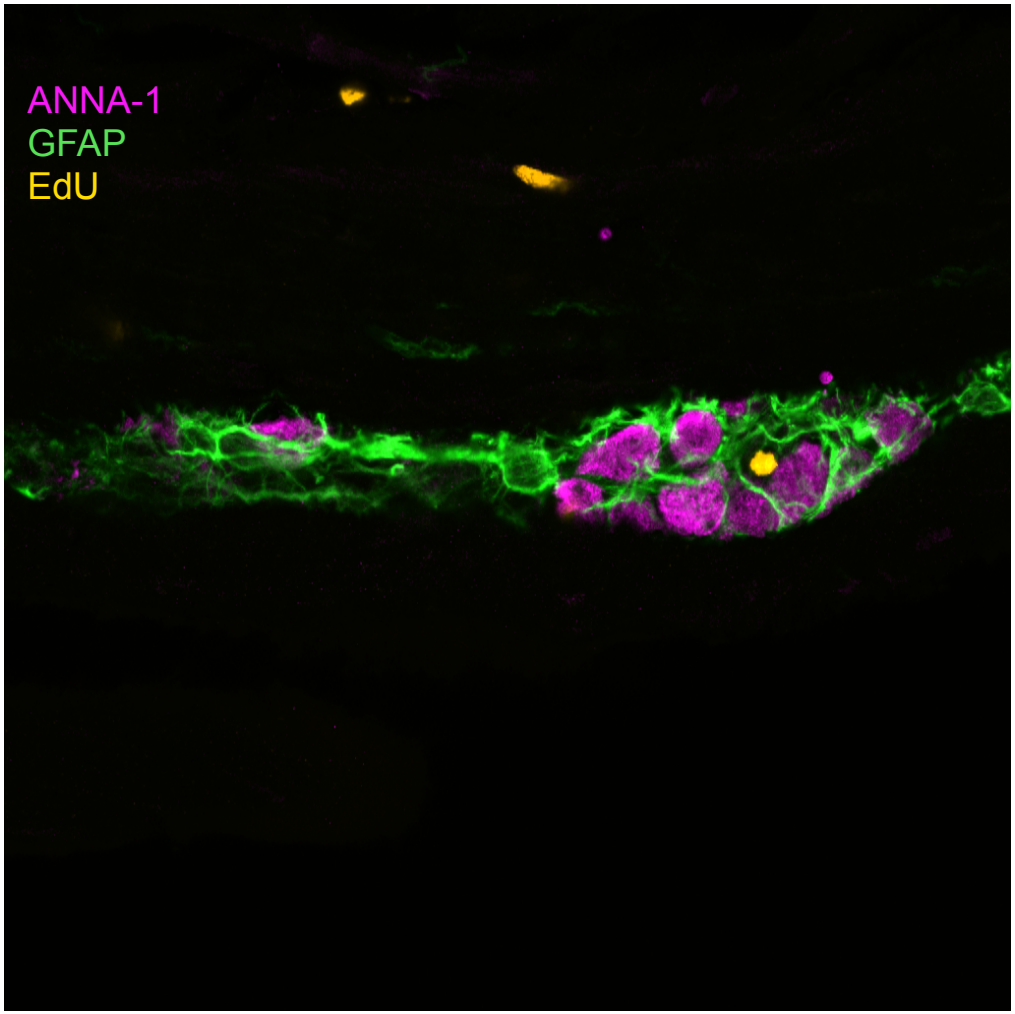

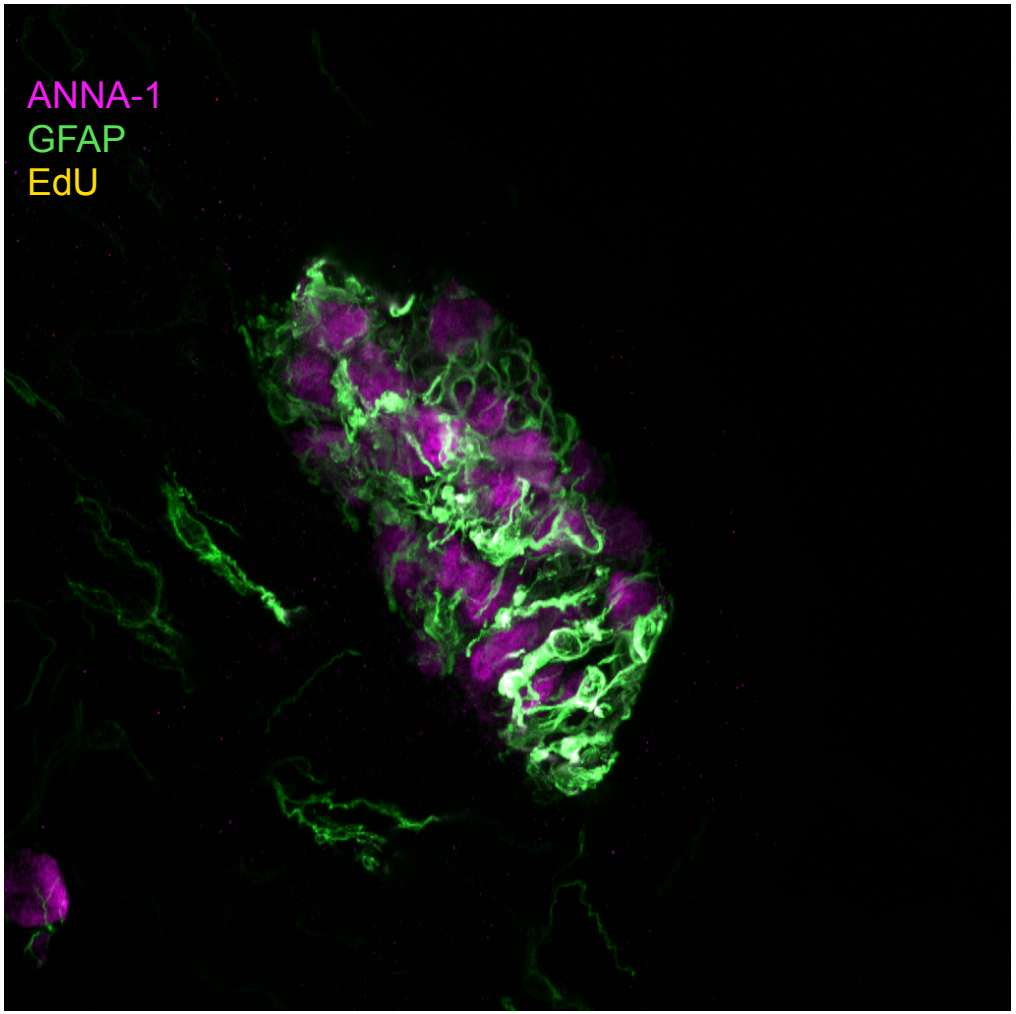

Infected untreated **Uninfected**

Figure 3.6.3.3.2.1 Representative images of myenteric plexus ganglia in the colon for each experimental group in the 12-week, "short repair window", experiment.
Benznidazole treatment began at 6-weeks post infection, with EdU being pulsed at weeks 9, 10 and 11. a) An image of the enteric neurons and glial cells in an infected treated colon, at 400x magnification. Image comprised of a compressed Z stack. White arrow indicates a putative EdU+ ANNA-1+ neuronal cell body. XZ and YZ orthogonal views of identified Edu+ANNA-1+ cell body give a 3D spatial context. b) Enteric neurons and glial cells in an infected untreated colon. c) Enteric neurons and glial cells in an uninfected control colon. Each image is a compressed Z-stack of 20 slices each with 1.03 μm thickness, captured at 400x magnification

Qualitatively, there was clear variability in EdU staining across the experimental groups (Fig. 3.6.3.3.2.1). In the infected treated group, there was no evidence of ANNA-1 and EdU co-localisation. In the representative image we noted a ganglionic EdU+ cell that was apposing neuronal cell bodies, but without obvious co-occurrence. The compressed z-stack image shows the EdU+ cell (indicated by the white arrow) residing medially between two ANNA-1+ cell bodies, amongst glial cells (Fig. 3.6.3.3.2.1a). The orthogonal views show the morphologically distinct EdU+ cell. Similar observations were made in enteric ganglia from infected untreated mice (Fig. 3.6.3.3.2.1b). Pink arrows in both infected treated and infected untreated indicate absence of ANNA-1 staining in regions of ganglia where it would normally be expected, consistent with neuronal damage occurring or persisting at week 12 post infection, irrespective of the alleviation of benznidazole treatment. As with the chronic experiment, there was less EdU staining in the uninfected control group (Fig. 3.6.3.3.2.2).

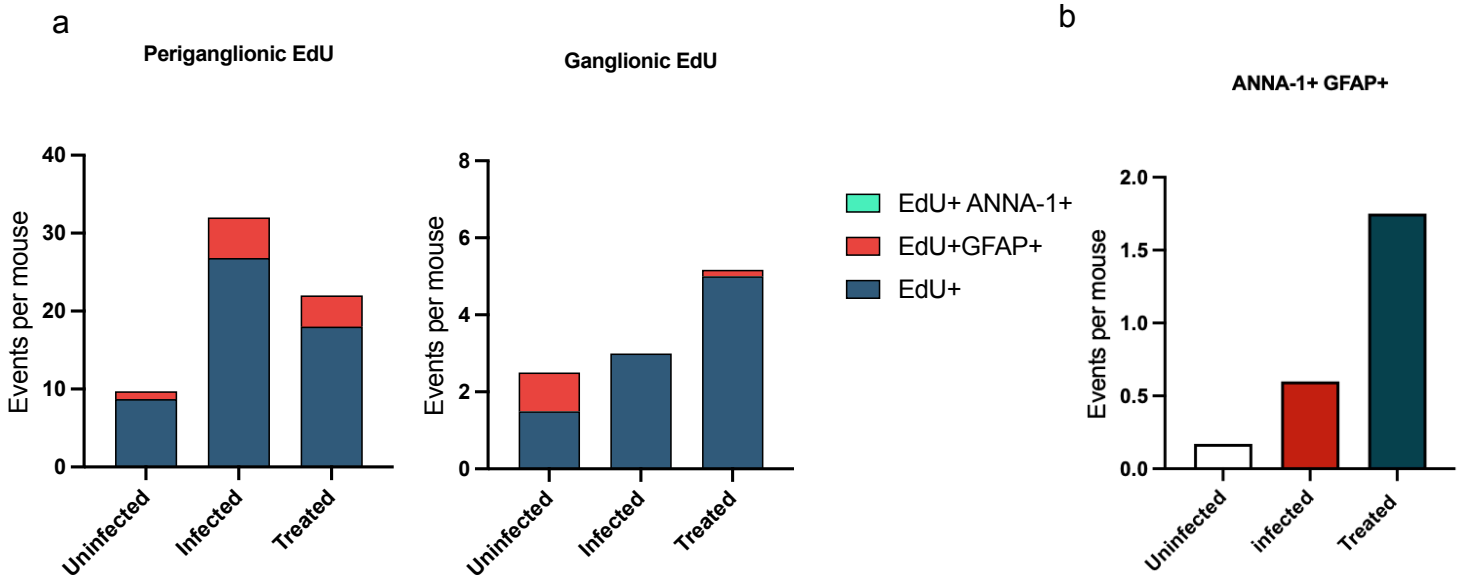

c

12 week experiment	EdU events					Non-EdU
Group	Ganglionic EdU+	Peri-ganglionic EdU+	EdU+ ANNA+	Ganglionic EdU+GFAP	Peri-ganglionic EdU+GFAP	ANNA+ GFAP+
Treated	20	72	0	4	16	7
Infected	15	134	0	0	26	3
Uninfected	9	52	0	1	6	1

Figure 3.6.3.3.2.2." Short repair window"
a). Graphs depicting the distribution of EdU + events in both the smooth muscle around the ganglionic space (Peri-ganglionic) and within the ganglionic structure (ganglionic). Total number of EdU positive cells were counted and grouped by location and co-localisation then normalised as events per mouse in each experimental group. In the peri-ganglionic space, the events per mouse were as follows: Uninfected; 8.70 EdU+, 1.0 EdU+ GFAP+. Infected: 26.80 EdU+, 5.20 EdU+GFAP+. Treated: 5 EdU+, 0.17 EdU+GFAP+. Within myenteric neurons, the events per mouse were as follows: Uninfected; 1.5 EdU+, 1.0 EdU+GFAP+; Infected; 6.5 EdU+, 3.5 EdU+GFAP+, 1.25 ANNA-1+GFAP+. Treated; 5.0 EdU+, 0 EdU+ANNA-1+, 0.17 EdU+GFAP+. b) Table showing ANNA-1+GFAP+ events per mouse. Uninfected; 0.17; infected 0.60; treated 1.75. Mice treated with benznidazole 6 weeks post infection, and pulsed with EdU at weeks 9, 10 and 11. Mice sacrificed 12 weeks post infection.

Overall, the trends observed were similar to the 33 week experiment, namely in the infected groups there was an upward trend of ganglionic EdU events occurring in the benznidazole treated than untreated infections (20 vs 15) and, conversely, more peri-ganglionic EdU events occurring in the infected untreated group than in the treated (134 vs 72). However, overall, there were substantially fewer total EdU+ events counted in the 12-week experiment (n=173) than the chronic experiment (n=574). This might be due to the broader EdU pulsing window in the chronic experiment, or due to there being less cellular replication activity in weeks 9,10 and 11 than at weeks 10, 12 and 16 post infection.

In this experiment there were no observed EdU+ ANNA-1+ events in any of the groups, unlike the three observed events in the chronic experiment. Moreover, in this experiment there was EdU+ GFAP+ co-localisation observed in the uninfected controls, but at a much lower occurrence than both the infected groups (Fig. 3.6.3.3.2.2c).

The rare ANNA-1+ GFAP+ events identified a slightly different trend compared to the chronic experiment (Fig 3.6.3.3.2.2.c). In the chronic experiment there were 5 events in both the infected and treated, averaging at 1.25 and 0.71 events per mouse respectively, with none noted in the uninfected. In the 12 week experiment the prevalence of ANNA-1+ GFAP+ cells was higher in the treated group, with 7 total events occurring at an average of 1.75 events per mouse. This was more than double that observed in the infected untreated group; 3 total events at 0.60 events per mouse. There was also one observed event in the uninfected control, suggesting this phenotype may not be infection exclusive as initially thought, but a mechanism

that is upregulated in response to infection and/or treatment. However, given the very low numbers of these events, these phenomena would need to be assessed with a substantially larger sample size.

3.7. Summary

Parasite burden

In the chronic experiment we observed a 25**%** cure rate, which affected interpretation of pooled data from the treated group. Despite this, there was no significant difference in *in vivo* bioluminescence signal between the treated and uninfected groups at any timepoint. This was similar to the 'short repair window' experiment, where in the two post-treatment timepoints (week 9 and 12) the bioluminescence signal in the treated was reduced to background levels. At weeks 9 and 12 the parasite burden of the infected untreated cohort was reduced in both experiments, indicative of an immune mediated reduction in parasite load.

Transit time

In the chronic experiment there was no significant difference in average transit time between treated and uninfected groups between weeks 18 and 33, except for week 30. There was a high degree of heterogeneity in gut function irrespective of the infection status, but much of the variability across this experiment was due to a combination of high rate of relapse, and low *n*. The key difference between the two experiments was at week 12. In the chronic experiment, the average transit time for both the infected and treated groups dropped as was the case for parasite burden, resulting in no significant difference in transit time between these two groups when compared to the uninfected. In the 'short repair window' experiment, despite the average transit time dropping, they remained significantly increased compared to the uninfected. There was also no significant difference between the infected and treated, which corroborated the experimental differences.

Colonic cellular proliferation

There were some similar trends in EdU-based observations of cellular proliferation events between the two experiments. There were more peri-ganglionic events per mouse than ganglionic, the treated cohort had the most frequently observed ganglionic events, and the untreated the most peri-ganglionic. However, there were more EdU+ events observed in the chronic experiment overall. The key differences between the experiments were with ANNA-1 co-localisation events. EdU+ in ANNA-1 expressing cells, although rare, were only observed in the chronic 'long repair window' experiment. Moreover, in the chronic experiment, the experimental group with the highest rate of ANNA-1+ GFAP+ co-expression was the untreated, whereas in the 'short repair window' experiment these events occurred more frequently in the treated group.

3.8 Discussion

3.8.1. Cure vs relapse

In the chronic experiment, the benznidazole cure rate was lower than previously described. Here were describe a 25% cure rate, with previous experiments outlining a cure rate of 60% (A.K, 2023). Moreover, in the 12-week experiment the benznidazole treated group exhibited a transit time delay at endpoint, despite having *in vivo* signal below detectable levels. This may suggest that a sub-set of mice may still have been infected, but below the detection threshold. This rendered it difficult when assessing the effect of sterile cure (as distinct from treatment) on transit delay accurately. The groups were still viable to investigate the tissue repair and functional transit recovery at this 12-week time point with the EdU analysis since the massive

reduction in parasite load, even if temporary, would likely enable repair and regeneration process to be activated to a greater extent than is the case of untreated infections.

3.8.2. Pathways for functional ENS repair

The incorporation of EdU by ANNA+ cells suggests proliferation of neuronal pre-cursors occurred between weeks 10 and 16 post infection, 1 to 7 weeks post treatment. The morphologies of these cells were not consistent with typical ANNA+ neuronal cell bodies, presenting as smaller and enveloped in ANNA-1+ signal. This suggests the presence of an intermediate proliferation stage, and not the direct transdifferentiation of glial cells to neurons, although these pathways are not mutually exclusive. This is consistent with published models where adult neurogenesis has been observed. In one study it was suggested that enteric neurons are regularly replaced as part of neuronal stem cell dependant homeostasis, which involves a high neuronal cell turnover of 4-5% a day (20). However, the claims of this study have been scrutinised as the results have not been reproducible, with follow up studies suggesting that enteric neurogenesis is absent, or extremely limited in a steady state (32). The mechanisms of the disputed ‘steady state enteric neurogenesis’ has been seen in settings of tissue damage, namely Hirschsprung’s disease (33) . Myenteric neurons fated for programmed death can be identified by cleaved caspase 3 labelling (20). Muscularis macrophages, that communicate with enteric neurons (34), conduct a robust phagocytic response to clear neuronal debris. Neuroepithelial stem cell protein (Nestin), a cytoskeletal intermediate filament phenotypically distinct from differentiated myenteric ganglia, give rise to adult myenteric neurons in the healthy gut, suggesting they are key candidates as enteric

neuronal precursor cells (ENPC). It has also been described that putative ENPCs in adult murine colon migrate into the myenteric plexus from extra-ganglionic locations (35). Serotonin (5-hydroxytryptamine (5-HT_4)), a prokinetic agent that acts on serotonin receptors in the intestine regulating peristalsis and gastric emptying (36), is implicated in the activation of extraganglionic Sox-10 expressing cells generating enteric neurons in (35).

By using these biomarkers of enteric neurogenesis, there is scope to further map the processes responsible for functional peristaltic improvement. By implementing an anti-Nestin antibody it could be possible to test whether some of the large number of EdU+ peri-ganglionic cells are neuronal precursor cells. It would be particularly interesting to dissect the trafficking associated with these sub-types, and whether or not a certain microenvironment around the myenteric plexus supports successful differentiation i.e. if the differentiation of Nestin+ cells is conditional on the ratio of pro/anti-inflammatory cytokines, or if parasites are present. Moreover, an abundant number of EdU+ GFAP+ events compared to uninfected means there is active proliferation of GFAP+ glial cells at sites of ENS damage and repair. This suggests a supportive role of enteric glia where they are likely to remain dormant under the normal ENS niche, and are activated in response to disruption of the environment by infection. This is consistent with what was described in chapter 2, where qualitative evidence for upregulation of GFAP signal was observed in cyclophosphamide treated mice, where immune regulation and communication may have become dysregulated. Contrary to this, a study where colitis was chemically induced by, dextran sulfate sodium (DSS), resulted in a substitutional increase in the rate of gliogenesis assessed by GFAP expression, a response that was eliminated in the

absence of 5-HT_4. This suggests that both neurogenic and gliogenic responses to intestinal inflammation are critically driven by local serotonin signalling (37). It would interesting to investigate if this is also the case in the setting of *T. cruzi* infection.

Benznidazole treatment does not seem to make much difference to the number of EdU+ GFAP+ cells compared to untreated infections. However, similar raw numbers of EdU+ GFAP+ cells does not consider the potential execution of differing functions in different situations or microenvironments. Glial cell recruitment can improve tissue function in the CNS (38), with a close relationship having been identified between neural stem cells and glia (39). GFAP-expressing progenitors share morphological and molecular characteristics of astrocytes (a major subset of CNS glial cells) (40), and glial cells replenish neurons lost in injured retina and adult carotid body (41). These processes are categorised as part of a 3-phase multicellular time course response to CNS damage (42). The first phase entails the inflammatory processes resulting in cell death, which prefaces the second phase: cell proliferation and tissue replacement. This involves a myriad of cells, including epithelial progenitors, fibroblast lineage cells, inflammatory cells, various glial cells and neural linage progenitor cells (scar forming astrocytes) (42). The functions of the fibroblast lineages and inflammatory cells reflect classic wound responses (43), whereas the proliferation of scar forming astrocytes are unique to the CNS (42). Astrocyte scarring surrounds the neuronal lesion and astroglial progenitors gather alongside inflammatory and fibroblast lineage cells (42). The micro-environment permits the long-term remodelling of the ECM within the neuronal lesion, which includes the modulation of collagen and glycoprotein components (44). There is also gradual and ongoing peri-ganglionic remodelling in the reactive perimeter opposing the neuronal

lesion (42). The majority of EdU+ cells observed in the ganglionic and peri-ganglionic space in this study were GFAP and ANNA-1 negative. In comparison, there was little replicative activity, as measured by EdU incorporation, in the uninfected group, which strongly suggests that these EdU+ cells are not components of steady state myenteric homeostasis. As outlined above in the CNS tissue remodelling process, a large influx of inflammatory cells, neuronal progenitors, and fibroblast progenitors surround neuronal lesions.

Although we are largely limited to speculation on the lineage of observed EdU+ cells that are negative for ANNA-1 or GFAP, I theorise those seen in the ganglionic space could be:

1. **Muscularis externa macrophages.** These tissue resident macrophages interact with the enteric neurons in response to damage and display a neuroprotective phenotype, elicited by neuron secreted TGF-β (45).
2. **Myofibroblasts/fibroblast progenitors.** Myofibroblasts are key in the pathophysiological process and possess contraction properties. Myofibroblasts secrete fibrillar collagen type I, III, IV, fibronectin and laminin which are components of the wound healing process (46) .
3. **Mesenchymal stromal cells (MSC).** MSC form gap junction mediated syncytium with smooth muscle layers, have receptors for neurotransmitters, and regulate smooth muscle contraction (47). MSC have platelet-derived growth factor receptor-alpha (PDGFRα) on their cell surface, which is essential for local cell growth, differentiation, and fibrosis. PDGFRα+ ligands such as Wnts, R-spondin 3 and bone morphogenic proteins maintain intestinal

environment homeostasis (48–50). In response to intestinal injury, PDGFRα+ cells secrete pro-inflammatory cytokines and matrix proteins (*Col1a1, Postn, Sparc, Has1*) suggesting MSC PDGFRα+ are also a key target for fibrotic pathogenesis in the GI tract (51). MSC could therefore be a feature of tissue and functional repair in both the treated and untreated infections and contribute to tissue pathology in the untreated.

4. **Enteric glial/neuronal precursors.** EdU+ cells that are negative for either GFAP or Hu (ANNA-1) could be developmental intermediate transitional forms i.e. they have lost GFAP expression but have not started expressing Hu proteins at this transient snapshot in time. Moreover, there may be similarities in the type 2/type 3 progenitor cells described above in CNS neurogenesis (Fig3.3.1) i.e. Nestin+, or Sox-10+ cells.

3.8.3. Co-expression of ANNA-1 and GFAP.

These cells were mainly present during or after *T. cruzi* infection but remain very rare. An initial explanation for this phenomenon was the neuroprotective processes of glia-neuron transdifferentiation. Since the morphology of these co-expressing cells resemble glial cells more closely than neuronal cell bodies, the hypothesis was neurons damaged by immune mediated mechanisms transdifferentiate to glial cells in an act of self-preservation and to support and protect other neurons. Conversely, local glial cells could transdifferentiate into neurons to replenish a depleted population. However, the primary caveat to this theory is that in most neurogenesis models GFAP expression is thought to switch off before neuronal identity is acquired (52). This may be suggestive that our system involves a distinct differentiation pathway not previously described. Moreover, one Hu isoform (HuR) can be

expressed by other cell types that are non-neuronal e.g: anti-ANNA-1 may be able to bind to epithelial and stromal cells, with previous studies noting HuR expression in proliferating progenitors in the crypts and epithelial cells in the lamina propria (53). Therefore, it may be possible that the co-expression with GFAP may not be of neuronal origin. It was considered there may be a technical explanation for this co-expression – the potential bleed through of signal between fluorescent channels. However, this is unlikely since GFAP was in the green channel (Alexafluor488) and ANNA-1 in the far-red channel (Alexafluor647) with a potential overlap of green emission being <2% within the excitation spectrum of the far-red channel, but 0% in the emission spectrum. It is also difficult to explain why technical artefacts would result in dual GFAP+ ANNA-1+ cell phenotype in infected and treated mice, but not in uninfected controls.

3.8.4. Peri-ganglionic EdU+ incorporation

The majority of EdU+ cells were outside the ganglionic space, with events observed spatially across the entire width of the smooth muscle layer. There were notably more peri-ganglionic events in the uninfected compared to the few observed ganglionic events, which likely reflects ongoing tissue homeostatic proliferative processes. The number of EdU+ cells increased in the infected untreated and the treated mice, with the difference between these two groups theorised to be a varying leukocyte populations associated with an active or cured/suppressed infection. Primary amongst those may be muscularis macrophages, which reside near neurons in the myenteric plexus, reside in both the circular and longitudinal muscle layers, and around interstitial cells of Cajal (54,55). The inflammatory profiles between the 12-week and 33-week experiment are likely to be different since EdU+ signal is a

retrospective snapshot in time. In the 12-week experiment, since the mice were culled a week after the final EdU injection, the EdU+ cells must have been present focally for at least a week. Whereas in the chronic experiment, observed EdU+ cells must have been present for at least 17 weeks. This does not take into account the influx or efflux of proliferating cells in either case e.g. peripheral blood EdU+ leukocytes destined for the smooth muscle layer. It is feasible that there are a more diverse range of immune cell types in the 12-week experiment such as monocyte derived macrophages, CD8+ T cells or mast cells, due to this reduced window for cellular efflux. In the chronic experiment there may be an increased ratio of tissue-resident memory CD8+ T cells (T_{rm}). Regulatory T cells (T_{treg}) also play a crucial role in the development of intestinal inflammation in inflammatory bowel disorder as a local imbalance between effector and T_{reg} cells (56). T_{rm} cells also release proinflammatory cytokines such as IFN-γ, IL-2, and TNF-α, which activate natural killer cells and dendritic cells, and others via upregulation of the vascular cell adhesion molecule (VCAM-1) (57). This activity may also explain the recurrence of pathological dysfunction in the treated cohort. To subtype the local inflammatory subset, it would be interesting to follow up this study with:

1. Anti-CD45 antibodies in a spatial (IFA) context, to allow for a full leukocyte count. With the addition of EdU it would be possible to determine which CD45+ cells were present at the time of EdU pulsing, and which CD45+ cells traffic in after. A caveat to this direction is that EdU is systemic, so cells in the bone marrow or lymph nodes that traffic to the gut would be indistinguishable from tissue resident cells. Spatial transcriptomics would be a suitable profiling assay to map CD45+ activity.

2. Anti-CD8 antibodies in an IFA context to allow for a population count of cytotoxic T-cells, which are critical for parasite control. Although it has been demonstrated there is an incomplete recruitment of T cells to colonic infection foci (58), it would be interesting to observe the ratio of T cells around the myenteric plexus in response to infection and treatment, and correlate with a transit functionality assay.
3. Labelling for CD206, a cell-surface protein on M2 macrophages, would be a useful marker for identifying local M2 specific phenotype (59). Moreover, by utilising flow cytometry, gating for $CX3CR1^{hi}MHCII^{hi}Ly6C^{low}$ would isolate muscularis macrophages (60). Anti-CCR2 antibody would help identify bone marrow, monocyte derived macrophages.
4. Labelling for γδ T cells in the intestine may be a suitable candidate for local tissue repair, as well as for myenteric host defence against *T. cruzi*. Migratory γδ T cells have been shown to be important for intestinal mediated defence against *Salmonella typhimurium* and *Toxoplasma gondii* in mice (61), but it has been suggested their main function is immunoregulatory and to maintain homeostasis at sites of injury (62). In an IBD model with αβ T cell-mediated pathology, γδ T cells have been shown to dampen the immune response to prevent further tissue damage (63). Moreover, in a DSS-induced colitis model, γδ T cells localised at sites of damage and induced cell proliferation through the production of the fibroblast growth factor, KGF (64).

The distinct elongated, flat and oval shaped nuclei of fibroblasts/myofibroblasts (31) were observed opposing ganglionic regions, and across the smooth muscle in the absence of ganglia as part of extraganglionic tissue repair. There is a high degree of

diversity and heterogeneity in intestinal fibroblast function and location (65). Crypt fibroblasts are located at varying locations in the crypts near intestinal epithelial stem cells (IESC) (65). PDGFRa^{hi} fibroblasts are 'crypt-top' fibroblasts and organise epithelial differentiation though the bone morphogenic proteins (BMP) and WNT ligands. This subset may include sub-epithelial myofibroblasts, as they express smooth muscle actin (αSMA) (65,66). CD81+ fibroblasts are 'crypt bottom' fibroblasts and are located within the sub-mucosa near vasculature (65). They act as a primary source of wingless-related integration sites (WNTs); *wnt2* and *wnt2b*, and the bone morphogenic protein (BMP) Gremlin 1 (67,68), and primarily function to maintain intestinal stem cell identity and proliferation (69). PDGFRa$_{low}$CD81- fibroblasts reside in the lamina propria and can be further divided in the large intestine by CD90+, Fbln+ populations (67). They primarily secrete basement membrane proteins and contribute to ECM and tissue remodelling (70). Fibroblasts are activated upon inflammatory stimuli and secrete a myriad of pro inflammatory and growth factors (KGF, TNF- α. FGF, IGF, IL-1R, VEGF, EGF, HGF, EGFR) (71). This drives immune cell recruitment and function, and paracrine signalling between fibroblasts to promote epithelial regeneration and ECM remodelling (69). In the DCD model it would be pertinent to follow up with labelling NS1—tensin-1; CDH11—cadherin-11 or PALLD—paladin for myofibroblasts (72), in order to assess the contribution of fibroblasts in functional tissue repair in ongoing chronic infections and after anti-parasitic chemotherapy.

3.8.5. Future directions

A follow up question would be to identify and quantify the sub-population of EdU+ cells across this 12-week post infection period. By determining a ratio of pro-

inflammatory markers and tissue repair markers in different experimental groups (uninfected, untreated, treated, relapsed) it would uncover what processes may be driving a) functional recovery, and b) functional relapse in treated mice. Moreover, a full quantitative analysis of neuronal and glial cells in whole mount colon tissue samples in the context of EdU incorporation would provide deeper, more convincing insights into the effects of benznidazole treatment on neuropathy development, to corroborate the functional data at the 12-week timepoint. By utilising apoptosis assays, e.g. TUNEL or cleaved caspase IFA labelling, the condition of the neurons can be more easily determined. Finally, by utilising an anti-luciferin antibody it would be possible to visualise parasitic presence in regions close to a) high EdU+ expression and b) the myenteric space.

3.9. References

1. Rassi A, Rassi A, Marin-Neto JA. Chagas disease. The Lancet. 2010 Apr;375(9723):1388–402.
2. Bittencourt AL. Congenital Chagas disease. Am J Dis Child. 1976 Jan;130(1):97–103.
3. Chadalawada S, Sillau S, Archuleta S, Mundo W, Bandali M, Parra-Henao G, et al. Risk of Chronic Cardiomyopathy Among Patients With the Acute Phase or Indeterminate Form of Chagas Disease: A Systematic Review and Meta-analysis. JAMA Netw Open. 2020 Aug 3;3(8):e2015072.
4. Rassi A, Rassi A, Little WC. Chagas' heart disease. Clin Cardiol. 2000 Dec;23(12):883–9.
5. Pinazo MJ, Cañas E, Elizalde JI, García M, Gascón J, Gimeno F, et al. Diagnosis, management and treatment of chronic Chagas' gastrointestinal disease in areas where Trypanosoma cruzi infection is not endemic. Gastroenterol Hepatol. 2010 Mar;33(3):191–200.
6. Ministério da Saúde. Secretaria de Vigilância em Saúde. [Brazilian Consensus on Chagas disease]. Rev Soc Bras Med Trop. 2005;38 Suppl 3:7–29.
7. PAHO. Guidelines for the diagnosis and treatment of Chagas disease . 2018.
8. Bern C, Montgomery SP, Herwaldt BL, Rassi A, Marin-Neto JA, Dantas RO, et al. Evaluation and Treatment of Chagas Disease in the United States. JAMA. 2007 Nov 14;298(18):2171.
9. Viotti R, Vigliano C, Lococo B, Alvarez MG, Petti M, Bertocchi G, et al. Side effects of benznidazole as treatment in chronic Chagas disease: fears and realities. Expert Rev Anti Infect Ther. 2009 Mar;7(2):157–63.
10. Morillo CA, Marin-Neto JA, Avezum A, Sosa-Estani S, Rassi A, Rosas F, et al. Randomized Trial of Benznidazole for Chronic Chagas' Cardiomyopathy. New England Journal of Medicine. 2015;373(14):1295–306.
11. Marin-Neto JA, Rassi A, Morillo CA, Avezum A, Connolly SJ, Sosa-Estani S, et al. Rationale and design of a randomized placebo-controlled trial assessing the effects of etiologic treatment in Chagas' cardiomyopathy: the BENznidazole Evaluation For Interrupting Trypanosomiasis (BENEFIT). Am Heart J. 2008 Jul;156(1):37–43.
12. Herbella FAM, Aquino JLB, Stefani-Nakano S, Artifon ELA, Sakai P, Crema E, et al. Treatment of achalasia: lessons learned with Chagas' disease. Dis Esophagus. 2008;21(5):461–7.
13. Villar JC, Perez JG, Cortes OL, Riarte A, Pepper M, Marin-Neto JA, et al. Trypanocidal drugs for chronic asymptomatic Trypanosoma cruzi infection. Cochrane Database Syst Rev. 2014 May 27;2014(5):CD003463.
14. Francisco AF, Jayawardhana S, Taylor MC, Lewis MD, Kelly JM. Assessing the Effectiveness of Curative Benznidazole Treatment in Preventing Chronic Cardiac Pathology in Experimental Models of Chagas Disease. Antimicrob Agents Chemother. 2018 Oct;62(10).
15. Lewis MD, Francisco AF, Taylor MC, Jayawardhana S, Kelly JM. Host and parasite genetics shape a link between Trypanosoma cruzi infection dynamics and chronic cardiomyopathy. Cell Microbiol. 2016 Oct;18(10):1429–43.
16. Khan AA, Langston HC, Costa FC, Olmo F, Taylor MC, McCann CJ, et al. Local association of Trypanosoma cruzi chronic infection foci and enteric neuropathic lesions at the tissue micro-domain scale. PLoS Pathog. 2021 Aug 23;17(8):e1009864.

17. Lewis MD, Kelly JM. Putting Infection Dynamics at the Heart of Chagas Disease. Trends Parasitol. 2016;32(11):899–911.
18. Gulati A. Understanding neurogenesis in the adult human brain. Indian J Pharmacol. 2015;47(6):583–4.
19. Overall RW, Walker TL, Fischer TJ, Brandt MD, Kempermann G. Different Mechanisms Must Be Considered to Explain the Increase in Hippocampal Neural Precursor Cell Proliferation by Physical Activity. Front Neurosci. 2016 Aug 3;10.
20. Kulkarni S, Micci MA, Leser J, Shin C, Tang SC, Fu YY, et al. Adult enteric nervous system in health is maintained by a dynamic balance between neuronal apoptosis and neurogenesis. Proceedings of the National Academy of Sciences. 2017 May 2;114(18).
21. Belkind-Gerson J, Graham HK, Reynolds J, Hotta R, Nagy N, Cheng L, et al. Colitis promotes neuronal differentiation of Sox2+ and PLP1+ enteric cells. Sci Rep. 2017;7(1):1–15.
22. Imayoshi I, Sakamoto M, Yamaguchi M, Mori K, Kageyama R. Essential Roles of Notch Signaling in Maintenance of Neural Stem Cells in Developing and Adult Brains. The Journal of Neuroscience. 2010 Mar 3;30(9):3489–98.
23. Okamura Y, Saga Y. Notch signaling is required for the maintenance of enteric neural crest progenitors. Development. 2008 Nov 1;135(21):3555–65.
24. Lewis MD, Francisco AF, Taylor MC, Jayawardhana S, Kelly JM. Host and parasite genetics shape a link between Trypanosoma cruzi infection dynamics and chronic cardiomyopathy. Cell Microbiol. 2016 Oct;18(10):1429–43.
25. Ward AI, Olmo F, Atherton RL, Taylor MC, Kelly JM. Trypanosoma cruzi amastigotes that persist in the colon during chronic stage murine infections have a reduced replication rate. Open Biol. 2020 Dec;10(12):200261.
26. Zeng C, Pan F, Jones LA, Lim MM, Griffin EA, Sheline YI, et al. Evaluation of 5-ethynyl-2'-deoxyuridine staining as a sensitive and reliable method for studying cell proliferation in the adult nervous system. Brain Res. 2010 Mar 10;1319:21–32.
27. King PH, Redden D, Palmgren JS, Nabors LB, Lennon VA. Hu Antigen Specificities of ANNA-I Autoantibodies in Paraneoplastic Neurological Disease. J Autoimmun. 1999 Dec;13(4):435–43.
28. Lewis MD, Francisco AF, Taylor MC, Jayawardhana S, Kelly JM. Host and parasite genetics shape a link between Trypanosoma cruzi infection dynamics and chronic cardiomyopathy. Cell Microbiol. 2016 Oct;18(10):1429–43.
29. Lewis MD, Francisco AF, Jayawardhana S, Langston H, Taylor MC, Kelly JM. Imaging the development of chronic Chagas disease after oral transmission. Sci Rep [Internet]. 2018;8(1):1–8. Available from: http://dx.doi.org/10.1038/s41598-018-29564-7
30. Zhang M, Wu C. The relationship between intestinal goblet cells and the immune response. Biosci Rep. 2020 Oct 30;40(10).
31. Ravikanth M, Soujanya P, Manjunath K, Saraswathi T, Ramachandran C. Heterogenecity of fibroblasts. Journal of Oral and Maxillofacial Pathology. 2011;15(2):247.
32. Virtanen H, Garton DR, Andressoo JO. Myenteric Neurons Do Not Replicate in Small Intestine Under Normal Physiological Conditions in Adult Mouse. Cell Mol Gastroenterol Hepatol. 2022;14(1):27–34.
33. Uesaka T, Nagashimada M, Enomoto H. Neuronal Differentiation in Schwann Cell Lineage Underlies Postnatal Neurogenesis in the Enteric Nervous System. Journal of Neuroscience. 2015 Jul 8;35(27):9879–88.

34. Margolis KG, Gershon MD, Bogunovic M. Cellular Organization of Neuroimmune Interactions in the Gastrointestinal Tract. Trends Immunol. 2016 Jul;37(7):487–501.
35. Liu MT, Kuan YH, Wang J, Hen R, Gershon MD. 5-HT4 receptor-mediated neuroprotection and neurogenesis in the enteric nervous system of adult mice. J Neurosci. 2009 Aug 5;29(31):9683–99.
36. Pithadia AB, Jain SM. 5-Hydroxytryptamine Receptor Subtypes and their Modulators with Therapeutic Potentials. J Clin Med Res. 2009 Jun;1(2):72–80.
37. Belkind-Gerson J, Hotta R, Nagy N, Thomas AR, Graham H, Cheng L, et al. Colitis induces enteric neurogenesis through a 5-HT4-dependent mechanism. Inflamm Bowel Dis. 2015 Apr;21(4):870–8.
38. Fellin T. Communication between neurons and astrocytes: relevance to the modulation of synaptic and network activity. J Neurochem. 2009 Feb;108(3):533–44.
39. Laranjeira C, Sandgren K, Kessaris N, Richardson W, Potocnik A, Vanden Berghe P, et al. Glial cells in the mouse enteric nervous system can undergo neurogenesis in response to injury. Journal of Clinical Investigation. 2011 Sep 1;121(9):3412–24.
40. Alvarez-Buylla A, Seri B, Doetsch F. Identification of neural stem cells in the adult vertebrate brain. Brain Res Bull. 2002 Apr;57(6):751–8.
41. Pardal R, Ortega-Sáenz P, Durán R, López-Barneo J. Glia-like Stem Cells Sustain Physiologic Neurogenesis in the Adult Mammalian Carotid Body. Cell. 2007 Oct;131(2):364–77.
42. Burda JE, Sofroniew M V. Reactive gliosis and the multicellular response to CNS damage and disease. Neuron. 2014 Jan 22;81(2):229–48.
43. Gurtner GC, Werner S, Barrandon Y, Longaker MT. Wound repair and regeneration. Nature. 2008 May 15;453(7193):314–21.
44. Klapka N, Müller HW. Collagen matrix in spinal cord injury. J Neurotrauma. 2006;23(3–4):422–35.
45. Viola MF, Chavero-Pieres M, Modave E, Delfini M, Stakenborg N, Estévez MC, et al. Dedicated macrophages organize and maintain the enteric nervous system. Nature. 2023 Jun;618(7966):818–26.
46. Klingberg F, Hinz B, White ES. The myofibroblast matrix: implications for tissue repair and fibrosis. J Pathol. 2013 Jan 12;229(2):298–309.
47. Kurahashi M, Kito Y, Hara M, Takeyama H, Sanders KM, Hashitani H. Norepinephrine Has Dual Effects on Human Colonic Contractions Through Distinct Subtypes of Alpha 1 Adrenoceptors. Cell Mol Gastroenterol Hepatol. 2020;10(3):658-671.e1.
48. McCarthy N, Manieri E, Storm EE, Saadatpour A, Luoma AM, Kapoor VN, et al. Distinct Mesenchymal Cell Populations Generate the Essential Intestinal BMP Signaling Gradient. Cell Stem Cell. 2020 Mar;26(3):391-402.e5.
49. Brügger MD, Valenta T, Fazilaty H, Hausmann G, Basler K. Distinct populations of crypt-associated fibroblasts act as signaling hubs to control colon homeostasis. PLoS Biol. 2020 Dec 11;18(12):e3001032.
50. Greicius G, Kabiri Z, Sigmundsson K, Liang C, Bunte R, Singh MK, et al. *PDGFRα* $^{+}$ pericryptal stromal cells are the critical source of Wnts and RSPO3 for murine intestinal stem cells in vivo. Proceedings of the National Academy of Sciences. 2018 Apr 3;115(14).
51. Chaen T, Kurosawa T, Kishi K, Kaji N, Ikemoto-Uezumi M, Uezumi A, et al. Transcriptome analysis of mesenchymal stromal cells of the large and small intestinal

smooth muscle layers reveals a unique gastrontestinal stromal signature. Biochem Biophys Rep. 2023 Jul;34:101478.
52. Duan CL, Liu CW, Shen SW, Yu Z, Mo JL, Chen XH, et al. Striatal astrocytes transdifferentiate into functional mature neurons following ischemic brain injury. Glia. 2015 Sep;63(9):1660–70.
53. Ghosh M, Aguila HL, Michaud J, Ai Y, Wu MT, Hemmes A, et al. Essential role of the RNA-binding protein HuR in progenitor cell survival in mice. J Clin Invest. 2009 Dec;119(12):3530–43.
54. Viola MF, Boeckxstaens G. Intestinal resident macrophages: Multitaskers of the gut. Neurogastroenterology and motility. 2020 Aug;32(8):e13843.
55. Takaki M. Gut pacemaker cells: the interstitial cells of Cajal (ICC). J Smooth Muscle Res. 2003 Oct;39(5):137–61.
56. Chen K, Gu X, Yang S, Tao R, Fan M, Bao W, et al. Research progress on intestinal tissue-resident memory T cells in inflammatory bowel disease. Scand J Immunol. 2023 Dec 17;98(6).
57. Lyu Y, Zhou Y, Shen J. An Overview of Tissue-Resident Memory T Cells in the Intestine: From Physiological Functions to Pathological Mechanisms. Front Immunol. 2022 May 31;13.
58. Ward AI, Lewis MD, Taylor MC, Kelly JM. Incomplete Recruitment of Protective T Cells Is Associated with Trypanosoma cruzi Persistence in the Mouse Colon. Infect Immun. 2022 Feb 17;90(2):e0038221.
59. Xu ZJ, Gu Y, Wang CZ, Jin Y, Wen XM, Ma JC, et al. The M2 macrophage marker CD206: a novel prognostic indicator for acute myeloid leukemia. Oncoimmunology. 2020;9(1):1683347.
60. Grainger JR, Konkel JE, Zangerle-Murray T, Shaw TN. Macrophages in gastrointestinal homeostasis and inflammation. Pflugers Arch. 2017 Apr 10;469(3–4):527–39.
61. Edelblum KL, Singh G, Odenwald MA, Lingaraju A, El Bissati K, McLeod R, et al. γδ Intraepithelial Lymphocyte Migration Limits Transepithelial Pathogen Invasion and Systemic Disease in Mice. Gastroenterology. 2015 Jun;148(7):1417–26.
62. Born W, Cady C, Jones-Carson J, Mukasa A, Lahn M, O'Brien R. Immunoregulatory functions of gamma delta T cells. Adv Immunol. 1999;71:77–144.
63. Kühl AA, Pawlowski NN, Grollich K, Loddenkemper C, Zeitz M, Hoffmann JC. Aggravation of intestinal inflammation by depletion/deficiency of γδ T cells in different types of IBD animal models. J Leukoc Biol. 2007 Jan 1;81(1):168–75.
64. Chen Y, Chou K, Fuchs E, Havran WL, Boismenu R. Protection of the intestinal mucosa by intraepithelial γδ T cells. Proceedings of the National Academy of Sciences. 2002 Oct 29;99(22):14338–43.
65. Brügger MD, Basler K. The diverse nature of intestinal fibroblasts in development, homeostasis, and disease. Trends Cell Biol. 2023 Oct;33(10):834–49.
66. McCarthy N, Kraiczy J, Shivdasani RA. Cellular and molecular architecture of the intestinal stem cell niche. Nat Cell Biol. 2020 Sep 3;22(9):1033–41.
67. Hong SP, Yang MJ, Cho H, Park I, Bae H, Choe K, et al. Distinct fibroblast subsets regulate lacteal integrity through YAP/TAZ-induced VEGF-C in intestinal villi. Nat Commun. 2020 Aug 14;11(1):4102.
68. McCarthy N, Manieri E, Storm EE, Saadatpour A, Luoma AM, Kapoor VN, et al. Distinct Mesenchymal Cell Populations Generate the Essential Intestinal BMP Signaling Gradient. Cell Stem Cell. 2020 Mar;26(3):391-402.e5.

69. Chalkidi N, Paraskeva C, Koliaraki V. Fibroblasts in intestinal homeostasis, damage, and repair. Front Immunol. 2022;13:924866.
70. Buechler MB, Pradhan RN, Krishnamurty AT, Cox C, Calviello AK, Wang AW, et al. Cross-tissue organization of the fibroblast lineage. Nature. 2021 May 27;593(7860):575–9.
71. Eming SA, Martin P, Tomic-Canic M. Wound repair and regeneration: Mechanisms, signaling, and translation. Sci Transl Med. 2014 Dec 3;6(265).
72. Grigorieva O, Basalova N, Vigovskiy M, Arbatskiy M, Dyachkova U, Kulebyakina M, et al. Novel Potential Markers of Myofibroblast Differentiation Revealed by Single-Cell RNA Sequencing Analysis of Mesenchymal Stromal Cells in Profibrotic and Adipogenic Conditions. Biomedicines. 2023 Mar 10;11(3):840.
73. Laddach A, Chng SH, Lasrado R, Progatzky F, Shapiro M, Erickson A, et al. A branching model of lineage differentiation underpinning the neurogenic potential of enteric glia. Nat Commun. 2023 Sep 22;14(1):5904.

<u>Chapter 4:</u> Exploring the potential for broader experimental DCD models, beyond the mouse.

4.1. Manuscript #3, Langston et al., 2023.

Harry Langston, Amanda Fortes Francisco, Ciaran Doidge, Chrissy H. Roberts, Archie A. Khan, Shiromani Jayawardhana, Martin C. Taylor, John M. Kelly, Michael D. Lewis.

Dynamics of *Trypanosoma cruzi* infection in hamsters and novel association with progressive motor dysfunction, PLoSNTD (in revision).

London School of Hygiene & Tropical Medicine
Keppel Street, London WC1E 7HT

T: +44 (0)20 7299 4646
F: +44 (0)20 7299 4656
www.lshtm.ac.uk

RESEARCH PAPER COVER SHEET

Please note that a cover sheet must be completed for each research paper included within a thesis.

SECTION A – Student Details

Student ID Number	1601186	**Title**	Mr
First Name(s)	Harry		
Surname/Family Name	Langston		
Thesis Title	Study of the Determinants of Enteric Neuropathy in Experimental Chagas disease		
Primary Supervisor	Michael Lewis		

If the Research Paper has previously been published please complete Section B, if not please move to Section C.

SECTION B – Paper already published

Where was the work published?			
When was the work published?			
If the work was published prior to registration for your research degree, give a brief rationale for its inclusion			
Have you retained the copyright for the work?*	**No**	Was the work subject to academic peer review?	**Yes**

*If yes, please attach evidence of retention. If no, or if the work is being included in its published format, please attach evidence of permission from the copyright holder (publisher or other author) to include this work.

SECTION C – Prepared for publication, but not yet published

Where is the work intended to be published?	Dynamics of Trypanosoma cruzi infeciton in hamsters and novel association with progressive motor dysfunction
Please list the paper's authors in the intended authorship order:	Harry Langston, Amanda Fortes Francisco, Ciaran Dodge, Chrissy H Roberts, Archie A Khan, Shiromani Jayawardhana, Martin C Taylor, John M Kelly, Michael D Lewis
Stage of publication	**Undergoing revision**

SECTION D – Multi-authored work

For multi-authored work, give full details of your role in the research included in the paper and in the preparation of the paper. (Attach a further sheet if necessary)	Writing: Review and editing. Additional roles included: Investigation, formal analysis, validation and visualisation. I performed all hamster specific histopatholoical analyses (Fig 3 and Fig 5). A full H&E inflammation assessment, and a fibrosis assessment (Picro sirius red) was conducted on both cardiac tissue and skeletal muscle.

SECTION E

Student Signature	
Date	

Supervisor Signature	
Date	

PLOS Neglected Tropical Diseases

Dynamics of Trypanosoma cruzi infection in hamsters and novel association with progressive motor dysfunction

--Manuscript Draft--

Manuscript Number:	
Full Title:	Dynamics of Trypanosoma cruzi infection in hamsters and novel association with progressive motor dysfunction
Short Title:	Imaging Trypanosoma cruzi infection in an experimental hamster model
Article Type:	Research Article
Keywords:	Chagas disease; Trypanosoma cruzi; trypanosomes; in vivo imaging; bioluminescence imaging; animal models; infection; infectious disease; protozoa; tissue tropism; histopathology; spastic diplegia; gait
Corresponding Author:	Michael D. Lewis University of Warwick Coventry, UNITED KINGDOM
Corresponding Author Secondary Information:	
Corresponding Author's Institution:	University of Warwick
Corresponding Author's Secondary Institution:	
First Author:	Harry Langston
First Author Secondary Information:	
Order of Authors:	Harry Langston
	Amanda Fortes Francisco
	Ciaran Doidge
	Chrissy H. Roberts
	Archie A. Khan
	Shiromani Jayawardhana
	Martin C. Taylor
	John M. Kelly
	Michael D. Lewis
Order of Authors Secondary Information:	
Abstract:	Chagas disease is a zoonosis caused by the protozoan parasite Trypanosoma cruzi. Clinical outcomes range from long-term asymptomatic carriage to cardiac, digestive, neurological and composite presentations that can be fatal in both acute and chronic stages of the disease. Studies of T. cruzi in animal models, principally mice, have informed our understanding of the biological basis of this variability and its relationship to infection and host response dynamics. Hamsters have higher translational value for many human infectious diseases, but they have not been well developed as models of Chagas disease. We transposed a real-time bioluminescence imaging system for T. cruzi infection from mice into female Syrian hamsters (Mesocricetus auratus). This enabled us to study chronic tissue pathology in the context of spatiotemporal infection dynamics. Acute infections were widely disseminated, whereas chronic infections were almost entirely restricted to the skin and subcutaneous adipose tissue. Neither cardiac nor digestive tract disease were reproducible features of the model. Skeletal muscle had only sporadic parasitism in the chronic phase, but nevertheless displayed significant inflammation and fibrosis, features also seen in mouse models. Whereas mice had normal locomotion, all

	chronically infected hamsters developed hindlimb muscle hypertonia and a gait dysfunction resembling spastic diplegia. With further development, this model may therefore prove valuable in studies of peripheral nervous system involvement in Chagas disease.
Suggested Reviewers:	Maria Terezinha Bahia Federal University of Ouro Preto: Universidade Federal de Ouro Preto mtbahia@nupeb.ufop.br Expert on Chagas disease experimental models
	Manu De Rycker University of Dundee School of Life Sciences M.DeRycker@dundee.ac.uk Expertise in translational medicine relating to trypanosomatid infections
	Jose Álvarez USP ICB: Universidade de Sao Paulo Instituto de Ciencias Biomedicas jmamosig@icb.usp.br Expertise in Chagas disease immunopathogenesis, including neuropathology
	Yaohe Wang Barts Cancer Institute yaohe.wang@qmul.ac.uk Senior author on recent review "Syrian Hamster as an Animal Model for the Study on Infectious Diseases"
Opposed Reviewers:	
Additional Information:	
Question	**Response**
Government Employee Are you or any of the contributing authors an employee of the United States government? Manuscripts authored by one or more US Government employees are not copyrighted, but are licensed under a CC0 Public Domain Dedication, which allows unlimited distribution and reuse of the article for any lawful purpose. This is a legal requirement for US Government employees. This will be typeset if the manuscript is accepted for publication.	No - No authors are employees of the U.S. government.
Financial Disclosure Enter a financial disclosure statement that describes the sources of funding for the work included in this submission. Review the submission guidelines for detailed requirements. View published research articles from *PLOS Neglected Tropical*	Yes

Diseases for specific examples. This statement is required for submission and **will appear in the published article** if the submission is accepted. Please make sure it is accurate. **Funded studies** Enter a statement with the following details: • Initials of the authors who received each award • Grant numbers awarded to each author • The full name of each funder • URL of each funder website • Did the sponsors or funders play any role in the study design, data collection and analysis, decision to publish, or preparation of the manuscript? Did you receive funding for this work?	
Please add funding details. as follow-up to "**Financial Disclosure** Enter a financial disclosure statement that describes the sources of funding for the work included in this submission. Review the submission guidelines for detailed requirements. View published research articles from *PLOS Neglected Tropical Diseases* for specific examples. This statement is required for submission and **will appear in the published article** if the submission is accepted. Please make sure it is accurate. **Funded studies** Enter a statement with the following details: • Initials of the authors who received each award • Grant numbers awarded to each author • The full name of each funder • URL of each funder website • Did the sponsors or funders play any role in the study design, data collection and analysis, decision to publish, or preparation of the manuscript?	The research was supported by UK Medical Research Council (https://www.ukri.org/councils/mrc/) grants MR/T015969/1 to J.M.K. and MR/R021430/1 to M.D.L.

Did you receive funding for this work?"	
Please select the country of your main research funder (please select carefully as in some cases this is used in fee calculation). as follow-up to "**Financial Disclosure** Enter a financial disclosure statement that describes the sources of funding for the work included in this submission. Review the submission guidelines for detailed requirements. View published research articles from *PLOS Neglected Tropical Diseases* for specific examples. This statement is required for submission and **will appear in the published article** if the submission is accepted. Please make sure it is accurate. **Funded studies** Enter a statement with the following details: • Initials of the authors who received each award • Grant numbers awarded to each author • The full name of each funder • URL of each funder website • Did the sponsors or funders play any role in the study design, data collection and analysis, decision to publish, or preparation of the manuscript? Did you receive funding for this work?"	UNITED KINGDOM - GB
Competing Interests On behalf of all authors, disclose any competing interests that could be perceived to bias this work. This statement will be typeset if the manuscript is accepted for publication. Review the instructions link below and	The authors declare they have no competing interests.

PLOS NTDs' competing interests policy to determine what information must be disclosed at submission.	
Data Availability Provide a **Data Availability Statement** in the box below. This statement should detail where the data used in this submission can be accessed. This statement will be typeset if the manuscript is accepted for publication. Before publication, authors are required to make all data underlying their findings fully available, without restriction. Review our PLOS Data Policy page for detailed information on this policy. Instructions for writing your Data Availability statement can be accessed via the Instructions link below.	All relevant data are within the manuscript and its Supporting Information files.

November 13th, 2023

Dear *PLOS Neglected Tropical Diseases*,

We would be grateful for your consideration of our manuscript entitled "Dynamics of *Trypanosoma cruzi* infection in hamsters and novel association with progressive motor dysfunction"

Over the last decade we have developed highly sensitive real-time imaging systems for *T. cruzi* infections in mice, enabling us to make significant progress in understanding Chagas disease pathogenesis and accelerating drug development (e.g. PMIDs: 34424944, 32302312, 30082291, 26918803, 26014936). Nevertheless, there have been justified concerns about the level of reliance on mouse models in the field and the fact that they do not adequately capture the broad range of clinical outcomes that are seen in humans infected with *T. cruzi*.

In our new manuscript we present the results from experiments aiming to develop the hamster as an alternative experimental model. This includes a detailed assessment of the course of infection, tissue tropism and tissue pathology, including the development of a remarkable progressive hindlimb gait condition resembling spastic diplegia. Our study contributes findings that will be of interest to the Chagas disease field and the broader NTD research community, including:

- A new model of *T. cruzi*-associated motor dysfunction that provides better opportunities to investigate peripheral neuropathy, which affects as many as 27% of Chagas disease patients, yet remains a neglected aspect of an already neglected disease.

- The identification of the skin as the only major reservoir site of chronic infection in hamsters. This is relevant to the understanding of *T. cruzi* transmission biology as well as holding parallels with the importance of skin parasitism in multiple NTDs and vector-borne infections e.g. African Trypanosomiasis, leishmaniasis, onchocerciasis etc.

- Proof of concept and open-source 3D printing files for adapting mouse vivo imaging instruments for hamster imaging. This could stimulate advances in a wide range of infectious disease fields where the hamster is the species of choice.

We hope that you will find our manuscript suitable for publication in *PLOS Neglected Tropical Diseases* and look forward to future correspondence.

Yours sincerely,

Michael Lewis, PhD
Associate Professor

Division of Biomedical Sciences
Warwick Medical School
University of Warwick
Coventry CV4 7AJ UK
T: (0)2476 574798
E: michael.d.lewis@warwick.ac.uk
www.warwick.ac.uk

Dynamics of *Trypanosoma cruzi* infection in hamsters and novel association with progressive motor dysfunction

Harry Langston[1,3], Amanda Fortes Francisco[1], Ciaran Doidge[1,4], Chrissy H. Roberts[2], Archie A. Khan[1], Shiromani Jayawardhana[1], Martin C. Taylor[1], John M. Kelly[1], Michael D. Lewis[1,5*]

[1] Department of Infection Biology, London School of Hygiene and Tropical Medicine, Keppel Street, London, WC1E 7HT, U.K.

[2] Department of Clinical Research, London School of Hygiene and Tropical Medicine, Keppel Street, London, WC1E 7HT, U.K.

[3] Current Address: Imperial College London, Exhibition Rd, South Kensington, London SW7 2BX, U.K.

[4] Current Address: Barts Cancer Institute, Queen Mary University of London, Charterhouse Square, London EC1M 6BQ, U.K.

[5] Current Address: Division of Biomedical Sciences, Warwick Medical School, University of Warwick, Coventry, CV4 7AJ, U.K.

Abstract

Chagas disease is a zoonosis caused by the protozoan parasite *Trypanosoma cruzi*. Clinical outcomes range from long-term asymptomatic carriage to cardiac, digestive, neurological and composite presentations that can be fatal in both acute and chronic stages of the disease. Studies of *T. cruzi* in animal models, principally mice, have informed our understanding of the biological basis of this variability and its relationship to infection and host response dynamics. Hamsters have higher translational value for many human infectious diseases, but they have not been well developed as models of Chagas disease. We transposed a real-time bioluminescence imaging system for *T. cruzi* infection from mice into female Syrian hamsters (*Mesocricetus auratus*). This enabled us to study chronic tissue pathology in the context of spatiotemporal infection dynamics. Acute infections were widely disseminated, whereas chronic infections were almost entirely restricted to the skin and subcutaneous adipose tissue. Neither cardiac nor digestive tract disease were reproducible features of the model. Skeletal muscle had only sporadic parasitism in the chronic phase, but nevertheless displayed significant inflammation and fibrosis, features also seen in mouse models. Whereas mice had normal locomotion, all chronically infected hamsters developed hindlimb muscle hypertonia and a gait dysfunction resembling spastic diplegia. With further development, this model may therefore prove valuable in studies of peripheral nervous system involvement in Chagas disease.

Author Summary

Chagas disease is a caused by American trypanosomes (*Trypanosoma cruzi*). These are microscopic parasites that circulate in wild mammals across most of the Americas and can also be transmitted to humans. Much of our knowledge about how *T. cruzi* causes Chagas disease comes from studies of infections in mice, but the data do not capture the full range of clinical outcomes seen in humans. For many other pathogens the hamster has proved to be a valuable model of human infections. We therefore aimed to apply some of the latest advances in *T. cruzi* infection imaging technology to studies in this alternative experimental model. In the early stages, parasites were widely disseminated throughout the body, but after several months parasites became almost entirely restricted to the skin. Hamsters did not show signs of heart or gut disease, which are common in humans, but they did develop skeletal muscle pathology. Stiffness in the hindlimbs grew progressively worse and resulted in a visibly altered gait, suggestive of damage to the nervous system. With further development, this model may therefore prove valuable in studies of peripheral nervous system involvement in Chagas disease.

Introduction

Chagas disease (American trypanosomiasis) is caused by infection with *Trypanosoma cruzi*, a protozoan parasite. Approximately 6 million people are infected and the disease causes ~10,000 deaths annually as well as a large morbidity burden in affected populations (1). Clinical outcomes are highly heterogeneous, encompassing muscle and nervous tissue pathologies affecting the heart and gastro-intestinal tract, as well as long-term asymptomatic carriage (2) Pathogenesis is thought to be primarily a result of collateral damage to infected tissues from the host's cellular immune response, which leads to fibrosis, microvascular abnormalities, denervation and consequent organ dysfunction (3-5).

Animal infection models are critical to research on the biological basis of Chagas disease. *T. cruzi* is a very cosmopolitan parasite in its natural host range (6) and a variety of species have been used in experimental settings, including rats, rabbits, dogs, guinea pigs, opossums and non-human primates, often reproducing important features of the human disease spectrum (7). Mice, however, are by far the most widely used species; in most cases they develop inflammatory cardiomyopathy and a few models are suitable for studying aspects of digestive disease. The compatibility of murine models with technologies such as bioluminescence imaging (BLI), which enable real-time monitoring of infections, is a major advantage and has led to significant advances in understanding how spatio-temporal infection dynamics relate to pathology development (8-10). Mice have been less well developed as models of advanced digestive megasyndromes, peripheral neuropathy or CNS infection, an important cause of acute mortality in human patients (11). Furthermore, the use of a few inbred mouse strains limits our ability to study the impact of host genetic diversity on disease pathogenesis and clinical outcome heterogeneity.

The aim of this study was to develop an *in vivo*/*ex vivo* BLI system for *T. cruzi* infection in the Syrian hamster, *Mesocricetus auratus*. Hamsters can show closer alignment with human diseases than mice for a variety of infectious agents, for example *Clostridium difficile*, SARS-CoV-2, West Nile Virus, adenoviruses, *Leishmania donovani* and *Schistosoma haematobium* (12-16). Hamsters have also been described as useful models of Chagas cardiac disease (17-23) and in some cases are reported to develop

77 a dilated large intestine indicative of megacolon (18) . They are also one of the few species readily
78 available, besides mice, whose physical size is compatible with standard *in vivo* imaging chambers. We
79 therefore reasoned that a hamster *T. cruzi* BLI system could add value to the landscape of experimental
80 Chagas disease *in vivo* models.

Methods

Parasites, Animals and Infections

T. cruzi CL Brener (genetic lineage TcVI) constitutively expressing the red-shifted firefly luciferase gene *PpyRE9h* (24) were used in all experiments. Infectious trypomastigotes were generated as previously described (24). Animals used were female CB17 SCID mice aged 8 – 10 weeks (bred in house), female BALB/c, C57BL6 and C3H/HeN mice aged 6 – 8 weeks (Charles River) and female Syrian hamsters aged 6 – 8 weeks old (Janvier Labs). Animals were acclimatised to the vivarium for 1 – 2 weeks prior to use in experiments. SCID mice were infected with 10^4 trypomastigotes and all other mice were infected with 10^3 trypomastigotes. Hamsters were infected with 5 x 10^3 or 10^5 trypomastigotes. Inocula were given as intra-peritoneal (i.p.) injections of 0.2 mL in sterile 1X Dulbecco's Phosphate Buffered Saline (DPBS).

Animal work was approved by the LSHTM Animal Welfare and Ethical Review Board and carried out under UK Home Office project licence (PPL 70/8207) in accordance with the UK Animals (Scientific Procedures) Act. Animals were maintained under specific pathogen-free conditions in individually ventilated cages, with 2 – 3 hamsters and 5 – 6 mice per cage, with a 12 hour light/dark cycle and *ad libitum* food and water. A minimum of 1 week's acclimatisation to the vivarium was implemented between the day of delivery and the start of an experiment. An investigator who was blinded to the infection/control group allocations assigned individual animals to cages. No randomisation procedure was used to allocate animals to infection or control groups. Animals were checked visually twice daily and weighed on average every two weeks. Humane end-points were any of the following: loss of >20% body weight, unwillingness to move, reluctance to feed and drink freely for >6 hours, loss of balance. No animals in this study reached any of the humane end-points.

Bioluminescence Imaging

Hamsters were injected with 150 mg/kg d-luciferin i.p., then anaesthetized using 2.5% (v/v) gaseous isoflurane in oxygen. To measure bioluminescence, hamsters were placed in a Lumina II In Vivo Imaging System (IVIS) (PerkinElmer) and images were acquired 10 – 20 minutes after d-luciferin administration using LivingImage v4.7. A custom 3D printed nosecone was used for continuous isoflurane delivery during imaging sessions (S1 Data). Exposure times varied between 30 seconds and 5 minutes, depending on bioluminescence signal intensity. After imaging, animals were revived and returned to cages. For *ex vivo* imaging, hamsters were injected with 150 mg/kg d-luciferin i.p., then sacrificed by ex-sanguination under terminal anaesthesia (400-600 mg/kg Pentobarbital Sodium) 7 minutes later. Trans-cardiac perfusion was performed with 20 mL 0.3 mg/mL d-luciferin in PBS. Organs and tissues were transferred to culture dishes, soaked in 0.3 mg/mL d-luciferin in PBS, and then imaged using the IVIS Lumina II. One hamster from the low inoculum group was excluded from further analysis because a bioluminescence signal was never detected, indicating that infection did not become established.

To estimate total parasite loads in live hamsters, regions of interest (ROIs) were drawn using Living Image v4.7 to quantify bioluminescence expressed as total flux (photons/second [p/s]). The detection threshold for *in vivo* imaging was determined using uninfected control hamsters. The line measurement tool in Living Image was used to quantify the degree of limb adduction by determining the distance between the two forepaws and between the two hindpaws in each image.

Ex vivo images of tissues and organs were scored for the presence of *T. cruzi* using a detection threshold for infection foci of at least 10 contiguous bioluminescent pixels of radiance $\geq 3x10^3$ p/s/cm^2/sr (8). Ex vivo parasite loads were inferred from tissue/organ-specific bioluminescence total flux (p/s) after subtracting the mean + 2SDs of matching samples from uninfected control hamsters (n = 7) to account for differences in background luminescence signal amongst different tissue and organ types. Tissue/organ-specific infection intensities were calculated as the fold change in bioluminescence

radiance (p/s/cm^2/sr), which normalises for differences in tissue sample surface areas, compared with the mean radiance for the matching tissue/organ type measured for uninfected control hamsters (n = 7).

Histopathology

Tissue samples were fixed in Glyo-Fixx (Epredia) for 24 – 72 hours, then dehydrated in an ethanol series, cleared in xylene (Sigma), and embedded in paraffin for histomorphometric analysis (8, 9). Five-micron tissue sections were stained with Haematoxylin and Eosin (H&E), picrosirius red or Masson's trichrome and analysed using a DFC295 camera attached to a DM3000 light-emitting diode microscope (Leica) as described (8, 9). Images were digitised using Leica Application Suite v4.5.0. For the inflammatory index, the total number of nuclei were counted in 10 - 15 randomly selected microscope fields of view (FOV, area at 400X magnification = 2.66 x 10^5 µm^2) per animal in H&E-stained sections. An inflammation index was calculated as the average cellularity (mean number of nuclei per FOV) for each animal. A significant increase in cellularity compared to uninfected controls was considered indicative of inflammation. For the fibrosis index, the proportion of total FOV area positive for collagen in picrosirius red- or Masson's trichrome stained sections (red or blue pixels respectively) was quantified, also in Leica Application Suite v4.5.0. A significant increase in collagen content compared to uninfected controls was considered indicative of fibrosis.

Statistics

Individual animals were used as the unit of analysis. Groups were compared using Student's *t*-test or one-way ANOVA, with Tukey's post-hoc correction in GraphPad Prism v.8.

Results

In vivo bioluminescence imaging permits long-term tracking of T. cruzi infection in hamsters

We infected hamsters with either a low (5,000) or high (100,000) inoculum of *T. cruzi* TcVI-CLBR trypomastigotes expressing the red-shifted luciferase reporter *PPy*RE9h (24). The resulting infections were monitored regularly by *in vivo* bioluminescence imaging (Fig 1A, 1B). For both inocula, parasite burdens proceeded through a typical acute phase wave that transitioned into a stable, long-term chronic infection. In the high inoculum group, the acute phase was 3-fold more intense and its peak occurred at 2 weeks post-infection (p.i.) rather than 4 weeks p.i. for the low inoculum group (Fig 1B). Spatially, *in vivo* imaging indicated that the acute phase infection was highly concentrated near to the injection site in the abdomen, but from 8 weeks p.i. onwards, the bioluminescence signal became widely distributed, multi-focal and dynamic between analysis time-points (Fig 1A). The size of the inoculum did not affect the level at which chronic parasite burdens stabilised, nor the spatio-temporal distribution of the infection. For further analyses, we focussed on the high inoculum approach because acute infections in the low inoculum group tended to be more variable.

Monitoring of animals identified gait abnormalities gradually developing during the chronic phase of infection, with pronounced hindlimb rigidity. Muscle mass was observed to be within normal limits at post-mortem. With respect to potential features of human Chagas disease, we observed significant splenomegaly, but no sign of cardiomegaly, digestive megasyndromes or constipation at the experimental end-point of 152-182 days p.i. (Fig 1C).

Skin is the primary reservoir of chronic parasite persistence in hamsters

T. cruzi displays a very broad cell and tissue tropism, but *in vivo* imaging does not permit unambiguous localisation of signals to organs. Therefore, to better understand infection dynamics in this model we conducted *ex vivo* bioluminescence imaging post-mortem, at the acute-chronic transition (34-38 days p.i.) and in the established chronic phase (152-182 days p.i.) (Fig 2A). At 34-38 days p.i., infection was almost universally detected across all the tissues and organs that were sampled (Fig 2A,

2B, 2D, 2F). In terms of absolute parasite loads (total bioluminescent flux/sec), the skin harboured the greatest proportion of parasites (58.0% ±19.2%) followed by several fat-rich organs each containing 5-10% of the total (GI mesentery, genito-urinary system, subcutaneous adipose, visceral adipose) (Fig 2D). Infection intensity, which takes into account the large variation in organ size, varied over more than three orders of magnitude. Of note, parasite loads measured in this way were relatively high in the skin, adipose, GI mesentery and genito-urinary system, moderately high in striated muscles (heart, skeletal muscle, abdomen/peritoneum) and relatively low in the GI tract, liver and spleen (Fig 2F).

In the established chronic phase, infection became undetectable in the majority of sites in the majority of individual animals (Fig 2A, 2C, 2E, 2G). It should be noted that the limit of detection is <20 parasites in the mouse colon (25), but the larger size of hamster organs likely reduces detection sensitivity. Persistent infection was mainly restricted to the skin and subcutaneous adipose tissue, with sporadic, usually small foci of infection in a few other organs, most often the skeletal muscle, spleen and lungs. In contrast to mouse models (9, 10), parasites were only rarely detected in the GI tract during the chronic stage. Considering absolute numbers, the skin harboured a large majority of the total parasites (93.4% ±3.8%) (Fig 2D, 2E) and also had the highest infection intensity (Fig 2G). Skin parasites could be detected in any skin region, and in the chronic phase they were typically present in approximately 20 to 30 discrete foci of infection (Fig 2A).

Occurrence of a hindlimb spastic diplegia-like syndrome in the hamster infection model

Cardiomyopathy is the most serious adverse clinical consequence of chronic *T. cruzi* infection in humans. Histopathology analysis of heart tissue samples from hamsters at 5 months p.i. indicated that inflammation and collagen content (a measure of fibrosis) were not significantly increased compared to uninfected control animals at the group mean level (Fig 3). However, some animals did display clear evidence of oedema, focal and diffuse inflammatory foci, and intermuscular fibro-fatty tissue replacement.

To better understand the gait abnormality that arose in the hamsters, we assessed its development over time (Fig 4A). This identified excessive bilateral hindlimb adduction, which was clearly progressive over the course of chronic infection and resembled the "scissor gait" seen in a number of human neuromuscular disorders, such as cerebral palsy (26, 27). The phenotype was highly significant and developed in 100% of chronically infected hamsters (Fig 4B). Histopathological analysis of hindlimb skeletal muscle identified significant perivascular and muscle parenchymal inflammation, fibrosis and fatty degeneration (Fig 5). To investigate whether the gait abnormality might be linked to the myositis (muscle inflammation) and intense fibrosis, we investigated if these histopathological features developed in a range of murine *T. cruzi* infection models (parasite strains TcI-JR and TcVI-CLBR in BALB/c, C57BL/6 and C3H/HeN mice), none of which develop the diplegia symptoms seen in hamsters. Significant myositis was present in 5 of the 6 parasite-mouse strain combinations, TcI-JR in C3H/HeN mice being the exception, and significant fibrosis was present in all 6 models (Fig 6). Both phenotypes occurred with a range of severities, with the most affected mouse models being broadly comparable to the hamster model: cellularity (myositis) increased 3-fold in TcVI-CLBR:C3H/HeN vs 4-fold for TcVI-CLBR:Hamster, and collagen content (fibrosis) increased ~4.5 fold in TcVI-CLBR:C3H/HeN vs 2-fold for TcVI-CLBR:Hamster. Fatty degeneration and parasite nests were also occasionally observed in murine skeletal muscle tissue. Thus, the diplegic gait in hamsters is highly unlikely to result directly from chronic parasite persistence, skeletal muscle inflammation or fibrosis, because these are all also common features of murine infections. A neuropathic aetiology therefore seems probable.

Discussion

Bioluminescence imaging has been widely applied to *T. cruzi* murine infections, but its utility to monitor Chagas disease progression in larger rodents has not been reported. Our aims were to investigate if this technology could provide new insights into parasite distribution patterns during long-term *T. cruzi* infection of hamsters and to establish if there was a link with pathological outcomes. The results demonstrate that *in vivo* imaging, using the highly sensitive system described here, is able to facilitate longitudinal monitoring of chronic *T. cruzi* infections in hamsters. Furthermore, *ex vivo* imaging revealed organ and tissue parasite tropism during both acute and chronic stage infections, and identified the reservoir sites within the hamster that provide a niche for long-term parasite survival.

There were both similarities and differences in comparison with typical infection profiles in mice, with one commonality being the pan-tropism of acute stage infections (24, 28-32). In terms of the heart, hamsters did not have detectable chronic infections localised to this organ and signs of cardiac pathology were only observed in a small subset of animals. Cardiac pathology typically is present in mice, although severity can vary substantially between parasite and mouse strains as, well as between individual animals, even when they are inbred (9, 33-35). The observation of a low rate of cardiomyopathy in hamsters may be significant, given that they are an outbred model, and only a minority of humans infected with *T. cruzi* develop heart disease symptoms (36). Previous studies in hamsters have reported more consistent cardiomyopathy as well as mortality rates ranging from 12 – 80% (17-19, 21-23, 37). However, here we observed 100% survival. This could reflect differences in virulence between strains because TcVI-CLBR also has low mortality, <10%, in mice in our laboratory (9). In addition, the 5-6 month post-infection period to which our study was limited may have been too short for cardiac pathology to develop more reproducibly.

Regarding the digestive tract, localised chronic infections were absent, apart from a few very weak bioluminescence signals in one or two animals. No signs of organ enlargement or constipation,

characteristic of digestive Chagas disease, were found. This contrasts with murine infections, where the GI tract is a major and almost universal site of long-term parasite persistence and chronic transit delays linked to the colon are significant in some parasite-mouse strain combinations (9, 38-41). GI tract samples from digestive Chagas disease patients have high frequencies of parasite DNA/antigen positivity (42-45). Overall, these data indicate that Syrian hamster infection with TcVI-CLBR is not a suitable model to study the cardiac or the digestive form of Chagas disease.

Two findings from the study are particularly noteworthy. Firstly. the predominance of the skin as a chronic reservoir of infection, and secondly, the hindlimb diplegic gait phenotype. In mouse models, we have shown that chronic skin infection is present in 80-90% of mice across multiple combinations of *T. cruzi* and host genetic strains (8, 25). Whereas in mice the skin and GI tract have a similar reservoir status, in the hamster our data indicate that the skin and subcutaneous adipose tissue harbour almost the entire parasite burden in the animal. Acute cutaneous manifestations of Chagas disease reported in humans include localised inoculation 'chagomas' – swellings associated with initial parasite entry sites (2) and, very rarely, more disseminated lesions (46). Skin lesions may also occur in cases of 're-activation' of a chronic infection in which immunosuppression, for example caused by HIV co-infection or post-transplant medications, causes expansion and spread of the parasite burden (47, 48). Although chronic *T. cruzi* infection in immunocompetent people is not associated with cutaneous pathology, this does not rule out the existence of a clinically silent skin-resident parasite population. This would have an obvious evolutionary advantage for *T. cruzi* in terms of ensuring onward transmission to its blood-feeding insect vector and would be in keeping with the biology of related trypanosomatids, such as *T. brucei* and *Leishmania donovani* (49, 50). It may also be relevant that the skin is the most common site affected by adverse reactions to the anti-parasitic drugs that are used to treat Chagas disease (51).

Skeletal muscle is a preferred site of infection for numerous human parasites e.g. *Sarcocystis,* . *Toxoplasma*, *Brugia*, *Ancylostoma*, and *Trichinella* spp., (52). Parasitism of this tissue is common in *T.*

cruzi infected mice, though the frequency and intensity appears to be rather model-dependent (9, 25, 39, 53). We observed hindlimb skeletal muscle-localised parasite bioluminescence in all hamsters at 34-38 days p.i., and in approximately half of them at 152-182 days p.i., although the infection intensity was relatively low. This tissue was characterised by significant chronic parenchymal and perivascular inflammation and fibrosis, which was also present in all six of the mouse models that we analysed. The hindlimb hypertonia and diplegic gait were hamster-specific; no locomotion defects were observed in mice, implying that tissue parasitism, inflammation and fibrosis are insufficient explanations. A motor neuron aetiology is probably the most suitable hypothesis for future work. Others have reported limb paralysis in *T. cruzi* infected mice (54, 55), but that is clearly a different phenomenon. While neither type of locomotive dysfunction have been linked to *T. cruzi* infection in humans, there is evidence of peripheral nervous system involvement in some Chagas disease cohorts at frequencies of 10% (56) to 27% (57). Skeletal muscle denervation, neuro-muscular junction, microvascular, mitochondrial and metabolic abnormalities have all been described (58-62). These are evidently under-studied aspects of Chagas disease and the potential translational value of the hamster model developed in this study should be explored further. It may also prove relevant to wider research on spastic diplegia.

Acknowledgements

The authors thank the LSHTM Biological Services Facility and Veterinary staff for technical support and helpful discussions.

References

1. Gómez-Ochoa SA, Rojas LZ, Echeverría LE, Muka T, Franco OH. Global, regional, and national trends of Chagas disease from 1990 to 2019: comprehensive analysis of the global burden of disease study. Global heart. 2022;17(1).

2. Pérez-Molina JA, Molina I. Chagas disease. Lancet (London, England). 2018;391(10115):82-94.

3. Marin-Neto JA, Cunha-Neto E, Maciel BC, Simoes MV. Pathogenesis of chronic Chagas heart disease. Circulation. 2007;115(9):1109-23.

4. Bonney KM, Luthringer DJ, Kim SA, Garg NJ, Engman DM. Pathology and Pathogenesis of Chagas Heart Disease. Annual Review of Pathology: Mechanisms of Disease. 2019;14(1):421-47.

5. Machado FS, Dutra WO, Esper L, Gollob KJ, Teixeira MM, Factor SM, et al. Current understanding of immunity to *Trypanosoma cruzi* infection and pathogenesis of Chagas disease. Seminars in Immunopathology. 2012;34(6):753-70.

6. Jansen AM, Xavier S, Roque ALR. Trypanosoma cruzi transmission in the wild and its most important reservoir hosts in Brazil. Parasit Vectors. 2018;11(1):502.

7. Chatelain E, Konar N. Translational challenges of animal models in Chagas disease drug development: a review. Drug design, development and therapy. 2015;9:4807.

8. Lewis MD, Francisco AF, Jayawardhana S, Langston H, Taylor MC, Kelly JM. Imaging the development of chronic Chagas disease after oral transmission. Scientific Reports. 2018;8(1):11292.

9. Lewis MD, Francisco AF, Taylor MC, Jayawardhana S, Kelly JM. Host and parasite genetics shape a link between *Trypanosoma cruzi* infection dynamics and chronic cardiomyopathy. Cell Microbiol. 2016;18(10):1429-43.

10. Khan AA, Langston HC, Costa FC, Olmo F, Taylor MC, McCann CJ, et al. Local association of *Trypanosoma cruzi* chronic infection foci and enteric neuropathic lesions at the tissue micro-domain scale. PLoS Pathog. 2021;17(8):e1009864.

11. Berkowitz AL, Raibagkar P, Pritt BS, Mateen FJ. Neurologic manifestations of the neglected tropical diseases. J Neurol Sci. 2015;349(1-2):20-32.

12. Nieto A, Domínguez-Bernal G, Orden JA, De La Fuente R, Madrid-Elena N, Carrión J. Mechanisms of resistance and susceptibility to experimental visceral leishmaniosis: BALB/c mouse versus syrian hamster model. Veterinary Research. 2011;42(1):39.

13. Toth K, Lee SR, Ying B, Spencer JF, Tollefson AE, Sagartz JE, et al. STAT2 knockout Syrian hamsters support enhanced replication and pathogenicity of human adenovirus, revealing an important role of type I interferon response in viral control. PLoS pathogens. 2015;11(8):e1005084.

14. Hutton ML, Mackin KE, Chakravorty A, Lyras D. Small animal models for the study of Clostridium difficile disease pathogenesis. FEMS Microbiology Letters. 2014;352(2):140-9.

15. Lee C-Y, Lowen AC. Animal models for SARS-CoV-2. Current opinion in virology. 2021;48:73-81.

16. Miao J, Chard LS, Wang Z, Wang Y. Syrian Hamster as an Animal Model for the Study on Infectious Diseases. Front Immunol. 2019;10:2329.

17. Cabrine-Santos M, Lages Silva E, Chapadeiro E, Ramírez LE. *Trypanosoma cruzi*: characterization of reinfection and search for tissue tropism in hamsters (*Mesocricetus auratus*). Experimental parasitology. 2001;99(3):160-7.

18. Ramírez LE, Lages-Silva E, Soares Júnior JM, Chapadeiro E. The hamster (*Mesocricetus auratus*) as experimental model in Chagas' disease: parasitological and histopathological studies in acute and chronic phases of *Trypanosoma cruzi* infection. Rev Soc Bras Med Trop. 1994;27(3):163-9.

19. Ramires FJ, Salemi VM, Ianni BM, Fernandes F, Martins DG, Billate A, et al. Aldosterone antagonism in an inflammatory state: evidence for myocardial protection. J Renin Angiotensin Aldosterone Syst. 2006;7(3):162-7.

20. Bilate AM, Teixeira PC, Ribeiro SP, Brito T, Silva AM, Russo M, et al. Distinct outcomes of *Trypanosoma cruzi* infection in hamsters are related to myocardial parasitism, cytokine/chemokine gene expression, and protein expression profile. J Infect Dis. 2008;198(4):614-23.

21. Bilate AM, Salemi VM, Ramires FJ, de Brito T, Silva AM, Umezawa ES, et al. The Syrian hamster as a model for the dilated cardiomyopathy of Chagas' disease: a quantitative echocardiographical and histopathological analysis. Microbes and Infection. 2003;5(12):1116-24.

22. Chapadeiro E, Silva EL, Silva AC, Fernandes P, Ramirez LE. Cardiac neuronal depopulation in hamsters (*Mesocricetus auratus*) chronically infected with *Trypanosoma cruzi*. Rev Soc Bras Med Trop. 1999;32(1):35-9.

23. Pimentel WS, Ramires FJ, Lanni BM, Salemi VM, Bilate AM, Cunha-Neto E, et al. The effect of beta-blockade on myocardial remodelling in Chagas' cardiomyopathy. Clinics (Sao Paulo). 2012;67(9):1063-9.

24. Lewis MD, Francisco AF, Taylor MC, Burrell-Saward H, McLatchie AP, Miles MA, Kelly JM. Bioluminescence imaging of chronic *Trypanosoma cruzi* infections reveals tissue-specific parasite dynamics and heart disease in the absence of locally persistent infection. Cell Microbiol. 2014;16(9):1285-300.

25. Ward AI, Lewis MD, Khan AA, McCann CJ, Francisco AF, Jayawardhana S, et al. *In Vivo* Analysis of *Trypanosoma cruzi* Persistence Foci at Single-Cell Resolution. mBio. 2020;11(4):e01242-20.

26. Koman LA, Smith BP, Shilt JS. Cerebral palsy. The Lancet. 2004;363(9421):1619-31.

27. Kheder A, Nair KPS. Spasticity: pathophysiology, evaluation and management. Practical Neurology. 2012;12(5):289-98.

28. Hyland KV, Asfaw SH, Olson CL, Daniels MD, Engman DM. Bioluminescent imaging of *Trypanosoma cruzi* infection. International journal for parasitology. 2008;38(12):1391-400.

29. Lenzi HL, Oliveira DN, Lima MT, Gattass CR. *Trypanosoma cruzi*: Paninfectivity of CL Strain during Murine Acute Infection. Experimental parasitology. 1996;84(1):16-27.

30. Guarner J, Bartlett J, Zaki SR, Colley DG, Grijalva MJ, Powell MR. Mouse model for Chagas disease: immunohistochemical distribution of different stages of *Trypanosoma cruzi* in tissues throughout infection. The American journal of tropical medicine and hygiene. 2001;65(2):152-8.

31. Postan M, Dvorak JA, McDaniel JP. Studies of *Trypanosoma cruzi* Clones in Inbred Mice: I. A Comparison of the Course of Infection of C3H/HEN- Mice with Two Clones Isolated from a Common Source. The American journal of tropical medicine and hygiene. 1983;32(3):497-506.

32. Melo R, Brener Z. Tissue tropism of different *Trypanosoma cruzi* strains. J Parasitol. 1978;64(3):475-82.

33. Postan M, Bailey JJ, Dvorak JA, McDaniel JP, Pottala EW. Studies of *Trypanosoma cruzi* Clones in Inbred Mice: III. Histopathological and Electrocardiographical Responses to Chronic Infection. The American journal of tropical medicine and hygiene. 1987;37(3):541-9.

34. Andrade SG. Influence of Trypanosoma cruzi strain on the pathogenesis of chronic myocardiopathy in mice. Memorias do Instituto Oswaldo Cruz. 1990;85(1):17-27.

35. Francisco AF, Jayawardhana S, Taylor MC, Lewis MD, Kelly JM. Assessing the Effectiveness of Curative Benznidazole Treatment in Preventing Chronic Cardiac Pathology in Experimental Models of Chagas Disease. Antimicrobial agents and chemotherapy. 2018;62(10).

36. Chadalawada S, Sillau S, Archuleta S, Mundo W, Bandali M, Parra-Henao G, et al. Risk of Chronic Cardiomyopathy Among Patients With the Acute Phase or Indeterminate Form of Chagas Disease: A Systematic Review and Meta-analysis. JAMA Network Open. 2020;3(8):e2015072-e.

37. dos Santos VM, de Lima MA, Cabrine-Santos M, de Stefani Marquez D, de Araújo Pereira G, Lages-Silva E, Ramírez LE. Functional and histopathological study of the pancreas in hamsters (*Mesocricetus auratus*) infected and reinfected with *Trypanosoma cruzi*. Parasitol Res. 2004;94(2):125-33.

38. Khan AA, Langston HC, Walsh L, Roscoe R, Jayawardhana S, Francisco AF, et al. Enteric nervous system regeneration and functional cure of experimental digestive Chagas disease with trypanocidal chemotherapy. In Preparation.

39. Santi-Rocca J, Fernandez-Cortes F, Chillón-Marinas C, González-Rubio M-L, Martin D, Gironès N, Fresno M. A multi-parametric analysis of *Trypanosoma cruzi* infection: common pathophysiologic patterns beyond extreme heterogeneity of host responses. Scientific Reports. 2017;7(1):1-12.

40. Silberstein E, Serna C, Fragoso SP, Nagarkatti R, Debrabant A. A novel nanoluciferase-based system to monitor *Trypanosoma cruzi* infection in mice by bioluminescence imaging. PLOS ONE. 2018;13(4):e0195879.

41. Calvet CM, Silva TA, Thomas D, Suzuki B, Hirata K, Siqueira-Neto JL, McKerrow JH. Long term follow-up of *Trypanosoma cruzi* infection and Chagas disease manifestations in mice treated with benznidazole or posaconazole. PLoS neglected tropical diseases. 2020;14(9):e0008726.

42. de Castro Côbo E, Silveira TP, Micheletti AM, Crema E, Adad SJ. Research on *Trypanosoma cruzi* and Analysis of Inflammatory Infiltrate in Esophagus and Colon from Chronic Chagasic Patients with and without Mega. Journal of tropical medicine. 2012:232646.

43. Adad SJ, Andrade DCdS, Lopes ER, Chapadeiro E. Contribuição ao estudo da anatomia patológica do megaesôfago chagásico. Rev I Med Trop. 1991;33:443-50.

44. da Silveira ABM, Arantes RME, Vago AR, Lemos EM, Adad SJ, Correa-Oliveira R, D'Avila Reis D. Comparative study of the presence of *Trypanosoma cruzi* kDNA, inflammation and denervation in chagasic patients with and without megaesophagus. Parasitology. 2005;131(05):627-34.

45. Pinto L, Schijman AG, Alonso-Padilla J, Lozano D, Torrico MC, Gamba P, et al. Molecular detection and parasite load of Trypanosoma cruzi in digestive tract tissue of Chagas disease patients affected by megacolon. Acta Trop. 2022;235:106632.

46. Rangel-Gamboa L, López-García L, Moreno-Sánchez F, Hoyo-Ulloa I, Vega-Mémije ME, Mendoza-Bazán N, et al. *Trypanosoma cruzi* infection associated with atypical clinical manifestation during the acute phase of the Chagas disease. Parasites & Vectors. 2019;12(1):506.

47. Riganti J, Maqueda MG, Piñero MCB, Volonteri VI, Galimberti RL. Reactivation of Chagas' disease: cutaneous manifestations in two immunosuppressed patients. International Journal of Dermatology. 2012;51(7):829-34.

48. Sartori AM, Sotto MN, Braz LM, Oliveira Júnior Oda C, Patzina RA, Barone AA, Shikanai-Yasuda MA. Reactivation of Chagas disease manifested by skin lesions in a patient with AIDS. Transactions of the Royal Society of Tropical Medicine and Hygiene. 1999;93(6):631-2.

49. Alfituri OA, Quintana JF, MacLeod A, Garside P, Benson RA, Brewer JM, et al. To the Skin and Beyond: The Immune Response to African Trypanosomes as They Enter and Exit the Vertebrate Host. Front Immunol. 2020;11:1250.

50. Singh OP, Tiwary P, Kushwaha AK, Singh SK, Singh DK, Lawyer P, et al. Xenodiagnosis to evaluate the infectiousness of humans to sandflies in an area endemic for visceral leishmaniasis in Bihar, India: a transmission-dynamics study. Lancet Microbe. 2021;2(1):e23-e31.

51. Morillo CA, Marin-Neto JA, Avezum A, Sosa-Estani S, Rassi AJ, Rosas F, et al. Randomized Trial of Benznidazole for Chronic Chagas' Cardiomyopathy. New England Journal of Medicine. 2015;373(14):1295-306.

52. Stewart GL, Giannini SH. Sarcocystis, Trypanosoma, Toxoplasma, Brugia, Ancylostoma, and Trichinella spp.: A review of the intracellular parasites of striated muscle. Experimental parasitology. 1982;53(3):406-47.

53. Weaver JD, Hoffman VJ, Roffe E, Murphy PM. Low-level parasite Persistence drives vasculitis and myositis in skeletal muscle of mice chronically infected with *Trypanosoma cruzi*. Infection and immunity. 2019;87(6):e00081-19.

54. Roffê E, Marino APMP, Weaver J, Wan W, de Araújo FF, Hoffman V, et al. *Trypanosoma cruzi* Causes Paralyzing Systemic Necrotizing Vasculitis Driven by Pathogen-Specific Type I Immunity in Mice. Infection and immunity. 2016;84(4):1123-36.

55. Bombeiro AL, Gonçalves LA, Penha-Gonçalves C, Marinho CRF, D'Império Lima MR, Chadi G, Álvarez JM. IL-12p40 Deficiency Leads to Uncontrolled *Trypanosoma cruzi* Dissemination in the Spinal Cord Resulting in Neuronal Death and Motor Dysfunction. PLOS ONE. 2012;7(11):e49022.

56. Genovese O, Ballario C, Storino R, Segura E, Sica RE. Clinical manifestations of peripheral nervous system involvement in human chronic Chagas disease. Arq Neuropsiquiatr. 1996;54(2):190-6.

57. Sica RE, Genovese OM, Gargia Erro M. Peripheral motor nerve conduction studies in patients with chronic Chagas' disease. Arq Neuropsiquiatr. 1991;49(4):405-8.

58. Laguens R, Cossio P, Diez C, Segal A, Vasquez C, Kreutzer E, et al. Immunopathologic and morphologic studies of skeletal muscle in Chagas' disease. The American journal of pathology. 1975;80(1):153.

59. Torres SH, Finol HJ, Montes de Oca M, Vásquez F, Puigbó JJ, Loyo JG. Capillary damage in skeletal muscle in advanced Chagas' disease patients. Parasitol Res. 2004;93(5):364-8.

60. Montes de Oca M, Torres SH, Loyo JG, Vazquez F, Hernández N, Anchustegui B, Puigbó JJ. Exercise performance and skeletal muscles in patients with advanced Chagas disease. Chest. 2004;125(4):1306-14.

61. Taratuto A, Pagano MA, Fumo T, Sanz OP, Sica RE. Histological and histochemical changes of the skeletal muscle in human chronic Chagas' disease. Arq Neuropsiquiatr. 1978;36(4):327-31.

62. Benavente OR, Patiño OL, Peña LB, Lugònes H, Kalala E, Meneclier CR, et al. Motor unit involvement in human acute Chagas' disease. Arq Neuropsiquiatr. 1989;47(3):283-6.

Figure Legends

Figure 1. Serial evaluation of *T. cruzi* CLBR infection in Syrian hamsters by *in vivo* bioluminescence imaging. A, B: Course of transgenic bioluminescent TcVI-CLBR infection in female Syrian hamsters tracked by *in vivo* imaging. **A:** Panels show an example series of ventral images for one hamster per group taken at the indicated times post-infection. Log-scale pseudocolour heat-map shows intensity of bioluminescence as a proxy for parasite load; minimum and maximum radiances are indicated. **B**: Chart shows the changes in mean ±S.E.M., total bioluminescence over time for hamsters inoculated with 5 x 10^3 (low inoculum, n = 3) or 1 x 10^5 (high inoculum, n = 8) parasites. Threshold lines are the mean (dashes) and the mean +2SD (dots) of background signal obtained for uninfected control hamsters (n = 7). **C**: Evaluation of organ sizes/weights and the number of faecal pellets present in the colon at 152-182 post-infection (high inoculum group (n = 8-9 with the exception of GI mesentery, n = 5, and faecal pellets n = 6), uninfected control group (n = 8, with the exception of GI mesentery and faecal pellets, n = 4). Asterisks indicate *p*-values for comparisons with the uninfected control group in multiple unpaired *t*-tests (*** $p<0.001$, * $p<0.05$).

Figure 2. Organ-specific infection profiles of *T. cruzi* CLBR in Syrian hamsters. Quantification of organ/tissue-specific parasite loads and densities in TcVI-CLBR-infected Syrian hamsters using *ex vivo* bioluminescence imaging at 34-38 days (n = 6) and 152-182 days (n = 9) post-infection. Images (**A**) show bioluminescence intensities for one representative animal per group. Layout of samples shown on the uninfected control image: 1 = liver (partial), 2 = lungs, 3 = heart (bisected), 4 = kidneys, 5 = spleen, 6 = visceral adipose, 7 = female reproductive system, 8 = bladder, 9 = skeletal muscle (from hindleg), 10 = oesophagus, 11 = stomach, 12 = small intestine, 13 = gastro-intestinal mesentery, 14 = peritoneum/abdominal muscle, 15 = caecum, 16 = colon, 17 = subcutaneous adipose, 18 = visceral adipose, 19 = skin. **B,C**: Quantification of total bioluminescent flux (photons/sec) as a proxy of parasite loads for each organ and tissue type at 34-38 days (**B**) and 152-182 days (**C**) post-infection. **D,E**: Charts

show the average proportional distributions of total measured *ex vivo* parasite loads (total flux, p/s) across the analysed set of organ and tissue types at 34-38 days (**D**) and 152-182 days (**E**) post-infection **F,G**: Quantification of bioluminescent radiance (photons/sec/cm^2/sr) as a proxy of infection intensity for each organ and tissue type expressed as fold change vs. matching organs or tissues from uninfected controls at 34-38 days (**F**) and 152-182 days (**G**) post-infection. Dashed line indicates detection threshold. In **B**, **C**, **F** and **G**, bars show the mean + S.E.M., and grey circles are data for individual hamsters.

Figure 3. Histopathological analysis of cardiac muscle tissue from *T. cruzi*-infected Syrian hamsters. Quantification of cellularity (**A**) and collagen content (**B**) as markers of myocardial inflammation and fibrosis, respectively. Bars show the means + S.E.M., and grey circles are data for individual hamsters. Uninfected control (n = 7), infected (n = 9). Images show representative example sections with haematoxylin and eosin (**A**), and picro-sirius red (**B**). Magnification 400X, scale bar = 50 µm.

Figure 4. Evaluation of limb adduction in *T. cruzi*-infected Syrian hamsters. A: Example ventral view images of an individual hamster under transient anaesthesia (gaseous isoflurane) at the indicated day post-infection, with an age-matched uninfected control. Red marker lines highlight the inter-hindpaw distances. **B – E**: Quantification of the distance between forepaws (**B**, **C**) and hindpaws (**D**, **E**). In **B** and **D**, data are shown as the mean ± S.E.M. over time, uninfected control (n=2), infected (n=4). In **C** and **E**, data are the mean + S.E.M at the endpoint, with grey circles showing the measurements for individual animals, uninfected control (n=5), infected (n=7) (**C**, **E**).

Figure 5. Histopathological analysis of quadriceps tissue from *T. cruzi*-infected Syrian hamsters. Quantification of cellularity (**A**) and collagen content (**B**) as markers of skeletal muscle inflammation and fibrosis, respectively. Bars show the means + S.E.M., and grey circles are data for individual hamsters. Uninfected control (n = 7), infected (n = 9). Images show representative example sections with

510 haematoxylin and eosin (**A**), and picro-sirius red (**B**). Magnification 400X, scale bar = 50 µm. *P*-values
511 shown are from Student's *t*-tests.
512
513 **Figure 6. Histopathological analysis of skeletal muscle tissue from multiple murine *T. cruzi***
514 **models. A:** Representative myocardial sections stained with haematoxylin and eosin, magnification
515 400X, scale bar = 100 µm. **B:** Quantitative histopathological analysis of myocardium samples obtained
516 at 154-174 days post-infection from the following groups: TcVI-CLBR-BALB/c (n = 9), TcVI-CLBR-
517 C57BL/6 (n = 10), TcVI-CLBR-C3H/HeN (n = 10), TcI-JR-BALB/c (n = 10), TcI-JR-C57BL/6 (n = 10), TcI-
518 JR-C3H/HeN (n = 8), uninfected control BALB/c, C57BL.6 and C3H/HeN (all n = 10). Myositis score is the
519 number of nuclei per image (6 x 10^4 μm^2). In **A** and **B**, black and white arrows indicate examples of
520 parasite nests and areas of adipose replacement respectively. **C:** Representative myocardial sections
521 stained with Masson's trichrome, magnification 400X, scale bar = 100 µm. **D:** Quantification of collagen
522 content (% blue area) as a marker of cardiac fibrosis severity in same groups as in **B**. Data are the means
523 +S.E.M. and are from two independent experiments. Asterisks indicate *p*-values for one way ANOVA
524 comparisons between infection status groups, with each mouse strain analysed independently (* $P <$
525 0.05; ** $P < 0.01$; *** $P < 0.001$).

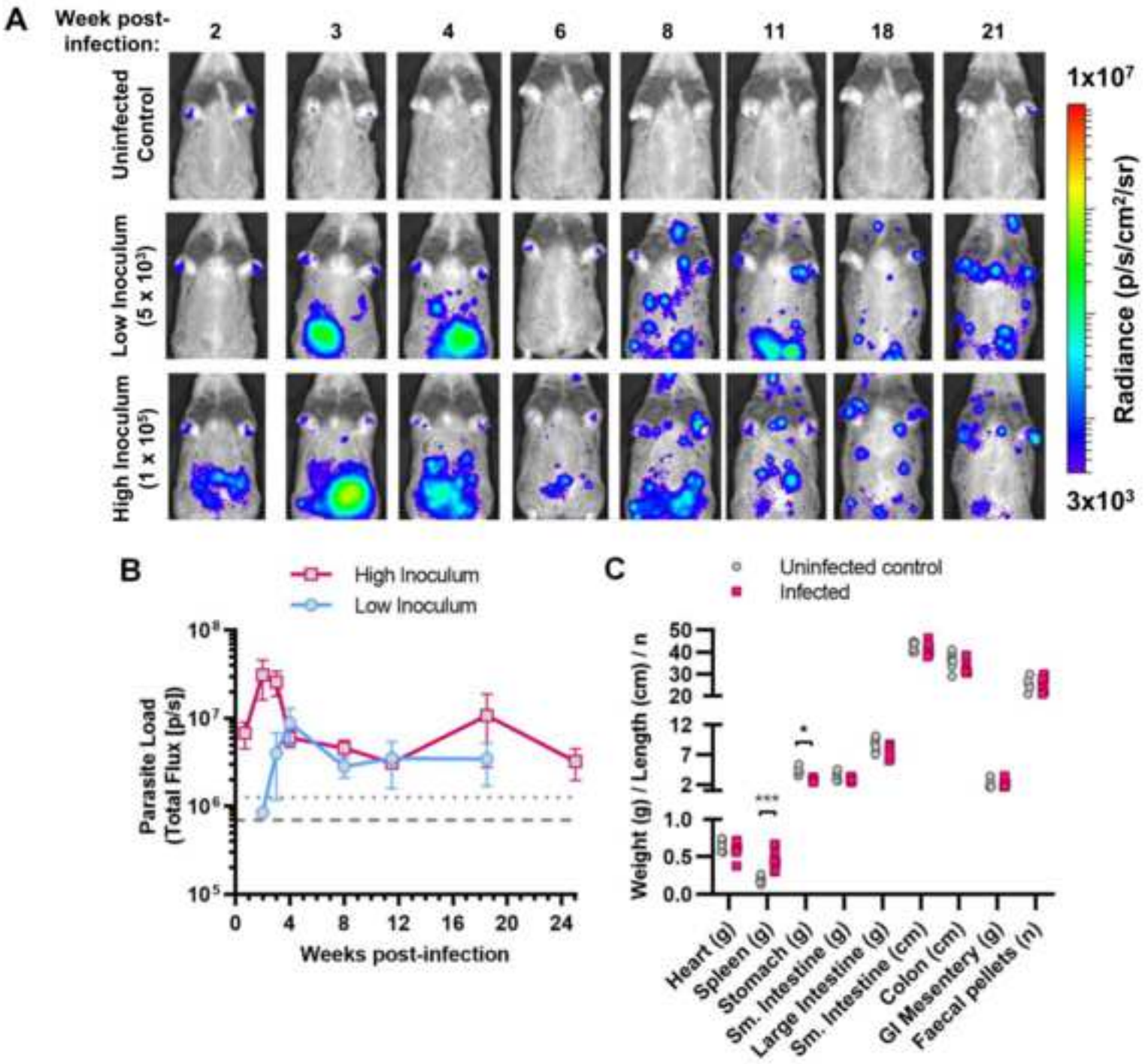

Figure 1.pdf

Figure 2.pdf

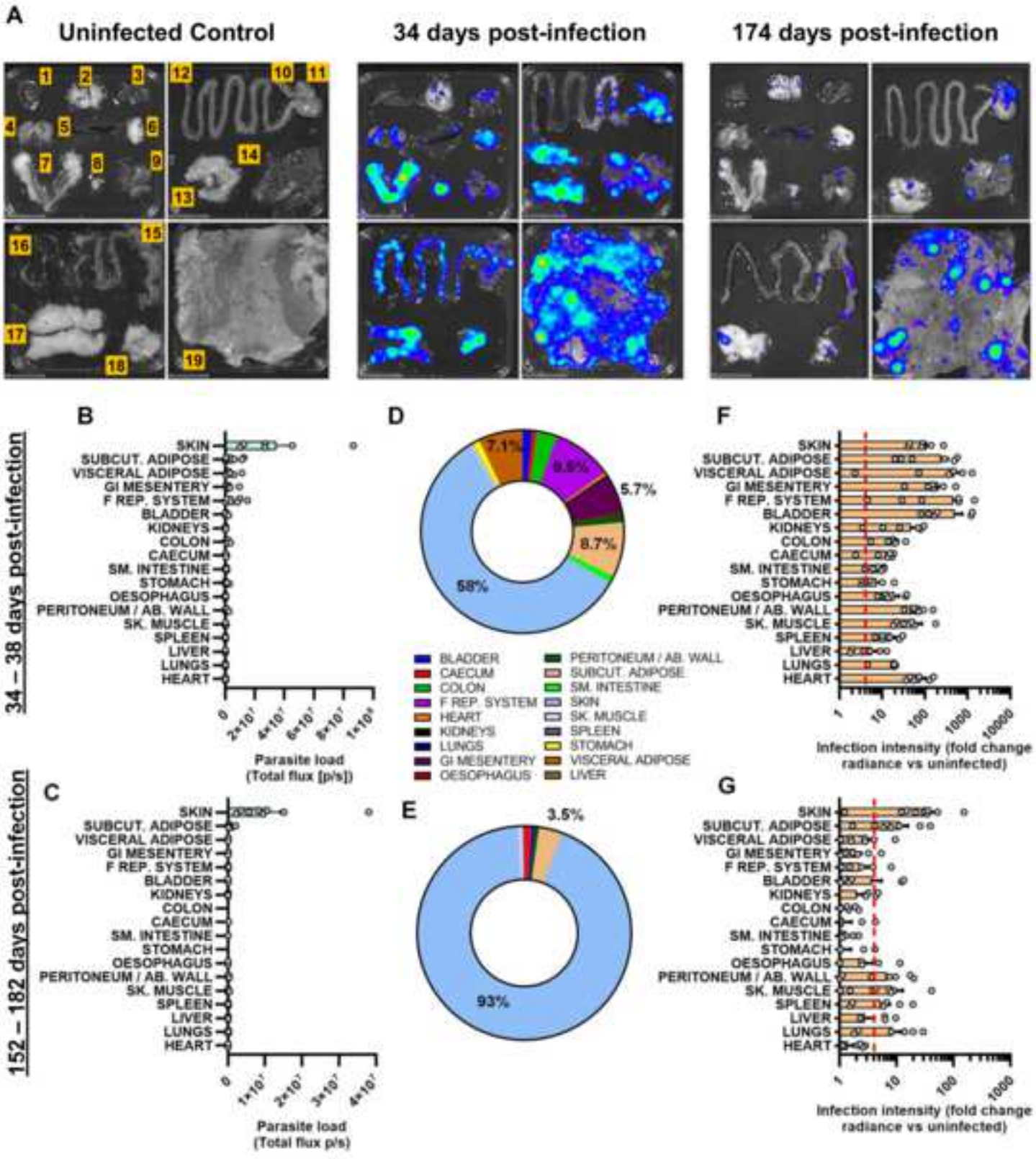
A
Uninfected Control
34 days post-infection
174 days post-infection
1
2
3
4
5
6
7
8
9
10
11
12
13
14
15
16
17
18
19
B
34 – 38 days post-infection
SKIN
SUBCUT. ADIPOSE
VISCERAL ADIPOSE
GI MESENTERY
F REP. SYSTEM
BLADDER
KIDNEYS
COLON
CAECUM
SM. INTESTINE
STOMACH
OESOPHAGUS
PERITONEUM / AB. WALL
SK. MUSCLE
SPLEEN
LIVER
LUNGS
HEART
0
2×10⁷
4×10⁷
6×10⁷
8×10⁷
1×10⁸
Parasite load
(Total flux [p/s])
D
7.1%
9.9%
5.7%
8.7%
58%
BLADDER
CAECUM
COLON
F REP. SYSTEM
HEART
KIDNEYS
LUNGS
GI MESENTERY
OESOPHAGUS
PERITONEUM / AB. WALL
SUBCUT. ADIPOSE
SM. INTESTINE
SKIN
SK. MUSCLE
SPLEEN
STOMACH
VISCERAL ADIPOSE
LIVER
F
SKIN
SUBCUT. ADIPOSE
VISCERAL ADIPOSE
GI MESENTERY
F REP. SYSTEM
BLADDER
KIDNEYS
COLON
CAECUM
SM. INTESTINE
STOMACH
OESOPHAGUS
PERITONEUM / AB. WALL
SK. MUSCLE
SPLEEN
LIVER
LUNGS
HEART
1
10
100
1000
10000
Infection intensity (fold change
radiance vs uninfected)
C
152 – 182 days post-infection
SKIN
SUBCUT. ADIPOSE
VISCERAL ADIPOSE
GI MESENTERY
F REP. SYSTEM
BLADDER
KIDNEYS
COLON
CAECUM
SM. INTESTINE
STOMACH
OESOPHAGUS
PERITONEUM / AB. WALL
SK. MUSCLE
SPLEEN
LIVER
LUNGS
HEART
0
1×10⁷
2×10⁷
3×10⁷
4×10⁷
Parasite load
(Total flux p/s)
E
3.5%
93%
G
SKIN
SUBCUT. ADIPOSE
VISCERAL ADIPOSE
GI MESENTERY
F REP. SYSTEM
BLADDER
KIDNEYS
COLON
CAECUM
SM. INTESTINE
STOMACH
OESOPHAGUS
PERITONEUM / AB. WALL
SK. MUSCLE
SPLEEN
LIVER
LUNGS
HEART
1
10
100
1000
Infection intensity (fold change
radiance vs uninfected)

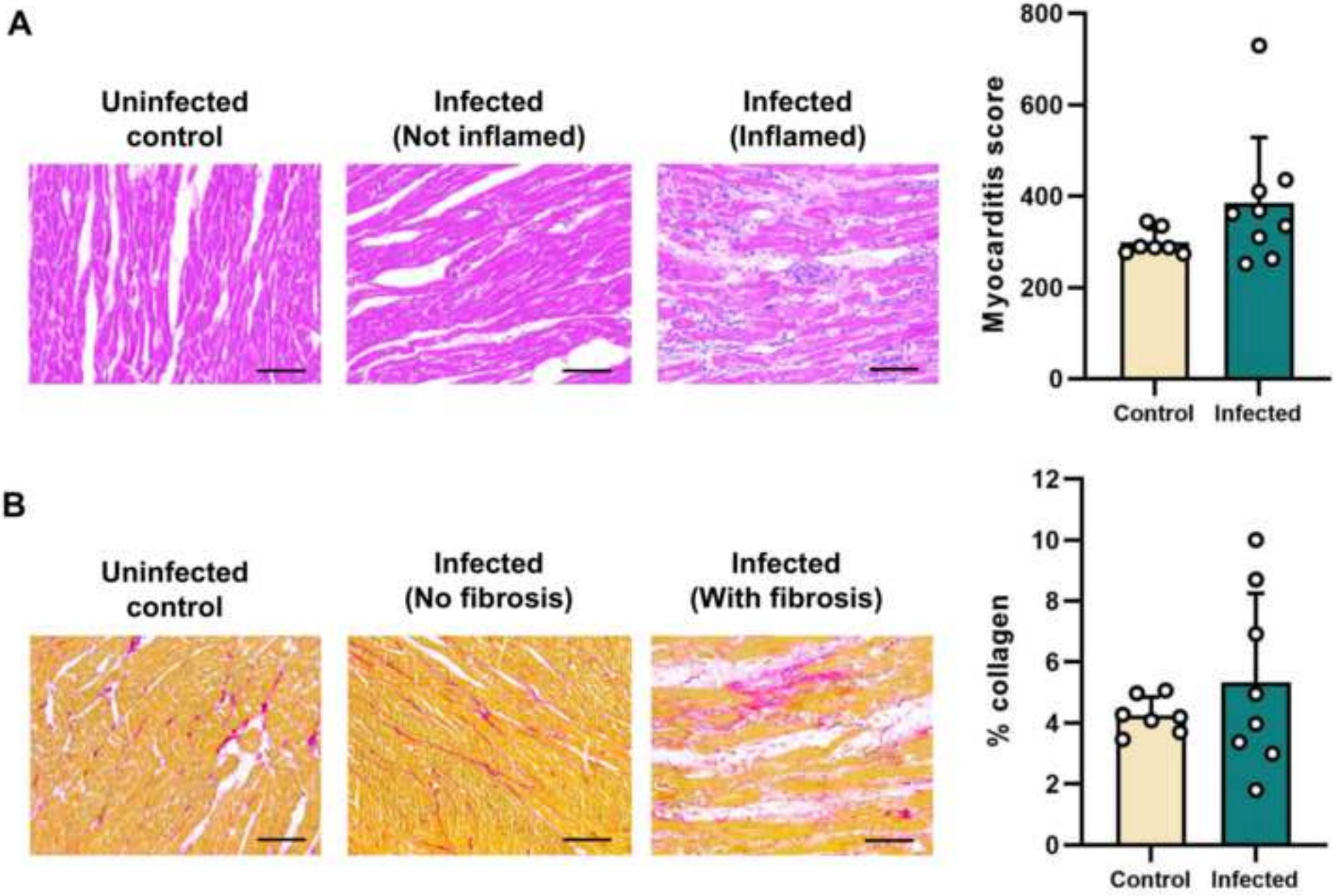

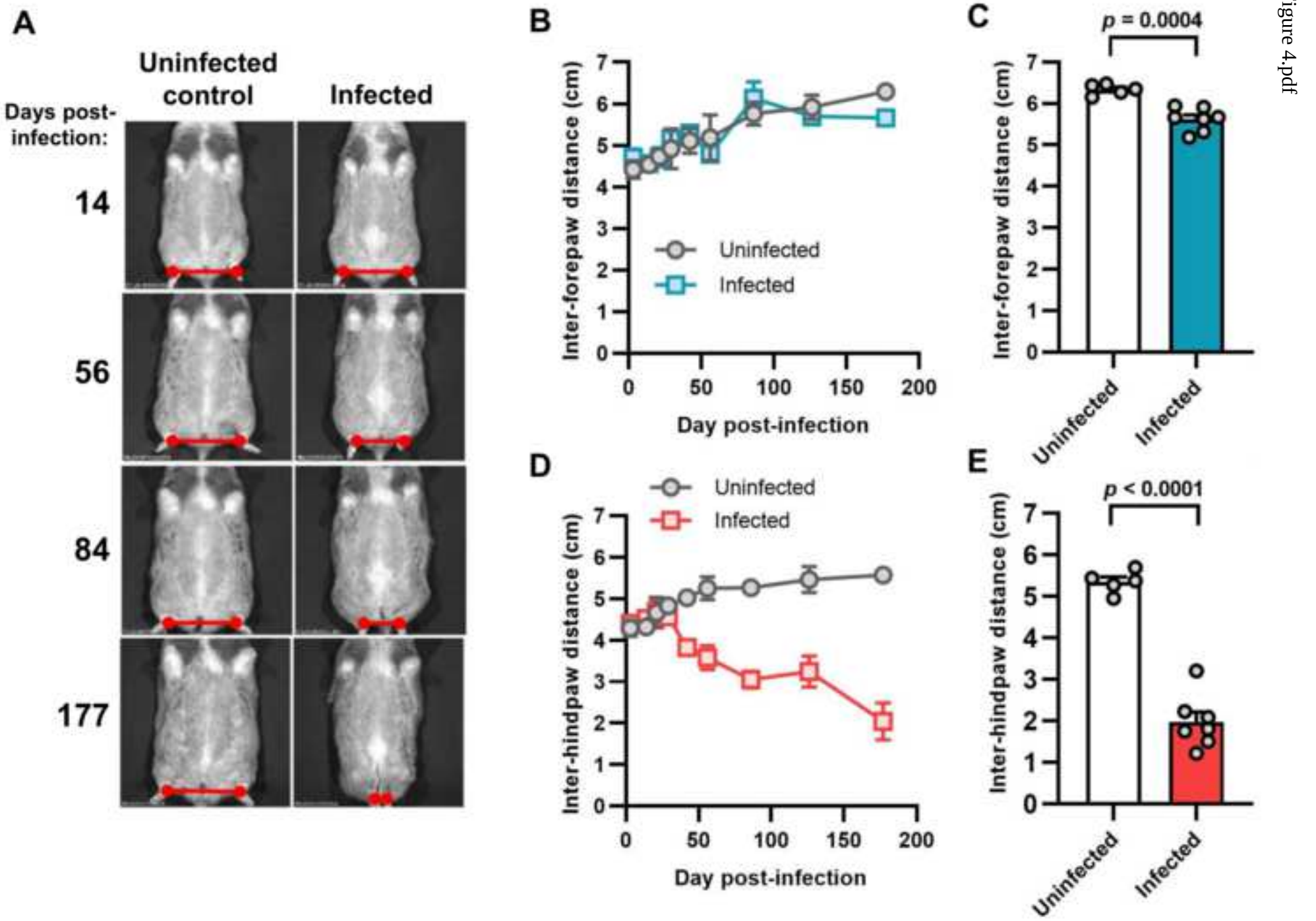

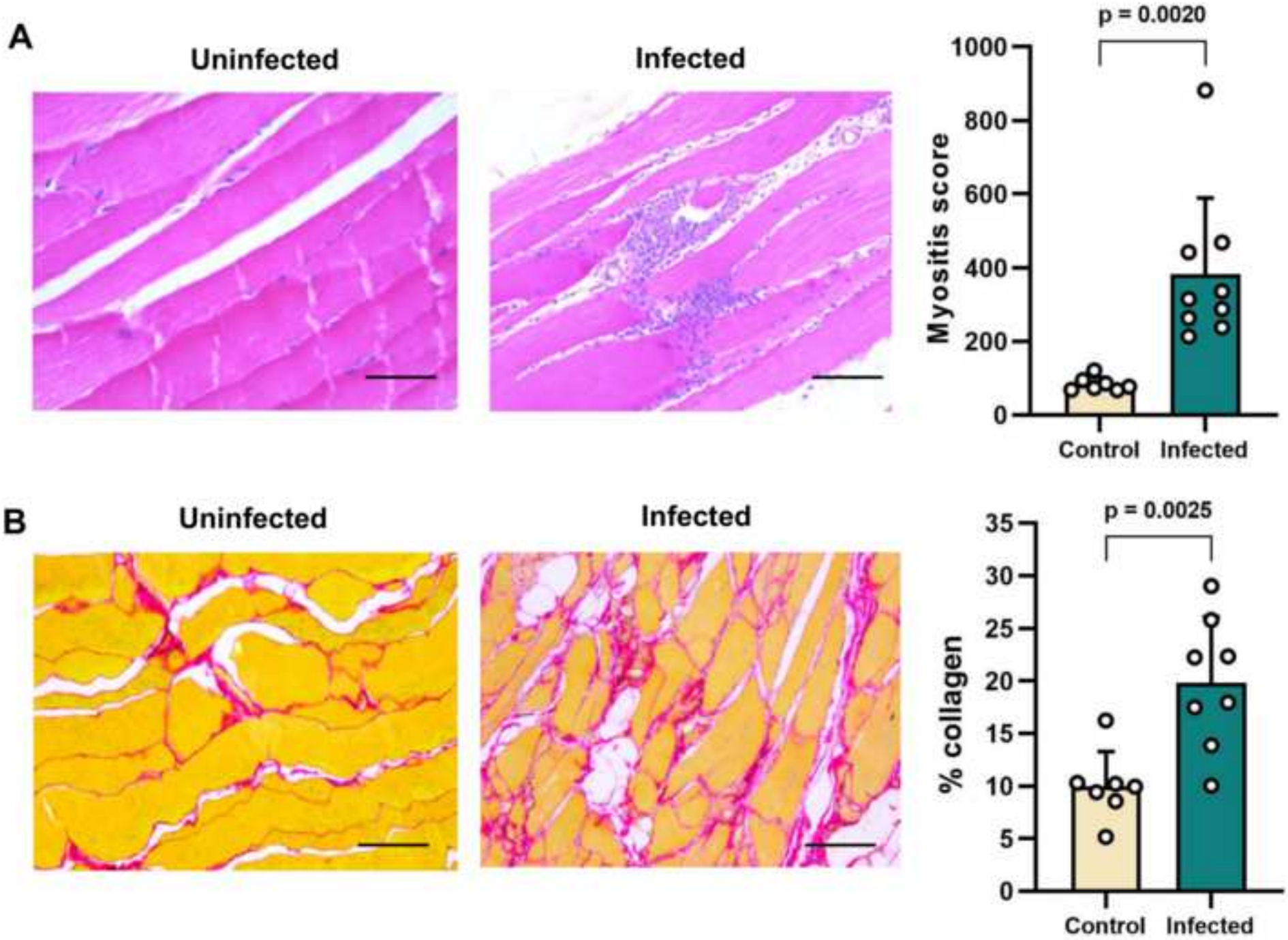

Figure 6.pdf

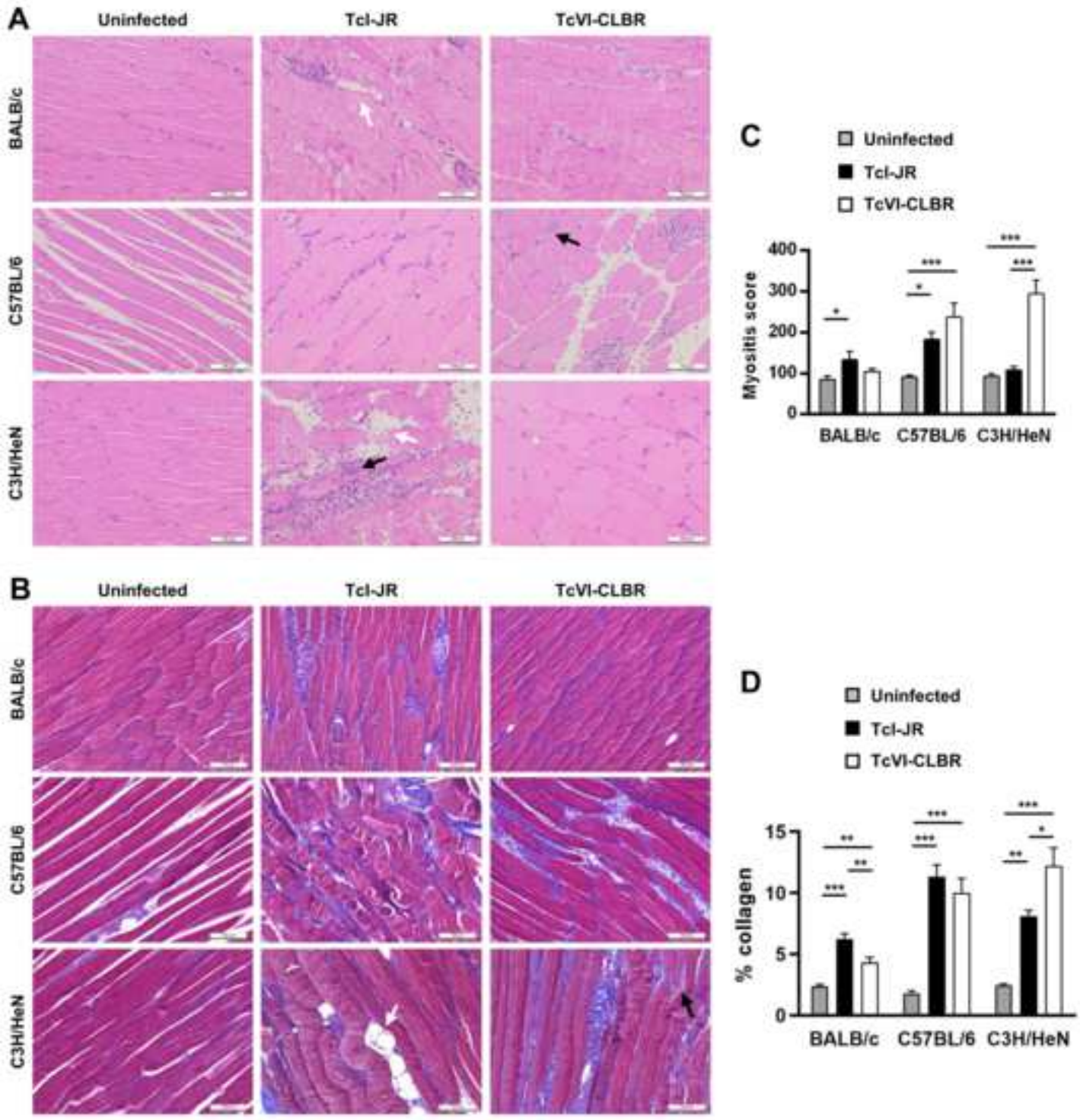

5. Concluding remarks

5.1. General discussion and summary

T. cruzi infection remains a major threat to human health in Latin America and is a growing concern for health systems across Europe and North America (1). Digestive Chagas disease (DCD) remains a neglected aspect of this neglected disease, with most of our understanding stemming from historical studies of human cadavers (2,3), advances in bioluminescence imaging (4–8), and the recent identification of a DCD model that reproduces some important aspects of human disease (9). At present, a vaccine for *T. cruzi* infection does not exist, and there is a weak rationale for benznidazole treatment of those affected by symptomatic DCD (10). There are three major questions currently impeding progress toward a better understanding of DCD, and subsequent refinement of drug and treatment options.

1. **Why is there so much heterogeneity in *T. cruzi* infection dynamics and outcomes?**
2. **What mechanistic pathways are responsible for enteric neuropathy and wound healing in DCD?**
3. **Is functional DCD pathology permanent, or is it pertinent to treat with antiprotozoal drugs at any stage of infection?**

In this thesis histopathological, immunological, functional, and bioluminescent *in vivo* assays were employed to help underpin our understanding of experimental Chagas disease to help answer these questions.

Firstly, a histopathological profile of the large intestine was developed for a ‘severe’ DCD model in C3H/HeN mice, and a ‘mild’ DCD model in BALB/c mice. Here, it was discovered that smooth muscle inflammation, iNOS expression, and enteric denervation were all features of the ‘severe’ model, but not the mild. This correlates with a previously identified functional GI transit deficit in this model (9). Moreover, iNOS protein expression was increased in the chronic phase of the ‘severe’ model, although *Nos2* RNA was significantly upregulated in both the ‘severe’ and ‘mild’ DCD models. This suggests that collateral damage to tissue and enteric neurons in the acute stage, via iNOS, is not the complete story as previously hypothesised (11).

This was further explored in chapter 2, where immunoregulatory and antiprotozoal treatments were employed *in vivo* to investigate the initial ‘triggering’ of functional transit delay between 2- and 3-weeks post-infection. Here, selective inhibition of iNOS had an inconclusive effect on transit time development, reinforcing the notion that iNOS as a lone effector is not sufficient to cause the enteric neuropathy responsible for dysperistalsis. However, as mentioned in Chapter 2.4.6.5, there were uncertainties surrounding both the dosage concentration and frequency of iNOS inhibition, which would require optimisation upon repeating this experiment. The principal findings from this study were that parasite burden in both cyclophosphamide and anti-CD8α treated mice increased significantly compared to infected controls, but a transit time delay did not develop in the cyclophosphamide group. This suggested that:

1. Increased parasite burden in the large intestine is not enough to cause dysperistalsis.

2. Cyclophosphamide-sensitive components of the immune response against *T. cruzi* are responsible for triggering dysperistalsis in the acute phase.
3. CD8+ T cells, despite being the critical effector in parasite control, are not responsible for dysperistalsis development.

In the pursuit of effector cells that may be responsible for this immune mediated enteric neuropathy, monocytes were identified as potential candidates informed by RNA upregulation of the genes encoding CCR2, CCR5 and ligands CCL2, 3, 4, 5 and 7 (Chapter 1, M. Lewis, unpublished). Upon monocyte depletion, iNOS+ populations increased, but mice exhibited highly variable transit times and parasite burdens making this phenotype difficult to interpret. However, the MC-21 treated transit times were not different to that of the uninfected controls, so there is suitable scope to further investigate monocytes as key candidates. The heterogeneity in results could be in line with the intrinsic disease outcome variability observed in experimental and human *T. cruzi* infection. However, repeating with an optimised dosing regimen, an increased sample size, and with confirmation of depletion via flow cytometry would be an essential follow up.

After investigating the ‘damage’ component of DCD, the aim of chapter 3 was to investigate the ‘tissue repair’ aspect. To do this EdU click reaction assays and multi-stain IFA was employed to identify proliferative cell populations following benznidazole treatment. The principal findings were that rare events of EdU co-localising with neuronal cell bodies were observed in the benznidazole treated cohort in a long exposure window between week 9-16 post infection, coinciding with a

‘normalisation’ window of transit function. This suggests that recovery of enteric neuron populations involves a proliferative pre-cursor stage.

The concept of adult neurogenesis is divisive in the field, however, Khan et al, (2023) demonstrated that a rebound in gut peristalsis function occurs in response to benznidazole treatment (Chapter 3). This, coupled with identifying proliferation in the myenteric ganglionic space in this study, lays the foundation for important and translatable research into functional peristaltic recovery, and may inform future research into DCD treatment regimes. Currently, it is argued there is ‘a point of no return’ for tissue pathology, and upon the onset of severe symptoms there is little incentive to treat (12–14). The data presented in this study (Chapter 3, Khan et al, 2023) suggests that optimal therapy would involve both sterile cure (or long-term suppression of parasites) and interventions to promote the existing tissue repair and regeneration pathways. In a Hirschsprung disease experimental model, a congenital disease that is characterised by agangliosis of the enteric nervous system in the large intestine (15), there have been developments in proof-of-concept enteric stem cell transplants (16). Here foetal human-derived enteric neural crest cells (ENCC’s) display engraftment, spread and differentiation toward local neurons and glia forming functional connectivity with endogenous ENS upon transplantation *in vivo* (16). This expands the prospective future clinical interventions possible for functional DCD.

Finally, a hamster model was used for *T. cruzi* infection and a novel association with progressive motor dysfunction was identified. This further validates the idea that host and parasite genetics are important in different disease outcomes.

5.2 Future directions

Here I provide comment on future work that can be built on the research presented in this thesis. These comments are ordered to correspond with the order of chapters.

Pathological and immunological components of experimental Chagas disease

In this study significant inflammation was observed in the smooth muscle layer of the large intestine of the 'severe' DCD model (TcI-C3H). A logical next step would be to phenotype and categorise the cells that comprise the inflammatory population. This will begin to inform which cells may be contributing to the inflammatory cascade and collateral damage to smooth muscle and enteric neurons. The proximal colon-mesentery junction, where significant focal pathology was noted, should be investigated in the context to the hypothesis proposed in Lewis and Kelly 2016 (17), that trafficking of parasites to and from permissive sites results in waves of re-infection followed by local inflammation. The identification of lymphoid follicles, and subsequent characterisation of their being T and B cell rich, requires following up. Firstly, are these structures important in parasite management or pathology? And does the frequency by which they are observed, the cellular activity, and size of the follicles vary under different infection conditions?

Finally, both BTNL1 and MARCO antibody staining requires further optimisation before firm conclusions can be made regarding the significance of either marker in the context of DCD. I propose using IFA and flow cytometry to gauge the location and frequency of these markers at a protein level to corroborate the RNA expression findings.

Investigating the parasite-immune axis in the initiation of gut dysfunction in acute stage experimental Chagas disease

Here, the most critical further optimisations reside with the dosing and validation of iNOS inhibiting and CCR2+ monocyte depleting treatments. The significance of iNOS is fundamental to our understanding of DCD, and investigating the true effect of iNOS inhibition on functional pathology is critical. Unfortunately, complications with flow cytometry data collection rendered a portion of the data to be unusable in the broader scope of this study. Repeating the flow cytometry with an expanded leukocyte phenotyping panel would be important in better understanding the colon-specific immunoregulatory effects. An additional arm of the *in* vivo experiment which could further identify contributory tissue-damage-cell-types, would include the specific inhibition of blood-circulating monocytes vs tissue resident myeloid cells. Moreover, depleting CD4+ T cells or even adding cytokine specific targets for flow cytometry (IFN- γ, IL-12, TNF-α) might help build important immune profiles of each treatment group. Finally, a full neuronal count as previously described (9) would be pertinent and fundamental to better understand the effect of each treatment on ENS integrity.

Does functional recovery correspond with tissue repair in experimental DCD?

Since the observation of EdU+ ANNA-1+ co-localisation events were rare, a repeat of both the 'long exposure' and 'short exposure' time points, with larger sample sizes, would be a recommended starting point. A full quantification of enteric neurons at week 12 post infection should also be conducted to investigate whether the recovery of transit time by this time point in both infected treated and infected untreated groups corresponds with increased enteric neuron viability. It may also be pertinent to expand beyond the context of the myenteric plexus. In the gastrointestinal tract there is scope to investigate the submucosal plexus, intra-muscular neurons, and interstitial cells of Cajal. Expanding further, the impact on extrinsic neuronal circuits such as the vagal (parasympathetic), and sympathetic nerves from prevertebral ganglia would be interesting. Both circuits travel through the mesentery tissue to connect to the gut which, as identified in chapter 1, is a site associated with focal smooth muscle pathology.

Exploring the potential for broader experimental DCD models, beyond the mouse model

There is scope for the refinement and reduction of animals in experimental Chagas disease. An *in vitro* colon explant system, previously developed at UCL (Navoly et al, 2021), has the potential to aid studies of *T. cruzi* infection. Initially, this system can be optimised for *T. cruzi* infection studies, allowing for multiple experiments to be conducted on a single dissected murine colon. A 3D explant model could bridge the gap between *in vitro* and *in vivo* systems, whereby *in vivo* GI infection dynamics can potentially be mimicked in an *in vitro* context. A full viability assessment could be conducted in order to gauge how long biopsied tissue can survive for culture. The

fundamental application of this system could be with short infection experiments on naïve, infected, or treated and cured tissue. A future direction of expanding DCD models could be using gut organoid technology. For example, a methodology has been established whereby embryonic and inducted pluripotent cells were used to generate human intestinal tissue containing a functional ENS (18). By utilising this approach, it is possible to forge an intermediate system that bridges the gap between simple *in vitro* cultures and *in vivo* applications. Moreover, the freedom to perform gene specific knockdowns in organoids, to investigate multiple experimental conditions at a time, and to potentially humanise mice, is a particularly exciting prospect for the future directions which experimental DCD research can venture into.

References

1. Rassi A, Rassi A, Marin-Neto JA. Chagas disease. The Lancet. 2010 Apr;375(9723):1388–402.
2. Tafuri WL, Maria TA, Lopes ER. [Myenteric plexus lesions in the esophagus, jejunum and colon of chronic chagasic patients. Electron microscopy study]. Rev Inst Med Trop Sao Paulo. 1971;13(2):76–91.
3. Köberle F. The causation and importance of nervous lesions in American trypanosomiasis. Bull World Health Organ. 1970;42(5):739–43.
4. Ward AI, Lewis MD, Taylor MC, Kelly JM. Incomplete Recruitment of Protective T Cells Is Associated with Trypanosoma cruzi Persistence in the Mouse Colon. Infect Immun. 2022 Feb 17;90(2):e0038221.
5. Ward AI, Lewis MD, Khan AA, McCann CJ, Francisco AF, Jayawardhana S, et al. In vivo analysis of trypanosoma cruzi persistence foci at single-cell resolution. mBio. 2020;11(4):1–13.
6. Lewis MD, Francisco AF, Taylor MC, Jayawardhana S, Kelly JM. Host and parasite genetics shape a link between Trypanosoma cruzi infection dynamics and chronic cardiomyopathy. Cell Microbiol. 2016;18(10):1429–43.
7. Lewis MD, Francisco AF, Jayawardhana S, Langston H, Taylor MC, Kelly JM. Imaging the development of chronic Chagas disease after oral transmission. Sci Rep [Internet]. 2018;8(1):1–8. Available from: http://dx.doi.org/10.1038/s41598-018-29564-7
8. Lewis MD, Fortes Francisco A, Taylor MC, Burrell-Saward H, Mclatchie AP, Miles MA, et al. Bioluminescence imaging of chronic Trypanosoma cruzi infections reveals tissue-specific parasite dynamics and heart disease in the absence of locally persistent infection. Cell Microbiol. 2014;16(9):1285–300.
9. Khan AA, Langston HC, Costa FC, Olmo F, Taylor MC, McCann CJ, et al. Local association of Trypanosoma cruzi chronic infection foci and enteric neuropathic lesions at the tissue micro-domain scale. PLoS Pathog. 2021 Aug 23;17(8):e1009864.
10. PAHO. Guidelines for the diagnosis and treatment of Chagas disease . 2018.
11. Arantes RME, Marche HHF, Bahia MT, Cunha FQ, Rossi MA, Silva JS. Interferon-γ-Induced Nitric Oxide Causes Intrinsic Intestinal Denervation in Trypanosoma cruzi-Infected Mice. American Journal of Pathology. 2004;164(4):1361–8.
12. PAHO. Guidelines for the diagnosis and treatment of Chagas disease . 2018.
13. Morillo CA, Marin-Neto JA, Avezum A, Sosa-Estani S, Rassi A, Rosas F, et al. Randomized Trial of Benznidazole for Chronic Chagas' Cardiomyopathy. New England Journal of Medicine. 2015;373(14):1295–306.
14. Marin-Neto JA, Rassi A, Morillo CA, Avezum A, Connolly SJ, Sosa-Estani S, et al. Rationale and design of a randomized placebo-controlled trial assessing the effects of

etiologic treatment in Chagas' cardiomyopathy: the BENznidazole Evaluation For Interrupting Trypanosomiasis (BENEFIT). Am Heart J. 2008 Jul;156(1):37–43.
15. Heuckeroth RO. Hirschsprung disease — integrating basic science and clinical medicine to improve outcomes. Nat Rev Gastroenterol Hepatol. 2018 Mar 4;15(3):152–67.
16. Cooper JE, Natarajan D, McCann CJ, Choudhury S, Godwin H, Burns AJ, et al. In vivo transplantation of fetal human gut-derived enteric neural crest cells. Neurogastroenterology & Motility. 2017 Jan 6;29(1).
17. Lewis MD, Kelly JM. Putting Infection Dynamics at the Heart of Chagas Disease. Trends Parasitol. 2016;32(11):899–911.
18. Workman MJ, Mahe MM, Trisno S, Poling HM, Watson CL, Sundaram N, et al. Engineered human pluripotent-stem-cell-derived intestinal tissues with a functional enteric nervous system. Nat Med. 2017 Jan;23(1):49–59.